CONFINED DETONATIONS AND PULSE DETONATION ENGINES

Edited by

Gabriel D. Roy
Office of Naval Research
Arlington, VA, USA

Sergei M. Frolov
N. N. Semenov Institute of Chemical Physics
Moscow, Russia

Robert J. Santoro
Pennsylvania State University
University Park, PA, USA

Sergei A. Tsyganov
Russian Foundation for Basic Research
Moscow, Russia

TORUS PRESS
Moscow 2003

ББК 24.54
Д 38
УДК 621.43:662.612.3

Confined Detonations and Pulse Detonation Engines / [Edited by
Д 38 G. Roy, S. Frolov, R. Santoro, and S. Tsyganov]. — Moscow: TORUS PRESS, 2003. — 384 p. Tabl. 14, ill. 219.

ISBN 5–94588–012–4

The volume contains 24 revised and edited articles on confined gaseous and spray deflagrations and detonations and their applications to pulse detonation propulsion written by world-known experts in detonation physics and propulsion. The articles include critical analyses of previous studies and controversial aspects of confined detonations, new experimental and theoretical results and findings, as well as numerous references to archival publications worldwide. The contents are organized in three parts: (1) Confined Deflagrations and Detonations; (2) Pulse Detonation Engines; and (3) Avenues of Future Research. The volume is prepared as a reference for practicing engineers and research scientists working in the field of combustion and propulsion.

ББК 24.54

ISBN 5–94588–012–4

Managing Editor T. Torzhkova
Technical Editor L. Kokushkina

Art Editor M. Sedakova
Cover Design A. Sevryugin

Printed in Russian Federation

PREFACE

Research on advanced propulsion has got several new focuses during the past several decades. One of them is the use of pulse detonations for producing enhanced thrust at both static and dynamic conditions. Thermodynamically, there are no doubts that detonation provides the best thermal efficiency of combustion in terms of minimal entropy of the exhaust jet. Based on this, a number of diligent efforts have been undertaken to show that proper utilization of the operation cycle does result in improved performance, in particular, for highly detonable gaseous fuel–oxygen mixtures. Transition to more realistic fuel–air mixtures poses, as expected, many problems. Some of the arising problems are akin to those typical of chemical propulsion. However, there are several issues that represent new scientific and technological challenges. The success in resolving these problems will determine the implementation of pulse detonation propulsion.

The recent interest in air-breathing and rocket pulse detonation engines (PDEs) has added new dimensions to the studies of detonation physics. Numerous new investigations on gas-phase and spray detonations have been started all over the world, in particular pertaining to detonation control and the effects of confinement. This is evident from the formation of collaborative teams by industry both in the U.S. and in Europe and sponsored research worldwide. Dedicated technical meetings and sessions on PDEs in combustion-related conferences are becoming very popular.

The U.S. Office of Naval Research (ONR)* and the Russian Foundation for Basic Research (RFBR) are among the principal sponsors in fundamental research on detonation. The International Colloquia on Advances in Experimentation and Computation of Detonations, held in 1998 at St. Petersburg, Russia, jointly sponsored by these organizations in association with ONR International Field Office — Europe, European Research Office of the U.S. Army, and Enas — Research & Education Co., and on Control of Detonation Processes, held in 2000 at Moscow, Russia, jointly sponsored by these organizations in association with ONR International Field Office — Europe, European Research Office of the U.S. Army, and the Scientific Council on Combustion and Explosion of the Presidium of the Russian Academy of Sciences, have further strengthened the awareness of this forefront in science and technology, and provided a forum for dialogue among specialists.

*The content of the information does not necessarily reflect the position or the policy of the United States Government and no official endorsement should be inferred.

In the current concepts of practical PDEs, confinement plays a very significant role. To concentrate on this issue, an International Colloquium on Advances in Confined Detonations has been organized. This Colloquium was sponsored by the U.S. ONR, ONR International Field Office — Europe, RFBR, and the Scientific Council on Combustion and Explosion of the Presidium of the Russian Academy of Sciences. The international scientific community responded overwhelmingly with over 50 papers from 9 countries. The extended abstracts of all presentations have been published earlier*.

This volume contains full manuscripts of selected contributions presented at the Colloquium. The articles were selected based on these criteria: their direct relevance to the topic, their significance, and international representation. The articles were thoroughly edited and organized in a uniform and easily readable manner with three parts: (1) Confined Deflagrations and Detonations; (2) Pulse Detonation Engines; and (3) Avenues of Future Research. In addition to new results and findings, the book includes critical analyses of previous studies and controversial aspects of confined detonations and numerous references to archival publications worldwide. The volume is prepared as a reference for practicing engineers and research scientists working in the field of combustion and propulsion.

This volume is the outcome of hard work of a number of people who have rendered their best, and we appreciate their contribution. The editors acknowledge the concern and diligence of the Torus Press staff. We thank all authors for preparing their papers and spending their time and efforts with the editors on improving the text, figures, and scope of their contributions to fit with the overall goals of the book.

Many thanks are due to Academician A.G. Merzhanov, Academician V.A. Kabanov, and Prof. A.A. Berlin for their valuable contribution to the organization of the Colloquium. We do hope that this book will contribute to transitioning the knowledge on detonations science to technology and applications.

December 2002

Gabriel D. Roy
Sergei M. Frolov
Robert J. Santoro
Sergei A. Tsyganov

*Roy, G., S. Frolov, R. Santoro, and S. Tsyganov, eds. 2002. *Advances in confined detonations.* Moscow, Russia: Torus Press.

CONTENTS

CONTRIBUTORS

V. S. AKSENOV
Department of Technical Physics
Moscow Physical Engineering Institute
(Technical University)
31, Kashirskoe Shosse
Moscow 115522, Russia

J. M. AUSTIN
Graduate Aeronautical Laboratories
California Institute of Technology
Pasadena, CA 91125, USA

D. I. BAKLANOV
Department of Gas Dynamics
High Energy Density Research Center
United Institute of High Temperature
Russian Academy of Sciences
13/19, Izhorskaya Str.
Moscow 127412, Russia

A. E. BARYKIN
Department of Combustion and Explosion
N. N. Semenov Institute
of Chemical Physics
Russian Academy of Sciences
4, Kosigin Str., Moscow 119991, Russia

V. Ya. BASEVICH
Department of Kinetics and Catalysis
N. N. Semenov Institute
of Chemical Physics
Russian Academy of Sciences
4, Kosigin Str., Moscow 119991, Russia

A. A. BORISOV
Department of Combustion and Explosion
N. N. Semenov Institute
of Chemical Physics
Russian Academy of Sciences
4, Kosigin Str., Moscow 119991, Russia

R. BRADLEY
Innovative Scientific Solutions, Inc.
Dayton, OH 45440, USA

C. M. BROPHY
Naval Postgraduate School
699 Dyer Road
Monterey, CA 93943, USA

J. BRUMBERG
Department of Mechanical and Nuclear
Engineering
Propulsion Engineering Research Center
The Pennsylvania State University
University Park, PA 16802, USA

G. CANTEINS
Laboratoire de Combustion
et de Détonique
UPR 9028 DU CNRS ENSMA
Université de Poitiers
1, Avenue Clément Ader
BP 40109, 86961
Futuroscope Cedex, France

A. CHANDY
University of Florida
Gainesville, FL 32611, USA

J.-Y. CHOI
Propulsion Engineering Research Center
The Pennsylvania State University
University Park, PA 16802, USA

C. CONRAD
Department of Mechanical and Nuclear Engineering
Propulsion Engineering Research Center
The Pennsylvania State University
University Park, PA 16802, USA

E. DANIAU
MBDA-F
8, rue Le Brix, BP 35
18020 Bourges CEDEX, France

D. DESBORDES
Laboratoire de Combustion
et de Détonique
UPR 9028 DU CNRS ENSMA
Université de Poitiers
1, Avenue Clément Ader
BP 40109, 86961
Futuroscope Cedex, France

R. N. ELSHIN
Department of Combustion and Explosion
N. N. Semenov Institute
of Chemical Physics
Russian Academy of Sciences
4, Kosigin Str., Moscow 119991, Russia

T. ENDO
Department of Aerospace Engineering
Nagoya University
Heiwaga-oka, Meito-ku, 5-207-9105
Nagoya 464-8603, Japan

A. V. FEDOROV
Institute for Theoretical
and Applied Mechanics
Russian Academy of Sciences
Siberian Division
Novosibirsk 630090, Russia

R. FERNANDEZ
NASA John H. Glenn Research Center
21000 Brookpark Road
Cleveland, OH 44135, USA

F. FRANZETTI
Laboratoire de Combustion
et de Détonique
UPR 9028 DU CNRS ENSMA
Université de Poitiers
1, Avenue Clément Ader
BP 40109, 86961
Futuroscope Cedex, France

S. M. FROLOV
Department of Combustion and Explosion
N. N. Semenov Institute
of Chemical Physics
Russian Academy of Sciences
4, Kosigin Str., Moscow 119991, Russia

K. FUJII
Department of Mechanical Engineering
Aoyama Gakuin University
6-16-1, Chitosedai, Setagaya-ku
Tokyo 157-8572, Japan

T. FUJIWARA
Department of Aerospace Engineering
Nagoya University
Heiwaga-oka, Meito-ku, 5-207-9105
Nagoya 464-8603, Japan

L. G. GVOZDEVA
Department of Gas Dynamics
High Energy Density Research Center
United Institute of High Temperature
Russian Academy of Sciences
13/19, Izhorskaya Str.
Moscow 127412, Russia

A. K. HAYASHI

Department of Mechanical Engineering
Aoyama Gakuin University
6-16-1, Chitosedai, Setagaya-ku
Tokyo 157-8572, Japan

J. HOKE

Innovative Scientific Solutions, Inc.
Dayton, OH 45440, USA

Y. HYODO

Safety and Reliability Management
Division, NASDA
Tokyo 105-8060, Japan

S. ITO

Department of Mechanical Engineering
Daido Institute of Technology
Nagoya 457-8530, Japan

M. S. IVANOV

Institute for Theoretical
and Applied Mechanics
Russian Academy of Sciences
Siberian Division
Novosibirsk 630090, Russia

K. KAILASANATH

Laboratory for Computational Physics
and Fluid Dynamics
Naval Research Laboratory
4555 Overlook Av.
Washington, DC 20375, USA

V. KATTA

Innovative Scientific Solutions, Inc.
Dayton, OH 45440, USA

Y. KENMOKU

Department of Mechanical Engineering
Aoyama Gakuin University
6-16-1, Chitosedai, Setagaya-ku
Tokyo 157-8572, Japan

S. KERAMPRAN

Centre de Developpement
des Technologies Nouvelles — ENSIETA
Brest, France

T. A. KHMEL

Institute for Theoretical
and Applied Mechanics
Russian Academy of Sciences
Siberian Division
Novosibirsk 630090, Russia

P. V. KOMISSAROV

Department of Combustion and Explosion
N. N. Semenov Institute
of Chemical Physics
Russian Academy of Sciences
4, Kosigin Str., Moscow 119991, Russia

T. S. KUAN

Department of Mechanical Engineering
Imperial College of Science,
Technology and Medicine
Exhibition Road
London SW7 2BX, UK

A. N. KUDRYAVTSEV

Institute for Theoretical
and Applied Mechanics
Russian Academy of Sciences
Siberian Division
Novosibirsk 630090, Russia

S.-Y. LEE

Department of Mechanical and Nuclear
Engineering
Propulsion Engineering Research Center
The Pennsylvania State University
University Park, PA 16802, USA

R. P. LINDSTEDT

Department of Mechanical Engineering
Imperial College of Science,
Technology and Medicine
Exhibition Road
London SW7 2BX, UK

F. H. MA

Propulsion Engineering Research Center
The Pennsylvania State University
University Park, PA 16802, USA

A. E. MAILKOV

Department of Combustion and Explosion
N. N. Semenov Institute
of Chemical Physics
Russian Academy of Sciences
4, Kosigin Str., Moscow 119991, Russia

D. MIKOLAITIS

University of Florida
Gainesville, FL 32611, USA

V. V. MITROFANOV

Lavrentyev Institute of Hydrodynamics
Russian Academy of Sciences
Siberian Division
Novosibirsk 630090, Russia

T. MIYASAKA

Department of Aerospace Engineering
Nagoya University
Heiwaga-oka, Meito-ku, 5-207-9105
Nagoya 464-8603, Japan

D. W. NETZER

Naval Postgraduate School
699 Dyer Road
Monterey, CA 93943, USA

Y. OKA

Nagoya Guidance and Propulsion Systems
Works
Mitsubishi Heavy Industries
Komaki 485-8561, Japan

S. PAL

Department of Mechanical and Nuclear
Engineering
Propulsion Engineering Research Center
The Pennsylvania State University
University Park, PA 16802, USA

D. E. PAXSON

NASA John H. Glenn Research Center
21000 Brookpark Road
Cleveland, OH 44135, USA

O. G. PENYAZKOV

Heat and Mass Transfer Institute
National Academy of Sciences of Belarus
15, P. Brovki Str.
Minsk 220072, Republic of Belarus

F. PINTGEN

Graduate Aeronautical Laboratories
California Institute of Technology
Pasadena, CA 91125, USA

S. A. POLIKHOV

Department of Combustion and Explosion
N. N. Semenov Institute
of Chemical Physics
Russian Academy of Sciences
4, Kosigin Str., Moscow 119991, Russia

G. D. ROY

U.S. Office of Naval Research
800 North Quincy Str.
Arlington, VA 22217, USA

R. J. SANTORO

Department of Mechanical
and Nuclear Engineering
Propulsion Engineering Research Center
The Pennsylvania State University
University Park, PA 16802, USA

S. SARETTO

Department of Mechanical and Nuclear
Engineering
Propulsion Engineering Research Center
The Pennsylvania State University
University Park, PA 16802, USA

F. SCHAUER

Air Force Research Laboratory
Propulsion Directorate
Wright-Patterson AFB
OH 45433, USA

N. B. SCHERBAK

Department of Gas Dynamics
High Energy Density Research Center
United Institute of High Temperature
Russian Academy of Sciences
13/19, Izhorskaya Str.
Moscow 127412, Russia

C. SEGAL

Department of Aerospace Engineering,
Mechanics and Engineering Science
University of Florida
Gainesville, FL 32611, USA

I. O. SHAMSHIN

Department of Combustion and Explosion
N. N. Semenov Institute
of Chemical Physics
Russian Academy of Sciences
4, Kosigin Str., Moscow 119991, Russia

J. E. SHEPHERD

Graduate Aeronautical Laboratories
California Institute of Technology
Pasadena, CA 91125, USA

M. A. SILAKOVA

Department of Combustion and Explosion
N. N. Semenov Institute
of Chemical Physics
Russian Academy of Sciences
4, Kosigin Str., Moscow 119991, Russia

J. O. SINIBALDI

Naval Postgraduate School
699 Dyer Road
Monterey, CA 93943, USA

J. W. SLATER

NASA John H. Glenn Research Center
21000 Brookpark Road
Cleveland, OH 44135, USA

A. M. STARIK

P. I. Baranov Central Institute
of Aviation Motors
2, Aviamotornaya Str.
Moscow 111116, Russia

J. STUTRUD

Air Force Research Laboratory
Propulsion Directorate
Wright-Patterson AFB
OH 45433, USA

S. I. SUMSKOI

Department of Technical Physics
Moscow Physical Engineering Institute
(Technical University)
31, Kashirskoe Shosse
Moscow 115522, Russia

N. S. TITOVA

P. I. Baranov Central Institute
of Aviation Motors
2, Aviamotornaya Str.
Moscow 111116, Russia

A. V. TROTSYUK

Institute for Theoretical
and Applied Mechanics
Russian Academy of Sciences
Siberian Division
Novosibirsk 630090, Russia

N. TSUBOI

Research Division for Space
Transportation, ISAS
Yoshinodai, Sagamihara
Kanagawa 229-8510, Japan

S. A. TSYGANOV

Department of Innovations
Russian Foundation for Basic Research
32a, Leninsky Prosp.
Moscow 119991, Russia

E. M. VAOS

Department of Mechanical Engineering
Imperial College of Science,
Technology and Medicine
Exhibition Road
London SW7 2BX, UK

A. A. VASIL'EV

Lavrentyev Institute of Hydrodynamics
Russian Academy of Sciences
Siberian Division
Novosibirsk 630090, Russia

B. VEYSSIÈRE

Laboratoire de Combustion
et de Détonique
UPR 9028 DU CNRS ENSMA
Université de Poitiers
1, Avenue Clément Ader
BP 40109, 86961
Futuroscope Cedex, France

R. D. WOODWARD

Department of Mechanical and Nuclear
Engineering
Propulsion Engineering Research Center
The Pennsylvania State University
University Park, PA 16802, USA

Y. WU

Propulsion Engineering Research Center
The Pennsylvania State University
University Park, PA 16802, USA

V. YANG

Propulsion Engineering Research Center
The Pennsylvania State University
University Park, PA 16802, USA

F. Y. ZHANG

Department of Aerospace Engineering
Nagoya University
Heiwaga-oka, Meito-ku, 5-207-9105
Nagoya 464-8603, Japan

S. A. ZHDAN

Lavrentyev Institute of Hydrodynamics
Russian Academy of Sciences
Siberian Division
Novosibirsk 630090, Russia

R. ZITOUN

Laboratoire de Combustion
et de Détonique
UPR 9028 DU CNRS ENSMA
Université de Poitiers
1, Avenue Clément Ader
BP 40109, 86961
Futuroscope Cedex, France

INTRODUCTION

The current focus on utilizing detonations for air-breathing propulsion has shifted from long-term studies of the possibility of fuel energy transformation in stabilized oblique detonation waves to investigations and practical development of propulsion engines operating on propagating detonations in a pulse mode. Contrary to the oblique-detonation concept that is applicable to hypersonic flight at velocities comparable or higher than the Chapman–Jouguet detonation velocity of the fuel–air mixture, the concept of a pulse detonation engine (PDE) is attractive for both subsonic and supersonic flight with the PDE as a main propulsion unit or as an afterburner in turbojet or turbofan propulsion system. In particular, PDE-based propulsion is attractive for flight Mach number up to about 4. Within this range of Mach number, solid rocket motors are known to be very efficient in terms of simplicity and high-speed capability, but they have a limited powered range. Turbojet and turbofan engines, due to their high specific impulse, provide longer range and heavier payloads, but at flight Mach number exceeding 2–3, they get too expensive. Ramjets and ducted rockets designed for flight Mach number up to 4 require solid rocket boosters to accelerate them to the ramjet takeover speed, which increases the complexity and volume of a propulsion system. Combined-cycle engines, such as turborockets or turboramjets, are also very complex and expensive for similar applications.

In a PDE, detonation is initiated in a tube that serves as the combustor. The detonation wave rapidly traverses the chamber resulting in a nearly constant-volume heat addition process that produces a high pressure in the combustor and provides the thrust. The operation of multitube PDE configurations at high detonation frequency (about 100 Hz and over) can produce a near-constant thrust. In general, the near-constant volume operational cycle of a PDE provides a higher thermodynamic efficiency compared to the conventional constant-pressure (Brayton) cycle used in gas turbines and ramjets. The advantages of PDEs for air-breathing propulsion are simplicity and easy scaleability, reduced fuel consumption, and intrinsic capability of operation from zero approach stream velocity to high supersonic flight speeds.

Confinement plays a predominant role in the PDE. On the one hand, it concentrates the initiation energy and serves to support the structure of the propagating detonation by reproducing transverse waves, whereas on the other hand, it can effectively destroy the detonation structure, decouple the lead shock wave from the reaction zones and quench the reaction. Current understanding of the confinement effects on deflagration and detonation is still not complete or satisfactory.

In order to use propagating detonations for propulsion and realize the PDE advantages mentioned above, a number of challenging fundamental and engineering problems has yet to be solved. These problems deal basically with a low-cost achievement and control of successive detonations in a propulsion device. It appears that even the phenomena associated with air purging through the duct with repeated pressure build-up, caused by energy deposition, and the gradual pressure relief are not fully understood so far, in particular at the supersonic approach stream velocity. To ensure rapid development of a detonation wave within a short cycle time, one needs to apply (*i*) efficient liquid fuel injection and air supply systems to provide fast and nearly homogeneous mixing of the components in the detonation chamber; (*ii*) low-energy source for detonation initiation to provide fast and reliable detonation onset; (*iii*) cooling technique for rapid, preferably recuperative, heat removal from the walls of the detonation chamber to ensure stable operation and avoid premature ignition of fuel–air mixture leading to detonation failure; ($i\nu$) geometry of the combustion chamber to promote detonation initiation and propagation at lowest possible pressure loss and to ensure high operation frequency; and (ν) control methodology that allows adaptive, active control of the operation process to ensure optimal performance at variable flight conditions, while maintaining margin of stability. In addition to the fundamental issues dealing with the processes in the detonation chamber, there are other issues such as (νi) efficient integration of PDE with inlets and nozzles to provide high performance; and (νii) efficient coupling of detonation chambers in a multitube PDE configuration. Among the most challenging engineering issues, is the durability of the propulsion system. As the structural components of the PDE are subject to repeated high-frequency shock loading and thermal deformations, considerable wear and tear can be expected within a relatively short period of time. The other problems are noise and vibration.

The global interest in the development of the PDE for propulsion has led to numerous studies on detonations, particularly pertaining to its control and confinement. This is evident from the formation of collaborative teams by universities and industry worldwide. Dedicated technical meetings and special minisymposia and sessions on PDEs in combustion-related conferences are becoming very popular. Several reviews have been already presented at various meetings (e.g., [1–11]) and published in archival journals [12–14].

During the period from 1998 to 2002, the U.S. Office of Naval Research (ONR) and the Russian Foundation for Basic Research (RFBR) have jointly sponsored

three International colloquia on detonations, in particular, those aspects of detonations that are directly relevant to the development of PDEs. In 1998, the International Colloquium on Advances in Experimentation and Computation of Detonations was held in St. Petersburg with the participation of more than 60 experts. In 2000, the International Colloquium on Control of Detonation Processes was organized in Moscow with more than 100 participants. The International Colloquium on Advances in Confined Detonations was held in 2002, again in Moscow, with more than 120 participants. As a result of these meetings, a number of books have been published containing extended abstracts of all presentations [15–17] and full manuscripts of selected papers presented at the colloquia [18, 19]. This volume is the continuation of the series of books of selected papers. Twenty four papers from those presented at the 2002 International Colloquium on Advances in Confined Detonations, constitute this book.

The goal of this book is to provide, based on the materials presented at the meeting, a text for those who are interested in recent accomplishments in basic and applied research on PDEs and some PDE design concepts. The book is subdivided into three parts: 1. Confined Deflagrations and Detonations; 2. Pulse Detonation Engines; and 3. Avenues of Future Research. The articles included in each section are briefly outlined below.

CONFINED DEFLAGRATIONS AND DETONATIONS

Reported by *Kerampran et al.* are the detailed experimental studies of pressure wave–flame interaction. Propane–air and acetylene–air flame behavior was studied in tubes of different lengths with one closed end and one open end. Trajectories of the first pressure wave generated by flame ignition at the closed end and several reflected waves were linked to the flame trajectory and pressure records. It has been found that the first pressure wave can play an important role in flame acceleration at early stages of its propagation. Depending on the stage at which interaction occurs between the flame front and the first pressure wave, various scenarios of flame acceleration are possible, including DDT.

Kuan et al. address one of the most challenging topics in computational combustion dynamics, that is, numerical simulation of transition from laminar or turbulent flame to explosion or detonation in a confined geometry. They apply two high Damköhler number based approaches to model the evolution of a turbulent gaseous explosion in a confined channel with obstacles. Both initially quiescent and preexisting turbulence fields are considered. Closures at the second moment level are utilized for both velocity and scalar fields. Comparison of predictions with velocity measurements indicates that the computational techniques applied are capable of describing quantitatively the flow field anisotropy and provide qualitatively correct flame dynamics.

Vasil'ev suggests an approach to design DDT accelerators providing the shortest possible distances of detonation run-up. The approach utilizes a number of repetitive obstacles of proper shape, spacing, and relative positioning mounted along the direction of combustion wave propagation. Optimization of the parameters of DDT-accelerators is based on considering the shear-flow pattern behind the row of similar obstructions. To initiate marginal detonations with characteristic spinning behavior, the author suggests to properly shift the obstructions for producing a swirl effect. The concept was validated experimentally with a number of reactive mixtures. In particular, it was possible to detonate a stoichiometric methane–air mixture in a 100-millimeter diameter tube at a distance of 2.5 to 3.0 m. With the DDT-accelerator, stoichiometric hydrogen–air and acetylene–air mixtures were detonated at about 0.5 m in a tube of 250-millimeter diameter.

Penyazkov, based on extensive experimental studies of near-limit detonations and transient deflagrations in tubes with a circular cross-section, suggests empirical criteria governing the existence of 'spinning' and 'galloping' detonation modes. According to these criteria, in a marginal, 'spinning,' detonation wave propagating in a tube of a given radius R, the ignition induction length behind the lead shock wave does not exceed $0.8R$. Transient 'galloping' detonations exhibit ignition induction lengths no longer than a unit tube diameter. These criteria were obtained by measuring ignition delays behind the reflected decaying detonations in acetylene–oxygen–diluent (Ar or N_2) mixtures at ambient temperature and different initial pressures. It is important that the criteria incorporate both mixture properties (ignition delay time and detonation velocity) and tube dimensions (radius).

Brophy et al. present studies of detonation diffraction from a small predetonator tube into a larger main combustor tube. A critical region of interest is at the predetonator exit plane where the exiting detonation wave experiences diffraction to the main combustor. To study the phenomenon, a rectangular two-dimensional (2D) detonation tube with an expanding nozzle was used and 2D numerical simulation was performed.

Trotsyuk et al. report their computational studies of regular and Mach reflection of shock and detonation waves on a wedge in a steady 2D supersonic flow of a stoichiometric hydrogen–oxygen mixture. It is shown that depending on the wedge inclination angle there exists a dual-solution domain where both regular and Mach reflection is possible under identical boundary conditions. The transition between the reflection modes in this domain may be activated by local perturbations of free-stream density. The study is directly relevant to scramjet propulsion concepts that use detonative combustion mode, and to RAM accelerators.

Starik & Titova present their computational findings on the possibility to control deflagration and detonation processes by means of selective excitation of vibrational or electronic degrees of freedom of reacting molecules. It has been shown that laser irradiation of hydrogen–oxygen and methane–oxygen mixtures

at wavelengths of 762 and 1268 nm allows one to activate supplementary channels of active radical formation and enhance considerably the chain mechanism of ignition. For example, laser excitation of oxygen molecules may result in detonation initiation by the shock wave with the postshock temperature as low as 500–600 K.

Pintgen et al. report the results of experimental visualization of the detonation structure in stoichiometric H_2–O_2 and H_2–N_2O mixtures diluted with Ar and N_2 exhibiting different cellular regularity. Simultaneous Schlieren and Planar Laser Induced Fluorescence visualizations were made. The mechanisms by which combustion occurs in the detonation fronts are discussed.

Segal et al. report their experimental study of shock-induced JP-10 droplet breakup in shock waves of Mach number 2. The study is aimed to better understand shock–droplet interactions for mixtures of JP-10 with high-energy-density fuel additives. Experiments have been performed in a double-diaphragm shock tube. Droplet breakup modes were registered by means of a high-speed camera. Careful synchronization of diaphragm rupturing and triggering of droplet injection, flash and camera's intensifier allowed measurement of the droplet breakup time.

Borisov et al. suggest a promising approach to initiate detonation-like processes by means of injecting a burning fuel-rich matter into air. For this purpose, they load nitromethane and flaked aluminum powder into a special injector. The injector is equipped with a bursting diaphragm. Ignition of the mixture results in its partial burning prior to diaphragm rupture, followed by ejection of the matter into a tube 120 mm in diameter and 3 m long filled initially with air. With this technique, blast waves propagating at the velocity of up to 1400 m/s and with overpressure of up to 30 atm were registered. To understand the nature of these blast waves, numerical studies were performed. Chemical reactions in the unburned ejected matter were shown to be considerably enhanced with entrained air and support blast wave propagation. The predictions were found to be consistent with experimental observations. The results of experimental and computational studies of specific impulse produced by gaseous detonations (propane–air, hydrogen–air, and propylene–air) and by nonsteady reactive shock waves generated by burning heterogeneous mixtures are also presented.

Fedorov & Khmel present 2D numerical solutions of three problems regarding shock wave propagation in an aluminum particle cloud suspended in oxygen. Their mathematical model is based on two-way coupled, two-temperature, two-velocity governing equations of gasdynamics of heterogeneous media. In the first problem, specific features of incident shock refraction and reflection as it propagates along the channel with long, rectangular-shaped cloud of particles, partly filling the channel cross-section, are considered. In the second, the effect of cloud dimension on initiation of heterogeneous detonation is studied. In the third, a possibility of detonation initiation behind the shock wave reflected from the channel end-wall is examined.

Frolov et al. report the results of their experimental studies of n-hexane and n-heptane spray deflagrations and detonations in air. The basic experimental facility comprises a straight test tube 51 mm in diameter and 1.5 m long and the air-assist atomizer that provides the entire mixture flow rate through the tube. The conditions required for direct detonation initiation in the fuel spray by means of a single electric discharge have been found. The effect of discharge time, shape, and location, insulating properties of the tube, tube shape and diameter, as well as atomizer performance are studied. It is shown that the combination of sources to promote direct detonation initiation allows one to considerably decrease the critical initiation energy, while keeping the predetonation distance and time very short as compared to the values characteristic for DDT. With two successively triggered electric discharges mounted at a certain optimal distance from each other, the total detonation initiation energy was found to be less than that required with a single discharge. It has been found that there exist resonant conditions for successive triggering of two discharges in order to initiate detonation. The detonation peninsula at the "initiation energy vs. triggering time delay" plane is very narrow. This indicates the necessity of careful synchronization of successive discharge triggering.

PULSE DETONATION ENGINES

Canteins et al. have developed a simple analytical model allowing for the evaluation of PDE performance and validated it against experimental data. Various factors influencing the performance have been analyzed. It has been shown that the specific impulse is a function of certain quasi-universal constant, K, specific heat ratio, detonation velocity, stoichiometric fuel mass concentration, and equivalence ratio. To improve the specific impulse, the lowest possible values of K and equivalence ratio should be used. It has been shown that attachment of a nozzle for supersonic ejector to a PDE is an efficient means for increasing the specific impulse. Contrary to nozzles of steady-flow engines, PDE nozzles operate at essentially unsteady conditions and their design and optimization require consideration of the whole operation process. When a detonation wave approaches the open end of the PDE tube, the high-pressure detonation products have a considerable expansion potential. Attachment of a nozzle to the end of the detonation tube makes it possible to gradually expand the gases and decrease the rate of pressure drop in the tube, thus increasing cycle thrust. On the other hand, the attachment of a nozzle results in increasing the length of the engine and therefore decreasing the operation frequency. Attachment of the supersonic ejector allows increasing the specific impulse without considerable decrease in the maximum operating frequency.

Kailasanath, based on the confidence gained from the detailed comparisons of his 1D simulations with experimental data for an ethylene–oxygen PDE, has put forward a general expression for the specific impulse of an idealized PDE operating on other fuels, like propane and JP-10. Based on the knowledge of the detonation wave plateau pressure and the Chapman–Jouguet detonation velocity of the test mixture, the PDE specific impulse can now be readily estimated. Reasons for existing controversies and discrepancies in PDE performance analyses are also discussed.

Fujiwara et al. provide theoretical assessment of the performance of an idealized, single-tube PDE at various flight conditions in terms of altitude and speed. The PDE is assumed to operate on hydrogen–air, hydrogen–oxygen, or JP-10–air mixtures with equivalence ratio varying from 0.7 to 1.3. The analytical expressions for the specific impulse and thrust have been derived based on the idealized representation of the PDE operation process.

Miyasaka et al. evaluate the performance of an idealized, single-tube, hydrogen–air PDE by means of a 2D numerical simulation. A particular emphasis in their study is given to the effect of open-boundary conditions and reactive mixture equivalence ratio on the specific impulse and time-averaged thrust density. It has been shown that the PDE impulse attains a maximum value for the stoichiometric mixture composition, while the specific impulse increases for the lower equivalence ratio. A comparison of time-averaged thrust density of PDE and typical turbofan engine VP2500 indicates higher efficiency of the former.

Mitrofanov & Zhdan report the results of theoretical and computational evaluation of PDE performance. Their study demonstrates that ideal PDE thrust is higher than that of a ramjet and by-pass turbojet engines under identical initial conditions. With the increase in the compression ratio, the advantages of PDE gradually decrease. Their predictions of specific impulse provided by a simple, quasi-steady-state one-dimensional (1D) and unsteady 2D models are within a 5% discrepancy. The discrepancy in head-thrust predictions provided by the models is about 40% that is attributed to cycle-to-cycle variations in fuel charge mass.

Ma et al. present the results of detailed computer simulation of flow dynamics in a thrust chamber of a three-tube, hydrogen–air PDE operating at a flight altitude of 9.3 km and Mach number of 2.1. The operation frequency of each tube was 333 Hz. The simulation approach is based on the space–time CESE method which circumvents the deficiencies of existing numerical methods for treating detonation and shock waves. The effects of various design attributes (tube configuration and nozzle shape) and operating parameters (cycle frequency and valve timing) on engine performance have been investigated systematically.

Tsuboi et al. present an experimental single-tube hydrogen–air pulse detonation facility to study propulsion performance. The tube is of rectangular cross-section, 4 cm wide, and less than 1 m long. The aim of the authors' experiments is to understand the effect of igniter position on the DDT length. A rectangular

cross-section for the detonation tube was selected to ensure correct comparison with numerical analyses. The numerical simulation of the flow in the tube was performed by using Euler equations with a detailed reaction model. Detonation transmission from a narrow predetonator channel into the wide thrust channel was numerically simulated.

Santoro et al. report their detailed experimental studies of detonation transmission from the ethylene–oxygen–nitrogen 33-millimeter diameter predetonator into the 109-millimeter diameter PDE thrust tube via a conical transition section of 10-degree divergence. Explosive mixtures of equivalence ratio 1.1 were used. The level of nitrogen dilution was varied from 0 to 3.76 for constant fuel and oxygen mass flow rates. The effect of obstacle-induced shock focusing and detonation wave overdrive on the transmission efficiency was also studied.

Baklanov et al. study sensitivity of pulse detonations in a water-cooled tube to the oxidizer-to-fuel ratio and Reynolds number of a detonation-preceding flow. Explosive mixtures of liquid (automobile gasoline of Octane number from 72 to 93, aviation gasoline, *n*-hexane, ethanol, and acetone) and gaseous (methane) hydrocarbons were tested. For liquid hydrocarbons, detonability limits were determined experimentally in tubes up to 36 mm in diameter and 7 m long. For gaseous hydrocarbons, the effect of turbulence generation in the detonation-preceding flow on the predetonation length was studied in the 36-millimeter diameter, 3-meter long tube. It is claimed that the results allow for more realistic calculations of PDE thrust and specific impulse as compared to the estimations based on idealized Chapman–Jouguet detonations.

Schauer & Stutrud present research results of a combined computational and experimental investigation of an innovative, premixed, four-detonation-tube, air-breathing PDE. The research includes detonation initiation in air without the use of excess oxygen and engine performance at various operating conditions. Experimental data are obtained for hydrogen–air as well as hydrocarbon–air mixtures and compared with theoretical results. Critical technology issues such as detonation initiation and propagation, valving, timing and control, instrumentation and diagnostics, variation in tube fill, equivalence ratio, repetition rate, and DDT, as well as performance prediction and analysis are addressed.

Fernandez et al. outline a fundamental analytical and experimental program of studies of pulse ejector performance. The concept entails a pulse ejector driven by the exhaust of a PDE simulator and is aimed at the development of a PDE combined-cycle propulsion system.

AVENUES OF FUTURE RESEARCH

The last chapter of the book written by *Roy* addresses the issues of future research that is needed for development of a practical PDE based on the results

of the open Panel Discussion entitled "Advantages and Specific System Applications of Pulse Detonation Engines." From the computational side, there is a need for comprehensively validated codes allowing for modeling realistic operating conditions of a PDE including variable flight conditions, transient mixing of reactants in the detonation chamber, and noninstantaneous detonation initiation via DDT or detonation transition, unstable mode of detonation propagation in the short detonation tube, conjugate heat transfer to tube walls and DDT-enhancing elements, momentum loss, misfires caused by premature ignitions, and many other factors usually neglected in ideal-cycle simulations. One has to take into account that each "nonideal" factor, while decreasing the efficiency up to several percent, negatively contributes to the overall efficiency, and the system performance deteriorates considerably. From the experimental point of view, there is a need for detailed studies of various techniques of detonation initiation with least energy requirements and, moreover, various combinations of those techniques providing an optimized hybrid approach. It is important to keep in mind that in actual PDEs, detonation is initiated under conditions thermally and dynamically different from those in single-pulse experiments. In general, understanding of confined repeated detonations and their propulsive performance require further study.

As can be seen from the brief synopsis of the articles, there has been considerable progress in research and development dealing with practical applications of detonations for propulsion devices. The research on high-speed deflagrations and detonations has spread worldwide, and a number of new findings are presented in this volume. Perhaps, the articles included in the book represent the cutting edge of science and technology that has occurred over the past couple of years.

REFERENCES

1. Eidelman, S., and W. Grossman. 1992. Pulsed detonation engines: Experimental and theoretical review. AIAA Paper No. 92-3168.
2. Bussing, T., and G. Pappas. 1994. An introduction to pulse detonation engines. AIAA Paper No. 94-0263.
3. Eidelman, S., X. Yang, and I. Lottati. 1995. Pulsed detonation engine: Key issues. AIAA Paper No. 95-3877.
4. Bussing, T., and G. Pappas. 1996. Pulse detonation theory and concepts. In: *Developments in 1996. High-speed vehicle propulsion systems.* Eds. S. N. B. Murthy and E. T. Curran. Progress in astronautics and aeronautics ser. Washington, DC: AIAA Inc. 165.
5. Eidelman, S. 1997. Pulse detonation engine: A status review and technology development road map. AIAA Paper No. 97-2740.

6. Eidelman, S., and W. Grossman. 1999. Pulsed detonation engine: Experimental and theoretical review. AIAA Paper No. 99-1067.
7. Kailasanath, K. 1999. Applications of detonation to propulsion: A review. AIAA Paper No. 99-1067.
8. Roy, G. D. 1999. Pulsed detonation phenomena for air-breathing propulsion. *14th ISABE Proceedings*. Florence, Italy. ISABE Paper No. 99-7127.
9. Kailasanath, K. 2001. Review of PDE research — performance estimates. AIAA Paper No. 2001-0474.
10. Desbordes, D., E. Daniau, and R. Zitoun. 2001. Pulsed detonation propulsion: Key issues. In: *High-speed deflagration and detonation: Fundamentals and control*. Eds. G. Roy, S. Frolov, D. Netzer, and A. Borisov. Moscow: Elex-KM Publ. 177–92.
11. Kailasanath, K. 2002. Recent developments in the research on pulse detonation engines. AIAA Paper No. 2002-0470.
12. Eidelman, S., W. Grossmann, and I. Lottati. 1991. Review of propulsion applications and numerical simulations of the pulse detonation engine concept. *J. Propulsion Power* 7(6):857–65.
13. Cambier, J.-L., and J. K. Tegner. 1998. Strategies for pulse detonation engine performance optimization. *J. Propulsion Power* 14(4):489–98.
14. Kailasanath, K. 2000. Review of propulsion applications of detonation waves. *AIAA J.* 38(9):1698–708.
15. Roy, G., S. Frolov, K. Kailasanath, and N. Smirnov, eds. 1998. *Advances in experimentation and computation of detonations*. Moscow, Russia: Enas Publ. 144.
16. Roy, G., S. Frolov, D. Netzer, and A. Borisov, eds. 2000. *Control of detonation processes*. Moscow, Russia: Elex-KM Publ.
17. Roy, G., S. Frolov, R. Santoro, and S. Tsyganov, eds. 2002. *Advances in confined detonations*. Moscow, Russia: Torus Press.
18. Roy, G., S. Frolov, K. Kailasanath, and N. Smirnov, eds. 1999. *Gaseous and heterogeneous detonations: Science to applications*. Moscow, Russia: Enas Publ.
19. Roy, G., S. Frolov, D. Netzer, and A. Borisov, eds. 2001. *High-speed deflagration and detonation: Fundamentals and control*. Moscow, Russia: Elex-KM Publ.

Editors

PART ONE

CONFINED DEFLAGRATIONS AND DETONATIONS

INFLUENCE OF THE PRESSURE WAVES GENERATED AT THE INITIAL STAGE OF FLAME PROPAGATION ON THE DDT PROCESS IN SMOOTH TUBES

S. Kerampran, D. Desbordes, and B. Veyssière

The possibility for a laminar flame, ignited at the closed end of a smooth horizontal tube, to accelerate during its propagation toward the opposite open end, is governed by the mechanisms of interaction between the flame front at its initial stage of propagation and the acoustic flow generated in the tube. When the initial value of the laminar flame speed is small ($\sim$ 3 m/s), acoustic oscillations of the flow inside the tube play a dominant role and the average flame front velocity along the tube changes very slowly. On the contrary, for higher initial laminar flame speeds, the flame propagation is less sensitive to acoustic oscillations, and reaches high velocity levels ($>$ 350 m/s) at the tube exit.

1 INTRODUCTION

In preceding works, the results of studies on flame propagation in smooth horizontal tubes closed at the ignition end and open at the other end have been presented for several reactive mixtures, tube lengths, and tube diameters [1, 2]. This configuration is of particular interest with regard to the problem of deflagration-to-detonation transition (DDT), since high flame velocities can be expected. Indeed, the expansion of the burnt gases at the closed end of the tube and the free flow of the fresh gas at the open end both contribute to increase the flame velocity. These previous studies have evidenced the major part played by the initial flame development, and the associated generation of pressure waves, on the subsequent flame propagation and change in flame velocity. This is of particular interest with regards to the occurrence of DDT in a smooth tube (i.e., without any turbulence enhancing mechanism, such as obstacles). In this respect, it is important to know which governing mechanisms enable an initially laminar flame to reach velocity levels high enough to allow DDT to occur. It was shown that different flame behaviors can be observed, depending on the initial spatial

flame velocity. In the case of initially slow flames, strong coupling between flame motion and acoustic pressure oscillations in the tube was observed, resulting in an oscillatory flame propagation. For faster flames, only temporary slowdowns of the flame front were observed, followed by continuous flame acceleration. It was concluded that the overall flame behavior resulted from a competition between the actual flame motion with respect to the fresh gas and the oscillatory flow of gases (both burnt and unburnt) in the tube.

The present paper further analyzes the initial stage of flame propagation, and focuses on the interaction of the first pressure waves generated by flame motion with the process of flame acceleration during this stage.

2 EXPERIMENTAL SETUP

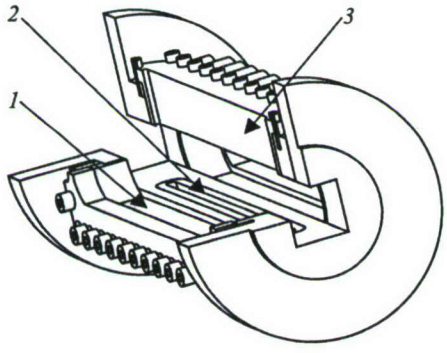

Figure 1 Schematic view of an element of the square cross-section tube (setup S2): *1* — lateral window (visualization); *2* — bottom window (laser sheet); and *3* — upper window (laser sheet)

Two experimental rigs have been used for this study. Both of them mainly consist of tubes closed at one end and open at the other. The first one (setup S1) is a Plexiglas tube of circular cross-section (21 mm in diameter) and variable length (from 0.22 to 2.72 m). This setup has been described in detail previously [1].

The other setup (setup S2) consists of a tube of square cross-section (with a side of 40 mm) and variable length (from 0.6 to 8.1 m). It is composed of 0.5-meter long sections, which can be equipped with 0.35-meter long windows on lateral sides, as shown in Fig. 1. Some elements are also equipped with windows on their upper and lower sides, so that laser sheets can be used for visualization. The tube inner surface has been designed to be as smooth as possible, paying attention in particular to roughness and gaps between tube elements. The tube can hold a static pressure of 50 atm.

For both setups, ignition is achieved at the closed end of the tube, by means of a heated wire, in order to ensure that the flame is initially laminar*. Flame

*Simple estimates show that under conditions of reported experiments, the Reynolds number of the expanded unburned gas in front of the flame exceeds the critical Reynolds number at the very beginning of flame ignition, and the flame-induced flow is likely to be turbulent rather than laminar, at least near tube walls. (*Editors' remark.*)

Table 1 Initial flame velocity V

Reactive mixture	Equivalence ratio, ϕ	Expansion ratio, α	Laminar burning velocity, S_u, m/s	$V = \alpha S_u$, m/s
Propane–air (P1)	1	8.0	0.38	3.0
Acetylene–air (A1)	1	8.5	1.38	11.7

emergence is detected with an ionization probe located as close to the heated wire as possible. Ignition takes place approximately at 1 cm from the closed end of the tubes.

Pressure is recorded with two Kistler 6031 gauges. One of them is systematically placed at the closed end of the tube. The other one can be located at various places along the tube. Flame propagation is recorded with a high framing rate video camera (Kodak Ektapro HS Motion Analyzer). Three kinds of visualization methods have been used: self-emitted light recordings, Schlieren, and laser sheet tomography. Depending on the flame velocity and visualization method used, the framing rates ranged from 2,250 (self-emitted light) to 27,000 frames per second (Schlieren).

Several reactive mixtures have been used over the course of the study, in order to vary the initial flame velocity, V. This velocity is given by $V = \alpha S_u$, α and S_u denoting, respectively, the expansion ratio (i.e., the ratio of the densities of the fresh and burnt gas) and the laminar burning velocity. This paper focuses on the results obtained with two stoichiometric mixtures of propane and acetylene with air, respectively, denoted hereafter as P1 and A1. The main characteristics of these reactive mixtures are presented in Table 1. The first mixture engenders a flame which may be considered as "slow" in the frame of this study, whereas a "fast" flame is produced by the second one.

3 INFLUENCE OF PRESSURE WAVES ON FLAME TRAJECTORY

A simple model is used to analyze the influence on flame trajectory, of the pressure wave generated at the beginning of flame propagation. It is based on the assumption that a compression wave (denoted C_0') is formed and propagates from the closed end of the tube at the time the flame ignites. It reflects at the open end of the tube as a rarefaction wave (denoted R_1), propagating backwards, and so forth. No interaction of this initial pressure wave with subsequently generated waves is considered. Its trajectory is correlated to flame trajectory (derived from

video recordings of flame propagation) and to pressure evolution recorded at the closed end of the tube.

Such an analysis is illustrated in Fig. 2, which shows the flame trajectories and pressure evolution at the closed end of the tube recorded in setup S2 for four different tube lengths in the case of mixture P1. On these diagrams, the trajectory of the initial pressure wave (C_0') generated by flame motion has been drawn, assuming this wave to be generated at the same time as the flame.

On the different diagrams of Fig. 2, one can observe the first pressure maximum, occurring at a fixed delay after ignition ($\sim$ 15 ms). Previous studies [2] have shown that this first pressure maximum is related to the initial development of the flame. It is reached by the time the flame touches the walls. However, its amplitude may be weakened if the reflected rarefaction wave (R_1) interacts sufficiently early with the flame. The critical value of the tube length under which this phenomenon can be observed depends on the initial flame velocity V and on the tube diameter. For the given setup (S2) and reactive mixture (P1), the critical tube length has been estimated to be between 2.1 and 2.6 m. Accordingly, the value of the first pressure maximum is the same for all tube lengths on Fig. 2.

It appears that in the case of a 2.6-meter long tube (Fig. 2*a*), the interaction of the flame front with the first rarefaction wave reflected at the open end of the tube, R_1, has no significant influence either on the flame trajectory or on the pressure evolution. This interaction occurs here at the same time as the first pressure maximum. Then, when the flame is met by wave C_1 (generated by the reflection of wave R_1' at the closed end of the tube) it stops (at $t = 28$ ms) and travels shortly backwards.

When the tube length is increased to 3.6 m (Fig. 2*b*), a change in the slope of the curve (occurring at $t \sim 20$ ms and denoted I_1 on the diagrams) appears on the pressure signal, during pressure decrease after the first maximum. The flame slows down at approximately the same time ($t = 20$ ms). As in the case of the previous tube length, the flame stops farther, when it is reached by wave C_1.

The diagrams obtained for 5.1-meter (Fig. 2*c*) and 6.1-meter (Fig. 2*d*) long tubes show that increasing the tube length increases the time during which the pressure decreases at a slower rate after point I_1. It also can be seen that the pressure starts decreasing more sharply again after the inflexion (point I_2) when the first reflected rarefaction wave (R_1) reaches the closed end of the tube. Regarding the flame trajectory, it seems that point I_1 corresponds to a slowdown of the flame. It accelerates again after wave R_1 has reached it. Attempting to apply this simplified model to analyze the influence of the initial pressure wave on the flame front becomes meaningless beyond this point, given the complex interaction of the reflected pressure waves with each other and the intrinsic dynamics of the flame itself.

The flame generated in mixture A1 is noticeably faster ($V = 11.7$ m/s) than the one observed in mixture P1. The interaction with the first reflected rarefac-

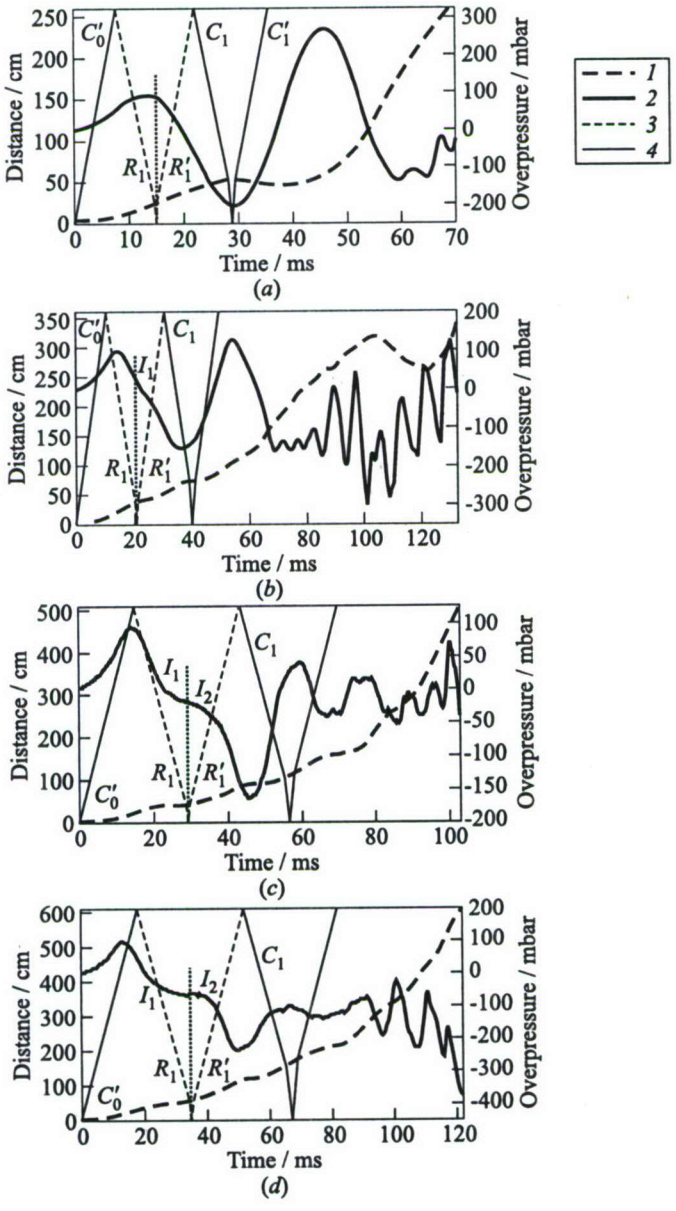

Figure 2 Flame front trajectory and pressure records at the closed end for different tube lengths, mixture P1, setup S2: (*a*) $L = 2.6$ m; (*b*) 3.6; (*c*) 5.1; and (*d*) $L = 6.1$ m. *1* — Flame trajectory; *2* — overpressure at the closed end; *3* — rarefaction wave; and *4* — compression wave

tion wave (R_1) occurs at a later stage of propagation and, therefore, the results obtained with this mixture offer more insight on the intrinsic behavior of the flame during its initial development. Flame trajectories and the corresponding pressure records obtained for three tube lengths in setup S1 have been displayed in Fig. 3. For the shortest tube ($L = 0.72$ m, Fig. 3*a*), the pressure record is very similar to those obtained with mixture P1 for the longest tubes, displaying an inflexion followed by a sharp pressure decrease seemingly triggered by wave R_1. The effects induced on flame trajectories are also the same as in the previous case: the flame slows down at the time the change in pressure slope I_1 is recorded and accelerates when it is caught up by wave R'_1.

In the case of larger tube lengths ($L = 1.22$ m, Fig. 3*b*; and $L = 1.72$ m, Fig. 3*c*), it can be observed on the pressure records that point I_1 is followed by an increase of the pressure (instead of a decrease for mixture P1), which stops at point I_2, i.e., approximately when the wave R_1 reaches the closed end. Figures 3*b* and 3*c* indicate that increasing the tube length results in an increase of the overpressure at point I_2. For those tube lengths, the flame velocity has become fairly high at this stage (of the order of 100 m/s) and it reaches the open end of the tube before the end of the first period of acoustic oscillations. Interaction of the flame front and wave R'_1 results in this case in a sharp increase of the flame velocity, enabling the flame to exit the tube at a near sonic velocity.

As long as the first reflected rarefaction wave R_1 has not met the flame, the flame behaves as it would propagate in a semi-infinite tube. Therefore, for this stage of propagation, it is interesting to analyze the intrinsic behavior of the flame. Experiments performed with mixture A1 are particularly useful in this respect, as stated above. The first part of the pressure record obtained with mixture A1 in setup S1 has been plotted for several tube lengths in Fig. 4. The dashed vertical lines indicate the time at which the first reflected rarefaction wave reaches the closed end of the tube, where the pressure gauge is located. It is apparent that the signals are in very good agreement until this time. On the part of the flame trajectory corresponding to this stage of propagation, a slowdown is systematically observed after the first pressure maximum (cf. Fig. 3). The subsequent pressure decrease should be attributed to the slowdown of the flame which is triggered by the increase of the contact surface between the flame and the tube walls: this results in a decrease of the flame surface and an increase of heat losses (both phenomena contributing to a decrease of flame velocity).

In the case of mixture A1, the initial stage of flame propagation can therefore be divided into three consecutive steps, as illustrated in Fig. 5 for a 1.72-meter long tube:

- Immediately after ignition ($0 < t < 2$ ms, in the given example), the flame acceleration is governed by its surface augmentation in spherical propagation. The first pressure maximum is reached at the end of this stage, when the flame touches the walls;

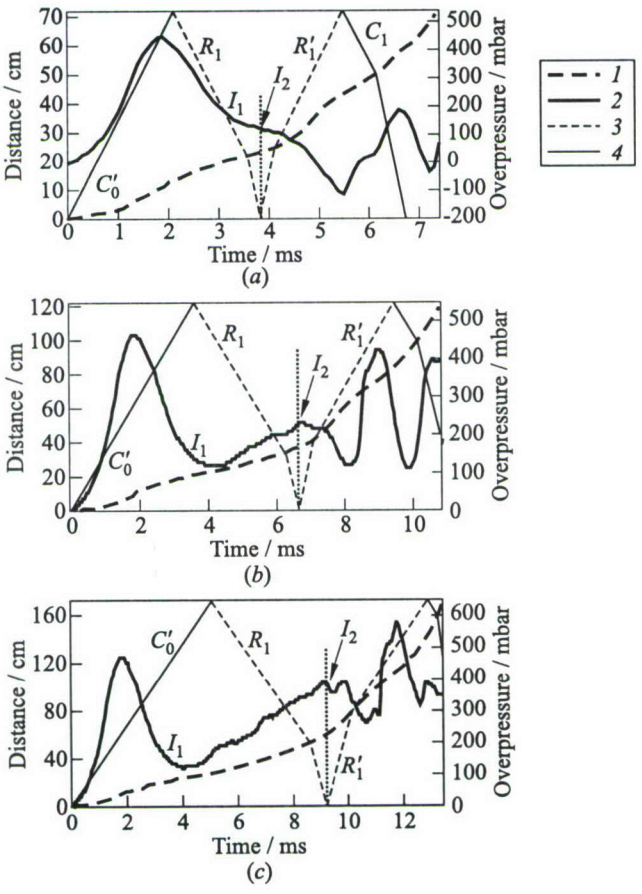

Figure 3 Flame front trajectory and pressure records at the closed end for different tube lengths: mixture A1, setup S1. (*a*) $L = 0.72$ m; (*b*) 1.22; and (*c*) $L = 1.72$ m. *1* — Flame trajectory; *2* — pressure at the closed end; *3* — rarefaction wave; and *4* — compression wave

- Then the flame elongates and slows down, due to the decrease of its surface, as explained above ($2 < t < 4$ ms). This stage is associated with the pressure decrease observed after the first maximum; and

- The flame velocity starts increasing again ($t > 4$ ms), but much more slowly than in the first stage. This induces a slow pressure increase. The first reflected rarefaction wave interacts with the flame front during this stage. It decreases the overpressure generated by flame motion while promoting flame acceleration, as shown on the diagram in Fig. 3*c*.

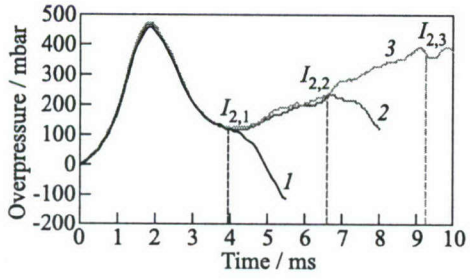

Figure 4 Beginning of the pressure records at the closed end of the tube: mixture A1, setup S1: *1* — $L = 0.72$ m; *2* — 1.22; and *3* — $L = 1.72$ m

Matters are a bit more complicated in the case of mixture P1. Since the flame generated by this mixture is slower than that obtained with mixture A1, the tube length plays a predominant role. Indeed, depending on the tube length, the flame can be reached by the first reflected rarefaction wave at different stages of its initial development. For tubes of 2.6-meter length or less, wave R_1 reaches the flame during the first step of its development, with little effect. In this case, the flame slows down and stops for the first time when it is reached by wave C_1. This first stop of the flame is due to the acoustic oscillations of the pressure in the tube. For tube lengths between 3.1 and 6.1 m, wave R_1 reaches the flame as it is slowing down after the first pressure maximum and induces an increase of its velocity. For longer tubes, the flame behavior is similar to the one observed for mixture A1. In this case, the first stop is due to the spontaneous slowdown of the flame. It must be noted that the tube lengths reported here depend on the initial value of flame velocity (and also on different factors, including the tube diameter).

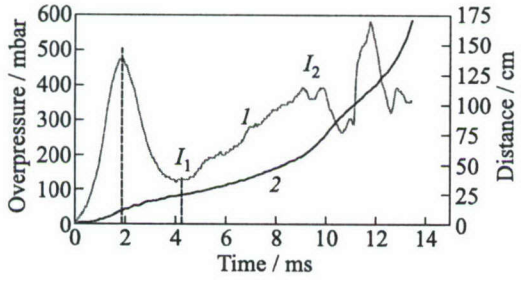

Figure 5 Decomposition of the pressure record (*1*) and flame trajectory (*2*): mixture A1, setup S1, $L = 1.72$ m

Obviously, the changes observed during the initial flame development result in very different evolutions of flame velocity. Let us examine the average flame velocity from the closed to the open end (denoted V_a), which has been plotted as a function of the tube length in Fig. 6, for both mixtures P1 and A1. As can be seen in the case of mixture A1 (Fig. 6*b*), V_a keeps on increasing with the tube length. Given the high values of V_a observed (> 350 m/s), DDT is very likely to occur at a subsequent stage of propagation, in this case. On the other hand, the dependence of V_a on tube length in the case of mixture P1 is not monotonic. As shown in Fig. 6*a*, increasing the tube length does not necessarily lead to a higher value of V_a. Furthermore, it can be noticed that the average flame velocity is bounded at approximately

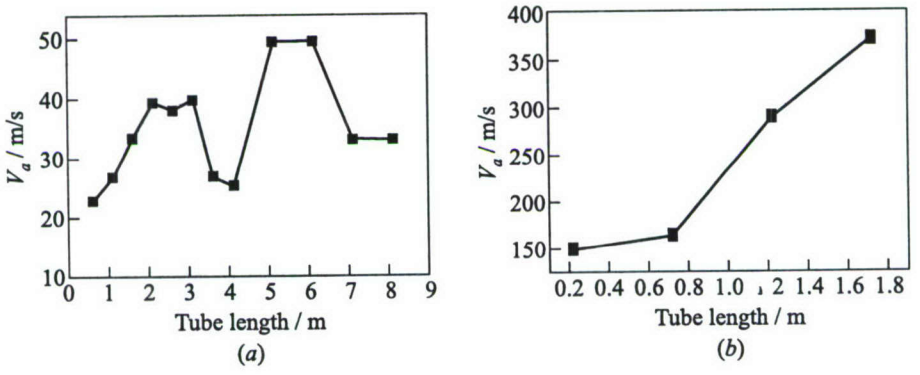

Figure 6 Average flame velocity, V_a, as function of the tube length: (a) mixture P1, setup S2; and (b) mixture A1, setup S1

50 m/s, which is far below the order of magnitude of velocities required for DDT to occur.

4 INFLUENCE OF PRESSURE WAVES ON THE FLAME FRONT STRUCTURE

In order to better analyze the interaction between the flame front and the pressure waves, a detailed photographic study of the early stage of propagation has been performed. Experiments have been done with the stoichiometric propane–air mixture (P1) in setup S2, with the visualization area located at the level of the second window of the tube (between 48 and 83 cm from the closed end). This permits the visualization of the interaction between the flame and the oscillatory flow. As seen above, the tube length plays the major part in the case of mixture P1. According to the results reported above, two cases must be distinguished, depending on the tube length: the visualized interaction may correspond either to the first flame stop (short tubes) or to the second one (long tubes).

1. The results obtained for a 2.1-meter long tube are presented in Fig. 7. On the self-emitted light frames, it can be observed that the flame is dome-shaped when entering the visualization zone. At $t = 24$ ms, it starts flattening. An inversion of the flame front curvature then becomes progressively apparent after $t = 25$ ms. The flame becomes indented, like a tulip flame, and breaks horizontally into two parts. During the inversion of flame curvature, the flame still propagates toward the open end of the tube, but its velocity decreases. At $t = 28$ ms, it starts propagating backwards. In spite of the blurred aspect of the frames, it seems that the upper and lower parts of the flame propagate transversally toward one another,

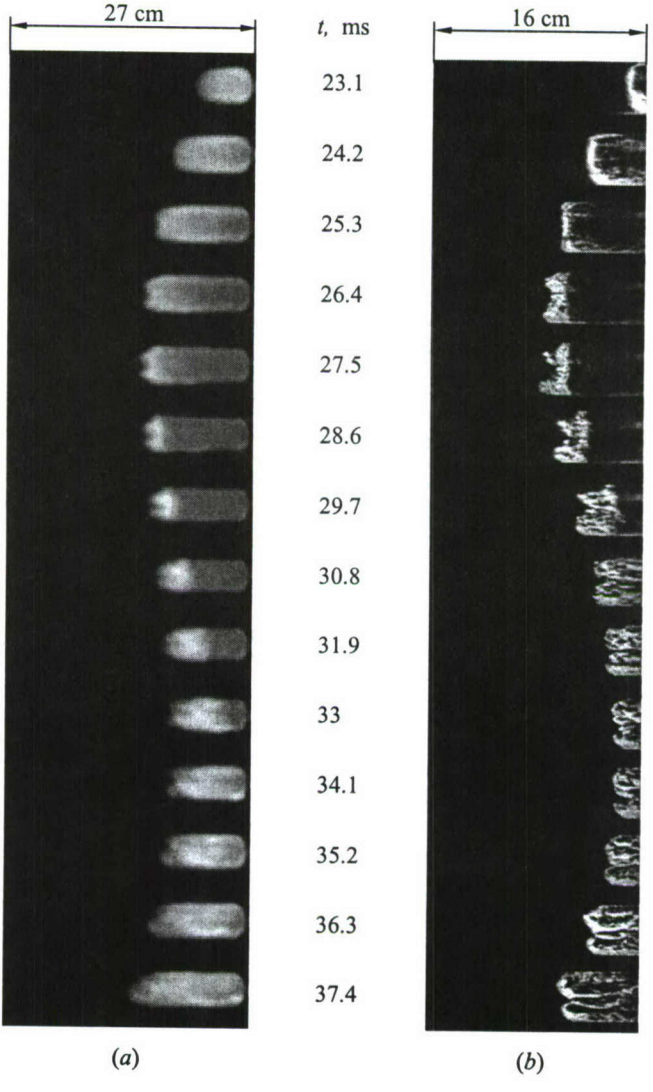

Figure 7 First stop of the flame: mixture P1, setup S2, tube length $L = 2.1$ m. (*a*) Self-emitted light, 4500 frames/s; and (*b*) Schlieren, 9000 frames/s

until they finally merge in the central part to form a unique flame front. Then, the flame resumes its propagation forward and its shape becomes much smoother after some 50 cm of propagation.

Schlieren frames obtained in the same conditions confirm this first analysis. The flattening and inversion of the flame front are clearly apparent on the frames at $t = 24$ and 25 ms. It can also be noted that the flame front becomes increasingly turbulent as the flame front curvature changes. When the flame resumes its propagation toward the open end of the tube, the turbulence has spread to the whole flame front.

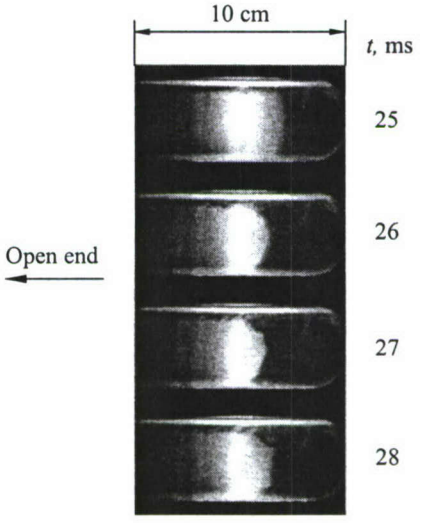

Figure 8 First stop of the flame for tubes shorter than 3.1 m: laser tomography, mixture P1, setup S2, tube length $L = 2.1$ m, 4500 frames/s

Figure 8 shows a sequence of flame front visualizations by laser sheet tomography. This visualization technique involves introducing a very dilute spray of micronic oil droplets in the reactive mixture and lighting a section of the tube by a laser sheet. Droplets diffuse the incident light which let the unburnt mixture appear as a bright zone. When the flame propagates, the oil droplets are vaporized in the flame front and no longer diffuse the incident light of the laser sheet: thus, the part of the tube containing burnt gases is dark on the tomographic frames. Here, a vertical laser sheet is used which allows the recording of the shape of the flame on a median vertical plane of the tube.

In Fig. 8, the first frame was taken after inversion of the curvature of the flame front. Subsequent evolution of the flame front is slightly complex: as seen above, the interaction with wave R_1 results in an indented flame. The upper and lower parts of the flame first propagate longitudinally along the walls, then radially toward each other ($t = 28$ ms). Another change in front curvature occurs in the central part of the flame. The merging of these three components (upper, central, and lower parts) of the flame front eventually results in a turbulent flame.

Therefore, the interaction of the flame with wave C_1 in the case of tubes shorter than 3.1 m can be divided in 4 stages:

- the flame slows down and flattens;
- curvature of the flame front is inverted, leading to the creation of an indentation; the flame eventually stops;

- the upper and lower parts of the flame propagate transversally toward the axis of the tube while the flame propagates backwards; and

- the flame resumes its propagation forward and becomes turbulent.

2. For tubes longer than 3.1 m, the flame is already indented when it reaches the visualization window (Fig. 9). This has been assumed to be a consequence of the spontaneous slowdown of the flame previously mentioned. It has not been possible to visualize this phenomenon, because it occurred in the 12.5-centimeter gap between the first and second windows of the tube. As a result, the frames presented in Fig. 9 illustrate the second slowdown of the flame, that is, the interaction of the flame front with the oscillatory flow in the case of long tubes. Although this phenomenon is similar to the one described for shorter tubes, several major differences can be observed, since the flame is no more smooth and regular when the interaction occurs in these particular conditions.

In Fig. 9, Schlieren frames show that the flame is strongly wrinkled before its velocity starts decreasing. Furthermore, it is split by a long and thin central indentation. Tomographic visualizations have enabled us to estimate this indentation to be approximately 20 cm long when the flame starts slowing down.

As the flame velocity decreases, the flame front becomes flat and the indentation disappears. Then, the flame stops and (at $t = 30$ ms) starts propagating backwards. It seems that the peripheral area of the flame is convected faster towards the closed end, whereas emergence of a tongue is observed in the center of the tube. This flame tongue seems to "struggle" to keep on moving in the forward direction. This phenomenon is clearly visible on the Schlieren frames, but not on the self-emitted light movies, which could be explained by the fact that this tongue is not as bright as the other parts of the flame. The peripheral part eventually disappears. The central tongue develops transversally (from $t = 35$ ms) until it fills the whole tube section when the whole flame resumes its propagation forward. The flame becomes again dome-shaped and its foremost part seems to be quite smooth. On the contrary, the flame wake becomes fairly turbulent.

In this case, the first interaction of the flame front with the oscillatory flow of gas in the tube can also be divided in 4 stages:

- the flame initially presents a long indentation and flattens as it slows down;

- the indentation disappears as the flame stops;

- a central tongue starts developing as the flame moves backwards, as a result of the competition between flame propagation and the oscillatory flow of gas; and

- the tongue develops in the whole section and the flame resumes its propagation forward.

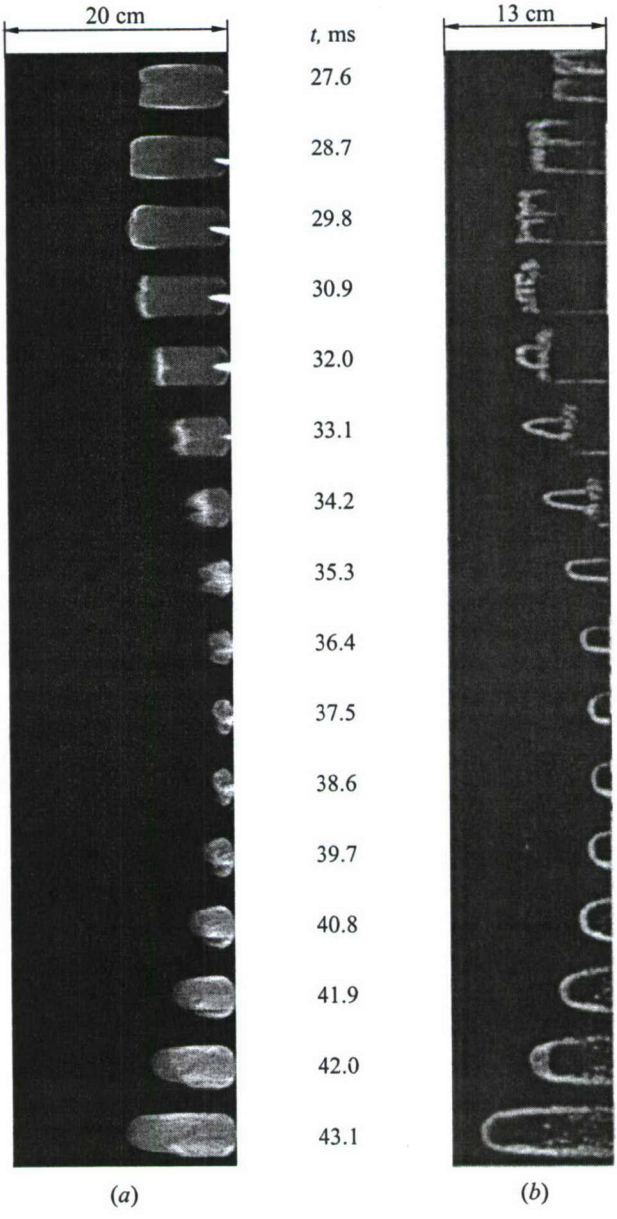

Figure 9 Second stop of the flame: mixture P1, setup S2, tube length $L = 3.6$ m. (a) Self-emitted light, 4500 frames/s, and (b) Schlieren, 9000 frames/s

5 CONCLUDING REMARKS

The very simplified analysis developed above, based on the interaction of the flame front with the flow created in the tube by the first pressure wave generated at the beginning of flame propagation, turns out to be a very efficient tool for interpreting the flame behavior. It confirms that flame propagation in the tube is strongly dependent on its interaction, at the very beginning, with the gas flow resulting from pressure wave generation by the flame front. For a gaseous mixture providing a low initial flame speed (3 m/s), flame propagation is deeply influenced by the gas flow in the tube and the augmentation of its average speed remains limited (< 50 m/s) even over long distances (6 m). It is impossible, in the present state of our knowledge, to predict whether such a flame will be able to accelerate by its own dynamics and reach typical values of velocity leading to DDT at a subsequent stage of propagation: addition of obstacles, or other devices able to generate a high level of turbulence, seems to be necessary to achieve this goal. Alternately, for a gaseous mixture having a higher initial flame speed (~ 12 m/s), flame propagation is hardly perturbed by the gas flow and acoustic waves: thus, the average flame speed increases rapidly and reaches values of the order of 350 m/s near the tube exit. In these conditions, DDT is very likely to occur in longer tubes within a short additional propagation distance. Detailed examination of the flame front at the moment of interaction with acoustic waves reveals that the flame is strongly modified during its interaction with the compression wave. Its curvature is inverted and it may be cut into two pieces or more. But at the same time, the increase of flame surface and turbulence generated by gas flow enhance the burning rate, allowing the flame to resume its propagation forwards. The overall behavior of the flame front results from the competition between these two opposite mechanisms. Further investigation of this problem is currently undertaken.

ACKNOWLEDGMENTS

The present work was supported by INERIS under Grant No. 780464.

REFERENCES

1. Kerampran, S., D. Desbordes, and B. Veyssière. 2000. Study of the mechanisms of flame acceleration in a tube of constant cross-section. *Combustion Science Technology* 158:71–91.
2. Kerampran, S., D. Desbordes, and B. Veyssière. 2001. Propagation of a flame from the closed end of a smooth horizontal tube of variable length. *18th Colloquium (International) on the Dynamics of Explosions and Reactive Systems.* Paper No. 110.

HIGHER MOMENT BASED MODELING OF TURBULENCE ENHANCED EXPLOSION KERNELS IN CONFINED FUEL–AIR MIXTURES

T. S. Kuan, R. P. Lindstedt, and E. M. Vaos

The transition of an initially laminar or turbulent deflagration to a confined gaseous explosion or detonation is of fundamental relevance to practical devices such as pulsed detonation engines (PDEs), and remains of key importance to on- and off-shore hazard assessment procedures. The topic is also one of the most challenging in contemporary physics and requires a detailed consideration of the interactions between unsteady high-speed turbulent flows and chemical kinetics. Furthermore, in many cases, fluid–wall interactions come to the fore. It is therefore, perhaps, not surprising that the subject has traditionally been treated either on the basis of shock dynamics in laminar flows, typically combined with simplified chemical kinetic expressions, or as a turbulent reacting flow closed at the eddy viscosity level in which the chemistry is considered to be in the high Damköhler number limit. The limitations associated with each approach are obvious and experimental data sets assembled over many decades show — without doubt — that the combined influence of chemistry and flow matters to the deflagration-to-detonation transition (DDT) process and by implication neither treatment is satisfactory. The current chasm in the theoretical treatment of turbulent gaseous explosions and detonation propagation studies must be bridged in order to provide a technically meaningful modeling capability for turbulence enhanced DDT processes. The focus of the present paper is to use detailed time-resolved experimental data sets to explore the ability of comprehensive moment based closures to reproduce time resolved flow field features up to the point of onset of detonation. A new reaction rate closure is also derived and evaluated. The experimental data set considered features a confined obstacle-accelerated premixed stoichiometric methane–air turbulent flame of physical relevance to PDEs. Time-resolved mean and root-mean squared (rms) profiles, obtained using laser Doppler anemometry, are used for comparisons with computational results along with

pressure traces and instantaneous spark Schlieren photographs. The main conclusions of the study are positive and the work does show that the application of higher moment based closures to model the flow field leading up to the onset of DDT yields surprisingly satisfactory results.

NOMENCLATURE

Latin Symbols

$\mathbf{b}$, b_{ij}	anisotropy tensor
B_{ijkl}, B^c_{ijkl}	scaling tensor for "rapid" redistribution and scrambling
c	reaction progress variable
C_0	generalized Langevin model constant
C_s	generalized gradient diffusion model constant
C_{ij}, C^c_{ij}	scaling tensor for "slow" redistribution and scrambling constants
C_R	reaction rate model constant
D_c	scalar laminar diffusivity
e	internal energy
G_{ij}	generalized Langevin model tensor
$\tilde{k}$	turbulence kinetic energy
M	molecular mass
p	pressure
P_{ij}, P_{ic}	Reynolds stress and scalar flux production terms
R	gas constant
S_c	reaction rate
t	time
T	temperature
T_{ijk}, T_{ijc}	Reynolds stress and scalar flux turbulent transport terms
$u_i = \{u, v, w\}$	velocity vector
u_L	laminar flame velocity
$\widetilde{u_i'' c''}$	scalar flux vector
$\widetilde{u_i'' u_j''}$	Reynolds stress tensor
$V_k \equiv (\nu\tilde{\varepsilon})^{1/4}$	Kolmogorov velocity
$x_i = \{x, y, z\}$	Cartesian coordinate vector
X	longitudinal coordinate in experimental setup
Y	transverse coordinate in experimental setup

Greek Symbols

α_1, α_2 $\beta_1, \beta_2, \beta_3$ $\gamma_1, \ldots, \gamma_6, \gamma^*$	generalized Langevin model parameters

δ_{ij}	Kronecker delta
$\tilde{\varepsilon}$	turbulent kinetic energy dissipation rate
$\tilde{\varepsilon}_c$	scalar dissipation rate
ε_{ij}, ε_{ic}	Reynolds stress and scalar flux dissipation terms
ζ	scaling parameter
μ	viscosity
ρ	density
ρ_o	density of unburned gas (reactants)
σ	Prandtl number
ϕ	equivalence ratio
ϕ_{ij}, ϕ_{ic}	pressure gradient correlation terms
Φ_{ij}, Φ_{ic}	mean pressure gradient terms

Superscripts

$\bar{}$	conventional mean value
$\tilde{}$	Favre averaged mean value
$'$	difference from conventional mean value
$''$	difference from Favre averaged mean value
$(\cdot)^D$	dilatation term
$(\cdot)^R$	redistribution term
$(\cdot)^S$	scrambling term
$(\cdot)^T$	transport term

Subscripts

c, s	related to scalar
t	turbulent

1 INTRODUCTION

Calculation methods for transient turbulent reacting flows must balance the fidelity of thermochemical and fluid mechanical closure aspects in order to provide technically useful results. The confined high-speed combusting flows considered here are dominated by flow–obstacle interactions and present a particular challenge. Chemical reaction occurs in the fine (unresolved) scales and must be modeled irrespective of the technique adopted for the flow field. Furthermore, flow interactions with solid boundaries, e.g., in the context of shock – (turbulent) boundary layer interactions, is a severe challenge for both unsteady Reynolds Averaged Navier–Stokes (RANS) approaches and Large Eddy Simulations (LES) even in the absence of chemical reaction. Temporal response issues and flowfield/turbulence interactions with chemistry also occupy central roles during the DDT phase in PDEs [1, 2] and in emerging propulsion devices in general [3].

The former are, in contrast to the majority of contemporary propulsion devices, intrinsically unsteady and cover an unusually wide spectrum of thermochemistry and physics. Examples of topics of practical relevance include fuel/mixture injection and obstacle (or shock) enhanced localized turbulent explosions resulting in a transition to detonation followed by the propagation of the resulting detonation and its interaction with confinement boundaries.

Key challenges that remain to be resolved during the latter stages of the DDT process include shock interactions with flames and boundary layers. However, two of the principal practical issues at present arguably concern the relative influences of fuel structures and turbulence on the transition process leading up to the actual onset of detonation. The chemical structure of the fuel has been shown experimentally to have a leading order influence on the transition process in smooth tubes [4]. It is also well established that the influence of turbulence reduces the sensitivity of the transition process to the point where alkane fuels, with the exception of methane, show a similar sensitivity. Lower alkenes and alkynes do, however, retain a greater propensity to DDT even in strongly turbulent environments [5]. An exceptionally wide range of turbulence Reynolds numbers is normally encountered during the transition process and the resulting complex interactions between flow and chemistry are likely to play a key role in device design. The resulting demands placed on computational design techniques are severe. Similar issues have for a long time prevailed in the context of hazards related studies of relevance to the modeling of turbulent gaseous explosions. Much of the work in the latter area has been performed in the context of successive studies sponsored by the CEC (DGXII) as part of the Major Technological Hazards Programme and a summary of some of the results has been presented by Arntzen *et al.* [6].

The modeling of turbulent gaseous explosions has to date exclusively featured different variants of closures at the eddy viscosity level. Generally, such closures have only proved adequate when turbulence is driven by local cross-stream gradients. In turbulent reacting flows, by contrast, variable density effects are at least comparable to, and usually outweigh, such generation mechanisms. A consequence of chemical reaction is the occurrence of velocity divergence leading to a reduction of turbulence levels due to the enhanced contribution of the strain components in the normal Reynolds stress "production" terms. However, volume expansion will also result in production due to preferential acceleration effects through mean pressure gradient terms in the respective transport equations. Similar considerations apply to the flux vector which may not necessarily be aligned with that of the scalar gradient and therefore result in "nongradient" transport. Effects of the type outlined above cannot be incorporated into eddy viscosity closures. Advantages of higher moment closures are that "history" and convection related effects on the evolution of turbulence are incorporated in a natural manner, while production terms by mean strain components appear in a closed form. Furthermore, effects induced by anisotropy generating mechanisms,

such as mean pressure gradients, are also included. Many of the latter features can be expected to be critical for the flows considered here as it may be expected that pressure gradient effects will have a significant impact upon the evolution of turbulence. The application of higher moment based closures to flows with strong pressure gradients is, however, not trivial and presents significant numerical challenges.

In the current context, it can also be expected that techniques capable of dealing with direct kinetic effects — with large deviations from equilibrium — will be required in order to model the full DDT process. At present, the transported probability density function (pdf) approach is the only method by which this can be achieved. Hulek & Lindstedt [7] have shown that one-dimensional transient premixed turbulent flames can be computed with a transported pdf closure at the joint velocity–scalar level. The molecular mixing terms were closed using a binomial Langevin model modified for joint velocity–scalar statistics [8]. Lindstedt & Vaos [9] subsequently explored the effects of different mixing models on the computed turbulent burning velocity and showed that both the binomial Langevin and Curl's mixing models perform well when combined with a closure at the second moment level. In both cases, the chemical reaction rate source term was extracted from laminar flame calculations and reduced to a one-step formulation. Time dependent calculations with realistic (large) scalar spaces ($\sim$ 20 independent scalars) are becoming increasingly feasible and are starting to appear [10] though exceptional computational resources are required.

In the present work, high Damköhler number techniques are applied to explore the ability of higher moment based closures for the flow field to reproduce major flow field features leading up to the point of onset of detonation. Catlin & Lindstedt [11] have shown that reaction rate expressions based on such assumptions are prone to numerical instabilities at the leading edge of turbulent premixed flames. The result is that the generally accepted leading order scaling between the turbulent burning velocity and turbulent velocity fluctuations is not reproduced in numerical calculations unless a Heaviside function is introduced at the leading edge. A further key observation is that the burning velocity eigenvalue is strongly dependent upon such modifications and that common approaches can be readily expected to lead to errors in excess of 100%. A further observation made is that the turbulent flame brush thickness has to be well resolved computationally in order to ensure physically meaningful results. The adherence to such, comparatively simple, requirements ensures that the intrinsic scaling behavior of the solved equations is retained. A recent study [12] has shown that the temporal evolution of gaseous explosions can be captured with useful accuracy and that alternative reaction rate closures based on a fractal assumption with the limiting cases of inner cut-off scales corresponding to the Kolmogorov and Gibson scales bracket key aspects of the experimental data.

Reliable experimental data is exceptionally difficult to procure for strongly transient turbulent flows but remain a prerequisite for a scientific evaluation of

different closure elements. The standard manner of evaluating predictive techniques with reference to single parameters, such as pressure rise or propagation velocity, is also insufficient. Furthermore, while visual information is helpful in advancing qualitative understanding, any detailed assessment of controlling mechanisms requires quantitative flow field information. It is therefore a striking deficiency that at the present time only two such data sets exist at meaningful Reynolds numbers [13–16]. The current work takes advantage of one of these data sets to provide an assessment of the ability of high Damköhler number based approaches to model qualitatively and quantitatively the evolution of a turbulent gaseous explosion in a confined channel. The case considered features a preexisting turbulence field generated through premixed fuel–air mixture injection at the closed end of a detonation tube [14, 16]. In the present work, closures at the second moment level are utilized for both velocity and scalar fields. The computational techniques applied are capable of describing phenomena such as flow field anisotropy and of providing qualitatively correct flame dynamics (e.g., [17]). The recent developments of comprehensive closures at this level [17, 18] is here followed by their application to model a transient multidimensional premixed turbulent flame.

2 GOVERNING EQUATIONS

The aerothermochemical fields are governed by the conservation equations for mass, momentum, and scalars cast in a density weighted form. Laminar diffusion terms and external force fields are neglected.

$$\frac{\partial \overline{\rho}}{\partial t} + \frac{\partial \overline{\rho}\widetilde{u}_l}{\partial x_l} = 0 \tag{1}$$

$$\frac{\partial \overline{\rho}\widetilde{u}_i}{\partial t} + \frac{\partial \overline{\rho}\widetilde{u}_l\widetilde{u}_i}{\partial x_l} = -\frac{\partial \overline{p}}{\partial x_i} - \frac{\partial \overline{\rho}\widetilde{u_l''u_i''}}{\partial x_l} \tag{2}$$

$$\frac{\partial \overline{\rho}\widetilde{c}}{\partial t} + \frac{\partial \overline{\rho}\widetilde{u}_l\widetilde{c}}{\partial x_l} = -\frac{\partial \overline{\rho}\widetilde{u_l''c''}}{\partial x_l} + \overline{S_c} \tag{3}$$

In the context of time dependent flows, it is important to note that changes in the velocity and scalar fields drive the generation of turbulence and that the feedback is provided through the turbulent correlation terms on the RHS of Eqs. (2) and (3). The latter are here treated through the corresponding transport equations for the Reynolds stresses:

$$\frac{\partial \overline{\rho}\widetilde{u_i''u_j''}}{\partial t} + \frac{\partial \overline{\rho}\widetilde{u}_l\widetilde{u_i''u_j''}}{\partial x_l} = \frac{\partial T_{ijl}}{\partial x_l} + P_{ij} + \Phi_{ij} + \phi_{ij} - \overline{\rho}\varepsilon_{ij} \tag{4}$$

and scalar fluxes (see Eq. (5)).

In Eq. (4), the terms on the RHS represent, in order, turbulent transport of the Reynolds stresses, effects of mean strain (or "production" P_{ij}), effects of mean pressure gradients (Φ_{ij}), the turbulent pressure strain term (ϕ_{ij}), and viscous dissipation ($\overline{\rho}\varepsilon_{ij}$), with

$$P_{ij} = -\overline{\rho}\left[\widetilde{u_i''u_l''}\frac{\partial \tilde{u}_j}{\partial x_l} + \widetilde{u_j''u_l''}\frac{\partial \tilde{u}_i}{\partial x_l}\right]$$

$$\Phi_{ij} = -\left[\overline{u_i''}\frac{\partial \overline{p}}{\partial x_j} + \overline{u_j''}\frac{\partial \overline{p}}{\partial x_i}\right]$$

$$\phi_{ij} = -\left[\overline{u_i''\frac{\partial p'}{\partial x_j}} + \overline{u_j''\frac{\partial p'}{\partial x_i}}\right]$$

The modeling of the pressure correlation terms in the Reynolds stress equations is the focal point of second moment closures. The terms can be decomposed into redistributive and isotropic parts and details can be found elsewhere (e.g., [17]). The latter may be further split into pressure transport and pressure dilatation terms. Redistribution terms are invariably modeled by recasting closures (derived on a constant density basis) in a density weighted form and a similar procedure is also applied to the pressure scrambling terms. An algebraic expression for the density weighted fluctuations forming part of the mean pressure gradient term can be derived. The corresponding scalar fluxes for the reaction progress variable are given below:

$$\frac{\partial \overline{\rho}\widetilde{u_i''c''}}{\partial t} + \frac{\partial \overline{\rho}\tilde{u}_l\widetilde{u_i''c''}}{\partial x_l} = \frac{\partial T_{ilc}}{\partial x_l} + P_{ic} + \Phi_{ic} + \phi_{ic} + \overline{u_i''S_c} - \overline{\rho}\varepsilon_{ic} \tag{5}$$

where

$$P_{ic} = -\overline{\rho}\left[\widetilde{u_l''c''}\frac{\partial \tilde{u}_i}{\partial x_l} + \widetilde{u_i''u_l''}\frac{\partial \tilde{c}}{\partial x_l}\right]\ ; \quad \Phi_{ic} = -\overline{c''}\frac{\partial \overline{p}}{\partial x_i}\ ; \quad \phi_{ic} = -\overline{c''\frac{\partial p'}{\partial x_i}}$$

The present study considers fully compressible flows with compressibility effects introduced via the solution of a conservation equation for the internal energy and the equation of state. The thermodynamic properties are evaluated from JANNAF polynomials and the temperature is calculated via a Newton iteration:

$$\begin{aligned} \frac{\partial \overline{\rho}\tilde{e}}{\partial t} + \frac{\partial \overline{\rho}\tilde{u}_l\tilde{e}}{\partial x_l} &= -\overline{p}\frac{\partial \tilde{u}_l}{\partial x_l} - \frac{\partial \overline{\rho}\widetilde{u_l''e''}}{\partial x_l} \\ -\overline{\rho}\widetilde{u_l''e''} &= \frac{\mu_t}{\sigma_t}\frac{\partial \tilde{e}}{\partial x_l} \\ pM &= \rho RT\,, \quad T = f(c,e) \end{aligned} \tag{6}$$

The treatment of flux terms in the internal energy equation presents a currently unresolved challenge and the principal role of Eq. (6) in the present context is to provide a treatment for the calculation of the temperature and density field. The turbulent kinetic energy, required in the evaluation of the "eddy viscosity," is determined from the solution of the Reynolds stress equations and the turbulent Prandtl number is assigned a value of 0.75.

The treatment of the pressure strain terms features a rearrangement into redistributive and isotropic parts with the latter decomposed into pressure transport and dilatation terms:

$$\phi_{ij}^R = -\left[\overline{u_i'' \frac{\partial p'}{\partial x_j}} + \overline{u_j'' \frac{\partial p'}{\partial x_i}} - \frac{2}{3}\delta_{ij}\overline{u_l'' \frac{\partial p'}{\partial x_l}}\right]$$

$$\phi_{ij}^T = -\left[\frac{2}{3}\delta_{ij}\overline{\frac{\partial p' u_l''}{\partial x_l}}\right]$$

$$\phi_{ij}^D = \left[\frac{2}{3}\delta_{ij}\overline{p' \frac{\partial u_l''}{\partial x_l}}\right]$$

The corresponding pressure strain term in the scalar flux equation may be recast in terms of pressure transport (T) and scrambling (S) terms:

$$\phi_{ic}^T = -\overline{\frac{\partial p' c''}{\partial x_i}}$$

$$\phi_{ic}^S = -\overline{p' \frac{\partial c''}{\partial x_i}}$$

The specific model expressions applied are described below.

3 SPECIFIC MODEL FORMS

The "return to isotropy" and "strain" redistribution parts are obtained from model formulations derived in nonreacting flows. Several suggestions exist at various levels of complexity. The model used here for illustrative purposes is that of Haworth & Pope [19] which is based on a stochastic Lagrangian Generalized Langevin Model (GLM) [20]. The latter features a nonlinear return to isotropy and has been calibrated and tested for a range of homogeneous turbulence and free shear flows. An important feature of the model is that it also yields a closure for the pressure scrambling term in the scalar flux equation and thus allows for

realizable modeling* of both pressure strain correlations. The "return" and "strain" redistribution parts take the following equivalent forms:

$$\phi_{ij} = \overline{\rho}\left[\frac{\tilde{\varepsilon}}{\tilde{k}}C_{ij}[\mathbf{b}] + B_{ijkl}[\mathbf{b}]\frac{\partial \tilde{u}_k}{\partial x_l}\right]\tilde{k}$$

$$= \overline{\rho}G_{ik}\widetilde{u_k''u_j''} + \overline{\rho}G_{jk}\widetilde{u_k''u_i''} + \overline{\rho}\left(C_0 + \frac{2}{3}\right)\delta_{ij}\tilde{\varepsilon} \quad (7)$$

where $\mathbf{b}$ denotes the anisotropy tensor. The corresponding model form for the scalar flux equation is

$$\phi_{ic} = \overline{\rho}\left[\frac{\tilde{\varepsilon}}{\tilde{k}}C_{ij}^{c}[\mathbf{b}] + B_{ijkl}^{c}[\mathbf{b}]\frac{\partial \tilde{u}_k}{\partial x_l}\right]\widetilde{u_j''c''} = \overline{\rho}G_{ik}\widetilde{u_k''c''} - \overline{\rho}\frac{\tilde{\varepsilon}_c}{\widetilde{c''^2}}\widetilde{u_i''c''}$$

In Eq. (7), the constant C_0 is assigned the value 2.1. The functional form for G_{ij} is linear in the mean velocity gradients and quasi-linear in the anisotropy tensor:

$$G_{ij} = \frac{\tilde{\varepsilon}}{\tilde{k}}(\alpha_1\delta_{ij} + \alpha_2 b_{ij}) + H_{ijkl}\frac{\partial \tilde{u}_k}{\partial x_l}$$

where

$$H_{ijkl} = \beta_1\delta_{ij}\delta_{kl} + \beta_2\delta_{ik}\delta_{jl} + \beta_3\delta_{il}\delta_{jk}$$
$$+ \gamma_1\delta_{ij}b_{kl} + \gamma_2\delta_{ik}b_{jl} + \gamma_3\delta_{il}b_{jk}$$
$$+ \gamma_4\delta_{kl}b_{ij} + \gamma_5\delta_{jl}b_{ik} + \gamma_6\delta_{jk}b_{il}$$

The model contains 11 coefficients of which 6 can be eliminated by exact constraints deduced form the Navier–Stokes equations. The remaining 5 were assigned values by matching experimental data [19] and no adjustment made in the present work:

$$\alpha_2 = 3.78 \qquad \beta_1 = -0.2 \qquad \beta_2 = 0.8 \qquad \beta_3 = -0.2$$
$$\gamma_1 = 0.0 \qquad \gamma_2 = 1.04 \qquad \gamma_3 = -0.34$$
$$\gamma_4 = 0.0 \qquad \gamma_5 = 1.99 \qquad \gamma_6 = -0.76$$

$$\alpha_1 = -\left[\frac{1}{2} + \frac{3}{4}C_0 + \alpha_2 b_{ii}^2 + \left(\beta_2 + \beta_3 + \frac{1}{3}\gamma^*\right)I_1 + \gamma^* I_2\right]$$

*Realizability principle has been introduced in turbulence modeling by Schumann U. 1977. *Physics Fluids* 20:721–25. This principle states that if a physical parameter is, e.g., nonnegative, then the model equations should satisfy this condition. (*Editors' remark.*)

where

$$\gamma^* \equiv \gamma_2 + \gamma_3 + \gamma_5 + \gamma_6$$

$$I_1 \equiv b_{ij} S^*_{ij} \qquad S^*_{ij} \equiv \frac{1}{2}\frac{\tilde{k}}{\tilde{\varepsilon}}\left[\frac{\partial \tilde{u}_i}{\partial x_j} + \frac{\partial \tilde{u}_j}{\partial x_i}\right]$$

$$I_2 \equiv b^2_{ij} S^*_{ij} \qquad b^2_{ij} \equiv b_{il} b_{lj}$$

$$\mathbf{b} = b_{ij} = \frac{\widetilde{u''_i u''_j}}{\widetilde{u''_k u''_k}} - \frac{\delta_{ij}}{3}$$

A number of closures have been suggested for the triple moments. However, the contributions of the diffusion terms to the overall budget of the Reynolds stresses and scalar fluxes is moderate and, consequently, the turbulent transport of the second moments is here modeled using the generalized gradient diffusion model of Daly & Harlow [21]:

$$\frac{\partial T_{ijl}}{\partial x_l} + \phi^T_{ij} = \frac{\partial}{\partial x_k}\left[C_s \overline{\rho}\frac{\tilde{k}}{\tilde{\varepsilon}}\widetilde{u''_k u''_l}\,\frac{\partial \widetilde{u''_i u''_j}}{\partial x_l}\right]$$

$$\frac{\partial T_{ilc}}{\partial x_l} + \phi^T_{ic} = \frac{\partial}{\partial x_k}\left[C_s \overline{\rho}\frac{\tilde{k}}{\tilde{\varepsilon}}\widetilde{u''_k u''_l}\,\frac{\partial \widetilde{u''_i c''}}{\partial x_l}\right]$$

The closure for the dissipation rate of the turbulent kinetic energy is obtained by the standard variable density transport equation model (e.g., [17, 22]).

4 CLOSURE FOR REACTION RATE RELATED TERMS

The closure for the chemical source term presents an interesting problem that entails the determination of an appropriate time scale for scalar turbulence. Traditionally, the closure for the scalar dissipation rate in the high Damköhler number regime is purely based on a constant timescale ratio leading to a direct relation to the mechanical time scale. The analysis is here pursued from the basis of differential models and the form proposed by Jones & Musonge [23] is used here for illustrative purposes:

$$\frac{\partial \overline{\rho}\tilde{\varepsilon}_c}{\partial t} + \frac{\partial \overline{\rho}\tilde{u}_l \tilde{\varepsilon}_c}{\partial x_l} = \frac{\partial}{\partial x_l}[J^{\varepsilon c}_l] + \left[C^{\varepsilon c}_1 \frac{\tilde{\varepsilon}}{\tilde{k}}\frac{P}{\tilde{\varepsilon}} + C^{\varepsilon c}_2 \frac{\tilde{\varepsilon}}{\tilde{k}}\frac{P_c}{\tilde{\varepsilon}_c} - C^{\varepsilon c}_3 \frac{\tilde{\varepsilon}}{\tilde{k}} - C^{\varepsilon c}_4 \frac{\tilde{\varepsilon}_c}{\widetilde{c''^2}}\right]\tilde{\rho}\varepsilon_c \quad (8)$$

In the above equation, C indicates a model constant, J a turbulent transport term, and the production terms (P, P_c) follow from the equations for the evolution of the Reynolds stresses and scalar fluxes. By virtue of Eq. (8), an algebraic expression for the scalar timescale can be derived if it is assumed that the evolution of the scalar dissipation rate is dominated by local source terms. The resulting form reduces to

$$\left[C_1^{\varepsilon c}\frac{\tilde{\varepsilon}}{\tilde{k}}\frac{P}{\tilde{\varepsilon}} + C_2^{\varepsilon c}\frac{\tilde{\varepsilon}}{\tilde{k}}\frac{P_c}{\tilde{\varepsilon}_c} - C_3^{\varepsilon c}\frac{\tilde{\varepsilon}}{\tilde{k}} - C_4^{\varepsilon c}\frac{\tilde{\varepsilon}_c}{\widetilde{c''^2}}\right] \cong 0$$

or

$$\frac{\tilde{\varepsilon}_c}{\widetilde{c''^2}} \cong \frac{1}{C_4^{\varepsilon c}}\left[C_1^{\varepsilon c}\frac{P}{\tilde{\varepsilon}} + C_2^{\varepsilon c}\frac{P_c}{\tilde{\varepsilon}_c} - C_3^{\varepsilon c}\right]\frac{\tilde{\varepsilon}}{\tilde{k}} = C_1^*\frac{\tilde{\varepsilon}}{\tilde{k}}$$

The above procedure may be regarded as typical for the derivation of the commonly adopted scalar time-scale ratio. The obvious requirement is that the sum of the terms in the square bracket does not vary significantly. Perhaps surprisingly, the value for the time-scale ratio is typically of order unity for passive scalars in many flows. In cases featuring reactive scalars, a similarly derived equation for the scalar dissipation rate includes additional specific terms in the form of correlations between scalar and reaction rate gradients:

$$\frac{\tilde{\varepsilon}_c}{\widetilde{c''^2}} \cong \left[C_1^* + \overline{S}_c^{\varepsilon}\right]\frac{\tilde{\varepsilon}}{\tilde{k}}$$

where

$$\overline{S}_c^{\varepsilon} = 2D_c\overline{\frac{\partial c''}{\partial x_l}\frac{\partial S_c}{\partial x_l}}$$

Borghi & Mantel [24] have performed a dimensional analysis and show that the above term is proportional to the Damköhler number. It has also been shown in [17, 18], based on a fractal analysis, that in the latter regime the time-scale ratio needs to be modified to account for flame propagation. Bray *et al.* [25] have recently evaluated a number of reaction rate closures in the context of the opposed jet geometry. The conclusions are interesting and suggest that the majority of reaction rate closures fail to predict qualitative trends correctly. Furthermore, it has been shown that irrespective of the level of closure adopted — algebraic or transport equation based — current models could generally not be calibrated to perform satisfactorily irrespective of the choice of modeling constant(-s). An exception was found to be the fractal based closure derived in [26] and discussed further in [17]. It must, however, be recognized that Bray *et al.* [25] also in this case show that there is a significant uncertainty relating to the appropriate modeling constant and that the value proposed [17] appears

too low. Based on the above considerations, the resulting modified expression for the time-scale ratio is proposed:

$$\frac{\tilde{\varepsilon}_c}{\widetilde{c''^2}} \cong \left[C_1^* + C_2^* \frac{\rho_0}{\overline{\rho}} \frac{u_L}{v_k}\right] \frac{\tilde{\varepsilon}}{\tilde{k}} = \left[C_1^* + C_2^* \frac{1}{\overline{\rho}} \frac{\sqrt{(\mu/\sigma)S_c}}{v_k}\right] \frac{\tilde{\varepsilon}}{\tilde{k}}$$

The reaction rate, S_c, is the integral across the corresponding (laminar) flame sheet and the viscosity (μ) and Prandtl number (σ) refer to the corresponding laminar properties evaluated at some inner reference plane. It is important to note that the above expression implies that burning velocity reductions at high Reynolds numbers are due to partial flame quenching and not to flame geometry related considerations. The limitations of the above derivation procedure and the resulting expression are obvious but to a large degree identical to those present in standard modeling approaches. From a practical perspective, however, the derived form ensures a consistent scaling behavior for turbulent burning velocities in the high Damköhler number regime of combustion. For the present case, the constant C_1^* has been assigned the standard value of 1, while the parameter C_2^* has been calibrated to the value of 1.2 on the basis of flames stabilized in an opposed jet geometry. The corresponding reaction rate expression follows from the assumption of a bimodal pdf:

$$\overline{S}_c = \overline{\rho} C_R \frac{\tilde{\varepsilon}_c}{\widetilde{c''^2}} \tilde{c}(1-\tilde{c}) \cong \overline{\rho} C_R \left[C_1^* + C_2^* \frac{\rho_0}{\overline{\rho}} \frac{u_L}{v_k}\right] \frac{\tilde{\varepsilon}}{\tilde{k}} \tilde{c}(1-\tilde{c})$$

The reaction rate constant C_R is assigned the value of 3.5 [27] and the above expression arguably constitutes an upper limit. The velocity – reaction rate correlation term is here closed through the assumption of a bimodal pdf [17]:

$$-\overline{\rho} \frac{\tilde{\varepsilon}_c}{\widetilde{c''^2}} \widetilde{u_i'' c''} + \overline{u_i'' S_c} = \frac{\overline{S}_c}{\widetilde{c''^2}} \left(\frac{1}{2} - \tilde{c}\right)$$

Different models for the pressure dilatation term have been proposed in [28] and [29]. The former suggestion has the virtue of being consistent with the assumed thermochemical conditions and, while the latter is heuristic in nature, it does not present problems in terms of realizability. In the present work, this term has been omitted as the influence is not expected to be large [29].

5 EXPERIMENTAL AND COMPUTATIONAL CONFIGURATION

The transition of a turbulent flame to a gaseous explosion in a confined pre-existing turbulent flow field is considered in the context of the data set produced in [14, 16]. The configuration yields overpressures of around 200 kPa and

peak bulk velocities around 400 m/s — both significantly higher than those reported [13, 15] for initially quiescent mixtures — and the turbulence velocities reach values of the order 40 m/s. Deflagration-to-detonation transition occurs in the same configuration for more reactive mixtures than the stoichiometric methane–air case reported here. The detonation tube features six interchangeable rectangular sections (72×34 mm) of length 1.825 m and two window sections of length 0.385 m. Initial turbulence is generated by an axisymmetric jet of 5-millimeter internal diameter centered in a plate at the ignition end of the flame tube. The flow field created by the injection of the premixed fuel–air mixture has been measured [14] and the data is here used in order to form the initial set of conditions. Ignition is obtained by two opposing electrodes placed symmetrically on either side of the jet centerline. A 5-millimeter thick obstacle with a height of 36 mm is placed downstream of the jet exit at a distance of 415 mm. The closure outlined above is here applied to the above geometry using a locally refined two-dimensional computational grid (~ 100 000 nodes) sufficient to provide a grid independent solution. The computations feature a second-order TVD scheme and an implicit predictor–corrector method with time splitting error control [11, 17].

The applied diagnostics include sixteen coaxial ionisation probes, used to detect flame arrival times, and six piezoelectric pressure transducers positioned along the channel. The flame propagation process was also visualised by means of spark Schlieren photography featuring a parallel beam of white light. Velocities were obtained using the standard dual-beam forward scatter laser Doppler anemometer arrangement and the data reduction technique reported in [15] applied. Velocity measurements along the axial (u-velocity) and vertical (v-velocity) directions have been obtained at 33 points above and downstream of the obstacle. All the points lie on the vertical plane passing through the axis of the flame tube. Sakthitharan [13] has shown, through flow field measurements across the detonation tube, that the flow is predominantly two-dimensional in the region close to the obstacle. Although there are temporal variations associated with the initial kernel growth (~ 10%), the reproducibility of the flame arrival at subsequent ports is excellent with comparatively small variations (~ 3%). The latter indicates that the development of the vortex structure downstream of the baffle is highly reproducible and relatively insensitive to initial variations. Problems do naturally arise with measurements of mean and, in particular, turbulence velocities in the current strongly accelerated flow. It is therefore expected that the measurement accuracy is significantly reduced following the onset of the explosion.

6 RESULTS AND DISCUSSION

Computed flame contours are compared with Schlieren images in Figs. 1 and 2. The relative times in the flame propagation cycle are close but not matched ex-

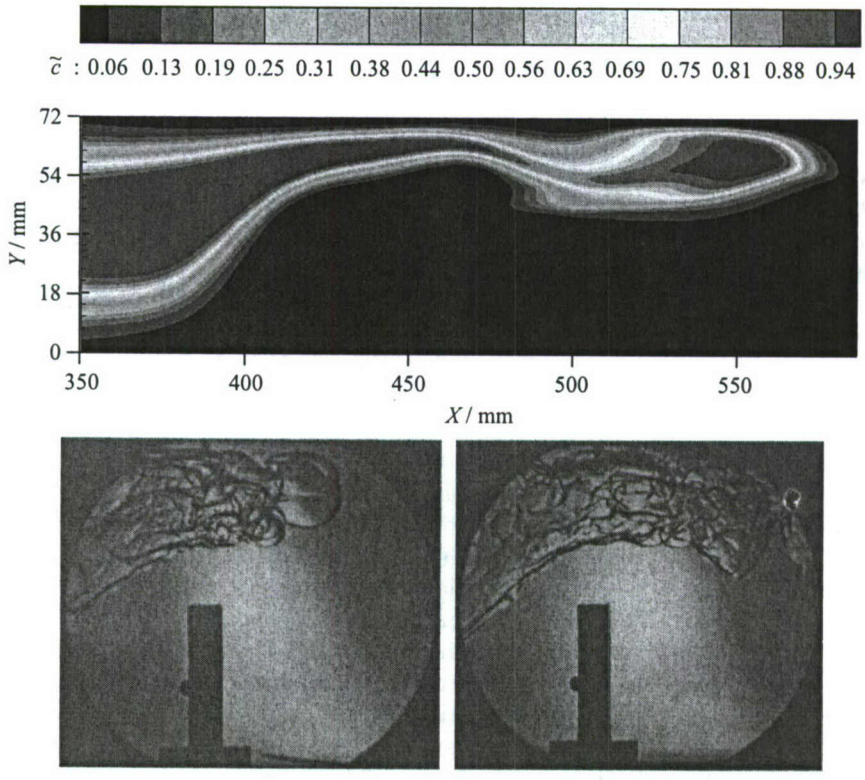

Figure 1 Comparison of computed (t = 14 ms) and measured stoichiometric methane–air flame images around the time the flame moves past the obstacle. The computation shows a later time and the Schlieren images illustrate the process leading up to the formation of the large-scale structures. (Refer color plate, p. I.)

actly and, furthermore, the Schlieren images are "line-of-sight" across the flame tube. Caution is therefore required in interpreting the images. However, it is seen that the creation of large-scale flame folds and the flame wrapping into the vortex are qualitatively reproduced by the computation. Clearly, the flow features large-scale instabilities along with strong turbulence generation in the shear layer and recirculation zone behind the obstacle. The large-scale instabilities are of order 10 mm with the wrinkling of the flame appearing to be of order 1 mm. The predicted pressure traces are compared with measurements in Fig. 3. Close to the ignition point, the agreement is very satisfactory as shown in Fig. 3*a*. However, it is also evident that peak pressures are somewhat underpredicted closer to the obstacle (Fig. 3*b*), though the shape of the pressure trace profile remains comparatively well reproduced.

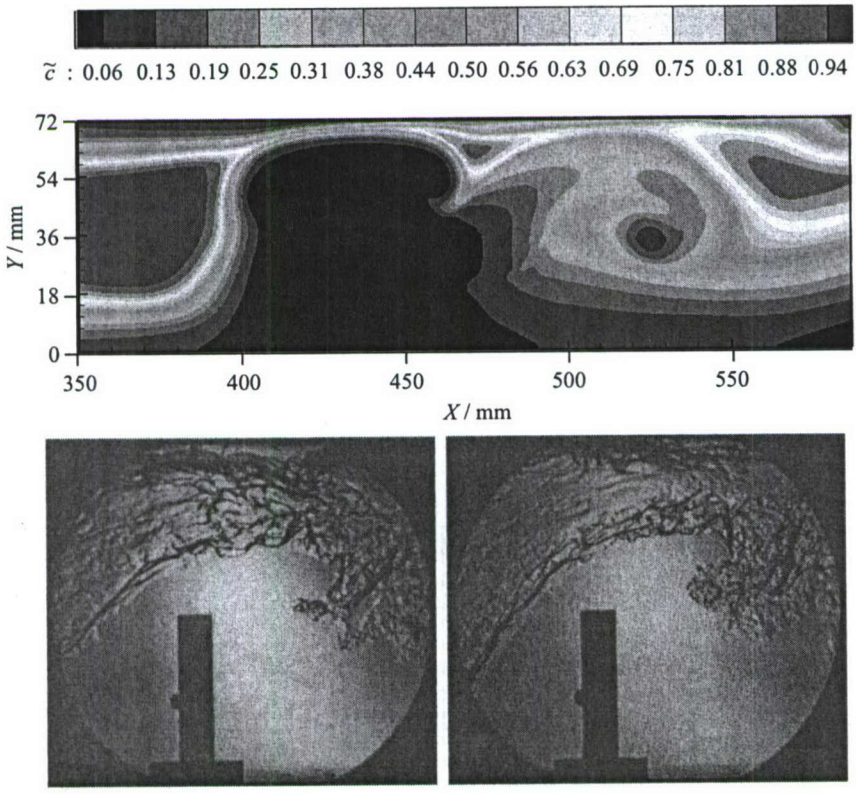

Figure 2 Comparison of experimental and computed (t = 15 ms) stoichiometric methane–air flame images at later times as compared to Fig. 1. Both the computations and the measurements clearly show large-scale instabilities propagating downstream of the obstacle. The experimental images show the superimposed turbulent flame wrinkling. The large-scale instabilities appear to be of order 10 mm and the flame wrinkling of order 1 mm. (Refer color plate, p. I.)

Further evidence that the predictions are qualitatively good and quantitatively reasonable can be found in the axial and cross-stream mean velocity profiles shown in Figs. 4 and 5 for the plane where the obstacle is located. The interaction of strong flow gradients in the *vena contracta* over the baffle with the explosion generated pressure pulses are exceptionally difficult to measure and it is likely that the experimental data underestimates the peaks in the bulk velocities. However, with the exception of the latter, the profile shapes and magnitudes are well reproduced for the axial (u) velocity component. The computations show strong oscillations in the burnt gas due to traveling pressure waves (evident in the pressure traces shown in Fig. 3) which clearly could not be captured by the meas-

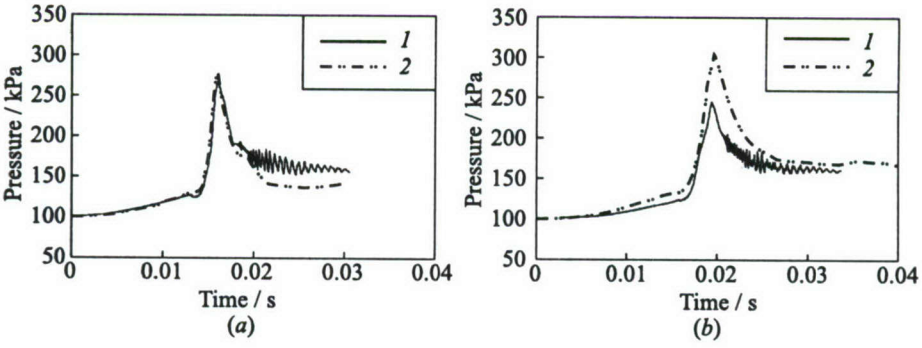

Figure 3 Comparison of computed (*1*) and measured (*2*) pressure traces for a turbulent gaseous explosion in a preexisting turbulence field. The figures show the pressure traces on both sides of the obstacle: (*a*) station 4 (0.03 m); and (*b*) station 2 (0.50 m)

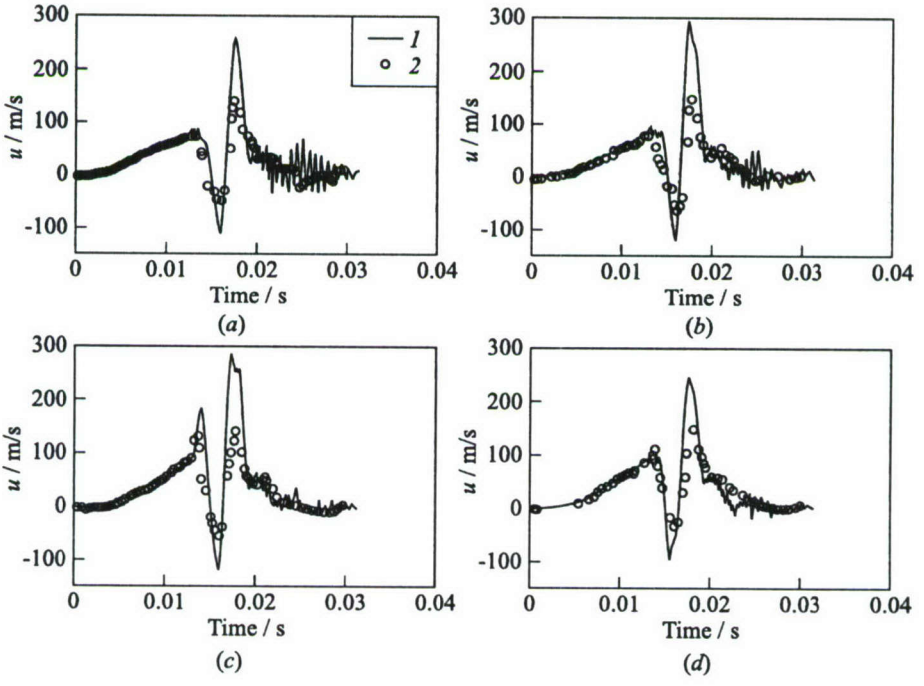

Figure 4 Comparison of computed (*1*) and measured (*2*) axial mean velocities at four measuring stations ((*a*) $Y = 42$ mm; (*b*) 48; (*c*) 54; and (*d*) 66 mm) along the plane $X = 415$ mm (directly above the obstacle) for a turbulent gaseous explosion in a preexisting turbulence field

urements. The agreement for the cross-stream (v) component is much less satisfactory. However, it can be noted that the flow velocities range from well in excess of 100 m/s close to the obstacle tip (42 mm) to around 10 m/s closer (10 mm) to the top wall. It may further be noticed that mean velocities are well reproduced until the onset of the explosion. Further away from the obstacle, at the 515-millimeter plane, the agreement between measurements and computations is generally satisfactory for the axial velocity component as shown in Fig. 6. However, it may be noted that the strongest flow accelerations again present what probably results in measurement difficulties. The qualitative and quantitative agreement for the cross-stream velocity component is very satisfactory as shown in Fig. 7 — despite the fact that the time evolution of the flow is extremely complex. It may also be noted that the flow acceleration is less severe in the cross-stream direction and hence greater confidence may be placed in experimental data.

The difficulties outlined above in the context of the determination of the bulk velocity field are naturally also present in the measurements of the turbulence

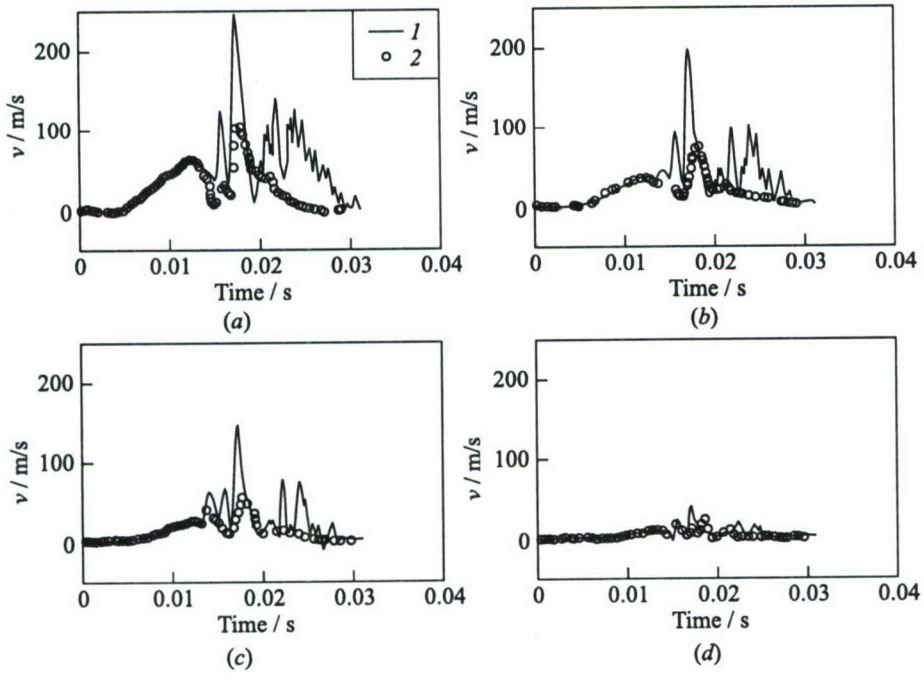

Figure 5 Comparison of computed (*1*) and measured (*2*) cross-stream mean velocities at four measuring stations ((*a*) $Y = 42$ mm; (*b*) 48; (*c*) 54; and (*d*) 66 mm) along the plane $X = 415$ mm (directly above the obstacle) for a turbulent gaseous explosion in a preexisting turbulence field

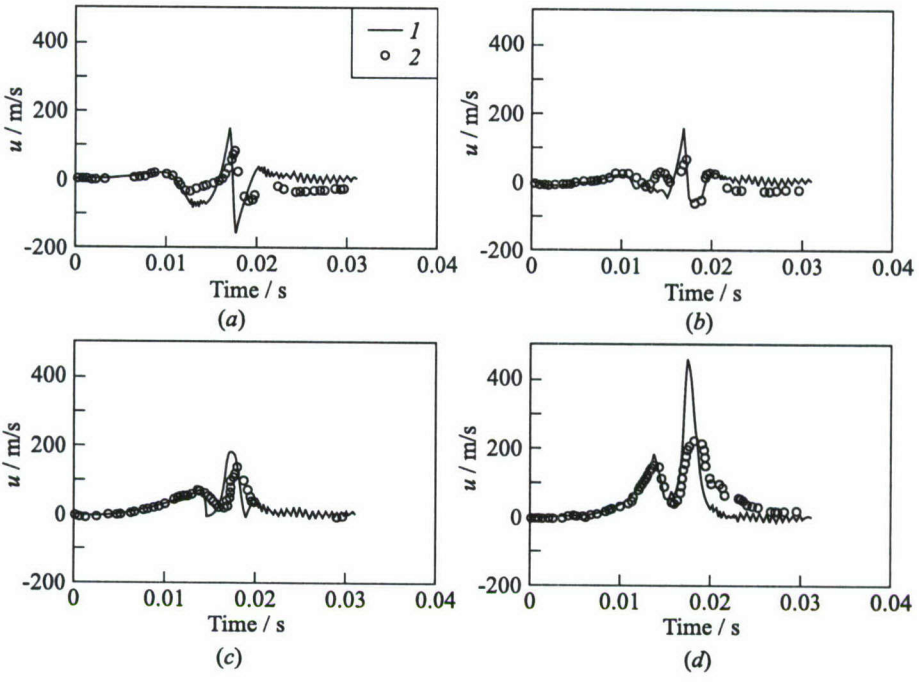

Figure 6 Comparison of computed (*1*) and measured (*2*) axial mean velocities at four measuring stations ((*a*) $Y = 9$ mm; (*b*) 18; (*c*) 36; and (*d*) 63 mm) along the plane $X = 515$ mm (100 mm downstream of the obstacle) for a turbulent gaseous explosion in a preexisting turbulence field

intensities. It is important to note that the vortex shedding and bulk flow instabilities do not satisfy the common criteria (e.g., irregularity) associated with turbulence (e.g., [30]). A scale separation associated with bulk and turbulent motion is evidently present in the current flow but becomes awkward to analyze both computationally and experimentally. The combination of a time window of 500 μs, used experimentally in order to gather sufficient statistics, along with the difficulties experienced by seeding particles in following flow, renders the measurements difficult to interpret. Nevertheless, up to the point of the onset of the explosion ($\sim$ 16–17 ms) there is fair agreement between computed and measured values of the axial component as shown in Fig. 8. Following the onset of the explosion the axial turbulence velocities — in particular — are very strongly affected and it is not possible to advance conclusions regarding the agreement between computed and measured values. The cross-stream velocity component is again much less affected and remains surprisingly well reproduced both qualitatively and quantitatively as shown in Fig. 9. A comparison of the results shown

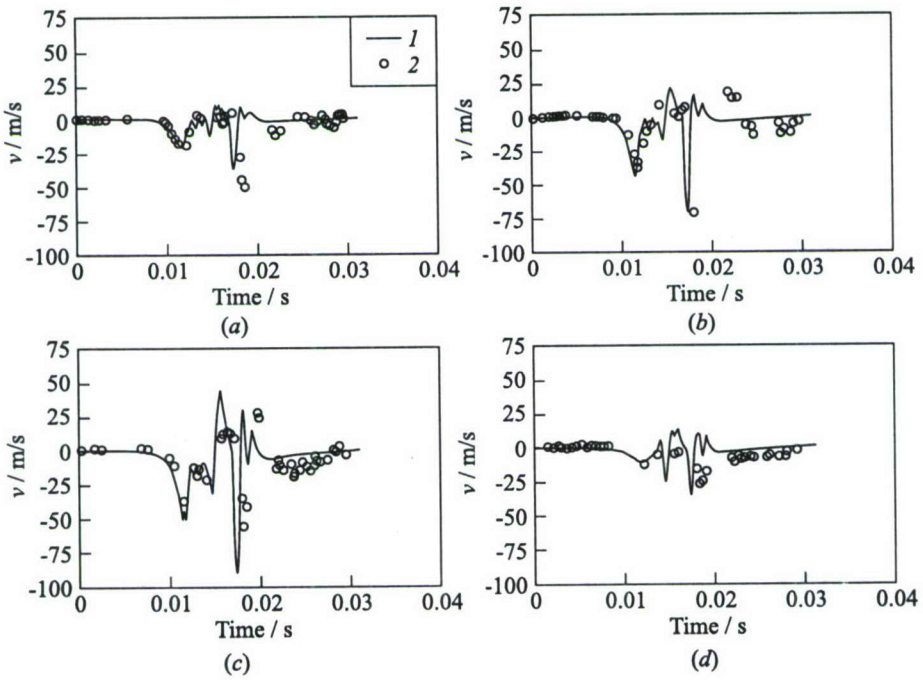

Figure 7 Comparison of computed (*1*) and measured (*2*) cross-stream mean velocities at four measuring stations ((*a*) $Y = 9$ mm; (*b*) 18; (*c*) 36; and (*d*) 63 mm) along the plane $X = 515$ mm (100 mm downstream of the obstacle) for a turbulent gaseous explosion in a preexisting turbulence field

in Figs. 7 and 9 is interesting and suggests that despite the difficulties associated with both measurements and computations, the overall agreement is encouraging. It is notable that the rapid changes in the velocity field and the resulting turbulence generation are both well captured. Perhaps surprisingly, the results indicate that the computational results are in many cases close to experimental uncertainties for the current exceptionally complex flow.

7 CONCLUDING REMARKS

The ability to model the formation and evolution of DDT kernels is of fundamental importance to a range of practical applications such as PDEs. In order to advance the subject, it is necessary to explore the sensitivity of the overall phenomena to the major closure elements of physical relevance to the problem.

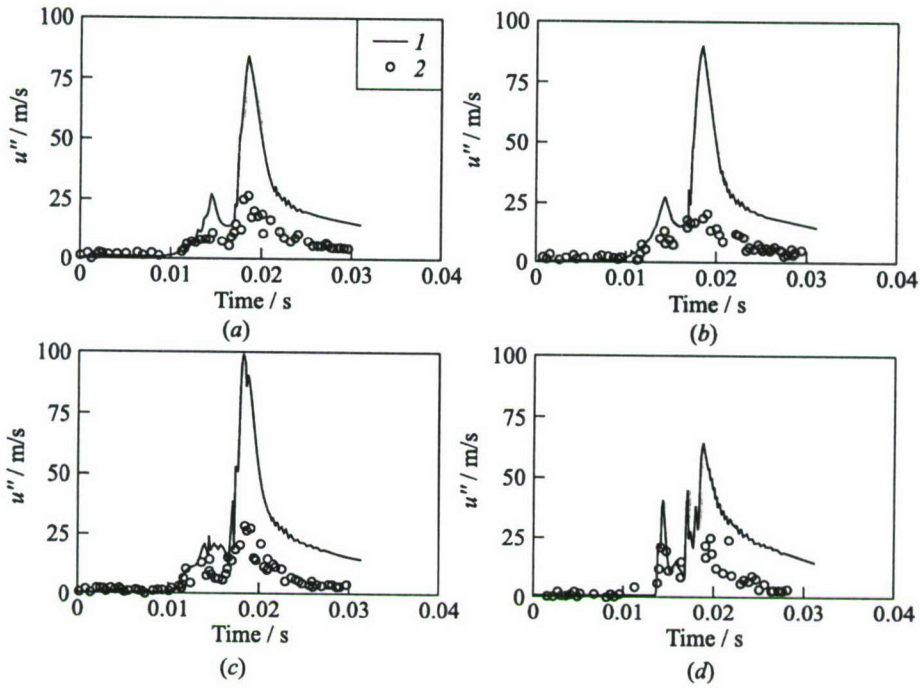

Figure 8 Comparison of computed (*1*) and measured (*2*) axial turbulence velocities at four measuring stations ((*a*) $Y = 9$ mm; (*b*) 18; (*c*) 36; and (*d*) 63 mm) along the plane $X = 515$ mm (100 mm downstream of the obstacle) for a turbulent gaseous explosion in a preexisting turbulence field.

Experimental work has shown that in many practical areas, the driving force for the transition can be found in the interaction of turbulence and chemistry, while in other cases it will reside with shock – (turbulent) boundary layer interactions. Both topics present similar — if not close to identical — modeling difficulties irrespective of the technique used for the flow field (e.g., LES or unsteady RANS). Nevertheless, it is naturally essential that a sensible reproduction of the flow field is achieved by the computational method of choice. In the absence of experimental data, such assessments are conjectural and the present work has used comparatively detailed data for turbulent gaseous explosion as a basis for comparisons. The experimental data set is naturally subject to significant uncertainties resulting from exceptionally difficult measurement conditions resulting from repeated flow acceleration/deceleration cycles. Despite such difficulties, the work has shown that the application of comprehensive higher moment closures to the modeling of the initial onset of DDT is technically possible and, furthermore, results in encouraging quantitative and qualitative agreement with

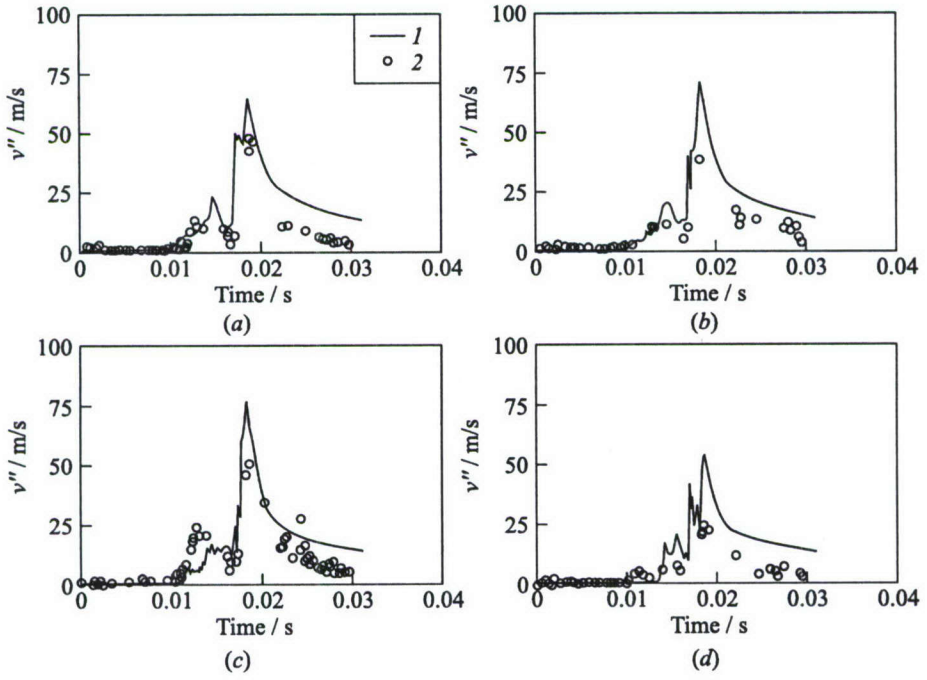

Figure 9 Comparison of computed (*1*) and measured (*2*) cross-stream turbulence velocities at four measuring stations ((*a*) $Y = 9$ mm; (*b*) 18; (*c*) 36; and (*d*) 63 mm) along the plane $X = 515$ mm (100 mm downstream of the obstacle) for a turbulent gaseous explosion in a preexisting turbulence field

measurements. It may be of interest to note that good agreement for other unsteady flows have also been obtained (e.g., [31]) using moment based methods. The turbulence–chemistry interactions can in principle be closed using a transported pdf approach combined with comprehensive autoignition chemistry. It is, however, likely that the scalar space required will be of order 20 species even for comparatively simple fuels (e.g., [32] and [33]) and, accordingly, the computational requirements are exceptional. The current finding is interesting as it suggests that improved closures for turbulence–chemistry interactions combined with the relative economy of unsteady RANS calculations may provide a route towards the modeling of obstacle/wall enhanced turbulence induced transition to detonation*.

*Note that the actual DDT process occurs when mean flow velocities attain the values of about 1000 m/s. It is considerably higher than the velocity range studied in the paper (200–300 m/s). (*Editors' remark.*)

ACKNOWLEDGMENTS

The authors wish to gratefully acknowledge the financial support of the EOARD under contract F61775-01-WE050 and the encouragement of Dr. F. Schauer, Dr. C. Raffoul, Dr. P. Ouzts, and Dr. G.D. Roy. The assistance of Miss S. Louloudi in preparing the manuscript is gratefully acknowledged.

REFERENCES

1. Roy, G.D. 1999. Pulsed detonation phenomena for air breathing propulsion. *14th Symposium (International) on Air Breathing Engines Proceedings.* ISABE Paper 99-7127.
2. Kailasanath, K. 2001. A review of PDE research — performance estimates. AIAA Paper No. 2001-0474.
3. Tishkoff, J.M., J.P. Drummond, T. Edwards, and A.S. Nejad. 1997. Future direction of supersonic combustion research: Air Force/NASA Workshop on Supersonic Combustion. AIAA Paper No. 97-1017.
4. Lindstedt, R.P., and H.J. Michels. 1988. Deflagration to detonation transition in alkane, alkene mixtures with O_2/N_2. *Combustion Flame* 72:63–72.
5. Lindstedt, R.P., and H.J. Michels. 1989. Deflagration to detonation transitions and strong deflagrations in alkane and alkene mixtures with air. *Combustion Flame* 76:169–82.
6. Arntzen, B.J., B. Hjertager, R.P. Lindstedt, W.P.M. Mercx, and N. Popat. 1995. Investigations to improve and assess the accuracy of computational fluid dynamic based explosion models. *J. Hazardous Materials* 45:1–25.
7. Hulek, T., and R.P. Lindstedt. 1996. Computations of steady-state and transient premixed turbulent flames using transported PDF methods. *Combustion Flame* 104:481–504.
8. Hulek, T., and R.P. Lindstedt. 1998. Joint scalar–velocity pdf modeling of finite rate chemistry in a scalar mixing layer. *Combustion Science Technology* 136:303–32.
9. Lindstedt, R.P., and E.M. Vaos. 2000. Modeling of mixing processes in nonisothermal and combusting flows. In: *Advances in Turbulence.* Ed. C. Dopazo. CIMNE Press 7:493–96.
10. Lindstedt, R.P., and T.S. Kuan. 2002. Prediction of steady and transient bluff body stabilized flames. *6th Workshop (International) on Measurements and Computations of Turbulent Nonpremixed Flames.* http://www.ca.sandia.gov/tdf/Workshop.html.
11. Catlin, C.A., and R.P. Lindstedt. 1991. Premixed turbulent burning velocities derived from mixing controlled reaction models with cold front quenching. *Combustion Flame* 85:427–39.

12. Colangelo, G., and R. P. Lindstedt. 2002. Higher moment based modeling of turbulence enhanced DDT kernels in confined fuel–air mixtures. In: *Advances in confined detonations*. Eds. G. Roy, S. Frolov, R. Santoro, and S. Tsyganov. Moscow, Russia: Torus Press. 3–11.

13. Sakthitharan, V. 1995. Time-resolved measurements of flame propagation over baffle-type obstacles. Ph.D. Thesis. Imperial College of Science, Technology and Medicine.

14. McCann, H. A. 1997. Time resolved measurements of propagating turbulent flames. Ph.D. Thesis. Imperial College of Science, Technology and Medicine.

15. Lindstedt, R. P., and V. Sakthitharan. 1998. Time resolved velocity and turbulence measurements in turbulent gaseous explosions. *Combustion Flame* 114:469–83.

16. Lindstedt, R. P., and H. A. McCann. 2001. Time resolved flow characteristics of confined turbulent gaseous explosions. *18th ICDERS Meeting Proceedings*. Seattle, WA.

17. Lindstedt, R. P., and E. M. Vaos. 1999. Modeling of premixed turbulent flames with second moment methods. *Combustion Flame* 116:461–85.

18. Lindstedt, R. P., and E. M. Vaos. 1998. Second moment modeling of premixed turbulent flames stabilised in impinging jet geometries. *27th Symposium (International) on Combustion Proceedings*. Pittsburgh, PA: The Combustion Institute. 957–62.

19. Haworth, D. C., and S. B. Pope. 1987. A pdf modeling study of self-similar turbulent free shear flows. *Physics Fluids* 30:1026–44.

20. Haworth, D. C., and S. B. Pope. 1986. A generalized Langevin model for turbulent flows. *Physics Fluids* 29:387–405.

21. Daly, B. J., and F. H. Harlow. 1970. Transport equations in turbulence. *Physics Fluids* 13:2634–49.

22. Jones, W. P. 1993. Turbulence modeling and numerical solution methods for variable density and combusting flows. In: *Turbulent reacting flows*. Academic Press. 309–74.

23. Jones, W. P., and P. Musonge. 1988. Closure of Reynolds stress and scalar flux equations. *Physics Fluids* 32:3589–604.

24. Borghi, R., and T. Mantel. 1994. A new model of premixed wrinkled flame propagation based on a scalar dissipation equation. *Combustion Flame* 96:443–57.

25. Bray, K. N. C., M. Champion, and P. A. Libby. 2001. Premixed flames in stagnation turbulence. Part V: Evaluation of models for the chemical source term. *Combustion Flame* 127:2023-40.

26. Lindstedt, R. P., and V. Sakthitharan. 1991. Modeling of compressible turbulent reacting flows. *8th Symposium on Turbulent Shear Flows*. Munich: Technical University.

27. Vaos, E. M. 1998. Second moment methods for turbulent flows with reacting scalars. Ph.D. Thesis. Imperial College of Science, Technology and Medicine.

28. Zhang, S., and C. J. Rutland. 1995. Premixed flame effects on turbulence and pressure related terms. *Combustion Flame* 102:447–61.

29. Hulek, T., and R. P. Lindstedt. 1996. Modeling of unclosed nonlinear terms in a pdf closure for turbulent flames. *J. Mathematical Computer Modeling* 24:137–47.

30. Tennekes, H., and J. L. Lumley. 1972. *A first course in turbulence.* MIT Press.

31. Durbin, P. A. 1995. Separated flows computations with the k–ε–v^2 model. *AIAA J.* 33:659–64.

32. Lindstedt, R. P., S. Louloudi, and E. M. Vaos. 2000. Transported PDF modeling of pollutant emissions in turbulent jet flames with comprehensive chemistry. *Proceedings of the Combustion Institute* 28:149–56.

33. Tang, Q., J. Xu, and S. B. Pope. 2000. Probability density function calculations of local extinction and NO production in piloted-jet turbulent methane–air flames. *Proceedings of the Combustion Institute* 28:133–39.

OPTIMIZATION OF ACCELERATORS OF DEFLAGRATION-TO-DETONATION TRANSITION

A. A. Vasil'ev

Efficient turbulence-generating device enhancing transition of confined slow flame to detonation has been suggested and tested for a number of gaseous fuel–oxygen and fuel–air mixtures at various initial pressures and tube diameters. Considerable shortening of the transition length as compared to the results in unblocked tubes was demonstrated. Some evidences on the effect of multipoint ignition on reduction of the transition length are reported.

1 INTRODUCTION

According to current knowledge, fast chemical reactions can be initiated in a combustible medium by three ways: (1) when a weak initiator ignites the mixture and low-velocity turbulent combustion (deflagration) is observed; (2) when the mixture is ignited with a weak initiator and then due to natural or artificial flame acceleration, the subsequent transition from deflagration to detonation occurs; and (3) when a strong initiator gives rise to a self-sustaining detonation wave (DW) in immediate proximity to the initiation point.

For cylindrical and spherical flames, the autoturbulization of the initially smooth flame front is the main reason of its acceleration and transition from laminar propagation to turbulent mode. Experimental evidences of deflagration-to-detonation transition (DDT) for cylindrical and spherical flames (due to autoturbulization only) are unknown. For plane flames in tubes, autoturbulization and wall effects supplement each other, and, at some conditions, DDT can be observed, in particular in long tubes and in fuel–oxygen mixtures. The degree of flame acceleration and the final mode of flame propagation are determined by many factors such as mixture sensitivity, initial pressure and temperature, flame topology, turbulence scales, wall roughness, etc.

The other possible reason of turbulence enhancement and increase in the degree of flame acceleration (in addition to flame autoturbulization) is the arti-

ficial forcing of the flame-induced flowfield with different obstacles, diaphragms, screens, wire meshes, Shchelkin spirals, spiral scrubbers, rods, etc. Such turbulence generators and amplifiers with repetitive elements are widely used in laboratory experiments, but they are not universal for different tubes and mixtures, especially for fuel–air systems. Positioning of repetitive elements at optimal locations may stimulate the development of high-intensity turbulence and result in efficient build-up of energy release, thus promoting DDT.

Strong initiation of DW was discussed at previous Colloquia* and is not discussed in this paper.

2 PRINCIPLES OF DDT ACCELERATION

Two aspects must be taken into account for "weak" ignition of combustible mixture in a tube.

First, the flame produced by a point igniter is spherical on the initial stage up to the moment of flame collision with tube walls†. Some distance is also needed for transformation of spherical flame to quasi-plane flame. For example, at distance L from the ignition point along a tube axis, the deviation of the curved flame front from the planar shape may be defined as $L(1-\cos\phi)/d$, where d is the tube diameter, ϕ is the angle at which the wave front is seen from the initiation point. If this deviation is required to be less than some small value δ, then L/d should satisfy the condition: $L/d \geq (1+4\delta^2)/8\delta$. For example, at $\delta = 1\%$, L/d should exceed 12. The ratio L/d can be reduced by using special generators of quasi-plane waves (GQPW). For obtaining DDT, a special DDT-accelerator must be placed downstream from the GQPW.

Second, to construct and optimize the DDT-accelerator, it is very important to know the type of accelerator elements, their dimensions, their orientation in tube cross-section, their displacement along the tube, etc. This issue is important not only for laboratory-scale tests, but also for new technologies (e.g., for pulse detonation engines operating on fuel–air mixtures). Some relevant aspects are discussed in this paper with term 'Optimization' used for maximal reduction of the DDT distance.

It is well known from the theory of shear layers (see, e.g., [1]) that obstacles in the flow give rise to turbulent shear layers. A simple scheme of Fig. 1 shows

*See, e.g., Vasil'ev, A. A., S. A. Zhdan, and V. V. Mitrofanov. 1999. Detonation initiation in gaseous and heterogeneous systems. In: *Gaseous and heterogeneous detonations: Science to applications*. Eds. G. Roy, S. Frolov, K. Kailasanath, and N. Smirnov. Moscow, Russia: Enas Publ. 25–38. (*Editors' remark.*)

†Actually, the flame is not spherical from the very beginning due to the flame-induced flow which elongates the flame along the tube axis. (*Editors' remark.*)

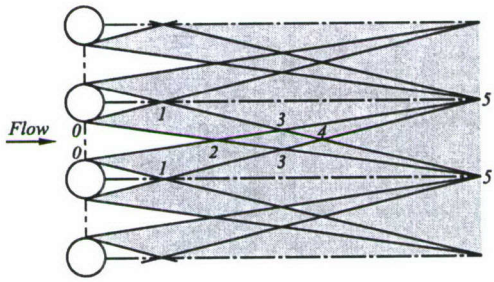

Figure 1 Schematic of turbulent shear layers behind obstructions

the turbulization zones behind several obstacles located in the same cross-section of the tube. The layers start from the periphery points *0* of obstacle and grow in downstream direction. Internal and external boundaries of a turbulent shear layer may be approximated by linear functions. Internal boundaries of the shear layer at each obstacle intersect at points *1* on the flow axis behind the obstacle at a distance $x_1 = d/(2\tan\beta)$, where d is the diameter of obstacle, and β is the inclination angle of the internal boundary of the shear layer from the flow axis. Starting from x_1, the shear layers interact with each other and the flow becomes fully turbulent behind each obstacle ('wake' turbulence).

If two neighboring obstacles are located at some distance, s, from each other, then the external boundaries of neighboring obstacles intersect at points *2* at the axial distance $x_2 = s/(2\tan\alpha)$, where α is the inclination angle of the external boundary of the shear layer from the flow axis. The undisturbed region *0–2–0* from the obstacles to cross-section x_2 is referred to as the zone of initial turbulence. Starting from x_2, the flow becomes turbulent all throughout the tube cross-section. Formation of isotropic turbulent flow behind the obstacles occurs up to points *5* with $x_5 = (d+2s)/(2\tan\alpha)$. After points *5*, the turbulence is only decaying (zone with self-similar turbulence decay). Thus, the region from x_2 to x_5 ('transition' zone) may be considered as the optimal location of next repetitive obstacles to further increase turbulence intensity.

From the optimization point of view, it is evident that distance x_1 must be equal to x_2. As a result, the following relationship must be valid: $d/s = \tan\beta/\tan\alpha \approx 1.5$ and $x_5 \approx 10d$. If the obstacles at some cross-section form the configuration similar to a wire mesh (grid), then the penetration factor defined as $\mu = s^2/(s+d)^2$ is $\mu \approx 0.16$ at optimal conditions. It should be mentioned that in aerodynamic wind tunnel, wire meshes with $\mu \approx 0.4$ are usually used to form the flow with low-intensity turbulece. At $\mu < 0.4$, the flow between the obstacles is accelerated to form jets and therefore high-intensity turbulence is generated, that is undesirable in a wind tunnel but useful for DDT.

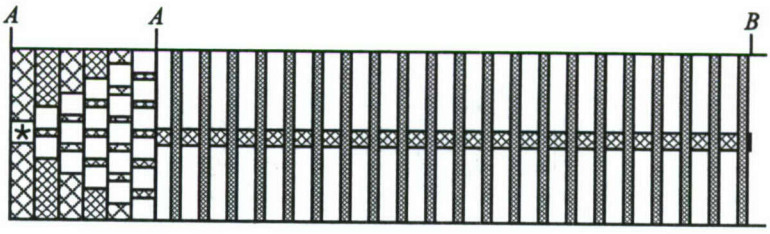

Figure 2 Schematic of the DDT-accelerator: AA — special device to expedite formation of a planar flame and AB — rows of obstructions. Symbol $\star$ denotes initiator position

3 CONSTRUCTION OF DDT-ACCELERATOR

The primary task of a DDT-accelerator is to accelerate the flame front from a laminar burning velocity of about dozens centimeters per second up to the detonation velocity of about two kilometers per second within the limited length of a detonation tube. It is commonly accepted that for providing such a great jump in the flame propagation velocity (up to 5 orders of magnitude) and to diminish the DDT length, the DDT-accelerator should use the obstructions of one specific geometry (e.g., either spirals, or disks, or rods). In the present work, the DDT-accelerator was constructed as a complex multisectional device consisting of obstructions of various shapes.

The artificial increase of turbulence intensity can be achieved by placing a number of repetitive obstacles along the direction of wave propagation. In addition, positions of similar obstacles in neighboring cross-sections must be shifted (turned) one relative to another to enhance turbulization process along the direction of wave propagation. The "turning" procedure is recommended especially for initiation of near-spinning detonations.

Lengths of individual sections, dimensions of the accelerating obstructions, and their mutual arrangement were selected from a condition of their maximum contribution to the effectiveness of the DDT-accelerator as a whole. Schematic of GQPW (AA) and multisectional DDT-accelerator (AB) for the tube geometry is demonstrated in Fig. 2. The design features of the Multisectional DDT-Accelerator (MSA) and GQPW represent technological "know how" and are protected by the patents of Russia and copyright certificates of the USSR [2–4].

4 EXPERIMENTS

The sections of tubes with MSA had transparent windows for optical registration along the side surface. The combustible mixtures were ignited by a weak

electrical igniter (similar to automobile spark plug) on the left end of the tube on its axis (symbol $\star$ in Fig. 2). The use of a weak electric discharge rather than a thermal igniter was dictated by a necessity of synchronization with camera (high-velocity photorecorder optically conjugated with the Schlieren system IAB-458). With this sort of initiator, no DDT was observed in the absence of GQPW and MSA for tested mixtures within the whole range of tested pressures. The energy of discharge was more than an order of magnitude lower than the critical energy, E^*, for detonation initiation. When triggered, the discharge created a shock wave (SW) with the velocity insignificantly exceeding the sound velocity. The SW magnitude was noticeably less than the magnitude required for shock-induced DDT to be obtained, when energetic exothermic centers arise in the region between SW and flame.

The DW velocity was measured by ionization gauges mounted along the tube. The signals from the gauges were directed through amplifiers to frequency meters operating in the mode of measuring time intervals. The detonation wave was considered stable if its velocity, D, had a scatter not exceeding 2% at the measuring bases between five ionization gauges. For fuel–air mixtures, the detonation tubes of $d_t = 100$ and 250 mm in diameter and 6 m long were used. The measurements of cell size were carried out by a conventional smoked-foil technique with metal foils mounted on an interior tube surface (foils 200 mm in length and πd_t in width were used). Track prints on the smoke layer were covered (for conservation) by a glue based on the plexiglas dissolved in dichlorethane.

5 EXPERIMENTAL RESULTS

Quasi-plane flames were investigated in tubes of constant cross-section of diameter $d_t = 20$–250 mm for gaseous mixtures of acetylene, hydrogen, ethylene, propane, methane, and vapors of acetone, gasoline, hydrogen peroxide, dimethylhydrazine, ammonia, etc. These fuels were mixed either with oxygen or air. Various methods of artificial turbulization of flame front were used. The search of an efficient MSA was carried out with different types of turbulizers, various blockage of tube cross-section, and a variety of laws of spatial distribution of the turbulizing elements in a tube cross-section and along the tube. The most efficient MSA of DDT was found for each individual tube and mixture. For example, for the stoichiometric methane–air mixture, the MSA-assisted DDT was obtained with a weak initiator in a laboratory-scale tube of diameter $d_t = 100$ mm. This mixture was the most insensitive mixture in the experiments. Nevertheless, the DDT length obtained was as short as $L_{\mathrm{DDT}} \approx 2500$–$3000$ mm $\approx (25$–$30)d_t \approx 10a$, i.e., spining detonation was obtained (here, a is the detonation cell width). Thus, DW in this mixture was formed at a distance of the order of 25–30 tube diameters.

Successful DDT acceleration was also obtained for other fuel–air and fuel–oxygen mixtures. For example, detailed experiments with $C_2H_2 + 2.5(O_2 +$

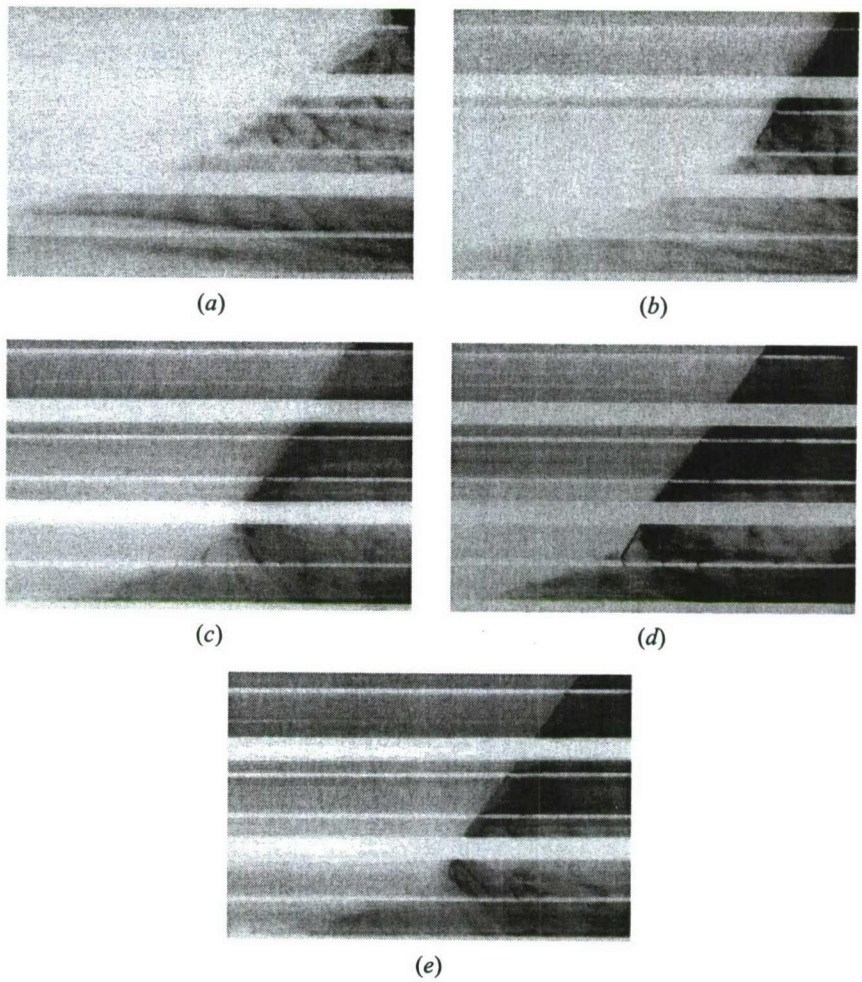

Figure 3 Streak records of DDT in stoichiometric hydrogen–air (a–d) and acetylene–air (e) mixtures at different initial pressures: (a) $P_0 = 0.3$ atm, (b) 0.5, (c) and (e) 1.6, and (d) $P_0 = 2.0$ atm. The records were obtained at the initial section of the tube 250 mm in diameter

zN_2) and C_2H_2–air mixtures were carried out. For the first mixture, the initial pressure, P_0, and amount of nitrogen, z, were varied in the ranges 0.04–1.40 atm and 0–3.76, respectively. For the second mixture, the equivalence ratio, ϕ, was varied at constant pressure $P_0 = 1.0$ atm. In this case, concentration limits of DDT were found in terms of ϕ.

The experimental values of $a(P_0)$, $a(z)$, $a(\phi)$, etc., obtained with the help of MSA, correlate well with calculated data [5] and data of other authors. Note

that the experimental dependence $a(\phi)$ has the typical U-shaped form similar to the dependence $a(c)$, where c is the molar fuel concentration.

It has been shown experimentally that MSA of DDT allows obtaining detonations in a broad range of fuel concentrations. For example, the data for acetylene–air mixtures demonstrate that DW is readily obtained for the fuel-lean mixtures, at $\phi_l < \phi < 1$, where ϕ_l is a lower detonability limit. At $\phi < \phi_l$, high-speed combustion rather than detonation was observed. With fuel-rich mixtures, $\phi > 1$, detonation is obtained in a wide range of fuel concentrations. The cell size a decreases with ϕ up to some minimum value in the vicinity of $\phi \approx 1.5$, and then $a(\phi)$ increases. Beginning approximately from $\phi \approx 2.0$, the amount of soot in detonation products increases noticeably: at $\phi \approx 2.5$, a soot layer of about 2–3 mm thick forms on tube walls that makes difficult the analysis of track prints on the smoked foil.

Figure 3 shows some streak-records of DDT in stoichiometric hydrogen–air and acetylene–air mixtures at different initial pressures. The records are obtained at the initial section of tube of $d_t = 250$ mm (in MSA region). The results of these experiments are presented in Fig. 4, with L_{DDT} measured from the begining of a multisectional DDT-accelerator mounted after GQPW. One can see that at $P_0 = 1.0$ atm, the system comprising GQPW + MSA ensures DDT in stoichiometric acetylene–air and hydrogen–air mixtures at a distance of about 450 mm ($\approx 1.8 d_t$).

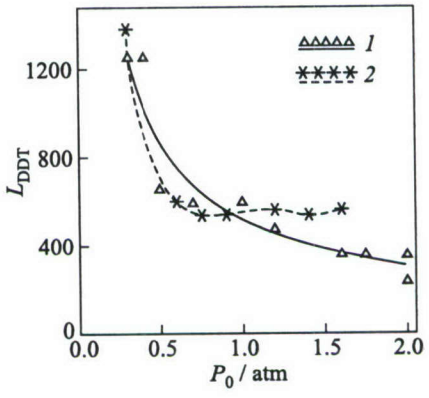

Figure 4 Measured DDT length as a function of pressure in a tube 250 mm in diameter for stoichiometric mixtures: H_2–air (*1*) and C_2H_2–air (*2*)

The effective DDT-accelerator avoids the use of a powerful explosive charge to initiate detonation. The DDT-distance correlates with the hazard potential of different explosive mixtures. At weak initiation, the critical ignition energy, E_{flame}, is usually used as the main hazard parameter. The quantitative criterion of DDT conditions has not been formulated yet because of the stochastic and multiparametric character of DDT phenomenon. Initiation of DW is also a multiparameter process, but for strong, point initiators, only one parameter — the critical detonation initiation energy, E^*, — may be considered as a measure of hazard potential: the less E^*, the more hazardous is the combustible mixture.

In this study, acceleration of flame front was obtained both due to its artificial turbulization during propagation through the obstructed area and due to

spatial redistribution of mixture igniters. In the latter case, the GQPW cannot be used, and DDT is obtained with MSA only. It has been shown that DDT can be successfully obtained with the help of multipoint ignition even under conditions when a single (summarized) igniter fails to ensure flame propagation with noticeable acceleration. For example, in mixture $2H_2 + O_2$, it was observed that at $P_0 = 2.5$ atm, a weak discharge did not initiate detonation; while, when using the multipoint ignition scheme, the DDT-phenomenon was observed even at $P_0 = 0.8$ atm. Thus, spatial distribution of igniters allows under certain conditions to considerably (by orders of magnitude) reduce the DDT length [6].

6 CONCLUDING REMARKS

A high-efficiency DDT-accelerator for transition of slow combustion to detonation has been constructed and tested for a number of explosive fuel–oxygen and fuel–air mixtures. Tubes of various diameters were used: from 20 to 250 mm. Considerable shortening of DDT length with using the DDT-accelerator was demonstrated. At weak initiation, the effect of significant (by orders of magnitude) decrease in the DDT length with spatial distribution of igniters has been observed.

ACKNOWLEDGMENTS

This work was supported in part by the Russian Foundation for Basic Research (Grant 02-01-00551).

REFERENCES

1. Abramovich, G. N., S. Yu. Krasheninnikov, A. N. Sekundov, and I. P. Smirnova. 1974. *Turbulent mixing of gaseous jets.* Moscow, Russia: Nauka.
2. Vasil'ev, A. A., S. B. Vorob'ev, Yu. A. Nikolaev, and I. I. Fridman. 1990. Device for cleaning the electrodes of electrical filters. Certificate of recognition. (In Russian.)
3. Vasil'ev, A. A., Yu. A. Nikolaev, A. V. Trotsyuk, and I. I. Fridman. 1992. Device of pulse combustion. Certificate of recognition. (In Russian.)
4. Ulianitsky, V. Yu., A. A. Vasil'ev, T. P. Gavrilenko, A. N. Krasnov, Yu. A. Nikolaev, and N. I. Podenkov. 1993. Barrel of a device for powder covering of surfaces with the use of gaseous detonations. Patent. (In Russian.)
5. Vasil'ev, A. A. 1995. *Near-critical regimes of gaseous detonation.* Novosibirsk.
6. Bannikov, N. V., and A. A. Vasil'ev. 1992. Multipoint ignition of a gas mixture and its influence on deflagration to detonation transition. *Combustion Explosion Shock Waves* 28(3):65–69.

NEAR-LIMIT PROPAGATION OF DETONATIONS IN ROUND TUBES

O. G. Penyazkov

Experimental study of the detonation structure near propagation limits was performed to evolve the quantitative criteria for the limits of stable and unstable detonations in round tubes. Observations were made with ion gages and pressure transducers to measure detonation velocity, chemical induction time, and pressure. Smoked foils have been applied for monitoring the detonation structure. Velocity history and reaction zone structure of spinning waves were investigated in detail. Below the limits, chemical reactivity of the mixture was explored by reflection of the leading shock front of decaying detonation from the end-flange of the tube. For different stages of the detonation decay, the ignition delay time behind the reflected shock front was measured by using the piezoelectric pressure gage. On the basis of the results obtained, two criteria were proposed for estimating the ranges of stable and unstable detonations.

1 INTRODUCTION

Different approaches based on experiments in finite length tubes have been established to define the conditions of detonation failure. Manson *et al.* [1] have proposed the limits to be determined from the condition of wave stability; they defined the stability on the basis of the fluctuations of local velocities from the mean value. Another approach is based on the analysis of the three-dimensional structure of detonation. Shchelkin [2] has suggested that the limits in tubes should be determined by the appearance of the single-head detonation structure. From measurements of detonation cell size, λ, in a smooth tube of diameter d, three different criteria were proposed. The first is the criterion $\lambda = \pi d$ [3], the second and the third ones are $\lambda = d$ [2] and $\lambda = 1.7d$ [4], respectively. Dupre *et al.* [5] have found that, for velocity fluctuation $\Delta V/V_{CJ} \approx 0.1$, the limit in cylindrical tube follows the criterion $\lambda = \pi d$, where V_{CJ} is the Chapman–Jouguet (CJ) detonation velocity.

One of the drawbacks of these approaches is that there is no direct link of the resulting correlations to the chemical kinetic rates relevant to the explosive mixture. At the same time, detonability limits are not only the specific property of the explosive mixture itself but depend on the boundary conditions, as well. Furthermore, the limits should also reflect the combined effects of reaction-kinetic behavior of the mixture and hydrodynamic features of the flow corresponding to the lowest stable detonation mode, i.e., single-head spinning detonation. Nevertheless, no generally accepted correlation between chemical properties of the mixture, detonation velocity, and characteristic dimensions of detonation tubes has been established so far for estimating the composition and pressure ranges for different near-limit modes of the detonation propagation. The objective of this work was to evolve such quantitative criteria for ranges of stable and unstable detonations in round tubes. Recent results on the propagation dynamics and reaction zone structure of spinning detonations are reported.

2 EXPERIMENTAL DETAILS

The near-limit propagation and failure of the detonation wave were investigated in the round, steel detonation tube 5.2 m long with inner diameter of 25.3 mm (Fig. 1). The aspect ratio of the tube, L/d (length-to-diameter ratio), was more than 200 to ensure adequate spacing for the observation of stable detonation. The 60-millimeter front section contained the driver gas, usually the stoichiometric $C_2H_2 + 2.5O_2$ mixture. This initiating mixture was separated from the experimental section by a brass diaphragm. The pressure of the driver gas was usually somewhat higher than that of the test mixture in order to initially overdrive the detonation. To secure the stable velocity regime in two measuring parts of the detonation tube, a minimum pressure ratio between the driver and test gases was maintained prior to initiation.

For all experiments, a combustible gas mixture 3.5% C_2H_2 + 26.5% O_2 + 70% Ar at different initial pressures and ambient initial temperature was used. The mixture was prepared by the method of partial pressures and kept for two days before use. Prior to the experiment, the detonation tube was pumped out twice to provide the pressure of $\sim 10^{-2}$ mm Hg. To lower the possible effect of parasite impurities, the tube was purged with the test gas before the secondary pumping.

Observations were made with ion gages and pressure transducers to measure detonation velocity and pressure, and large smoked foils to monitor the detonation structure. The measuring part of the tube was equipped with nine ports placed at 39.75-millimeter intervals. The step between ports was equal to a half-length of the spin pitch, $\pi d/2$, of spinning detonation. Each port consisted of four ion gages. The gage positions and their orientation with respect to the

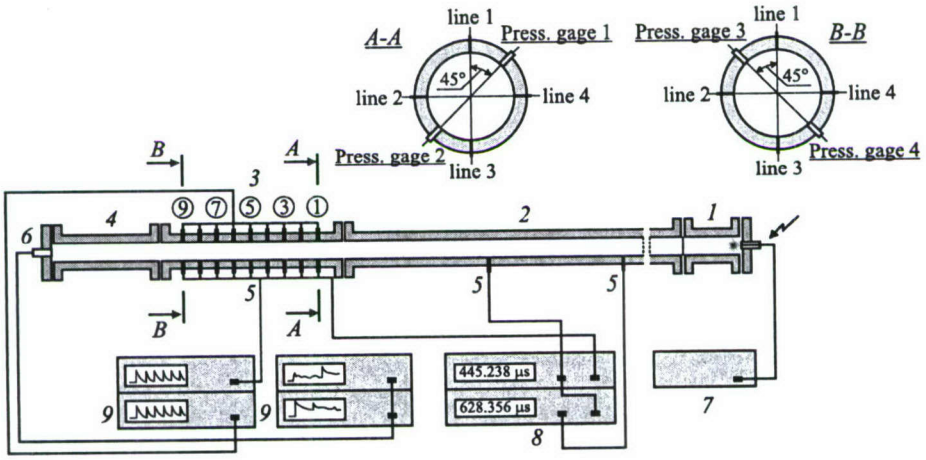

Figure 1 Schematic of the experimental setup: *1* — ignition chamber; *2* — detonation tube; *3* — test section; *4* — section for smoked-foil measurements; *5* — ion gages; *6* — pressure transducer; *7* — ignition unit; *8* — time detector; and *9* — digital oscilloscopes

tube axis are shown in Fig. 1. Thus, the detailed velocity evolution of the arising reaction zones and shock fronts could be measured over a 31.6-centimeter test section. A 290-centimeter long section of the tube was used in order to obtain soot imprints of detonation travel. The section was connected to the main channel without changing the open flow area and equipped with a mechanical system to fix the smoked foils. The end-flange of the tube was equipped with a piezoelectric pressure transducer to perform pressure, velocity, and chemical induction time measurements. The signals registered were recorded on storage oscilloscopes interfaced with a personal computer.

The detonation limits were found in terms of initial pressure. The limit was easily recognized: in the detonability region, the initially overdriven detonation in the test mixture settled to the final steady-state velocity, but below the limiting pressure, the detonation propagation suddenly failed. The detonation structure in the latter case disintegrates into a precursor shock wave and a deflagration front propagating in the shock-compressed gas. The leading shock wave eventually decays. The detachment zone between the shock and combustion waves rapidly grows and, depending on the initial pressure and mixture composition, the reaction front tends to transit to the slow deflagration mode, or highly unstable near-limit phenomena, like "galloping" detonation, accompanied by eventual reignition and decay of detonation. Nevertheless, flow parameters inside the detachment zone, i.e., pressure, temperature, and velocity, sometimes are similar to those existing in the detonation structure before the decay. Chemical reactivity of the mixture under these transient conditions was explored by

reflection of the leading shock wave from the end-flange of the tube (Fig. 1). For different stages of the detonation destruction, the chemical induction times behind the reflected shock front were measured by using the piezoelectric pressure gage.

3 EXPERIMENTAL RESULTS

The limiting initial pressure for a confined detonation in a round tube of diameter d, below which a detonation could not propagate, corresponded to the criterion for detonation limits in round tubes $\lambda \cong \pi d$.

As the critical value of initial pressure was approached, single-head spinning detonations were observed and the detonation velocity decreased rapidly. Figure 2 illustrates the typical soot imprints of single-head spin detonation structure propagating along the round tube near the extinction limit. As seen in Fig. 3, the detonation velocity deficit as compared with the CJ velocity reaches the maximum at the pressure range I (spinning detonation), and decreases slowly as the initial pressure grows. The effect of initial pressure is substantial for marginal detonations when the cell size of the mixture is larger than one tube diameter. In this case, the intensification of energy release due to interactions of transverse waves with the tube wall is the main mechanism for maintaining the wave propagation at a higher velocity. Under these conditions, the influence of viscous effects at the walls on the detonation velocity is the largest. As the initial pressure or tube cross-section grow, the new zones of high-energy release formed by collisions of transverse waves in the bulk of the flow gradually start to dominate the detonation propagation. In a high-pressure region, the energy

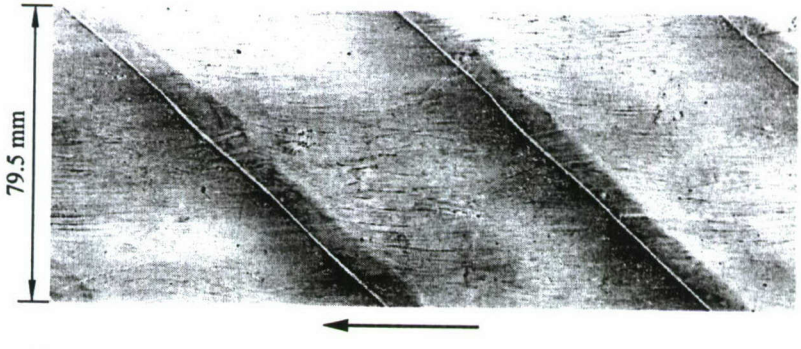

Figure 2 Negative copy of smoked film corresponding to propagation of spinning detonation: initial pressure $P_0 = 45.6$ mm Hg; 3.5% C_2H_2 + 26.5% O_2 + 70% Ar mixture. Arrow shows direction of wave propagation

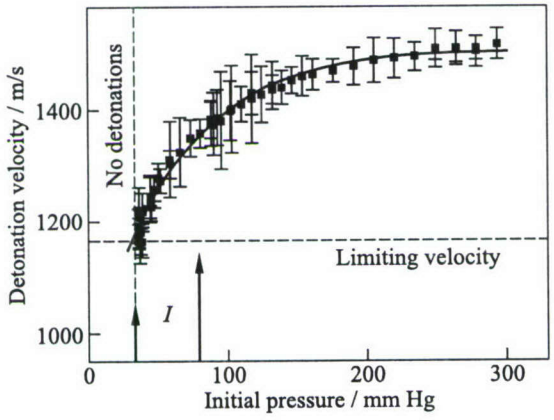

Figure 3 Detonation velocity vs. initial pressure for 3.5% C_2H_2 +26.5% O_2 + 70% Ar mixture

release in the bulk of the flow determines the structure and velocity of detonation. Consequently, the detonation velocity deficit decreases slowly and tends to the natural limit, which is defined by boundary-layer effects and heat loss to the wall.

Significant velocity fluctuations of the reaction front were recorded over the test sections for single-head spin detonations. Figure 4 illustrates the typical dynamics of a spinning wave that was measured by means of two lines of ion gages mounted along the tube. Clearly, the detonation velocity exhibits the oscillatory behavior — a property that becomes more pronounced near the propagation limits. The flame velocity in the marginal detonation periodically attains a maximum value, V_{max}, with further decay to a minimum value, V_{min}. Figure 5 shows the ranges of the flame velocity attained within the spin pitch during

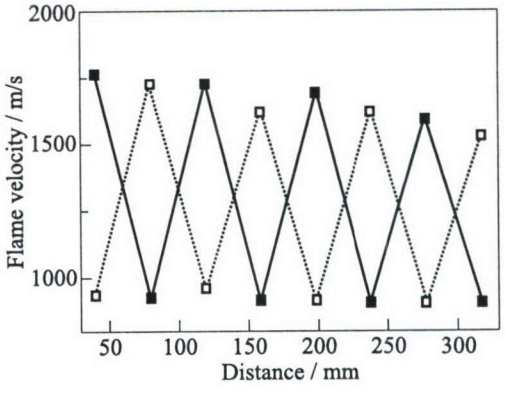

Figure 4 Measured history of flame velocity in the single-head spinning detonation propagating along a round tube for 3.5% C_2H_2 + 26.5% O_2 + 70% Ar mixture at initial pressure of P_0 = 37 mm Hg. Solid and open symbols correspond to velocity measurements by two different lines of ion gages

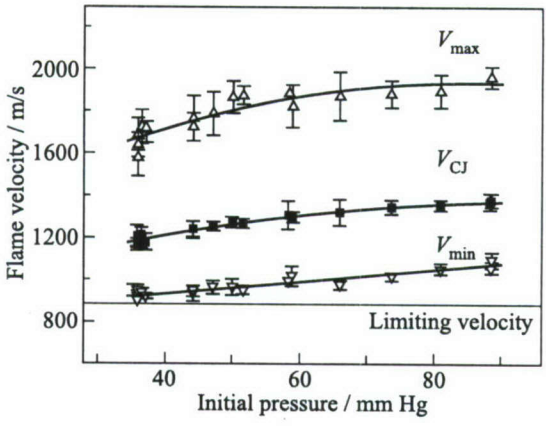

Figure 5 Ranges of flame velocity for 3.5% C_2H_2 + 26.5% O_2 + 70% Ar mixture within a spin pitch of the spinning detonation vs. initial pressure

propagation of the spinning detonation wave. Quantitatively, the ranges of the measured velocities are $(0.77–1.41)V_{CJ}$, that agrees well with predictions of Lefebvre *et al.* [6] for marginal detonations.

Ion gages also provide the tool for monitoring the reaction zone shape during detonation travel. The measured dependence of the flame curvature, S_{fl}, on the initial pressure of the mixture is presented in Fig. 6. The flame curvature was defined as the distance between the near and far edges of the reaction front along the tube. As seen from the figure, at high pressures, the detonation front can be approximately considered as planar. For single-head spinning detonations, the flame curvature reaches the peak value $S_{fl} \cong 1.1R$, where R is the tube radius. This is consistent with earlier observations of Ul'yanitsky [7] who studied the spatial shape of single-head spinning detonations by using pressure transducers. For the maximum curvature of the leading shock front, S_{sh}, of the spinning detonation wave, his measurements gave the same value: $S_{sh} \cong 1.1R$.

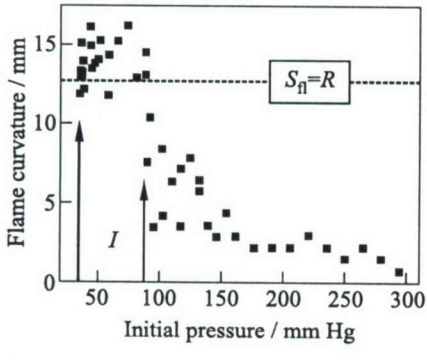

Figure 6 Flame front curvature of detonation wave vs. initial pressure of 3.5% C_2H_2 + 26.5% O_2 + 70% Ar mixture. Range *I* corresponds to single-head spinning detonations

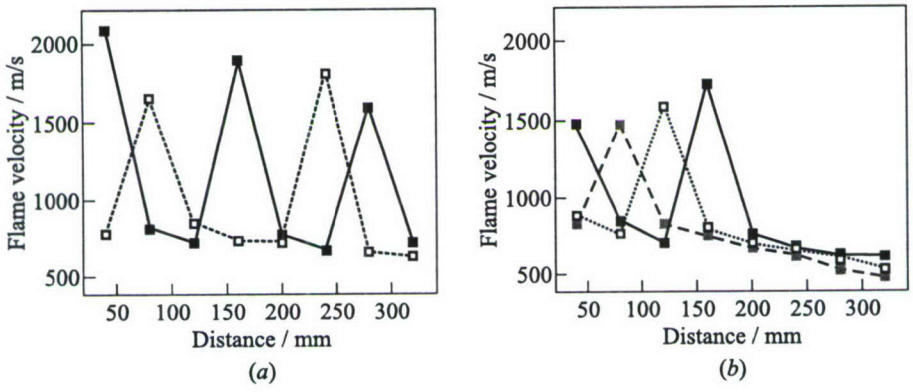

Figure 7 Typical velocity histories of the decay of the spinning detonation along the test section below the pressure limit for 3.5% C_2H_2 + 26.5% O_2 + 70% Ar mixture at initial pressure (*a*) P_0 = 35.9 mm Hg; and (*b*) P_0 = 35.3 mm Hg. Solid and open symbols correspond to velocity measurements by two different lines of ion gages

Below the pressure limit, the detonation decays. The leading shock front decouples from the reaction front, and strong interaction between shock and flame fronts disappears. The structure of the spinning detonation wave vanishes and the reaction front no more exhibits the rotary motion along the circumference of the tube. The flame first acquires a characteristic "tulip" shape and then transforms to a regular turbulent flame.

Figure 7 shows typical stages of detonation destruction in the test section. As seen, the frequency of flame velocity oscillations decreases (Fig. 7*a*) and the reaction front attains the final quasi-steady-state turbulent flame velocity (Fig. 7*b*). Under these transient conditions, normal reflection of the leading shock wave can still result in secondary ignition of the mixture. To measure the chemical induction time behind a reflected shock wave, pressure transducers have been used. In addition, the conventional smoked-foil technique has been employed to visualize self-ignition phenomena near the end-flange of the tube. Figure 8 presents pressure (*a*) and smoked-foil (*b*) records obtained in the same run. The induction period was defined as the time interval between the beginning of the normal reflection of the incident shock wave and the second pressure spike caused by self-ignition of a shock-compressed reactive mixture. The distance from the reflecting wall to the location where the self-ignition occurs (referred to as the induction length behind the reflected shock wave), was also determined from the smoked-foil records. The self-ignition process in the precompressed reactive mixture is accompanied by intense shock waves or secondary detonations which leave traces on a soot layer (Fig. 8*b*). When the arising secondary detonation overtakes the front of a reflected shock, the cellular structure corresponding to the overdriven detonation appears on the smoked foil.

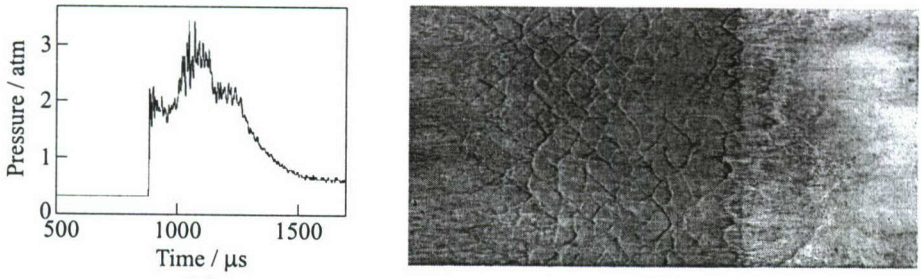

Figure 8 Pressure (a) and smoked-foil (b) records of gas self-ignition behind the shock wave reflected from the end-wall for 3.5% C_2H_2 + 26.5% O_2 + 70% Ar mixture

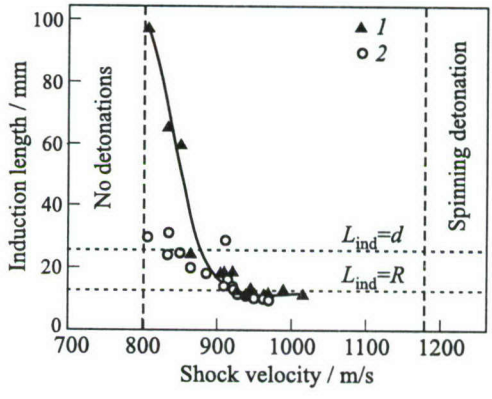

Figure 9 Induction zone length vs. velocity of the leading shock wave: *1* — induction time measurements; and *2* — smoked foils

Clearly, the intensity of a transient shock wave heading the primary decaying spinning detonation depends on the stage of detonation failure. To estimate the induction length behind this shock wave, a simple relation: $L_{\text{ind}} = \tau_{\text{ind}} V$ was used, where τ_{ind} is the chemical induction time corresponding to the stagnation temperature and pressure of the gas flow behind the shock, and V is the shock velocity*. Figure 9 shows the estimated induction length vs. shock velocity of decaying detonations. As seen, most of the data fall in the region for which the induction length is lower than tube diameter, $d = 2R$, and larger than tube radius, R. As the shock velocity approaches the limiting velocity of spinning

*The induction length behind a propagating shock wave is usually determined as the product of the induction time, based on post-shock flow temperature and pressure, and the post-shock velocity in the frame of reference attached to the shock. (*Editors' remark.*)

detonation (see Fig. 3), the induction lengths approach the value $L_{\text{ind}} \approx 0.8R$. The extrapolation of this data provides the criterion for the range of stable detonations in round tubes:

$$\tau_{\text{ind}} V \leq 0.8R$$

For unstable near-limit propagation phenomena, like "galloping detonation," another criterion could be proposed:

$$0.8R < \tau_{\text{ind}} V \leq d$$

These relationships include chemical properties of the mixture, shock wave velocity, and characteristic dimensions of the channel, and may be useful for the analyses of limiting conditions governing propagation of stable and unstable detonations in case of tubular confinements.

4 CONCLUDING REMARKS

Quantitative criteria governing the limits of stable and unstable detonations in round tubes have been suggested. These criteria are based on the detailed experimental studies of marginal acetylene–oxygen–diluent detonations and link key parameters responsible for propagation behavior of the wave near extinction limits. The proposed relationships include ignition delay time corresponding to stagnation temperature and pressure of the gas flow behind the leading shock front, leading shock wave velocity and diameter, or radius, of the tube. These criteria provide a tool to estimate the composition and pressure ranges of stable and unstable detonations in case of tubular confinements.

ACKNOWLEDGMENTS

This work was partially funded by INTAS Grant No. 99-00464.

REFERENCES

1. Manson, N., C. Brochet, J. Brossard, and Y. Pujol. 1963. Vibratory phenomena and instability of self-sustained detonations in gases. *9th Symposium (International) on Combustion Proceedings*. London: Academic Press. 461.
2. Shchelkin, K.I. 1959. Two stages of unstable combustion. *Sov. J. Experimental Theoretical Physics* 36:600.

3. Kogarko, S. M., and Ya. B. Zeldovich. 1948. Detonation of gaseous mixture. *Dokl. Acad. Nauk SSSR.* (*Transaction of the USSR Academy of Sciences*) 63:553.

4. Moen, I. O., M. Donato, R. Knystautas, and J. H. Lee. 1981. The influence of confinement on the propagation of detonation near the detonability limits. *18th Symposium (International) on Combustion Proceedings.* Pittsburgh, PA: The Combustion Institute. 1615.

5. Dupre, G., R. Knystautas, and J. H. Lee. 1986. Near-limit propagation of detonation in tubes. In: *Dynamics of explosions.* Eds. J. R. Bowen, J.-C. Leyer, and R. I. Soloukhin. Progress in astronautics and aeronautics ser. New York, NY: AIAA Inc. 106:244–59.

6. Lefebvre, M. H., J. W. Weber, and E. S. Oran. 1997. Numerical simulations of a marginal detonation: Wave velocities and transverse wave flow structure. In: *Fluid mechanics and its applications. The IUTAM Symposium Proceedings.* Eds. M. Champion and B. Deshaies. Dordrecht–Boston–London: Kluwer Academic Publ. 39:347–58.

7. Ul'yanitsky, V. Yu. 1980. Experimental study of bulk structure of spin detonation. *Combustion Explosion Shock Waves* 16(1):105.

INITIATOR DIFFRACTION LIMITS IN A PULSE DETONATION ENGINE

C. M. Brophy, J. O. Sinibaldi, D. Netzer, and K. Kailasanath

A coaxial initiator geometry, currently being used on an integrated pulse detonation engine (PDE) system, is being characterized by both experimental and computational efforts. The goal of the parallel research efforts is to develop the ability to accurately model and predict the detonation diffraction process from a small "initiator" combustor to a larger diameter main combustor so that a detailed understanding of the mechanisms responsible for successful transmissions can be obtained. Single-shot detonation experiments have been performed on axisymmetric and two-dimensional (2D) diffraction geometries for ethylene and propane mixtures involving both oxygen and air as the oxidizer. Homogeneous and heterogeneous mixtures involving the use of fuel–oxygen mixture in the smaller combustor and fuel–air mixture elsewhere have demonstrated the increased benefit of generating an overdriven detonation condition near the diffraction plane for enhanced transmission. Mach reflections have been observed on the outer wall downstream of the diffraction plane for the 2D geometry and appear to be the primary reinitiation mechanisms for the reestablished fuel–air detonations for that geometry. A combination of spontaneous reignition and wall reflection of existing shock waves was observed to be present in the successful axisymmetric cases.

1 INTRODUCTION

The interest in PDEs has increased dramatically in recent years due to their high theoretical performance and wide range of potential applications [1]. Practical operation of these systems requires the use of fuels that have already gained acceptance/approval by the military and/or aviation industry, such as kerosene-based Jet-A, JP-5, or JP-10. The use of such fuels has inherent difficulties since such fuel–air mixtures are difficult to detonate [2, 3], especially in a repetitive and reliable manner. Therefore various research teams are currently investigating the use of an initiator, which consists of a small tube or auxiliary combustor filled

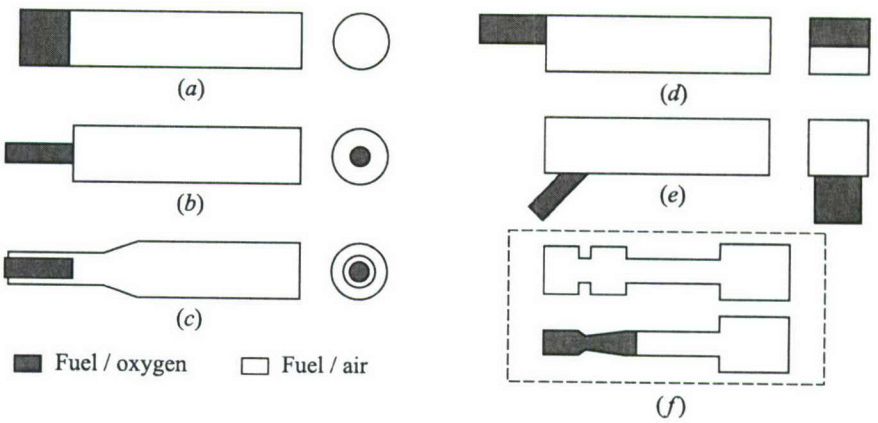

Figure 1 Sample results for C_2H_4–O_2 diffraction tests: (*a*)–(*e*) general examples of initiator concepts, and (*f*) pure fuel–air and hybrid designs

with mixtures highly sensitive to detonation as the means to initiate a detonation in a larger main combustor containing a less sensitive fuel–air mixture. Thus, the importance of detonation diffraction or transmission from the small tube into a larger main combustor tube often arises.

Various initiator concepts exist and can vary from coaxial designs to transverse or splitter plate concepts just to name a few. Most concepts operate on fuel–oxygen mixtures while others utilize a blend of oxygen-enriched air as the oxidizer. Although the use of oxygen provides excellent reliability, repeatability, and a very rapid ignition event, the minimization of the oxygen required is of paramount importance since it is treated as "fuel" for specific impulse (I_{sp}) and specific fuel consumption (SFC) calculations and directly reduces the overall system performance. Thus, efficient coupling between an initiator and the larger combustor is of high importance. Some examples of initiator designs are shown in Fig. 1, but many more exist at the concept level. Concept (*a*) simply involves the use of an oxygen–fuel "plug" at the head-end of a combustor. This concept has been shown to work well, but often requires the use of a substantial amount of oxygen. Initiator concepts (*b*) and (*c*) utilize a smaller combustor which "transmits" a fuel–oxygen detonation wave into a larger combustor containing the fuel–air mixture. Concept (*b*) possesses a solid back wall at the diffraction plane while concept (*c*) allows the wave to diffract initially to slightly larger diameter, but with less confinement than in (*b*). The first three concepts have been investigated by Naval Postgraduate School (NPS) in regards to their applicability to hydrocarbon/air PDE concepts. Concepts (*d*) and (*e*) are two that have been explored on a limited scale computationally and little work exists in the open literature. The last concepts depicted as caption (*f*) are examples of hybrid designs, which

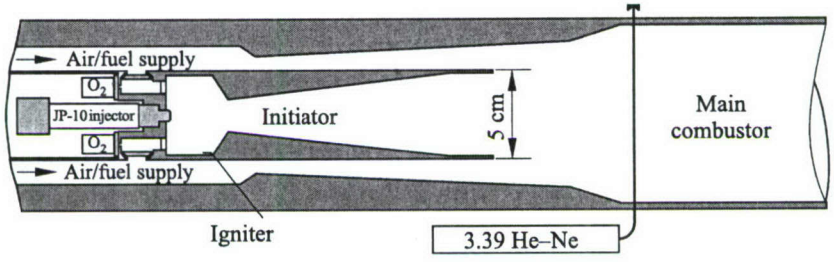

Figure 2 Valveless PDE geometry

may use wall shaping/confinement and/or shock reflection/focusing to promote the generation of a detonation wave. Both concepts could also be used solely with air as the oxidizer, but would likely be limited in operational frequency, reliability, and also require additional axial length for the deflagration-to-detonation transition (DDT) process to occur. The lower initiator depicted as caption (f) is representative of the actual initiator in use today on the NPS PDE geometry.

The PDE geometry under development at NPS utilizes a continuous air flow design, which does not possess valves for the air supply to the combustion chamber. The geometry utilizes the initiator approach depicted as caption (c) in Fig. 1, where the initiator combustor operates on an oxygen-enriched air–fuel mixture to rapidly and reliably generate a detonation wave which can then be used to initiate the less sensitive fuel–air mixture located in the main combustor, see Fig. 2. The absence of a large valve on the air flow has permitted a convenient flow path to rapidly fill, detonate, and purge the combustion chamber at rates up to 100 Hz, but has also introduced difficulties into the initiation process due to lowered confinement conditions when compared to conventional PDE concepts which involve some type of valve on the air supply. A critical region of interest is at the initiator exit plane where the exiting detonation wave experiences a diffraction to the main combustor. The concern for this area of the system is the motivation for the effort to characterize the effects of the diffraction condition between main combustor and the initiator at the diffraction plane. The effects of diameter ratio (D/D_0), mixture variation (overdrive), and varying degrees of confinement are being evaluated so that a more optimized condition can exist.

A large body of historical work has investigated the classical case of detonation transmission from a confined tube to an unconfined volume [4] for homogeneous mixtures. The well documented critical diameter value of 13 times the cell size (λ) of the mixture for transmission of a detonation wave to an unconfined volume has been verified many times to hold true for most mixtures. The 13λ value has been shown to be specifically valid for mixtures containing more irregular cell spacing, typically fuel–air mixtures with higher activation energies. Mixtures containing highly regular detonation cell structure, such as argon-diluted fuel–

oxygen mixtures have been shown to often require a larger critical diameter than the 13λ rule, thus revealing the increased importance of wavefront structure during the diffraction processes in producing gas-dynamic hot spots for spontaneous reignition to occur. The increased irregularity in the cellular structure for fuel–air mixtures often aids in the adjustment to sudden expansion conditions and can be interpreted as possessing more levels of instability and therefore more modes by which spontaneous reinitiation may occur near a critical diameter value [5].

Teodorczyk *et al.* [6] and Oran *et al.* [7, 8] have looked at the reinitiation mechanisms of Mach reflections at a rigid wall from the propagation of a quasi-detonation in an obstacle-laden channel and an imparting spherical blast wave on a rigid wall, respectively. Both studies stress the importance of the rapid reignition sites immediately behind the generated Mach stems at the wall. Murray *et al.* [9] also demonstrated the importance of shock–shock and shock–wall collisions for different exit conditions at the diffraction plane, including tube bundles, annular orifices, and cylindrical diffraction. The reinitiation mechanism associated with the Mach reflections observed in those studies is extremely important for initiator concept (*c*) described earlier. It also becomes increasingly important as the combustor diameter approaches the cell size of the mixture and few transverse waves exist to assist with adjusting to the expansion condition occurring at the diffraction plane. The reinitiation process for such conditions appears to be a very local process and the influence of the wave front structure [10] and reflection cannot be ignored during analysis.

In [11, 12], the effects of overdriving a detonation wave during diffraction from a smaller combustion tube to a larger volume have been investigated. In both studies, it was determined that a definitive benefit existed when a detonation wave was allowed to propagate into a less reactive mixture immediately before diffraction occurred, thus creating an overdriven condition in the less reactive mixture. Recently, Murray *et al.* [13] investigated the direct benefit of utilizing a fuel–oxygen driver section, an initiator, and transmitting the generated detonation wave into a fuel–air mixture in order to generate the overdriven condition. Overall values of the effectiveness of driver–receptor mixtures and diameter ratios approached 30 for some conditions indicating a dramatic reduction in the required critical diameter for the receptor mixture. Thus, a combination of Mach reflections and overdriven conditions are the mechanisms which appear to dominate initiator transmissions on the scale of most PDEs and will be responsible for the successful application in such systems.

2 EXPERIMENTAL SETUP

The single-shot imaging experiments were performed on a test apparatus, schematically shown in Fig. 3, which allows for either circular or 2D diffraction into

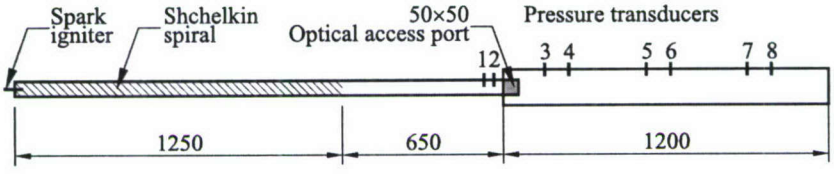

Figure 3 Experimental setup used for single-shot experiments. Dimensions in mm

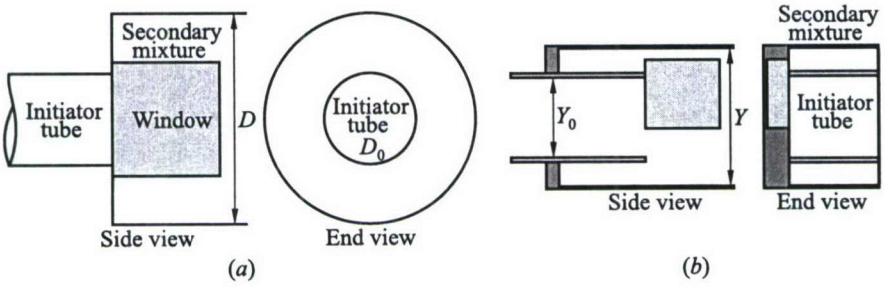

Figure 4 Optical access test section configurations used for imaging studies: (*a*) axisymmetric test section, and (*b*) two-dimensional test section

a larger combustor. A 50.8-millimeter inner diameter, 1.9-meter long combustor was used as the initiating combustor for all tests. A Shchelkin spiral was installed at the head-end of the combustor to promote the rapid formation of the fuel–air detonations. For the axisymmetric case, the detonation wave exiting from the initiating combustor was then allowed to diffract into a larger circular combustor with a maximum diameter of 127 mm. The detonation wave exiting from the initiating combustor was converted into a 50.8×50.8 mm square wave over a 250-millimeter axial length for the 2D imaging tests. The test sections used for each series of testing provided 49.5×49.5 mm of optical access near the diffraction plane and are shown in Fig. 4. Additional diameter and channel ratios were obtained by the insertion of sleeves and channel plates.

The mixtures investigated were composed of ethylene–oxygen and ethylene–air at various equivalence ratios and were injected dynamically into the system at the head-end of the test apparatus. A 3.39-micrometer infrared (IR) HeNe laser was transmitted across the combustor 25.4 mm upstream of the diffraction plane so that the fuel–oxygen to fuel–air interfaces could be located spatially and characterized temporally. The typical mixture transition interface between the fuel–oxygen and fuel–air mixtures was approximately 60 mm in length and was completed before the diffraction plane. All gaseous flow rates were determined from metering orifices. Detonation wave speeds were monitored using Kistler

603B1 pressure transducers along the combustor axis to monitor the initial and final velocities in each combustor. If a wave speed indicative of a Chapman–Jouguet (CJ) detonation was not observed within 500 mm from the diffraction plane, the test condition was considered unsuccessful.

The detonation wave diffraction at the initiator/main detonation tube was observed using high-speed Schlieren and CH* chemiluminescence imaging which utilized a 10-nanometer FWHM interference filter centered at 430 nm and both DRS Hadland and Princeton Instruments intensified CCD cameras. Preliminary computational results from detailed simulations such as density and CH* species concentration contours have been compared against the experimental data and show good agreement. An explicit algorithm, Flux-Corrected Transport, was used for the computational study. It has been shown to be very efficient and accurate for integrating high-speed reactive flows, typical of detonations. Flux-Corrected Transport is a conservative, monotonic algorithm with fourth-order phase accuracy. The results presented utilized a two-step global chemistry model. In this model, the induction step is followed by an energy release step. Induction time data from shock-tube experiments is used for characterizing the first step. The energy release is terminated at the CJ plane by specifying the mixture composition and terminating the chemical reactions beyond this plane (frozen flow assumption). The computational results analyzed a larger spatial area than the experiments and provided additional species and spatial imaging information where diagnostics were not possible.

3 RESULTS

3.1 Axisymmetric Geometry

The first series of tests performed on the axisymmetric geometry ($D/D_0 = 2.5$) were for homogeneous mixtures of either C_2H_4–air or C_2H_4–O_2 at varying equivalence ratios. All tests were performed at a nominal pressure and temperature of 100 kPa and 285 K, respectively. The diffraction of the fuel–oxygen detonations was observed to remain successful until an equivalence ratio of 0.2 was reached. Due to the cell size of this extremely lean mixture, the detonation wave was not observed to successfully diffract into the larger combustor. The behavior was in good agreement with the 13λ rule, sample results are listed in Table 1[†]. Computational and experimental results are shown together in Fig. 5 and show good agreement. The computational results depict density gradients while the experimental results reveal strong CH* emission from the heat release regions behind

[†]The approximate empirical 13λ rule has been established for detonation transmission to the unconfined space rather than for the geometry like shown in Fig. 4*a* with relatively low D/D_0 ratio. (*Editors' remark.*)

Table 1 Sample results for C_2H_4–O_2 diffraction tests

Fuel/oxidizer	ϕ	d_c, mm*	V_{CJ}, m/s**	V_{exit}, m/s	V_{exit}/V_{CJ}
Ethylene–air	1.0	325.0	1824	718	0.394
Ethylene–O_2	1.0	4.0	2376	2439	1.026
Ethylene–O_2	0.8	5.7	2268	2341	1.034
Ethylene–O_2	0.6	9.7	2138	2215	1.036
Ethylene–O_2	0.4	22.3	1974	2043	1.035
Ethylene–O_2	0.2	157.5	1719	720	0.419
Propane–O_2	1.0	8.3	2361	2434	1.031
Propane–O_2	0.8	10.7	2252	2331	1.035
Propane–O_2	0.6	16.4	2123	2196	1.034
Propane–O_2	0.5	17.0	2090	2171	1.039
Propane–O_2	0.4	37.4	1958	830	0.424

*d_c is the critical tube diameter based upon the 13λ rule.
**V_{CJ} is the CJ detonation velocity.

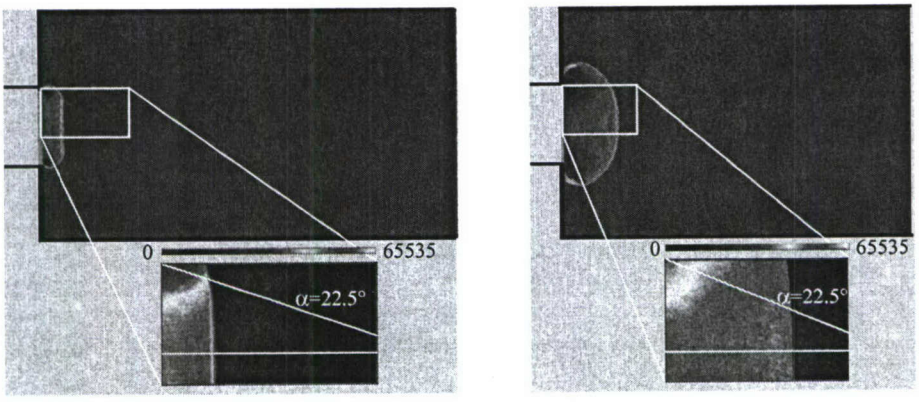

Figure 5 Stoichiometric C_2H_4–O_2 detonation wave undergoing diffraction. Computational density contours are shown on top, and experimental CH* chemiluminescence images are shown on the bottom. The 0–65535 color scale represents increasing emission (a.u.). (Refer color plate I.)

the incident shock. No substantial decoupling was observed. The angle, α, depicted in Fig. 5 represents the leading expansion wave from the diffraction plane.

The second series of tests was to evaluate the same geometry but with fuel C_2H_4–air mixtures. No successful transitions were expected or observed for this case, both computationally and experimentally. The minimum cell size for C_2H_4–air mixtures is approximately 25 mm and is relevant to the mixture just above an equivalence ratio of 1.0. The critical tube diameter, d_c, required based upon

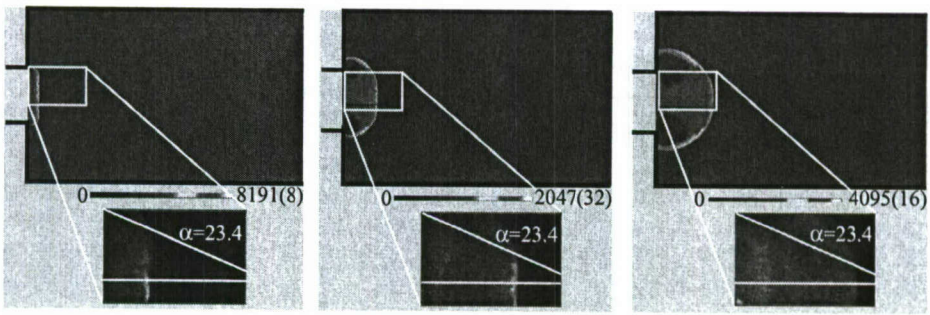

(*a*) (*b*) (*c*)

Figure 6 Transmission of C_2H_4–air ($\phi = 1.0$) detonation from 50.8-millimeter initiator to 127-millimeter combustor: (*a*) $t = 25$ μs, (*b*) 40, and (*c*) $t = 55$ μs. The color scales represent increasing emission (a.u.) and vary to preserve detail. (Refer color plate II.)

13 cell sizes would therefore be approximately 325 mm, well above the diameter of 50.8 mm used in this study. Sample results are shown in Fig. 6. The propagation of the failure line due to the expansion is illustrated on the experimental images and clearly reveals itself by the observed lower reaction rates on the periphery of the remaining detonation core. Good overall agreement was found between the computational and experimental results, although the computational results appear to predict a larger amount of curvature of the diffracting wavefront. This may require another look at the chemistry used in the model.

The third condition evaluated on the axisymmetric case was that of an overdriven condition. The test matrix evaluated the transmission of selected initiator mixtures into a stoichiometric fuel–air mixture. Two diameter cases were evaluated and the results are presented in Fig. 7. Representative computational and experimental images are shown in Fig. 8 for a stoichiometric initiator and receptor condition. Time sequenced CH^* images are presented in Fig. 9 and reveal the relative level of heat release behind the detonation front as the wave experiences the expansion. Plate (*c*) of Fig. 9 shows a region of spontaneous rapid chemical reaction, likely due to the collision of two laterally propagating shock waves. This appeared to be a very common observation on many of these tests. The reinitiation mechanisms for the near-critical conditions appear to be combination of spontaneous reignition behind the diffracting shock front, seen in the experimental images, as well as reinitiation sites along the periphery wall due to strong Mach reflections. The computational results revealed the strong wall reinitiation sites before evidence of their contribution was observed in the experimental portion of the program, thereby directly aiding in providing a better overall view of the developing flow field. A wider range of initiator conditions is planned for the computational work.

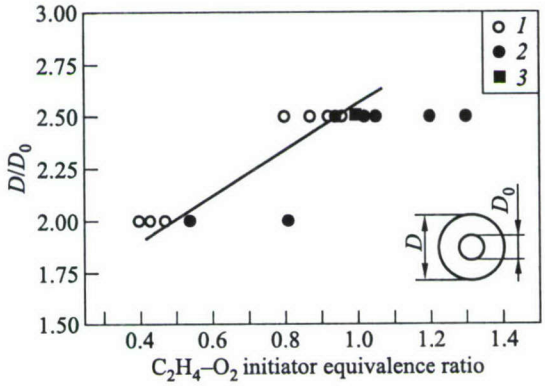

Figure 7 Results for axisymmetric geometry with various initiator mixtures driving a stoichiometric C_2H_4–air main combustor; D_0 = 50.8 mm; initial pressure 100 kPa (nominal); initial temperature 283 K; at ϕ = 0.4 uncertainty ±0.1; at ϕ = 1.4 uncertainty ±0.04: *1* — unsuccessful; *2* — successful; and *3* — computational result

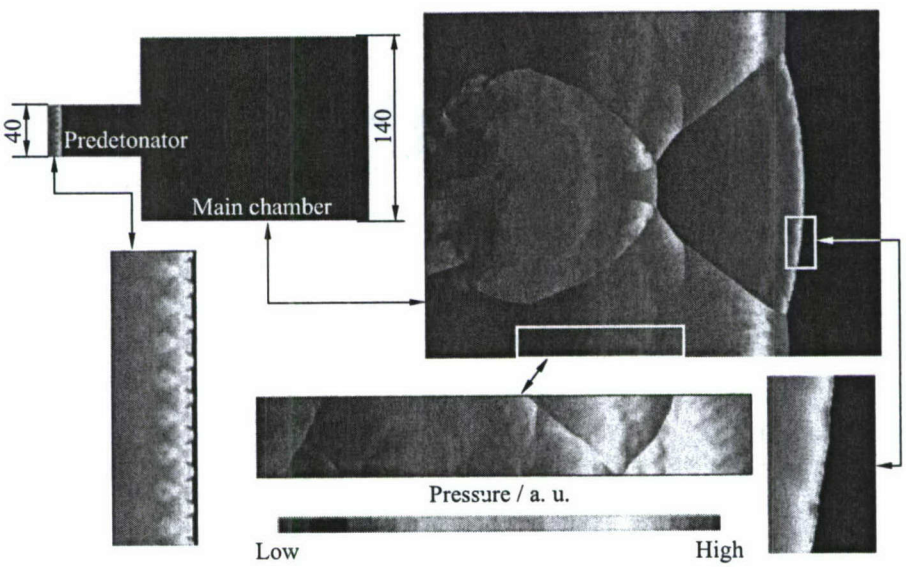

Figure 8 Experimental and computational results for the numerical point in Fig. 7. Dimensions in mm. Color scales represent increasing pressure (a.u.) and vary to preserve detail. (Refer color plate II.)

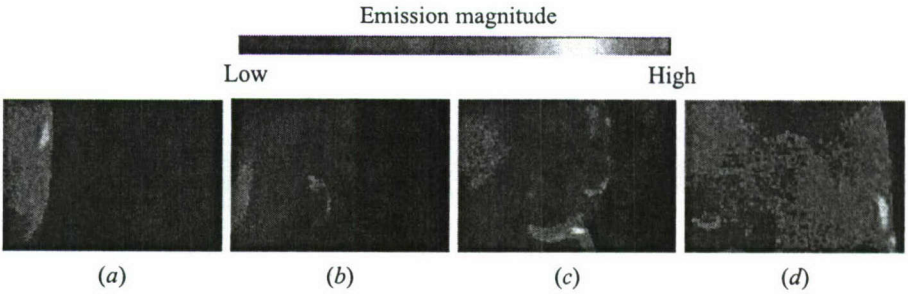

Figure 9 CH* chemiluminescence images of a successful axisymmetric diffraction of a locally overdriven C_2H_4–air detonation ($\phi = 1.0$) from a 50.8- to 127-millimeter circular combustor: (*a*) $t = 12$ μs, (*b*) 19, (*c*) 26, and (*d*) $t = 33$ μs. (Refer color plate III.)

Two-Dimensional Geometry

The 2D geometry evaluated the behavior of an overdriven detonation diffraction at a rapid expansion region, but only on one axis. The head-wall confinement present on the axisymmetric case was also removed so that the geometry was representative of initiator type (*c*) in Fig. 1. The result was a 2D test section which provided diffraction on one axis in order to provide more appropriate optical access for the Schlieren and CH* imaging. The results are for test conditions similar to the axisymmetric case, but with varying vertical diffraction conditions rather than the cylindrical cases evaluated earlier.

The first series of images taken was of the natural luminosity of the detonation wave as it propagated through the test section field of view. This was done to provide estimates of the general luminosity for the conditions to be evaluated, yet it immediately revealed the presence of strong wall reflections immediately downstream of the diffraction plane, seen as plate (*c*) in Fig. 10. The interference filter for the CH* images was then added and images were obtained for three expansion conditions. Results for $Y/Y_0 = 1.33$ and 2.0 are shown in Figs. 11 and 12, respectively. They reveal the presence of regions of increased chemical reaction near the walls of the test section, as expected. As mentioned earlier, this observation was very repeatable and is due to the strong Mach reflections resulting from the residual shock of the decaying blast wave. A schematic of what was believed to have occurred is shown in Fig. 13 and appears to agree with computational results from Oran & Boris [8] and Kailasanath & Patnaik [14]. Plate (*d*) in Fig. 11 shows the CH* emission commonly found to occur with the near-wall Mach stem reflection and the resulting increase in local reaction rate. This behavior was normally observed at distances greater than $1.0Y_0$ from the diffraction plane.

Figure 14 summarizes the successful and unsuccessful test conditions for which detonation transmission occurred for the ethylene–air mixtures. The re-

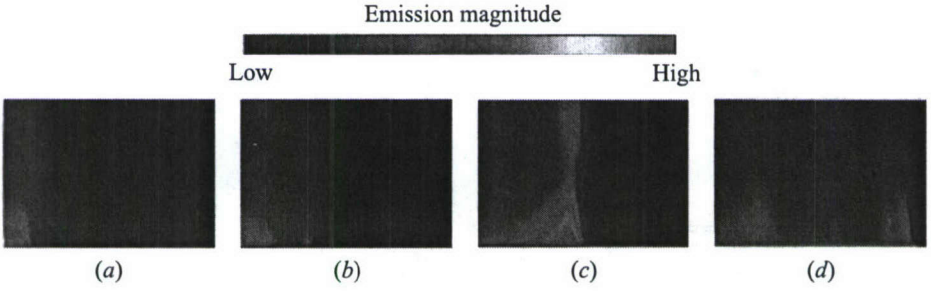

Figure 10 Images of the visible emission from a successful two-dimensional diffraction of a locally overdriven C_2H_4–air ($\phi = 1.0$) detonation in the square detonation tube geometry ($Y/Y_0 = 1.33$): (*a*) $t = 15$ μs, (*b*) 22, (*c*) 29, and (*d*) $t = 36$ μs. (Refer color plate III.)

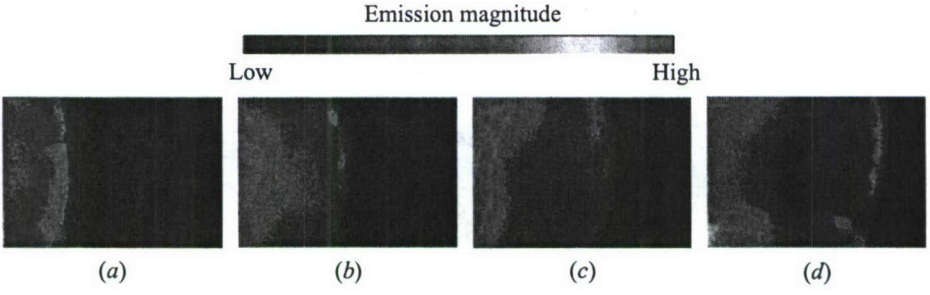

Figure 11 C_2H_4–air ($\phi = 1.1$) detonation transmission in the two-dimensional geometry ($Y/Y_0 = 1.33$): (*a*) $t = 15$ μs, (*b*) 22, (*c*) 29, and (*d*) $t = 36$ μs. (Refer color plate III.)

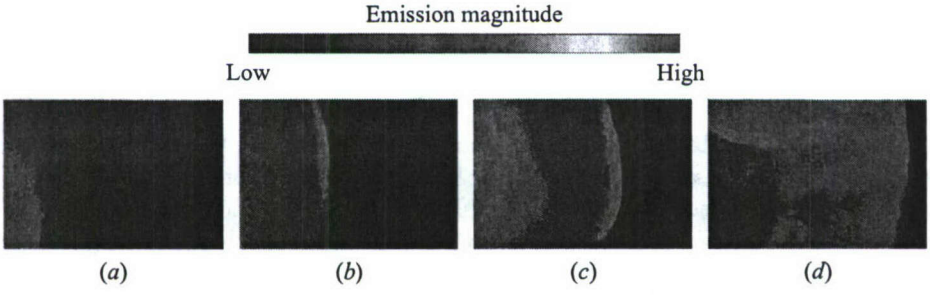

Figure 12 CH^* chemiluminescence images of a successful diffraction of a locally overdriven C_2H_4–air ($\phi = 1.1$) detonation in the two-dimensional geometry ($Y/Y_0 = 2.0$): (*a*) $t = 15$ μs, (*b*) 22, (*c*) 29, and (*d*) $t = 36$ μs. (Refer color plate III.)

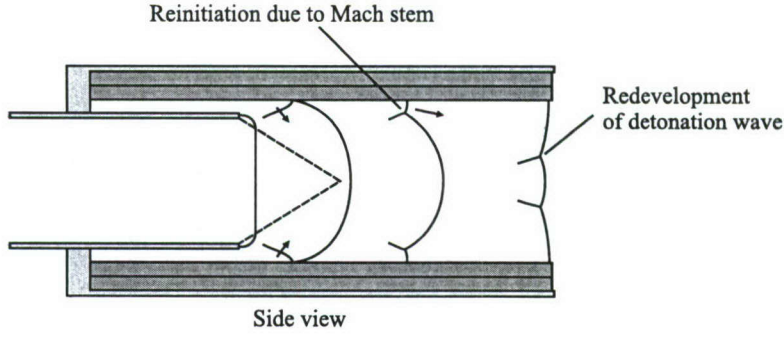

Figure 13 Representation of the observed detonation diffraction/reinitiation process (two-dimensional diffraction geometry)

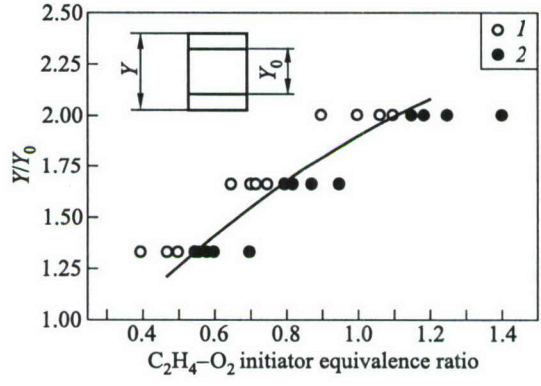

Figure 14 Results for the two-dimensional diffraction geometry. Main combustor — stoichiometric C_2H_4–air; Y_0 = 50.8 mm; initial pressure 100 kPa (nominal); initial temperature 283 K; at ϕ = 0.4 uncertainty ±0.1; at ϕ = 1.4 uncertainty ±0.04: *1* — unsuccessful; and *2* — successful

quired initiator strength (equivalence ratio) was found to be higher than the axisymmetric case†. This is likely due in part to the decrease in confinement at the diffraction plane and the fact that the wall reflection from the 2D geometry does not possess the benefits of wall curvature found on the axisymmetric geometry‡. The effect of wall curvature has been found to be important for the generation of "X"-shaped compression waves and increased local heating.

†Empirical critical condition for detonation transition from a 2D rectangular channel to the unconfined volume is Y_{0c} = (3–6)λ or Y_{0c} = 10λ at most, where Y_{0c} is the critical channel width. In view of it, 2D diffraction should seemingly be less sensitive to the initiator strength than the axisymmetric diffraction with d_c = 13λ. (*Editors' remark.*)

‡As a matter of fact, due to the difference in the divergence factor between 3D and 2D geometry, the effect should be opposite. (*Editors' remark.*)

With the exception of an occasional reignition due to a localized explosion some distance behind the leading shock, it appears that the shock reflection at the confining surface of the outer wall is the basic mechanism for reinitiation in this geometry. (Due primarily to the increased heating and associated chemical activity behind the Mach stem which provides the rapid energy release required for reinitiation.) It is believed that if the exiting detonation wave from the initiator can be tailored to possess a very large Mach number, the transmission across the diffraction will be substantially enhanced.

4 CONCLUDING REMARKS

Comparison of the computational results to the experimental observations show good agreement for the ethylene mixtures and generates confidence in the ability to predict detonation diffraction for other specified geometries. It is felt that the case of confined detonation diffraction for homogeneous ethylene mixtures is well understood, but that heterogeneous or partially confined conditions which involve complex shock reflections need additional study.

The reliable generation of Mach stems along the wall downstream of the diffraction plane for coaxial initiators/combustors will be a valuable mechanism to take advantage of in an actual engine since they do not depend directly on the cell size, but on the strength of the exiting shock wave and the physical diffraction condition. However, the sensitivity of the mixture to reignition can be correlated to the cell size.

The situation involving a flowing coaxial region of air, such as on an actual engine, has not yet been investigated, but it is planned to be evaluated in the next phase of this study. The effect of turbulence and increased kinetic energy should be to improve the overall transmissibility of the geometry. Turbulence intensity measurements will be made so that additional flow field parameters can be introduced into the numerical model to evaluate sensitivities. Additional computational results will evaluate these effects in conjunction with the experimental test program.

ACKNOWLEDGMENTS

This work was sponsored by Dr. Gabriel Roy of the Office of Naval Research. The authors would like to thank Harry Connor and Lt. Mike Fludovich at NPS for assisting with this work.

REFERENCES

1. Kailasanath, K. 2002. Recent developments in the reseach on pulse detonation engines. AIAA Paper No. 2002-0470.

2. Lee, J. H. S., and C. M. Guirao. 1982. Fuel–air explosions. *Conference (International) on Fuel–Air Explosions Proceedings.* Waterloo, Ontario: University of Waterloo Press. 1005.
3. Beeson, H. D., R. D. McClenagan, W. J. Pitz, C. K. Westbrook, and J. H. S. Lee. 1991. Detonabilty of hydrocarbon fuels in air. In: *Dynamics of detonations and explosions: Detonations.* Eds. A. L. Kuhl, J.-C. Leyer, A. A. Borisov, and V. A. Sirignano. Progress in astronautics and aeronautics ser. Washington, DC: AIAA Inc. 133:19–36.
4. Knystautas, R., J. H. Lee, and C. M. Guirao. 1982. The critical tube diameter for detonation failure in hydrocarbon–air mixtures. *Combustion Flame* 48:63.
5. Moen, I. O., M. Donato, R. Knystautas, and J. H. Lee. 1981. The influence of confinement on the propagation of detonations near the detonability limit. *18th Symposium (International) on Combustion Proceedings.* Pittsburgh, PA: The Combustion Institute. 1615–22.
6. Teodorczyk, A., J. H. Lee, and R. Knystautas. 1991. Photographic study of the structure and propagration mechanisms of quasidetonations in rough tubes. In: *Dynamics of detonations and explosions: Detonations.* Eds. A. L. Kuhl, J.-C. Leyer, A. A. Borisov, and V. A. Sirignano. Progress in astronautics and aeronautics ser. Washigton, DC: AIAA Inc. 133:223–40.
7. Oran, E. S., D. A. Jones, and M. Sichel. 1992. Numerical simulations of detonation transmission. *Proc. Royal Society London A* 436:267–97.
8. Oran, E. S., and J. P. Boris. 1993. Ignition in a complex Mach structure. In: *Dynamics aspects of detonations.* Eds. A. L. Kuhl, J.-C. Leyer, A. A. Borisov, and W. A. Sirignano. Progress in astronautics and aeronautics ser. Washington, DC: AIAA Inc. 153:241–52.
9. Murray, S. B., F. Zhang, and K. B. Gerrard. 2001. The influence of driver power and receptor confinement on pre-detonators for pulse detonation engines. *18th Colloquium (International) on the Dynamics of Explosions and Reactive Systems Proceedings.* Seattle, WA.
10. Edwards, D. H., G. O. Thomas, and M. A. Nettleton. 1979. The diffraction of a planar detonation wave at an abrupt area change. *J. Fluid Mechanics* 95:79–96.
11. Desbordes, D. 1988. Transmission of overdriven plane detonations: Critical diameter as a function of cell regularity and size. In: *Dynamics of explosions.* Eds. A. L.Kuhl, J. R. Bowen, J.-C. Leyer, and A. A. Borisov. Progress in astronautics and aeronautics ser. Washington, DC: AIAA Inc. 114:170–85.
12. Desbordes, D., and A. Lannoy. 1991. Effects of a negative step of fuel concentration on critical diameter of diffraction of a detonation. In: *Dynamics of detonations and explosions: Detonations.* Eds. A. L. Kuhl, J.-C. Leyer, A. A. Borisov, and V. A. Sirignano. Progress in astronautics and aeronautics. Washington, DC: AIAA Inc. 133:170–86.
13. Murray, S. B., P. A. Thibault, F. Zhang, D. Bjerketvedt, A. Sulmistras, G. O. Thomas, A. Jenssen, and I. O. Moen. 2001. The role of energy distribution on the transmission of detonation. In: *High-speed deflagration and detonation: Fundamentals and control.* Eds. G. Roy, S. Frolov, D. Netzer, and A. Borisov. Moscow, Russia: Elex-KM Publ. 139–62.
14. Kailasanath, K., and G. Patnaik. 2001. Multilevel computational studies of pulse detonation engines. *ISABE Meeting Proceedings.* Bangalore, India. ISABE Paper No. 2001-1172.

NUMERICAL SIMULATION OF REFLECTION OF DETONATION AND SHOCK WAVES IN SUPERSONIC FLOWS

A. V. Trotsyuk, A. N. Kudryavtsev, and M. S. Ivanov

Numerical simulations were performed to study regular and Mach reflections of detonation and shock waves in chemically reacting flows. A finite volume TVD scheme with a high-order MUSCL reconstruction procedure was used in this work. The two-dimensional (2D) time dependent Euler equations were applied to describe a supersonic flow over a wedge in a channel. It has been found that, as for nonreacting shock waves, there is a dual solution domain, where the existence of both regular and Mach reflections is possible under identical boundary conditions. It is shown that in the case of the Mach reflection, a Mach stem is a section of the front of an unsteady overdriven multifront detonation wave. Retaining the wedge angle unchanged, influence of channel geometry on the Mach reflection was investigated. The simulations have shown that different types of local perturbations of the free-stream flow might cause the transition from regular to Mach reflection. The detachment criterion of transition was also examined.

1 INTRODUCTION

In studying the detonation phenomenon in gas mixtures, much attention is traditionally paid to investigation of the multifront (cellular) structure of a self-sustained unsteady detonation wave (DW) propagating in a quiescent mixture, determination of the critical conditions of detonation initiation (critical value of the initiation energy), and marginal regimes of DW propagation.

Development of new promising scramjets that use the detonation mode of combustion requires a detailed study of interaction of oblique shock waves (SW) and DW in steady flows. These studies are also necessary to create effective RAM accelerators, since the oblique DW is the most important element in the

flow structure around an accelerated body in the accelerator barrel. The idea to use DW as the ignition mechanism in high-speed propulsion devices goes back to 1946 [1]. A number of experimental, theoretical, and numerical studies of this concept were reported in the past and recently there has been a renewed interest in this subject [2–10].

In nonreacting gasdynamics, the flow structure in the case of regular (RR) and Mach (MR) reflection of SW and the criteria of transition between these types of reflections have been studied in many theoretical, experimental, and numerical papers. It is known that there are two principal conditions, the von Neumann criterion, α_N, and the detachment criterion, α_D, at which the transition from one type of reflection to the other occurs in a steady flow. Here, α is the angle between SW and the free-stream velocity vector, and $\alpha_N < \alpha_D$. There is a dual solution domain with $\alpha_N < \alpha < \alpha_D$, where both types of reflections are possible. A hysteresis phenomenon is also possible, where the transition from RR to MR and back occurs at different values of a variable flow parameter (e.g., the angle α or the flow Mach number).

At the Institute for Theoretical and Applied Mechanics (ITAM) of the Siberian Branch of the Russian Academy of Sciences, a hysteresis of the RR to MR transition (both in terms of the wave angle and the Mach number) was obtained for the first time [11, 12]; the effect of the Reynolds number on the Mach stem height was revealed [13]; stability of RR and MR to perturbations was examined [13, 14]; three-dimensional (3D) MR of SW was calculated for the first time [14], and the wave and Mach surface shapes were obtained; a hysteresis was achieved for the 3D case [14], and a new type of 3D reflection of SW (combined reflection) was found [15]. The latter type of reflection was experimentally confirmed in investigations performed at ITAM [15].

As compared to reflection of oblique detonations, the interaction of oblique DW with each other, SW, or a solid surface has not been adequately studied.

The main objective of the present work is to study the flow structure with reflection of oblique SW and DW in a steady supersonic flow of a chemically reacting mixture and the transition from RR to MR.

2 PROBLEM FORMULATION AND PHYSICAL MODEL

The simulation was performed for a flow of a homogeneously premixed mixture $2H_2 + O_2$ at $p_0 = 0.2$ bar, $T_0 = 298.15$ K, and inflow Mach number $M_{in} = 5.5$. A 2D supersonic flow of the mixture over a compression body, represented by a wedge of angle θ and length of the compression surface w, in a channel with an inlet cross-section H and outlet cross-section h was considered (see Fig. 1). In contrast to simulation of SW reflection in an inert medium, for a chemically

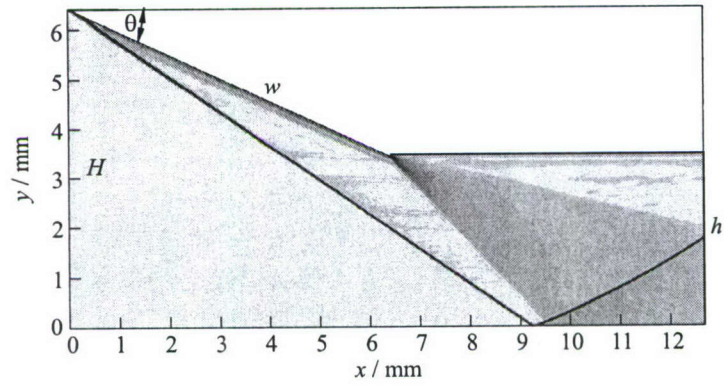

Figure 1 Numerical Schlieren picture of the flow field with regular reflection of shock waves in $2H_2 + O_2$ mixture: $p_0 = 0.2$ bar, $T_0 = 298.15$ K, $M_{in} = 5.5$, $\theta = 25°$, and $h/w = 0.5$

reacting flow, there is a characteristic velocity, namely, the Chapman–Jouguet (CJ) detonation velocity, D_{CJ}, and an intrinsic length scale. As for the length scale, the detonation cell width, a_0, is often used. Another parameter commonly used for the characteristic length scale is the calculated thickness of an idealized one-dimensional, steady reaction zone of DW. For the specified mixture and initial conditions, one has: $D_{CJ} = 2757$ m/s, and $M_{CJ} = 5.13$. The value of M_{CJ} is the lower limit for M_{in}. In the present simulation, the value of H was retained constant for any changes in θ and h/w. Thus, the inlet mass flow rate, $m_{in} = \rho_0 c_0 M_{in} H$, was constant for different channel geometries.

Hereinafter, the following notations are used: ρ is the density; u and v are the fluid velocities in the x and y directions, respectively; E and U are the total energy and internal energy per unit mass; E_D is the mean dissociation energy of the reaction products; μ is the mean molar mass of mixture; μ_a, μ_{min}, and μ_{max} are the molar masses of mixture in the atomic, extremely dissociated, and extremely recombined states, respectively; Y is the induction parameter with $Y = 1$ at the beginning and $Y = 0$ at the end of the induction zone; p is the pressure; T is the temperature; R is the gas constant; a is the width of the detonation cell; the subscript 0 denotes the quantities in the initial state.

The dynamics of the compressible, chemically reacting flow was described by the 2D Euler equations

$$\frac{\partial \mathbf{q}}{\partial t} + \frac{\partial \mathbf{F}(\mathbf{q})}{\partial x} + \frac{\partial \mathbf{G}(\mathbf{q})}{\partial y} = \mathbf{W} \tag{1}$$

where

$$\mathbf{q} = (\rho, \rho u, \rho v, \rho E, \rho\mu, \rho Y)^T$$
$$\mathbf{F}(\mathbf{q}) = (\rho u, p + \rho u^2, \rho uv, u(p + \rho E), \rho u\mu, \rho uY)^T$$
$$\mathbf{G}(\mathbf{q}) = (\rho v, \rho uv, p + \rho v^2, v(p + \rho E), \rho v\mu, \rho vY)^T$$
$$\mathbf{W} = (0, 0, 0, 0, \rho W_\mu, \rho W_Y)^T$$
$$E = U + \frac{u^2 + v^2}{2}$$

W_μ and W_Y are the rates of change of μ and Y, respectively; superscript "T" denotes the transposition.

Put the origin of coordinates to the left bottom corner of a computational domain as shown in Fig. 1. The x-axis is then directed from left to right along the lower domain boundary, and the y-axis is directed upwards, normal to the x-axis.

Chemical transformations in the mixture were described by the two-step kinetic model (including the induction step and the heat release step) [16]:

at $0 < Y \leq 1$:

$$W_Y = -\frac{1}{\tau_{\text{ind}}}, \quad W_\mu = 0, \quad U = \frac{1}{\gamma_0 - 1}\frac{p}{\rho} + E_{\text{D}}\left(\frac{1}{\mu_0} - \frac{1}{\mu_{\min}}\right)$$

at $Y = 0$:

$$W_Y = 0, \quad W_\mu = W_\mu(T, \mu, \rho), \quad U = U(T, \mu)$$

The first, induction, step ($0 < Y \leq 1$) was modeled in accordance with experimental kinetics [17]:

$$\tau_{\text{ind}} = 4.17 \cdot 10^{-14}[\text{O}_2]^{-1/2}[\text{H}_2]^{-1/2} \exp\frac{18{,}100}{RT} \ [\text{mole·s/cm}^3] \qquad (2)$$

After the completion of the induction period, $Y = 0$. The subsequent heat release step is described by the following model [18, 19]:

$$W_\mu(T, \mu, \rho) = \frac{4K_+\rho^2}{\mu}\left(1 - \frac{\mu}{\mu_{\max}}\right)^2 - A_2 T^{3/4}\rho\left[1 - \exp\left(-\frac{\vartheta}{T}\right)\right]^{3/2} \exp\left(-\frac{E_{\text{D}}}{RT}\right)\left(\frac{\mu}{\mu_{\min}} - 1\right)$$

together with the caloric equation of state [19]:

$$U(T, \mu) = E_D\left(\frac{1}{\mu} - \frac{1}{\mu_{\min}}\right) + \left[\frac{3}{4}\left(\frac{\mu}{\mu_a} + 1\right) + \frac{3}{2}\left(\frac{\mu}{\mu_a} - 1\right)\frac{\vartheta/T}{\exp(\vartheta/T) - 1}\right]\frac{RT}{\mu}$$

correlated with the adopted kinetic model by taking into account the second law of thermodynamics.

All of the constants entering the last two equations and pertaining to the gaseous mixture under study were calculated according to [18, 19]: E_D = 459.2089 kJ/mol, $\mu_{min} = \mu_a$ = 6.005 g/mol, μ_{max} = 18.016 g/mol, μ_0 = 12.011 g/mol, $A_2 = 4.646561 \cdot 10^{10}$ m^3/(kmol·s·K$^{3/4}$), $K_+ = 6 \cdot 10^8$ m^6/(kmol^2·s), ϑ = 4000 K, and γ_0 = 1.397.

The system of governing equations was closed by the thermal equation of state for ideal gas:

$$\frac{P}{\rho} = \frac{RT}{\mu}$$

The boundary conditions on the different boundaries of the computational domain were as follows (see Fig. 1): a uniform supersonic flow is imposed on the left upstream side; supersonic outflow conditions are implemented on the right downstream side; nonpermeable conditions are specified on the upper solid wall; the lower side is a plane of symmetry so in the case of Eulerian approach it is equivalent to a perfect wall and nonpermeable conditions are adopted at it. To implement these boundary conditions in the computational code, the procedures described in [20] were used.

3 NUMERICAL METHOD

The hyperbolic system (1) was solved numerically using the finite-volume scheme with the fourth-order MUSCL TVD reconstruction [21] and the advanced HLLC algorithm [22] for an approximate solution of the Riemann problem. In implementation of this algorithm for the case of a chemically reacting mixture, the "energy relaxation method" [23] was used. This method eliminates the problem of numerical solution of the Riemann problem for a medium with a complicated nonlinear equation of state (including that with a variable ratio of specific heats). Integration in time was performed with a second-order accuracy by using new, recently developed, additive, semi-implicit Runge–Kutta methods [24]. In this case, the characteristic values of the Courant number were CFL = 0.2–0.3.

A body-fitted, quadrilateral grid was used with typical values of node numbers N_x = 600 and N_y = 200 in x- and y-direction, respectively. To ensure the independence of the computational results on grid resolution, some of the runs were checked with the doubled number of nodes in each direction. It was found that the agreement between the coarse and fine grid results was very close.

4 RESULTS OF CALCULATIONS

As in the case of nonreacting SW, there is a dual solution domain, where the existence of both RP and MR is possible under identical boundary conditions. Figure 1 shows the numerical Schlieren visualization of RR of an oblique SW for a wedge angle of $\theta = 25°$. The study of reflection of nonreacting SW shows that h/w is one of the governing parameters; in the present case, $h/w = 0.5$. For an inert SW at a given combination of M_{in}, θ (or shock-wave angle α), and γ, there is an upper limit of h/w, i.e., h/w_{max}. This limit is determined by h_{max}, i.e., the situation when the leading characteristic of the expansion fan, which is formed at the trailing edge of the wedge, intersects the incident SW. For the present simulation, $h/w_{max} = 0.6145$. The channel height was $H = a_0$, i.e., it was chosen to be equal to the transverse size of the detonation cell in a freely propagating, unsteady, multifront DW. The predicted cell size for the specified mixture and initial conditions is $a_0 = 0.64$ cm. This value is in very good agreement with the experimental results (see [25]). The computation described shows that, for the above parameters, the temperature behind both the incident and reflected waves is not sufficiently high, and the induction zone length is greater than the computational domain. In this case, the flow structure is similar to RR in an inert medium [11–15].

Figure 2 shows the case of MR; all geometric dimensions and flow parameters are similar to those in Fig. 1. The flow structure behind the Mach stem is similar to the flow structure behind the front of a multifront (cellular), unsteady, propagating DW [25]. There are unsteady transverse waves on the Mach stem, which are periodically reflected from the plane of symmetry and from the flow region in the vicinity of the triple point. The motion of these waves along the Mach stem changes its shape significantly. The behavior of these transverse waves corresponds to the behavior of transverse waves behind the front of an unsteady multifront DW. This gives grounds to consider that the Mach stem is a section of the front of an overdriven DW with a degree of overdrive approximately equal to $M_{in}/M_{CJ} = 1.07$.

In contrast to MR in an inert medium, the Mach stem for a chemically reacting flow is unsteady. The detonation front moves upstream or downstream. This study revealed that, at fixed values of M_{in} and θ, h/w is the governing parameter. The simulations were performed for $\theta = 25°$.

For values of h/w up to 0.7 (that is greater than h/w_{max}), the Mach stem inevitably moves upstream up to the inlet boundary. For this case, one has an unstarted 2D converging nozzle. If h/w exceeds some critical value, the Mach stem arises, goes downstream, and vanishes, so one has RR as the final stationary configuration. This evolution of the flow was obtained for $h/w = 0.8$. Hence, the critical value of h/w is between 0.7 and 0.8. The closer h/w is to this value, the lower is the velocity of upstream or downstream motion of the unsteady Mach stem, and the greater is the CPU time for calculation of the

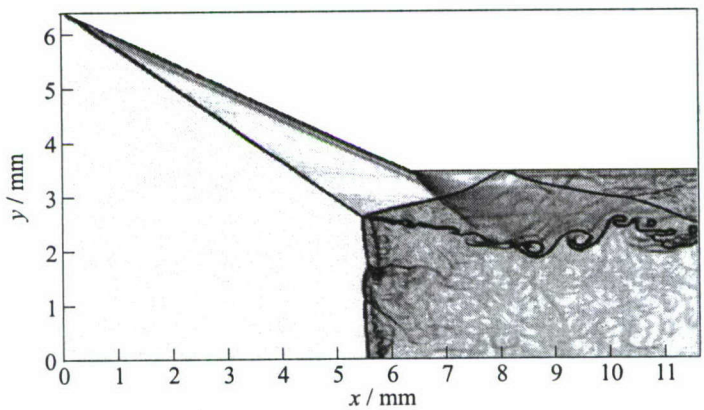

Figure 2 Numerical Schlieren picture of the flow field with Mach reflection of shock waves in $2H_2 + O_2$ mixture: $p_0 = 0.2$ bar, $T_0 = 298.15$ K, $M_{in} = 5.5$, $\theta = 25°$, and $h/w = 0.5$

final flow configuration. Based on these considerations, the authors believe that the Mach stem is in the state of unstable equilibrium for h/w exactly equal to the critical value. The results of numerical simulation of MR allow one to formulate the following problem: for a given mixture and chosen value of H, which combinations of M_{in} and θ in a certain range of h/w ensure the existence of a steady MR configuration (as for nonreacting SW)?

In the study described above, RR served as the initial steady flow configuration. Regular reflection was formed if the computations were started at the initial conditions of a uniform flow with gas parameters in the computational domain similar to those at the inlet boundary. The SW configuration at different times during flow evolution is shown in Fig. 3. The final steady RR is shown in Fig. 3*d*.

To obtain MR, a technique that was previously applied in investigations of nonreacting SW reflections was used [13, 14]. Similar to previous simulations, the present study showed that different local perturbations of the free-stream flow may initiate transition from RR to MR in the dual-solution domain. Here, the problem of finding the minimum size and amplitude of perturbations for the successful transition from RR to MR was not the aim of study, i.e., the critical conditions for such transformation were not studied. A square "spot" with dimensions from $0.2h$ to $0.5h$ in both directions was placed at the axis of symmetry. This disturbance was introduced into the flow upstream of the reflection point. The computations were performed for two different types of perturbations.

The first type of disturbances consisted of instantaneous changes in density from ρ_0 to $0.1\rho_0$ in this region; all other flow parameters remained unchanged. Figure 4 shows the interaction between this local perturbation and steady SW

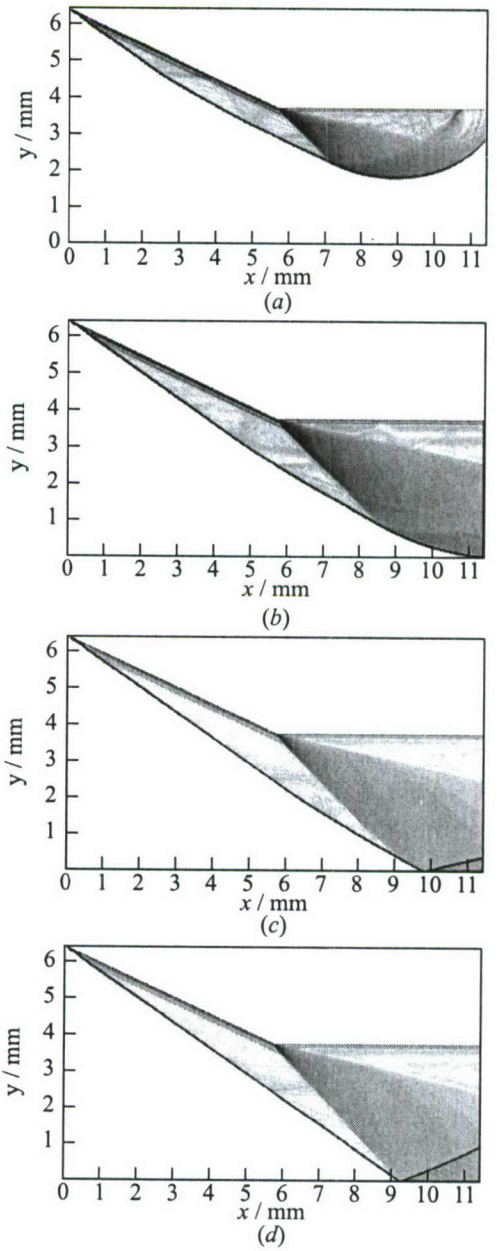

Figure 3 Sequence of numerical Schlieren pictures of the flow field showing the formation of regular reflection ($\theta = 25°$ and $h/w = 0.6$). Time (in μs) is: (*a*) 1.56, (*b*) 3.43, (*c*) 4.48, and (*d*) 31.62

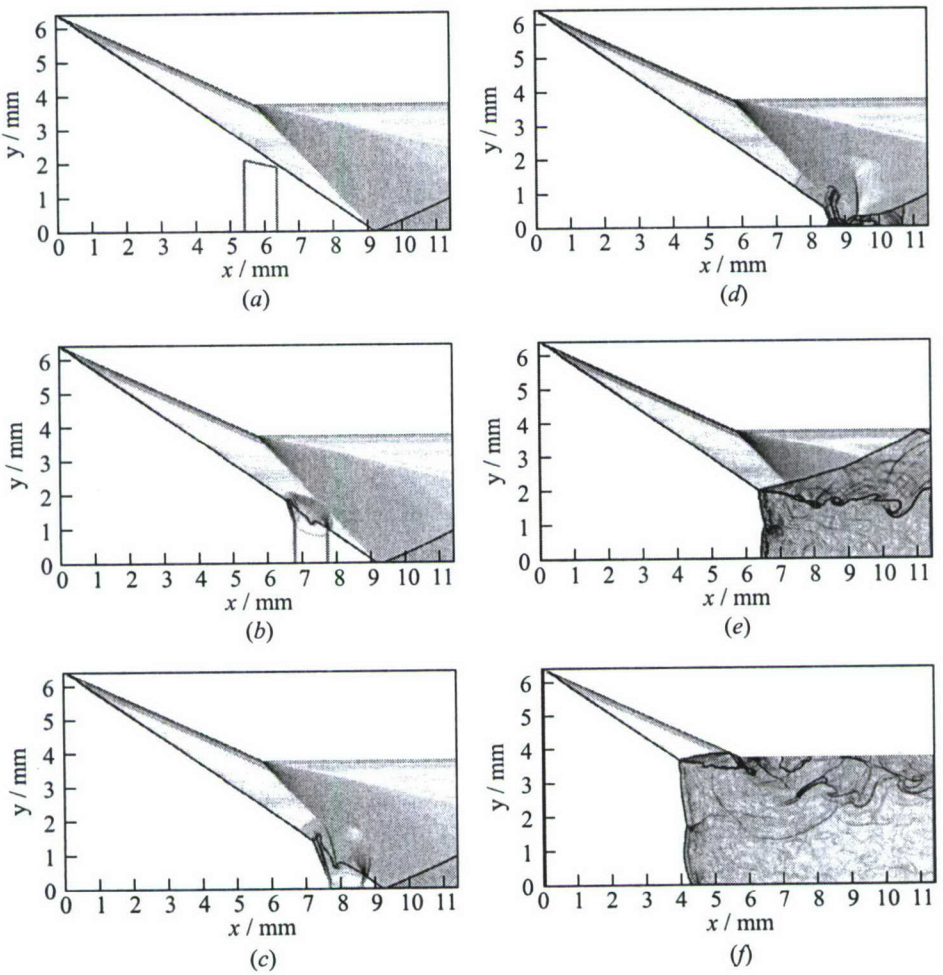

Figure 4 Sequence of numerical Schlieren pictures of the flow field showing the interaction of disturbance with shock wave structure of regular reflection and the Mach stem emergence and evolution ($\theta = 25°$ and $h/w = 0.6$). Time (in μs) from the moment of "spot" introducing is: (*a*) 0.246, (*b*) 0.706, (*c*) 1.00, (*d*) 1.569, (*e*) 43.697, and (*f*) 116.104

with RR. The appearance of the Mach stem and its subsequent evolution are seen in Figs. 4*d*–4*f*. The physical reason for MR is a refraction of an incident SW on this low-density region and temporary existence of SW with a larger angle of incidence than the detachment criterion angle, α_D, determined for the perturbed "spot" parameters [14].

In the second type of disturbances, all flow parameters in the region described above were changed to those behind a normal steady SW. There is another possibility for this type of perturbation [3]: the velocity in the perturbed "spot" can be set to zero. In both cases, the local normal SW is formed near the axis of symmetry and interacts with the existing steady SW structure.

Creation of the normal SW by both types of disturbances is the key mechanism of transition from RR to MR in chemically reacting mixtures*. The temperature behind the normal SW is much greater than that behind the incident oblique SW. Thus, due to the strong dependence of induction period, τ_{ind}, on temperature (see Eq. (2)), the value of τ_{ind} behind the normal SW is low. Hence, the heat release successfully starts at a short distance (short induction zone) behind the leading SW. This results in the formation of an unsteady, multifront DW — Mach stem.

For the adopted value of M_{in}, the wedge angle (i.e., flow deflection angle) of $\theta = 25°$ corresponds approximately to the middle of the dual solution domain for nonreacting SW (Fig. 5). Determination of the boundaries of this region for chemically reacting flow is another problem of interest.

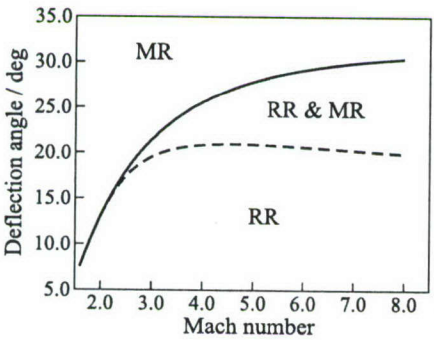

Figure 5 Theoretical criteria of shock wave reflection transition: deflection angle θ vs. inlet Mach number, M_{in}. The case of nonreacting shock waves in $2H_2 + O_2$ mixture, $\gamma_0 = 1.397$. Detachment criterion — solid line, and von Neumann criterion — dashed line. MR — Mach reflection, RR — regular reflection

Numerical investigation of the von Neumann criterion is a rigorous methodological problem for computational fluid dynamics. For finite volume schemes, the Mach stem height can become comparable with the computational cell size as θ approaches θ_N. Therefore, the detachment criterion is better to examine. For a nonreacting SW, the value of θ for the detachment criterion is $\theta_D = 28.55°$ at $M_{in} = 5.5$ (see Fig. 5). The simulations were started from $\theta > \theta_D$, and the initial conditions described above were used with $h/w = 0.6$. Unsteady MR was achieved up to $\theta = 28.60°$. For this angle, the numerical Schlieren pictures of the flow at different time are shown in Fig. 6 (compare with Fig. 3). It is interesting to note that at the earlier stage of flow evolution, there is an unsteady RR (Fig. 6*b*). The reflection point moves upstream, and, after some delay, the

*Other effects like those produced by the wall boundary layer can also play an important role. (*Editors' remark.*)

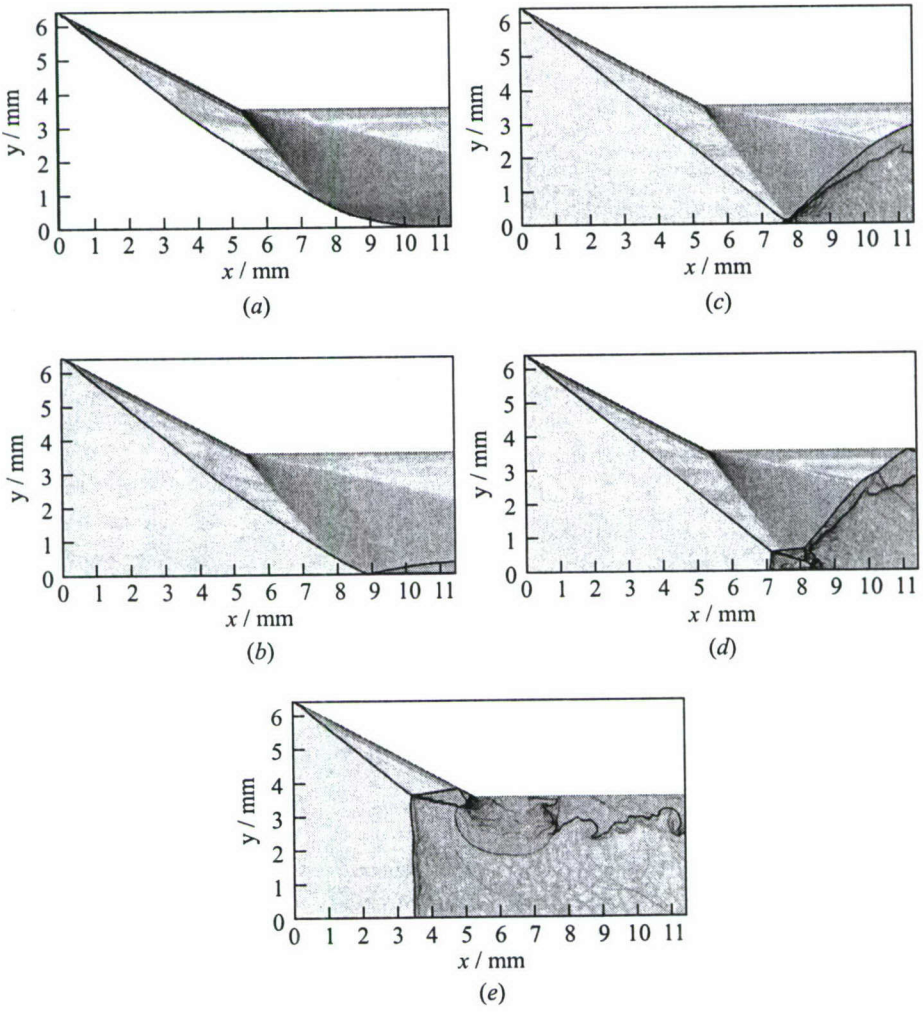

Figure 6 Sequence of numerical Schlieren fields showing the formation of Mach reflection ($\theta = 28.6°$ and $h/w = 0.6$). Time (in μs) is: (*a*) 3.016, (*b*) 3.587, (*c*) 9.014, (*d*) 9.966, and (*e*) 29.069

Mach stem appears (Fig. 6*c*). Subsequent growth of the Mach stem is shown in Figs. 6*d*–6*e*. The computations were finished when the Mach stem reached the inlet boundary.

This analysis of the RR flow structure provides some grounds to believe that the dual solution domain for the given size of the channel and M_{in} is very close or coincides with one for the nonreacting SW (Fig. 5).

5 CONCLUDING REMARKS

Numerical investigations of RR and MR in a supersonic chemically reacting flows have been performed by a high-order MUSCL TVD scheme. It has been found that, as for nonreacting SW, there is a dual solution domain, where the existence of both RR and MR is possible under identical boundary conditions. In the case of MR, the Mach stem is a section of the front of an unsteady, overdriven, multifront DW. The study has revealed that h/w is one of the governing parameters. Depending of its value, the Mach stem inevitably moves upstream to the inlet boundary or vanishes. The simulations have shown that different local perturbations of the free-stream flow may initiate transition from RR to MR. The detachment criterion has been examined. It has been found that, for the size of the computational domain under consideration and for the adopted value of inlet flow Mach number, the detachment wedge angle is very close or coincides with the value relevant to a nonreacting SW.

ACKNOWLEDGMENTS

This work was supported by the Russian Foundation for Basic Research under Grant 02-03-32548.

REFERENCES

1. Roy, M. 1946. *Comptes rendus a l'Academie des Sciences.* Paris.
2. Glenn, D. E., and D. T. Pratt. 1988. Numerical modeling of standing oblique detonation waves. AIAA Paper No. 88-0440.
3. Fujiwara, T., A. Matsuo, and H. Nomoto. 1988. A two-dimensional detonation supported by a blunt body or a wedge. AIAA Paper No. 88-0098.
4. Cambier, J.-L., H. Adelman, and G. P. Menees. 1990. Numerical simulation of an oblique detonation wave engine. *J. Propulsion Power* 6(3):315–23.
5. Li, C., K. Kailasanath, and E. S. Oran. 1994. Detonation structure behind oblique shocks. *Physics Fluids* 6(4):1600–11.
6. Shepherd, J. S. 1994. Detonation waves and propulsion. In: *Combustion in high-speed flows.* Eds. J. Buckmaster, *et al.* Dordrecht–Boston–London: Kluwer Academic Publ. 173–420.
7. Matsuo, A., K. Fujii, and T. Fujiwara. 1995. Flow features of shock-induced combustion around projectiles traveling at hypervelocities. *AIAA J.* 33(6):1056–63.
8. Li, C., K. Kailasanath, and E. S. Oran. 1997. Detonation structures generated by multiple shocks on ram-accelerator projectiles. *Combustion Flame* 108:173–86.

9. Kasahara, J., T. Endo, K. Nishide, D. Yahata, N. Yoshikawa, and T. Fujiwara. 1999. Experimental study on oxyhydrogen oblique detonation around hypersonic projectile. *22nd Symposium (International) on Shock Waves Proceedings.* Eds. G. J. Ball, *et al.* London 1:303–8.

10. Bezgin, L., A. Ganzhelo, O. Gouskov, V. Kopchenov, and Yu. Yarinov. 1999. Some estimations of a possibility to utilize shock-induced combustion in propulsion systems. In: *Gaseous and heterogeneous detonations: Science to applications.* Eds. G. Roy, S. Frolov, K. Kailasanath, and N. Smirnov. Moscow, Russia: Enas Publ. 285–300.

11. Ivanov, M. S., S. F. Gimelshein, and A. E. Beylich. 1995. Hysteresis effect in stationary reflection of shock waves. *Physics Fluids* 7(4):685–87.

12. Ivanov, M. S., G. Ben-Dor, T. Elperin, A. N. Kudryavtsev, and D. V. Khotyanovsky. 2001. Flow-Mach-number-variation-induced hysteresis in steady shock wave reflection. *AIAA J.* 39(5):972–74.

13. Ivanov, M. S., S. F. Gimelshein, and G. N. Markelov. 1998. Statistical simulation of the transition between regular and Mach reflection in steady flows. *Computers Math. Appl.* 35(1/2):113–25.

14. Ivanov, M. S., G. N. Markelov, A. N. Kudryavtsev, and S. F. Gimelshein. 1998. Numerical analysis of shock wave reflection transition in steady flows. *AIAA J.* 36(11):2079–86.

15. Ivanov, M. S., D. Vandromme, V. M. Fomin, A. N. Kudryavtsev, A. Hadjadj, and D. V. Khotyanovsky. 2001. Transition between regular and Mach reflection of shock waves: New numerical and experimental results. *Shock Waves* 11(3):199–207.

16. Korobeinikov, V. P., V. A. Levin, V. V. Markov, and G. G. Chernyi. 1972. Propagation of blast waves in a combustible gas. *Acta Astronautica* 17:529–37.

17. White, D. R. 1966. Density induction times in very lean mixtures of D_2, H_2, C_2H_2, and C_2H_4 with O_2. *11th Symposium (International) on Combustion Proceedings.* Berkeley, CA. 147–54.

18. Nikolaev, Yu. A., and P. A. Fomin. 1982. Analysis of equilibrium flows of chemically reacting gases. *Combustion Explosion Shock Waves* 18(1):53–58.

19. Nikolaev, Yu. A., and D. V. Zak. 1988. The agreement of models of chemical reactions in gases with the second law of thermodynamics. *Combustion Explosion Shock Waves* 24(4):87–90.

20. Godunov, S. K., ed. 1976. *Numerical solution of multidimensional problems of gaseous dynamics.* Moscow, Russia: Nauka.

21. Yamamoto, S., and H. Daiguji. 1993. Higher-order-accurate upwind schemes for solving the compressible Euler and Navier–Stokes equations. *Comput. Fluids* 22(2/3):259–70.

22. Batten, P., M. A. Leschziner, and U. C. Goldberg. 1997. Average-state Jacobians and implicit methods for compressible viscous and turbulent flows. *J. Computational Physics* 137:38–78.

23. Coquel, F., and B. Perthame 1998. Relaxation of energy and approximate Riemann Solvers for general pressure laws in fluid dynamics. *SIAM J. Numer. Anal.* 35(6):2223–49.

24. Shen, J. W., and X. Zhong. 1996. Semi-implicit Runge–Kutta schemes for nonautonomous differential equations in reactive flow computations. AIAA Paper No. 96-1969.

25. Trotsyuk, A. V. 1999. Numerical simulation of the structure of two-dimensional gaseous detonation of an H_2-O_2–Ar mixture. *Combustion Explosion Shock Waves* 35(5):549–58.

KINETICS OF IGNITION OF GASEOUS MIXTURES BY RESONANT LASER RADIATION

A. M. Starik and N. S. Titova

A kinetic model to describe combustion and detonation of hydrogen–oxygen mixtures preconditioned by laser-induced excitation of molecular oxygen to the $a^1\Delta_g$ and $b^1\Sigma_g^+$ electronic states has been developed. Mechanisms of reaction runaway in an adiabatic reactor and in a supersonic flow behind an oblique shock wave are analyzed. It is shown that in terms of characteristic reaction times, excitation of oxygen molecules to the $b^1\Sigma_g^+$ electronic state is more efficient than to the $a^1\Delta_g$ state. The comparative analysis of the efficiency of different approaches to initiate combustion and detonation in combustible mixtures is made. It is shown that the approach based on the excitation of O_2 molecules by resonant laser radiation is more efficient than the laser-induced thermal ignition.

1 INTRODUCTION

A possibility to intensify combustion and detonation processes by different physical means has been widely discussed during several tens of years [1–5]. First attempts to affect flames by electric field refer to early '70s of the last century. Since approximately the same time, various plasmochemical approaches to control combustion were considered. One of promising and least energy consuming methods to efficiently control deflagration and detonation of combustible mixtures is the selective excitation of vibrational or electronic degrees of freedom of reacting molecules. Recent studies demonstrated that preliminary excitation of molecular vibrations of H_2 and N_2 molecules as well as excitation of the first electronic state of oxygen molecules $a^1\Delta_g$, can reduce the self-ignition temperature and significantly decrease the induction and combustion zone lengths behind a detonation front induced by an inclined shock wave in a supersonic flow [6, 7]. The reason for these effects is the decrease of the barrier of endoergic reactions with participation of excited molecules. Oxygen molecules excited to the second electronic state, $b^1\Sigma_g^+$, should be more effective in overcoming the activation barrier than $O_2(a^1\Delta_g)$ molecules. Therefore the abundance of $O_2(b^1\Sigma_g^+)$ molecules in a reacting mixture should result in a stronger effect on combustion processes

than the presence of $O_2(a^1\Delta_g)$ molecules. One of effective means to selectively excite molecules is laser irradiation of the gaseous medium. In this case, the irradiation frequency should be in resonance with the frequency of a corresponding vibration–rotation or electronic–vibration molecular transition.

This paper deals with the analysis of a possibility to control ignition and detonation of H_2–O_2 mixtures by means of exciting O_2 molecules to the $a^1\Delta_g^+$ or $b^1\Sigma_g^+$ electronic states by using resonant laser radiation.

2 KINETIC MODEL

It is known that a fairly complete scheme of 29 reactions involving H, O, OH, H_2O, H_2, O_2, HO_2, H_2O_2, and O_3 species should be used to adequately describe ignition of H_2–O_2 mixtures in a wide range of initial temperatures and pressures, even without regard for excited molecules. The abundance of electronically excited molecules $O_2(a^1\Delta_g)$ and $O_2(b^1\Sigma_g^+)$ in the mixture requires consideration of additional reaction channels. First, it is necessary to specify processes with participation of $O_2(a^1\Delta_g)$ and $O_2(b^1\Sigma_g^+)$ molecules. Second, the reactions involving $O(^1D)$ atom should be involved as this species forms in the course of electronic–electronic exchange [8]. Reactions involving nonexcited molecules, electronically excited $O_2(a^1\Delta_g)$ and $O_2(b^1\Sigma_g^+)$ molecules, and $O(^1D)$ atoms are listed in Table 1 and numerated from 1 to 76. The appropriate rate coefficients for forward $k_{+q}(T)$ and backward $k_{-q}(T)$ reactions in the Arrhenius form $k_q(T) = A_q T^{n_q} \exp(-E_{aq}/T)$ are also given in Table 1. Here, T is the gas temperature, E_{aq} is the activation energy for the qth reaction, and A_q is the preexponential factor.

Consider in more detail the problem of calculating the reaction rates of processes involving excited molecules $O_2(a^1\Delta_g)$, $O_2(b^1\Sigma_g^+)$, and atoms $O(^1D)$. Excitation of the vibrational and electronic states of reacting molecules is known to decrease the barrier of endoergic reactions [9]. The rate constants for these reactions at $E_e < E_{aq}^0$, where E_e is the energy of an excited state of reacting molecules, and E_{aq}^0 is the activation energy of the qth chemical reaction involving nonexcited molecules, may be written in a conventional form:

$$k_{eq}(T) = A_q T^{n_q} \exp\left(-\frac{E_{aq}^e}{T}\right) \tag{1}$$

where E_{aq}^e is the activation energy of chemical reaction involving excited molecules. Consider how the E_{aq}^e value can be calculated for the exchange reaction:

$$AB(e) + C = A + BC$$

where $AB(e)$ denotes the molecule AB excited to the electronic state "e." According to [9], for the potential energy surfaces of forward, U_1, and reverse, U_2, reactions, one can write:

Table 1 List of reactions involved in kinetic model

No.	Reaction	k_{+q} $(\mathrm{cm}^3/\mathrm{mol})^{m-1}\cdot\mathrm{s}^{-1}$			k_{-q} $(\mathrm{cm}^3/\mathrm{mol})^{m-1}\cdot\mathrm{s}^{-1}$		
		A_q	n_q	E_{aq}	A_q	n_q	E_{aq}
1.	$H_2O + M = OH + H + M$	1(24)	−2.2	59,000	2.2(22)	−2	0
2.	$H_2 + M = 2H + M$	2.2(14)	0	48,300	9(17)	−1	0
3.	$O_2(X^3\Sigma_g^-) + M = O(^3P) + O(^3P) + M$	5.4(18)	−1	59,400	6(13)	0	−900
4.	$O_2(a^1\Delta_g) + M = O(^3P) + O(^3P) + M$	5.4(18)	−1	48,008			
5.	$O_2(b^1\Sigma_g^+) + M = O(^3P) + O(^3P) + M$	5.4(18)	−1	40,415			
6.	$OH + M = O(^3P) + H + M$	8.5(18)	−1	50,830	7.1(18)	−1	0
7.	$H_2 + O(^3P) = OH + H$	1.8(10)	1	4,480	8.3(9)	1	3,500
8.	$H_2 + O(^1D) = OH + H$	$0.95 \cdot 6.6(13)$	0	0			
9.	$O_2(X^3\Sigma_g^-) + H = OH + O(^3P)$	2.2(14)	0	8,455	1.3(13)	0	350
10.	$O_2(a^1\Delta_g) + H = OH + O(^3P)$	1.1(14)	0	3,188	5.8(12)	0	6,224
11.	$O_2(b^1\Sigma_g^+) + H = OH + O(^3P)$	1.1(14)	0	1,620			
12.	$H_2O + O(^3P) = 2OH$	5.8(13)	0	9,059	5.3(12)	0	503
13.	$H_2O + O(^1D) = 2OH$	1.32(14)	0	0			
14.	$H_2O + H = OH + H_2$	8.4(13)	0	10,116	2(13)	0	2,600
15.	$H_2 + O_2(X^3\Sigma_g^-) = 2OH$	1.7(15)	0	24,200	1.7(13)	0	24,100
16.	$H_2 + O_2(a^1\Delta_g) = 2OH$	1.7(15)	0	17,906			
17.	$H_2 + O_2(b^1\Sigma_g^+) = 2OH$	1.7(15)	0	14,657			
18.	$HO_2 + M = O_2(X^3\Sigma_g^-) + H + M$	$q_X \cdot 2.1(15)$	0	23,000	1.5(15)	0	−500
19.	$HO_2 + M = O_2(a^1\Delta_g) + H + M$	$q_a \cdot 2.1(15)$	0	23,000	1.5(15)	0	−500
20.	$HO_2 + M = O_2(b^1\Sigma_g^+) + H + M$	$q_b \cdot 2.1(15)$	0	23,000	1.5(15)	0	−500
21.	$H_2 + O_2(X^3\Sigma_g^-) = H + HO_2$	1.9(13)	0	24,100	1.3(13)	0	0
22.	$H_2 + O_2(a^1\Delta_g) = H + HO_2$	2.1(13)	0	18,216	6(12)	0	1,518
23.	$H_2 + O_2(b^1\Sigma_g^+) = H + HO_2$	2.1(13)	0	11,508			
24.	$H_2O + O(^3P) = H + HO_2$	4.76(11)	0.372	28,743	1(13)	0	540
25.	$H_2O + O(^1D) = H_2 + O_2(X^3\Sigma_g^-)$	1.32(12)	0	0			
26.	$H_2O + O_2(X^3\Sigma_g^-) = OH + HO_2$	1.5(15)	0.5	36,600	3(14)	0	0

Continued

Table 1 List of reactions involved in kinetic model (*Continued*)

No.	Reaction	k_{+q} $(\mathrm{cm}^3/\mathrm{mol})^{m-1}\cdot\mathrm{s}^{-1}$			k_{-q} $(\mathrm{cm}^3/\mathrm{mol})^{m-1}\cdot\mathrm{s}^{-1}$		
		A_q	n_q	E_{aq}	A_q	n_q	E_{aq}
27.	$H_2O + O_2(a^1\Delta_g) = OH + HO_2$	1.5(15)	0.5	25,209			
28.	$H_2O + O_2(b^1\Sigma_g^+) = OH + HO_2$	1.5(15)	0.5	17,616			
29.	$H_2O + OH = H_2 + HO_2$	7.2(9)	0.43	36,100	6.5(11)	0	9,400
30.	$2OH = H + HO_2$	1.2(13)	0	20,200	2.5(14)	0	950
31.	$OH + O_2(X^3\Sigma_g^-) = O(^3P) + HO_2$	1.3(13)	0	28,200	5(13)	0	500
32.	$OH + O_2(a^1\Delta_g) = O(^3P) + HO_2$	1.3(13)	0	17,132			
33.	$OH + O_2(b^1\Sigma_g^+) = O(^3P) + HO_2$	1.3(13)	0	10,111			
34.	$OH + O_2(X^3\Sigma_g^-) = O(^1D) + HO_2$				$q_X \cdot 3.96(13)$	0	0
35.	$OH + O_2(a^1\Delta_g) = O(^1D) + HO_2$				$q_a \cdot 3.96(13)$	0	0
36.	$OH + O_2(b^1\Sigma_g^+) = O(^1D) + HO_2$				$q_b \cdot 3.96(13)$	0	0
37.	$H_2O_2 + M = 2OH + M$	1.2(17)	0	22,900	9.1(14)	0	−2,650
38.	$H + H_2O_2 = H_2 + HO_2$	1.7(12)	0	1,900	6(11)	0	9,300
39.	$H + H_2O_2 = H_2O + OH$	5(14)	0	5,000	2.4(14)	0	40,500
40.	$2HO_2 = H_2O_2 + O_2(X^3\Sigma_g^-)$	1.8(13)	0	500	3(13)	0	21,600
41.	$2HO_2 = H_2O_2 + O_2(a^1\Delta_g)$				3(13)	0	10,717
42.	$2HO_2 = H_2O_2 + O_2(b^1\Sigma_g^+)$				3(13)	0	4,510
43.	$HO_2 + H_2O = H_2O_2 + OH$	1.8(13)	0	15,100	1(13)	0	910
44.	$OH + HO_2 = H_2O_2 + O(^3P)$	5.2(10)	0.5	10,600	2(13)	0	2,950
45.	$H_2O + O_2(X^3\Sigma_g^-) = H_2O_2 + O(^3P)$	3.4(10)	0.5	44,800	8.4(11)	0	2,130
46.	$H_2O + O_2(a^1\Delta_g) = H_2O_2 + O(^3P)$	3.4(10)	0.5	34,079			
47.	$H_2O + O_2(b^1\Sigma_g^+) = H_2O_2 + O(^3P)$	3.4(10)	0.5	27,195			
48.	$O_3 + M = O(^3P) + O_2(X^3\Sigma_g^-) + M$	4(14)	0	11,400	6.9(12)	0	−1050
49.	$O_3 + M = O(^3P) + O_2(a^1\Delta_g) + M$	4(14)	0	22,790			
50.	$O_3 + M = O(^3P) + O_2(b^1\Sigma_g^+) + M$	4(14)	0	30,384			

Continued

Table 1 List of reactions involved in kinetic model (*Continued*)

No.	Reaction	k_{+q} $(cm^3/mol)^{m-1}\cdot s^{-1}$			k_{-q} $(cm^3/mol)^{m-1}\cdot s^{-1}$		
		A_q	n_q	E_{aq}	A_q	n_q	E_{aq}
51.	$O_3+H=OH+O_2(X^3\Sigma_g^-)$	2.3(11)	0.75	0	4.4(7)	1.44	38,600
52.	$O_3+H=OH+O_2(a^1\Delta_g)$				4.4(7)	1.44	27,209
53.	$O_3+H=OH+O_2(b^1\Sigma_g^+)$				4.4(7)	1.44	19,616
54.	$O_3+O(^3P)=2O_2(X^3\Sigma_g^-)$	1.1(13)	0	2,300	1.2(13)	0	50,500
55.	$O_3+O(^3P)$ $=O_2(X^3\Sigma_g^-)+O_2(a^1\Delta_g)$				1.2(13)	0	39,732
56.	$O_3+O(^3P)$ $=O_2(X^3\Sigma_g^-)+O_2(b^1\Sigma_g^+)$				1.2(13)	0	32,761
57.	$O_3+O(^1D)$ $=2O_2(X^3\Sigma_g^-)$	$0.095\cdot 1.44(14)$	0	0			
58.	$O_3+O(^1D)$ $=O_2(X^3\Sigma_g^-)+O_2(a^1\Delta_g)$	$0.063\cdot 1.44(14)$	0	0			
59.	$O_3+O(^1D)$ $=O_2(X^3\Sigma_g^-)+O_2(b^1\Sigma_g^+)$	$0.032\cdot 1.44(14)$	0	0			
60.	$O_3+O(^1D)=O_2(X^3\Sigma_g^-)$ $+O(^3P)+O(^3P)$	$0.81\cdot 1.44(14)$	0	0			
61.	O_3+OH $=HO_2+O_2(X^3\Sigma_g^-)$	$q_X\cdot 9.6(11)$	0	1,000	9(8)	0	0
62.	O_3+OH $=HO_2+O_2(a^1\Delta_g)$	$q_a\cdot 9.6(11)$	0	1,000			
63.	O_3+OH $=HO_2+O_2(b^1\Sigma_g^+)$	$q_b\cdot 9.6(11)$	0	1,000			
64.	$O_3+H_2=OH+HO_2$	6(10)	0	10,000			
65.	O_3+HO_2 $=OH+2O_2(X^3\Sigma_g^-)$	$q_X\cdot 2(10)$	0	1,000			
66.	$O_3+HO_2=OH$ $+O_2(X^3\Sigma_g^-)+O_2(a^1\Delta_g)$	$q_a\cdot 2(10)$	0	1,000			
67.	$O_3+HO_2=OH$ $+O_2(X^3\Sigma_g^-)+O_2(b^1\Sigma_g^+)$	$q_b\cdot 2(10)$	0	1,000			
68.	$O_3+O_2(a^1\Delta_g)$ $=2O_2(X^3\Sigma_g^-)+O(^3P)$	3.13(13)	0	2,840			
69.	$O_3+O_2(b^1\Sigma_g^+)$ $=2O_2(X^3\Sigma_g^-)+O(^3P)$	9(12)	0	0			
70.	$2O_2(a^1\Delta_g)$ $=O_2(b^1\Sigma_g^+)+O_2(X^3\Sigma_g^-)$	4.2(−4)	3.8	−700			
71.	$O_2(a^1\Delta_g)+M$ $=O_2(X^3\Sigma_g^-)+M$						
	$M=O,H$	4.2(8)	0	0			
	$M=O_3$	2.4(9)	0	0			
	$M=O_2$	1.02(6)	0	0			
	$M=H_2$	2.7(6)	0	0			
	$M=H_2O,OH,HO_2,H_2O_2$	3.36(6)	0	0			

Continued

Table 1 List of reactions involved in kinetic model (*Continued*)

No.	Reaction	k_{+q} $(\text{cm}^3/\text{mol})^{m-1}\cdot\text{s}^{-1}$			k_{-q} $(\text{cm}^3/\text{mol})^{m-1}\cdot\text{s}^{-1}$		
		A_q	n_q	E_{aq}	A_q	n_q	E_{aq}
72.	$O_2(b^1\Sigma_g^+)+M = O_2(a^1\Delta_g)+M$						
	$M = O, H$	4.8(10)	0	0			
	$M = O_3$	1.08(13)	0	0			
	$M = O_2$	2.76(7)	0	0			
	$M = H_2$	4.92(11)	0	0			
	$M = H_2O, OH, HO_2$	4.02(12)	0	0			
	$M = H_2O_2$	6(12)	0	0			
73.	$O(^1D) + O_2(X^3\Sigma_g^-)$ $= O(^3P) + O_2(a^1\Delta_g)$	$0.2 \cdot 1.92(13)$	0	−67			
74.	$O(^1D) + O_2(X^3\Sigma_g^-)$ $= O(^3P) + O_2(b^1\Sigma_g^+)$	$0.8 \cdot 1.92(13)$	0	−67			
75.	$O(^1D) + O_2(a^1\Delta_g)$ $= O(^3P) + O_2(b^1\Sigma_g^+)$	3(13)	0	0			
76.	$O(^1D) + M = O(^3P) + M$						
	$M = O, H, O_3, O_2$	1.92(13)	0	−67			
	$M = H_2$	$0.05 \cdot 6.6(13)$	0	0			
	$M = H_2O, OH, HO_2, H_2O_2$	7.2(12)	0	0			

Remark: $A(n)$ corresponds to $A \cdot 10^n$.

$$U_1 = \Delta H + E_a^0 \exp\left(\frac{r}{r_1}\right)$$

$$U_2 = (\Delta H + E_a^0) \exp\left(-\frac{r}{r_2}\right)$$

where ΔH is the thermal effect of reaction, r_1 and r_2 are the action radii of exchange forces for reactants and products, respectively. For reactions involving molecules excited to the electronic state "e," the potential energy surface is determined by the expression:

$$U_1^e = \Delta H + E_e + E_a^0 \exp\left(\frac{r}{r_1}\right)$$

At the point of intersection of potential energy surfaces for forward and reverse reactions, $U_1^e = U_2$. With a conventional assumption that $r_1 = r_2$ [9], the expression for E_a^e may be written in the form:

$$E_a^e = \frac{1}{2}\left(\sqrt{(\Delta H + E_e)^2 + 4E_a^0(\Delta H + E_a^0)} - (\Delta H + E_e)\right) \qquad (2)$$

Equations (1) and (2) were used to calculate the rate constants for forward reactions Nos. 4, 5, 16, 17, 27, 28, 32, 33, 46, and 47 and for reverse reactions

Nos. 41, 42, 52, 53, 55, and 56. Note that this approach cannot be applied to calculate the rate constant for (*i*) reactions with $E_a^0 = 0$, and (*ii*) reactions with $O_2(b^1\Sigma_g^+)$ molecules, when the value of activation energy is of the same order of magnitude as the energy of the excited state $b^1\Sigma_g^+$ (E_e = 18,984 K). The first type of reactions includes the reactions producing oxygen molecules in different electronic states $X^3\Sigma_g^-$, $a^1\Delta_g$, and $b^1\Sigma_g^+$. The second type includes reactions of chain propagation: $H + O_2(b^1\Sigma_g^+) = OH + O$ and $H_2 + O_2(b^1\Sigma_g^+) = HO_2 + H$.

To estimate the rate coefficients for the reactions of the first type, the procedure suggested in [10] has been used. It was assumed that the probability of production of O_2 molecules in electronic states $X^3\Sigma_g^-$, $a^1\Delta_g$, and $b^1\Sigma_g^+$ is determined by its degeneration multiplicity, q_e. For the ground state $X^3\Sigma_g^-$, $q_X = 0.5$; for $a^1\Delta_g$ state — $q_a = 0.33$; and for $b^1\Sigma_g^+$ — $q_b = 0.17$. This way, the rate coefficients for reactions Nos. 18–20, 34–36, 61–63, and 65–67 have been determined.

The rate coefficients for chain propagation reactions with $O_2(a^1\Delta_g)$ molecules (Nos. 10 and 22) were presented in [7]. For the reactions of the same type with $O_2(b^1\Sigma_g^+)$ molecules (Nos. 11 and 23), the rate coefficients were derived using Eqs. (1) and (2), taking into account that the values of ΔH and E_a^0 correspond to reactions Nos. 10 and 22, and $E_a = \Delta E_{ba}$, with ΔE_{ba} = 7,593 K. For reactions Nos. 8, 13, 25, 57–60, and 73–76 with excited oxygen atoms $O(^1D)$, the rate coefficients were selected using recommendations [8, 11]. The rate coefficients for processes of electronic–electronic (E–E) exchange and electronic–translational (E–T) relaxation of $O_2(b^1\Sigma_g^+)$ and $O_2(a^1\Delta_g)$ molecules (Nos. 70–72) were taken from [12]. For the reactions that lack the Arrhenius data in Table 1, the rate constants were determined using the principle of detailed equilibrium.

$O_2(a^1\Delta_g)$ and $O_2(b^1\Sigma_g^+)$ molecules are generated by laser irradiation with the frequency in resonance with the frequency corresponding to the center of spectral line of the electronic–vibration transition $m(e', v', j', K') \rightarrow n(e'', v'', j'', K'')$, where $e' \equiv X^3\Sigma_g^-$, $e'' \equiv a^1\Delta_g$ or $b^1\Sigma_g^+$, v' and v'' are the vibrational quantum numbers, j', K' and j'', K'' are the rotational quantum numbers in the ground ($X^3\Sigma_g^-$) and in the electronically excited ($a^1\Delta_g$ or $b^1\Sigma_g^+$) states. The analysis has been performed for ${}^QP(9)$ branch of transition with $v' = v'' = 0$ ($j' = 10$, $j'' = K' = K'' = 9$). The wavelength $\lambda_I = 1.268$ μm corresponds to $X^3\Sigma_g^- \rightarrow a^1\Delta_g$ transition and $\lambda_I = 762$ nm to $X^3\Sigma_g^- \rightarrow b^1\Sigma_g^+$ transition. The scheme of low electronic terms of O_2 molecule and corresponding transitions are shown in Fig. 1. Note that these transitions are allowed in the magnetic dipole approximation [13].

The suggested kinetic model assumes that the time of radiation-induced transition $\tau_I \gg \tau_R, \tau_V$, where τ_R and τ_V are the characteristic times of rotational and vibrational relaxation. In this case, at $t \gg \tau_R, \tau_V$, the translational, rotational, and vibrational degrees of freedom of molecules in the mixture are in thermodynamic equilibrium which is not disturbed by chemical reactions. The excited molecules $O_2(a^1\Delta_g)$, $O_2(b^1\Sigma_g^+)$, and atoms $O(^1D)$ are considered as individual chemical species.

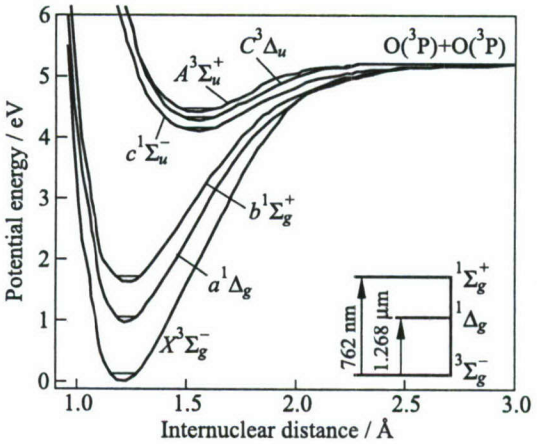

Figure 1 Scheme of the electronic terms of oxygen molecule

3 IGNITION OF STAGNANT MIXTURE BY RESONANT LASER RADIATION

Consider ignition of a premixed stagnant, homogeneous H_2–O_2 mixture irradiated by a laser pulse at resonant wavelength $\lambda_I = 1.268$ μm or 762 nm of duration τ_p. Evolution of hydrodynamic parameters in the irradiated region is governed by the hierarchy of characteristic times of different macro- and micro-transport processes [13]. For nonreacting, inviscid gas, these are: the time of propagation of the acoustic vibrations across the beam, τ_a; times of multicomponent, τ_D^i, and thermal diffusion, τ_{T_i}, for the ith species; heat-conduction time, τ_λ; time of induced transition, τ_I; duration of radiation pulse, τ_p; and time of changing the state of the medium under the action of striction force, τ_F. For reacting gas, the list of characteristic times should be supplemented with a characteristic time of the qth chemical reaction for the ith species, τ_{iq}^{ch}. The latter determines the time of ignition delay (or induction time), τ_{in}.

The processes in $2H_2 + O_2$ mixture were simulated in the region irradiated by a laser beam with Gaussian radial intensity distribution, $I(r,t) = I_0(t)\exp(-r^2/R_a^2)$, where R_a is the beam radius, and $I_0(t) = I_0$ at $0 < t \leq \tau_p$, $I_0(t) = 0$ at $t > \tau_p$, with $I_0 = 1$–20 kW/cm^2, $R_a = 10$ cm, and the initial pressure and temperature $P_0 = 10^3$–10^4 Pa, $T_0 = 300$–700 K, respectively. For these conditions, at $\lambda_I = 762$ nm, the simulation results are: $\tau_I \approx 10^{-5}$–$6 \cdot 10^{-3}$ s, $\tau_a \approx 2 \cdot 10^{-4}$ s, $\tau_D \sim \tau_{T_i} \sim \tau_\lambda \approx 0.3$–$10$ s, $\tau_F \approx 0.5$–10 s.

Consider ignition at $\tau_a \ll \tau_p \sim \tau_I \leq \tau_{\mathrm{in}} \ll \tau_D, \tau_F$. Under specified conditions, the value of the absorption coefficient, k_ν, varies from $8 \cdot 10^{-5}$ up to $2 \cdot 10^{-3}$, and, consequently, $k_\nu^{-1} \ll R_a$. Therefore, the influence of the longitudi-

nal variation of the parameters on their distribution in a beam cross-section may be ignored. Also, the rate of spontaneous emission for the $O_2(a^1\Delta_g)$, $O_2(b^1\Sigma_g^+)$, and $O(^1D)$ states is significantly less than the rates of chemical reactions. At $t > \tau_a$, it may be assumed that $P(r,t) = P_a$, where P_a is the pressure in the undisturbed gas ($P_a = P_0$). With this in mind, the set of equations governing the ignition process in the irradiated zone, $r < R_a$, may be written in the form:

$$\frac{\partial N_i}{\partial t} = G_i + q_I^i$$

$$\rho\frac{\partial E}{\partial t} = k_\nu I - \rho\sum_{i=1}^{3} h_{0i}q_I^i - \rho\sum_{i=1}^{M} h_{0i}G_i$$

$$G_i = \sum_{q=1}^{M_1} S_{iq}, \quad S_{iq} = (\alpha_{iq}^- - \alpha_{iq}^+)[R_q^+ - R_q^-], R_q^{+(-)} = k_{+(-)q}\prod_{j=1}^{n_q^{+(-)}} N_j^{\alpha_{jq}^{+(-)}}$$

$$q_I^i = \ell_{Ii}W_{Ii}\left(\frac{g_{ni}}{g_{mi}}N_m - N_n\right), \; W_I = \frac{\sigma_{mn}I}{h\nu_I}, \; \sigma_{mn} = \frac{\lambda_{mn}^2}{4\pi b_D}A_{mn}\sqrt{\frac{\ln 2}{\pi}}H(x,a)$$

$$k_\nu = \sigma_{mn}\left(\frac{g_n}{g_m}N_m - N_n\right), \; E = \sum_{i=1}^{M} C_{VT}^i T, \; C_{VT}^i = \frac{R}{\mu}\gamma_i\left(\frac{3}{2} + C_R^i + C_V^i\right)$$

$$C_V^i = \sum_{\ell=1}^{L_i}\left(\frac{\theta_{i\ell}}{T}\right)^2\frac{\exp(\theta_{i\ell}/T)}{[\exp(\theta_{i\ell}/T)-1]^2}, \; \mu = \sum_{i=1}^{M}\mu_i\gamma_i, \; \gamma_i = \frac{N_i}{N}, \; N = \sum_{i=1}^{M} N_i$$

where ρ and T are the gas density and temperature, respectively; N_i is the number density of molecules (or atoms) of the ith sort ($i = 1$, 2, and 3 correspond to $O_2(X^3\Sigma_g^-)$, $O_2(a^1\Delta_g)$, and $O_2(b^1\Sigma_g^+)$, respectively); μ_i is their molecular mass; h_{0i} is the entalphy of formation of the ith species; M is the total number of species in the mixture; $C_R^i = 1$ for species consisting of linear molecules, and $C_R^i = 1.5$ for species consisting of nonlinear molecules; θ_{ij} is the characteristic vibrational temperature of the jth mode for the ith species ($j = 1, \ldots, L_i$); M_1 is the number of reactions that produce (or deplete) the ith species of the mixture; α_{iq}^+ and α_{iq}^- are the stoichoimetric coefficients of the qth reaction; $n_q^{+(-)}$ is the number of species involved in forward (+) and reverse (−) reactions, $k_{+(-)q}$ are the rate constants of these reactions; R is the universal gas constant; k_B is the Boltzmann constant; ℓ_{Ii} is the number of quanta lost or acquired by the ith species during laser-induced transitions; N_m and N_n are the numbers of molecules at the low and upper states of the transition $m \to n$; g_m and g_n are the corresponding degeneracy multiplicities; h is the Plank constant; λ_{mn} is the wavelength at the center of the line due to absorbing transition $m \to n$; A_{mn} is the Einstein coefficient for this transition; b_D is the Doppler width of the line at its half-height; and $H(x,a)$ is the Voigt function which was calculated with due regard for the Doppler and collisional mechanisms of spectral line broadening [8].

Ignition of combustible mixture is caused by initiation of chain-branching reactions. For H_2–O_2 (air) mixtures, these reactions, in general, involve O and H atoms, and OH radicals. Formation of these species is represented in the kinetic scheme and is specified by the time τ_{iq}^{ch}. Removal of active radicals from the reaction zone occurs due to chain termination reactions and diffusion processes. Ignition of the mixture occurs if the condition $\tau_{iq}^{ch} < \tau_D^i$ (i = O, H, OH) is satisfied.

Consider first formation of active atoms O and H, and OH radicals under irradiation of $2H_2 + O_2$ mixture at $\lambda_I = 1.268$ μm and 762 nm. Figure 2 shows the evolution of species mole fractions, γ_i, vs. time during ignition in the absence of radiation (a), under irradiation at $\lambda_I = 1.268$ μm (b), and $\lambda_I = 762$ nm (c) at $I_0 = 10$ kW/cm^2, $\tau_p = 10^{-3}$ s. One can see that excitation of oxygen molecules to the $a^1\Delta_g$ state by radiation with $\lambda_I = 1.268$ μm and to the $b^1\Sigma_g^+$ state by radiation with $\lambda_I = 762$ nm leads to a significant decrease of the induction time. In the absence of irradiation at $T_0 = 600$ K and $P_0 = 10^3$ Pa, the value of τ_{in} is 1.5 s (note that the value of τ_{in} was defined as the time taken for H atoms to achieve maximum concentration). Under irradiation at $\lambda_I = 1.268$ μm and at $\lambda_I = 762$ nm with the energy input of $E_{in} = 10$ J/cm^2 ($E_{in} = I_0\tau_p$), the result is $\tau_{in} = 0.15$ s and $4.56 \cdot 10^{-3}$ s, respectively.

Excitation of O_2 molecules to the $a^1\Delta_g$ and $b^1\Sigma_g^+$ states leads to the change in dynamics of species concentrations during induction time. This is caused by additional channels of H, O, and OH species formation. Excitation of O_2 molecules to the $b^1\Sigma_g^+$ state results in production of $O_2(a^1\Delta_g)$ molecules. This occurs due to E–T relaxation of the $O_2(b^1\Sigma_g^+)$ state via reaction No. 72 and higher value of W_I for $X^3\Sigma_g^- \rightarrow b^1\Sigma_g^+$ transition compared with the rate of induced transition $X^3\Sigma_g^- \rightarrow a^1\Delta_g$. The concentration of $O_2(a^1\Delta_g)$ at $t = \tau_p$ is substantially higher (by a factor of 50) than under excitation of oxygen molecules directly to the $a^1\Delta_g$ state by resonant radiation with $\lambda_I = 1.268$ μm. Therefore, irradiation at $\lambda_I = 762$ nm is more efficient in reducing τ_{in} as compared with irradiation at $\lambda_I = 1.268$ μm.

Collisional E–T relaxation of the $O_2(b^1\Sigma_g^+)$ state leads to a slight increase of the gas temperature under irradiation at $\lambda_I = 762$ nm. At $T_0 = 600$ K, $P_0 = 10^3$ Pa, and $I_0 = 5$ kW/cm^2, $\tau_p = 10^{-3}$ s, the temperature grows up to 647 K at $t = \tau_p$. Increasing I_0 or E_{in} results in further temperature rise. This is illustrated by Fig. 3 that shows the evolution of the gas temperature under irradiation of $2H_2 + O_2$ mixture at $\lambda_I = 1.268$ μm and 762 nm, $I_0 = 5$; 10; and 20 kW/cm^2, $\tau_p = 10^{-3}$ s. Note that at given I_0 and τ_p values, the radiation energy $E_s = I\tau_p k_\nu / N_1$ absorbed by a single oxygen molecule is very small (for $\lambda_I = 762$ nm, E_s is 0.082; 0.15; and 0.3 eV, respectively; for $\lambda_I = 1.268$ μm, E_s is $1.2 \cdot 10^{-2}$; $2.4 \cdot 10^{-3}$; and $4.8 \cdot 10^{-3}$ eV, respectively). Reduction in the induction time under irradiation of H_2–O_2 mixture at $\lambda_I = 762$ nm is mainly caused by new channels of O, H, and OH species formation and promotion of chain mechanism of combustion, rather than heating of the gas in the irradiation

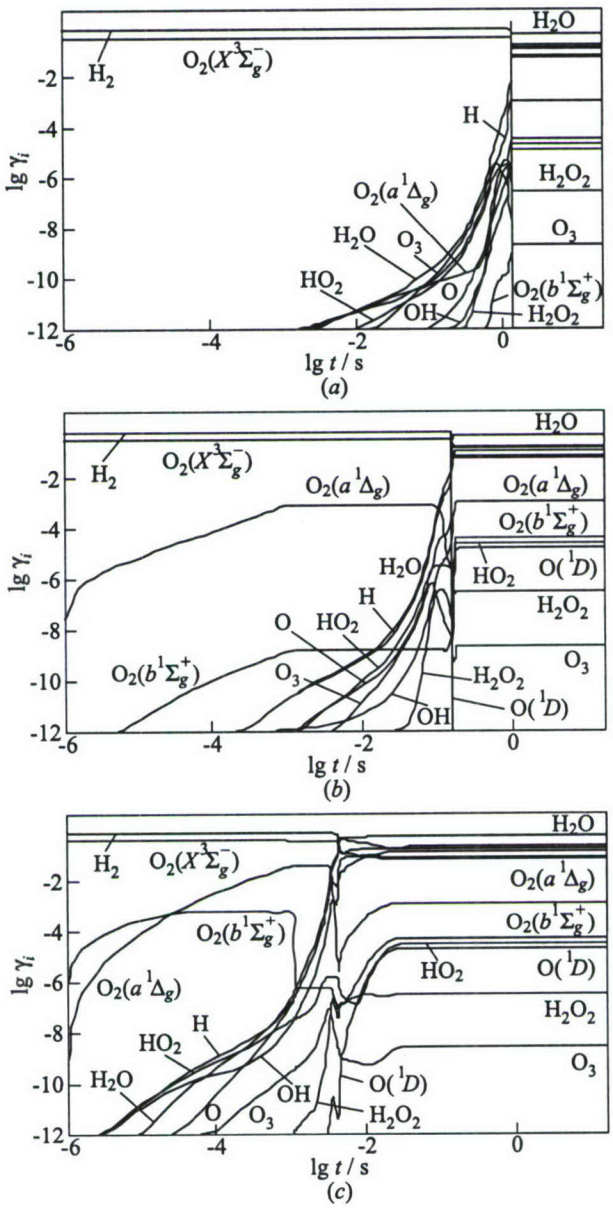

Figure 2 Predicted time histories of species mole fractions during ignition of $2H_2 + O_2$ mixture at $T_0 = 600$ K, $P_0 = 10^3$ Pa in the absence of radiation (a) and under irradiation with $\lambda_I = 1.268$ μm (b) and $\lambda_I = 762$ nm (c) at $I_0 = 10$ kW/cm^2, $\tau_p = 10^{-3}$ s

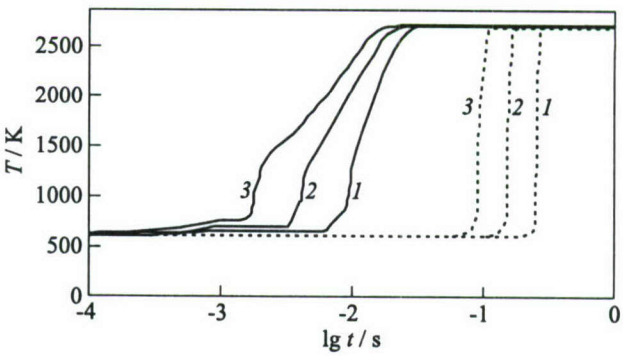

Figure 3 Predicted evolution of temperature during ignition of $2H_2 + O_2$ mixture ($T_0 = 600$ K, $P_0 = 10^3$ Pa) under resonant irradiation at $\lambda_I = 1.268$ μm (dotted curves) and 762 nm (solid curves); $\tau_p = 10^{-3}$ s, $I_0 = 5$ (*1*); 10 (*2*); and 20 kW/cm^2 (*3*)

zone. As a matter of fact, increase of temperature to $T = 688$ K at $t = 10^{-3}$ s in the irradiated region at $I_0 = 10$ kW/cm^2, $\tau_p = 10^{-3}$ s, $T_0 = 600$ K, and $P_0 = 10^3$ Pa may lead to decrease in the τ_{in} value to only 0.14 s. This time is by a factor of 30 longer than the predicted induction time with regard for chain reactions caused by abundance of $O_2(a^1\Delta_g)$ and $O_2(b^1\Sigma_g^+)$ molecules in the irradiated zone.

Figure 4 shows the histories of the rates, S_{iq}, of reactions producing O, H, and OH during combustion of the $2H_2 + O_2$ mixture under irradiation at $\lambda_I = 1.268$ μm and 762 nm. In the absence of irradiation, the principal reaction of chain initiation is $H_2 + O_2 = 2OH$ (No. 15). The second step in the chain propagation is $H_2 + OH = H_2O + H$ (reverse reaction No. 14). H atoms produced in this process react with O_2, thus favoring the formation of O atoms (reaction No. 9). O atoms further react with H_2 to yield hydrogen atoms again (reaction No. 7). These reactions complete chain-branching mechanism of H_2–O_2 mixture combustion. Irradiation at $\lambda_I = 1.268$ μm results in excitation of O_2 molecules to the $a^1\Delta_g$ state that launches new channels of O, H, and OH formation. The representative reactions Nos. 10, 16, and 68 proceed much faster than the corresponding processes with nonexcited oxygen molecules. Fast formation of H, O, and OH species enhances the chain mechanism of combustion and reduces the induction time and self-ignition temperature.

Under irradiation at $\lambda_I = 762$ nm, in addition to $O_2(a^1\Delta_g)$ molecules, the $O_2(b^1\Sigma_g^+)$ molecules are also abundant in noticeable amount. Therefore the processes Nos. 17 and 23 with participation of $O_2(b^1\Sigma_g^+)$ become the main reactions of chain initiation. Reaction No. 17 results in OH radical formation and reaction No. 23 produces H atoms. Due to abundance of $O_2(a^1\Delta_g)$ molecules (at $I_0 = 10$ kW/cm^2, $\tau_p = 10^{-3}$ s, the concentration of $O_2(a^1\Delta_g)$ at $t = \tau_p$ attains

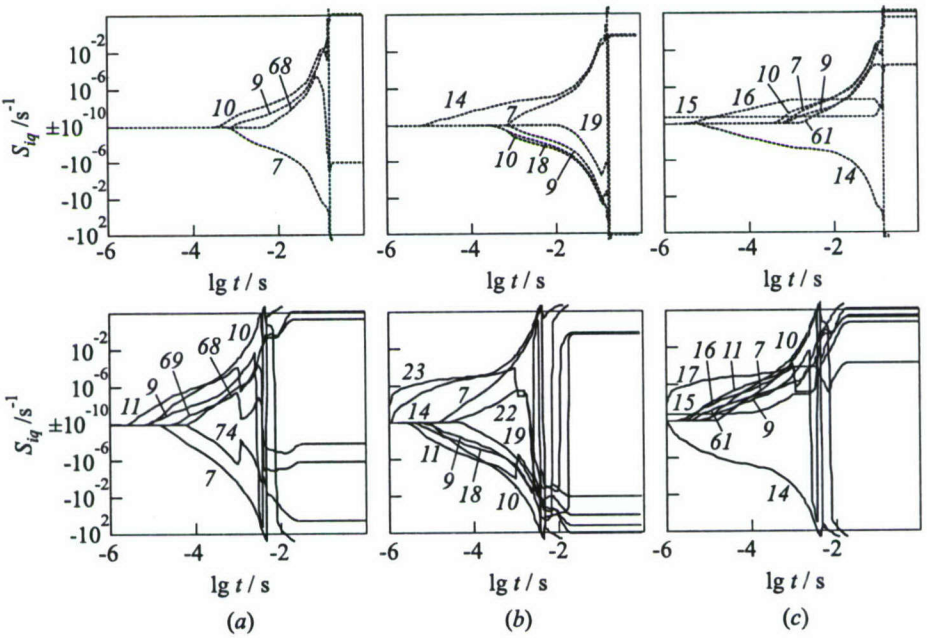

Figure 4 Predicted time histories of production (+) and depletion (−) rates S_{iq} for H (*a*), O (*b*), and OH (*c*) species during ignition of $2H_2 + O_2$ mixture at $T_0 = 600$ K and $P_0 = 10^3$ Pa under laser irradiation at $\lambda_I = 1.268$ μm (dashed curves) and $\lambda_I = 762$ nm (solid curves); $I_0 = 10$ kW/cm^2, $\tau_p = 10^{-3}$ s

3%), formation of O atoms at initial stage of ignition occurs in chain-branching reactions Nos. 10 and 11. Enhancement of chain mechanism of combustion in this case is more efficient than under excitation of O_2 molecules to the $a^1\Delta_g$ state by laser radiation with $\lambda_I = 1.268$ μm at the same values of I_0 and τ_p.

It is interesting to compare efficiencies of the laser-induced thermal method of combustion initiation with that used in this issue. In the thermal method, laser radiation is used to heat the combustible mixture [3]. The method considered in this paper is based on excitation of oxygen molecules to the $a^1\Delta_g$ and $b^1\Sigma_g^+$ electronic states. The comparison is shown in Fig. 5 in terms of the dependencies $\tau_D^{\mathrm{H}}(T_0)$ of the diffusion time of H atoms vs. initial temperature T_0, and $\tau_{\mathrm{in}}(T_0)$ computed at $P_0 = 10^3$ Pa, $I_0 = 1$; 5; and 10 kW/cm^2, $\tau_p = 10^{-3}$ s. The first method relates to laser-induced thermal ignition when radiation energy absorbed by oxygen molecules at $\lambda_I = 762$ nm transforms to translational degrees of freedom of molecules and results in increasing the temperature of the mixture. The second method relates to the excitation of oxygen molecules to the $b^1\Sigma_g^+$ state. One can see that the method based on excitation of O_2 molecules

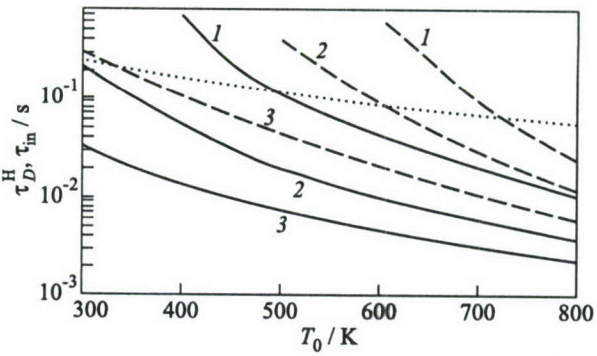

Figure 5 Predicted dependencies of $\tau_D^{\mathrm{H}}(T_0)$ (dotted curve) and $\tau_{\mathrm{in}}(T_0)$ under irradiation of $2H_2 + O_2$ mixture ($P_0 = 10^3$ Pa) at $\lambda_I = 762$ nm, $I_0 = 1$; 5; 10 kW/cm^2 (curves *1–3*) $\tau_p = 10^{-3}$ s for the case of excitation of $O_2(b^1\Sigma_g^+)$ state by laser radiation (solid curves), and when absorbed radiation energy transforms to the thermal energy of the mixture (dashed curves)

by resonant laser radiation is much more efficient than laser-induced thermal ignition. Excitation of O_2 molecules leads to a more significant reduction in τ_{in} and in the self-ignition temperature, T_{ign}. The value of T_{ign} may be estimated from equation $\tau_{\mathrm{in}}(I_0, T_0) = \tau_D^{\mathrm{H}}(T_0)$. At $I_0 = 5$ kW/cm^2, this method allows the decrease of T_{ign} to 300 K, while the laser-induced thermal method allows the decrease of T_{ign} to only 600 K.

4 MIXTURE IGNITION IN SUPERSONIC FLOW

Consider now the supersonic flow of premixed H_2–O_2 mixture with a stationary shock wave (Fig. 6). The shock wave front is assumed to incline to angle $\beta < 90°$ with respect to the approach stream velocity vector u_0. In front of the shock, at the interval $[x_0 - \delta, x_0]$, laser radiation with $I_0 = \mathrm{const}$ and with the frequency in resonance with the frequency of electronic–vibrational transitions mentioned above affects the combustible mixture. Here, x_0 is the position of the shock front. In this case, besides characteristic times governing the excitation of O_2 molecules by laser radiation in stagnant gas, the spatial scales of radiation exposure come into great importance. These are: the absorption length, L_ν ($L_\nu = k_\nu^{-1}$), and the length of irradiated zone, δ. The latter is connected with τ_p and flow velocity, i.e., $\delta = \tau_p u_0$.

Consider the case when $\delta \ll L_\nu$. The equations governing the flow of reacting mixture along the x-axis (x-axis is aligned with the gas particle trajectory) may be written in the form:

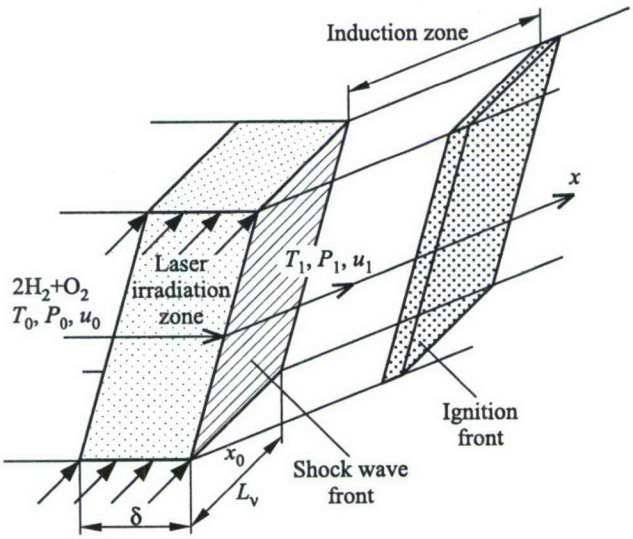

Figure 6 Schematic of the flow with laser-induced ignition behind the inclined shock front

$$u\frac{dN_i}{dx} = G_i + q_I^i\,; \qquad u\frac{du}{dx} + \frac{1}{\rho}\frac{dP}{dx} = 0\,; \qquad \frac{dH}{dx} + u\frac{du}{dx} = \frac{k_\nu I}{\rho u}$$

$$H = \sum_{i=1}^{M} h_{0i}\gamma_i + C_pT\,; \qquad C_p = \sum_{i=1}^{M} C_{VT}^i + \frac{R}{\mu}$$

Parameters behind the shock front (further labeled by subscript 1) are found from the equations of mass, momentum, and energy conservation assuming that species concentrations remain unchanged in the shock front. At low temperatures in the irradiation zone in front of the shock, the rates of chemical reactions are significantly less than the rates of radiation-induced transitions and the rate of E–T relaxation for the $a^1\Delta_g$ and $b^1\Sigma_g^+$ states. In this region, the evolution of $O_2(a^1\Delta_g)$ and $O_2(b^1\Sigma_g^+)$ concentrations is specified by several characteristic times: time τ_I; time of collisional relaxation of excited states of oxygen molecules, τ_R; and irradiation time, $\tau_p = \delta/u_0$. Immediately behind the shock front, the temperature and pressure of the mixture increase stepwise and chemical reactions start. This is clearly seen in Fig. 7 showing variation of concentrations and gas temperature along the x-axis in the irradiation region and behind the shock in $2H_2 + O_2$ mixture ($T_0 = 300$ K and $P_0 = 10^3$ Pa) for $\lambda_I = 762$ nm, $I = 10$ kW/cm^2, $\delta = 0.5$ m, Mach number of undisturbed flow $M_0 = 6$, and $\beta = 25°$. The abundance of excited molecules $O_2(a^1\Delta_g)$ and $O_2(b^1\Sigma_g^+)$ in the reaction zone leads to intensification of chain mechanism of combustion and initiation

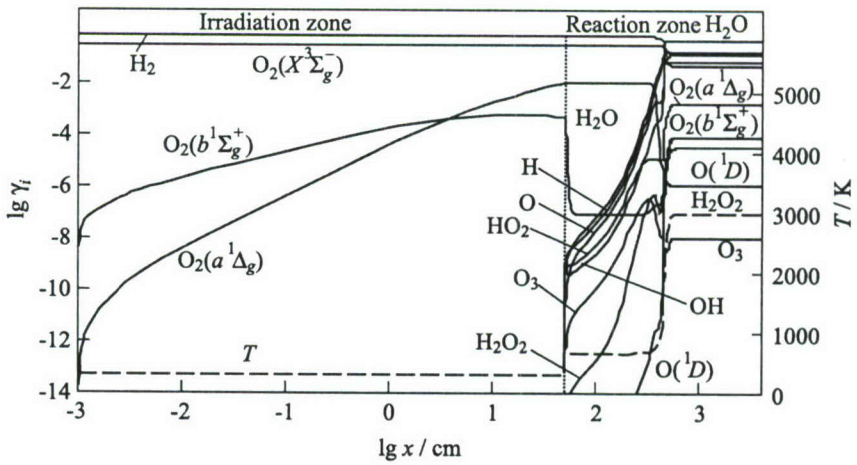

Figure 7 Predicted evolution of temperature (dashed curve) and species mole fractions (solid curves) in the irradiation zone and in the reaction zone behind an inclined shock at $P_0 = 10^3$ Pa, $T_0 = 300$ K, $M_0 = 6$, and $\beta = 25°$. The flow of the $2H_2 + O_2$ mixture is subject to laser irradiation with $\lambda_I = 762$ nm, $I_0 = 10$ kW/cm^2, and $\delta = 0.5$ m. Vertical dotted line denotes shock location

of ignition at distance $L_{in} = 3.9$ m from the shock front. In the absence of irradiation, $L_{in} \sim 1$ km, i.e., there is a lack of ignition.

Increase in I_0 and τ_p results in further reduction of the induction zone length at given values of P_0, T_0, β, and M_0. Initial pressure, P_0, has a strong effect on L_{in}, too. The dependence of L_{in} on P_0 at $M_0 = 6$, $\beta = 25°$, $T_0 = 300$ K, and different values of the input radiation energy: $E_{in} = 0.3$; 1; and 3 J/cm^2, with $\lambda_I = 762$ nm is shown in Fig. 8. To compare the efficiency of this method of detonation initiation and the laser-induced thermal method, the corresponding dependencies of $L_{in}(P_0)$ are also plotted in Fig. 8*. The length of induction zone, L_{in}, was calculated for two more cases: (*i*) in the absence of irradiation, and (*ii*) when total absorbed radiation energy with $\lambda_I = 762$ nm is consumed for mixture heating in front of the shock. There exist three ranges of P_0 for each value of E_{in}. In the first, L_{in} decreases with P_0. In the second, L_{in} increases with P_0. The boundary value, P_{0b}, separating these ranges increases with E_{in}. In the third range of P_0, L_{in} decreases again with P_0. The boundary value of P_0 that separates the second and third ranges, P_{0c}, also increases with E_{in}. The existence of P_{0b} and the increase in L_{in} at $P_0 > P_{0b}$ are due to formation of chemically inert H_2O_2 molecules and decrease in O, H, and OH concentrations

*For detonation initiation in the bulk flow, a large amount of irradiation energy is still required. In case of a faster localized ignition, the predetonation distance can be still significant. (*Editors' remark.*)

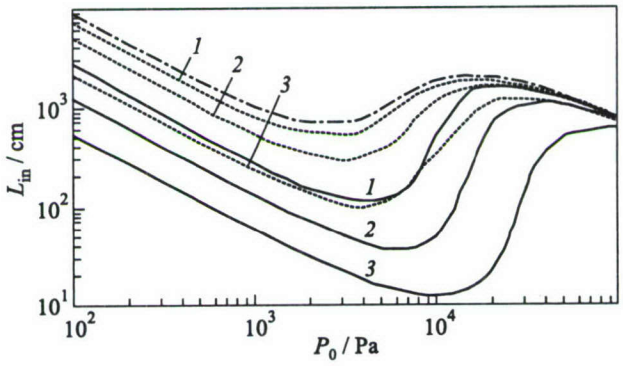

Figure 8 Induction zone length, L_{in}, as a function of initial pressure P_0 for $2H_2 + O_2$ mixture at $T_0 = 300$ K, $M_0 = 6$, and $\beta = 30°$ behind a shock front under irradiation at $\lambda_I = 762$ nm and $E_{\text{in}} = 0.3$; 1; 3 J/cm^2 (curves *1–3*) when irradiation produces $O_2(a^1\Delta_g)$ and $O_2(b^1\Sigma_g^+)$ molecules (solid curves), and when the absorbed energy is consumed on gas heating (dotted curves). Dash-dotted curve corresponds to the absence of irradiation

at relatively low temperature ($T_1 = 650$ K) and high pressure behind the shock front [14].

It is clearly seen that excitation of O_2 molecules to the $b^1\Sigma_g^+$ state by laser radiation with $\lambda_I = 762$ nm is significantly more effective in terms of L_{in} reduction than gas heating due to absorption of radiation. The difference in L_{in} values for these two methods is the largest at $P_{0b} < P < P_{0c}$. For $E_{\text{in}} = 3$ J/cm^2, this difference at $P_0 = 2{\cdot}10^4$ Pa attains the factor of 100. Under abundance of $O_2(a^1\Delta_g)$ and $O_2(b^1\Sigma_g^+)$ molecules formed in the irradiation zone, the detonation wave can be initiated at a small distance from the shock front. Indeed, at $E_{\text{in}} = 3$ J/cm^2 and $P_0 = 10^4$ Pa, the predicted value of L_{in} is about 13 cm. In the absence of irradiation at $P_0 = 10^4$ Pa, $L_{\text{in}} = 19$ m. Note, excitation of O_2 molecules by laser radiation has a high efficiency to initiate detonation at $P_0 < P_{0c}$. At $P_0 > P_{0c}$, irradiation of O_2 molecules does not provide a significant reduction of L_{in}.

5 CONCLUDING REMARKS

Laser-induced excitation of metastable $O_2(a^1\Delta_g)$ and $O_2(b^1\Sigma_g^+)$ molecules provides an efficient means for detonation initiation in a supersonic flow. This is caused by launching additional channels of O, H, and OH species formation and enhancement of chain mechanism of combustion. As molecular oxygen is a strong oxidizer for gaseous fuels, this method can be applied to control deflagration and detonation processes for a whole number of combustible mixtures, in particular, for hydrocarbon–air systems.

ACKNOWLEDGMENTS

This work was supported by the Russian Foundation for Basic Research, Grants 02-01-00703 and 02-02-16915.

REFERENCES

1. Jaggers, H. C., and A. Von Engel. 1971. The effect of electric fields on the burning velocity of various flames. *Combustion Flame* 16(3):275–85.
2. Weinberg, F. J., ed. 1986. *Advanced combustion methods.* London: Academic Press.
3. Tanoff, M. A., M. D. Smooke, R. E. Teets, and J. A. Sell. 1995. Computational and experimental studies of laser-induced thermal ignition in premixed ethylene–oxidizer mixtures. *Combustion Flame* 103(4):253–80.
4. Arnold, S. T., A. A. Viggiano, and R. A. Moriss. 1997. Rate constants and branching ratios for the reactions of selected atmospheric primary cations with *n*-octane and *iso*-octane (2,2,4-trimethylpentane). *J. Physical Chemistry A* 101(49):9351–58.
5. Ma, J. X., D. R. Alexander, and D. E. Polulain. 1998. Laser spark ignition and combustion characteristics of methane–air mixtures. *Combustion Flame* 112(4):492–506.
6. Starik, A. M., and N. G. Dautov. 1996. The effect of vibrational excitation of molecules on the dynamics of detonation combustion of H_2 + air mixtures behind shock waves. *High Temperature* 34(5):726–39.
7. Starik, A. M., and N. S. Titova. 2001. Initiation of combustion and detonation in $H_2 + O_2$ mixtures by excitation of electronic states of oxygen molecules. In: *High-speed deflagration and detonation: Fundamentals and control.* Eds. G. Roy, S. Frolov, D. Netzer, and A. Borisov. Moscow, Russia: Elex-KM Publ. 63–78.
8. Starik, A. M., and O. V. Taranov. 1999. Kinetics of ozone formation in the middle atmosphere under irradiation at $\lambda = 1.27$ μm and 762 nm. *Chemical Physics Reports* 18(3):435–50.
9. Rusanov, V. D., and A. A. Fridman. 1984. *Physics of chemically active plasma.* Moscow, Russia: Nauka.
10. Zakharov, A. I., K. S. Klopovskii, A. P. Osipov, A. M. Popov, O. B. Popovicheva, T. V. Rakhimova, V. A. Samorodov, and A. P. Sokolov. 1988. Kinetics of processes excited by self-maintained glow discharge in oxygen. *Plasma Physics Reports* 14(3):327–33.
11. Atkinson, R., D. I. Baulch, R. A. Cox, R. F. Hampson, J. A. Kerr, and J. Troe. 1992. Evaluated kinetic and photochemical data for atmospheric chemistry: Supplement IV. *J. Physical Chemistry Reference Data* 21(6):1125–568.
12. Kulagin, Yu. A., L. A. Shelepin, and V. I. Yarygina. 1994. Kinetics of processes in gaseous media containing metastable oxygen. *Transactions of the P. N. Lebedev Physical Institute of the Russian Academy of Sciences* 228:166–227.
13. Grabovskii, V. I., and A. M. Starik. 1994. Characteristics of the changes in the refractive index due to interaction of a radiation pulse with an inverted medium. *Quant. Electronics* 24(4):340–45.
14. Starik, A. M., and N. S. Titova. 2001. On mechanisms of low-temperature initiation of combustion in $H_2 + O_2$ (air) mixtures by exciting vibrational degrees of freedom of the reagents. *Chemical Physics Reports* 19(9):1681–99.

DETONATION FRONT STRUCTURE: VARIETY AND CHARACTERIZATION

F. Pintgen, J. M. Austin, and J. E. Shepherd

The structure of multifront or cellular detonation waves has been studied using Schlieren, planar laser-induced fluorescence (PLIF) imaging of the OH radical, and soot foils in three mixtures with varying regularity. These are: stoichiometric H_2–O_2 diluted with Ar, stoichiometric H_2–O_2 diluted with N_2, and stoichiometric H_2–N_2O diluted with N_2, all at 20 kPa initial pressure. Very different structures are observed in each mixture. These differences are most striking on the PLIF images, which are used as a starting point for a qualitative discussion and interpretation of the features seen on the Schlieren images and soot foils. It is clear that the detonation propagation mechanism in mixtures with irregular cellular structure may be much more complex than in mixtures with regular cellular structure.

1 INTRODUCTION

Many researchers have investigated the structure of propagating detonation waves experimentally and more recently, through numerical simulation. The initial evidence of the multifront or "cellular" structure of detonation waves was obtained by Denisov & Troshin [1] using foils covered with a thin layer of soot, by White [2] with interferometry, and Schlieren methods by Soloukhin [3]. The interferometric measurements demonstrated the existence of secondary transverse waves propagating nearly perpendicular to the front and a curved front structure with abrupt changes in slope at triple points where the secondary waves joined the main front. The modern view of the structure of multifront detonations was initiated with the pioneering work of Voitsekhovskii *et al.* [4].

The simple technique of soot foils has been used extensively to investigate the shock configurations of the front and, in particular, to study the wave configurations at the triple points. Lee *et al.* [5] made stroboscopic Schlieren photographs through a sooted window to show the tracks are closely associated with the triple points on the detonation front, although the physical mechanism by which the tracks are made in the soot layer is still unclear. Soot-foil track angles may be

used to calculate triple-point configurations using shock polars once the angle of the track and the velocity of the leading shock through the cell are known [6–9]. These techniques and numerical simulation were used recently by Pintgen *et al.* [10] to calculate OH contours at the triple point for comparison with PLIF images.

Soot foils have also been previously used to characterize the cellular regularity of detonation structure. Strehlow [11] and Libouton *et al.* [12] classified many mixtures in this manner and observed that highly Ar-diluted mixtures have a very regular structure while N_2-diluted mixtures have a more irregular structure. In C_2H_2–N_2O–Ar mixtures, Libouton *et al.* [12] also observed "substructure" — cellular soot foil tracks similar in appearance to the large-scale structure but appearing at multiple scales smaller than the main cell size. The substructure cells are observed on the soot tracks in the upstream apex of the main cell and increase in size as the velocity of the Mach stem decays. They are usually not observed in the second half of the main cell.

Schlieren and interferometry have previously been used to visualize shock and reaction zone structure in detonation waves. Because of the difficulties associated with interpreting these images in three dimensions, many studies have been performed in narrow channels [4, 13, 14]. Subbotin [9] reported different triple point structures in different mixtures. Using Schlieren images, Subbotin calculated that the transverse waves were unreactive in irregular (CH_4–O_2) mixtures and reactive in a regular (H_2–O_2–Ar) mixture. Subbotin also reported islands of unburnt gas that become isolated from the main front after a triple point collision. Such "unburnt pockets" were also observed in Schlieren images [15].

Previous researchers have made substantial progress in describing the structure of multifront (cellular structure) detonation waves. One of the key issues that remains unresolved is the precise nature of the combustion processes within the reaction zone. To make progress on this issue, it is necessary to use techniques that are sensitive to chemical species and spatially resolve the structure in the front. For detonation front studies on irregular mixtures in wide channels, integrating techniques such as direct imaging of chemiluminescence appear to be limited in value. Much more promising are the techniques such as PLIF that allow the dissection of the flow into planar sections.

Andersen *et al.* [16] used laser-induced predissociation fluorescence (LIPF) to obtain images of oscillations along the reaction zone front of detonation waves, Eder [17] made LIPF images of fast deflagrations, and Pintgen [18] used OH PLIF to image the cellular character of the reaction zone structure of detonations. Very striking features with a "keystone" shape were observed by Pintgen [18] in many mixtures and it was demonstrated previously [10] that these features can be interpreted in terms of classical shock-induced combustion for mixtures highly diluted with argon. The appearance of these features can be related to the oscillations in shock front strength and the substantial changes in the OH concentration across the shear layer associated with the triple points. The keystone

features appeared more irregular for the N_2-diluted mixtures than for Ar-diluted mixtures. The present study is an extension of the authors' previous work and focuses on differences observed in mixtures with various degrees of all regularity.

Experimental Technique

The experiments were carried out in a 280-millimeter diameter detonation tube coupled by a 150-millimeter square "cookie-cutter" to a 150-millimeter square test section. The overall length of the facility is 8 m; the length of the cookie-cutter and test section is 1.5 m. The tube is evacuated to approximately 0.04 kPa before each filling procedure, which is based on the partial pressure of each species. The detonation is initiated directly by a thin copper wire exploding in a small amount (10% of the tube volume) of acetylene–oxygen mixture which is injected into the tube immediately prior to ignition. Pressure traces and detonation velocities are obtained from six pressure transducers located along the facility, three of which are in the test section. Soot foils were placed on the sidewalls of the test section as well as on the end plate of the test section.

Simultaneous Schlieren and OH PLIF visualizations are made through two 184-millimeter diameter windows in the side walls of the test section. The light source for the Schlieren system is a Q-switched ruby laser with a 50-nanosecond pulse width. The Schlieren system is a typical Z-setup using two concave mirrors of focal length of 1 m. The transmitted light passes through a narrow bandpass filter to eliminate self-light from the detonation and is imaged onto 80×100 mm black and white Polaroid (3000 ISO) film. The laser system for the PLIF setup consists of a tuneable dye laser (Scanmate2E, Lambda Physik) with a frequency doubling unit which is pumped by an excimer-laser (COMPex102, Lambda Physik). The pulse energy of the excimer laser is 300 mJ and the pulse width is approximately 17 ns. A Coumarin 153 dye was used in the dye-laser to obtain a narrow band ultraviolet (UV) light with a pulse energy of about 6.5 mJ. The frequency was tuned to 284.008 nm which corresponds to the immediate vicinity of two OH-transitions: $A^2\Sigma^+ \leftarrow X^2\Pi_i(1,0)\ Q_2(8)$ and $A^2\Sigma^+ \leftarrow X^2\Pi_i(1,0)\ Q_1(9)$.

The UV laser beam is directed by mirrors to propagate along the tube axis and formed into a light sheet by the combination of cylindrical lens (focal length −25 mm) and a spherical lens (focal length 1000 mm). The light sheet enters the test section through a quartz window in the center of the test section end plate. The induced fluorescence which is perpendicular to the light sheet, passes through a 184-millimeter diameter quartz glass window, and is filtered by a bandpass filter (centerline 313 nm, FWHM 10 nm) before being imaged by a 576×384 pixel 12-bit intensified CCD-Camera (Princeton Instruments ITE/ICCD-576). The image is formed by a 105-millimeter f/4.5 UV-transmitting lens (Nikkon UV-Nikkor). The camera was gated by a 90-nanosecond pulse of 900 V. Depending on the height of the field of view of the camera, which was varied between 80

and 30 mm, the light sheet-forming optics were readjusted such that the usable light sheet height was optimized. For simultaneous Schlieren and PLIF experiments, the camera had to be placed out of the optical path of the Schlieren setup and therefore at a slight angle (under 15°) to the desired perpendicular position relative to the light sheet. The resulting distortion was corrected by postprocessing the PLIF image using a test-pattern to match images obtained from both systems.

Two photo diodes detecting the light pulse emitted from the ruby laser and the dye-laser verified that the time between acquiring the Schlieren image and the PLIF image was less than 200 ns. The current investigation is qualitative rather than quantitative due to the nonuniformity of the light sheet and locally varying effects influencing the fluorescence intensity. These effects include varying excited state population which depends on the local thermodynamic state and molecular effects like quenching which is influenced by the number density of the quenching species. Three-dimensional effects due to the orientation of the cellular structure to the light sheet are evident on the end-plate soot foils.

2 RESULTS

This work is a part of a larger program in detonation research which has as one goal the understanding of the combustion mechanisms and dynamics of detonation fronts. To this end, experiments were carried out with several different mixtures, all using hydrogen as the fuel. Stoichiometric H_2–O_2–Ar, H_2–O_2–N_2, and H_2–N_2O–N_2 mixtures were investigated. The H_2–O_2–Ar mixture represents a mixture with a very regular cellular structure. The N_2-diluted H_2–O_2 mixture is an example of an irregular cellular structure, whereas the H_2–N_2O mixture diluted with N_2 has a highly irregular cellular structure. Previously, cellular substructure has been observed in the H_2–N_2O system [12]. All experiments were conducted at an initial temperature of 25 °C and initial pressure of 20 kPa. One PLIF and one Schlieren image are obtained from each experiment. Schlieren images, pressure histories, and soot foil records indicate the detonations are multifront, self-sustaining waves within the test section. Many images in the course of the experiments have been obtained and only a few examples are shown here.

Ar-Diluted H_2–O_2 Mixtures

The detonation velocities were within 1.5% of the Chapman–Jouguet values for the 80% and 85% Ar-diluted H_2–O_2 mixtures in the round cross-section of the facility. The soot foils placed in the test section confirmed the expected high regularity of this mixture (Fig. 1*a*). The cell size for the 80% and 85% Ar-diluted cases was measured to be 22 and 48 mm which is 7 and 3 times less, respectively, than the test section dimension. The regularity is seen in the relatively small

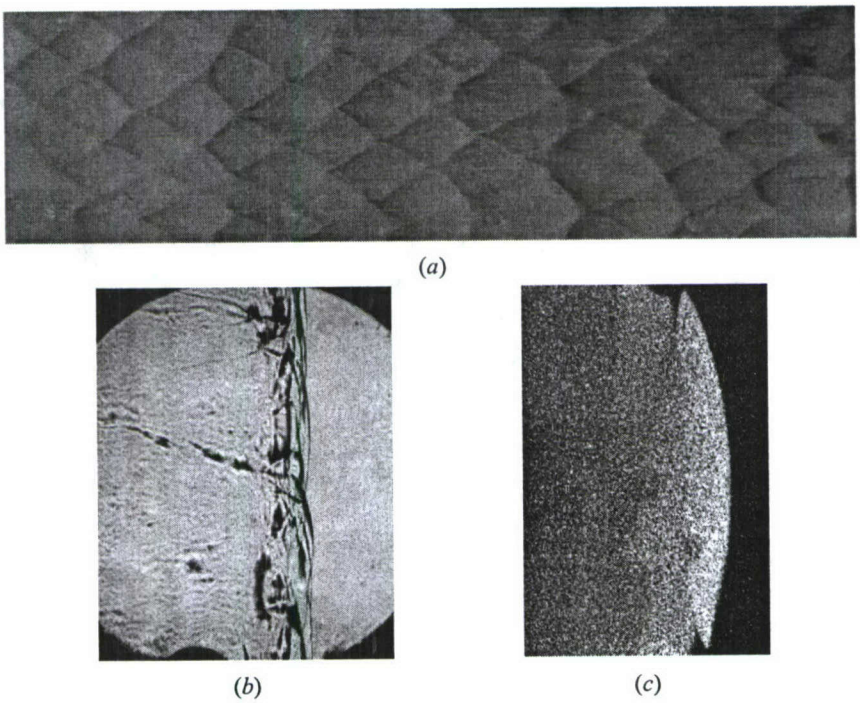

Figure 1 (*a*) Side wall soot foil (image height 150 mm) of 85% Ar-diluted stoichiometric H_2–O_2 mixture. (*b*) Schlieren image of detonation front (image height 150 mm) and (*c*) PLIF image of OH fluorescence behind the detonation front (image height 30 mm) in a 87% Ar-diluted stoichiometric H_2–O_2 mixture. The initial pressure is 20 kPa for all mixtures, the detonation wave propagates from left to right in all images

variations in the cell size. End-plate soot foils show that the two planes of the detonation are not repeatably orthogonally aligned to the side walls for every experiment. The orthogonal structure appears to be most often observed for the 80% Ar-diluted mixture.

Transverse waves extending into the unburned region can be identified on the Schlieren images. The visibility of the transverse waves depends in large part on the alignment of the waves relative to the optical axis. The transverse waves are most clearly visible when the waves are propagating in two orthogonal families that are parallel to the test section walls. In these cases, as shown in Fig. 1*b*, the flow field behind the main front appears to be composed of periodic transverse shock waves with a spacing on the order of the cell size. The leading shock wave is imaged as a sharp line with a smooth contour. There do not appear to be any significant small-scale features visible in the Schlieren images.

In PLIF images (Fig. 1*c*) for these Ar-diluted mixtures, a distinct front is seen which corresponds to the sharp increase in OH concentration at the end

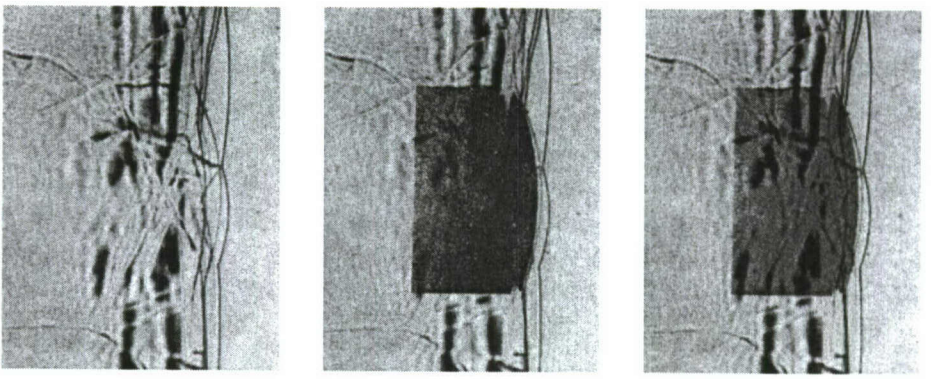

(*a*) (*b*) (*c*)

Figure 2 87% Ar-diluted stoichiometric H_2–O_2 mixture: (*a*) Schlieren image; (*b*) superposition of false color PLIF image with Schlieren image; and (*c*) overlay of PLIF and Schlieren image. Schlieren image is 50 mm high and PLIF image is 30 mm high

of the induction zone. The PLIF images reveal a very smooth reaction front punctuated periodically with the previously reported [10] "keystone" features associated with the oscillation of the detonation front velocity. The keystone is bounded by a discontinuity in reactivity across the shear layers that emanate from the triple points at the intersection of the transverse waves and main front. This can be most clearly seen in Fig. 2, which shows an overlay of the Schlieren and PLIF images. The PLIF image is a close-up and the straight edges on top, bottom, and left are associated with the PLIF-image boundaries. Near the top of the image, a transverse wave can clearly be seen and is associated with the triple point shown in the Schlieren image.

The role of the transverse waves is not completely resolved but in many of Ar-diluted cases it has been examined, they do not appear to play an essential role in the combustion (Figs. 1*b* and 1*c*). The "keystone" is less pronounced in some cases and may depend on the stage in the cell cycle when the image is captured. Other than three-dimensional effects associated with the misalignment of the transverse waves with respect to the light sheet, the OH distribution appears to be contiguous. The reaction front is slightly curved behind the incident shock and the Mach stem. The discontinuity across the shear layer appears as a smooth straight line at the highest resolution (20 pixel/mm) used in these experiments.

N_2-Diluted H_2–O_2 Mixtures

For the N_2-diluted H_2–O_2 mixtures, the soot foils (Fig. 3*a*) indicate a wider range of cell sizes and track angles compared to the Ar-diluted mixtures with

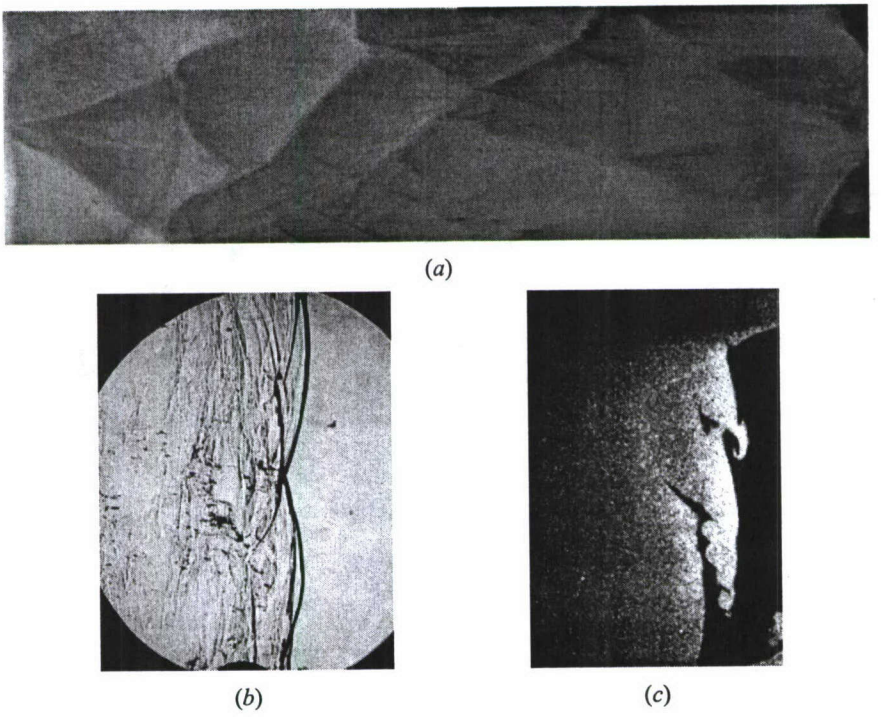

Figure 3 (*a*) Side wall soot foil (image height 150 mm); (*b*) Schlieren image of detonation front (image height 150 mm); and (*c*) PLIF image of OH fluorescence behind the detonation front (image height 50 mm) in a stoichiometric H_2–O_2 mixture diluted with 72% N_2. The initial pressure is 20 kPa for all mixtures and the detonation wave propagates from left to right in all images

a comparable cell size. The cell size for 45% N_2 and 65% N_2 was measured to be 22 and 55 mm, respectively. The wave system at the front rarely appears to be aligned in an orthogonal fashion to the test section walls and coherent transverse wave structures are not visible on the Schlieren images (Fig. 3*b*) or end-plate soot foils (not shown). On the Schlieren images, the leading shock wave appears to be much less planar than for the Ar-diluted mixture with the same cell size. The curved sections visible along the front do not correspond to the cell size measured on the soot foils. In part, this may also be due to the integrating effect of the Schlieren image and the lack of coherence in the transverse wave structures. Behind the shock front, small-scale variations in density gradients are visible at a distance up to one cell size downstream of the leading shock. The PLIF images show that the reaction front is much more distorted (Figs. 3*c* and 4) than in the Ar-diluted cases. For cell sizes up to 55 mm and resolutions up to 10 pixel/mm, the "keystone" features associated with the cellular structure

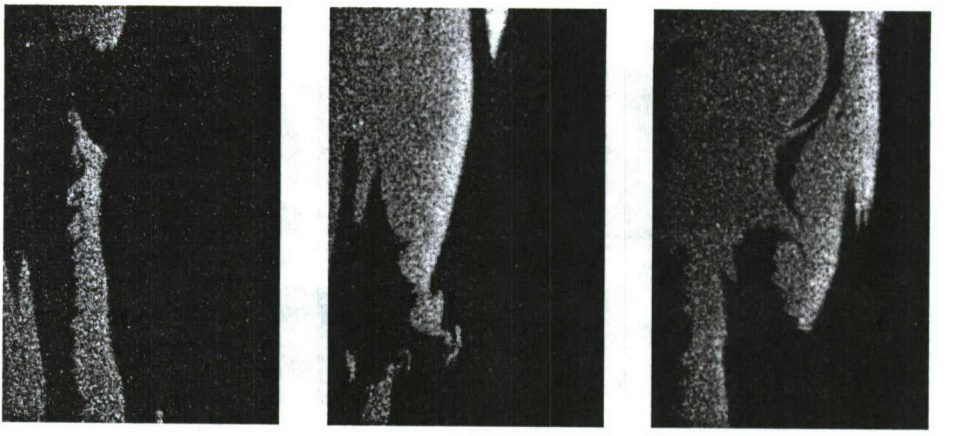

(*a*) (*b*) (*c*)

Figure 4 Selection of PLIF images of OH fluorescence behind the detonation front in a stoichiometric H_2–O_2 mixture diluted with N_2. The initial pressure is 20 kPa and the detonation wave propagates from left to right in all images. Image height: (*a*) 30 mm; (*b*) and (*c*) 50 mm

are still seen, but the front separating regions of high and low fluorescence are in general much more wrinkled. Disturbances in the OH front are visible on scales less than the cell size determined from soot foil measurements. For high resolution (20 pixel/mm) imaging and higher N_2-dilution (72.7%) cases, features are visible which resemble those commonly associated with Kelvin–Helmholtz instability for shear layers.

These features were not observed in the case of Ar-diluted mixtures with similar velocity differences and only sometimes observed in N_2-diluted mixtures. The authors speculate that lack of consistent observation of shear-layer instabilities is related to the resolution of the images and the size of the cells in comparison to the test section dimensions. A possible explanation for the differences in Ar- and N_2-diluted mixtures is the difference in extent of the OH concentration gradient across the shear layer in the two cases (see the discussion below). Further investigation is required to resolve this issue. The complex nature of the flow field suggests that simultaneous planar imaging of the shock front and OH front will be required to make progress on this aspect.

H_2–N_2O–N_2 Mixtures

For the H_2–N_2O–N_2 compositions, 50% and 60% N_2-diluted mixtures were investigated and cell sizes of 42 mm and 70 mm measured on the soot foils. In both cases, substructure was seen on the side-wall soot foils (Fig. 5*a*). The structure

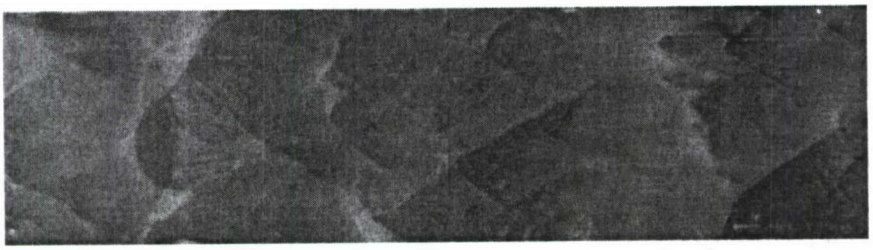

(*a*)

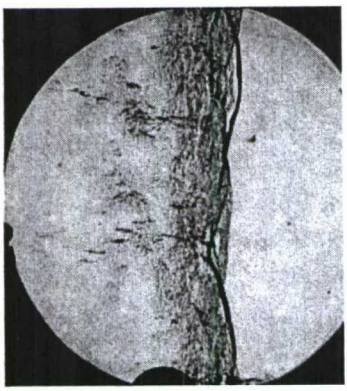

(*b*)

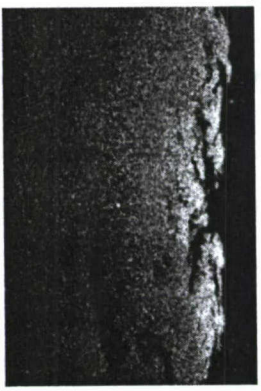

(*c*)

Figure 5 (*a*) Side wall soot foil (image height 150 mm); (*b*) Schlieren image of detonation front (image height 150 mm); and (*c*) PLIF image of OH fluorescence behind the detonation front (image height 45 mm) in a H_2–N_2O–$3N_2$ mixture. The initial pressure is 20 kPa

originates at the upstream end (apex) of the cells and persists until the middle of the cell. The size of the substructure cells increases with increasing distance downstream from the cell apex. The end-plate soot foils (not shown) also showed the highly irregular structure seen on the side wall soot foils.

The Schlieren images (Fig. 5*b*) reveal that the leading shock front is strikingly different than the previous cases studied. In addition to the smooth curved waves observed with Ar- and N_2-diluted mixtures, "rough" portions with fine scale disturbances on the front can be observed. The region immediately behind the main shock front contains fine-scale density fluctuations that persist for a distance of about one cell size behind the front. The large-scale cellular structure as seen in the other two mixtures is not as striking for the 60% N_2-diluted mixture and vanishes nearly entirely for the 50%-diluted case on the Schlieren images. The transverse waves are difficult to discern due to the presence of small-scale density disturbances. The complexity of the flow makes relating Schlieren images to PLIF images even more difficult than in the N_2-diluted case.

The PLIF image (Fig. 5*c*) is clearly different from either the Ar- or N_2-diluted cases. The "keystone" features are not as distinct and the OH front is very rough rather than smooth. Instead of a contiguous front, there appear to be isolated irregular regions of low intensity embedded within the high-intensity region behind the main OH front.

3 DISCUSSION

Several new features have been observed in the present experiments that were not seen in the previous studies [10, 18]. The most significant are (*i*) shear-layer type disturbances on the OH front in N_2-diluted mixtures; and (*ii*) fine-scale density and OH front disturbances in H_2–N_2O–N_2 mixtures.

The presence of features commonly associated with shear-layer instabilities is hardly surprising given the large velocity differences that three-shock models [10] predict across the contact surface between the flow behind the Mach stem and the reflected wave. Visual evidence of turbulent shear layers was seen in earlier Schlieren images (see p. 76, Shot 136 of Akbar [19] obtained in the Graduate Aeronautical Laboratory of the California Institute of Technology in a stoichiometric H_2–O_2 mixture with 88% Ar dilution). What is somewhat surprising is that these features are not also observed on the PLIF OH front images in 87% Ar-diluted mixtures but are visible in the 72.7% N_2-diluted mixture. The authors speculate that the difference in visibility by the OH PLIF technique is due to the difference in OH concentration across the shear layers in these two cases: Apparently in the N_2-diluted cases, a large OH concentration difference occurs across a substantial extent of the shear layer while in the Ar-diluted cases, the OH concentration is only appreciably different very close to the triple point. Evidence of shear layer instability for the highly N_2-diluted mixtures is very faint on the Schlieren images. The authors believe that this is due to the rather modest density gradients in the shear layers as compared to the shock waves, lack of alignment of the shear layers with respect to the optical path, and the obscuring effects of the small-scale density fluctuations distributed randomly behind the leading shock front.

The appearance of the OH PLIF images for the H_2–N_2O mixtures is intriguing. On the basis of authors' previous work with Ar-diluted mixtures, it was anticipated that the substructure visible on the soot foils might be manifested as a superposition of "keystone" features of varying sizes. Instead, it is difficult to recognize distinct keystones in the OH PLIF images and transverse waves that would be associated with the substructure are difficult to observe on the Schlieren images. With the current resolution, the ordered features seen for the Ar-diluted mixtures are not seen on any scale. The fine-scale structure in the Schlieren images taken together with the fine-scale wrinkling of the OH fronts

suggests that velocity and density fluctuations on a scale much smaller than the main cell width are important issues in mixtures with highly irregular cellular structure.

4 CONCLUDING REMARKS

Several experimental techniques were used to investigate different properties of the flow field behind propagating detonation waves. Three mixtures were chosen as representative of regular, irregular, and very irregular cellular structure. In Ar-diluted H_2–O_2 mixtures with regular structure, soot foils show a very regular pattern, Schlieren images show disturbances to the main front in the order of the cell size, and "keystone" features are seen in the PLIF images. In more irregular N_2-diluted H_2–O_2 mixtures, soot foils show a wider range of cell sizes, and Schlieren images show structures with a scale smaller than the cell width. Highly N_2-diluted mixtures exhibit features on the PLIF images which suggest the instability of the shear-layer. In very irregular H_2–N_2O–N_2 mixtures, features with a size much smaller than the main cell width appear, soot foils show substructure, a finely subdivided, more unstructured flow field is visible on the Schlieren images, and very convoluted OH fronts are observed in the PLIF images. From the photographic evidence, it appears that shear flow instabilities and fine-scale wrinkling of the OH front may play a role in the combustion mechanism of mixtures with irregular cellular structure. Continued experimentation and improved diagnostics are needed to fully resolve the nature of the combustion processes within the detonation front in the case of mixtures with highly irregular cellular structure.

ACKNOWLEDGMENTS

This work was supported by the Office of Naval Research, Multidisciplinary University Research Initiative *Multidisciplinary Study of Pulse Detonation Engine*, grant 00014-99-1-0744, subcontract 1686-ONR-0744.

REFERENCES

1. Denisov, Y., and Y. Troshin. 1959. Pulsating and spinning detonation of gaseous mixtures in tubes. *Dokl. Akad. Nauk* 125:110–13.
2. White, D. 1961. Turbulent structure in gaseous detonations. *Physics Fluids* 4:465–80.

3. Soloukhin, R. 1965. Multiheaded structure of gaseous detonation. *Combustion Flame* 9:51–58.
4. Voitsekhovskii, B., V. Mitrofanov, and M. Topchian. 1963. *Struktura fronta detonastii v gasakh.* Novosibirsk: Akad. Nauk, USSR. (Translation: 1966. *The structure of a detonation front in gases.* Rep. FTD-MT-64-527. Foreigh Technology Division. Wright-Patterson A.F.B., Ohio.)
5. Lee, J., R. Soloukhin, and A. Oppenheim. 1969. Current views on gaseous detonation. *Astronautica Acta* 14:565–84.
6. Strehlow, R., R. Liaugminas, R. Watson, and J. Eyman. 1967. Transverse wave structure in detonations. *11th Symposium (International) on Combustion Proceedings.* Pittsburg, PA: The Combustion Institute. 683–92.
7. Oppenheim, A., J. Smolen, and L. Zajac. 1968. Vector polar method for the analysis of wave intersections. *Combustion Flame* 12:63–76.
8. Urtiew, P. 1970. Reflections of wave intersections in marginal detonations. *Astronautica Acta* 15:335–43.
9. Subbotin, V. 1975. Two kinds of transverse wave structures in multifront detonation. *Combustion Explosion Shock Waves* 11(1):96–102.
10. Pintgen, F., C. A. Eckett, J. M. Austin, and J. E. Shepherd. 2003 (in press). Direct observations of reaction zone structure in propagating detonations. *Combustion Flame.*
11. Strehlow, R. 1969. The nature of transverse waves in detonations. *Astronautica Acta* 14:539–48.
12. Libouton, J., A. Jacques, and P. Van Tiggelen. 1981. Cinétique, structure et entretien des ondes de détonation. *Actes du Colloque International Berthelot–Vieille–Mallard–Le Chatelier Proceedings.* Bordeaux, France 2:437–42.
13. Edwards, D., G. Hooper, and R. Meddins. 1972. Instabilities in the reaction zones of detonation waves. *Astronautica Acta* 17(4–5):475–85.
14. Strehlow, R., and A. Crooker. 1974. The structure of marginal detonation waves. *Acta Astronautica* 1:303–15.
15. Oran, E. T., J. Boris, J. Picone, and D. Edwards. 1982. A study of detonation structure: The formation of unreacted gas pockets. *19th Symposium (International) on Combustion Proceedings.* Pittsburg, PA: The Combustion Institute. 573–82.
16. Andersen, P., W. Reckers, H. Wagner, E. Dabora, and H. Voges. 1992. The structure of gaseous detonations as revealed by laser-induced fluorescence of the OH-radicals. *Zeitschrift fur Physicalische Chemie neue Folge* 175:129–43.
17. Eder, A. 2001. Brennerverhalten schnallnaher und überschall-schneller Wasserstoff-Luft Flammen. Ph.D. Thesis. Munich. Germany: Technische Universität München.
18. Pintgen, F. 2000. *Laser-optical visualization of detonation structures.* Diplomarbeit, Lehrstuhl für Thermodynamik: Technische Universität München / Graduate Aeronautical Laboratories: California Institute of Technology, Munich, Germany.
19. Akbar, R. 1997. Mach reflection of gaseous detonations. Ph.D. Thesis. Rensselaer Polytechnic Institute, Troy, New York.

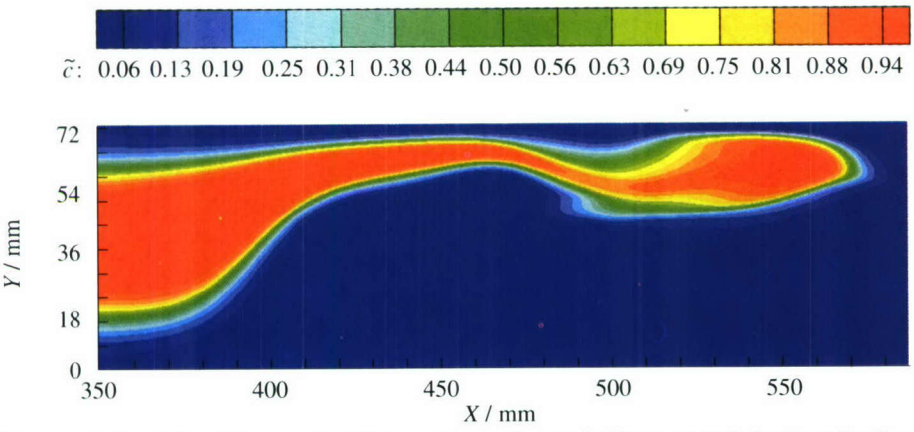

Computed (t = 14 ms) image of stoichiometric methane air flame around the time the flame moves past the obstacle (plate 5 mm thick and 36 mm high located at x = 415 mm). (Refer Kuan *et al.*, Fig. 1, p. 30.)

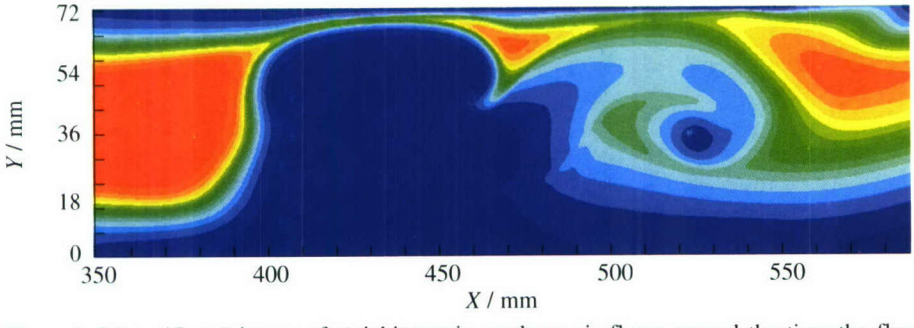

Computed (t = 15 ms) image of stoichiometric methane air flame around the time the flame moves past the obstacle (plate 5 mm thick and 36 mm high located at x = 415 mm). (Refer Kuan *et al.*, Fig. 2, p. 31.)

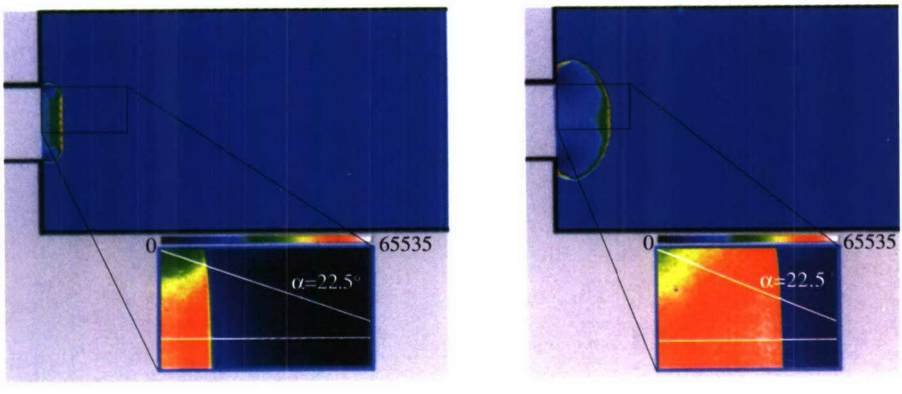

Stoichiometric C_2H_4 O_2 detonation wave undergoing diffraction. Computational density contours are shown on top, and experimental CH* chemiluminescence images are shown on the bottom. The 0 65535 color scale represents increasing emission (a.u.). (Refer Brophy *et al.*, Fig. 5, p. 65.)

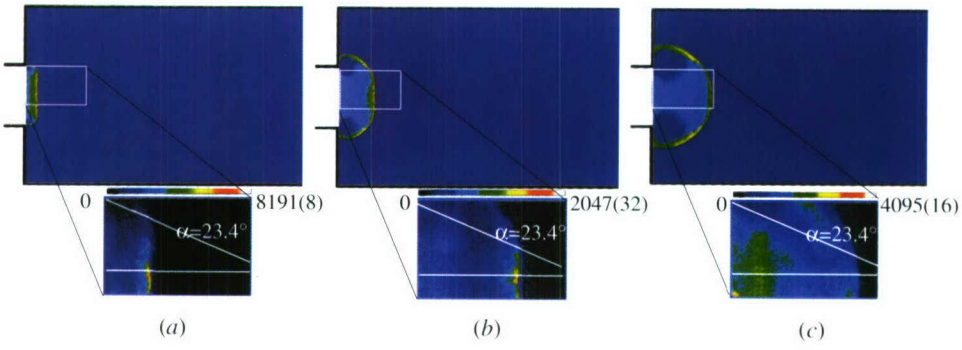

Transmission of C_2H_4 air ($\phi = 1.0$) detonation from 50.8-millimeter initiator to 127-millimeter combustor: (*a*) $t = 25$ μs, (*b*) 40, and (*c*) $t = 55$ μs. The color scales represent increasing emission (a.u.) and vary to preserve detail. (Refer Brophy *et al.*, Fig. 6, p. 66.)

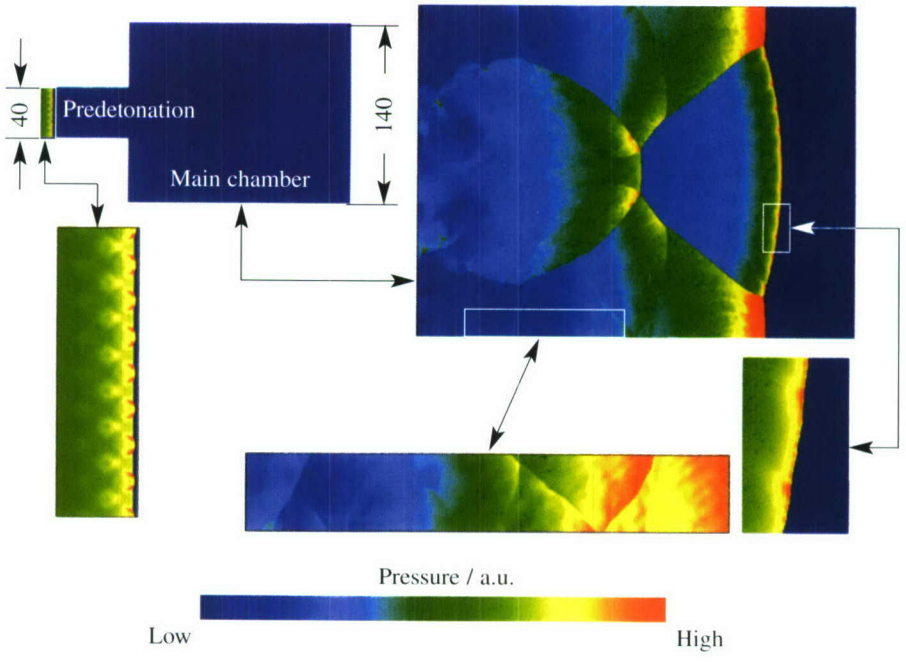

Experimental and computational results for the numerical point in Fig. 7, p. 67. Dimensions in mm. Color scales represent increasing pressure (a.u.) and vary to preserve detail. (Refer Brophy *et al.*, Fig. 8, p. 67.)

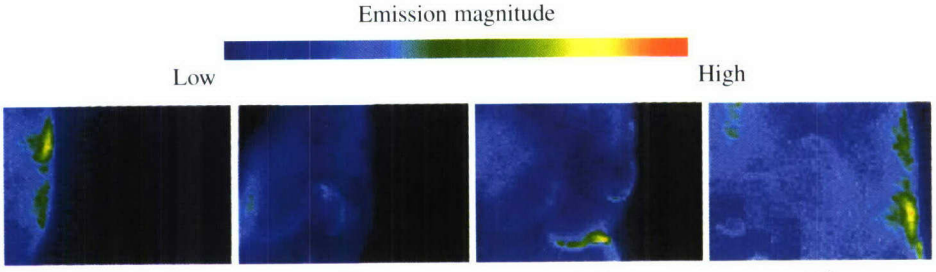

(*a*) (*b*) (*c*) (*d*)

CH* chemiluminescence images of a successful axisymmetric diffraction of a locally overdriven C_2H_4 air detonation ($\phi = 1.0$) from a 50.8- to 127-millimeter circular combustor: (*a*) $t = 12$ μs, (*b*) 19, (*c*) 26, and (*d*) $t = 33$ μs. (Refer Brophy *et al.*, Fig. 9, p. 68.)

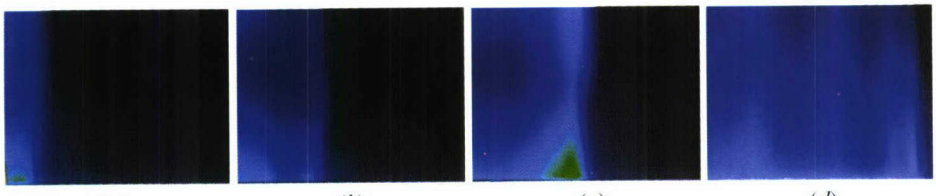

(*a*) (*b*) (*c*) (*d*)

Images of the visible emission from a successful two-dimensional diffraction of a locally overdriven C_2H_4 air ($\phi = 1.0$) detonation in the square detonation tube geometry ($Y/Y_0 = 1.33$): (*a*) $t = 15$ μs, (*b*) 22, (*c*) 29, and (*d*) $t = 36$ μs. (Refer Brophy *et al.*, Fig. 10, p. 69.)

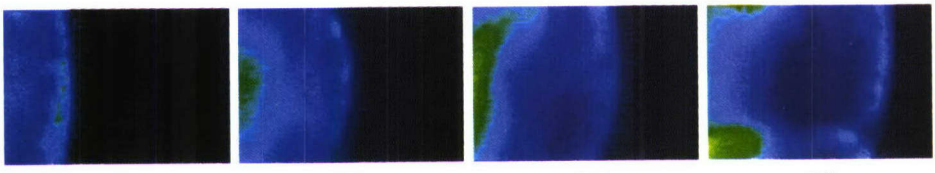

(*a*) (*b*) (*c*) (*d*)

C_2H_4 air ($\phi = 1.1$) detonation transmission in the two-dimensional geometry ($Y/Y_0 = 1.33$): (*a*) $t = 15$ μs, (*b*) 22, (*c*) 29, and (*d*) $t = 36$ μs. (Refer Brophy *et al.*, Fig. 11, p. 69.)

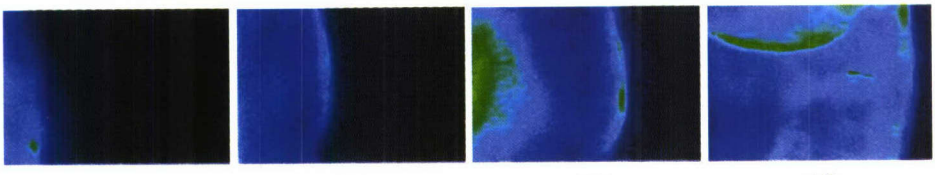

(*a*) (*b*) (*c*) (*d*)

CH* chemiluminescence images of a successful diffraction of a locally overdriven C_2H_4 air ($\phi = 1.1$) detonation in the two-dimensional geometry ($Y/Y_0 = 2.0$): (*a*) $t = 15$ μs, (*b*) 22, (*c*) 29, and (*d*) $t = 36$ μs. (Refer Brophy *et al.*, Fig. 12, p. 69.)

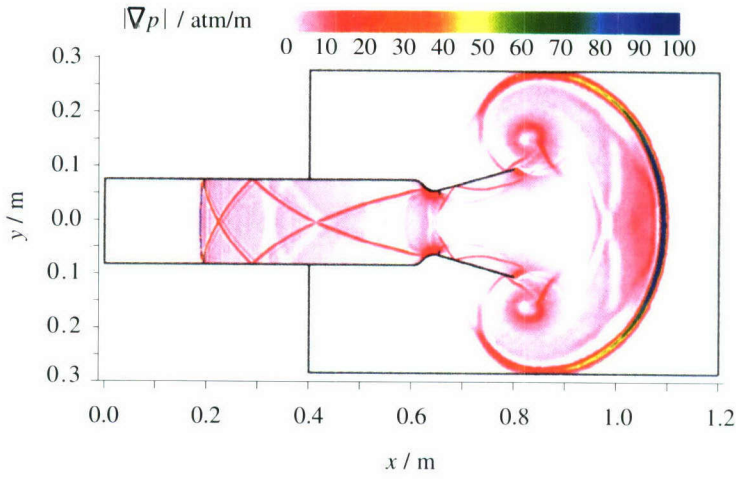

(*b*)

Snapshot of pressure-gradient field at $t = 0.80$ ms ($\tau_{cycle} = 3$ ms, $\tau_{close} = 2.1$ ms). (Refer Ma *et al.*, Fig. 4*b*, p. 239.)

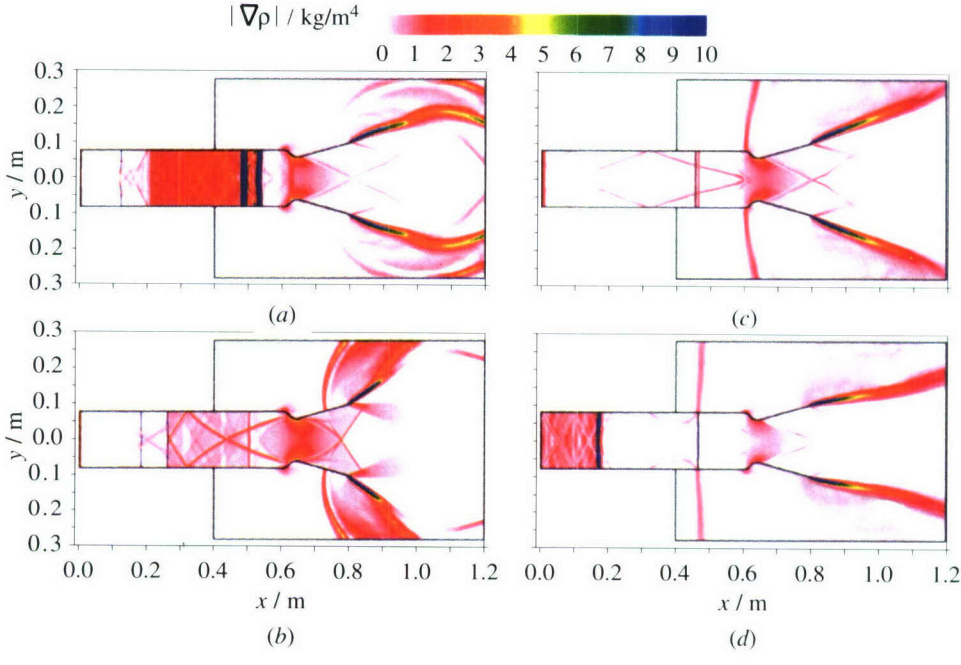

Time evolution of density-gradient field during 5th cycle of operation ($\tau_{cycle} = 3$ ms, $\tau_{close} = 2.1$ ms): (*a*) $t = 12.20$ ms; (*b*) 12.80; (*c*) 13.50; and (*d*) $t = 14.50$ ms. (Refer Ma *et al.*, Fig. 5, p. 240.)

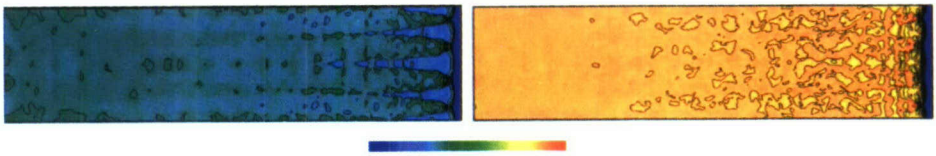

Initial conditions in the detonation tube. The detonation propagates from left to right: (*a*) pressure; and (*b*) temperature. (Refer Tsuboi *et al.*, Fig. 6, p. 254.)

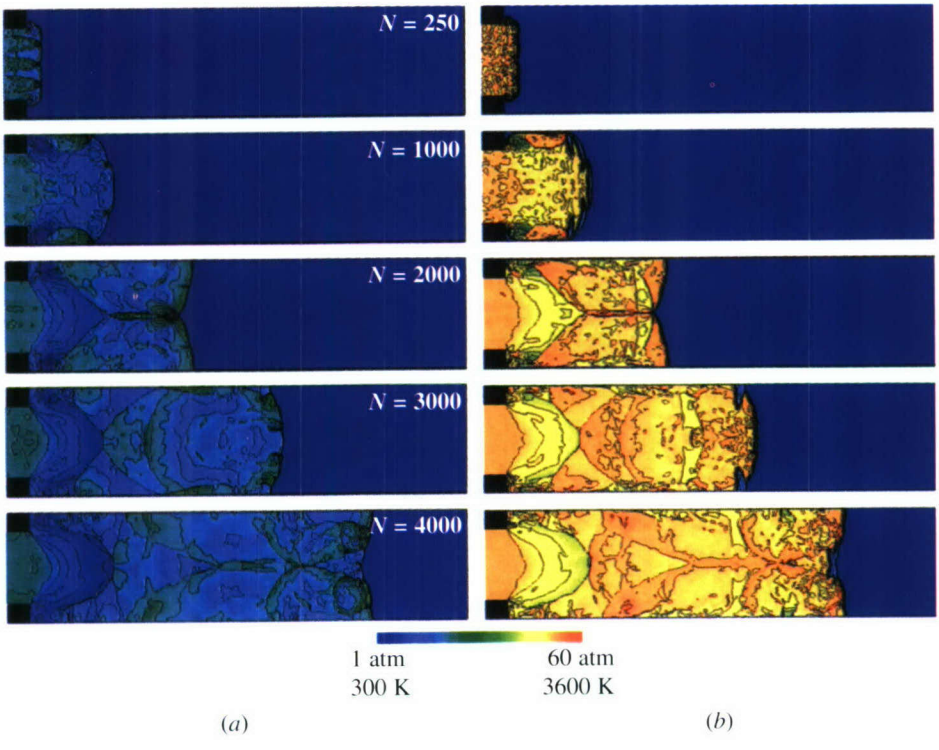

Predicted evolution of pressure (*a*) and temperature (*b*) for Case 1. (Refer Tsuboi *et al.*, Fig. 7, p. 255.)

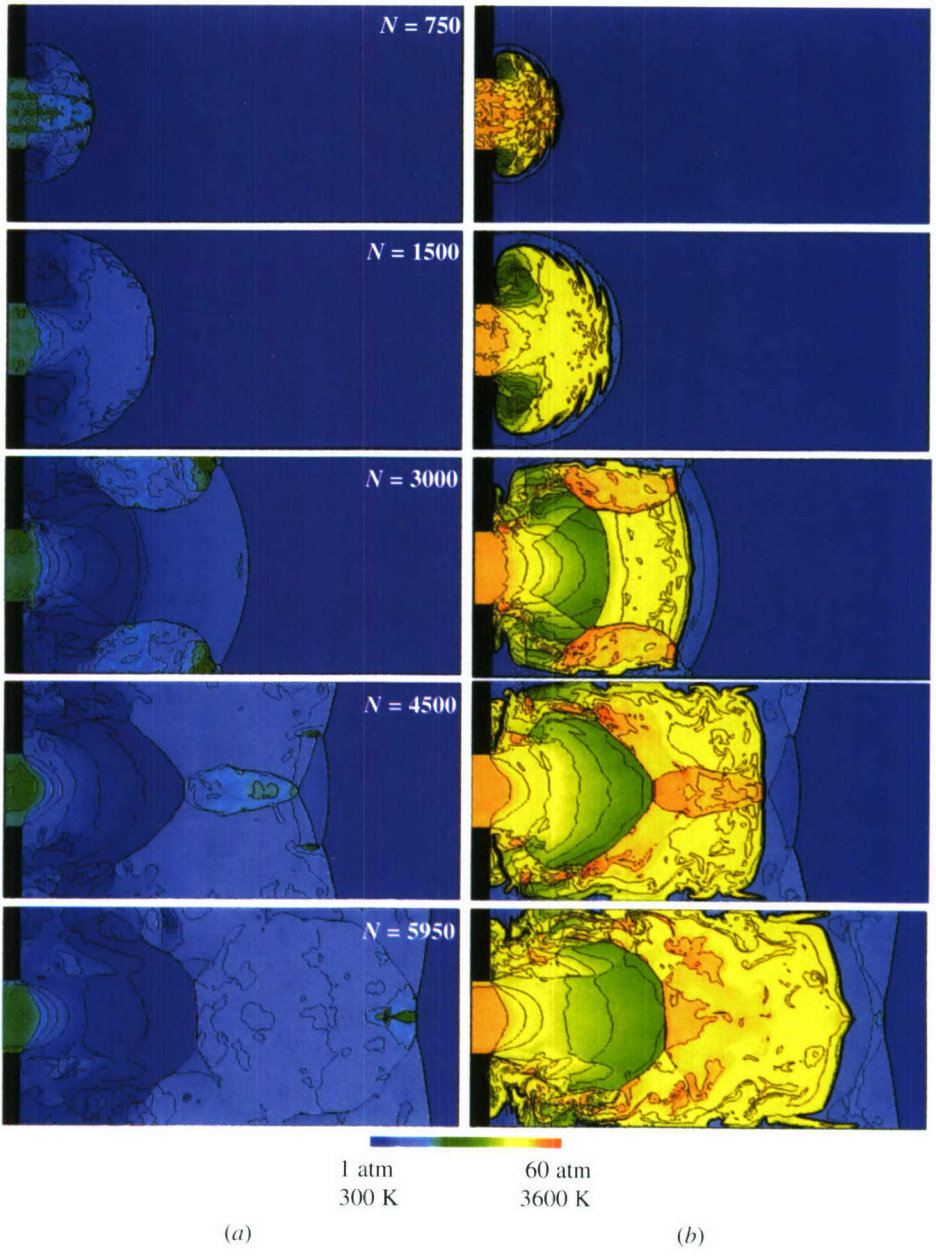

Predicted evolution of pressure (*a*) and temperature (*b*) for Case 2. (Refer Tsuboi *et al.*, Fig. 8, p. 256.)

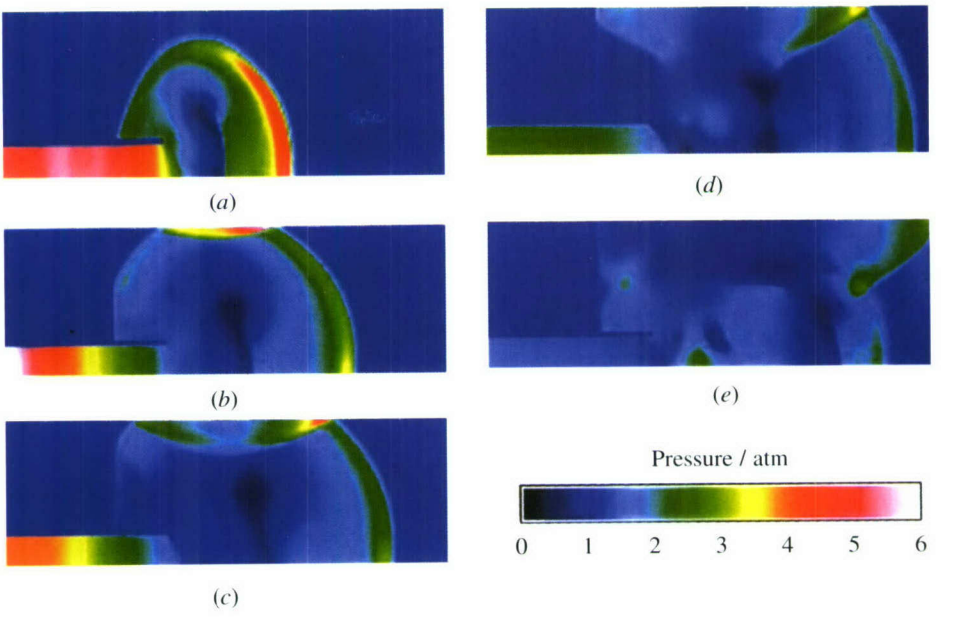

CFD pressure contours of hydrogen oxygen detonation exiting the PDE tube: (*a*) $t = 0.087$ ms; (*b*) $t = 0.115$ ms, the shock reflects off the tunnel wall; (*c*) $t = 0.142$ ms, the reflected shock has propagated further along the tunnel centerline; (*d*) $t = 0.170$ ms, there is interference between shock waves and expansions; and (*e*) $t = 0.198$ ms. At $t = 0.0188$ ms, the detonation is at the PDE tube exit plane. (Refer Fernandez *et al.*, Fig. 4, p. 309.)

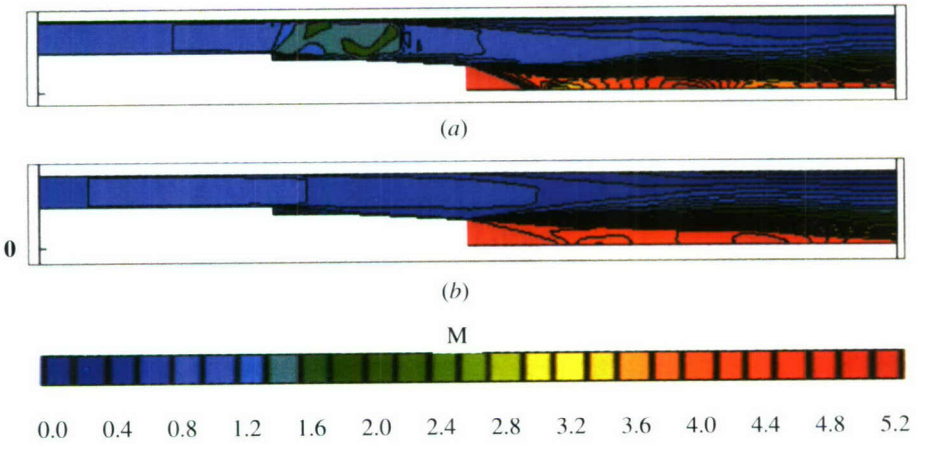

Calculated Mach contours for cases A1 (*a*) and B1 (*b*) with the nozzle flow on. (Refer Fernandez *et al.*, Fig. 12, p. 321.)

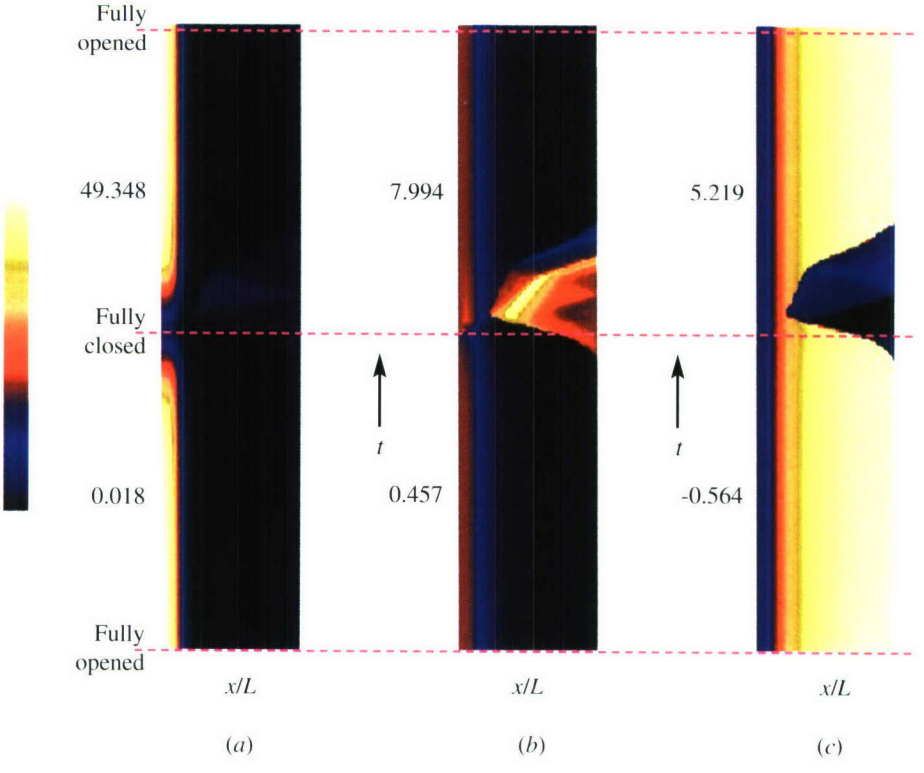

Pressure (*a*), temperature (*b*), and Mach contours (*c*) over one 60-hertz cycle of a Mach 5 nozzle using a linear valve. Numbers beside contours represent high and low values in the x t space. All values have been nondimensionalized. (Refer Fernandez *et al.*, Fig. 5, p. 310.)

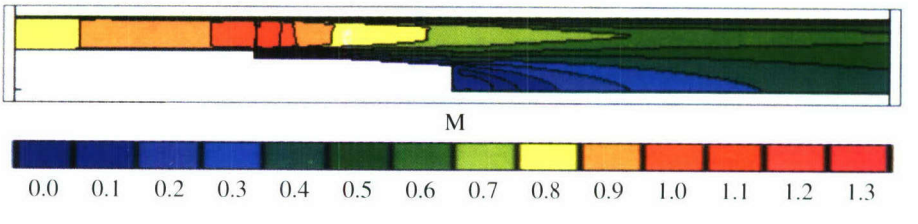

Calculated Mach contours for case A2, the analysis with the nozzle off. (Refer Fernandez *et al.*, Fig. 13, p. 322.)

BREAKUP OF DROPLETS UNDER SHOCK IMPACT

C. Segal, A. Chandy, and D. Mikolaitis

These studies evaluate shock–droplet interactions for mixtures of JP-10 with ethyl-hexyl nitrate, a compound used in the automotive industry to accelerate the reactions in diesel engines. The interest derives from this and other high-energy-density (HED) fuels capability to accelerate the ignition processes in practical devices, such as, for example, a Pulse Detonation Engine (PDE). Initial studies involve Mach 2 shock interactions with a stream of individual, 0.8-millimeter diameter droplets, to be followed by 0.4-millimeter droplets impacted by stronger shocks, up to Mach 5. Previous studies indicated that addition of HED to JP-10 did not accelerate ignition delay times, however, the preignition processes including droplet dispersion, vaporization, and mixing, along with the higher exothermicity of the HED formulations can contribute to reduce the ignition energy required for direct initiation of detonations. Furthermore, the inclusion of HED additives can contribute to the sustainability of detonation waves once they are formed. In the results presented here, the more rapid droplet breakup of mixtures of JP-10 with 5% and 10% ethyl-hexyl nitrate was observed.

1 BACKGROUND

Droplet–shock interactions have been studied extensively and several breakup modes have been described, including vaporization, aerodynamic material stripping, and heating [1–3]. It has been shown that, depending on the jet geometry and the aerodynamic regime, liquid jet column and, subsequently, the formed droplets, undergo several different breakup mechanisms. Early experimental studies indicated the presence of two critical Weber numbers, We_{c1} for primary and We_{c2} for the secondary breakup modes. The We_c variation as a function of the droplet diameter has been identified in these early works and some influence

of liquid viscosity on critical Weber numbers has been found. Later studies determined that the critical Weber numbers depended on flow regime, Reynolds number Re, and Ohnesorge number Oh [4].

The mechanism to which the mass stripping is attributed was found dependent on the flow regime with surface deformation and rupture being characteristic for large convective flows in a crosswise direction relative to the jet column, whereas under quiescent conditions, the column breakup is due to surface instabilities [5]. These observations obtained for water injection were consistent with the observations of Ranger & Nicholls [2] on single droplets who determined that even in the case of strong air–liquid interaction, such as those caused by the passage of a shock wave across a liquid droplet, the disruption of the droplet is due to the shear formed at the droplet surface causing a stripping of the boundary layer but, otherwise, without any visible effect of the shock–droplet interaction. Some disagreement exists in the regime of strong shocks as previous reports in the Russian literature indicated that strong shocks might induce an "explosion" of the droplet before aerodynamic stripping takes effect [4].

It has been shown that at an initial stage, the droplet is deformed to an ellipsoid of revolution under the drag effects*. Unsteady wave disturbances grow on the surface and a boundary layer is formed on upwind side of the droplet. Blowout of boundary layer appears after some induction time. It takes place until a critical deformation is reached and the droplet is transformed into a disk with a thickness $\sim 0.1d_0$ (d_0 is the initial diameter). Then the disk breaks forming several smaller droplets. The induction time is estimated to be $\sim 2t^*$, while the time of breakup $\sim 2.5t^*$, where $t^* = (d_0/v)(\rho_l/\rho_g)^{1/2}$ is some characteristic breakup time, with v, ρ_l, and ρ_g standing for gas velocity, and liquid and gas densities, respectively, [4]. Further correlations have been suggested for droplet mass reduction in time depending on various stages of the breakup. These earlier results have been confirmed by recent data on primary and secondary droplet breakup modes presented by Chou *et al.* [5] under conditions of low-speed crossflow velocities. In the experiments described below, higher speeds are encountered and the characteristic times appear to increase due to inertial effects.

A recent analysis of 2–3 mm diameter, viscous and viscoelastic droplets breakup under high accelerations at Mach 2 to 3 offered by Joseph *et al.* [6], reveals the sequences of the breakup events including the deformation, bag and bag-stamen formation and, finally, mist formation. Breakup at these large accelerations is attributed to the onset of Rayleigh–Taylor instabilities.

In this study, the analysis is focused on higher accelerations with smaller sized droplets, i.e., 0.4–0.8 mm, and, in particular, the breakup of mixtures formed

*Actually, the shape of the deformed droplet only resembles the shape of ellipsoid of revolution. (*Editors' remark.*)

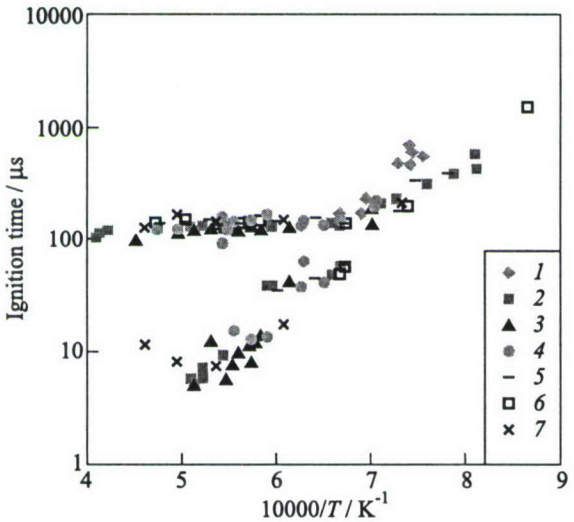

Figure 1 Ignition delay time of JP-10 with additives: *1* — United Technologies Research Center (UTRC) results [8] (included for comparison), *2* — JP-10, *3* — 10% methylated pentacycloundecane (MPCU) alkene dimer, *4* — 50% MPCU alkine dimer, *5* — 10% nitronorbornane, *6* — 20% nitronorbornane, and *7* — 20% dinitronorbornane

by addition of detonation sensitizing compounds to existing liquid hydrocarbons to identify the potential of these additives to enhance the relevant processes present in PDEs. Specifically, in this study, ethyl-hexyl nitrate has been added in concentrations of 5% and 10% on a mass fraction basis to JP-10 and shocks of nominally Mach 2 have been generated to study the extent to which the nonhomogeneity of the mixture accelerates the droplets breakup process. In an initial study of ignition times of these mixtures in air [7], the 5% ethyl-hexyl nitrate mixtures did not show faster ignition times when compared with pure JP-10. Furthermore, none of the other HED compounds included in that study indicated accelerated ignition times within the 1000–2500 K temperature interval, as indicated in Fig. 1. Theoretical analyses [9] have shown that JP-10 has a substantial affinity to destroy free radicals, which may explain the inability of HED to accelerate JP-10 ignition. The usefulness of certain compounds to accelerate detonation or other ignition processes depends largely on the particular molecular structure that results in one reaction mechanism or another [10]. Due to the limiting availability of appropriate compounds suitable for this application, i.e., compounds which (*a*) exhibit sufficient chemical and physical stability, and (*b*) maintain high-energy density, an appropriate compound for detonation enhancement has not been identified in this study.

However, the droplet breakup and vaporization processes are enhanced by the nonhomogeneity of the mixture and the net result is the acceleration of the processes that precede ignition. Indeed, during the experiments described before mixtures of JP-10 with ethyl-hexyl nitrate ignited after the passage of the reflected shock, whereas droplets of pure JP-10 did not. Visualization of the breakup sequence shows faster droplets breakup of JP-10 with additives compared to pure JP-10.

2 EXPERIMENTAL SETUP

The experimental setup is based on the shock tube shown in Fig. 2. The length of the driven section (minus test section length) is 6.1 m. It is made of 4-inch Schedule 80 seamless tube. The driver section is 1.8 m in length. Helium is used as the driver gas and heated, when necessary, until a nominal operating condition of 500 K and 54 atm absolute is attained to generate Mach 5 shocks. At the same time, the driven section/test section is evacuated to a pressure of 0.20 atm absolute and maintained at nominal room temperature. Double diaphragms are employed because with such an arrangement the pressure difference between the driver and driven gases can be precisely controlled even if the diaphragm burst pressure is uncertain. In the experiments described below, the variation in the Mach number ranged between 2.0 and 2.16 for a nominal Mach 2 condition with

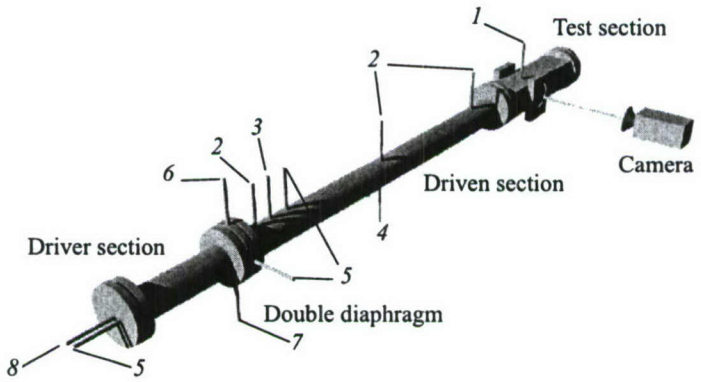

Figure 2 Schematic diagram of the shock tube with test section, droplet injection mechanism, and recording devices: *1* — droplet generator; *2* — high-speed pressure transducers; *3* — low-speed pressure transducer; *4* — vacuum port; *5* — thermocouples; *6* — diaphragm chamber bleed; *7* — low-speed pressure transducer; and *8* — helium input and low-speed pressure transducer

a corresponding variation in the Weber (We) number from 4200 to 4300 for pure JP-10 droplets.

A droplet injection mechanism has been calibrated for the droplet size and dispersion designed for the experiments. Several droplets are captured within the viewing port of the test section. Images are recorded with a Princeton Instruments Intensified Pentamax® Camera using 150-microsecond duration, 300-joule pulse-flash lamp. Within the duration of this flash, the intensifier is triggered twice at an interval of 125 μs. Each intensifier trigger lasts for 60 ns, thereby obtaining, in general, two images of the droplets on the same frame, as indicated in Fig. 3. The viewing window has been set initially for 15 × 15 mm for the JP-10 droplets and reduced subsequently to 6 × 6 mm to increase image resolution.

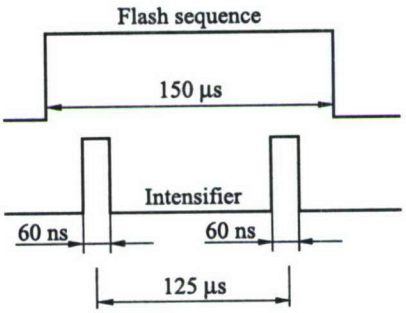

Figure 3 Experimental timing. The droplets injection takes place during the diaphragm breakup. The flash lasts for 150 μs. During this interval, the intensifier is triggered twice for 60-nanosecond duration at an interval of 125 μs, thus recording two images on the same frame

The triggering of the droplet injection, flash, and camera's intensifier is done by detecting the diaphragm rupturing with one of the high-speed pressure transducers and delaying the trigger by a precalculated length of time based on the speed of the generated shock. These pressure transducers have small piezoelectric elements that can detect rapid variations in pressure with resonance response of 1 MHz. The signal from the high-speed pressure transducer is sampled at a rate of 500 kHz. Thus, all the times in the experiment were fixed and known, with the only variation due to material differences from one set of diaphragms to the other.

3 RESULTS

Figure 4 shows a sequence of images collected in different experiments with a nominal Mach 2 flow with pure JP droplets. The field of view in these experiments was 6 × 6 mm. Only a vertical strip of the image is shown. The Mach number ranged between 2.11 to 2.26 and resulted in a Weber number range from 3890 to 5160, therefore the droplets are in the regime of catastrophic breakup. The shock velocity at Mach 2 is 690 m/s and the speed of the air behind the incident shock is 435 m/s. The Reynolds numbers were around 11,000 and the Ohnesorge numbers around 0.015. Since the timing of the shock arrival is measured from the dynamic transducers and the timing of the other events is linked

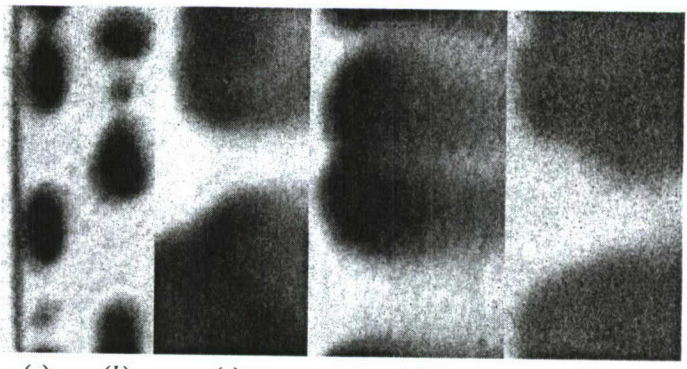

(*a*) (*b*) (*c*) (*d*) (*e*)

Figure 4 Dynamics of JP-10 droplet breakup: (*a*) shock arrival; (*b*) at 5 μs after shock impact the droplets begin to flatten (M = 2.2, We = 5060); (*c*) at 30 μs from the impact the droplets have begun to deform and material is being stripped from the regions of higher shear (M = 2.11, We = 3890); (*d*) at 46 μs the droplets experience a substantial disruption; the finer mist is carried along by the air faster than the denser, more inert, droplet core (M = 2.26, We = 5150); and (*e*) at 90μs the droplets have essentially disintegrated into a fine mist (M = 2.22, We = 4796)

to the dynamic pressure transducers, an exact time of the event shown in the images can be deducted. Figure 4*a* shows 0.8-millimeter-diameter droplets at the time of shock arrival. The droplets in this image have not acquired a spherical shape yet.

The shock does not show deformations despite the cumulative effects of diaphragm rupture, travel through the 6-meter long tube and transition from the round cross-section of the shock tube to the square cross-section of the test section. Figure 4*b* is taken at 5 μs after the shock impact and the droplets begin to flatten under the aerodynamic drag. Figure 4*c* taken at 30 μs from the impact shows droplets that have begun to deform under the impact and material is being stripped from the regions of higher shear. This is more clearly indicated in the top droplets in the figure that have partially coalesced. These effects are shown more clearly in Fig. 4*d*, taken at 46 μs after the impact, when the droplets experience a substantial disruption and the finer mist carried along by the air faster than the denser, more inert, droplet core. This breakup is similar to that observed in previous studies of aerodynamic droplet shattering. Figure 4*e*, taken at 90 μs, indicates that the droplets have essentially disintegrated into a fine mist.

At lower gas speed and higher droplets' surface tension, formation of bag structures and breakup into smaller droplets has been observed following the initial droplet deformation into a disk [5]. In the current experiment, these

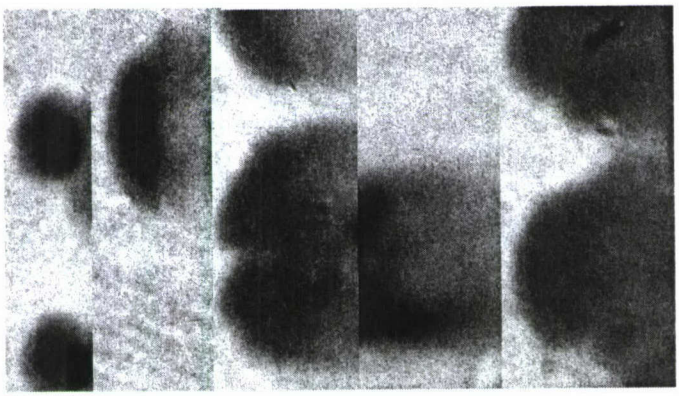

(*a*) (*b*) (*c*) (*d*) (*e*)

Figure 5 Dynamics of JP-10 + 5% ethyl-hexyl nitrate droplet breakup: (*a*) prior to the shock arrival; (*b*) at 16 μs after the shock impact the droplets are deformed and initial material is removed at the periphery of droplet (M = 2.27, We = 4854); (*c*) at 30 μs a substantial deformation of the droplet with significant material removal (M = 2.15, We = 3897); (*d*) and (*e*) at 52 (M = 2.25, We = 4686) and 150 μs (M = 2.31, We = 5198), respectively, indicate complete disintegration of the droplets within the field of view

smaller droplets are not observed, primarily due to the large We number. A mist with scales smaller than the camera resolution, which was 1.2 μm/pixel, was visible both in the pure JP-10 and in the mixture of JP-10 with additives. Based on acceleration estimates, the axial displacement of the droplets at these experimental conditions was 0.85 mm for the first 50 μs after the shock impact, which represents 1.3 droplet diameter [7].

Droplets of heterogeneous composition appear to break faster than single compounds. Figure 5 shows a breakup sequence for droplets of JP-10 with 5% ethyl-hexyl nitrate. The Mach number ranged from 2.15 to 2.31 and the Weber numbers ranged from 3900 to 5200 based on mixture measured surface tension. Figure 5*a* shows the droplet prior to the shock arrival. Due to the experiment timing these droplets have acquired a spherical shape. Figure 5*b* shows droplets at 16 μs after the shock impact. The droplets are deformed and initial material removal at the periphery of droplet where the shear is stronger has begun. Figure 5*c*, taken at 30 μs from the impact, shows a substantial deformation of the droplet with significant material removal. This situation is more evident in the half portion of the top droplet, whereas the lower droplets have coalesced following deformation. Figures 5*d* and 5*e*, taken at 52 and 150 μs, respectively, indicate complete disintegration of the droplets within the field of view. Within 70 μs after the shock reached the droplet, the motion of the droplet,

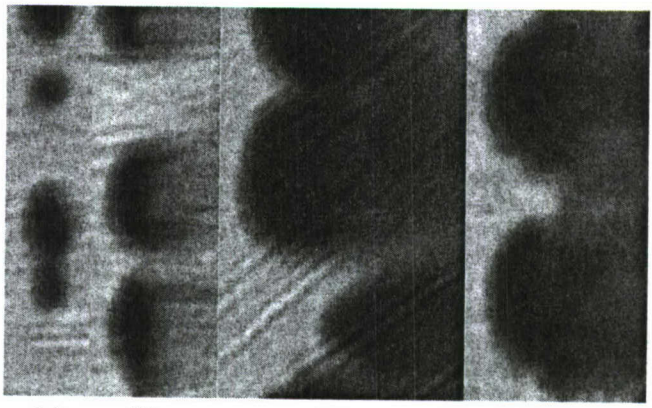

(*a*) (*b*) (*c*) (*d*)

Figure 6 Dynamics of JP-10 + 10% ethyl-hexyl nitrate droplet breakup: (*a*) before shock arrival; (*b*) at 22 μs deformation and initial breakup (M = 2.11, We = 3512); (*c*) and (*d*) at 60 (M = 2.24, We = 4489) and 135 μs (M = 2.3, We = 4982), respectively, the droplets experience a significant breakup becoming clouds of fine mist

based on acceleration estimates, was 1.2 mm, which is a 1.5 droplet diameter in these experiments.

A similar situation is noted in Fig. 6 for mixtures of 10% ethyl-hexyl nitrate in JP-10. At 22 μs, the deformation and initial breakup is evident while at later times, 60 and 135 μs, respectively, the droplets have experienced a significant breakup becoming, essentially, clouds of fine mist.

4 CONCLUDING REMARKS

A set of hydrocarbon compounds that have been blended in JP-10 to accelerate the chemical decomposition did not sensitize the fuel for enhanced detonation. Subsequently, ethyl-hexyl nitrate has been selected to evaluate its effects on JP-10 droplet breakup under Mach 2 shocks impact. This study indicated the following:

- The experimental regime was characterized by We numbers around 4000 resulting in all cases in catastrophic breakup without formation of bag-like structures or primary and secondary breakup, as usually noticed at We number an order of magnitude lower;
- The droplets breakup at these conditions follows the deformation – material stripping – disintegration phases due to aerodynamic shear;

- Addition of 5% to 10% ethyl–hexyl nitrate to JP-10 accelerates the droplet breakup in comparison with pure JP-10 at these experimental conditions to a certain extent, however, the effect is not drastic;
- As a result, it is not expected that inclusion of this compound as a blend in JP-10 will substantially accelerate the physical disintegration of fuel droplets in a PDE application;
- Analyses of the effects of the shocks with higher Mach number and of smaller droplet diameters are needed, including shock/spray interactions at conditions more realistic to PDE operation;
- Although droplet breakup has not dramatically increased, the effects of HED can be materialized through increased energy deposition that would contribute to detonation sustainability. In view of it and, in particular, for accelerating the chemical decomposition through detonation sensitization, specifically designed HED compounds are needed.

ACKNOWLEDGMENTS

This work was performed under ONR contract N00014-99-1-0745.

REFERENCES

1. Buzukov, A. A. 1963. Droplets and jets destruction by air shock wave. *Sov. J. Applied Mechanics Technical Physics* 2:154–58.
2. Ranger, A. A., and J. A. Nicholls. 1969. The aerodynamic shattering of liquid drops. *AIAA J.* 7(2):285–90.
3. Fuller, R., P.-K. Wu, K. Kirkendall, and A. Nejad. 1997. Effects of injection angle on the breakup processes of liquid jets in subsonic crossflows. AIAA Paper No. 97-2966.
4. Volynsky, M. S. 1948. On droplets breakup in an air stream. *Doklady AN USSR* 67(2):301–4; and: 1949. Study of droplets breakup in a gas stream. *Doklady AN USSR* 68(2):237–40; quoted in: Livingston, T., C. Segal, M. Schindler, and V. A. Vinogradov. 2000. Penetration and spreading of liquid jets in an external–internal compression inlet. *AIAA J.* 38(6):989–94.
5. Chou, W.-H., L. P. Hsiang, and G. M. Faeth. 1997. Dynamics of drop deformation and formation during secondary breakup in the bag breakup regime. AIAA Paper No. 97-0797.
6. Johnson, D. D., J. Belanger, and G. S. Beavers. http://www.aem.umn.edu/research/Aerodynamic_Breakup.

7. Mikolaitis, D. W., C. Segal, and A. Chandy. 2002 (submitted). Ignition delay for JP-10/air and JP-10/high energy density fuel/air mixtures. *J. Propulsion Power.*
8. Colket, III, M. B., and L. J. Spadaccini. 2001. Scramjet fuel autoignition study. *J. Propulsion Power* 17:315–23.
9. Varatharajan, B., and F. A. Williams. 2001. Chemistry of hydrocarbon detonations. *14th ONR Propulsion Meeting Proceedings*. Eds. G. Roy and F. Mashayek. 105–10.
10. Colangelo, G., and R. P. Linstedt. 2002. High-moment based modeling of turbulence enhanced DDT kernels in confined fuel–air mixtures. In: *Advances in confined detonations*. Eds. G. Roy, S. Frolov, R. Santoro, and S. Tsyganov. Moscow, Russia: Torus Press. 3–11.

JETS OF FUEL-RICH COMBUSTION PRODUCTS DISCHARGED IN AIR AS A SOURCE OF IMPULSE

A. A. Borisov, A. E. Mailkov, M. A. Silakova, R. N. Elshin, P. V. Komissarov, S. I. Sumskoi, I. O. Shamshin, and A. E. Barykin

The idea of using a high-pressure jet produced by self-ignition or burning of a monopropellant in a small closed volume and injected in the main combustion chamber filled with air as a source of a high-intensity reactive shock wave in the chamber carrying a large impulse is tested both experimentally and by numerical modeling. Fuel-rich energetic materials, such as nitromethane (NM) (both pure and in combination with kerosene) and isopropyl nitrate (IPN), are used as model monopropellants. The injected products react with air in the main chamber to support reactive shock waves that spread at a velocity of up to 1400 m/s. Numerical modeling suggests that burning of the jet material in air can be efficient only if precautions are taken to significantly enhance jet mixing with air in the chamber. It also demonstrates that under certain conditions, unsteady reactive shock waves can be more efficient impulse generators than detonation of a homogeneous monopropellant mixture with air. Measured impulses provide evidence of incomplete burning of the injected material. Possible modifications of the chamber geometry and injection procedure are discussed.

1 INTRODUCTION

Chapman–Jouguet (CJ) detonation is believed to be an ideal regime to be used in pulse detonation engines (PDEs). However, this regime brings about serious problems that if not solved, the PDE designer would face insurmountable obstacles. Among these problems are: (*i*) filling of the chamber with air and fuel within a very short time period; (*ii*) provision of nearly perfect mixing between the components (which is needed because detonation can be initiated and propagates within quite a narrow equivalence ratio range); (*iii*) preevaporation of liquid fuels (experiments show that such fuels as kerosene can not be detonated

in a duct if the vapor phase pressure in the mixture is insufficient [1]); ($i\nu$) initiation of detonation within short distances available in engines (apart from the necessity of very large energy inputs for direct initiation of detonation or special very sophisticated measures speeding up the DDT process, steady CJ detonations in real engines would hardly be attained because CJ detonation in fuel–air mixtures sets in within distances of no less than 1.5 m); and, finally, (ν) limiting tube diameter of detonation which rapidly increases as the ambient pressure drops (e.g., at 0.2 bar, propane–air mixtures cannot detonate in tubes less that 100 mm in diameter). Thus, if even all the above-listed problems are successfully solved, the burning regime in the PDE chamber is inevitably unsteady and the detonation velocity is below the CJ value by about 10%–15%.

Are any other approaches that allow one to avoid the aforementioned difficulties and, at the same time, are as efficient as detonation of the mixture in the chamber? The present work explores the possibility of combining mixing and reactive shock generation in a single process. This can be done by injecting a preconditioned fuel in the main chamber filled with air [2–4]. Preconditioning means preheating of the fuel to a temperature that would provide its fast spontaneous reaction with the ambient air in the course of their mixing. If the pressure in the jet is high enough to drive a strong shock wave at the initial stage of discharge that would be supported at later stages by the fuel reaction within the mixing layer, the burning process would be similar, at least to some extent, to detonation.

The approach eliminates most of the difficulties inherent in detonation engines, namely, the jet initiates the reaction, so that the initiation problem is no longer critical. The same applies to fuel preevaporation and detonation limits, because the injected material is preheated, gasified, contains reactive species, and reacts with air with no limitations. The combustion chamber needs refilling with air only, which is much easier to arrange than to fill it with a fuel–air mixture. As to the essentially unsteady nature of the flow, it is, as mentioned above, inevitable in a short combustion chamber. The only problem left is mixing, but its solution requires other approaches than those in the case of detonation of premixed components.

The questions to be answered are:

- How efficient is the unsteady process produced by a jet?
- What is the flow structure and the reaction intensity and efficiency?
- What should be done to enhance the mixing process?

High-pressure jets can be generated by self-igniting (in a preheated volume) or igniting with a spark either a liquid monopropellant rich in the fuel component (and then injecting the partially reacted material in air) or a small amount of a monopropellant to raise the pressure in the injector and inject in the main chamber the products of its decomposition together with a conventional hydrocarbon fuel. The intention of this study is to answer the aboveformulated questions.

2 EXPERIMENTAL SETUP

Experiments were conducted in tubes schematically shown in Fig. 1. In the first version of the setup, the tube was 3 m long and 120 mm of inner diameter. The tube was equipped with 5 pressure gauges spaced 50 cm apart to monitor the wave velocity and pressure profiles. The injector is a thick-walled steel cylinder screwed in the end flange.

In tests with monopropellant self-ignition, the injector is placed in an electric furnace. The opposite tube end is open. Liquid NM in an amount of 4–9 g with small additives of Al powder (0.3 or 0.5 g) is poured in the injector closed with a diaphragm. In tests with no self-ignition, the mixture is ignited with a pyrotechnic primer. The injector diameter-to-length ratio is varied from 1/5 to 1/12 to find an optimal value at which the wave velocity and pressure amplitude

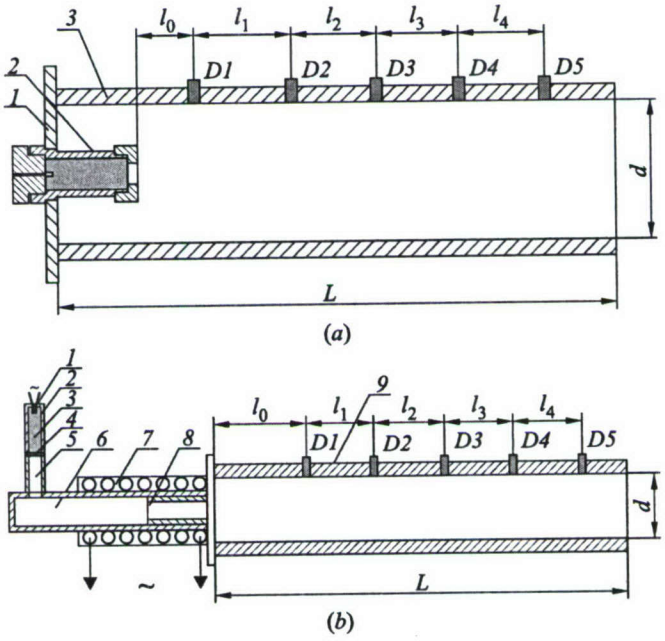

Figure 1 (*a*) Schematic of the experimental setup for studying propagation of reactive shock waves produced by injection of hot fuel into a combustion chamber: *1* — butt flange, *2* — injector, and *3* — steel tube. Distances between the gauges are $l_0 = 25$ cm, $l_1 = l_2 = 50.5$ cm, $l_3 = l_4 = 50$ cm, tube diameter $d = 120$ mm, and tube length $L = 3$ m. (*b*) Experimental apparatus in which NM is self-ignited in the injector: *1* — primer; *2* — container; *3* — propellant; *4* — separating diaphragm; *5* — duct; *6* — injector; *7* — furnace; *8* — orifice; and *9* — tube. $d = 95$ mm, $L = 135$ cm; $l_0 = 30$ cm; $l_1 = 22.5$ cm; $l_2 = 23$ cm; and $l_3 = l_4 = 22.5$ cm

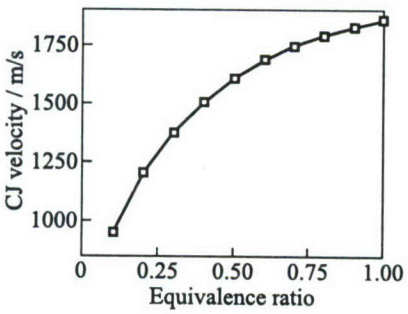

Figure 2 Chapman–Jouguet detonation velocity vs. equivalence ratio for IPN–air mixtures. Equivalence ratio 1.0 corresponds to $m_{[oxid]}/m_{[fuel]} = 4.24851$, where "oxid" = "air"

are the greatest. Inasmuch as NM contains too much of oxygen in its molecule and the heat of its combustion in air is low, in the next set of tests IPN was used as a fuel. Isopropyl nitrate cannot be ignited with a primer, therefore it is ignited either by gradually heating the injector until self-ignition occurs or rapidly admitting the liquid in the preheated injector. Experiments with self-ignition are conducted in a tube 1.35 m long and 95 mm in diameter equipped with 5 pressure gauges.

To assess the efficiency of the process suggested to produce thrust, the shorter tube is suspended and the impulse is measured by the pendulum technique. Since the measured impulse depends on the conditions of fuel discharge, the efficiency of heterogeneous jets in producing impulse is assessed in comparative tests in which experiments with heterogeneous jets are compared with detonation of homogeneous mixtures. Detonation in homogeneous mixtures is initiated by detonating a small volume of a stoichiometric propylene–oxygen mixture in the tube. The impulse produced by the initiator is measured in a run where the tube is filled with air and subtracted from the impulse measured in runs with a fuel–air mixture present in the tube. The saturated vapor pressure of NM and IPN is too low to allow one to prepare a stoichiometric NM or IPN–air mixture in the tube. Moreover, both liquids are easily adsorbed by the tube walls. Therefore, a lean IPN mixture was detonated and the actual fuel concentration was estimated by the average measured detonation velocity using the calculated dependence of the CJ detonation velocity on fuel concentration shown in Fig. 2.

3 EXPERIMENTAL RESULTS

In experiments with NM, the highest wave velocities (up to 1400 m/s) and pressure of about 30 atm are observed at injector diameter-to-length ratios (L/d) ranging between 1/12 and 1/8. The wave parameters measured near the injector are higher because the amount of NM is insufficient to make a stoichiometric mixture with air in the tube. The representative pressure records in the tube are shown in Fig. 3. At smaller L/d ratios, only low-velocity regimes (with velocities of about 600 m/s) were observed. These results and the long pressure pulses provide evidence of an intense reaction between the injected material and air.

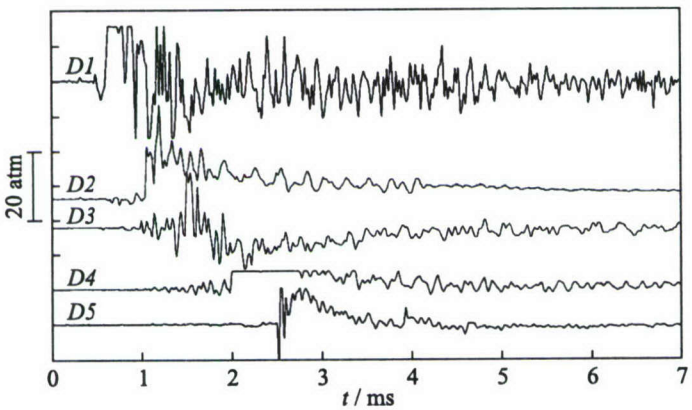

Figure 3 Representative pressure records of the reactive shock generated in the tube upon injection of a reacting Al + NM jet. Fuel: 8 cm^3 NM + 0.5 g Al. Initiator: primer cap. Pressure signal from gauge *D1* is cut from above by electronic circuit. Measured wave velocity between *D1* and *D2*: $U_1 = 1260$ m/s; *D2–D3*: $U_2 = 1215$ m/s; *D3–D4*: $U_3 = 1040$ m/s, and *D4–D5*: $U_4 = 1040$ m/s

To increase the amount of fuel to its stoichiometric content, 1.8 cm^3 of kerosene (JP-type) is poured on the diaphragm closing the injector. As seen in Fig. 4, burning of a small amount of NM in the injector sprayed and preheated kerosene to cause its spontaneous reaction with air.

Experiments with IPN are performed with the hope that the reaction of its decomposition products with air would produce stronger reactive shock waves. Figure 5 shows the recorded pressure profiles. The amount of IPN in this case is stoichiometric, and the charge is initiated by gradually heating the monopropellant in the injector. The pressure records indicate that only a small fraction of the injected fuel reacts with air and mostly near the injector.

The detonation velocity measured in a propylene mixture is indicated in Fig. 6. As seen, the process is unsteady even with the very high initiation energy used. The second important point is that the steady CJ detonation does not set in (the final velocity is below the calculated level). The measured impulse for a stoichiometric propylene–air mixture ranges between 1730 and 1600 s. The detonation wave initiated in a homogeneous IPN–air mixture is also unsteady (Fig. 7). The measured specific impulse of IPN ranges between 600 and 700 s for the homogeneous mixtures and between 250–300 s for heterogeneous IPN jets. The specific impulse of NM measured in jet experiments is close to 150 s. To understand why the impulse produced by homogeneous mixtures is about twice as high as the impulse generated by jets and to find the ways to make the injection process efficient, numerical modeling of the unsteady flow produced by reactive jets was performed.

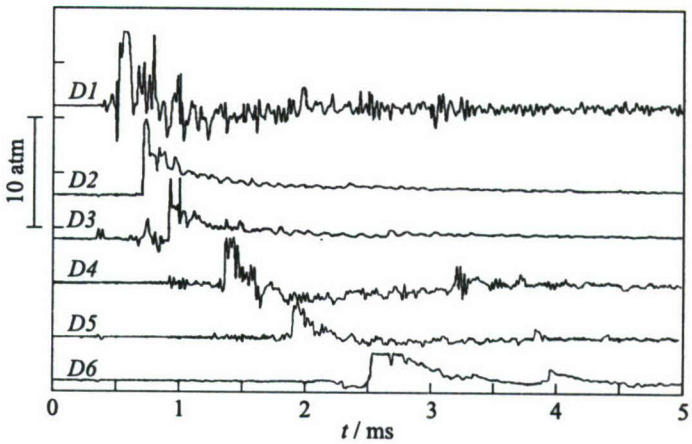

Figure 4 Representative records of the wave generated upon injection of a reacting 4 cm^3 NM+0.2 g Al + 1.8 cm^3 kerosene. Initiator: primer cap. Measured wave velocity between *D1* and *D2*: $U_1 = 1390$ m/s; *D2–D3*: $U_2 = 1170$ m/s; *D3–D4*: $U_3 = 1165$ m/s, and *D4–D5*: $U_4 = 950$ m/s

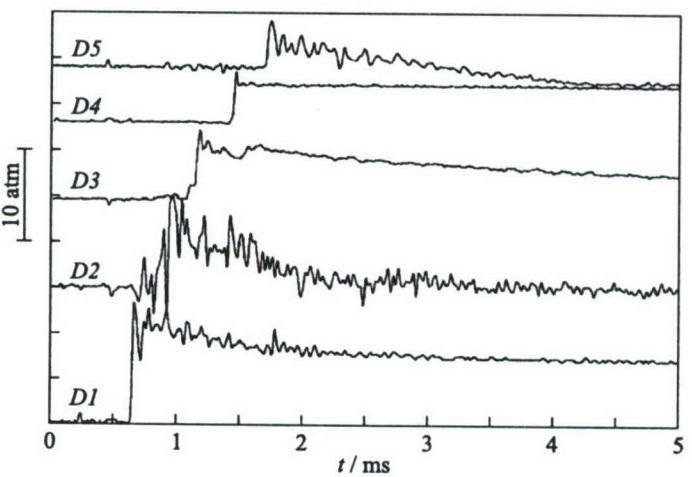

Figure 5 Pressure records for IPN self-ignition, $m_{IPN} = 3.5$ g. Measured wave velocity between *D1* and *D2*: $U_1 = 1125$ m/s; *D2–D3*: $U_2 = 920$ m/s; *D3–D4*: $U_3 = 680$ m/s, and *D4–D5*: $U_4 = 805$ m/s

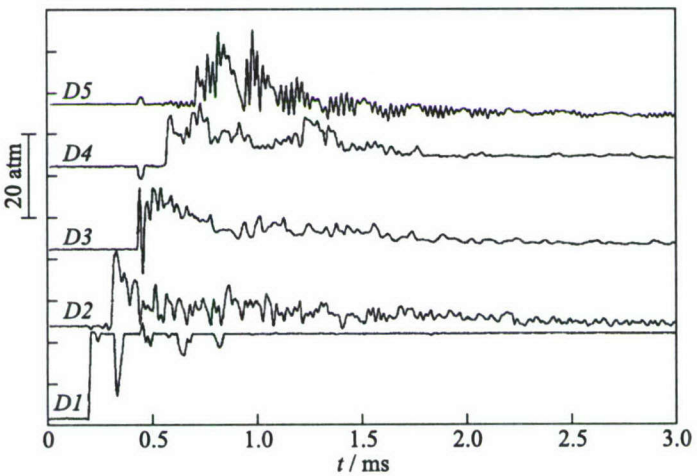

Figure 6 Measurements of the specific impulse produced by detonation of a stoichiometric gaseous mixture (C_3H_6 + air, initiator $C_3H_6 + O_2$ mixture). Measured impulse is 1730 s. Measured wave velocity between *D1* and *D2*: $U_1 = 2000$ m/s; *D2–D3*: $U_2 = 1840$ m/s; *D3–D4*: $U_3 = 1635$ m/s, and *D4–D5*: $U_4 = 1635$ m/s

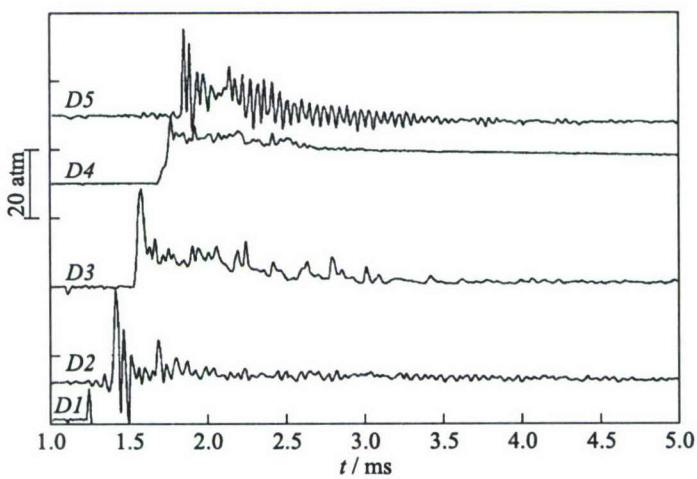

Figure 7 Detonation of IPN–air mixture (1.15 g IPN). Measured impulse is 730 s. Measured wave velocity between *D1* and *D2*: $U_1 = 1330$ m/s; *D2–D3*: $U_2 = 1700$ m/s; *D3–D4*: $U_3 = 1330$ m/s, and *D4–D5*: $U_4 = 1660$ m/s

4 NUMERICAL MODELING

A two-dimensional gasdynamic code is developed to model multiphase flows. It allows for an arbitrary number of condensed and gaseous components, homogeneous and heterogeneous chemical reactions, interactions between condensed particles, and an arbitrary number of mesh refinement levels. The traditional burning-time equation is used for decomposition and burning of condensed particles and Arrhenius-type global equation is used for homogeneous reactions. To analyze the flow pattern and compare computations (wave velocities and impulses) with experiment, the following problems are solved:

(1) Injection of a NM + Al (95/5) mixture through the injector orifice in a tube of the same size as in the experiment; charge weight is 9.0 g;

(2) Detonation of the same mixture homogeneously distributed in the tube;

(3) Injection of 3.5 g of IPN in a 1.2-meter long tube; and

(4) Detonation of a homogeneous IPN spray in the same tube.

Modeled are also detonations of stoichiometric hydrogen–air and propane–air mixtures in a 0.8-meter long tube.

A simple analysis suggests that, to generate an intense initial shock wave, the pressure in the injector must be high; however, in contrast to low-pressure jets, in this case, the products expand at almost equal velocities in the axial and radial directions. Thus, the products are expected to expel a significant portion

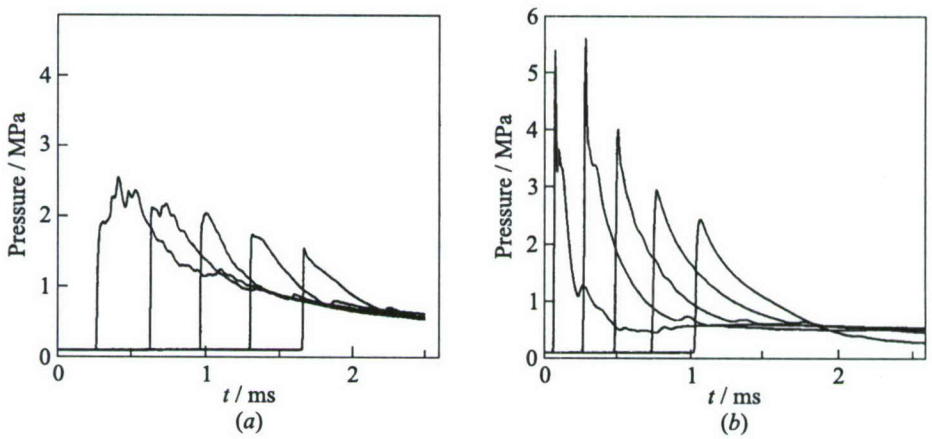

Figure 8 Pressure–time histories at various tube sections: (*a*) NM + Al injection; and (*b*) instantaneous mixture reaction within the injector. Positions of gauges are 0.25 m, 0.76, 1.26, 1.76, and 2.26 m

of air from the tube. Numerical computations are performed to assess the fuel fraction not participating in the reaction with air and find the ways of increasing the burning efficiency. Unfortunately, the process within the injector is too complicated and many factors governing it are unknown, therefore at present it is not amenable to modeling. This necessitates several assumptions. In order to fit the pressure at which the injector diaphragm bursts in the experiment, it was assumed that initially 10% of the propellant reacts at a constant volume. Furthermore, it was also assumed that the initial size of liquid drops in the jet is 25 μm. This allows the wave velocities to approximately fit the experiment. Figure 8 shows the pressure profiles in the tube for a NM + Al jet and detonation of a homogeneous mixture. The pressure profiles are quite similar to the measured ones; the behavior of the calculated wave velocity (see Fig. 9) is also similar to that observed in the experiment. That the reaction between the products and air takes place only at the jet head is illustrated by Fig. 10 where the pressure peaks locally at each time instant. The low efficiency of fuel oxidation by air oxygen is seen from Fig. 11 where time histories of the mass fractions (referred to the amount of the component to be formed in the propellant decomposition

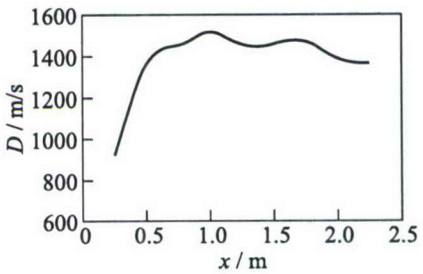

Figure 9 Wave front velocity vs. time. NM/Al injection, x is the distance from the injector

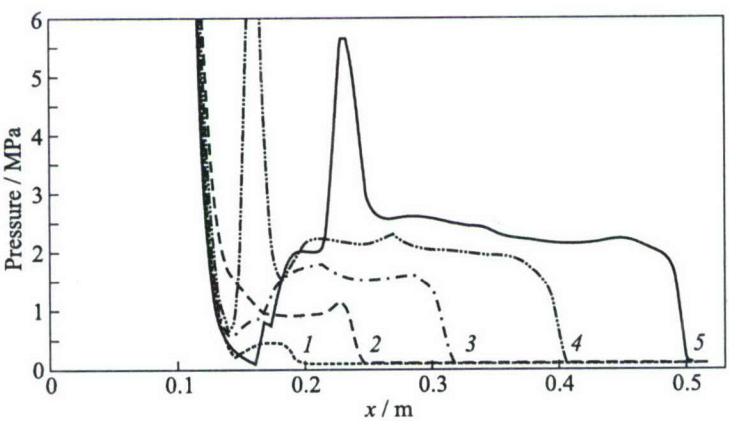

Figure 10 Axial pressure profiles at the initial stage of injection after diaphragm bursting: *1* — $t = 0.075$ ms, *2* — 0.15, *3* — 0.225, *4* — 0.3, and *5* — $t = 0.375$ ms

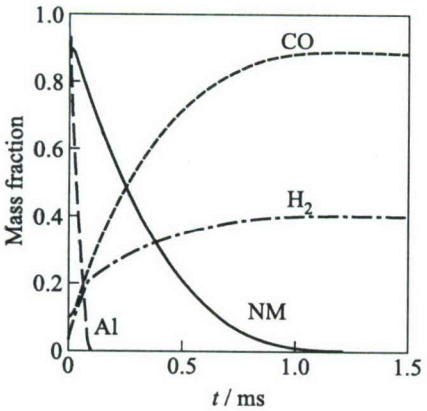

Figure 11 Mass fractions of the mixture components integrated over the tube volume

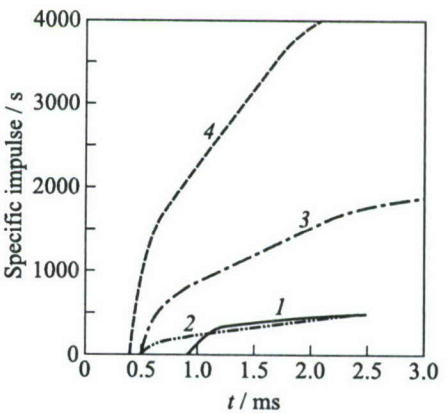

Figure 12 Time histories of the specific impulse at the open tube end. Injection of NM/Al, open (*1*) and closed ends (*2*); *3* — propane–air; and *4* — hydrogen–air

reaction) of fuel components are plotted. Thus, only about 15% of CO formed is oxidized. Calculations of injection of partially reacted NM in the tube filled with oxygen also revealed a very low burnt fraction of the injected material. The unburnt fraction of H_2 and CO is greater in the IPN jet.

The basic characteristic of engine efficiency is the impulse produced by fuel combustion. In general, the impulse depends on the chamber and nozzle geometry. Therefore, as in experiment, the impulse produced by detonation of a homogeneous propellant–air mixture and by injecting the propellant in air is compared under identical conditions. The impulse is calculated by the thrust at the closed and open tube ends. Time histories of the specific impulse are illustrated in Fig. 12. The results of calculations are listed in Table 1.

Table 1 Results of calculations

	I_{sp}, s	
	Open end	Closed end
NM + Al (injection)	442	—
NM + air (homogen.)	455	495
IPN (injection)	241	273
IPN (homogen.)	671	686
Propane + air	1867	1911
Hydrogen + air	4145	

5 DISCUSSION

As computations show, the major reason of incomplete burning of the injected material is that the jet expands too fast and produces a plug flow at the beginning of the tube. Thus, the mixing layer area is reduced to the jet head only, therefore the major fuel fraction is not oxidized in air. This is illustrated in Fig. 13 where the oxygen concentration clearly shows formation of a plug flow at the initial discharge stage, which means that the area of the layer where fuel mixes with air is insufficient for the fuel to be consumed within the chamber. The experiment suggests even poorer mixing efficiency and a lesser fraction of decomposed propellant. This indicates that, on the one hand, the jet expansion should be restricted, and on the other, the jet must be split in several smaller jets to drastically enhance the mixing process keeping the jet velocity at a high

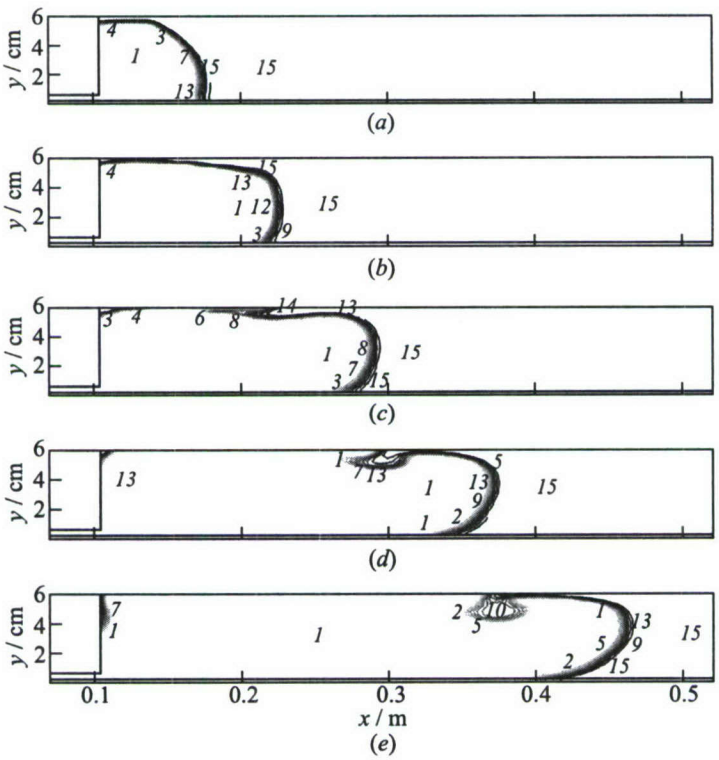

Figure 13 Predicted oxygen concentration maps (*1* corresponds to zero mass fraction, and *15* — to 0.233) at various instants upon injection of a heterogeneous charge (9 g NM + 0.5 g Al) in the tube: (*a*) $t = 0.075$ ms, (*b*) 0.15, (*c*) 0.225, (*d*) 0.3, and (*e*) $t = 0.375$ ms

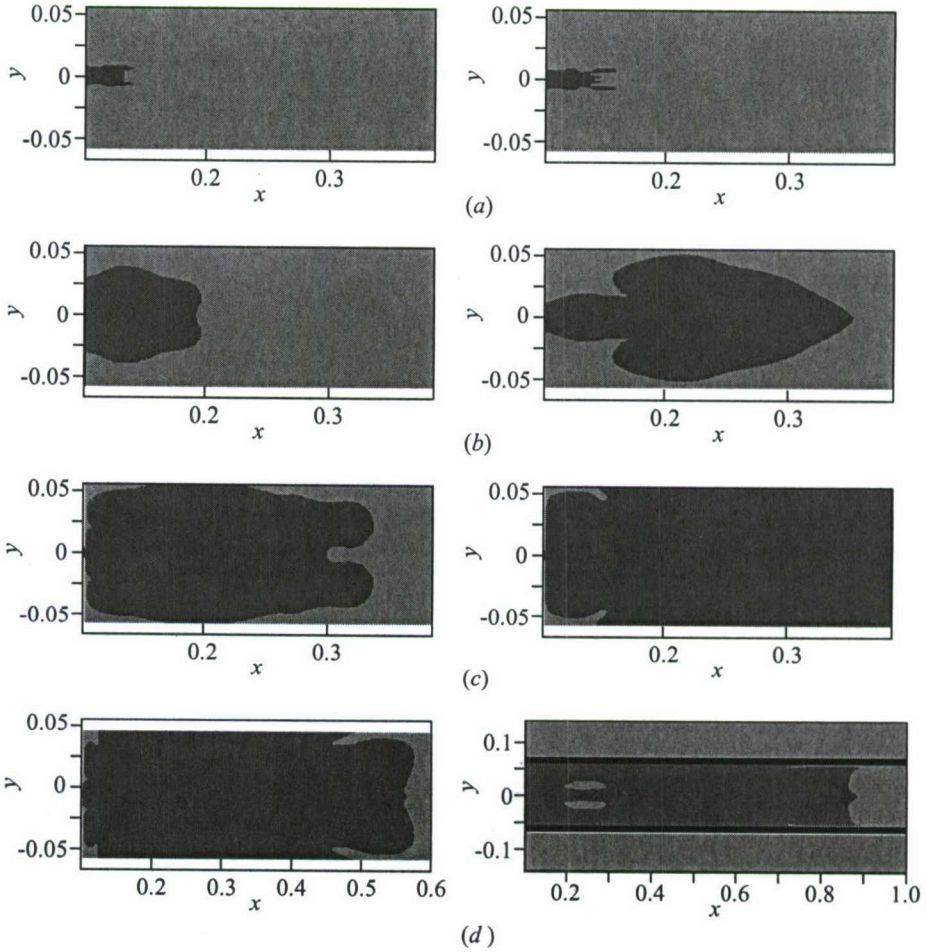

Figure 14 Jet profiles (90% concentration of the injected material) under different conditions. Variable injection pressure p and time t, at time instants 1 ms (left) and 2 ms (right) after injection: (a) $p = 40$ atm, $t = \infty$; (b) $p = 60$ atm, $t = 10$ ms; (c) $p = 170$ atm, $t = 5$ ms; and (d) $p = 450$ atm, $t = 1$ ms. The x and y scales are in m

level. This can be done either by confining the jet in a tube of a smaller diameter with perforations to eject the propellant and products of its decomposition into the main chamber as the jet spreads through the smaller tube or by injecting the decomposition products through several orifices distributed over the chamber. Turbulizing obstacles can increase the mixing rate, their design and arrangement in the chamber are to be ascertained by numerical modeling. Lowering the injection pressure would drastically increase the mixing surface area

(see Fig. 14); however, the jet velocity drops significantly, therefore the pressure in the injector is another factor to be used in optimizing the mixing process.

The most important finding that follows from computations is that the impulse produced by a NM jet is nearly equal to that of the detonation, in spite of the fact that only a small fraction of the jet material is oxidized by air. This is attributed to the longer pressure pulses resulting from the lesser energy left in the reaction products, higher density and velocity of the fluid discharged from the tube as compared to the detonation wave issuing from the tube. Somewhat surprising is also the fact that the experimental impulse of detonation of a homogeneous propylene–air mixture is virtually equal to the calculated one, although the recorded wave velocity is lower than the CJ velocity.

6 CONCLUDING REMARKS

Experiments have revealed that:

- Both self-ignition of monopropellant and its ignition with a weak source in an injector can produce a reacting jet issuing in air that supports a strong shock wave spreading at a velocity of up to 1400 m/s;
- Combination of NM with kerosene is a promising way of generation of reactive shock waves (it is demonstrated that kerosene driven by the issuing NM decomposition products does react behind the wave);
- Measured specific impulse generated by NM and IPN jets is about 150 and 210 s, respectively; and
- Injection of the IPN decomposition products at two sites along the tube increases the specific impulse to 286 s.

Numerical calculations show that:

- Low efficiency of heterogeneous jets is due to poor mixing of the jet material with air because the high-pressure jets expand too fast, reach the walls, and dramatically reduce the mixing surface area;
- Possible ways of improving the efficiency of jets in generation of impulse are: injection of fuel-rich products at several points along the combustion chamber, the use of a monopropellant as a driver and igniter of a conventional hydrocarbon fuel to inject it in the chamber in the form of a fine preheated spray, placement of turbulizers in the chamber to enhance mixing, or changing the injection pressure profile (to start with a low pressure and then increase it to, say, a few hundreds of atmospheres; and

– Under certain conditions, the specific impulse produced by unsteady reactive shock waves can be even higher than the impulse generated by CJ detonation of the same amount of fuel homogeneously distributed in the chamber.

ACKNOWLEDGMENTS

This work was partly supported by the U.S. Office of Naval Research and Russian Foundation for Basic Research.

REFERENCES

1. Borisov, A.A. 1999. Initiation of detonation in gaseous and two-phase mixtures. In: *Gaseous and heterogeneous detonations: Science to applications*. Eds. G. Roy, S. Frolov, K. Kailasanath, and N. Smirnov. Moscow, Russia: Enas Publ. 3–24.
2. Borisov, A.A. 2002. Initiation of detonation-like processes by injecting a liquid monopropellant into air. In: *Advances in confined detonations*. Eds. G. Roy, S. Frolov, R. Santoro, and S. Tsyganov. Moscow, Russia: Torus Press. 133–38.
3. Borisov, A.A. 2002. Comparison of impulse generated by gaseous detonations and shock waves supported by heterogeneous reactions. In: *Advances in confined detonations*. Eds. G. Roy, S. Frolov, R. Santoro, and S. Tsyganov. Moscow, Russia: Torus Press. 158–60.
4. Borisov, A.A. 2002. Impulse production by injection fuel rich combustion products in air. *15th ONR Propulsion Meeting Proceedings*. Eds. G.D. Roy, and A.K. Gupta. College Park, MD: University of Maryland. 219–24.

FORMATION OF TWO-DIMENSIONAL DETONATION STRUCTURES IN ALUMINUM GAS SUSPENSION IN A CHANNEL

A. V. Fedorov and T. A. Khmel

Two-dimensional (2D) effects at detonation initiation in a cloud of aluminum particles partly filling a plane channel are studied numerically based on the mathematical model of detonation in aluminum particle suspension in oxygen and verified by experimental data. Detonation is initiated by a planar shock wave (SW) entering the cloud or reflecting from the channel end-wall. Different scenarios of detonation formation depending on the incident SW amplitude and profile are revealed. The influence of cloud width on detonation initiation or failure is analyzed. Nonsteady flow dynamics and complex 2D flow structure accompanying shock/detonation wave propagation along the channel are discussed. It is shown that detonation wave propagation is quasi-stationary with periodic fluctuations of the front shape and flow parameters. The mean propagation velocity corresponds to strong (in case of supported incident shock wave) or normal detonation wave. In one case of supported incident SW, a quasi-stationary detonation with the propagation velocity considerably lower than the Chapman–Jouguet (CJ) velocity is obtained.

1 INTRODUCTION

Capability of aluminum particle suspensions to detonate in oxygen and air has been confirmed experimentally [1–4]. A certain discrepancy in the measured propagation velocities indicates that the detonation was not always steady. The value of 1.6 km/s [1] is considered as the most credible value of the CJ detonation velocity for the aluminum suspension of stoichiometric composition in oxygen [4, 5].

Mathematical modeling of detonation waves in aluminum suspensions in oxygen and air and theoretical investigations of stationary detonation structure were performed in [3, 5–8]. A mathematical model based on the formalism of heterogeneous medium mechanics supplemented with an overall chemical reaction was

developed in [5, 7, 8]. The model provides a reasonable agreement with experiments [1] on the dependence of the detonation velocity on initial particle concentration and agrees with available experimental data on ignition delay and characteristic combustion time. Taking into account the presence of unburnt particles in detonation products (about 10% of the initial particle mass concentration [1]), the theoretical analysis of detonation in aluminum suspension in oxygen revealed a nonideal character of stationary detonations [7, 8]. Nonmonotonic heat release caused by simultaneous thermal and chemical relaxation between the gas and particles results in a possibility of weak (underdriven) stationary detonation regimes (although the detonation velocity is close to the CJ value). The mathematical model [5, 7, 8] was applied to study detonation initiation in a one-dimensional (1D) formulation [9, 10]. In particular, the problem of SW interaction with a particle cloud of infinite width was considered in [10], where scenarios and criteria of detonation initiation by supported and decaying incident shock waves were obtained. The present work is an extension of [10] to a 2D case, when the particle cloud occupies only a part of the channel cross-section.

A plane channel partly filled with gas (oxygen) and partly with a gas suspension of aluminum particles is considered. A planar SW first propagates in the gas along the channel and then enters the cloud. The shock wave can be either continuously supported or attenuated by an adjacent rarefaction wave. A similar problem for a cloud of nonreactive particles was considered in [11]. Transverse effects arising when the shock wave enters the cloud as well as the processes accompanying shock propagation, refraction and reflections were analyzed. Some results on detonation formation in a suspension of reactive particles are also presented in [11] for the case of strong supported incident SW with the propagation velocity exceeding the characteristic CJ velocity. Even in this case, the detonation flow pattern appears to be unsteady with periodic fluctuations of the front shape and velocity. Nevertheless, the mean propagation velocity corresponds well to a strong stationary detonation regime. The opposite case when the incident SW velocity is lower than the CJ detonation velocity is also of interest. The other unknown issue is a possibility to initiate detonation in a cloud of finite width by the incident SW that is attenuated by the adjacent rarefaction wave. Also, if the incident SW amplitude is insufficient for direct detonation initiation, the conditions for particle ignition and combustion may be created by SW reflection from the channel end-wall. The corresponding problem in 1D formulation was studied in [9], where strongly overdriven detonation regimes were obtained with very high values of pressure and temperatures in the near-wall region.

The objectives of the present work are to study the influence of the cloud width on detonation initiation, to investigate specific features of 2D detonation structure, and to analyze the dynamics of combined shock/detonation wave propagation in the cloud at different incident SW amplitudes and profiles.

2 PROBLEM FORMULATION

Consider a plane channel of infinite length partly filled with a cloud of spherical aluminum particles uniformly dispersed in gaseous oxygen. The semi-infinite cloud is of a rectangular shape and is attached to the bottom channel wall. The residual volume of the channel is filled with gaseous oxygen. A planar shock wave, initially propagating along the channel in gas, interacts with the cloud. Two types of incident shock waves are considered: (*i*) externally supported (i.e., characterized by stepwise rectangular parameter profiles), and (*ii*) decaying due to adjacent rarefaction wave (i.e., having a triangular velocity profile). Shock wave penetration into the cloud either results in particle ignition or creates the conditions for detonation initiation after subsequent reflection from the channel end-wall.

The governing equations follow from the conservation laws of mass, momentum, and energy for each phase in a two-velocity two-temperature approach of mechanics of heterogeneous media. Equations of state and the equation of overall chemical reaction close the system. In addition, ignition criterion and incomplete particle burning are taken into account [8, 10, 11]:

$$\frac{\partial \rho_i}{\partial t} + \frac{\partial \rho_i u_i}{\partial x} + \frac{\partial \rho_i v_i}{\partial y} = (-1)^{i-1} J$$

$$\frac{\partial \rho_i u_i}{\partial t} + \frac{\partial [\rho_i u_i^2 + (2-i)p]}{\partial x} + \frac{\partial \rho_i u_i v_i}{\partial y} = (-1)^{i-1} (-f_x + J u_2)$$

$$\frac{\partial \rho_i v_i}{\partial t} + \frac{\partial (\rho_i u_i v_i)}{\partial x} + \frac{\partial [\rho_i v_i^2 + (2-i)p]}{\partial y} = (-1)^{i-1} (-f_y + J v_2) \qquad (1)$$

$$\frac{\partial \rho_i E_i}{\partial t} + \frac{\partial [\rho_i u_i (E_i + (2-i)p/\rho_1]}{\partial x} + \frac{\partial [\rho_i v_i (E_i + (2-i)p/\rho_1)]}{\partial y} = (-1)^{i-1} (-q - f_x u_2 - f_y v_2 + J E_2)$$

$$p = \rho_1 R T_1 , \quad E_1 = \frac{u_1^2 + v_1^2}{2} + c_{v,1} T_1 , \quad E_2 = \frac{u_2^2 + v_2^2}{2} + c_{v,2} T_2 + Q \qquad (2)$$

$$J = \frac{\rho}{\tau_\xi} \max [0, (\xi - \xi_k)] \exp \left(-\frac{E_a}{R T_2} \right) \max [0, \operatorname{sign}(T_2 - T_{\text{ign}})] \qquad (3)$$

Here, p is the pressure; $\rho_i = m_i \rho_{ii}$, u_i, v_i, E_i, and $c_{v,i}$ are mean densities, velocities, total energy per unit mass, and specific heats of the components; m_i is the volume concentration of the ith phase, ρ_{ii} is the material density ($i = 1, 2$; indices 1 and 2 refer to gas and particle phase, respectively); T_1 and T_2 are

the gas and particle temperatures, respectively; Q is the heat effect of chemical reaction; $\gamma_1 = R/c_{v,1}$ is the adiabatic exponent; $\xi = \rho_2/(\rho_1 + \rho_2)$ is the relative mass concentration of particles; E_a is the activation energy; ξ_k is the mass concentration of unburnt particles; T_{ign} is the ignition temperature; and τ_ξ is the characteristic combustion time.

Interaction between the phases is determined with regard for a drag coefficient of a spherical particle in a supersonic flow [12]:

$$f = \frac{3m_2\rho_{11}}{4d} c_D\,|u_1 - u_2|\,(u_1 - u_2)\,, \quad q = \frac{6m_2\lambda_1}{d^2}\mathrm{Nu}\,(T_1 - T_2)$$

$$c_D(\mathrm{Re}, \mathrm{M}_{12}) = \left[1 + \exp\left(-\frac{0.43}{\mathrm{M}_{12}^{4.67}}\right)\right]\left(0.38 + \frac{24}{\mathrm{Re}} + \frac{4}{\sqrt{\mathrm{Re}}}\right) \tag{4}$$

$$\mathrm{Nu} = 2 + 0.6\mathrm{Re}^{1/2}\mathrm{Pr}^{1/3}\,, \quad \mathrm{Re} = \frac{\rho_{11} d|u_1 - u_2|}{\mu}\,, \quad \mathrm{M}_{12} = \frac{|\,u_1 - u_2\,|\sqrt{\rho_{11}}}{\sqrt{\gamma_1 p}}$$

In Eqs. (4), d is the particle diameter; c_D is the drag coefficient; λ_1 and μ are the coefficients of thermal conductivity and viscosity of the gas; Re, Nu, Pr, and M are the Reynolds, Nusselt, Prandtl, and Mach numbers, respectively.

Initial conditions for the case when the cloud is unbounded in the x-direction have the form:

$$t = 0\,, \quad \phi = \begin{cases} \phi_{\text{SW}}\,, & 0 \le x < X_{\text{SW}}\,, & 0 \le y \le Y \\ \phi_0\,, & X_{\text{SW}} \le x < X_{\text{cl}}\,, & 0 \le y \le Y \\ \phi_{\text{cl}}\,, & X_{\text{cl}} \le x < +\infty\,, & 0 \le y < D \\ \phi_0\,, & X_{\text{cl}} \le x < +\infty\,, & D \le y \le Y \end{cases} \tag{5}$$

Here, $\phi = \{\rho_1, \rho_1 u_1, \rho_1 v_1, \rho_1 E_1, \rho_2, \rho_2 u_2, \rho_2 v_2, \rho_2 E_2\}$ is the solution vector, $\phi_{\text{SW}}(x)$ describes the plane SW in gas, X_{SW} indicates the initial position of the incident SW. Values ϕ_0 and ϕ_{cl} refer to the initial state of gas (outside the cloud), and mixture (inside the cloud), respectively; X_{cl} determines the position of the front cloud boundary; D is the cloud width; and Y is the channel width. The boundary conditions on the channel walls ($y = 0$, $y = Y$) correspond to nonadherent, impermeable, and adiabatic walls:

$$v_i = 0\,, \quad \frac{\partial u_i}{\partial y} = \frac{\partial T_i}{\partial y} = \frac{\partial \rho_i}{\partial y} = 0 \quad i = 1, 2$$

The initial state ϕ_o or ϕ_{cl} depending on y is taken as the condition on the right boundary, which moves in the course of calculations as far as the leading shock wave propagates in the x-direction.

The initial values of mixture parameters and constants are assumed to be similar to those in [10, 11]: $p_0 = 1$ bar, $T_{10} = T_{20} = 300$ K, $T_{ign} = 900$ K, $\xi_{0cl} = 0.55$, $E_a = 10^6$ J/kg, and $Q = 2.94 \cdot 10^6$ J/kg. The particle diameter is 5 μm and the cloud width varies from 2 to 8 cm in the 10-centimeter wide channel. The amplitude of the incident shock wave is determined by its Mach number, M_0, defined with respect to the sonic velocity in the initial gas. In the numerical calculations, M_0 varies from 3 to 5.

The problem (1)–(5) is solved numerically on a rectangular 2D uniform grid using a TVD-scheme for the gaseous phase and the MacCormack scheme for the particle phase. The method was previously tested and applied for calculations of 1D and 2D detonations in gas suspensions of aluminum particles [9–11].

3 NUMERICAL RESULTS

3.1 Detonation Initiation by a Supported Incident Shock Wave

A supported SW entering the aluminum particle cloud initiates detonation if its amplitude is sufficiently large. In the 1D case, the shock Mach number, M_0, must be no less than 3.5 for particles of 5 μm in size [10]. In 2D calculations, if the propagation velocity of the incident SW is greater than the normal detonation velocity in the particle suspension (at $M_0 = 5$), then the cloud width does not affect the scenario of detonation initiation. Strong (overdriven) detonation regimes develop in the cloud of finite width [11] similar to 1D results [10]. Nevertheless, the main specific feature of detonation in the finite-width cloud is its nonstationary dynamics with a certain periodicity caused by transverse waves propagation and reflections from the upper and bottom channel walls [11]. The transverse pressure wave initially arises when the SW interacts with the front of the cloud and the combustion zone appears. Fluctuations induced by the transverse waves affect the shape of the detonation front, its propagation velocity, position of a point with maximum pressure in the detonation front, and other flow characteristics.

Here, the case is considerd when the incident shock wave velocity is less than the normal detonation velocity but the conditions required for particle ignition and detonation formation are ensured. This occurs, for example, at $M_0 = 4$ (i.e., the shock velocity is 1.38 km/s, the CJ detonation velocity is 1.56 km/s at $\xi_{0cl} = 0.55$), when an overdriven detonation wave with the velocity of 1.6 km/s forms in 1D formulation [10]. The numerical calculations for the 2D problem show that the transverse mixture motion behind the leading shock wave is quite intense and affects the development of the combustion zone. Figure 1*a* shows the dynamics of the incident SW of $M_0 = 4$ in terms of gas density profiles on the bottom wall with the time step of 0.05 ms for two values of the cloud width: $D = 2$ cm (solid curves) and 4 cm (dashed curves). As seen, the

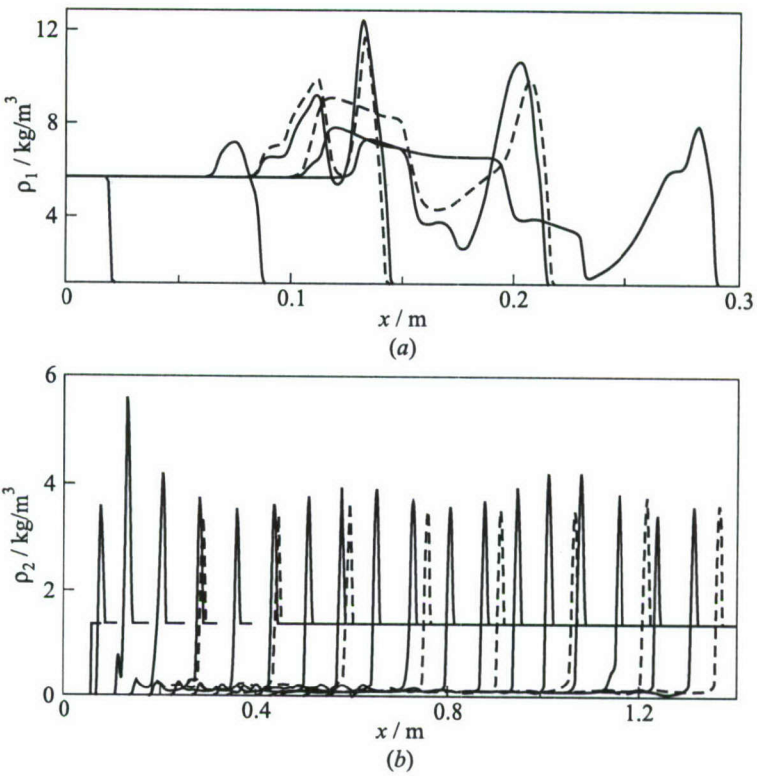

Figure 1 Transverse flow effects in the course of detonation initiation by a shock wave of $M_0 = 4$ at $y = 0$; $D = 2$ cm (solid curves, $t = 0.05$ ms), and $D = 4$ cm (dashed curves, $t = 0.1$ ms)

gas density drops behind the leading shock, which is similar to 1D detonation structure. Nevertheless, the detonation wave forms and propagates in a quasi-stationary regime (al least, at $D \geq 2$ cm) that is confirmed by Fig. 1*b* (particle density profiles). It is seen that the particle density amplitude exhibits a periodic behavior and decreases with the cloud width. The existence of a thin layer of high particle density behind the leading shock wave (known as the ρ-layer [8]) and the residual unburnt particles confirms the detonation character of the flow. The flow structure and the cloud shape behind the front are plotted in Fig. 2*a* for $D = 2$ cm in terms of gas temperature maps and in Fig. 2*b* for $D = 4$ cm in terms of particle density shadow images at three times. Gas temperature distribution reveals the region of detonation products and residual unburnt particles, which is characterized by higher temperatures than the pure gas outside the cloud even behind the shock wave. The transverse wave in this case causes the front

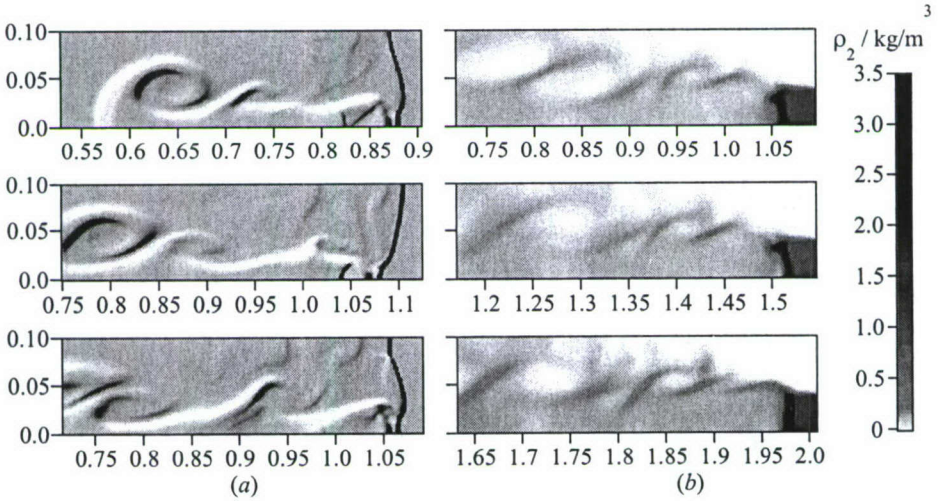

Figure 2 Flow fluctuations and vortex structures at the combined shock/detonation wave propagation induced by the supported incident SW of $M_0 = 4$ at $t = 0.6$ ms (upper frame), 0.75 (middle frame), and 0.9 ms (bottom frame): (*a*) $D = 2$ cm, gas temperature-gradient maps; and (*b*) $D = 4$ cm, particle density shadow images. Plotted along X and Y axes are the longitudinal and transverse coordinates (in m)

shape fluctuations, so that a vortex periodically arises in the area where the shock and detonation waves collide with each other. Along with the longitudinal gas velocity, transverse discontinuity on the cloud boundary affects unsteadiness and nonuniformity of the remaining particle cloud surface that is seen in Fig. 2*b*. The mean propagation velocity is close to the CJ velocity at $D = 4$ cm and is somewhat less at $D = 2$ cm (about 1.5 km/s) but the whole process has no trend to decay at least at a distance up to 3.5 m (2.4 ms). Thus, in the case of supported incident SW, the detonation wave propagates quasi-stationary with the mean velocity less than the CJ velocity.

3.2 Interaction of Decaying Incident Shock Wave with Particle Cloud

Consider the case when the incident SW is attenuated by an adjacent rarefaction wave and has the triangular (or initially trapezoid) pressure profile. The initial conditions are as follows:

$$t = 0\,, \quad \phi_{\mathrm{SW}}(x) = \begin{cases} \phi_{\mathrm{SW}}\,, & X_{\mathrm{RS}} \le x \le X_{\mathrm{SW}} \\ \phi_{\mathrm{RW}}(x)\,, & X_{\mathrm{RW}} \le x \le X_{\mathrm{RS}} \\ \phi_{\mathrm{R}}\,, & 0 \le x \le X_{\mathrm{RW}} \end{cases}$$

Here, $X_{RS} \leq X_{SW}$ is the initial position of the first characteristic in the rarefaction wave, X_{RW} is the point of its contact to the zone of steady flow, $\phi_R = \phi_{RW} X_{RW}$, determined from the condition f_0 ($X = X_{RW}$). The value of incident SW reserved energy is also specified as [10]:

$$W = \int_{X_{RW}}^{X_{SW}} (\rho_1 E_1 - \rho_{10} E_{10})\, dx$$

along with the incident SW amplitude and the cloud width.

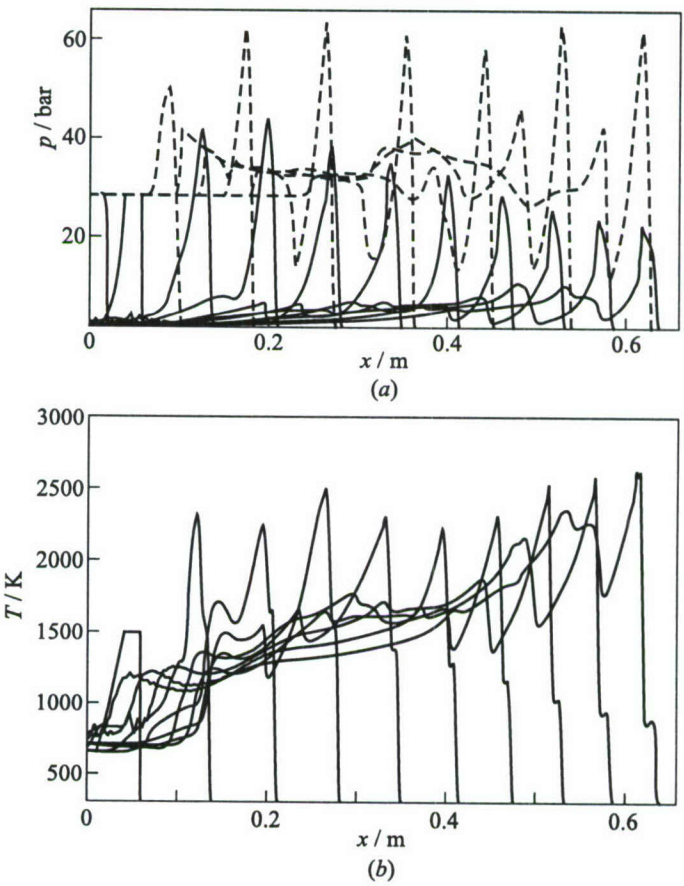

Figure 3 Detonation structure disintegration behind a decaying incident SW (W = 1.27 MJ/m^2, solid curves) and detonation formation behind a supported incident SW (dashed curves), D = 2 cm, M_0 = 5, and δt = 0.05 ms

The shock wave decays in the gas outside the cloud. Thus, when the SW interacts with the cloud of finite width it may either further decay or accelerate if energy deposition in the post-shock flow due to particle combustion in the cloud overcomes this decay. In the latter case, one may expect establishment of a stationary (or quasi-stationary) detonation regime. In 1D formulation [10], the following conditions are required for detonation formation: the amplitude of incident SW should be sufficient to ensure particle ignition, and the energy of the incident SW should be sufficient to compensate the rarefaction wave effect and to provide detonation formation. In the 2D case, additionally, a sufficient cloud width is required to support the combined shock/detonation wave propagation in the channel.

Figure 3 shows the decay of detonation formed at insufficient cloud width (solid curves showing pressure and temperature profiles along the bottom wall, $y = 0$, with the time step 0.05 ms at $D = 2$ cm, $M_0 = 5$, $W = 1.27$ MJ/m^2). Here, the leading SW decelerates and decays in the cloud although in the 1D case (at $D = 10$ cm), the value of the energy accumulated by the incident SW is sufficient for detonation formation [10]. The temperature distributions reveal separation of the leading SW and the combustion front and the increase of the

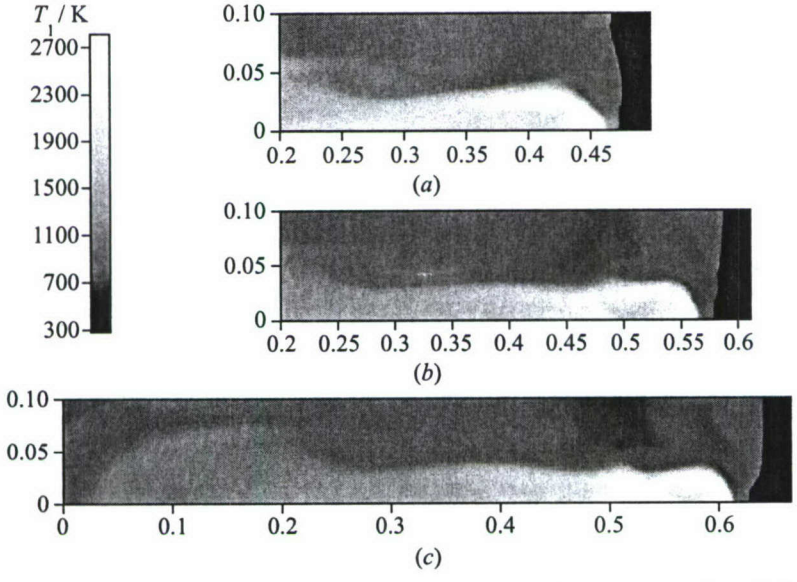

Figure 4 Temperature maps indicating that the combustion zone lags behind a decaying attenuated incident SW, $M_0 = 5$, $W = 1.27$ MJ/m^2, $D = 2$ cm: (*a*) $t = 0.3$ ms; (*b*) 0.4; and (*c*) $t = 0.45$ ms. Plotted along X and Y axes are the longitudinal and transverse coordinates (in m)

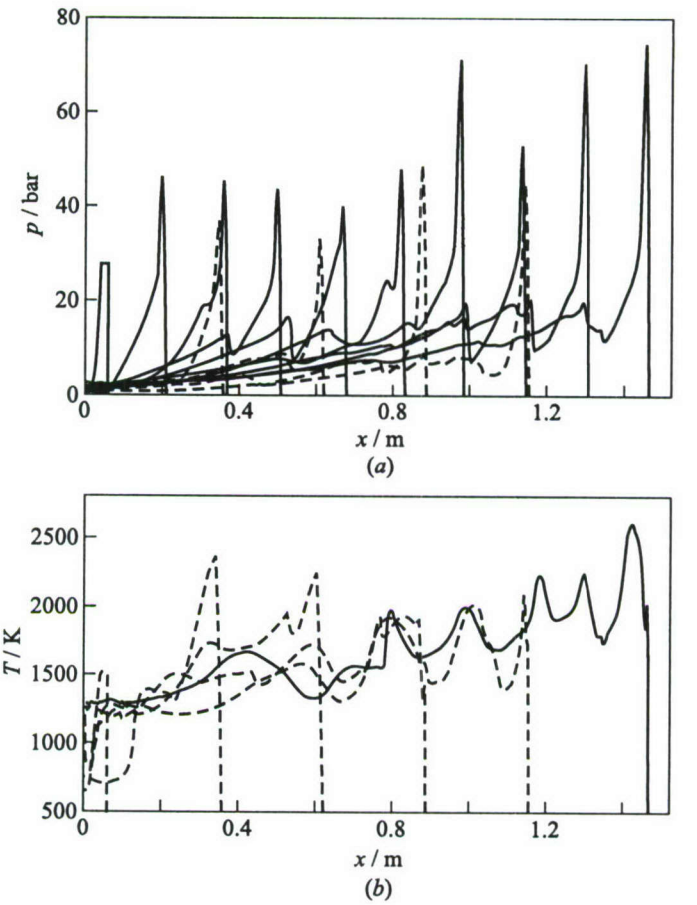

Figure 5 Dynamics of detonation formation ($D = 8$ cm, $\Delta t = 0.1$ ms, solid curves) and decay ($D = 4$ cm, $\Delta t = 0.2$ ms, dashed curves), $M_0 = 5$, $W = 1.27$ MJ/m^2

ignition delay. Figure 4 presents 2D maps of gas temperature at three times confirming that the combustion zone lags behind the leading SW. At 0.45 ms, the SW propagation velocity is about 1 km/s and tends to decrease. Dashed curves in Fig. 3 correspond to the case of the supported incident SW of the rectangular pressure profile which initiates strong detonation wave in the cloud.

The results similar to the case with $D = 2$ cm are obtained at $D = 4$ cm under the same conditions. In the latter case, the combustion front at some instant overtakes and amplifies the leading SW to form a detonation-like structure. However, the SW amplitude is insufficient to provide steady-state detonation propagation in the channel and the rarefaction wave weakens the SW front

leading to temperature decrease (see dashed curves in Fig. 5, time step 0.2 ms). The mean propagation velocity is 1.35 km/s till $t = 0.8$ ms, which is much less than the CJ detonation velocity. Thus, the detonation fails to develop in these cases.

Increase in the cloud width to $D = 8$ cm at the fixed value of W provides detonation formation followed by quasi-steady-state propagation. Solid curves in Fig. 5 show the corresponding pressure profiles at $y = 0$ with the time step of 0.1 ms and temperature profile at $t = 0.9$ ms. Obviously, the flow exhibits unsteady dynamics although the pressure and temperature distributions immediately behind the leading SW resemble the detonation structure. Comparing the last profiles in Figs. 5*a* and 5*b* at $x < 1.25$ m, one can see that the temperature profile is oscillatory while pressure oscillations are absent. In accordance to the equation of state (2), this indicates the nonuniformity in the mixture density. The mean propagation velocity in the interval from 0.6 to 0.9 ms is 1.61 km/s, i.e., slightly exceeding the CJ detonation velocity. One may expect that this slightly overdriven detonation wave will be further attenuated by the rarefaction wave to the CJ detonation regime, as it was observed in the 1D formulation.

Increasing the incident SW energy provides detonation formation in the cloud of smaller width. For example, at $M_0 = 5$ and $W = 1.84$ MJ/m^2, the cloud width of $D = 6$ cm is sufficient for detonation development. In this case, the detonation wave propagation has also an oscillatory dynamics and remains unsteady over a long period of time. Figure 6 shows detonation formation and propagation at $D = 6$ cm in terms of gas temperature maps that reveal a complex flow structure in the cloud of residual particles. As compared with Fig. 4, one can see that in Fig. 6 the combustion zone is attached to the leading SW rather than lagging behind it. In spite of the rarefaction wave affecting the SW from outside the cloud, sustained propagation of the combined shock/detonation wave takes place. This is confirmed in Fig. 7 by the pressure distributions along the bottom wall up to $t = 1$ ms (*a*) and from $t = 1$ to 2 ms (*b*). The mean propagation velocity established by $t = 2$ ms corresponds to the CJ detonation velocity (1.56 km/s). Thus, interaction of a decaying incident SW with a cloud of finite width results in development of a quasi-stationary detonation regime with the mean velocity very close to the CJ detonation velocity. The necessary initiation conditions are provided by the incident SW amplitude, SW accumulated energy, and the cloud width.

3.3 Detonation Formation at Shock Wave Reflection from Channel End-Wall

Consider the case when the incident SW amplitude is insufficient to directly initiate detonation at entering the cloud, but ignition of particles is still possible

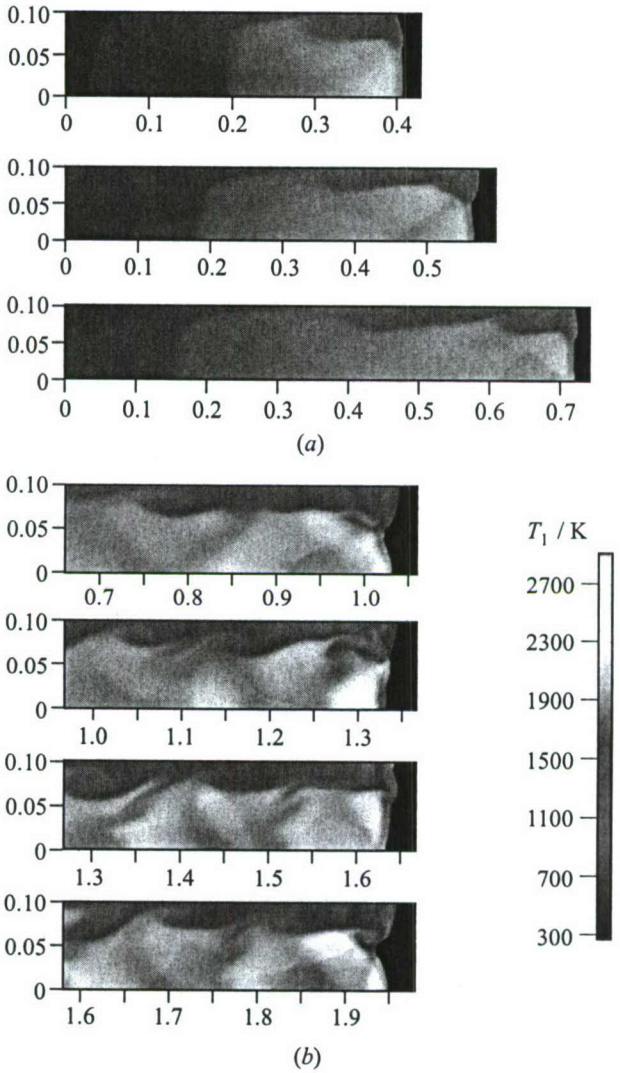

Figure 6 Detonation initiation and propagation (with a decaying incident SW), $M_0 = 5$, $W = 1.84$ MJ/m^2, $D = 6$ cm, gas temperature maps: (a) initial stage, $\Delta t = 0.1$ ms; and (b) developed flow, $\Delta t = 0.2$ ms. Plotted along X and Y axes are the longitudinal and transverse coordinates (in m)

behind the SW reflected from the channel end-wall. At the value of $M_0 = 3$, such conditions arise for the mixture under study. The mixture in front of the reflected SW is already heated and compressed by the primary SW, i.e., its thermodynamic state is different from the initial state of the mixture. In the 1D

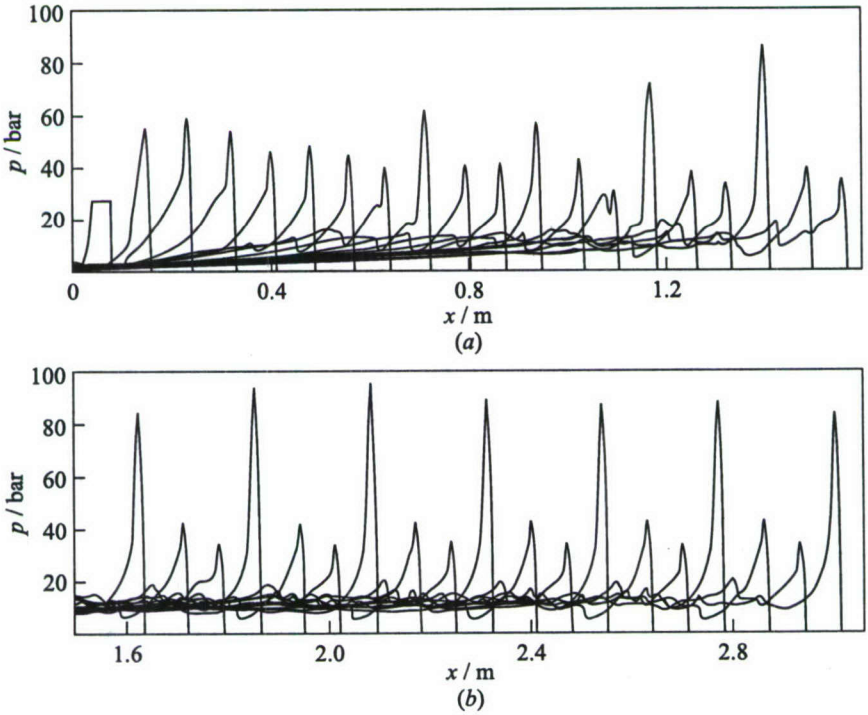

Figure 7 Dynamics of detonation formation and quasi-stationary propagation induced by a decaying incident SW; $M_0 = 5$; $W = 1.27$ MJ/m^2, $D = 6$ cm, $y = 0$, and $\Delta t = 0.05$ ms

formulation of this problem, overdriven (strong) stationary detonation regimes were obtained in [9] using a simplified representation of relaxation processes. Here, the channel of finite length is considered that should be taken into account in the problem formulation (see Section 2). In the cloud of finite width and length, the detonation-like flow arising at SW reflection exists for a finite period of time and cannot attain a stationary or quasi-stationary propagation mode. The flow structure immediately after SW reflection in the cloud 2 cm wide and 1.5 m of initial length is presented in Fig. 8 with the time step of 0.2 ms (a part of the channel 0.6 m long attached to the end-wall is shown). Particle dispersion behind the primary SW results in the vortex-like cloud shape with increasing cloud width in front of the reflected shock. The temperature-gradient maps reveal a complex flow structure behind the reflected shock. Particle dispersion behind the arising detonation wave is much more intense and is also of a vortex type. The detonation-induced gas flow over the cloud is also affected by transverse waves. The inclined transverse waves are clearly observed in the

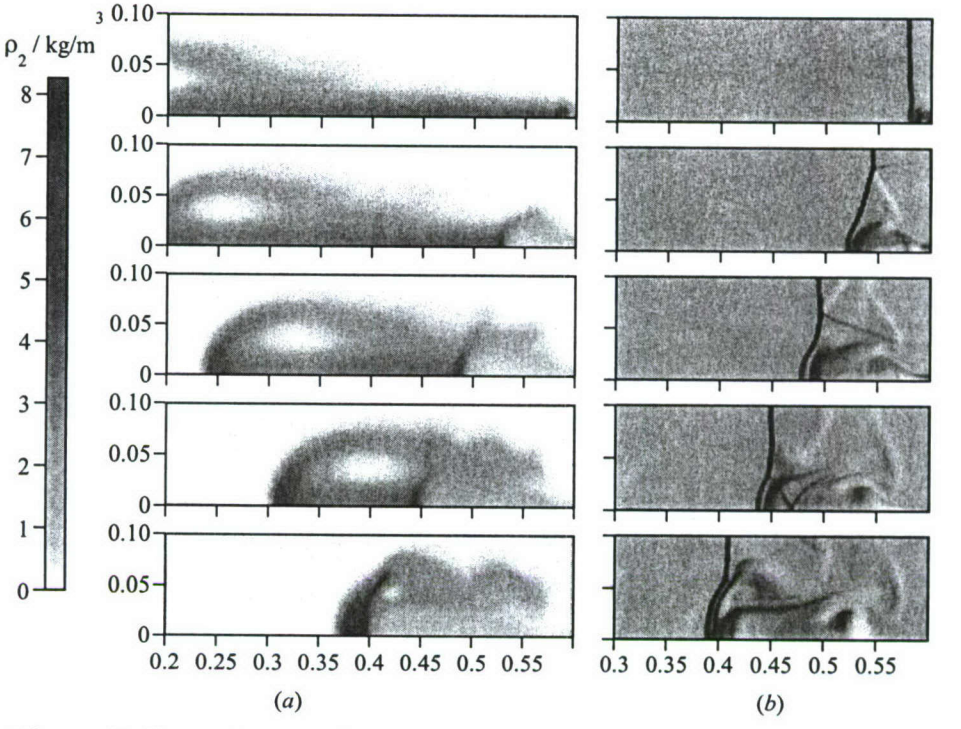

Figure 8 Detonation wave formation in a narrow cloud after shock reflection from the channel end-wall, $M_0 = 3$, $D = 2$ cm, $\Delta t = 0.2$ ms: (a) particle density shadow images; and (b) gas temperature-gradient maps. Plotted along X and Y axes are the longitudinal and transverse coordinates (in m)

upper gas temperature-gradient maps of Fig. 8. Due to the transverse motion and essential dust spreading, the detonation wave formed is not as strong as in the 1D formulation. Maximum predicted values of gas temperature and pressure attain 2050 K and 102 bar, respectively. Thus, the decrease of the cloud width results in weakening of the detonation formed at SW reflection, as compared to clouds of infinite width.

4 CONCLUDING REMARKS

Based on the mathematical model of detonation of aluminum particle suspension in oxygen, several problems of detonation initiation in clouds of finite width are investigated. The following dynamic features are revealed:

- Strong incident shock waves ($M_0 \geq 5$) initiate strong (overdriven) detonation waves in the cloud, irrespectively of the cloud width;

- Detonation initiation by a supported SW of small amplitude (with the propagation velocity less than the CJ detonation velocity in the mixture) depends on the cloud width. Formed at $M_0 = 4$ in a sufficiently wide cloud, the detonation-induced flow is characterized by periodic vortex generation on the cloud surface and flow nonuniformity behind the front. Quasi-stationary propagation with the mean velocity less than the CJ detonation velocity is observed;

- With a decaying incident SW of $M_0 = 5$, detonation formation in the cloud depends on the SW accumulated energy and cloud width. Insufficient cloud width results in formation of a detonation-like structure followed by structure disintegration into a decaying leading SW and lagging combustion front;

- Detonation initiated by a decaying incident SW in a cloud of sufficient width is characterized with nonstationary periodic dynamics and nonuniform gas and particle parameter distributions. The mean propagation velocity of detonation corresponds to the CJ detonation velocity;

- If the amplitude of the incident SW is insufficient for direct detonation initiation in the cloud (e.g., at $M_0 = 3$), detonation formation is possible behind the SW reflected from the channel end-wall. The process is essentially unsteady. The decrease in the cloud width leads to weakening of the detonation.

ACKNOWLEDGMENTS

This work was supported by the Russian Foundation for Basic Research (Grant No. 00-01-00891).

REFERENCES

1. Strauss, W A. 1968. Investigation of the detonation of aluminum powder – oxygen mixtures. *AIAA J.* 6:1753–61.
2. Tulis, A. J., and J. R. Selman. 1982. Detonation tube studies of aluminum particles dispersed in air. *19th Symposium (International) on Combustion Proceedings.* Pittsburgh, PA: The Combustion Institute. 655.

3. Borisov, A. A., B. A. Khasainov, and B. Veyssiere. 1991. Detonation of aluminum suspensions in air and oxygen. *Chemical Physics Reports* 10(2):250–72.
4. Ingignoli, W., B. Veyssiere, and B. A. Khasainov. 1999. Study of detonation initiation in unconfined aluminum dust clouds. In: *Gaseous and heterogeneous detonations: Science to applications*. Eds. G. Roy, S. Frolov, K. Kailasanath, and N. Smirnov. Moscow, Russia: Enas Publ. 337–49.
5. Fedorov, A. V. 1992. Structure of the heterogeneous detonation of aluminum particles dispersed in oxygen. *Combustion Explosion Shock Waves* 28:277–86.
6. Afanasjeva, E. A., and V. A. Levin. 1987. Ignition and combustion of aluminum particles behind shock and detonation waves. *Combustion Explosion Shock Waves* 23(1):8–14.
7. Fedorov, A. V., and T. A. Khmel'. 1996. Types and stability of detonation flows of aluminum suspension in oxygen. *Combustion Explosion Shock Waves* 32:181–90.
8. Fedorov, A. V., T. A. Khmel', and V. M. Fomin. 1999. Nonequilibrium model of steady detonations in aluminum particles — oxygen suspensions. *Shock Waves* 9:313–18.
9. Fedorov, A. V., and T. A. Khmel'. 1999. Numerical simulation of shock wave initiation of heterogeneous detonation of aerosuspension of aluminum particles. *Combustion Explosion Shock Waves* 35:288–95.
10. Fedorov, A. V., and T. A. Khmel'. 2002. Numerical simulation of detonation initiation with a shock wave entering a cloud of aluminum particles. *Combustion Explosion Shock Waves* 38:101–8.
11. Fedorov, A. V., and T. A. Khmel'. 2002. Interaction of a shock wave with a cloud of aluminum particles in a channel. *Combustion Explosion Shock Waves* 38:206–14.
12. Boiko, V. M, V. P, Kiselev, S. P. Kiselev, A. N. Papyrin, S. V. Poplavsky, and V. M. Fomin. 1997. Shock wave interaction with a cloud of particles. *Shock Waves* 7:275–86.

INITIATION OF CONFINED SPRAY DETONATION BY ELECTRIC DISCHARGES

S. M. Frolov, V. Ya. Basevich, V. S. Aksenov, and S. A. Polikhov

Experimental results on the effect of various means on the critical initiation energy of spray (*n*-hexane and *n*-heptane) detonation are presented. Spray detonation is initiated by a single electric discharge or by two discharges triggered successively in a tube with the flow of air and fine fuel drops produced by an air-assist atomizer. The effects of discharge time, shape, and location, insulating properties of the tube, tube shape and diameter, atomizer performance, distance between igniters and time delay between their triggering on detonation initiation are studied. It is shown that the combination of the means promoting direct detonation initiation allows one to considerably decrease the critical initiation energy, while keeping the predetonation distance and time very short as compared to the values characteristic for deflagration-to-detonation transition (DDT).

1 INTRODUCTION

One of the most challenging problems encountered in the development of air-breathing liquid-fueled pulse detonation engines (PDEs) is detonation initiation in hydrocarbon fuel sprays within distances and time periods that are feasible for propulsion applications. To develop a PDE, there is a need for experimental data on detonation initiation and propagation in heterogeneous fuel–air mixtures under well-defined conditions. The latter applies to the initiation source and methods, initiator location, energy deposition history, geometry and physical properties of the confinement, homogeneity and properties of the fuel–air mixture, etc.

As the energy requirements for direct detonation initiation in fuel–air mixtures are very stringent, various initiation promoting means have to be combined, including reactive mixture preconditioning [1, 2], formation of a stratified mixture composition in the vicinity of initiators [3, 4], and cumulation of blast waves [5, 6]. The use of distributed external energy sources to artificially accelerate an initially weak shock wave to detonation by stimulating strong coupling

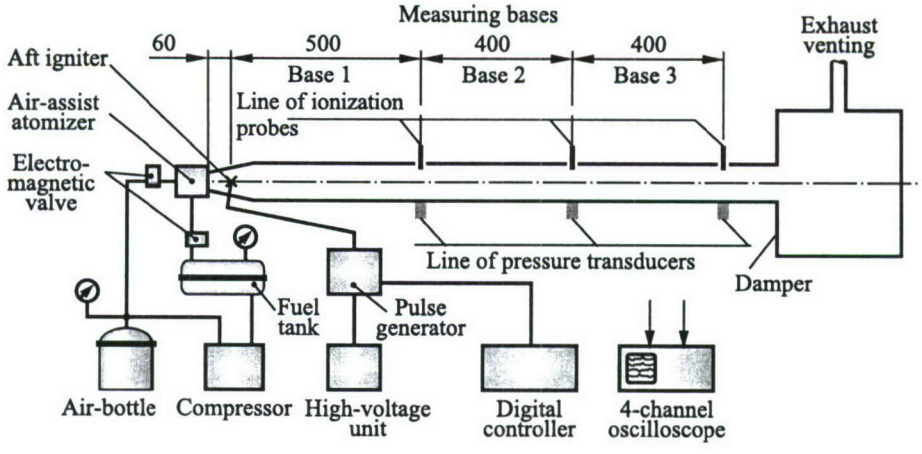

Figure 1 Sketch of the experimental setup. Dimensions in mm

between the shock and chemical energy deposition is also one of the promising techniques to decrease the initiation energy and shorten the predetonation distance [7–9].

This paper addresses some of these issues and exploits various possibilities to minimize the energy requirements for direct initiation of spray detonation.

2 BASIC EXPERIMENTAL SETUP AND RESULTS OF EXPERIMENTS

2.1 Detonation Tube

The basic test facility is a steel tube 51 mm (2 in.) in inner diameter and 1.5 m long (Fig. 1). To create a two-phase flow in the facility, a specially designed air-assist atomizer is mounted at the left end of the tube. The atomizer is attached to the detonation tube via the expanding cone nozzle. The right end of the tube is connected to atmosphere via the detonation arrester — a big steel barrel with packing made of metal ribbon.

The air supply system comprises a compressor, air-bottle and air solenoid valve. The liquid fuel supply system consists of pressurized fuel tank and a fuel solenoid valve. The air-bottle and fuel tank are pressurized to preset pressure values before each run. When the solenoid valves are activated, air and fuel are directed to the atomizer that provides the entire mixture flow rate through the detonation tube. Pulse flow duration is chosen such that the air pressure in the

air-bottle decreases by 10% of its initial value. In most of reported experiments, pulse duration was about 1 s.

Ignition of the two-phase flow is facilitated by a powerful electrical igniter fed with a high-voltage unit via pulse generator. The igniter consists of the primary and the secondary discharges (3-electrode scheme, see Fig. 2).

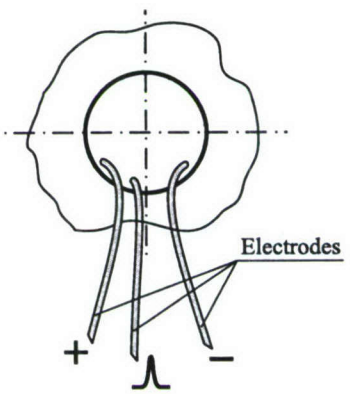

Figure 2 Cross-sectional view of igniter

The primary discharge is of fixed (usually 57 J) energy. (The energy is calculated based on the rated capacitance, C, and voltage, U, i.e., $E = CU^2/2$.) It produces plasma to trigger the secondary discharge of considerably higher energy. The igniter is located inside the cone nozzle at a distance of 60 mm downstream from the atomizer. In the basic configuration, the capacitance of the secondary discharge is 600 μF. The characteristic time of discharge is 100 ± 10 μs as can be seen from Fig. 3*a*. Figure 3*a* shows the discharge current measured by the Rogovsky coil mounted on the high-voltage cable (cable length is 40 cm). The signal of Fig. 3*a* was obtained at a voltage of 2500 V and rated capacitance of 300 μF. The current trace is close to a sine wave.

The detonation tube is equipped with lateral ports for auxiliary electrical igniters, pressure transducers, and ionization gauges. Three measuring stations were activated (see Fig. 1). The first station is located 500 mm downstream from the igniter. The second and third stations are located 900 and 1300 mm downstream from the igniter, respectively. At the measuring stations, both a

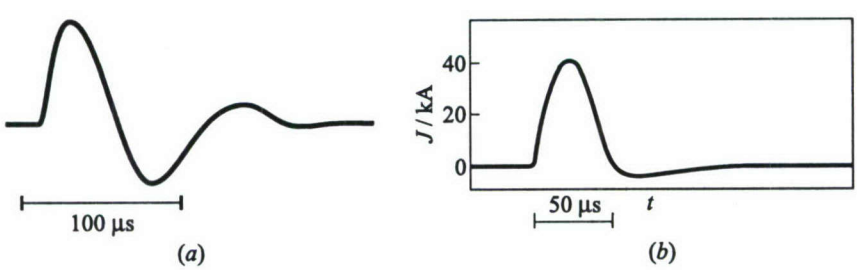

Figure 3 Discharge current measured by the Rogovsky coil mounted on the high-voltage cable: (*a*) discharge of basic configuration with the shape close to sine wave with the oscillation period of 100 ± 10 μs; and (*b*) optimized discharge shape with duration of about 50 μs

pressure transducer and an ionization gauge are mounted at the opposite tube walls. Piezoelectric pressure transducers were flush mounted with the inner tube wall and were used to measure shock wave arrival time and pressure profiles at the station. Ionization gauges were inserted into the detonation tube to a certain depth (usually 20 mm) and were used to measure flame arrival time at the station. Measuring Base 1 comprises the igniter and the first measuring station, so that the characteristic distance is 500 mm. Measuring Base 2 consists of the first and second measuring stations and is 400 mm long. Measuring Base 3 consists of the second and third measuring stations and is also 400 mm long. A digital controller (based on a PC) controls opening and closing of the air and fuel solenoid valves and triggering of the igniter.

2.2 Atomizers

Several air-assist atomizers were designed, fabricated, and tested. Figure 4*a* shows the sketch of the atomizer used in the basic configuration (referred to as atomizer A2-1). Air is supplied via two radial channels. Liquid fuel (*n*-hexane or *n*-heptane) is supplied via one 0.28-millimeter-diameter axial channel into the air channel. The mean diameter of drops produced by the atomizer is close to 5 μm [8]. The air-bottle and fuel tank were pressurized to preset pressure values (usually 6.00 ± 0.05 and 4.80 ± 0.05 atm, respectively) before each run. These values were found in a series of experiments aimed at establishing the optimal fuel-supply pressure at a given air pressure. This optimal pressure provided the maximum flame propagation velocity when other conditions were fixed. The atomizer of the basic configuration provided flow rate of air of about 20 liters per second. Measurements of air-flow velocity generated by atomizer A2-1 in the

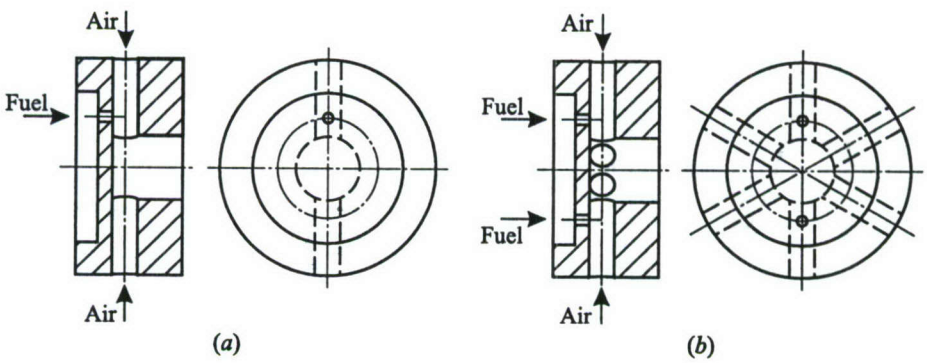

Figure 4 Sketch of air-assist atomizers used in experiments: (*a*) atomizer A2-1, and (*b*) atomizer A6-2

detonation tube by the Pitot technique have shown that, starting from distance of 260 mm downstream from the atomizer, the mean flow velocity is nearly constant across the tube and equal to (10 ± 1) m/s.

2.3 Spray Detonation Initiation by Single Igniter

The aim of the tests was to determine the critical energy of direct detonation initiation by a single discharge. At ignition energy below 3.130 kJ, no detonation was observed in the basic setup. Increase in the ignition energy from 3.130 to 3.324 kJ (that corresponds to the voltage of 3300 V at the secondary discharge) resulted in detonation initiation in the detonation tube with n-hexane–air mixture. Further increase of the ignition energy from 3.324 to 3.732 kJ produced no effect on the detonation parameters. The detonation wave propagated at constant mean velocity of (1780 ± 100) m/s at measuring bases 2 and 3.

Figure 5 summarizes the results of experiments for n-hexane with different voltage at the secondary discharge electrodes. Dashed and solid curves correspond to measured flame and shock wave velocities, respectively, at corresponding measuring bases (denoted by numbers *1*, *2*, and *3*). Due to poor accuracy of pressure measurements at low ignition energies, measurements of shock wave velocity were performed beginning from a voltage of 2000 V. It follows from Fig. 5 that increase in the secondary discharge voltage from 0 to 2000 V shows almost no effect on the flame propagation velocity at measuring bases 2 and 3. Contrary to flame behavior at these measuring bases, flame velocity at base 1 gradually increases with the voltage. Finally, at the voltage exceeding 3300 V, a detonation wave arises at all measuring bases from 1 to 3. In other words, at the ignition energy exceeding about 3.2 kJ, direct initiation of detonation in

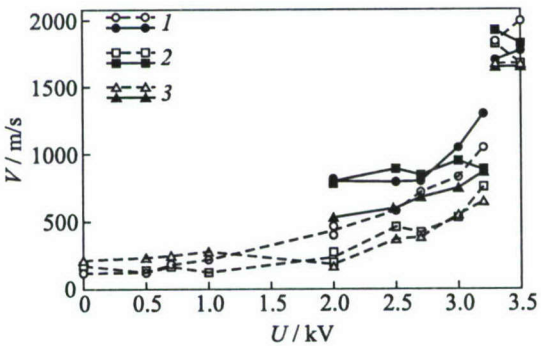

Figure 5 Measured shock wave (solid curves) and flame front (dashed curves) velocities vs. igniter voltage for n-hexane–air mixture

n-hexane spray has been obtained. This value will be referred to as the critical energy for direct detonation initiation in the basic setup.

Note that positioning of the igniter at the distance 100 mm downstream from its position in the basic setup results in increasing the critical voltage from 3200 to 4100 V, i.e., increasing the critical initiation energy by more than 60%.

A similar set of experiments has been performed for *n*-heptane. In the run with the secondary igniter voltage of 3300 V (corresponding to critical conditions of detonation initiation in *n*-hexane spray), *n*-heptane spray did not detonate. Increase of the ignition energy from 3.324 to 3.732 kJ resulted in direct detonation initiation in *n*-heptane spray. Thus, under conditions of the basic setup, the critical energy for direct detonation initiation in *n*-heptane spray is about 3.7 kJ.

3 OPTIMIZATION STUDIES WITH SINGLE IGNITER

The aim of optimization studies is to decrease the energy of electric discharge required for direct detonation initiation, by improving certain elements of the basic experimental setup. For the sake of conformity, all initial optimization tests were carried out with a single 3-electrode igniter of Fig. 2 with the rated capacitance of its high-voltage block fixed at 600 μF, i.e., the optimization tests were aimed at decreasing the minimal voltage required for direct detonation initiation. Structural parameters varied are (*i*) the dielectric properties of the transition cone surface in the vicinity of the discharge electrodes, (*ii*) the type of air-assist atomizer, (*iii*) detonation tube diameter, and (*iv*) the shape of transition section between the atomizer and the detonation tube. Functional parameters varied are (*i*) the shape and duration of electric discharge, (*ii*) the fuel pressure in the fuel-supply system, and (*iii*) the discharge voltage.

3.1 Optimization of Discharge Parameters

To improve the efficiency of electric discharge in terms of transition of the electric energy to the test mixture, the following two principal measures were taken: (*i*) the interior surface of the transition cone connecting the atomizer and detonation tube was covered with a 1-millimeter thick layer of dielectric thermoresistant lacquer. This measure avoided the discharge between the igniter electrodes and the grounded metal transition cone; and (*ii*) the electric connection between electrodes and high-voltage capacitors was made by using a coaxial cable rather than separate bars. These measures led to modification of the discharge current shape and decrease in effective discharge duration from about 100 to about 50 μs (see Fig. 2*b*). With the discharge of improved efficiency, the critical voltage required for direct detonation initiation in *n*-hexane spray decreased

from 3200 to 2200 V, resulting in more than two-fold decrease in the critical detonation initiation energy (from 3.2 to 1.5 kJ). Further decrease of discharge duration from 50 to 40 μs did not show any significant effect on the initiation energy.

3.2 Optimization of Atomizer

Shown in Fig. 4*b* is another atomizer (referred to as A6-2) used in the experiments. It has six air supply radial channels and two fuel supply axial channels. Flow rate of air provided by the atomizer is about 30 liters per second at air overpressure of 6 atm. This atomizer produces higher level of turbulence in the flow as compared to atomizer A2-1, while providing an approximately similar drop size distribution. Experiments with atomizer A6-2 at optimized fuel supply pressure have shown that this atomizer provides somewhat higher combustion wave velocities in *n*-hexane spray at relatively low discharge voltage as compared to atomizer A2-1.

In contrast to tests with atomizer A2-1, the tests with atomizer A6-2 exhibited formation of shock waves with steeper leading front at measuring station 1300 mm. Nevertheless, with atomizer A6-2, detonation was initiated at voltages of 2100–2200 V, i.e., there was no considerable difference in the performance of atomizers A2-1 and A6-2.

3.3 Optimization of Detonation Tube Geometry

All experiments discussed above were performed in the detonation tube of the basic configuration (51 mm in diameter). To study the effect of tube diameter on the critical detonation initiation energy, the experimental setup was modified. A thick-walled plastic tube 36 mm in diameter and 440 mm long was inserted into the main tube. The insert was properly fixed at the atomizer transition cone by means of a supplementary converging cone and sealed at the far end by means of an O-ring. The insert provided approximately 1.4-fold decrease in the tube diameter. The experiments were carried out with atomizer A6-2. Starting from voltages of 1800–1850 V, reproducible detonation-like mode of combustion was registered in the experiments. The detonation velocity obtained on the basis of pressure measurements was at the level of 1600–1700 m/s. Clearly, decrease in tube diameter resulted in decreasing the critical detonation initiation energy: 1.4-fold decrease in the tube diameter resulted in decreasing the critical initiation energy from 1.5 to 1.08 kJ, i.e., approximately 1.4 times.

To study the effect of tube diameter in more detail, a new experimental setup was fabricated with the detonation tube 27 mm in diameter (Fig. 6). In this setup, the atomizer assembly with the transition cone is the same as in the

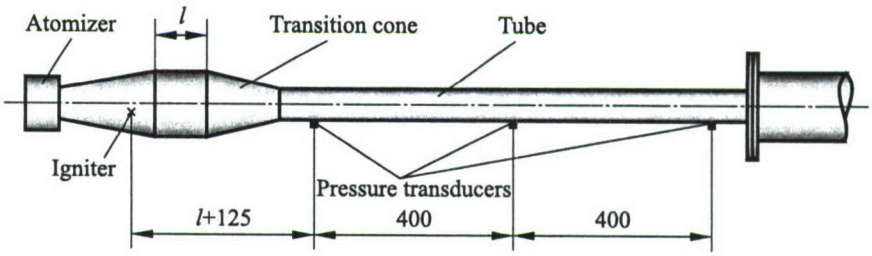

Figure 6 Experimental setup with the detonation tube of diameter 27 mm. Dimensions in mm

basic configuration. Internal diameter of the outer edge of the transition cone is 51 mm. To connect the transition cone with the new detonation tube, two possibilities are foreseen: either immediately through the converging cone 65 mm long, or through the cylindrical section of length l followed by the converging cone (see Fig. 6).

Figure 7 shows the results of experiments in the new setup without the cylindrical transition section (i.e., at $l = 0$). As the shock wave exhibits a smeared front at the first measuring station, the shock wave velocity is measured at the tube section from the igniter to the second measuring station (measuring base 1 in Fig. 6 is 525 mm long), and from the second to third measuring station (measuring base 2 in Fig. 6 is 400 mm long).

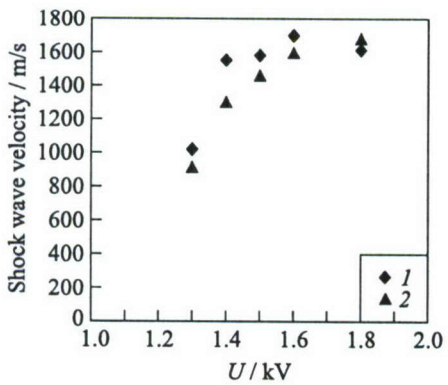

Figure 7 Measured shock wave velocities vs. discharge voltage (n-hexane spray) at two measuring bases 1 (*1*) and 2 (*2*). Detonation tube 27 mm in diameter (no cylindrical insert). Atomizer A6-2. Igniter of improved efficiency

Contrary to Fig. 5, the dependency of the shock wave velocity on the igniter voltage in Fig. 7 is very smooth, i.e., there is no evident abrupt change in the mode of combustion front propagation after the characteristic value of 800–1000 m/s. Starting from voltages of 1500–1600 V, the shock wave velocity is about 1500–1700 m/s, which is at the level of detonation velocity. Such a regular variation of the shock wave velocity at measuring bases 1 and 2 with discharge voltage may be explained by the proximity of the tube diameter (27 mm) to the limiting tube diameter for n-hexane–air mixture.

Voltages of 1500–1600 V, relevant to detonation initiation in the small tube, correspond to initiation energies of 0.73–0.82 kJ, respectively. Thus, almost a two-fold decrease in the tube diameter (as compared to the basic configuration) resulted in about a two-fold decrease of the critical energy of detonation initiation by a single discharge down to the value of 700–800 J. Note that the energy requirements for detonation initiation before the optimization studies was about 3.2 kJ for *n*-hexane spray.

The cylindrical transition section (see Fig. 6) does not improve the overall picture of the phenomenon under study. For example, at $l = 90$ mm, the critical voltage required for detonation initiation is 1900 V, which corresponds to the initiation energy of 1.14 kJ. This energy is 40% higher than 0.8 kJ obtained for the tube without the cylindrical transition section.

The other series of optimization tests was made with the configuration of Fig. 6 with the converging cone section replaced by abrupt transition from the cylindrical section 51 mm in diameter to the detonation tube 27 mm in diameter. With this modification, the critical igniter voltage increased to 2100 V (1.4 kJ in terms of energy).

One more series of tests was made with replacing the secondary discharge capacitance of basic configuration (600 μF) by the capacitance of 400 μF. In this case, the minimal voltage of about 1900 V was required to initiate detonation of the *n*-hexane spray, other conditions being similar to the experiments relevant to Fig. 6. This voltage corresponds to the critical initiation energy of about 0.8 kJ, which was obtained previously.

4 OPTIMIZATION STUDIES WITH TWO IGNITERS

As is well known, critical conditions for detonation initiation are based on the necessity of strong coupling between a shock wave and energy deposition. In the approach of Sections 2 and 3, a shock wave of high amplitude and proper duration was required to ensure the coupling due to the high activation energy of exothermic chemical reactions in the fuel–air mixture. Such a shock wave was produced by a single powerful electric discharge.

Fundamentally, it does not matter how the energy is deposited into the post-shock flow: spontaneously, due to shock-induced chemical reactions, or by means of inducing chemical reactions with an external energy source. The latter approach implies the use of an external energy source to artificially induce exothermic reactions closely behind a relatively weak shock wave in order to stimulate the strong coupling. Clearly, in this case, the external energy source should be distributed rather than concentrated and should provide pulse or continuous coupling of energy deposition with a propagating shock wave.

Originally, the idea of using external sources to drive a detonation was proposed by Zel'dovich & Kompaneetz [10]. They have shown theoretically that motion of an ignition source in a compressible reactive mixture at the characteristic detonation velocity would result in formation of a self-sustaining detonation in a long run. To model the moving ignition source, Zel'dovich and co-workers [11, 12] considered the nonuniformly preconditioned reactive mixture, implying that the initial gradient of autoignition delay time will produce a similar effect. As a matter of fact, it has been proved computationally that temperature and composition nonuniformities in the reactive mixture preconditioned to autoignition may result in spontaneous onset of detonation. Thibault *et al.* [13] reported their one-dimensional numerical study of the situation when the external energy source traveled at a constant velocity in an inert compressible medium. It has been proved that the strength of the shock wave arising in the medium depends on the energy source velocity and attains a maximum value when this velocity approaches the characteristic detonation velocity based on the specific energy (per unit mass of gas) deposited by the source, which substantiated the original idea of Zel'dovich & Kompaneetz computationally. Later, Yoshikawa *et al.* [14] extended the analysis to take into account coupling between the moving energy source and the shock wave. Lee & Moen [15] have suggested the SWACER mechanism (abbreviation for Shock Wave Amplification by Coherent Energy Release) and applied it to qualitatively explain the experimental findings in photochemical initiation of detonation [16], detonation initiation by injecting hot turbulent jets into explosive mixture [17], and 'explosion in the explosion' phenomenon during deflagration-to-detonation transition [18]. Recently, Frolov *et al.* [7–9] provided experimental substantiation of the ideas and mechanisms discussed herein. In their experiments, a weak shock wave was accelerated in the reactive mixture by means of in-phase triggering of seven spark igniters in the course of shock wave propagation along the tube. Detonation-like regimes have been obtained at a distance of 0.6–0.7 m in stoichiometric gaseous C_3H_8–$(O_2 + 3N_2)$ and C_3H_8–air mixtures under normal conditions in a tube 51 mm in diameter (the same tube as that shown in Fig. 1). The other finding of [7–9] is that the critical energy of detonation initiation with several igniters is less than that obtained with a single igniter.

The aim of the current tests with two igniters was to initiate spray detonation by controlled successive triggering of two electric discharges rather than using a single discharge as in Sections 2 and 3, and to check whether the previous findings of the authors are valid for liquid-fuel sprays in the given experimental setup.

Figure 8 shows the sketch of the experimental setup used in this optimization study. Tube *1* and atomizer *2* in this setup are actually the same as those shown in Figs. 1 and 4*a*.

In this configuration, in addition to the aft igniter *3* used earlier, a lateral igniter *4* is mounted at a distance X. The igniters used in the tests were two identical 3-electrode igniters (as in Fig. 2) with identical high-voltage blocks

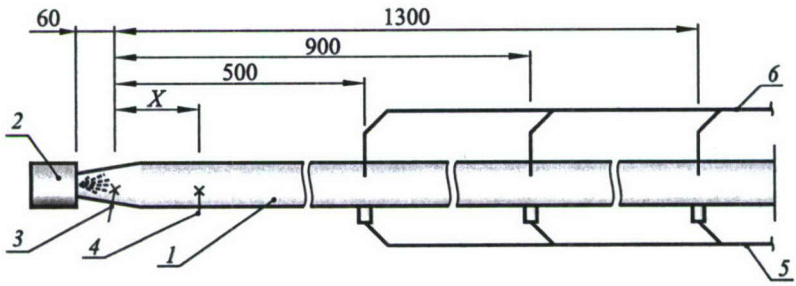

Figure 8 Schematic of the detonation tube: *1* — detonation tube of Fig. 1, *2* — air-assist atomizer, *3* — aft igniter, *4* — lateral igniter, *5* — line of pressure transducers, *6* — line of ionization probes, X is the distance between successively triggered igniters *3* and *4*

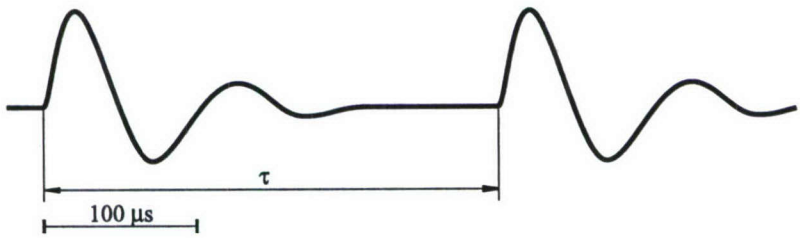

Figure 9 Discharge current in a two-discharge circuit measured by the Rogovsky coil mounted on the high-voltage cable. The signal was obtained at a voltage of 2500 V and rated capacitance of 300 μF for each discharge. The second (lateral) igniter is triggered 300 μs after the first (aft) igniter

(each of 300 μF rated capacitance). During the tests, both igniters were subject to the same voltage U. The discharge triggering time of the igniters is controlled with a controller. The controller provides time-delayed impulses to successively trigger, via the commuting field, the individual high-voltage blocks of the igniters with a preset time delay. The time delay can be varied over a wide range (from 50 to 500 μs) with an interval of 10 μs. Figure 9 shows a typical discharge current in a two-discharge circuit measured by the Rogovsky coil mounted on the high-voltage cable. The signal of Fig. 9 was obtained at a voltage of 2500 V and rated capacitance of 300 μF for each discharge. The second (lateral) igniter is triggered 300 μs after the first (aft) igniter (time interval τ in Fig. 9).

As in the tests with a single igniter, three measuring stations are activated. The first station is located 500 mm downstream from the aft igniter. The second and third stations are located 900 and 1300 mm downstream from the aft igniter, respectively. At the measuring stations, both pressure transducers *5* (see Fig. 8) and ionization gauges *6* are mounted at the opposite tube walls.

There were 4 test series depending on distance X between two successively triggered igniters: (I) $X = 100$ mm; (II) 200; (III) 300; and (IV) 400 mm.

4.1 Series I: 100-Millimeter Distance Between Igniters

The experimental procedure encountered a number of steps dealing with 'tuning' the controller in terms of a preset delay time for triggering the lateral igniter located at distance of 100 mm downstream from the aft igniter. The aim of the 'tuning' was to obtain a detonation wave at the second and third measuring bases at the lowest possible total ignition energy.

The procedure was as follows. After triggering the aft igniter, the blast wave arrival time at location of lateral igniter was measured by using the signal from pressure transducer installed at $X = 100$ mm. As the blast wave at this tube section had a smeared rather than a sharp front, the arrival times of the lead and the rear front portions were detected. Thus, the shock arrival time at location of lateral igniter was represented by two lines at the "voltage vs. triggering delay time" plane, as lines *1* and *2* in Fig. 10. (Plotted along the X-axis in Fig. 10 is the delay time τ for triggering the lateral igniter. Plotted along the Y-axis is the voltage at high-voltage blocks of the igniters). It follows from analyzing the distance between lines *1* and *2* (along the τ-axis) that the width of the blast wave front at $X = 100$ mm is 15–25 μs.

Based on these measurements, a first approximation for the time delay of triggering the lateral igniter was obtained for the next run. This time delay was preset in the controller. The next run encountered time-delayed triggering of the lateral igniter after the aft igniter. The blast wave velocity at second and third bases was then measured at this preset value of the triggering time. In the subsequent runs, the time delay of ignition triggering was varied in a certain vicinity of this value to reveal the best conditions for blast wave amplification to detonation. Then the voltage was decreased and a new test series at lower total ignition energy was performed. At each stage of the procedure, several runs were performed to collect the statistics on the reproducibility of the results. It has been found that the results were satisfactorily reproducible.

Figure 10 summarizes the results of experiments for n-hexane sprays. Plus and minus signs correspond to reliable "go" and "no go" detonation conditions both at second and third measuring bases. The curve separates plus and minus signs and interpolates the conditions required for detonation initiation. Clearly, there exists a pronounced detonation peninsula within the range of delay time $\tau = 50$–150 μs.

It follows from Fig. 10 that there exist resonant conditions for lateral igniter triggering in terms of the delay time τ (the optimum delay time is $\tau \approx 100$ μs). The lowest voltage required for detonation initiation with two successively triggered igniters is 3000 V instead of 3300 V relevant to a single aft igniter (lower

dotted level in Fig. 10) and instead of 4100 V relevant to a single lateral igniter (upper dotted level in Fig. 10) of the doubled (600 μF) rated capacitance. The "width" of the detonation peninsula is about 40 μs at 3300 V and 10 μs at 3000 V. The importance of discharge synchronization is evident from the fact that the increase in the voltage over the optimized value of 3000 V at the fixed time delay of 100 μs results in detonation initiation failure at $3400 < U < 3800$ V. At small delays $\tau < 30$ μs, the total energy required for detonation initiation was somewhat higher than the upper level relevant to the single lateral igniter.

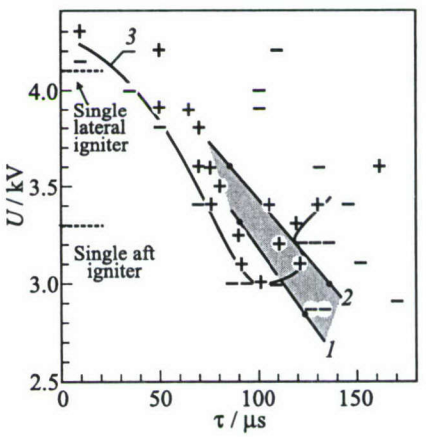

Figure 10 Results of experiments on initiation of n-hexane spray detonation by two successively triggered igniters mounted 100 mm from each other. Plus and minus signs correspond to reliable "go" and "no go" detonation conditions. Curve separates plus and minus signs and interpolates the conditions required for detonation initiation. Shaded area between lines *1* and *2* corresponds to the arrival time of the initial shock at location of lateral igniter

Combined consideration of the curve in Fig. 10 with lines *1* and *2* indicates that the necessary condition for the resonance is proper synchronization of lateral igniter triggering with the arrival of the blast wave generated by the aft igniter. The characteristic interval between blast wave arrival and discharge triggering varies from 10 to 35 μs. Similar to the findings of [7, 9], for obtaining detonation, the lateral igniter should be triggered somewhat prior to the arrival of a blast wave to the igniter location.

4.2 Series II: 200-Millimeter Distance Between Igniters

Figure 11 summarizes the results of experiments for $X = 200$ mm. It follows from Fig. 11 that there also exist resonant conditions for lateral igniter triggering in terms of the delay time τ. The lowest voltage required for detonation initiation with two successively triggered igniters is now 2500 V (with the optimum delay time of 270 μs) instead of 3000 V relevant to the case with $X = 100$ mm. The "width" of the detonation peninsula is now about 50 μs at 3000 V and 10 μs at 2500 V. At a fixed delay time, e.g., 270 μs, detonation arises at 2500 V and does not arise at higher voltage (2600 to 2900 V) that indicates the necessity of careful synchronization of the igniter triggering with the arrival of the blast wave gener-

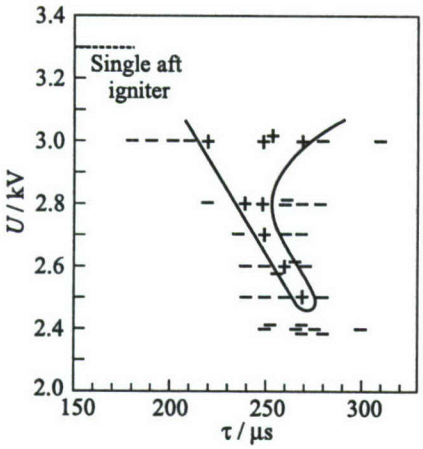

Figure 11 Results of experiments on initiation of n-hexane spray detonation by two successively triggered igniters mounted 200 mm from each other

ated by the aft igniter. The decrease in voltage from 3300 V (dotted line in Fig. 11 corresponding to the critical voltage of the single aft igniter) to 2500 V indicates an almost 75% decrease in the total ignition energy and 3.5-fold decrease in the energy deposited by each of the two igniters as compared to the energy of single aft igniter required for direct detonation initiation. As compared to energy requirements for detonation initiation by a single lateral igniter (4100 V, 600 μF), two successively triggered igniters allow to decrease the total initiation energy by a factor of 2.7, with the energy of each successive igniter 5.4 times lower than that required for a single lateral igniter to initiate detonation.

4.3 Series III: 300-Millimeter Distance Between Igniters

Figure 12 summarizes the results of experiments for $X = 300$ mm. The lowest voltage required for detonation initiation with two successively triggered igniters is now 3000 V, i.e., it is higher than in the case with $X = 200$ mm (2500 V) and close to that found for the case with $X = 100$ mm (3000 V). The optimum delay time is 370 μs. The "width" of the detonation peninsula is about 20 μs at 3000 V.

4.4 Series IV: 400-Millimeter Distance Between Igniters

Figure 13 summarizes the results of experiments for $X = 400$ mm. The lowest voltage required for detonation initiation with two successively triggered igniters is now higher than 3000 V, as there was no detonation detected at second and third measuring bases. Instead of detonation, the blast wave propagating at velocity 900–1400 m/s was detected at measuring base 3. Nevertheless, the highest detected blast wave velocity (1400 m/s) was attained if $\tau = 430$ μs.

As a result of these tests it has been found that:

(1) There exist resonant conditions for successive triggering of two igniters that have to be met in order to initiate detonation;

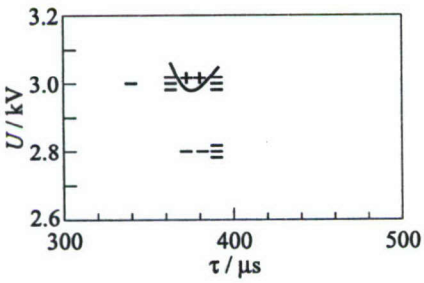

Figure 12 Results of experiments on initiation of *n*-hexane spray detonation by two successively triggered igniters mounted 300 mm from each other

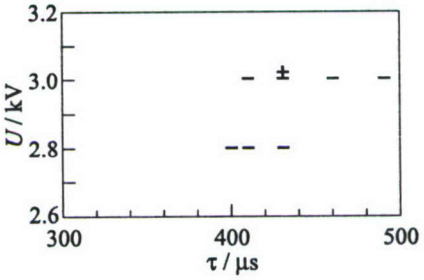

Figure 13 Results of experiments on initiation of *n*-hexane spray detonation by two successively triggered igniters mounted 400 mm from each other

(2) The minimal total detonation initiation energy by successively triggered igniters is lower than that required for direct detonation initiation by a single igniter;

(3) The detonation peninsula at the "initiation energy vs. triggering time delay" plane is very narrow that indicates the necessity of careful synchronization of successive discharge triggering;

(4) The resonant conditions for detonation initiation by successively triggered igniters depend on the distance between the igniters: there exists an optimum spacing between igniters that allows for the largest decrease in the total initiation energy; and

(5) The energy deposited by each igniter at resonant conditions is considerably lower than that typical for a single igniter to initiate detonation.

5 CONCLUDING REMARKS

Based on the studies described above, the following conclusions can be formulated.

For direct initiation of spray detonation with a single igniter and minimum energy requirements, (*i*) it is worth to use the igniter located at the closed end of the detonation tube; (*ii*) the discharge area should be properly insulated to avoid electric loss to the metal tube walls; (*iii*) discharge duration should be minimized to at least 50 μs; (*iv*) the detonation tube should be preferably of diameter close to the limiting tube diameter. In this case, detonation initiation by a single discharge shows relatively low energy requirements (e.g., 700–800 J

for n-hexane–air mixture); and (ν) gradual transition between the volume with electric discharge (combustion chamber) and the detonation tube should be used; this allows to efficiently cumulate the arising shock wave into the detonation tube.

Further decrease in the total detonation initiation energy can be achieved by using several successively triggered igniters rather than a single igniter. The tests with two successively triggered igniters revealed the following main findings: (*i*) there exist resonant conditions for successive triggering of two igniters that have to be met in order to initiate detonation; (*ii*) the minimal total detonation initiation energy is lower than that required for direct detonation initiation by a single igniter; and (*iii*) the detonation peninsula at the "initiation energy vs. triggering time delay" plane is very narrow and indicates the necessity of careful synchronization of successive discharge triggering.

In general, it has been shown that various means can be used to considerably decrease the initiation energy of spray detonation while keeping the predetonation distance at a level less and even much less than 1 m and the predetonation time, both feasible for PDE applications. Contrary to DDT involving partial blockage of tube cross-section with turbulence-generating elements, the techniques studied herein do not produce much additional drag and the detonation tube is essentially smooth-walled. It is expected that with the combination of the reported findings it will be possible to decrease the total initiation energy of n-hexane spray detonation to lower than 300–400 J. Further experimental studies with the setup of Fig. 6 and several successively triggered igniters will show whether this expectation is realistic.

ACKNOWLEDGMENTS

This work was partly supported by the U.S. Office of Naval Research and Russian Foundation for Basic Research.

REFERENCES

1. Brophy, C.M., D.W. Netzer, J. Sinibaldi, and R. Jonson. 2001. Detonation of JP-10 aerosol for pulse detonation applications. In: *High-speed deflagration and detonation: Fundamentals and control.* Eds. G. Roy, S. Frolov, D. Netzer, and A. Borisov. Moscow, Russia: Elex-KM Publ. 207–22.
2. Levin, V.A., J.N. Nechaev, and A.I. Tarasov. 2001. A new approach to organize operation cycles in pulsed detonation engines. In: *High-speed deflagration and detonation: Fundamentals and control.* Eds. G. Roy, S. Frolov, D. Netzer, and A. Borisov. Moscow, Russia: Elex-KM Publ. 223–38.

3. Frolov, S. M., V. Ya. Basevich, and A. A. Vasil'ev. 2001. Detonation of JP-10 aerosol for pulse detonation applications. In: *High-speed deflagration and detonation: Fundamentals and control.* Eds. G. Roy, S. Frolov, D. Netzer, and A. Borisov. Moscow, Russia: Elex-KM Publ. 315–32.

4. Knappe, B. M., and C. F. Edwards. 2002. Investigation of spray detonation characteristics using a controlled, homogeneously seeded two-phase mixture. *15th ONR Propulsion Meeting Proceedings.* Eds. G. D. Roy and A. K. Gupta. College Park, MD: University of Maryland. 172–77.

5. Korobeinikov, V. P., V. V. Markov, I. V. Semenov, P. D. Pedrow, and S. Wojcicki. 2001. Detonation of JP-10 aerosol for pulse detonation applications. In: *High-speed deflagration and detonation: Fundamentals and control.* Eds. G. Roy, S. Frolov, D. Netzer, and A. Borisov. Moscow, Russia: Elex-KM Publ. 289–302.

6. Santoro, R. J., S.-Y. Lee, C. Conrad, J. Brumberg, S. Saretto, P. Lecat, S. Pal, and R. D. Woodward. 2002. Deflagration-to-detonation transition studies for multicycle PDE applications. In: *Advances in confined detonations.* Eds. G. Roy, S. Frolov, R. Santoro, and S. Tsyganov. Moscow, Russia: Torus Press. 243–49.

7. Frolov, S. M., V. Ya. Basevich, and V. S. Aksenov. 2001. Detonation initiation by controlled triggering of multiple electric discharges. *14th ONR Propulsion Meeting Proceedings.* Eds. G. D. Roy and F. Mashayek. Chicago: University of Illinois at Chicago. 202.

8. Frolov, S. M., V. Ya. Basevich, V. S. Aksenov, and S. A. Polikhov. 2002. Initiation of spray detonation by successive triggering of electric discharges. In: *Advances in confined detonations.* Eds. G. Roy, S. Frolov, R. Santoro, and S. Tsyganov. Moscow, Russia: Torus Press. 150–57.

9. Frolov, S. M., V. Ya. Basevich, V. S. Aksenov, and S. A. Polikhov. 2002 (accepted). Detonation initiation by controlled triggering of electric discharges. *J. Propulsion Power.*

10. Zel'dovich, Ya. B., and A. S. Kompaneetz. 1955. *The theory of detonation.* Moscow, Russia: Gostekhteorizdat.

11. Zel'dovich, Ya. B., V. B. Librovich, G. M. Makhviladze, and G. I. Sivashinski. 1970. On the development of detonation in a non-uniformly preheated gas. *Acta Astronautica* 15:313–21.

12. Zel'dovich, Ya. B., B. E. Gelfand, S. A. Tsyganov, S. M. Frolov, and A. N. Polenov. 1988. Concentration and temperature nonuniformities of combustible mixtures as a reason of pressure waves generation. In: *Dynamics of explosions.* Eds. A. Kuhl, J. R. Bowen, J.-C. Leyer, and A. A. Borisov. Progress in astronautics and aeronautics ser. New York: AIAA Inc. 114:99.

13. Thibault, P. A., N. Yoshikava, and J. H. Lee. 1978. Shock wave amplification through coherent energy release. *1978 Fall Technical Meeting of the Eastern Section of the Combustion Institute.* Miami Beach, FL.

14. Yoshikava, N., P. A. Thibault, and J. H. Lee. 1979. Shock wave amplification in non-uniformly preconditioned gas mixtures. *1979 Spring Technical Meeting of the Canadian Section of the Combustion Institute.* Kingston, Ontario.

15. Lee, J. H. S., and I. O. Moen. 1980. The mechanism of transition from deflagration to detonation in vapor cloud explosions. *Progress Energy Combustion Science* 6(4):359.

16. Lee, J. H., R. Knystautas, and N. Yoshikawa. 1978. Photochemical initiation of gaseous detonation. *Acta Astronautica* 5(11–12):971–82.

17. Knystautas, R., J. H. Lee, I. O, Moen, and H.-Gg. Wagner. 1979. Direct initiation of spherical detonation by a hot turbulent gas jet . *17th Symposium (International) on Combustion Proceedings*. Pittsburgh, PA: The Combustion Institute. 1235.

18. Oppenheim, A. K. 1972. *Introduction to gasdynamics of explosions. Courses and lectures*. Wien–New York: Springer-Verlag, International Center for Mechanical Sciences 48.

PART TWO

PULSE DETONATION ENGINES

PDE — POSSIBLE WAYS FOR SPECIFIC IMPULSE IMPROVEMENT

G. Canteins, F. Franzetti, R. Zitoun, D. Desbordes, and E. Daniau

Pulse detonation engine (PDE) specific impulse, I_{sp}, is derived from direct impulse measurements using detonation pressure records on the closed end of the PDE combustion chamber and a ballistic pendulum arrangement. A simple analytical model validated against experimental data provides the specific impulse based on the Chapman–Jouguet (CJ) characteristics of the reactive mixture used. This simple expression is then developed in the case of an air-breathing engine and the main parameters governing the specific impulse are presented. Based on these results, ways for improving I_{sp} of an air-breathing PDE are detailed and the advantages of a dual-flow, supersonic ejector, PDE are summarized.

1 INTRODUCTION

The advantages of a PDE over conventional propulsion systems are based on estimates of its performance. Currently, only very little experimental data are available. Because of unsteady dynamics, analysis of such engines is more complex than that of a steady engine. As a result, there is significant uncertainty in the performance and, hence, the actual propulsive potential of PDEs.

This paper reports the results of experimental and theoretical studies on the propulsive performance of a generic PDE, which comprises a cylindrical tube open at one end into the atmosphere and closed at the other end by the thrust wall, at static conditions. The detonation is considered to be an ideal plane CJ wave initiated at the thrust wall.

Impulse and thrust are obtained in single-cycle experiments for different reactive mixtures and PDE geometries. The results are compared with Taylor and Zel'dovich self-similar flow analyses. Specific impulse of the generic PDE, I_{sp}, is then directly expressed in terms of the CJ characteristics of the mixture. This expression for I_{sp} is developed for the case of high CJ detonation pressure. The parameters controlling the specific impulse are presented and studied.

2 TAYLOR–ZEL'DOVICH SELF-SIMILAR SOLUTION

Once the plane CJ detonation wave is produced instantaneously in the plane of the thrust wall and propagates without losses from left to right (see Fig. 1), a right-propagating, centered rarefaction wave follows the detonation front. Rear condition of the rarefaction wave adjustment to the tube end wall (zero flow velocity $u = 0$) defines the position of the tail of the rarefaction wave which is approximately half of the distance travelled by the detonation wave. The gaseous detonation products occupying the space between the end wall and the tail of the rarefaction wave (so-called "detonation kernel") are at constant thermodynamic state and quiescent. The overall flow field behind the detonation wave is self-similar and is well known as the Taylor–Zel'dovich wave.

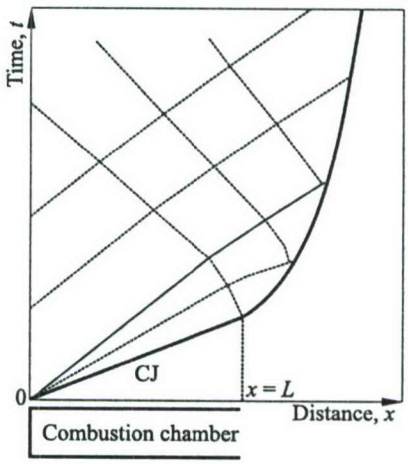

Figure 1 Taylor–Zel'dovich self-similar flow field

For a polytropic gas with constant ratio of specific heats, γ, the entire flow field depends only on the distance travelled by the detonation, γ, and the CJ detonation parameters [1].

3 SIMPLIFIED ANALYTICAL MODEL OF I_{sp}

A simple model of I_{sp} is based on the assumption that the impulse is equal to the time integral of the overpessure over the thrust wall, so the pressure loss at PDE walls is neglected. As a result, the specific impulse is only a function of overpressure level and duration.

Ballistic pendulum tests show that there is a good correlation between the integrated pressure signal and direct impulse measurements in the case of 50-millimeter diameter (2 in.) tubes. The first step in the analysis is to measure accurately the history of the thrust wall overpressure when detonation is initiated at the thrust wall (see Fig. 2). Measurements were performed with Kistler 603B fast-response pressure gages (rise time of about 1.5 μs) for the stoichiometric C_2H_4–O_2 mixture. As the ignition device, a predetonation tube with a low-energy automotive spark plug was used. The volume of this predetonation tube was small (less than 5%) as compared with the volume of the main combustion

chamber (CC). The main detonation chamber was rather short (only 100 mm), so the overall PDE cycle duration was less than 1 ms and the pressure signal did not exhibit temperature-induced drift. The detonation cell size of $C_2H_4 + 3O_2$ mixture is very small (less than 1 mm), therefore the detonation can be considered as a plane self-sustained wave traveling from the thrust wall to the open end.

As follows from Fig. 2, during a certain time, the overpressure on the thrust wall is constant. The time integral of the pressure signal will give the impulse produced by detonation.

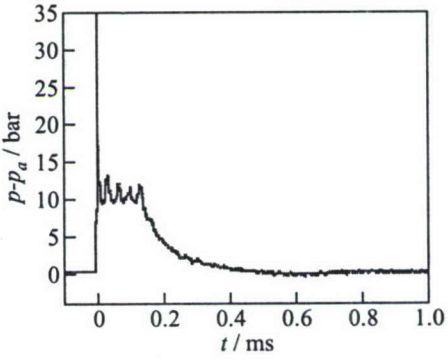

Figure 2 Typical overpressure signal at the thrust wall

Taking into account that the flow behind the CJ detonation wave is self-similar, one can try to determine I_{sp} in the dimensionless form. The dimensionless time, τ, can be defined as $\tau = t/t_{CJ}$, where t_{CJ} is the time needed for the detonation to exit the main detonation chamber. As the detonation wave propagates at the velocity D_{CJ}, $t_{CJ} = L_{CC}/D_{CJ}$, where L_{CC} is the length of the main detonation chamber.

To normalize pressure, the Taylor–Zel'dovich "detonation kernel" pressure, p_k, is a convenient parameter. In this case, the dimensionless overpressure is defined as $\Pi = (p - p_a)/(p_k - p_a)$.

The impulse, I, is given by the integral:

$$I = S_{CC}\int_0^\infty (p_k - p_a)\Pi(t)\,dt = S_{CC}(p_k - p_a)\int_0^\infty \Pi(\tau)\frac{L_{CC}}{D_{CJ}}\,d\tau$$

$$= S_{CC}(p_k - p_a)\frac{L_{CC}}{D_{CJ}}\int_0^\infty \Pi(\tau)\,d\tau = \frac{(p_k - p_a)V_{CC}}{D_{CJ}}\int_0^\infty \Pi(\tau)\,d\tau$$

where S_{CC} is the thrust wall cross-section area and $V_{CC} = L_{CC}S_{CC}$ is the volume of the CC. Introducing the dimensionless impulse parameter, $J' = \int \Pi(\tau)\,d\tau$, one arrives at the following relationship for the impulse:

$$I = J'\frac{(p_k - p_a)V_{CC}}{D_{CJ}}$$

The mixture-based specific impulse is defined as:

$$I_{sp} = J'\frac{(p_k - p_a)V_{CC}}{gV_{CC}\rho_0 D_{CJ}}$$

and, finally, after applying the Taylor–Zel'dovich solution,

$$I_{sp} = \frac{J'}{g\rho_0 D_{CJ}} \left[p_{CJ} \left(\frac{\gamma+1}{2\gamma} \right)^{2\gamma/(\gamma-1)} - p_a \right]$$

where ρ_0 is the initial mixture density, p_{CJ} is the CJ detonation pressure, and g is the acceleration of gravity.

Figure 3 presents the overpressure signal of Fig. 2 in the dimensionless form. The positive impulse could be considered as represented by the area of a rectangle of height $\Pi = 1$ and base K in Fig. 3, equal to $J'_{max} = \int_0^{\tau^+} \Pi(\tau)d\tau$. In this case, the value of K is roughly 5.15. This value corresponds to the maximum rather than overall impulse, i.e., the negative overpressure phase is not taken into account. Note that the negative overpressure phase is caused by over-expansion of the detonation products and exists only in single-cycle experiments. In actual multicycle PDEs, this effect is negated due to injection of fresh reactive mixture.

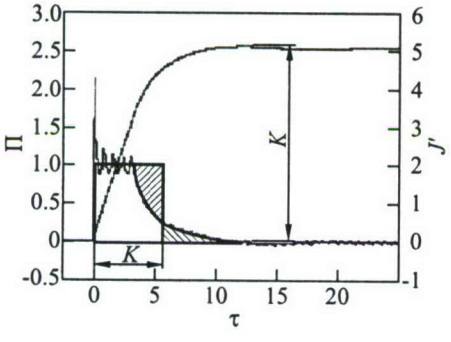

Figure 3 Thrust-wall impulse and K-factor

Thus, the PDE specific impulse can be expressed in terms of the CJ detonation parameters of a specific reactive mixture and the value of the K-factor.

For Pulse Detonation Rocket Engine (PDRE), the mixture-based specific impulse is equal to:

$$I_{sp} = \frac{K}{g\rho_0 D_{CJ}} \left[p_{CJ} \left(\frac{\gamma+1}{2\gamma} \right)^{2\gamma/(\gamma-1)} - p_a \right] \tag{1}$$

For air-breathing PDE, the fuel-based specific impulse is equal to (approximate relation):

$$I_{sp} = \frac{K}{g\rho_0 D_{CJ} Y_{st}\phi} \left[p_{CJ} \left(\frac{\gamma+1}{2\gamma} \right)^{2\gamma/(\gamma-1)} - p_a \right] \tag{2}$$

where ϕ is the mixture equivalence ratio, and Y_{st} is the ratio of fuel mass to total mixture mass at $\phi = 1$. If one takes into account the negative overpressure phase, the value of K should be decreased by roughly 5%.

4 EXPERIMENTAL VALIDATION

Self-similarity of the detonation-induced flow field in the CC allows one to determine governing parameters of the phenomenon. However, the overall PDE cycle, and particularly, the late phase of the exhaust of the detonation products into the atmosphere, is not self-similar. To investigate this issue and validate the aforementioned approach, single-cycle experiments with a CC of two different lengths, 100 mm (4 in.) and 150 mm (5.9 in.) filled with $C_2H_4 + 3O_2$ (Fig. 4) or $C_2H_2 + 2.5O_2$ (Fig. 5) mixtures at different initial pressures (1.5, 1.0, and 0.7 bar for the 100-millimeter CC and $C_2H_4 + 3O_2$ mixture; 1.0, 0.7, 0.5, and 0.4 bar for the 150-millimeter CC and $C_2H_2 + 2.5O_2$ mixture). In these experiments, the CJ detonation peak pressure was 51.2, 34.1, 23.9, 34.5, 24.2, 17.3, and 13.8 bar, respectively.

Figure 6 shows the pressure signals of Figs. 4 and 5, in a dimensionless form. All seven signals in Fig. 6 are pretty similar but exhibit some minor differences. The decrease of the detonation pressure brings to a decrease of the positive overpressure time, τ^+, during the second half of the exhaust phase. To emphasize the mentioned differences, Fig. 7 shows dimensionless impulse curves for 3 of the signals of Fig. 6. The durations of the positive and negative overpressure phases are slightly shortened when p_{CJ} decreases. For example, τ^+ decreases from 12 to 8, when the CJ detonation pressure drops from 51.2 to 13.8 bar. This decrease of the overpressure time with the decrease of the detonation pressure indicates that K is not a constant, but varies with the detonation pressure. Thus, for mixtures

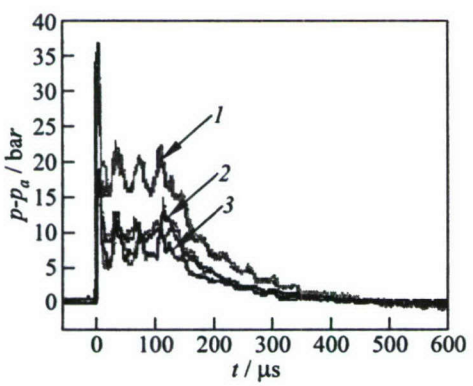

Figure 4 Measured thrust-wall overpressure histories in $C_2H_4 + 3O_2$ mixture at different initial pressures: *1* — p_0 = 1.5 bar; *2* — 1.0; and *3* — p_0 = 0.7 bar

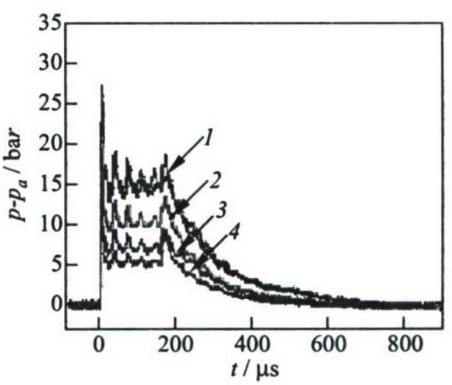

Figure 5 Measured thrust-wall overpressure histories in $C_2H_2 + 2.5O_2$ mixture at different initial pressures: *1* — p_0 = 1.0 bar; *2* — 0.7; *3* — 0.5; and *4* — p_0 = 0.4 bar

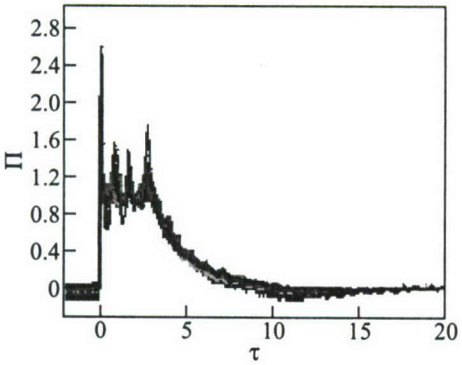

Figure 6 Dimensionless thrust-wall overpressure histories for 7 different mixtures, pressures, and geometry configurations, shown in Figs. 4 and 5

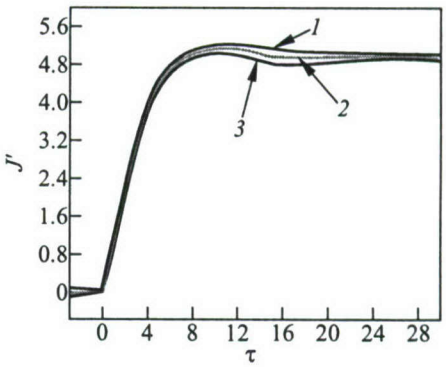

Figure 7 Dimensionless impulse histories for $C_2H_4 + 3O_2$ mixture at different initial pressures: *1* — $p_{CJ}/p_a = 54$; *2* — 34; and *3* — $p_{CJ}/p_a = 24$

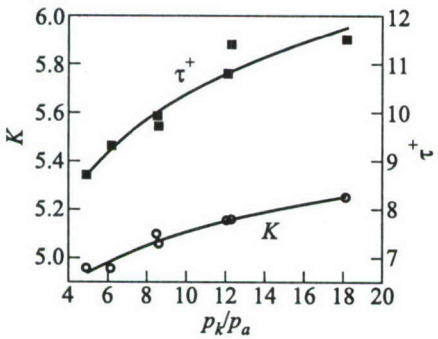

Figure 8 Positive overpressure duration, τ^+, and K-factor as functions of p_k

with high detonation pressure (generally fuel–oxygen mixtures), the value of K is between 5.0 and 5.2. For fuel–air mixtures with a lower detonation pressure, the value of K is predominantly in the range from 4.7 to 4.9 (Fig. 8).

Remember that the values of K are based on the positive impulse only. If one wants to take into account the negative overpressure phase, those values have to be reduced by approximately 5%.

Detonation in longer tubes (with length-to-diameter ratio, L/d, up to 10) has also been studied. In the longer tubes, the measured impulse was found to be 5% to 10% lower than the impulse measured in shorter tubes. This effect is probably due to the heat loss to the tube wall of the CC: longer residence times of the detonation products result in higher heat loss in long tubes as compared to short tubes.

Table 1 summarizes the calculated fuel-based specific impulse for different mixtures. The I_{sp} was determined using $\gamma = 1.15$ and a conservative assumption that $K = 4.7$. Results of direct measurements of the impulse with a ballistic pendulum were reported [2–4] and correlate well with the results of Table 1.

Table 1 Calculated fuel-based specific impulse for different reactive mixtures (based on positive impulse only)

Mixture	P_{CJ}, bar	D_{CJ}, m/s	ρ_0, kg/m^3	Y_{st}	I_{sp}, s
H_2 + 2.38 air	15.63	1971	0.843	0.0284	4630
CH_4 + 9.52 air	17.18	1803	1.114	0.0551	2210
C_2H_4 + 14.28 air	18.45	1830	1.162	0.0637	1965
C_2H_6 + 16.67 air	17.99	1803	1.166	0.0588	2090
C_3H_8 + 23.81 air	18.27	1801	1.188	0.0603	2040
JP-10 + 66.67 air	18.40	1783	1.221	0.0661	1850

5 CASE OF HIGH CJ DETONATION PRESSURE

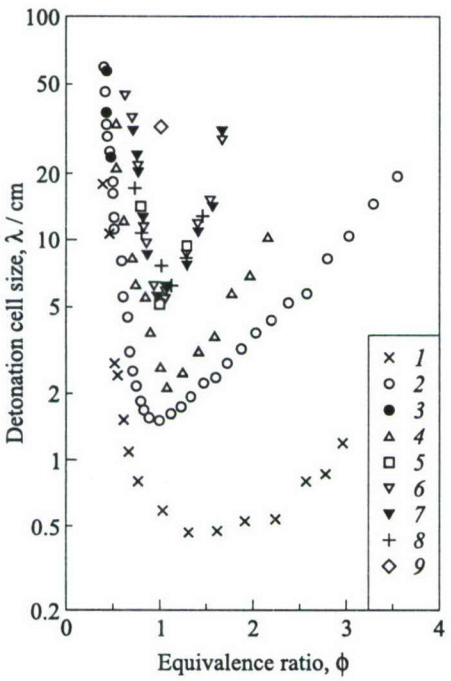

Figure 9 Detonation cell size vs. equivalence ratio for different fuel–air compositions [5]: *1* — C_2H_2; *2*, *3* — H_2; *4* — C_2H_4; *5* — C_2H_6; *6*, *7* — C_3H_8; *8* — C_4H_{10}; *9* — CH_4 (open symbols correspond to smoked foil measurements, filled symbols — to pressure oscillation measurements)

In this section, the ways to increase the specific impulse of air-breathing PDEs with a high CJ detonation pressure are discussed.

The main problem with fuel–air mixtures is their poor detonability, as the characteristic detonation cell size ranges between 15 mm (stoichiometric H_2–air mixture) and 55–60 mm (stoichiometric Fig. 9).

For a given mixture, the detonability is highest for an equivalence ratio generally between 1.0 and 1.2, and decreases dramatically for fuel-lean mixtures. The critical energy for the direct detonation initiation is proportional to the third power of the cell size, so fuel-lean mixtures are very difficult to detonate.

One means to increase the detonability of a reactive mixture is to increase the initial pressure. The cell size decreases linearly with the initial pressure, therefore a modest increase of the initial pressure can result in a large decrease of the critical energy required for detonation initiation. As a useful side effect,

the increase of the initial pressure also increases the CJ detonation pressure by the same factor.

5.1 Generic Relation

For air-breathing PDE, at $p_k \gg p_a$ (e.g., at $p_k > 10p_a$, when $p_{CJ} > 30p_a$), Eq. (2) can be written as:

$$I_{sp} \approx \frac{K}{g\rho_0 D_{CJ} Y_{st}\phi}\left[p_{CJ}\left(\frac{\gamma+1}{2\gamma}\right)^{2\gamma/(\gamma-1)}\right]$$

Applying the well-known relationship, $p_{CJ} \approx \rho_0 D_{CJ}^2/(\gamma+1)$, results in the following formula for the specific impulse:

$$I_{sp} \approx K\frac{D_{CJ}}{g(\gamma+1)Y_{st}\phi}\left(\frac{\gamma+1}{2\gamma}\right)^{2\gamma/(\gamma-1)} \tag{3}$$

or

$$I_{sp} \approx K\left(\frac{\gamma+1}{2\gamma}\right)^{2\gamma/(\gamma-1)}\frac{u_{CJ}}{gY_{st}\phi}$$

where u_{CJ} is the flow velocity behind the CJ detonation wave in the frame of reference attached to the lead shock.

5.2 Main Parameters Effects

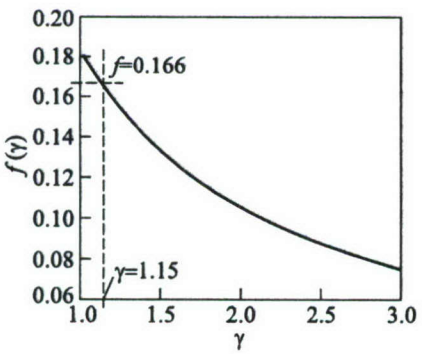

Figure 10 Effect of γ

Effects of Specific Heat Ratio

The function $f(\gamma)$, where $f = ((\gamma+1)/2\gamma)^{2\gamma/(\gamma-1)}/(\gamma+1)$, is plotted in Fig. 10. As function f decreases with γ, the ratio of specific heats should be as low as possible. At the same time, one can see that I_{sp} cannot be increased much even if mixtures with low γ are used. At $\gamma = 1.15$ (dashed lines in Fig. 10), function f equals to 0.166, so a generic value of 0.166 can be selected.

Effects of D_{CJ}, ϕ, and Fuel Type

Chapman–Jouguet detonation velocity, D_{CJ}, equivalence ratio, ϕ, and fuel type are interdependent and enter Eq. (3) in the combination $D_{CJ}/(gY_{st}\phi)$. Note that

$$Y_{st} = \frac{m_{fuel}}{m_{fuel} + m_{oxyd}} = \frac{f_{sto}}{f_{sto} + 1}$$

is the ratio of the fuel mass and the overall mixture mass, and is a function of the fuel composition and molecular mass. Velocity D_{CJ} is related to the heat of chemical reaction and, therefore, is linked to the mixture equivalence ratio, ϕ, for a given reactive mixture. As ϕ decreases, the available chemical heat of the reactive mixture decreases and D_{CJ} decreases too but to a lesser extent (following a square-root dependence on ϕ).

Using the mixture of equivalence ratio of 0.80 should then increase the I_{sp} by 12% and equivalence ratio of 0.70 will give a 20% gain in I_{sp}. A lower equivalence ratio will result in higher I_{sp}, but the sharp decrease in the detonability of the reactive mixture will preclude the use of too fuel-lean mixtures.

From a performance (not a system) point of view, hydrogen, with its high D_{CJ} and low f_{sto} values, seems to be the best fuel for PDE applications.

For a PDRE operating on a stoichiometric reactive mixture, Eq. (1) is reduced to:

$$I_{sp} \approx 0.166 \frac{K D_{CJ}}{g}$$

or

$$I_{sp} \approx 0.356 \frac{K u_{CJ}}{g}$$

At $K = 5.15$ (simple case of CC without nozzle), $I_{sp} \approx 1.83 u_{CJ}/g$.

As the flow velocity, u, behind the CJ detonation wave in the laboratory frame of reference is the $\gamma/(\gamma+1)$ part of D_{CJ}, roughly 55% of the PDRE specific impulse comes from the flow velocity and 45% comes from the overpressure.

Effect of K-Factor

Since K-factor is in essence the duration of the useful work of detonation products on the thrust wall, one means to increase K is to attach a nozzle to the CC. Because of a large expansion potential of high-pressure detonation products at the CC exit, which is lost for propulsion in a simple PDE configuration without nozzle, their controlled expansion will allow to recover a nonnegligible thrust.

To demonstrate the effect of nozzle, a simple calculation, based on one-dimensional, unsteady Flux-Corrected Transport method was performed. Predicted behavior of the flow Mach number u/c (c is the local sound velocity) inside

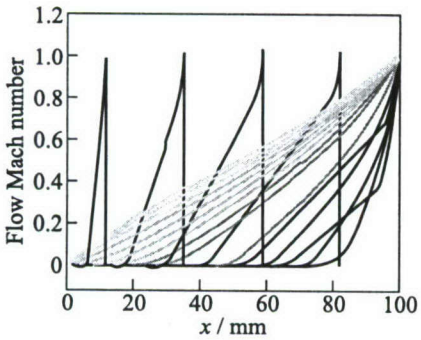

Figure 11 Calculated flow Mach number at different times inside the PDE combustion chamber in case of detonation initiation at the thrust wall

the CC is shown in Fig. 11. The flow at the CC exit is sonic during the greater part of the exhaust of the detonation products, so attachment of a nozzle (cylindrical or divergent) should increase the impulse.

However, a nozzle may also affect the time required for pressure in the CC to drop to a specific value (e.g., $p = 1$ atm) when a fresh mixture should be injected. Therefore, the overall cycle time will be shorter for a shorter CC without nozzle, i.e., when rapid expansion occurs at the exit.

Some relevant results were already reported in a previous publication [6], therefore only the main findings are presented here (see Figs. 12 and 13). Parameter β in Figs. 12 and 13 is the ratio of the nozzle length to the CC length. Measurements were performed at atmospheric conditions and so the nozzle was filled with air at ambient pressure. A major part (up to 80%–90%) of the increase in the specific impulse could be linked to the exhaust of this additional mass of gases. In case of a multicycle PDE, when the nozzle is filled with low-density detonation products, the gain in the specific impulse should be less than the claimed values.

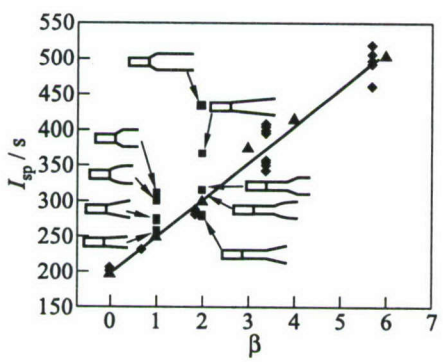

Figure 12 Nozzle effect on I_{sp} (solid line corresponds to cylindrical nozzle)

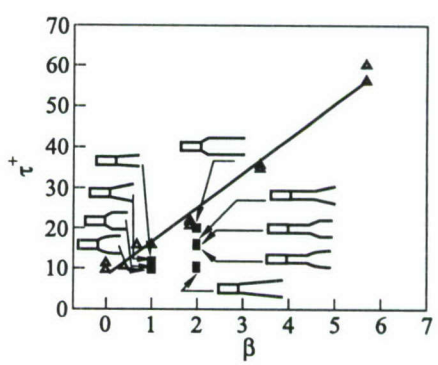

Figure 13 Nozzle effect on the dimensionless positive overpressure duration (solid line corresponds to cylindrical nozzle)

Since the exit cross-section area of all nozzles in Figs. 12 and 13 is greater than that of an adapted nozzle in a continuous flow regime, those nozzles could be considered as over-expanding ones. As the nozzle pressure ratio is decreased below the design point, a compression wave develops inside the nozzle that raises the static pressure at the nozzle exit to the ambient pressure level. As the pressure ratio is further reduced, the location of the compression wave shifts upstream and its strength increases, affecting more the pressure distribution at the nozzle wall. At the end of the exhaust phase of a PDE cycle, this compression wave enters the combustion chamber and impacts the thrust wall, providing additional thrust but also delaying the filling phase (see Fig. 14).

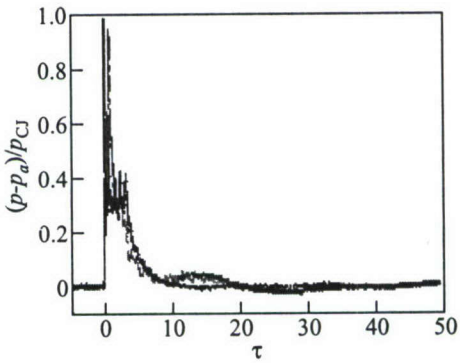

Figure 14 Measured thrust-wall overpressure history for a PDE with a large overexpanding nozzle

This effect can be used for controlling the injection phase and increasing the initial pressure in the CC just like a dashpot in a two-stroke piston engine.

The attachment of a nozzle is a practical way for improving the PDE specific impulse. However, this improvement is not costless. For a cylindrical nozzle, the cost is a reduction in maximum operating frequency and, probably, also an increase in the PDE thermal loading (due to longer residence times of the detonation products in the CC). For a divergent nozzle, the cost is the drag induced by the increase in the frontal area.

Thus, an outlet device that will show a higher exhaust-flow momentum than a cylindrical nozzle without sharp increase in the frontal area characteristic to a divergent nozzle hopefully will provide the best performance. This device could be a supersonic ejector nozzle. The other alternative is a double-flux PDE.

6 SUPERSONIC EJECTOR

One of the ways to increase I_{sp} of a subsonic air-breathing PDE is to add a coaxial tube of larger diameter around the CC, acting as supersonic ejection nozzle (see Fig. 15). This configuration minimizes the drag induced by the nozzle and may preserve the overall cycle time.

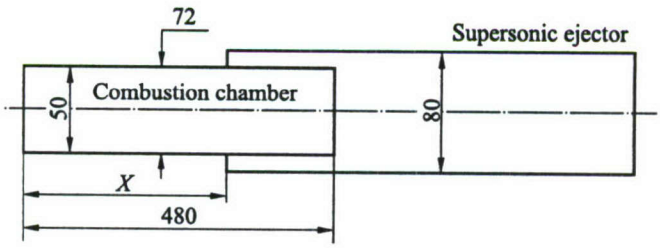

Figure 15 Experimental setup with supersonic ejector. Dimensions in mm

Figure 16 shows some examples of the performance measured with a CC 480 mm long, 50 mm in internal diameter, and 72 mm in external diameter with attached external cylindrical nozzle 80 mm in inner diameter and different lengths: 1000, 850, 700, 500, and 400 mm.

Without nozzle, I_{sp} obtained both by integrating the thrust wall pressure signal and by the ballistic pendulum method, are in the range 170–180 s, which is very close to the results obtained elsewhere [2]. Depending slightly on the overlapping distance, X (see Fig. 15), the I_{sp} of the PDE with a supersonic ejector nozzle, measured by the ballistic pendulum method, ranges from 265 to 277 s for a 1-meter long ejector, which corresponds to a gain of about 50%. As the ejector length reduces, the specific impulse decreases but stays over 170 s.

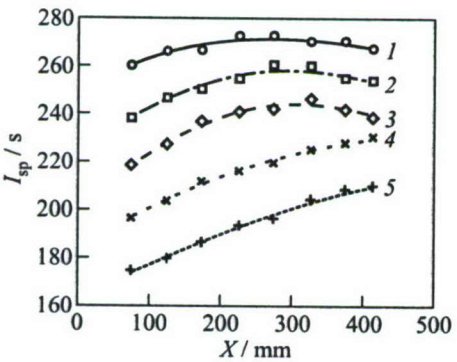

Figure 16 Measured specific impulse of PDE with attached supersonic ejector nozzles of different length vs. the overlapping distance, X (see Fig. 15): *1* — 1000 mm; *2* — 850; *3* — 700; *4* — 500; and *5* — 400 mm

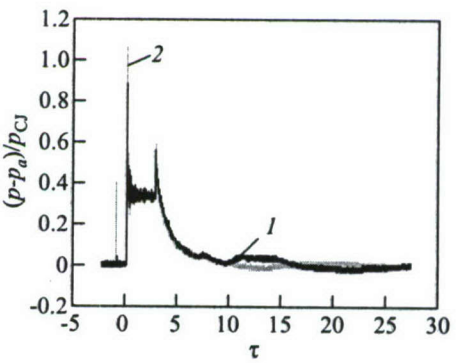

Figure 17 Comparison of measured thrust-wall overpressure signals with (*1*) and without (*2*) nozzle

Comparison of thrust wall pressure signals with and without nozzle (see Fig. 17) indicates a slight overpressure at $10 < \tau < 15$, which is comparable (but slightly shorter) to the one found in Fig. 14.

The increase in I_{sp} is maximum for X between 200 and 300 mm, corresponding to a 720–820-millimeter long nozzle, i.e., to β of 1.5–1.7. This 50% gain in I_{sp} compares favorably with the results for cylindrical nozzles, where a β value of 1.5–1.7 will increase I_{sp} by (at most) 37%–42%.

Thus, the supersonic ejector seems to be an efficient way to increase the specific impulse of the air-breathing PDE without considerable decrease in the maximum operating frequency and increase in the drag. Some additional parametric investigations are currently under way for the optimization of the basic design (i.e., the length and the internal diameter of the supersonic ejector in relation to the dimensions of the CC).

7 CONCLUDING REMARKS

Experimental investigations were recently undertaken to measure propulsive performance of a PDE. A simple analytical model, based on Taylor–Zel'dovich self-similar flow theory, was developed and validated against single-cycle experimental data. This model was shown to provide PDE performance in terms of the CJ parameters of the reactive mixture used. A quasi-universal constant, named K-factor, varying slightly between 4.7 and 5.2 has been defined for the simplest PDE configuration.

This analytical model was applied to the air-breathing PDE with a high CJ detonation pressure. It was shown that in this case, the specific impulse is a function of K, γ (ratio of specific heats), D_{CJ} (CJ detonation velocity), Y_{st} (stoichiometric fuel mass concentration), and ϕ (equivalence ratio).

To attain a maximum specific impulse, K and D_{CJ} should be as high as possible and γ, Y_{st}, and ϕ should be as low as possible. Parameters γ, Y_{st}, and D_{CJ} depend on the reactive mixture and cannot be varied over a wide range. Therefore, only parameters K and ϕ can be used for improving the PDE specific impulse.

The use of fuel-lean mixtures improves the specific impulse greatly but the accompanying sharp drop in detonability will probably preclude the use of too lean mixtures with equivalence ratio below 0.7.

It can be seen that hydrogen, with a high D_{CJ} and very low Y_{st}, is the best fuel for attaining maximum specific impulse from a performance point of view.

The effects of the initial pressure and temperature of the reactive mixture were also addressed. A combination of high initial pressure with low equivalence ratio could allow a nonnegligible gain of I_{sp} without decreasing the reactive

mixture detonability. The only difficulty seen is the practical realization of such a system.

Taking into account that the exit of the CC is sonic during the major part of the exhaust of the detonation products, attachment of a nozzle appears to be a convenient means for increasing the specific impulse.

Experiments in atmospheric conditions have shown that:

- with cylindrical nozzles, the I_{sp} increases linearly with the length of the nozzle but the overall cycle time increases, and the maximum operating frequency decreases accordingly;
- with diverging nozzles, the increase in I_{sp} is much higher than with cylindrical nozzles of the same length and in the case of fast-diverging nozzles (i.e., bell-shaped), the overall cycle time remains unchanged; and
- supersonic ejector of moderate diameter increases the I_{sp} more than a cylindrical nozzle of the same length, but does not degrade the maximum operating frequency and does not increase the frontal area and drag as the diverging nozzles do.

REFERENCES

1. Stanyukovich, F. P. 1960. Unsteady motion of continuous media. Pergamon Press.
2. Zdhan, S. A., V. V. Mitrofanov, and A. I. Sychev. 1994. Reactive impulse from the explosion of a gas mixture in a semi-infinite space. *Combustion Explosion Shock Waves* 30(5):633–57.
3. Cooper, M., S. I. Jackson, J. M. Austin, E. Wintenberger, and J. E. Shepherd. 2001. Direct experimental impulse measurements for detonations and deflagrations. AIAA Paper No. 2001-3812.
4. Zitoun, R., E. Daniau, and D. Desbordes. 2001 (accepted). Thrust, impulse and specific impulse for different reactive mixtures in detonation regime. *Shock Waves.*
5. Knystautas, R., C. Guirao, J. H. S. Lee, and A. Sulmistras. 1984. Measurement of cell size in hydrocarbon–air mixtures and prediction of critical tube diameter, critical initiation energy and detonability limits. *Dynamics of shock waves, explosions, and detonations.* Eds. J. R. Bowen, N. Manson, A. K. Oppenheim, and R. I. Soloukhin. Progress in astronautics and aeronautics ser. NY: AIAA Inc. 94:23–37.
6. Daniau, E., R. Zitoun, C. Couquet, and D. Desbordes. 2001. Effects of nozzles of different length and shape on the propulsion performance of pulsed detonation engines. In: *High-speed deflagration and detonation: Fundamentals and control.* Eds. G. Roy, S. Frolov, D. Netzer, and A. Borisov. Moscow, Russia: Elex-KM Publ. 251–62.

ON THE PERFORMANCE OF PULSE DETONATION ENGINES

K. Kailasanath

Performance estimates of an idealized pulse detonation engine (PDE) consisting of a tube closed at one end and open at the other are derived from numerical simulations. The effects of chemical recombination on the calculated performance are explored using a detailed chemistry model and a simplified two-step chemistry model in which the composition is frozen at the Chapman–Jouguet (CJ) equilibrium conditions. The impact on the computed performance is shown to be smaller than uncertainties introduced due to initial conditions typically used for detonation initiation. The computed performance for an ethylene–oxygen mixture in a long tube is shown to be in excellent agreement (within 5%) with experimental data. The results from various simulations are generalized to derive a simple expression for estimating the performance. Various performance measures are also estimated from an ideal thermodynamic cycle analysis. These estimates are found to be larger than those obtained from the numerical simulations as well as from some previous theoretical estimates. Various reasons for this difference and methods to enhance the computed performance are also suggested.

1 INTRODUCTION

There are several reasons for investigating PDEs such as simplicity of the device, ability to operate over a range of speeds from zero to hypersonic and overall performance. Key issues in the development of PDE have been identified [1]. Among these, the performance of PDEs has been a controversial topic with many claims and counter claims [2]. A review of previous computational studies [3] showed significant variation in the reported performance of even an idealized PDE (a tube closed at one end and open at the other) under static conditions working on a stoichiometric hydrogen–air mixture. Even the thermodynamic advantages of the detonation cycle over the constant-pressure Brayton cycle have been reported to vanish rapidly under flight conditions [4]. Studies [5] have also suggested that the performance of PDEs is significantly inferior to that

of a ramjet. Others have blamed the unsteady processes in PDE for reduced propulsive efficiency [6].

As part of the U.S. Office of Naval Research program on PDEs, the Naval Research Laboratory is developing and applying computational tools to gain a better understanding of the operation and performance of PDEs [7]. At the International Colloquium on Control of Detonation Processes, factors that control the performance of the idealized PDE under static conditions have been identified [8]. Then, detailed time-dependent numerical simulations [9] were used to show that the primary reason for the reported variation in the computed performance of the hydrogen–air PDE could be the choice of numerical boundary conditions at the exhaust end of PDE. There was also some dependence on the initial conditions used in numerical simulations. More recently, numerical simulations with boundary conditions that are believed to be a good representation of the physical problem have been conducted and the results compared to detailed experimental observations [10, 11].

In this paper, the effects of detonation initiation energies and chemical recombination on the computed performance are discussed. Comparisons with experimental data are presented and a general expression derived for estimating the performance of PDEs. These results are also compared against the theoretical performance estimates recently reported in the literature [12]. Methods to enhance the performance of the idealized PDE and progress to date on resolving some of the controversies mentioned earlier are also reported.

2 NUMERICAL MODEL

Since the results presented in this paper are derived primarily from numerical simulations, the computational approach and numerical model are discussed first. The computational approach adopted is to solve the compressible, time-dependent, reactive flow, conservation equations for the density, momentum, total energy, and the concentrations of individual species. The terms in the conservation equations representing the different physical and chemical processes are solved separately and coupled using timestep splitting techniques [13]. This procedure allows the individual processes to be integrated by appropriate and efficient techniques and permits the easy substitution and elimination of different submodels for the individual processes, as needed for specific applications. For the short duration, single-cycle simulations discussed in this paper, the diffusive and thermal processes will have a negligible effect and, hence, only the convective flow with chemistry is considered.

For the high-speed reactive flows that are typical of detonations, an explicit algorithm such as the Flux-Corrected Transport [14] is very efficient and accurate for integrating the fluid convection. Flux-Corrected Transport is a conservative,

monotonic algorithm with fourth-order phase accuracy. With various initial and boundary conditions, this algorithm has been used previously to solve a wide variety of problems involving detonations.

Results with both a detailed multistep chemistry model as well as a two-step global chemistry model are presented. Since there is significant uncertainty in the rates as well as the mechanisms appropriate for hydrocarbon detonations, PDE simulations with detailed chemistry are presented only for a hydrogen–air mixture. In these simulations, a comprehensive model for hydrogen combustion with 8 species and 48 reactions was used. The reaction set is solved at each timestep with CHEMEQ, an integrator for stiff ordinary differential equations [15]. A two-step global reaction model [16] is used for the other fuels (ethylene, propane) considered. In this model, the induction step is followed by an energy release step. Induction time data from shock-tube experiments are used for characterizing the first step. The energy release is terminated at the CJ plane by specifying the mixture composition and terminating the chemical reactions beyond this plane (frozen flow assumption). By directly comparing the results using this model with those using a detailed chemistry model, the effects of neglecting the late time recombination can be estimated. Because of the uncertainties still present in the mechanism and rates for ethylene under detonative conditions, this comparative study has been carried out for an idealized PDE operating on a stoichiometric hydrogen–air mixture and is reported next.

3 PERFORMANCE ESTIMATES OF AN IDEALIZED PULSE DETONATION ENGINE

The idealized PDE consists of a tube closed at one end and open at the other end. This is a simple geometry both for computational simulations as well as for obtaining detailed experimental diagnostics. This is not an actual flying engine but can be considered as an idealization to the thrust tube of a more complex engine consisting of multiple tubes with inlets and nozzles. The details of calculating the various performance measures (thrust, impulse, fuel-, and mixture-based specific impulses) of this PDE have been discussed earlier by a number of investigators (e.g., [1, 2, 9, 17]) and are not repeated here.

3.1 Effects of Chemical Recombination

One of the controversies mentioned earlier was the effect chemical dissociation and recombination will have on performance estimates [4]. Earlier simulations [3, 9] of a hydrogen–air PDE with detailed chemistry that includes the appropriate dissociation and recombination effects implicitly did not show a significant effect. However, those simulations were for short tubes (10 to 20 cm

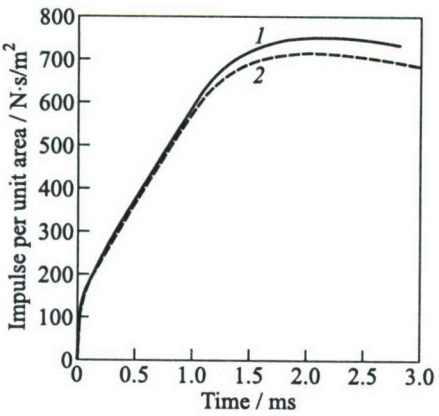

Figure 1 Chemistry effects on the time histories of the impulse (per unit area) from simulations of a 60-centimeter long PDE operating on a stoichiometric hydrogen–air mixture. The solid line (*1*) is from simulations using detailed chemistry and the dashed line (*2*) is from simulations using the two-step chemistry model

in length). It is possible that for longer tubes, where more time is available for the detonation products to undergo recombination reactions before being evacuated from the tube, the result could be more significant. To explore this issue, detonation in tubes of various lengths (10 to 60 cm) filled with a stoichiometric hydrogen–air mixture initially at 298 K and 1 atm, were simulated using both the detailed chemistry model as well as the two-step chemistry model. As mentioned before, the two-step model includes dissociation effects in the shocked flow but assumes that the mixture is chemically frozen at the CJ state. Hence, all long-term energy addition due to recombination is neglected. The detailed chemistry simulations include these effects. The impulse from simulations of a 60-centimeter long PDE tube using the two models is shown in Fig. 1. The peak impulse is different by 5.3% and translates into an equivalent gain in specific impulse due to chemical recombination effects. These observations are similar to those made recently in another computational study [18].

3.2 Detonation Initiation

The effects of parameters used for initiating detonations in simulations have been discussed previously [2, 9, 17] and estimated to be as much as 27%. Clearly, this is an unacceptable uncertainty and needs to be reduced. Use of lower energy initiators and longer tubes have been suggested [9]. Typically, a high-pressure and temperature zone of a certain width near the closed-end of the tube is used for initiating detonations in simulations. A series of global-chemistry simulations was carried out with various temperatures, pressures, and zone widths. The impulse from two cases (both for 60-centimeter long tubes) using a high-energy and a low-energy initiator is shown in Fig. 2. The peak values differ by about 17%. However, the peak specific impulse for the two cases is 4439 and 4161 s, differing by only 6.3%. This is because the mass of fuel used for initiation

is also larger for the case with the higher impulse. A 2-centimeter zone near the closed end of the tube at 50 atm and 3000 K was used as the high-energy initiator while a 0.2-centimeter zone at 20 atm and 2000 K was used for the lower energy initiator. These simulations again emphasize the importance of considering the contribution from initiators in making performance estimates. These effects could overshadow the differences due to neglecting chemical recombination effects. Direct performance measurements in experiments also show the impact of transition devices that are typically used to aid in the initiation of detonations [19].

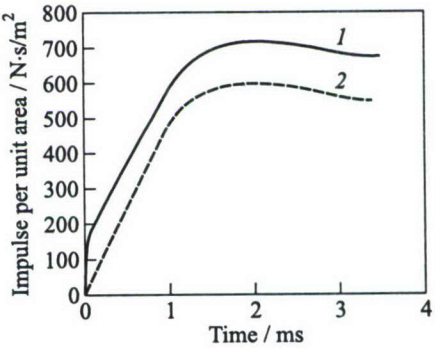

Figure 2 Effect of initiation energies on the time histories of the impulse (per unit area) from simulations of a 60-centimeter long PDE operating on a stoichiometric hydrogen–air mixture. The solid line (*1*) is from simulations using the high-energy initiator and the dashed line (*2*) is from simulations using a lower-energy initiator

3.3 Comparison of Computed Performance with Experimental Data

In performing direct comparisons between the predictions of numerical simulations and experimental data, the effects of factors such as the initiators used and the boundary conditions at the open end of the tube must be considered. The difficulties in isolating the effects of detonation initiators or transition devices can be reduced by focusing on easily detonable mixtures such as acetylene–oxygen or ethylene–oxygen. The ambiguity with specifying the open boundary conditions can be removed by conducting multidimensional simulations in which the exit plane of the thrust tube is an interior point. These simulations are expensive because the regions outside the tube (such as a dump tank) also need to be included in the computational domain. Such simulations have already been carried out [20]. In addition to providing information for direct comparison with experimental data, the results from these simulations have been used to determine better approximations for open boundary conditions for use in one-dimensional (1D) simulations.

The measured head-end pressure history [10] from experiments at Stanford University for a stoichiometric C_2H_4–O_2 mixture initially at 1 atm and 298 K is compared with the results from 1D numerical simulations in Fig. 3. The very good agreement in the pressure histories also results in very good agreements in the impulses and specific impulses estimated from the pressure histories. The

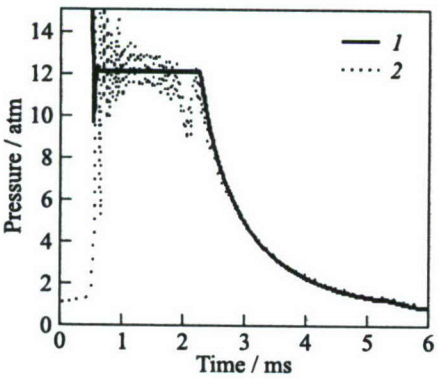

Figure 3 Comparison of the head-end pressure history predicted by one-dimensional numerical simulations (*1*) with experimental data from Stanford University (*2*)

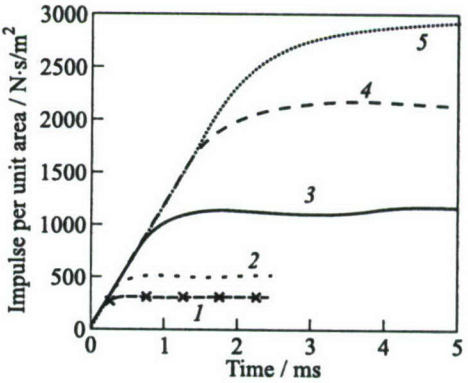

Figure 4 The computed impulse (per unit area) from PDE tubes of various length: *1* — 10 cm; *2* — 20; *3* — 50; *4* — 100; and *5* — 135 cm

impulse per unit area calculated from the pressure history for the 1.35-meter long tube is 2820 N·s/m^2. This corresponds to 2089 N·s/m^3 for the impulse per unit volume and that is in excellent agreement with the estimates of about 2100 N·s/m^3 from a different set of experiments at California Institute of Technology [19]. Those experiments also give a value of about 170 s for the mixture-based specific impulse when no transition devices are used.

The mixture-based specific impulse computed from the data in Fig. 3 is 165 s, which is in excellent agreement with the estimate from the Stanford University data (163 s) but significantly lower than the value of about 200 s reported in some other experiments [21]. Although those measurements were thought to be independent of the length of the tube, there may be some effect of the initiator and detonation transition present in those data, which are primarily for tubes of comparatively short length. This possibility was explored further by simulating PDEs of various thrust-tube lengths. The calculated impulses for various cases (tube lengths varying from 10 to 135 cm) are shown in Fig. 4. It is clearly evident from the figure that the impulse from the 10-centimeter long tube is more than half the impulse from the 20-centimeter long tube. However, the impulse scales quite well with tube length for tubes that are longer than about 50 cm. The specific impulses for the various cases have also been calculated and show that the value corresponding to the 10-centimeter long tube simulation (one of the primary tubes used in the experiments of [21]) is about 198 s, in excellent agreement with their experimental data. In summary, good estimates for the propulsive performance measures of a stoichiometric ethylene–oxygen mixture initially at 1 atm are about 2100 N·s/m^3 for the impulse per unit area

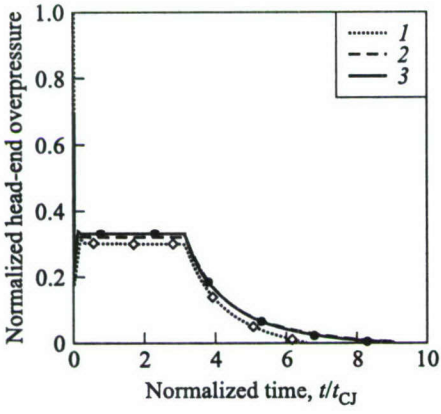

Figure 5 The normalized head-end overpressure shown as a function of the normalized time for three different PDEs operating on: *1* — ethylene–oxygen; *2* — propane–oxygen; and *3* — ethylene–air mixture

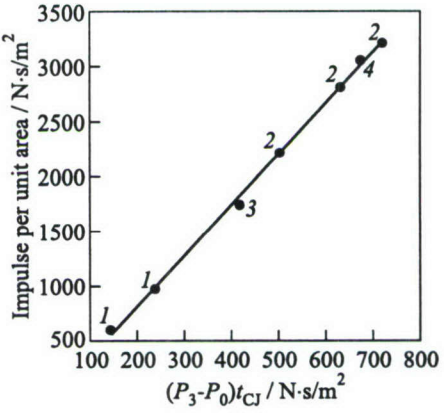

Figure 6 The generalized impulse (per unit area) from a series of simulations of PDEs operating on different fuels. The various numbers refer to different mixtures as follows: *1* — hydrogen–air, *2* — ethylene–oxygen, *3* — ethylene–air, and *4* — propane–oxygen

(independent of length), about 163–170 s for the mixture-based I_{sp} and 725–750 s for the fuel-based I_{sp}.

3.4 Generalization of the Results

With the confidence gained from the detailed comparisons with experimental data as well as the excellent agreement on the overall performance, simulations have been carried out of PDEs operating on other fuel–oxygen and fuel–air mixtures. The results from the various cases have been analyzed and the head-end overpressure from three mixtures: ethylene–oxygen, ethylene–air, and propane–oxygen, are shown in Fig. 5. The overpressure shown in the figure is the difference between the plateau pressure (P_3) and the ambient pressure (P_0) and has been normalized by the CJ pressure corresponding to the specific mixture. The time scale has been normalized using the detonation transit time (t_{CJ}), which is the length of the PDE tube divided by the CJ detonation velocity of the mixture. The general agreement among the three sets of data on the normalized coordinates suggests that these two normalized parameters are indeed key factors in determining the performance. Therefore, the impulse per unit area from the various cases has been shown in Fig. 6 as a function of the product of the two parameters, $P_3 - P_0$ and t_{CJ}. More than one data point for a mixture indicates data from simulations with different tube lengths.

What this generalization implies is that one can estimate the impulse from an idealized PDE knowing the plateau pressure, P_3, and the detonation velocity. That is, the impulse per unit area is given by:

$$\frac{I}{\text{Area}} = 4.65\,(P_3 - P_0)\,t_{CJ}$$

This expression derived from numerical simulations is similar to the expressions for I_{sp} obtained from theoretical analysis [22] and experiments [1, 23]. The constants of proportionality are slightly different in the various studies suggesting some dependence on the details of the particular configuration such as initiators or tube lengths used for deriving the correlation.

4 THERMODYNAMIC CYCLE ANALYSIS OF A DETONATION ENGINE

A number of investigators have carried out thermodynamic cycle analysis to show that heat addition using a detonation wave results in higher thermodynamic efficiencies than heat addition using a constant pressure process. Typically, this is done for a limited set of chosen conditions and questions have been raised about conditions that have not been reported. A recent comprehensive study [12] shows that the ideal detonative cycle is indeed more efficient than the ideal constant-volume Humphrey and the ideal constant-pressure Brayton cycles under all conditions. The relative advantage does decrease with increasing inlet compression temperature ratios and, hence, will decrease with increasing flight Mach numbers. The thermodynamic cycle efficiencies have been related to overall performance measures using conventional steady-state analysis. The appropriateness of this approach to an inherently unsteady device is questionable but is worth considering as an additional performance estimate.

The maximum I_{sp} shown in [12] (their Fig. 7) for static conditions (and inlet temperature ratio of unity) is only about 3500 s. Since the results are said to be valid for hydrogen and hydrocarbon fuels and are thought to be an upper estimate, it is curious that the computed performance measures reported above for a stoichiometric hydrogen–air mixture are all higher than this reported maximum value. An independent cycle analysis similar to those reported by Heiser & Pratt [12] was carried out for the mixtures considered in this study.

The current thermodynamic cycle analysis gives an efficiency of 0.46 for a stoichiometric hydrogen–air mixture initially at 298 K and 1 atm. Using the approach given in [12], this translates into a force for unit mass flow rate (specific thrust) of 1802 N·s/kg and a fuel-based I_{sp} of 6257 s for the ideal cycle. The differences between two estimates using identical analysis, is probably due to

differences in the fuel–air ratios and heat input values used. Consistent with the definition of the ideal cycle, heat input corresponding to the lower heating value of hydrogen and a fuel–air ratio corresponding to the stoichiometric value has been used in the current analysis. Even if the effective heat added to the flow is reduced by 50% (due to say, dissociation effects or other "losses"), a fuel-based I_{sp} of about 4000 s is obtained for the stoichiometric hydrogen–air mixture under the conditions noted above. Even this number is significantly larger than the maximum value presented in [12].

4.1 Effects of Forward Flight

Detailed simulations of the effects of forward flight require the specification of a geometry. With the current level of understanding, this is premature. The thermodynamic cycle analysis discussed above can be used to estimate the effects of forward flight. The conditions corresponding to a Mach 2.1 flight at an altitude of 9.3 km have been specified in [5]. These include a flight velocity of 640 m/s, ambient temperature of 228 K, and a combustor inflow static temperature of 428 K. Using these values, an ideal thermodynamic cycle efficiency of 0.69, specific thrust of 1660 N·s/kg, and I_{sp} of 5764 s have been calculated for the stoichiometric hydrogen–air mixture. While the thrust and I_{sp} are lower by about 8%, they do not drop off rapidly with increasing flight speeds because of the increase in the thermodynamic cycle efficiency. Similar calculations carried out for a stoichiometric ethylene–air mixture show a reduction in specific thrust from 1688 to 1544 N·s/kg and an I_{sp} reduction from 2531 to 2316 s for a change in operating conditions from static to Mach 2.1. This is again a reduction of only about 8.5% in the idealized performances.

4.2 Comparison of Performance Estimates

The value for fuel-based specific impulse obtained from numerical simulations of the idealized PDE operating on a stoichiometric hydrogen–air mixture is 4161 s while the value from the ideal cycle analysis is 6257 s. There may be several reasons for this difference. While the geometry has been idealized as a straight tube abruptly open to the outside, the thermodynamic processes have not been explicitly idealized. The numerical simulations include the effects of chemical dissociation and recombination while the ideal cycle analysis assumes the entire lower heating value is available. Therefore, the ideal cycle analysis should indeed give larger values than the numerical simulations.

It is difficult to correlate the various station conditions in the classical cycle analysis with those observed in the numerical simulations. The simulations capture the inherent unsteadiness of the PDE and are only for a single cycle. It is

possible that a more realistic PDE consisting of multiple tubes and a common inlet and nozzle can better approximate a "steady engine." Meanwhile, it must be recognized that the classical thermodynamic cycle analysis and performance measures derived from it are really for a "steady" engine that happens to have heat addition using a detonation wave and are not specific to a PDE.

The flow expansion process at the exit of the tube may be more gradual with the addition of a nozzle than that observed in the current simulations where the tube opens abruptly into the ambient atmosphere. This observation is consistent with earlier reports of a better performance with boundary conditions that allow for a slower relaxation rate at the open end of the tube [9]. In fact, conducting simulations identical to those reported here for the stoichiometric hydrogen–air mixture but with an effectively slower relaxation process for the pressure at the exit of the tube, a higher value of about 5100 s is observed. The addition of a nozzle will also enhance the performance due to the well-established partial fuel-fill effect [2, 24]. Separating the gain in performance from the better expansion of the detonation products from the gain due to the partial fuel-fill effect could be a challenging task.

Another issue that is often brought up is the relative merits of the ideal detonation cycle and the ideal constant-pressure Brayton cycle. Again following the approach prescribed by Heiser & Pratt [12], the ideal thermodynamic cycle efficiencies of the Brayton cycle have been calculated for the different mixtures and physical conditions discussed in this paper. Under all conditions discussed in this paper, the ideal performance of the detonation cycle is found to be better than that of the Brayton cycle. Consider, for example, the case of the stoichiometric hydrogen–air mixture at the Mach 2.1 flight conditions specified earlier. For the Brayton cycle, the calculations yield a specific thrust of 1283 N·s/kg and a specific impulse of 4490 s. Recall that the corresponding values for the detonation cycle were 1660 N·s/kg and 5764 s. That is, an engine operating at the Mach 2.1 flight conditions under the ideal detonation cycle has a performance gain of over 28%, when compared to the ideal Brayton cycle. Indeed, the performance advantage does drop with increasing flight speeds but is still substantial.

5 CONCLUDING REMARKS

Several controversies concerning the estimation of the performance of PDE have been discussed and progress noted in their resolution. The effects of including detailed chemical kinetics in PDE simulations were shown to be small. Recombination effects do increase the performance when long systems are considered but the increase is comparable to uncertainties in the performance due to initiation conditions typically used in numerical simulations. Experimental performance measurements also depend on the method used to initiate detonations. By con-

sidering long systems and easily detonable mixtures, the effects of initiator uncertainties can be minimized. Such simulations have been carried out and the results are found to be in very good agreement (within 5%) with data from different experiments. A general expression for the performance of the idealized PDE has also been derived from numerical simulations. This expression is in general agreement with corresponding expressions from theoretical analysis and experiments.

Performance measures based on an ideal thermodynamic cycle analysis has been calculated for a detonation engine. These values are higher than those obtained from the numerical simulations and experiments and the reasons for this difference have been discussed. The effects of forward flight on the ideal performance are found to be small for the conditions investigated. Methods to enhance the performance of the ideal PDE have also been briefly discussed.

In the ideal thermodynamic cycle analysis discussed in this paper, the same value was used consistently for the heat supplied (corresponding to the lower heating value) for all cycles. An argument can be made that the effective heat added will be less for the detonation cycle than for the Brayton cycle because of more dissociation "losses" at the higher temperatures encountered in detonations. Considering such nonideal effects as well as a better representation of the processes in an actual PDE on the cycle diagram could alter the performance advantages noted here.

ACKNOWLEDGMENTS

This work is sponsored by Mechanics and Energy Conversion Division of the Office of Naval Research under the direction of Dr. Gabriel Roy. The authors wish to thank the PDE research group at Stanford University headed by Prof. R. Hanson for providing the data used in the comparison.

REFERENCES

1. Desbordes, D., E. Daniau, and R. Zitoun. 2001. Pulsed detonation propulsion: Key issues. In: *High-speed deflagration and detonation: Fundamentals and control.* Eds. G. Roy, S. Frolov, D. Netzer, and A. Borisov. Moscow, Russia: Enas Publ. 177–92.
2. Kailasanath, K. 2001. A review of PDE research — performance estimates. AIAA Paper No. 2001-0474.
3. Kailasanath, K., C. Li, and G. Patnaik. 1999. Computational studies of pulse detonation engines: A status report. AIAA Paper No. 99-2634.
4. Povinelli, L. A. 2001. Impact of dissociation and sensible heat release on pulse detonation and gas turbine engine performance. ISABE-2001-1212. Bangalore, India.
5. Yang, V., Y. H. Wu, and F. H. Ma. 2001. Pulse detonation engine performance and thermodynamic cycle analysis. *14th ONR Propulsion Meeting Proceedings.* Eds. G. D. Roy and F. Mashayek. Chicago, IL. 165–70.

6. Razi Nalim, M., and Z. A. Izzy. 2001. Rotary ejector enhanced pulse detonation system. AIAA Paper No. 2001-3613.
7. Kailasanath, K., C. Li, and G. Patnaik. 2001. Multilevel computational studies of pulse detonation engines. ISABE-2001-1172. Bangalore, India.
8. Kailasanath, K., G. Patnaik, and C. Li. 2001. On factors controlling the performance of pulsed detonation engines. In: *High-speed deflagration and detonation: Fundamentals and control.* Eds. G. Roy, S. Frolov, D. Netzer, and A. Borisov. Moscow, Russia: Enas Publ. 193–206.
9. Kailasanath, K., and G. Patnaik. 2000. Performance estimates of pulsed detonation engines. *Proc. Combustion Institute* 28:595–601.
10. Jenkins, T. P., S. T. Sanders, K. Kailasanath, C. Li, and R. K. Hanson. 2000. Diode laser-based measurements for model validation in pulse detonation flows. *25th JANNAF Airbreathing Propulsion Meeting Proceedings.* Monterey, CA.
11. Kailasanath, K. 2002. Recent developments in the research on pulse detonation engines. AIAA Paper No. 2002-0470.
12. Heiser, W. H., and D. T. Pratt. 2002. Thermodynamic cycle analysis of pulse detonation engines. *J. Propulsion Power* 18(1):68–76.
13. Oran, E. S., and J. P. Boris. 1987. *Numerical simulation of reactive flow.* New York: Elsevier,
14. Boris, J. P., and D. L. Book. 1973. Flux corrected transport I: SHASTA, a fluid transport algorithm that works. *J. Computational Physics* 11(1):38–69.
15. Young, T. R., and J. P. Boris. 1977. Solving stiff ordinary differential equations assciated with chemical kinetics of reactive-flow problems. *J. Physical Chemistry* 81:2424–27.
16. Kailasanath, K., E. S. Oran, J. P. Boris, and T. R. Young. 1985. Determination of detonation cell size and the role of transverse waves in two-dimensional detonations. *Combustion Flame* 61:199–209.
17. Cambier, J. L., and J. K. Tegner. 1997. Strategies for PDE performance optimization. AIAA Paper No. 97-2743.
18. Povinelli, L. A., and S. Yungster. 2002. Airbreathing pulse detonation engine performance. NASA/TM-2002-211575.
19. Cooper, M., S. Jackson, J. Austin, E. Wintenberger, and J. E. Shepherd. 2001. Direct experimental impulse measurements for detonations and deflagration. AIAA Paper No. 2001-3812.
20. Li, C., K. Kailasanath, and G. Patnaik. 2000. A numerical study of flow field evolution in a pulse detonation engine. AIAA Paper No. 2000-0314.
21. Zitoun, R., and D. Desbordes. 1999. Propulsive performances of pulsed detonations. *Combustion Science Technology* 144:93–114.
22. Wintenberger, E., J. Austin, M. Cooper, S. Jackson, and J. E. Shepherd. 2001. An analytical model for the impulse of a single-cycle pulse detonation engine. AIAA Paper No. 2001-3811.
23. Falempin, F., D. Bouchaud, B. Forrat, D. Desbordes, and E. Daniau. 2001. Pulsed detonation engine: Possible application to low cost tactical missile and to space launcher. AIAA Paper No. 2001-3815.
24. Zhdan, S. A., V. V. Mitrofanov, and A. I. Sychev. 1994. Reactive impulse from the explosion of a gas mixture in a semiinfinite space. *Combustion Explosion Shock Waves* 30(5):657–63.

THEORETICAL ASSESSMENT OF PDE PERFORMANCE AT VARIOUS FLIGHT CONDITIONS

T. Fujiwara, T. Endo, T. Miyasaka, F. Y. Zhang, and Y. Oka

Although a pulse detonation engine (PDE) is considered in this analysis as an air-breathing engine, the fuel and air introduced into the combustion chamber are assumed to come to a stagnant condition after closing the supply valves. Performance assessment is done, using the theoretical analysis recently derived and published by Endo & Fujiwara [1], and based upon a fundamental assumption of zero deflagration-to-detonation transition (DDT) distance.

1 INTRODUCTION

Recent computational and experimental studies on PDE have been reported elsewhere [2, 3]. For estimating the performance of an air-breathing engine, it is very important to consider different flight conditions. In this paper, the fuel and air introduced into a combustion chamber are assumed to attain a stagnant condition after closing supply valves. The PDE performance has been estimated under the calculated stagnant conditions at different flight speed and altitude and fuel–oxidizer combinations using a simplified theoretical Endo & Fujiwara formula [1].

2 FLIGHT CONDITIONS AND INITIAL CONDITIONS IN PDE

Flight conditions utilized in the present assessment are listed in Table 1.

The following initial conditions inside the PDE have been calculated from flight conditions: initial oxidizer density ρ_{o1}, initial fuel density ρ_{f1}, initial mixture density ρ_1, air mass flow rate $\dot{m}_o$, and fuel mass flow rate $\dot{m}_f$.

Table 1 Assumed flight conditions

Item	Unit	Conditions
Flight altitude	ft	0; 20,000; 30,000; 40,000
Flight Mach number		$0.8 \sim 3.0$ (0.2 increment)
Engine diameter	m	0.2, 0.35, 0.5
Engine length	m	1.0
Fuel–oxidizer		H_2/air, JP-10/air, H_2/O_2
Equivalence ratio ϕ		0.7, 1.0, 1.3

Table 2 Assumed static pressure and temperature at various altitudes

Flight altitude, ft	Static pressure p_∞, Pa	Temperature T_∞, K
0	101,325	288
20,000	46,603	249
30,000	30,150	225
40,000	18,824	203

After acquiring the total temperature and pressure from flight conditions, the total pressure at the combustion chamber inlet is calculated by taking into account the ram recovery factor. Performance assessment is carried out for a stationary mixture, where the mixture density ρ_1 is calculated from the total temperature and total pressure at the combustion chamber inlet. In addition, the air mass flow rate $\dot{m}_o$ and fuel mass flow rate $\dot{m}_f$ are calculated, as is shown below.

First, the atmospheric static pressure and temperature are given from the flight altitude, as indicated in Table 2.

Then, the given quantities p_∞, T_∞, and flight Mach number, M, can yield the total pressure, p_s, and total temperature, T_s, as

$$T_s = T_\infty \left[1 + \frac{\gamma - 1}{2}\mathrm{M}^2\right] \tag{1}$$

$$p_s = p_\infty \left[1 + \frac{\gamma - 1}{2}\mathrm{M}^2\right]^{\gamma/(\gamma-1)} \tag{2}$$

where the air specific heat ratio γ is 1.382 at the flight altitude 0 ft, while $\gamma = 1.382$ at 20,000 ft, $\gamma = 1.381$ at 30,000 ft, and $\gamma = 1.380$ at 40,000 ft. In the case of pure oxygen, $\gamma = 1.4$ and is fixed for all altitudes. Next, the ram recovery factor, η, is calculated from the flight Mach number as

$$\eta = \begin{cases} 1, & \mathrm{M} < 1 \\ 1 - 0.075(\mathrm{M} - 1)^{1.35}, & \mathrm{M} \geq 1 \end{cases} \tag{3}$$

Using the ram recovery factor, the total pressure at the combustion chamber inlet is given by

$$p_{is} = \eta p_s \tag{4}$$

The total pressure at the combustion chamber inlet, p_{is}, and total temperature, T_s, determine, for a given equivalence ratio, ϕ, the initial oxidizer, fuel, and mixture densities, ρ_{o1}, ρ_{f1}, and ρ_1, respectively:

$$\rho_{o1} = \frac{p_{is}/T_s}{fR_f + R_o} \tag{5}$$

$$\rho_{f1} = f\rho_{o1} \tag{6}$$

$$\rho_1 = \rho_{o1} + \rho_{f1} \tag{7}$$

where R_f and R_o denote the gas constants of the fuel and oxidizer, while f is the fuel–air ratio given by:

$$f = C\phi\frac{W_f}{W_o} \tag{8}$$

Here, W_f and W_o indicate the molecular masses of fuel and oxidizer, respectively, whereas C is the ratio of stoichiometric coefficients: 0.402 for hydrogen–air, 2/17 for JP-10–air, and 2.0 for hydrogen–oxygen mixtures.

Next, the air mass flow rate, $\dot{m}_o$, and fuel mass flow rate, $\dot{m}_f$, are given by the following equations:

$$\dot{m}_o = Sp_{is}\sqrt{\frac{\gamma}{R_oT_s}}\mathrm{M}\left[1 + \frac{\gamma - 1}{2}\mathrm{M}^2\right]^{(\gamma+1)/(2(\gamma-1))} \tag{9}$$

$$\dot{m}_f = f\dot{m}_o \tag{10}$$

where S is the PDE cross-section.

3 PERFORMANCE ASSESSMENT

Impulse and thrust are obtained using the theoretical formula derived by Endo & Fujiwara [1], as is shown below.

The present PDE is a straight, constant-cross-section tube with one upstream end closed at $x = 0$ and the other downstream end $x = L$ open. For simplicity, the gas is assumed to be polytropic and having no viscosity or heat conductivity. Assuming that the flow inside the PDE is one-dimensional, consider one cycle

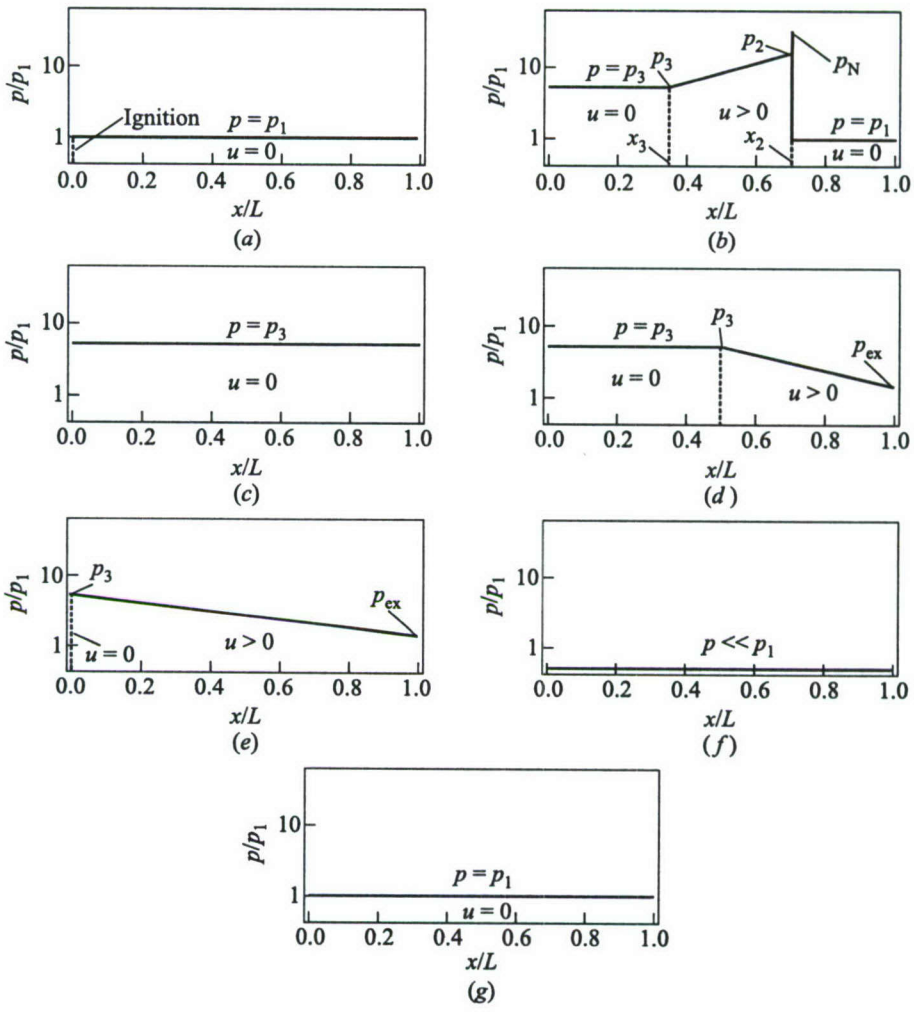

Figure 1 Temporal evolution of pressure distribution: (*a*) $t = 0$; (*b*) $0 < t < t_I$; (*c*) $t = t_I$; (*d*) $t_I < t < t_{II}$; (*e*) $t = t_{II}$; (*f*) $t = t_{III}$; and (*g*) $t = T_{cyc}$

of PDE operation. Initially, as shown in Fig. 1*a*, the PDE is filled up with a quiescent and uniform combustible mixture, having parameters ρ_1, p_1, γ_1, and u_1 (= 0), where subscript "1" indicates the initial state. At $t = 0$, the combustible gas is ignited at the location $x = 0$, from which a Chapman–Jouguet (CJ) detonation wave propagates toward the open end (direct initiation or zero DDT distance).

Although the burnt gas is accelerated toward the open end of the PDE by the detonation wave, the condition $u = 0$ has to be satisfied at the closed end, causing the deceleration of burnt gas between the detonation front and the closed end. This deceleration occurs in the form of the self-similar rarefaction wave that accompanies the detonation front, as shown in Fig. 1*b*. The front of the rarefaction wave is coincident with the CJ plane (indicated by subscript 2) of detonation, while the rear end of the rarefaction wave (shown by subscript 3) proceeds toward the closed end of the PDE with parameters ρ_3, p_3, γ_3 $(= \gamma_2)$, and u_3 $(= 0)$ at $0 \leq x \leq x_3$. Specifying the time instant when $x_3 = L$ as $t = t_I$, the state of the entire gas within the PDE is expressed by ρ_3, p_3, $\gamma_3(= \gamma_2)$, and $u_3(= 0)$, as shown in Fig. 1*c*. The time interval $0 \leq t \leq t_I$ will be referred to as the "combustion phase."

At $t = t_I$, another rarefaction wave starts traveling with the sound speed a_3 from the open end toward the closed end of the PDE, until the time instant $t = t_{II}$, when it reaches the closed end, as shown in Figs. 1*d* and 1*e*. Due to the action of this rarefaction wave, the burnt gas is exhausted out of the open end until the time instant $t = t_{III}$, as shown in Fig. 1*f*. The time interval $t_I \leq t \leq t_{III}$ will be referred to as the "exhaust phase." At $t = t_{III}$, a fresh combustible mixture starts to fill the PDE until time $t = T_{\text{cyc}}$, as shown in Fig. 1*g*. Thus, the time increment T_{cyc} can be considered as the "cycle time" of PDE operation, and the time interval $t_{III} \leq t \leq T_{\text{cyc}}$ will be referred to as the "fill phase."

4 ANALYSIS

At $t = t_I$, the physical quantities at the CJ plane are given by the Hugoniot relation, with the assumption that the initial internal energy of the mixture is negligible [4]:

$$p_2 = \frac{\gamma_1 \mathrm{M}_{\mathrm{CJ}}^2}{\gamma_2 + 1} p_1 , \quad D_2 = D_{\mathrm{CJ}} = \sqrt{2(\gamma_2^2 - 1)q} \tag{11}$$

where $\mathrm{M}_{\mathrm{CJ}} = D_{\mathrm{CJ}}/a_1$ is the propagation Mach number of the CJ detonation, D_{CJ} is the propagation velocity of the CJ detonation, and q is the heat effect of combustion. Neglecting the detonation wave thickness, the instantaneous location of the CJ plane is determined as $x_2 = D_2 t = D_{\mathrm{CJ}} t$, while the von Neumann spike pressure, p_N, is expressed as

$$p_N = \frac{2\gamma_1 \mathrm{M}_{\mathrm{CJ}}^2}{\gamma_1 + 1} p_1 \tag{12}$$

Since the front of the self-similar rarefaction wave behind the detonation coincides with the CJ plane 2, the rarefaction front conditions are ρ_2, p_2, γ_2, u_2,

and D_2. Parameters of the rear end 3 of the rarefaction wave specified by the boundary condition $u_3 = 0$ are given by self-similar wave mechanics [5]:

$$x_3 = \frac{1}{2} x_2 , \quad D_3 = a_3 = \frac{1}{2} D_{\mathrm{CJ}} \tag{13}$$

$$p_3 = \left(\frac{\gamma_2 + 1}{2\gamma_2} \right)^{(\gamma_2+1)/(\gamma_2-1)} \frac{\gamma_1 \mathrm{M}_{\mathrm{CJ}}^2}{2\gamma_2} p_1 \tag{14}$$

Although these solutions are not exactly valid after the detonation has reached the open end of the PDE, the duration of the combustion phase is, for simplicity, evaluated as

$$t_1 = \frac{L}{D_3} = \frac{2L}{D_{\mathrm{CJ}}} \tag{15}$$

As mentioned above, at time $t = t_I$ the conditions in the PDE are ρ_3, p_3, γ_3 $(= \gamma_2)$, and u_3 $(= 0)$. Thus, during the combustion phase $(0 \le t \le t_I)$, the pressure $p_w(t)$ at the closed end of the PDE (source of thrust) is equal to p_3.

At $t = t_I$, a rarefaction wave starts traveling from the open end to the closed end of the PDE with the sound speed a_3, giving the travel time

$$t_{II} - t_I = \frac{L}{a_3} = \frac{2L}{D_{\mathrm{CJ}}} \tag{16}$$

and

$$t_{II} = \frac{2L}{D_{\mathrm{CJ}}} + t_I = \frac{4L}{D_{\mathrm{CJ}}} \tag{17}$$

The gas conditions at the open end of the PDE at $t_I \le t \le t_{II}$ are derived from the self-similar solutions [5] as:

$$\rho_{\mathrm{ex}} = \rho_1 (\gamma_2 + 1) \gamma_2^{-(\gamma_2+1)/(\gamma_2-1)} , \qquad u_{\mathrm{ex}} = a_{\mathrm{ex}} = \frac{1}{\gamma_2 + 1} D_{\mathrm{CJ}} \tag{18}$$

Thus, the exhaust mass flow rate per unit area is given as

$$\begin{aligned} \rho_{\mathrm{ex}} u_{\mathrm{ex}} &= \rho_3 D_{\mathrm{CJ}} 2^{2/(\gamma_2-1)} (\gamma_2 + 1)^{-(\gamma_2+1)/(\gamma_2-1)} \\ &= \left(\frac{2}{\gamma_2 + 1} \right)^{(\gamma_2+1)/(\gamma_2-1)} \rho_3 a_3 \end{aligned} \tag{19}$$

At $t = t_I$, the total gas mass per unit area within the PDE is $\rho_3 L$, therefore duration of the exhaust phase can be evaluated as:

$$\begin{aligned} t_{III} - t_I = \frac{\rho_3 L}{\rho_{\mathrm{ex}} u_{\mathrm{ex}}} &= \frac{L}{D_{\mathrm{CJ}}} 2^{-2/(\gamma_2-1)} (\gamma_2 + 1)^{(\gamma_2+1)/(\gamma_2-1)} \\ &= \frac{L}{a_3} \left(\frac{\gamma_2 + 1}{2} \right)^{(\gamma_2+1)/(\gamma_2-1)} \end{aligned} \tag{20}$$

During a part of the exhaust phase, $t_I \leq t \leq t_{II}$, the rarefaction wave front has not reached the closed end, giving the closed-end pressure as $p_w(t) = p_3$. During the rest of the exhaust phase, $t_{II} \leq t \leq t_{III}$, a linear decrease of the closed-end pressure is assumed:

$$p_w(t; t_{II} \leq t \leq t_{III}) = p_3 \left(1 - \frac{t - t_{II}}{t_{III} - t_{II}}\right) \tag{21}$$

where

$$t_{III} = \left[1 + \left(\frac{\gamma_2 + 1}{2}\right)^{(\gamma_2+1)/(\gamma_2-1)}\right] \frac{2L}{D_{\mathrm{CJ}}} \tag{22}$$

At last, consider several more quantities related to the PDE performance. Denoting the PDE fill time as τ_f (> 0), the cycle time of PDE operation, T_{cyc}, is given as

$$\begin{aligned} T_{\mathrm{cyc}} = t_{III} + \tau_f &= \left[1 + \left(\frac{\gamma_2 + 1}{2}\right)^{(\gamma_2+1)/(\gamma_2-1)}\right] \frac{2L}{D_{\mathrm{CJ}}} + \tau_f \\ &> \left[1 + \left(\frac{\gamma_2 + 1}{2}\right)^{(\gamma_2+1)/(\gamma_2-1)}\right] \frac{2L}{D_{\mathrm{CJ}}} \end{aligned} \tag{23}$$

The predicted closed-end pressure is then summarized as

$$p_w(t) = \begin{cases} p_3\,, & 0 \leq t \leq t_{II} \\ p_3 \left(1 - \dfrac{t - t_{II}}{t_{III} - t_{II}}\right), & t_{II} \leq t \leq t_{III} \\ 0\,, & t_{III} \leq t \leq T_{\mathrm{cyc}} \end{cases} \tag{24}$$

as shown in Fig. 2.

Using this expression, the impulse per unit PDE area generated during one cycle is defined as:

$$\begin{aligned} I_{\mathrm{cyc}} &= \int_0^{T_{\mathrm{cyc}}} p_w(t)\, dt \\ &= \frac{1}{2\gamma_2} \left(\frac{\gamma_2 + 1}{2\gamma_2}\right)^{(\gamma_2+1)/(\gamma_2-1)} \left[3 + \left(\frac{\gamma_2 + 1}{2}\right)^{(\gamma_2+1)/(\gamma_2-1)}\right] \rho_1 D_{\mathrm{CJ}} L \end{aligned} \tag{25}$$

where the relationship $a_1^2 = \gamma_1 p_1 / \rho_1$ is used. For the time-averaged thrust per unit area, $p_{\mathrm{av}} = I_{\mathrm{cyc}} / T_{\mathrm{cyc}}$, one finally obtains:

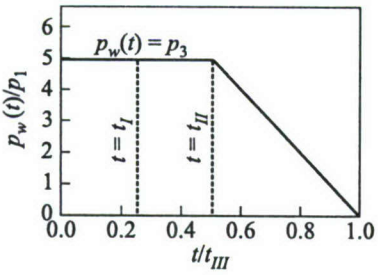

Figure 2 Pressure acting on the thrust wall as a function of time

Table 3 Chapman–Jouguet detonation velocities (m/s)

Fuel–oxidizer	ϕ		
	0.7	1.0	1.3
Hydrogen/air [6]	1780	1960	2060
JP-10/air [3]	1650	1790	1820
Hydrogen/oxygen [6]	2560	2850	3060

$$p_{\text{av}} = \frac{1}{2\gamma_2}\left(\frac{\gamma_2+1}{2\gamma_2}\right)^{(\gamma_2+1)/(\gamma_2-1)} \frac{\left[3+[(\gamma_2+1)/2]^{(\gamma_2+1)/(\gamma_2-1)}\right]\rho_1 D_{\text{CJ}} L}{\left[1+[(\gamma_2+1)/2]^{(\gamma_2+1)/(\gamma_2-1)}\right](2L/D_{\text{CJ}})+\tau_f}$$

$$< \frac{1}{4\gamma_2}\left(\frac{\gamma_2+1}{2\gamma_2}\right)^{(\gamma_2+1)/(\gamma_2-1)} \frac{3+[(\gamma_2+1)/2]^{(\gamma_2+1)/(\gamma_2-1)}}{1+[(\gamma_2+1)/2]^{(\gamma_2+1)/(\gamma_2-1)}}\rho_1 D_{\text{CJ}}^2 \qquad (26)$$

5 EVALUATION OF PDE FILL TIME

The PDE fill time, τ_f, is required to theoretically assess the performance, as indicated by Eq. (26). Time τ_f is given by:

$$\tau_f = \frac{\rho_1 SL}{\dot{m}_o + \dot{m}_f} \qquad (27)$$

6 GRAPHICAL REPRESENTATION OF PERFORMANCE

Using Eqs. (25) and (26), (*i*) the impulse per unit mass of fuel (specific impulse), (*ii*) the averaged thrust per unit fuel mass flow rate, and (*iii*) the time-averaged thrust per unit area (thrust density), have been evaluated as functions of flight Mach number for three different equivalence ratios. Note that the impulse and thrust are independent of the PDE tube cross-section area or diameter. It is assumed that for hydrogen–air and hydrogen–oxygen mixtures $\gamma_2 = 1.4$ and for JP-10–air mixture $\gamma_2 = 1.25$. Since the CJ velocity is slightly dependent on pressure, the CJ velocities at 1 atm are used as typical reference values which are given in Table 3.

7 SPECIFIC IMPULSE

The impulse per unit mass of fuel or oxidizer, i.e., the specific impulse, is defined as the ratio between the impulse per unit area of Eq. (25) and the supplied fuel or oxidizer per unit area as follows:

$$I_{\mathrm{sp},f} = \frac{I_{\mathrm{cyc}}}{\rho_{f1} L g}; \qquad I_{\mathrm{sp},o} = \frac{I_{\mathrm{cyc}}}{\rho_{o1} L g} \tag{28}$$

where g is the acceleration of gravity.

Using Eq. (25), Eqs. (28) can be rewritten as:

$$I_{\mathrm{sp},f} = \frac{1}{2\gamma_2}\left(\frac{\gamma_2+1}{2\gamma_2}\right)^{(\gamma_2+1)/(\gamma_2-1)}\left[3+\left(\frac{\gamma_2+1}{2}\right)^{(\gamma_2+1)/(\gamma_2-1)}\right] D_{\mathrm{CJ}}\frac{1+f}{fg}$$

$$I_{\mathrm{sp},o} = \frac{1}{2\gamma_2}\left(\frac{\gamma_2+1}{2\gamma_2}\right)^{(\gamma_2+1)/(\gamma_2-1)}\left[3+\left(\frac{\gamma_2+1}{2}\right)^{(\gamma_2+1)/(\gamma_2-1)}\right] D_{\mathrm{CJ}}\frac{1+f}{g} \tag{29}$$

which indicates that the fuel-based specific impulse $I_{\mathrm{sp},f}$ or oxidizer-based specific impulse $I_{\mathrm{sp},o}$ in Eq. (29) is dependent on the specific heat ratio, γ_2, the CJ detonation velocity, D_{CJ}, and the fuel–air ratio, f, which are determined by the fuel–air combination and its equivalence ratio. Thus, by fixing γ_2 and assuming that D_{CJ} is a function of the fuel–air combination and its equivalence ratio [6], $I_{\mathrm{sp},f}$ and $I_{\mathrm{sp},o}$ are independent of flight altitude and Mach number (Fig. 3).

The results of theoretical analysis give the following findings:

(1) The fuel-based specific impulse $I_{\mathrm{sp},f}$ is greater for a lower equivalence ratio, while the oxidizer-based specific impulse $I_{\mathrm{sp},o}$ behaves oppositely.

(2) The maximum impulse $I_{\mathrm{sp},f}$ is attained for the hydrogen/air combination, which is higher than twice of any other combinations; the JP-10–air mixture shows slightly higher $I_{\mathrm{sp},f}$ than the hydrogen–oxygen mixture.

(3) The $I_{\mathrm{sp},o}$ value is similar for all three fuel–oxidizer combinations.

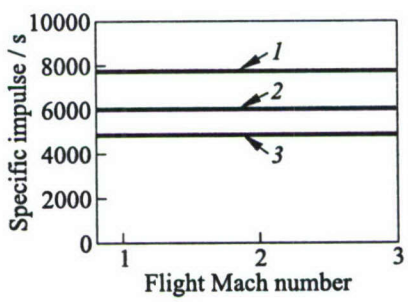

Figure 3 Fuel-based specific impulse for H_2–air mixture as a function of equivalence ratio (1 — $\phi = 0.7$; 2 — 1.0; and 3 — $\phi = 1.3$) and flight Mach number

8 AVERAGED THRUST FOR UNIT MASS FLOW RATE OF FUEL OR OXIDIZER

The time-averaged thrust per unit mass flow rate of fuel or oxidizer is calculated from the ratio between the time-averaged thrust per unit area of Eq. (26) and the mass flow rate of fuel or oxidizer per unit area as follows:

$$F_{\mathrm{sp},f} = \frac{p_w}{\dot{m}_f/S}; \qquad F_{\mathrm{sp},o} = \frac{p_w}{\dot{m}_o/S} \tag{30}$$

The calculated results are summarized in Fig. 4. The following findings are worth noting:

(1) For all the fuel–oxidizer combinations, the time-averaged thrust per unit mass flow rate of fuel, $F_{\mathrm{sp},f}$, and oxidizer, $F_{\mathrm{sp},o}$, slightly increase with flight altitude.

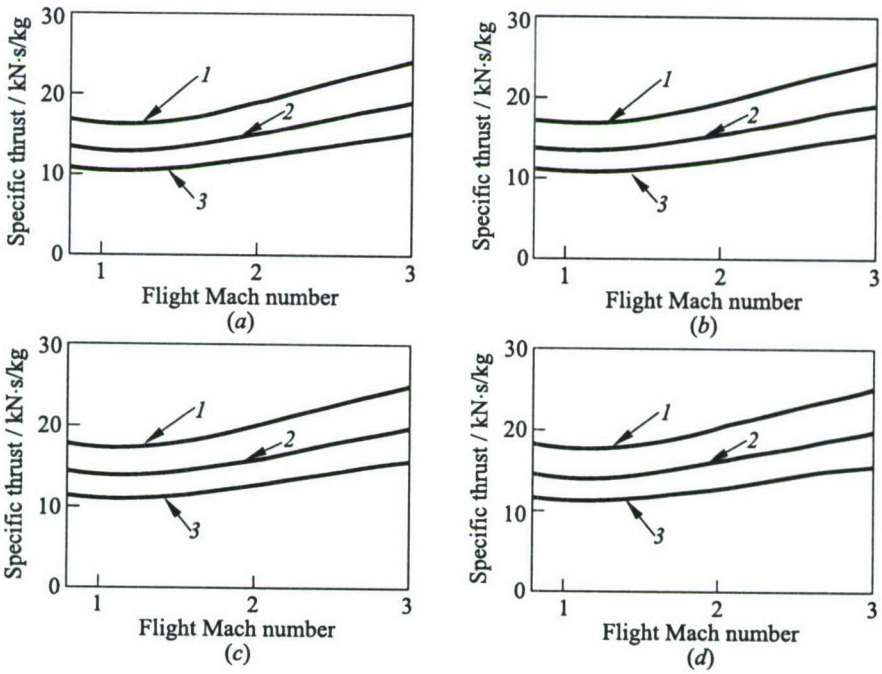

Figure 4 Time-averaged thrust per unit fuel mass flow rate (specific thrust) for JP-10–air mixture as a function of equivalence ratio (*1* — $\phi = 0.7$; *2* — 1.0; and *3* — $\phi = 1.3$), flight Mach number and altitude: (*a*) altitude 0 ft; (*b*) 20,000; (*c*) 30,000; and (*d*) 40,000 ft

(2) For all the fuel–oxidizer combinations, $F_{\mathrm{sp},f}$ and $F_{\mathrm{sp},o}$ attain minimum at flight Mach number 1.

(3) For all the fuel–oxidizer combinations, $F_{\mathrm{sp},f}$ becomes greater at lower equivalence ratio, whereas $F_{\mathrm{sp},o}$ behaves oppositely.

(4) $F_{\mathrm{sp},f}$ is the highest for hydrogen–air mixture, whereas $F_{\mathrm{sp},o}$ is the highest for hydrogen–oxygen mixture.

9 AVERAGED THRUST PER UNIT AREA

The time-averaged thrust per unit area, i.e., the thrust density, p_{av}, is given by Eq. (26). The summary of computational results is as follows:

(1) For all the fuel–oxidizer combinations, p_{av} increases with the flight altitude and Mach number as shown in Fig. 5.

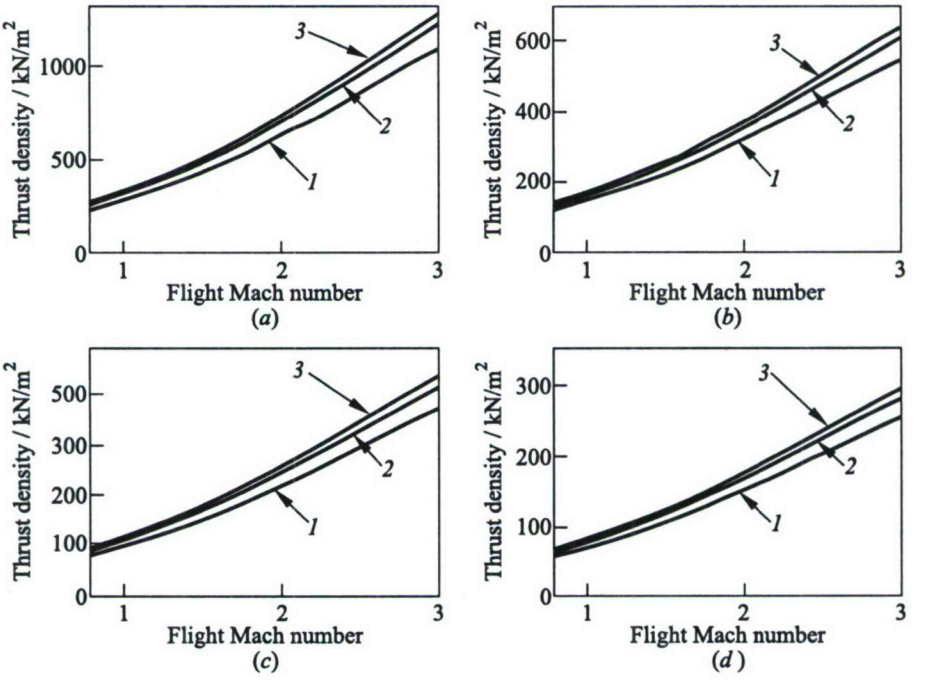

Figure 5 Thrust density for H_2–air mixture as a function of equivalence ratio (*1* — $\phi = 0.7$; *2* — 1.0; and *3* — $\phi = 1.3$), flight Mach number and altitude: (*a*) altitude 0 ft; (*b*) 20,000; (*c*) 30,000; and (*d*) 40,000 ft

(2) For all the fuel–oxidizer combinations, p_{av} becomes higher at higher equivalence ratios.

10 CONCLUDING REMARKS

The analytical expressions for the PDE specific impulse and thrust have been derived based on the idealized representation of the single-tube PDE operation process. Based on the expressions, the PDE performance has been evaluated in terms of flight altitude and speed, as well as fuel–oxidizer combination (hydrogen–air, or JP-10–air) and mixture equivalence ratio.

REFERENCES

1. Endo, T., and T. Fujiwara. 2002. A simplified analysis on a pulse detonation engine model. *Transactions of Japan Society for Aeronautical and Space Science* 44:217–22.
2. Hayashi, A. K., and T. Fujiwara. 2002. Recent progress of Japanese PDE research. AIAA Paper No. 2002-0475.
3. Brophy, C. M., J. O. Sinibaldi, D. W. Netzer, and R. G. Johnson. 2000. Operation of a JP-10/air pulse detonation engine. AIAA Paper No. 2000-3591.
4. Landau, L. D., and E. M. Lifshitz. 1987. *Fluid mechanics.* Ch. 14. 2nd ed. Oxford: Butterworth–Heinemann.
5. Landau, L. D., and E. M. Lifshitz. 1987. *Fluid mechanics.* Ch. 10. 2nd ed. Oxford: Butterworth–Heinemann.
6. Glassman, I. 1996. *Combustion.* Ch. 5. 3rd ed. Academic Press.
7. Endo, T., and T. Fujiwara. 2003 (submitted). Analytical estimation of thrust-plateau duration in pulse detonation engines. *Transactions of Japan Society for Aeronautical and Space Science.*

THEORETICAL ASSESSMENT OF PDE PERFORMANCE USING TWO-DIMENSIONAL NUMERICAL ANALYSIS

T. Miyasaka, T. Fujiwara, F. Y. Zhang, Y. Hyodo, Y. Oka, and S. Ito

To evaluate the performance of a pulse detonation engine (PDE), a two-dimensional (2D) analysis for a straight single-tube PDE in an external environment is performed. The combustible mixture is hydrogen–air with the equivalence ratio varied between 0.5 and 1.25. As a result of numerical simulations, better understanding of relevant physical processes in one PDE cycle and the dependence of PDE performance on the equivalence ratio are obtained.

1 INTRODUCTION

Pulse detonation engine has received considerable attention as a promising propulsion device [1]. Detonation has been simulated using 2D codes because of its cellular structure [2, 3]. In contrast, PDE has been extensively studied using one-dimensional (1D) codes [1, 4]. However, in the 1D codes, it is difficult to set adequate boundary conditions at the exit plane, although PDE performance depends strongly on the boundary condotions [1].

In this paper, a 2D analysis of the operation process of a straight, single-tube PDE is performed depending on the fuel–oxidizer equivalence ratio and flight conditions.

2 ANALYZED CONDITIONS AND MODELING

In the present analysis, a small 2D PDE of length $L = 10$ cm and width $W = 2$ cm is considered, along with the region representing the ambience (Fig. 1). The combustible mixture used is hydrogen–air with the equivalence ratio, ϕ, varied between 0.5 and 1.25. Other initial conditions are shown in Table 1.

The aerodynamic drag of the PDE is not evaluated as it depends not only on the shape of the air intake, but also on the entire engine shape.

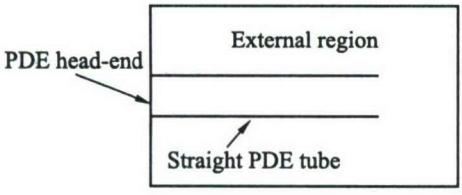

Figure 1 Computational domain

The governing equations are the 2D Euler equations supplemented with the conservation equations for each chemical species. A Cartesian coordinate system with x-axis directed along the PDE tube and y-axis directed across the PDE tube is used. In a vector form and in a general coordinate system (ξ, η), the governing equations can be written as follows:

$$\frac{\partial \hat{\mathbf{U}}}{\partial t} + \frac{\partial \hat{\mathbf{F}}}{\partial \xi} + \frac{\partial \hat{\mathbf{G}}}{\partial \eta} = \hat{\mathbf{S}} \tag{1}$$

where $\hat{\mathbf{U}}$ is the vector of conserved quantities, $\hat{\mathbf{F}}$ and $\hat{\mathbf{G}}$ are the convective vector terms in ξ- and η-directions, and $\hat{\mathbf{S}}$ is the source term vector. The vector quantities in Eq. (1) are written in terms of the density, ρ, x-velocity component, u, y-velocity component, v, and total energy $E = \rho(u^2 + v^2)/2 + \sum_{s=1}^{9} \rho_s e_s$, as follows:

$$\hat{\mathbf{U}} = \frac{1}{J}\begin{bmatrix} \rho \\ \rho u \\ \rho v \\ E \\ \rho_s \end{bmatrix}, \qquad \hat{\mathbf{F}} = \frac{1}{J}\begin{bmatrix} \rho\hat{U} \\ \rho u\hat{U} + \xi_x P \\ \rho v\hat{U} + \xi_y P \\ (E+P)\hat{U} \\ \rho_s\hat{U} \end{bmatrix}$$

$$\hat{\mathbf{G}} = \frac{1}{J}\begin{bmatrix} \rho\hat{V} \\ \rho u\hat{V} + \eta_x P \\ \rho v\hat{V} + \eta_y P \\ (E+P)\hat{V} \\ \rho_s\hat{V} \end{bmatrix}, \qquad \hat{\mathbf{S}} = \frac{1}{J}\begin{bmatrix} 0 \\ 0 \\ 0 \\ 0 \\ \dot{\omega}_s \end{bmatrix} \tag{2}$$

where $J = 1/(x_\xi y_\eta - x_\eta y_\xi)$ is the Jacobian for variable transformation, $\hat{U} = \xi_x u + \xi_y v$ and $\hat{V} = \eta_x u + \eta_y v$ are the contravariant velocities, P is the pressure, ξ_x, ξ_y,

Table 1 Initial conditions

Domain	Mixture	Initial pressure	Initial temperature
Inside PDE	$2\phi H_2 + O_2 + 3.76N_2$	51 kPa	298.15 K
External region	$O_2 + 3.76N_2$	51 kPa	298.15 K

η_x, and η_y are the metric tensors, and $\dot{\omega}_s$ is the mass production rate of chemical species s. A total of 8 reacting species: H_2, O_2, O, H, OH, HO_2, H_2O, H_2O_2, and 1 inert species, N_2, are included in the present detailed chemistry analysis, based on Jachimowski's modified 19-reaction model [3, 5], which possibly causes a complicated stiffness problem in chemical source terms.

3 NUMERICAL TECHNIQUE

The problem is solved by using the Harten–Yee's, non-MUSCL-type, second-order-upwind explicit-TVD numerical scheme [6]. Due to the necessity to resolve a 2D detonation wave and associated entire flowfield for a long time with high resolution, the following 2nd-order-accurate time-splitting method is used:

$$\hat{\mathbf{U}}_{i,j}^{n+1} = L_\eta\left(\frac{\Delta t}{2}\right) L_\xi\left(\frac{\Delta t}{2}\right) L_c(\Delta t) L_\xi\left(\frac{\Delta t}{2}\right) L_\eta\left(\frac{\Delta t}{2}\right) \hat{\mathbf{U}}_{i,j}^{n} \qquad (3)$$

where the chemical reaction operator L_c is treated by a semi-implicit scheme, from the viewpoint of stiffness in source terms.

Computational time is greatly reduced by adopting a space-splitting method. Although the combustion process (from ignition to the arrival of a detonation wave at the PDE open end) is confined within a PDE tube, the outflow of burnt gas from the PDE is associated with the outside region, necessitating the use of two different grids shown in Figs. 2 and 3.

3.1 Analysis of Combustion Process

During propagation of a detonation wave from initiation to the PDE exit, the computational grid shown in Fig. 2 is used, which consists of (i) a coarse Grid I

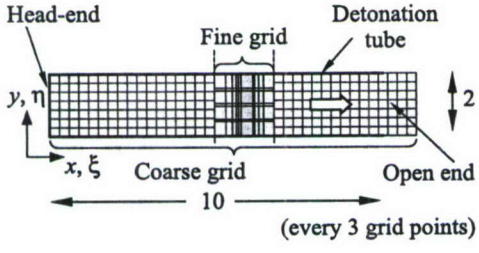

Figure 2 Two grid systems used to analyze the detonation process in the PDE. Dimensions in cm

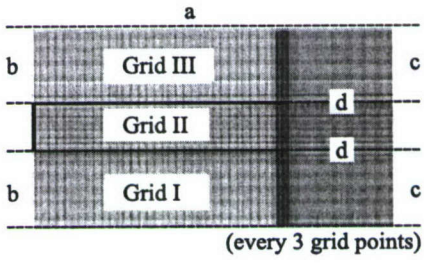

Figure 3 Three grid systems used to analyze exhaust process (outside and inside of the PDE)

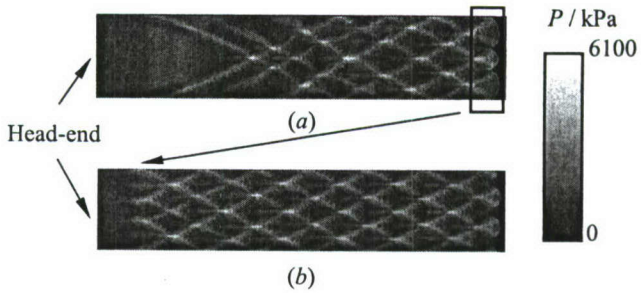

Figure 4 (*a*) Computational smoked-foil record of detonation propagation started from the 1D CJ profile. (*b*) Computational smoked-foil record of the detonation wave started from the 2D profile relocated from frame (*a*)

(spacing 1 mm, total number of grid points $\xi \times \eta = 116 \times 23$) over the entire PDE length, and (*ii*) a fine Grid II (minimum grid spacing 10 μm, total number of grid points $\xi \times \eta = 68 \times 203$) moving with the propagating detonation front. After applying the operation of Eq. (3), the conserved quantities are exchanged between Grids I and II at both ends of Grid II. Wall boundary conditions are set to be adiabatic, noncatalytic and slip. Until the time of detonation arrival, the conditions at the PDE exit are fixed as the initial conditions.

In conventional analyses of detonations with a zero DDT distance, a 1D Chapman–Jouguet (CJ) detonation profile is often used as the initial condition, which needs a few-centimeter-long run-up distance to form a 2D structure. Since this run-up distance can be too long in the present case of a short PDE with $L = 10$ cm, performance assessment could be seriously influenced. Thus, the present technique is as follows: First, a 1D CJ detonation is set up at the head-end of the PDE followed by its development to a fully 2D structure. Next, this 2D detonation profile is relocated as an initial condition to the head-end of the PDE which is filled up with an unburnt gas mixture (Fig. 4).

3.2 Analysis of Outflow Process

Grids I and III used to analyze the outflow of burnt gas, which includes the external region of PDE, are shown in Fig. 3: The coarse Grids I and III (spacing in ξ-direction is 100–1000 μm, in η-direction — 200–300 μm, total number of grid points — $\xi \times \eta = 303 \times 111$) are used only for the external region, while the medium Grid II is used for the PDE tube (spacing in ξ-direction is 100–1000 μm, in η-direction — 200 μm, total number of grid points — $\xi \times \eta = 303 \times 105$). In order to properly describe the outflow process, all three grids concentrate more grid points in the neighborhood of the open end. The wall condition is "slip," while on the boundary "a" and on the subsonic outflow boundary "c"

the pressure is set to the constant ambient value and the other quantities are extrapolated. On the supersonic outflow boundary "c," all physical quantities are extrapolated. On the supersonic inflow boundary "b," all physical quantities are fixed and correspond to the outside flow conditions, whereas on the subsonic inflow boundary "b," all quantities except for density are fixed and correspond to the outside flow condition; density is extrapolated from downstream. On the grid boundary "d," where grid points are overlapped between two grids, the conserved quantities at two outside points are replaced by the points of another grid.

4 RESULTS OF ANALYSIS

4.1 Pressure Contours

Figures 5*a*–5*c* show the calculated pressure contours for $\phi = 1.0$ at $t = 43$ μs, 80, and 310 μs, while Fig. 6 shows the longitudinal pressure distribution along the PDE centerline for the same time instants. In Fig. 5*a*, the detonation has just arrived at the PDE open end, while in Fig. 5*b* the detonation front is expanding in the external region as a nonreactive blast wave. Figure 6 shows that at $t = 80$ μs the expansion wave has started to propagate from the PDE open end toward the head-end. With time, the pressure inside the PDE tube decreases until the head-end pressure, P_h, drops down to the initial pressure, $P_h = P_i$, at $t = 310$ μs. In operation of a realistic PDE, this is the time to initiate the 2nd cycle by starting to fill a PDE with a new portion of fuel and oxidizer.

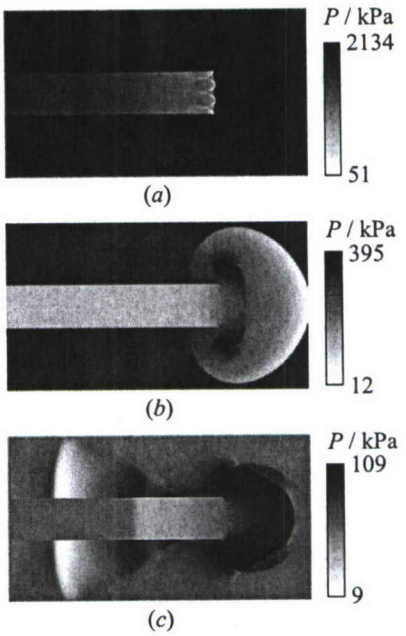

Figure 5 Calculated pressure contours at $t = 43$ μs (*a*), 80 (*b*), and 310 μs (*c*) for $\phi = 1.0$

4.2 History of Head-End Pressure

The time history of pressure at the center of the PDE head-end, $P_{h,c}$, is shown in Fig. 7 for different equivalence ratios. As shown elsewhere in computational/experimental studies of PDEs, the head-end pressure history consists of three distinct stages; (*a*) initiation, (*b*) plateau, and (*c*) relaxation. The first, initiation, stage (*a*) is caused by the detonation initiation, which strongly depends

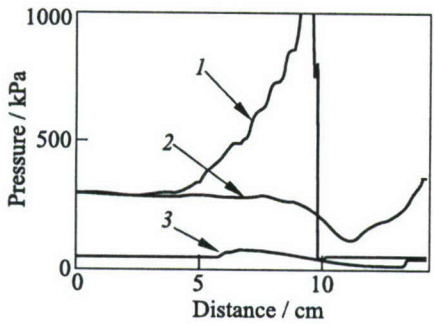

Figure 6 Calculated pressure distribution along the PDE tube centerline at $t = 43$ μs (*1*), 80 (*2*), and 310 μs (*3*) for $\phi = 1.0$

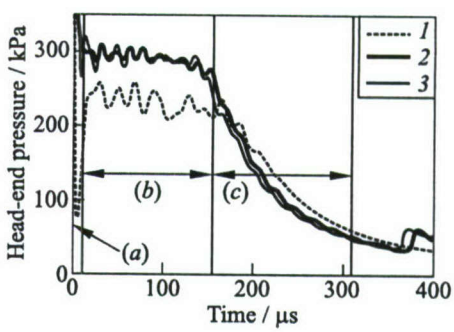

Figure 7 Calculated histories of the pressure at the center of the PDE head-end for three values of mixture equivalence ratio: *1* — $\phi = 0.5$; *2* — 1.0; and *3* — $\phi = 1.25$; characteristic stages: (*a*) initiation, (*b*) plateau, and (*c*) relaxation

on the initial conditions in the numerical analysis; a high pressure is observed when a 2D detonation profile is utilized in the beginning. The plateau period (*b*) is maintained until the expansion wave generated at the PDE open end reaches the head-end. Thereafter, the relaxation period (*c*) starts due to the action of expansion waves originating at the PDE open end. With the decrease of the equivalence ratio, ϕ, the plateau and relaxation times increase due to reduction of the detonation velocity, D_{CJ}, whereas the plateau pressure decreases, as shown in Fig. 7.

4.3 Impulse per Unit Area

The impulse per unit area, I_{cyc}, can be evaluated from the PDE head-end pressure history as:

$$I_{cyc} = \frac{1}{W} \int_0^W \int_0^{t_{cyc}} (P_h - P_i)\, dy\, dt\,, \quad [\mathrm{N{\cdot}s/m^2}] \tag{4}$$

Here, W is the head-end cross-section area and the cycle time, t_{cyc}, is the time from the start of the computation to the instant when the PDE head-end pressure reaches the initial value, P_i, i.e., the time for detonation and exhaust. Note, however, that with this approach (*i*) t_{cyc} is underevaluated because, initially, the detonation has already traveled 1 cm downstream from the PDE head-end, and (*ii*) the obtained impulse is influenced by the adopted initial condition. To eliminate these effects, the detonation initiation time and impulse were corrected, resulting in longer cycle time, t_{cyc}, as shown in Fig. 8. The corrected cycle time,

t_{cyc}, in Fig. 8 is longer for lower equivalence ratios, which favors higher impulse values. At the same time, a lower equivalence ratio is associated with a lower plateau pressure, and as a result the calculated impulse is essentially lower for lower equivalence ratios; this trend becomes dominant at lower equivalence ratios, like $\phi = 0.5$, when a 16% decrease is observed in comparison with the impulse at $\phi = 1.0$.

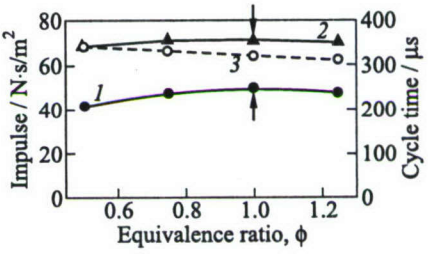

Figure 8 Calculated dependencies of I_{cyc} (*1* — 2D analysis and *2* — theory) and t_{cyc} (*3*) on equivalence ratio ϕ

Now, the present dependency of impulse on the equivalence ratio is compared with the theoretical solution of Endo & Fujiwara [7]. According to the theory, the impulse per unit area, I_{cyc} [N·s/m^2], is given by*:

$$I_{cyc} = \frac{1}{2\gamma_2}\left(\frac{\gamma_2+1}{2\gamma_2}\right)^{(\gamma_2+1)/(\gamma_2-1)}\left[3+\left(\frac{\gamma_2+1}{2}\right)^{(\gamma_2+1)/(\gamma_2-1)}\right]\rho_1 D_{CJ} L \quad (5)$$

where ρ_1 is the initial mixture density, D_{CJ} is the CJ detonation velocity, and γ_2 is the ratio of specific heats for the detonation products. Setting $\gamma_2 = 1.4$, one obtains:

$$I_{cyc} = 0.085\rho_1 D_{CJ}\,, \quad [\text{N·s/m}^2] \quad (6)$$

The result of Eq. (6) is plotted in Fig. 8 and compared with the present 2D numerical analysis. Clearly, similar trends can be seen between the theory and the current numerical analysis, i.e., the maximum impulse is attained for a stoichiometric mixture, $\phi = 1.0$ (shown by arrows), although the numerical analysis gives a considerably lower impulse. The reason for such a difference is the oversimplification of the theoretical model where, for example, the relaxation of pressure upon arrival of the expansion wave at the PDE head-end is assumed linear. The numerical analysis gives a realistic pressure relaxation that is steeper than linear, as shown in Fig. 7, due to existence of the external flowfield.

4.4 Specific Impulse

Fuel-based specific impulse, I_{sp}, can be derived from I_{cyc} by using the formula:

*See: Fujiwara, T., T. Endo, T. Miyasaka, F. Y. Zhang, and Y. Oka. Theoretical assessment of PDE performance at various flight conditions. p. 203–14. (*Editors' remark.*)

$$I_{\mathrm{sp,f}} = \frac{\text{[1-cycle impulse per unit area]}}{\text{[Supplied fuel mass per unit area} \times g\text{]}} \tag{7}$$

or

$$I_{\mathrm{sp,f}} = \frac{1}{W}\int_0^W \int_0^{t_{cyc}} (P_h - P_i)\, dy\, dt \Big/ \int_0^L \rho_{f1} g\, dx\,, \text{ [s]} \tag{8}$$

where ρ_{f1} is the fuel density during the PDE fill stage. As shown in Fig. 9, the fuel-based specific impulse $I_{\mathrm{sp,f}}$ strongly depends upon ϕ in contrast with I_{cyc}, due to the dependence of ϕ on ρ_{f1}. Thus, $I_{\mathrm{sp,f}}$ becomes higher for lower ϕ, e.g., at $\phi = 0.5$ the value of the $I_{\mathrm{sp,f}}$ is by 1770 s higher than $I_{\mathrm{sp,f}}$ for the stoichiometric mixture. This is an interesting result for selecting a cruise condition.

4.5 Thrust Density

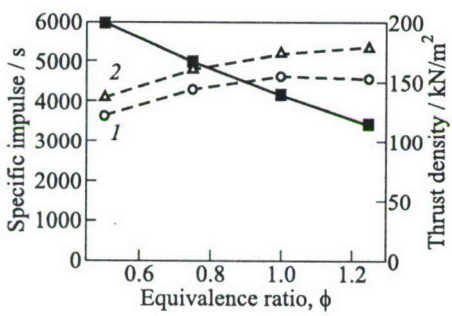

Figure 9 Calculated fuel-based specific impulse, $I_{\mathrm{sp,f}}$, (solid curve) and thrust density (dashed curves) (*1* — 2D analysis and *2* — theory at $\tau_f = 0$) as functions of equivalence ratio, ϕ

The thrust density, p_w, (average thrust per unit area) can be derived from I_{cyc} using the following equation:

$$p_w = \frac{I_{\mathrm{cyc}}}{t_{\mathrm{cyc}} + \tau_f} \tag{9}$$

where τ_f denotes the characteristic time of PDE fill with the fresh fuel–air mixture, which depends upon the geometry of air intake. Calculated thrust density at $\tau_f = 0$ is plotted in Fig. 9. Assumption of $\tau_f = 0$ gives the upper limit for p_w. Similar to the dependencies for the impulse per unit area, I_{cyc}, and the cycle time, t_{cyc}, given in Fig. 8, the dependence of thrust density, p_w, on the equivalence ratio, ϕ, is weak.

At $\tau_f = 0$, the theory [7] gives the relationship:

$$p_w = \frac{1}{4\gamma_2}\left(\frac{\gamma_2+1}{2\gamma_2}\right)^{(\gamma_2+1)/(\gamma_2-1)} \frac{3 + ((\gamma_2+1)/2)^{(\gamma_2+1)/(\gamma_2-1)}}{1 + ((\gamma_2+1)/2)^{(\gamma_2+1)/(\gamma_2-1)}} \rho_1 D_{\mathrm{CJ}}^2 \tag{10}$$

which at $\gamma_2 = 1.4$ transforms to

$$p_w = 0.106 \rho_1 D_{\mathrm{CJ}}^2 \tag{11}$$

According to Fig. 9, the theoretical value of thrust density, p_w, is higher than the numerical one. The reason for the arising difference is the same as for the

impulse per unit area. However, the difference between the predicted p_w values is only 10%–20%, which is less than the difference in the predicted values of the impulse per unit area shown in Fig. 8. At $\phi > 0.75$, both theory and 2D numerical simulation give weak dependence of p_w on ϕ.

4.6 Thrust in Real Flight

As indicated by the theoretical result of Eq. (10), which is based upon the assumption of a developed CJ detonation with zero DDT distance, the thrust density p_w is independent of the PDE length. This is numerically verified by Kawai & Fujiwara [8, 9], who varied the PDE length between 10 and 40 cm in 2D calculations. In the present analysis, the PDE length is short (10 cm), but the results are in line with the earlier findings.

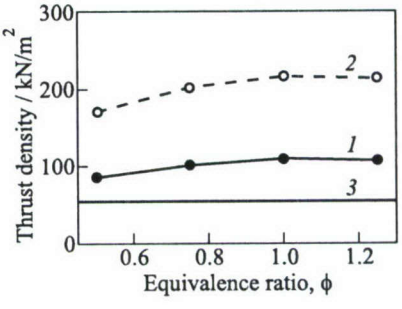

Figure 10 Calculated thrust density (at nonzero τ_f) of the PDE (*1* — extrapolated for initial pressure of 101 kPa; and *2* — 2D analysis for initial pressure of 51 kPa) compared with turbofan VP2500 (*3*)

To introduce realistic values for the fuel fill time, τ_f, which has been assumed zero in Eqs. (10) and (11), the numerical results of Kawai & Fujiwara [8, 9] were used. It has been shown that the PDE fill time with fuel–air mixture from the neighborhood of the PDE head-end is always 30% of a cycle time (assuming zero DDT length), irrespective of the PDE length*. The corrected thrust density, p_w, is shown in Fig. 10, where the value for initial pressure of $p_1 = 101$ kPa is extrapolated by using the initial pressure dependency of thrust density given by Eq. (11);

$$p_w \sim \rho_1 \sim P_1 \tag{12}$$

Interestingly, a PDE operating on the hydrogen–air mixture of initial pressure of 1 atm shows the thrust density 4 times higher than turbofan engine VP2500.

It is worth to note that all the results obtained are based on the assumption of zero DDT distance. Inclusion of a finite DDT distance into theoretical/numerical analyses would certainly lower the PDE performance: the impulse per unit area and thrust density. Only direct detonation initiation, i.e., zero DDT distance, can be relevant to the results of present assessments.

*See also Fujiwara, T., and S. Kawai. 2002. Numerical analysis of oxyhydrogen pulse detonation engine cycles. In: *Advances in confined detonations.* Eds. G. Roy, S. Frolov, R. Santoro, and S. Tsyganov. Moscow, Russia: Torus Press. 213–20. (*Editors' remark.*)

5 CONCLUDING REMARKS

The performance of an idealized, single-tube, hydrogen–air PDE has been evaluated using 2D numerical simulation. A particular emphasis has been given to the effect of open-boundary conditions and reactive mixture equivalence ratio on the specific impulse and time-averaged thrust density. It has been shown that the PDE impulse attains a maximum value for the stoichiometric mixture composition, while the specific impulse increases for the lower equivalence ratio. A comparison of time-averaged thrust density of PDE and typical turbofan engine VP2500 indicates higher efficiency of the former.

REFERENCES

1. Kailasanath, K.. 2001. A review of PDE research — performance estimates. AIAA Paper No. 2001-0474.
2. Taki, S., and T. Fujiwara. 1978. Numerical analysis of two-dimensional nonsteady detonations. *AIAA J.* 16:73–77.
3. Matsuo, A., K. Fujii, and T. Fujiwara. 1995. Flow features of shock-induced combustion around projectile traveling at hypervelocities. *AIAA J.* 33.
4. Fujiwara, T., K. Fukiba, and T. Miyasaka. 2001. Efficiency study of PDE based on quasi-one-dimensional calculation of detonation. *Chemical Physics Reports* 6:99–104.
5. Jachimowski, J. 1988. An analytical study of the hydrogen–air reaction mechanism with application to scramjet combustion. NASA TP2791.
6. Yee, H. C. 1987. Upwind and symmetric shock-capturing schemes. NASA Technical Memorandum 89464.
7. Endo, T., and T. Fujiwara. 2002. A simplified analysis on a pulse detonation engine model. *Transactions of Japan Society for Aeronautical and Space Science* 44(146):217–22.
8. Kawai, S., and T. Fujiwara. 2002. Numerical analysis of 1st and 2nd cycles of oxyhydrogen PDE. AIAA Paper No. 2002-0929.
9. Kawai, S., and T. Fujiwara. 2002 (submitted). Numerical analysis of 1st and 2nd cycles of oxyhydrogen PDE. *AIAA J.*

CALCULATION OF THRUST PERFORMANCE OF AN IDEAL PULSE DETONATION ENGINE

V. V. Mitrofanov and S. A. Zhdan

Quasi-steady-state and two-dimensional (2D) unsteady formulations of the pulse detonation engine (PDE) operating cycle problem were formulated. Calculations of thrust characteristics were performed under certain assumptions that idealize real processes. It was found that at flight Mach number M = 0–3.6 and compression ratio p_2/p_1 = 1–80, PDE thrust characteristics are always better than those of a ramjet and a one-spool turbojet. As for specific impulse, the ideal PDE is only second after the ideal by-pass turbojet with a high by-pass ratio, but surpasses the latter in terms of the head thrust. As the compression ratio p_2/p_1 increases, the advantage of PDE gradually decreases.

1 INTRODUCTION

Pulse detonation engines are considered promising for air-breathing propulsion at flight Mach number M = 0–3. Various designs of such engines were proposed [1–6]. In the simplest version, PDE consists of the following units: (*i*) air inlet (AI) for continuous intake and compression of air from the ambient atmospheric pressure p_1 to a certain stagnation pressure p_2; (*ii*) receiver, where the air supplied by AI is in a stagnant state at pressure p_2; (*iii*) valve distribution system which directs air from the receiver to detonation chambers in a given time sequence; ($i\nu$) detonation chamber unit (DC) which consists of a bundle of identical cylindrical tubes with supersonic nozzles at the exit; (ν) fuel tanks and systems of fuel injection in DC correlated with air injection; and (νi) systems for detonation initiation in DC.

In all DCs, the following identical sequence of processes occurs cyclically: filling the volume with compressed air and addition of fuel to form a charge of explosive fuel–air mixture (FAM); detonation of FAM with the closed inlet valve, accompanied by a sudden pressure rise; and efflux of the detonation products through the nozzle, providing jet momentum. Jet thrust pulsations and noise effects may be reduced by shifting the phase of the processes in different DCs. Air in the AI is compressed by dynamic head pressure and/or a compressor. In

general, the PDE under consideration corresponds to schematics in [4–6]. In the present work, the thrust characteristics of such a PDE were calculated under certain assumptions idealizing the real processes.

2 PROBLEM FORMULATION

To define thrust characteristics of the PDE described above, consider two mathematical models of the operation cycle under the following assumptions which idealize real processes. Air and detonation products are assumed to be ideal gases with constant specific heats (the ratio $\gamma = C_p/C_v$). Air compression in the AI and its flow in DC, as well as exhaust of the detonation products are isentropic without friction and heat loss to the walls. The compressor in AI (if present) has a 100% efficiency and is actuated by a separate engine, which does not produce own thrust and consumes the same fuel with a 100% efficiency. Detonation of FAM is simulated by instantaneous release of energy Q per unit mass of air in the chamber segment of length $L_0 \leq L$, where L is the total length of DC.

Quasi-Steady-State Model (Model 1)

First, consider a quasi-steady-state formulation of the problem. In addition to the assumptions listed above, it is assumed that the chamber and nozzle flows are one-dimensional and divided into three stages. At stage 0, after instantaneous energy release ($\rho = const$) on the segment $x \in (0, L_0)$, the pressure in DC instantaneously levels out at a value of p_3 that corresponds to the conservation of entropy of detonation products and total internal energy of the gases in the chamber. At stage I ($0 < t \leq t_1$), there is a quasi-steady-state gas outflow through the nozzle at chamber pressure $p(t)$, which gradually decreases from p_3 to p_2. At $t_1 < t \leq t_2$, a steady-state stage II takes place. At this stage, the remaining products are expelled from the chamber by the next portion of air and FAM at constant pressure p_2 and constant velocity of gas motion inside the chamber, $u_c \ll c_c$. The cross-section areas of the nozzle throat and exit are selected such that the nozzle-exit pressure at stage II is equal to p_1 and the condition $u_c \ll c_c$ still holds. Under these assumptions and at $L_0 = L$ (i.e., the fill ratio $\xi = L_0/L = 1$), the thrust characteristics of PDE are determined by the following set of algebraic equations:

$$\frac{p_2}{p_1} = \pi\,; \quad \frac{\rho_2}{\rho_1} = \pi^{1/\gamma}\,; \quad \frac{c_2^2}{c_1^2} = \pi^{1-1/\gamma}\,; \quad \rho_3 = \rho_2$$

$$\frac{p_3}{p_2} = \frac{c_3^2}{c_2^2} = 1 + \gamma(\gamma - 1)\frac{Q}{c_2^2}; \quad c(t) = c_3(1 + at)^{-1}$$

$$a = \frac{\gamma - 1}{2}\left(\frac{2}{\gamma + 1}\right)^{0.5(\gamma+1)/(\gamma-1)} \frac{c_3 S_{\min}}{LS_c}; \quad \frac{p(t)}{p_3} = \left(\frac{c(t)}{c_3}\right)^{2\gamma/(\gamma-1)}$$

$$t \le t_1 = \frac{1}{a}\left(\left(\frac{p_3}{p_2}\right)^{0.5(1-1/\gamma)} - 1\right); \quad t_2 = \frac{\gamma - 1}{2a}\left(\frac{p_3}{p_2}\right)^{0.5(1-1/\gamma)}$$

$$\nu = (t_1 + t_2)^{-1}; \quad \mathrm{M}_4^2 = \frac{2}{\gamma - 1}\left(\pi^{1-1/\gamma} - 1\right) + \frac{u_c^2}{c_4^2}$$

$$c_4^2 = c_3^2\left(\frac{p_1}{p_3}\right)^{1-1/\gamma}$$

$$\frac{J}{c_1} = \frac{2}{\gamma + 1}\left(\mathrm{M}_4 + \frac{1}{\gamma \mathrm{M}_4}\right)\frac{c_3}{c_2}\left(1 - \left(\frac{c_2}{c_3}\right)^{1+1/\gamma}\right)$$

$$+ \mathrm{M}_4\left(\frac{c_2}{c_3}\right)^{1/\gamma}\left(1 - \frac{t_1}{\gamma \mathrm{M}_4^2 t_2}\right) - \mathrm{M}_1$$

$$\frac{F}{S_c p_1} = \frac{\nu J \rho_2 L}{p_1}; \quad \frac{c_1^2 \mathrm{M}_1^2}{2} + \frac{c_1^2}{\gamma - 1} + \frac{N}{G} = \frac{\gamma + 1}{2(\gamma - 1)}c_2^2$$

where p, ρ, c, and u are the pressure, density, speed of sound, and flow velocity, respectively; $\mathrm{M} = u/c$ is the Mach number; subscript 1 refers to external air parameters; subscript 2 refers to stagnation air parameters in the receiver; subscript 3 corresponds to chamber parameters at the beginning of stage I; subscript 4 denotes flow parameters at the nozzle exit, subscript c denotes chamber parameters at stage II; the values without subscripts characterize a variable state in the chamber at stage I; G is the mass of the air consumed by PDE per second; N is the compressor engine power; t_1 and t_2 are the durations of stages I and II, respectively; ν is the operation frequency; J is the mean impulse per unit mass of air passing through the chamber (air-based specific impulse); $S_{\min}$ is the cross-section area of the nozzle throat; and $F/(S_c p_1)$ is the dimensionless jet thrust per unit cross-section area of the DC.

Two-Dimensional Unsteady Model (Model 2)

In order to check the validity of the assumptions adopted in the quasi-steady-state model 1, the following problem for an ideal PDE was formulated and solved numerically in a 2D unsteady formulation. A detonation chamber is assumed

to be a cylindrical tube of length L and radius r_c with a supersonic exit nozzle (throat radius $r_{\min}$). The ambient medium is air with pressure p_1 and temperature T_1. At $t = 0$, the entire tube (or its part $0 < x < L_0$) is filled with FAM at pressure p_2 and temperature T_2. The inlet valve in the tube (located at $x = 0$) is closed. Next, there is an instantaneous explosion ($\rho = const$) of FAM with the heat effect per unit mass of the mixture Q, and gas flows out through the nozzle. At $t = t_1$, when the pressure at the inlet edge of the tube becomes equal to the receiver pressure p_2, the valve opens and all residual detonation products are expelled from the chamber by the next portion of air and FAM. At $t = t_2$, the contact surface between the fresh mixture and detonation products reaches the coordinate $x = L$, the valve is closed and an instantaneous explosion of FAM in the cylindrical tube (or in its part $0 < x < L_0$) takes place again, i.e., the new cycle starts. The task is to determine the efflux dynamics and jet momentum over the period $\Delta t = t_1 + t_2$. The dynamics of the gas in the chamber is governed by the following equations:

$$(\rho r)_t + (\rho u r)_x + (\rho v r)_r = 0$$

$$(\rho u r)_t + [(\rho u^2 + p) r]_x + (\rho u v r)_r = 0$$

$$(\rho v r)_t + (\rho u v r)_x + [(\rho v^2 + p) r]_r = p$$

$$(E r)_t + [(E + p) u r]_x + [(E + p) r]_r = 0$$

where ρ is the density; p is the pressure; u and v are the components of the velocity vector; $E = \rho[e + (u^2 + v^2)/2]$; and $e = p/((\gamma - 1)\rho)$. The behavior of the gas outside the chamber was considered in a bounded region with the volume approximately equal to 10^3 of the chamber volume, i.e., at $r = R$ ($R \approx 10$–$15 r_c$), undisturbed parameters of the atmosphere were kept.

All variables of the gas-dynamic equations were normalized by the initial parameters of relevant dimensions: p_1, ρ_1, L, $u_1 = \sqrt{p_1/\rho_1}$, and L/u_1. The formulated problem has 7 dimensionless similarity parameters:

$$\pi = \frac{p_2}{p_1}, \quad \theta = \frac{T_2}{T_1}, \quad \xi = \frac{L_0}{L}, \quad q = \frac{Q}{u_1^2}, \quad \gamma, \quad \delta = \frac{r_{\min}}{r_c}, \quad \frac{r_c}{L}$$

They are determined from the initial stagnation parameters, FAM characteristics, and the chamber geometry. For the correct comparison of the 2D unsteady model with the quasi-steady-state approximation, the numerical values of the first six parameters were the same as in the calculations with model 1. The value of parameter $r_c/L = 1/12$ was fixed.

3 RESULTS OF CALCULATIONS

Model 1. In the calculations, the following values of governing parameters were used: $\gamma = 1.4$, $c_1 = 300$ m/s, $Q/c_1^2 = 18.75$, and $u_c = c_1/3$. The value of $\pi = p_2/p_1$ was varied. The flight Mach number was varied from 0 to the value $M_1 = M_4$ corresponding to air compression in an ideal air inlet of a ramjet without a compressor. Some results of calculations are shown in Table 1.

Table 1 Predicted specific impulse and thrust of the ideal PDE, ramjet, and turbojet (the results of calculations based on unsteady 2D model are given in brackets)

π	$\frac{p_3}{p_1}$	M_4	ν, Hz	J/c_1				$F/(Sp_1)$, (PDE)	
				at $M_1 \ll 1$		at $M_1 = M_4$			
				PDE	TJE	PDE	Ramjet	$M_1 \ll 1$	$M_1 = M_4$
2	19.2	1.05	42(40)	3.87(3.68)	2.80	2.82	1.76	1.24(0.74)	0.905
3	26	1.36	43(43.5)	4.20(4.03)	3.46	2.84	2.10	1.85(1.17)	1.25
4	32.2	1.56	43.6(44)	4.44(4.29)	3.83	2.88	2.27	2.43(1.56)	1.58
6	43.8	1.83	44.4(46)	4.75(4.61)	4.29	2.92	2.46	3.54(2.33)	2.18
10	64.4	2.16	46(48)	5.11(4.98)	4.77	2.95	2.61	5.72(3.80)	3.30
20	109	2.60	48(52)	5.55(5.48)	5.32	2.95	2.72	10.66(7.33)	5.66
40	186	3.06	50(55)	5.97(6.03)	5.81	2.91	2.75	19.5(14.1)	9.5
80	320	3.54	52(59)	6.38(6.67)	6.27	2.84	2.73	35.9(27.6)	16.0

Analysis of dependencies of J/c_1 for PDE (at $M_1 = M_4$) on the compression ratio π at fixed Q (Fig. 1) demonstrates a nonmonotonous variation of the specific impulse with π. In the range $10 < \pi < 20$, the specific impulse for PDE reaches the maximum. The thrust characteristics of PDE are compared with the characteristics of a ramjet:

$$\frac{J}{c_1} = M_4\sqrt{1+\frac{B}{\kappa}} - 1$$

$$B = \frac{(\gamma-1)Q}{c_1^2}$$

$$\kappa = \left(\frac{p_2}{p_1}\right)^{1-1/\gamma}$$

calculated under similar idealizations and the same compression ratios $\pi = p_2/p_1$. It

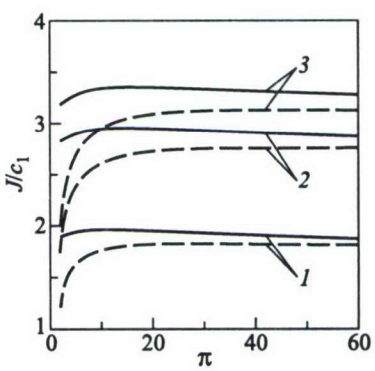

Figure 1 Predicted dependence of the normalized specific impulse, J/c_1, for PDE (solid curves) and ramjet (dashed curves) on the compression ratio, π: *1* — $Q = 1$ MJ/kg; *2* — 1.6875; and *3* — $Q = 2$ MJ/kg

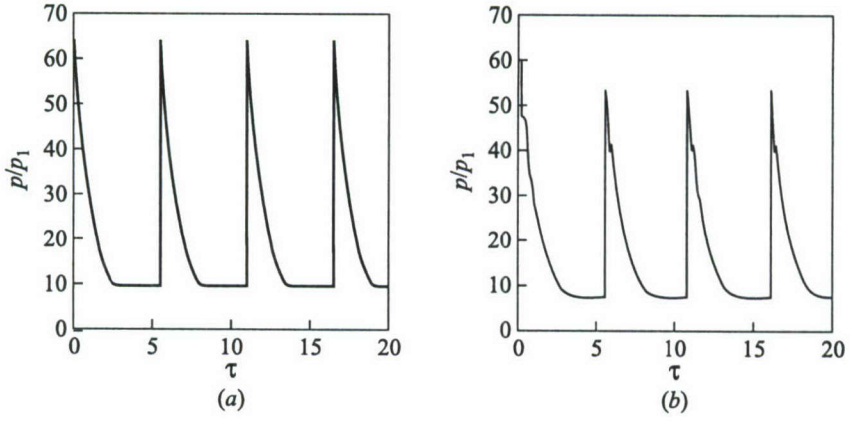

Figure 2 Predicted dependence of the normalized inlet pressure, p/p_1, in the detonation chamber on nondimensional time, $\tau = t\sqrt{p_1/\rho_1}/L$ ($\pi = 10$; $\xi = 1$; $\delta = 0.46$); (a) model 1; and (b) model 2

is assumed that in a ramjet, combustion occurs without loss of stagnation pressure. The results of calculations at M = 0–3.6 and $p_2/p_1 = 1$–80 show that the thrust characteristics of the PDE are always better than those of a ramjet and a one-spool turbojet. As to specific impulse, an ideal PDE is only second after the ideal by-pass turbojet with a high by-pass ratio, but surpasses the latter in terms of the head thrust (last column of Table 1). At the same time, when the compression ratio p_2/p_1 is increased, the advantage of PDE gradually decreases.

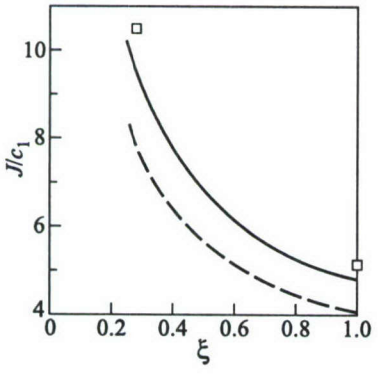

Figure 3 Predicted dependence of the PDE normalized specific impulse, J/c_1, on chamber fill ratio, $\xi = L_0/L$, at fixed $\pi = 10$. Model 1: □; model 2: solid curve — $\delta = 0.46$ and dash curve — $\delta = 1$

Model 2. As a result of the numerical solution of the 2D unsteady problem, distributions of gas-dynamics parameters in the chamber at different time t and time dependencies of pressure $p(t)$ at the tube entry ($x = 0$), as well as mass flux $M(t) = \int_s \rho u\, ds$ and the momentum flux $I(t) = \int_s (p + \rho u^2 - p_1)\, ds$ at the nozzle exit were obtained. It is found that after the first irregular cycle, the solution of the unsteady problem becomes periodic with a constant period Δt. Some results of calculations are shown in Table 1 and in Figs. 2 and 3. The calculations relevant to model 2 show that the specific impulse (per unit mass of

air) decreases by 5% because of intrinsic flow unsteadiness and nonuniformity. Obviously, these losses can be reduced by nozzle optimization. The reduction of thrust is more considerable, up to 40%. This is caused by a decrease in pressure, density, and, hence, mass of the gases filling the chamber in each cycle, while the operating frequency is kept constant. The decrease of the average pressure in the filled chamber is confirmed by comparison of dependencies $p(t)$ (see Fig. 2), obtained in two formulations of the problems for identical initial data.

Calculations show that with decreasing the fill ratio ξ, the air-based specific impulse, J, of PDE increases (Fig. 3) and the thrust, F, and cycle frequency, ν, decrease. It is worth noting that in the absence of the nozzle (i.e., at $\delta = 1$ or $S_{\min} = S_c$), the unsteady calculations give 18% decrease in the specific impulse (dashed curve in Fig. 3). At $\xi = 1/4$–$1/3$, $\pi = 4$–40, and $M_1 \ll 1$, the values of the specific impulse of the order of $J \approx 3000$ m/s were obtained which correspond to the thrust specific fuel (propane) consumption of about 0.12 kg/h/N.

4 CONCLUDING REMARKS

It was found that at M = 0–3.6 and $p_2/p_1 = 1$–80, thrust characteristics of the idealized PDE are always better than those of the idealized ramjet and one-spool turbojet. The encouraging agreement of results obtained by using models 1 and 2 indicates that algebraic formulae of quasi-steady-state model provide good estimates for the specific impulse J (within 5%) of PDE. Therefore, in order to find the optimal thrust characteristics of an ideal PDE, model 1 can be recommended as the starting approach without time consuming 2D calculations. Model 2 can be recommended for the subsequent stages of PDE design optimization to determine more precisely thrust characteristics.

ACKNOWLEDGMENTS

This work was supported by the Russian Foundation for Basic Research (Grant No. 02-01-00551).

REFERENCES

1. Frolov, S. M., V. Ya. Basevich, A. A. Belyaev, and M. G. Neuhaus. 1999. Application of fuel blends for controlling detonability in pulsed detonation engines. In: *Gaseous and heterogenous detonations: Science to applications*. Eds. G. Roy, S. Frolov, K. Kailasanath, and N. Smirnov. Moscow, Russia: Enas Publ. 313–30.

2. Desbordes, D. 2000. Pulsed detonation propulsion: Key issues. In: *Control of detonation processes*. Eds. G. Roy, S. Frolov, D. Netzer, and A. Borisov. Moscow, Russia: Elex-KM Publ. 166–71.

3. Furlong, E. R., I. A. Leyva, and S. R. Sanderson. 2000. MEMS-based pulse detonation engine for small scale propulsion applications. In: *Control of detonation processes*. Eds. G. Roy, S. Frolov, D. Netzer, and A. Borisov. Moscow, Russia: Elex-KM Publ. 219–21.

4. Eliseev, Yu. S., E. F. Manushin, V. E. Mikhal'tsev, M. I. Osipov, and I. G. Surovtsev. 2000. *Theory and design of gas-turbine and combined installations*. 2nd issue. Part 2. Moscow, Russia: Bauman Moscow State Technical University Publ.

5. Schauer, F., J. Stutrud, and R. Bradley. 2001. Detonation initiation studies and performance results for pulsed detonation engine applications. AIAA Paper No. 2001-1129.

6. Remeev, N. Kh., V. V. Vlasenko, R. A. Khakimov, and V. V. Ivanov. 2001. Condition and problems of detonation ramjet technology development. *Chemical Physics* 20(7):119–29.

MODELING OF MULTITUBE PULSE DETONATION ENGINE DYNAMICS

F. H. Ma, J.-Y. Choi, Y. Wu, and V. Yang

This paper deals with the modeling and simulation of the thrust chamber dynamics of air-breathing pulse detonation engines (PDEs). The system under consideration includes a supersonic inlet, a rotary valve, a multitube combustor, and a common nozzle. The analysis treats the conservation equations of mass, momentum, energy, and species concentration in two dimensions. Chemical kinetics is modeled using a one-step overall reaction scheme, which is calibrated with a detailed model for a stoichiometric hydrogen–air system. The governing equations and their associated boundary conditions are numerically solved by means of a recently developed Space–Time Conservation Element/Solution Element (CE/SE) method, which circumvents the deficiencies of existing numerical methods for treating detonation waves and shock discontinuities. The resultant computer code is further parallelized using the Message-Passing-Interface (MPI) library to improve its efficiency. The combustion and gasdynamic processes involved in a multitube PDE are studied in detail. The effects of operation frequency and valve close-up time on the engine propulsive performance are examined. Calculations are also conducted for a single-tube PDE for comparison. Results show that the multitube design substantially modifies the system dynamics and reduces the degree of unsteadiness within the engine.

1 INTRODUCTION

Pulse detonation engines are unsteady propulsion devices that produce periodic impulse by utilizing repetitive detonation. They differ from conventional propulsion engines in two major ways: unsteady operation and detonation combustion. Recently, PDEs have attracted considerable attention because of their advantages in thermodynamic cycle efficiency, hardware simplicity, operation stability, and reliability [1, 2].

A typical PDE cycle operation includes four basic processes [1, 2]: initiation of detonation wave, propagation of detonation wave, exhaust of combustion

products, and refilling of reactants. Studies on this subject have been conducted for several decades. The first reported work on intermittent detonation is attributed to Hoffman [3] in 1940. Both acetylene and benzine fuels were employed with oxygen. The work was terminated during World War II. Nicholls *et al.* [4] and Dunlap *et al.* [5] reinitiated the effort in the 1950s. They performed a series of single-shot detonation experiments with hydrogen–oxygen, hydrogen–air, acetylene–oxygen, and acetylene–air mixtures in a 6-foot tube. In a similar setup, Krzycki [6] performed an experimental investigation using propane–air mixtures and concluded that the intermittent detonation device was not promising for propulsion application. Possibly due to this conclusion, most experimental works related to PDEs were suspended in the late 1960s. Helman *et al.* [7] reexamined the PDE concept in the late 1980s, carrying out experiments using ethylene–oxygen and ethylene–air mixtures. The self-aspirating feature of an air-breathing PDE was successfully demonstrated. Since then, there has been a growing interest in PDEs as a propulsion technology for both aircraft and missile systems. Several reviews have been available in the literature. Eidelman *et al.* [8, 9] reviewed the progress made up to the 1980s. Kailasanath conducted a series of reviews, such as the application of detonation to propulsion [10, 11], PDE performance estimates [12], and PDE nozzle effects [13]. A more recent review by Kailasanath [14] discussed several important topics, including atomization, fuel–oxidizer mixing, detonation initiation, multiphase detonations, diagnostics of detonation flows, and numerical simulations.

Numerical investigation of PDE system performance and dynamics has been seriously attempted. Most of the previous studies, however, were limited to the behavior of a single-tube detonation chamber. Research on multitube PDEs commenced just recently. Mohanraj *et al.* [15] presented an approximate model for a PDE with five detonation tubes. Time accurate one-dimensional solutions of the flowfield were obtained for only one tube. Their results showed that the filling process in a multitube PDE could be markedly different from that for a single-tube PDE. Although this approach saves computational effort, the resultant error due to the model approximation is difficult to estimate and may likely be quite large. Ebrahimi *et al.* [16] conducted two-dimensional (2D) simulations for a dual-tube PDE, but with only one shot of operation. The pressure induced by the detonation in the neighboring tube is nearly as large as that produced by the detonation itself. The shock wave produced by the detonation is sufficient to initiate combustion in the adjacent tube filled with fresh propellants.

In view of the limitations of existing studies, the present paper attempts to investigate the system performance and dynamics of multitube air-breathing PDEs with repetitive operation by means of 2D simulations. Figure 1 shows schematically the physical model under consideration. It includes a co-axial supersonic inlet with mixed compression, a rotary valve, a combustion chamber consisting of multiple detonation tubes, and a common convergent-divergent (CD) nozzle. The inlet is designed for the flight condition with an altitude of 9.3 km and a

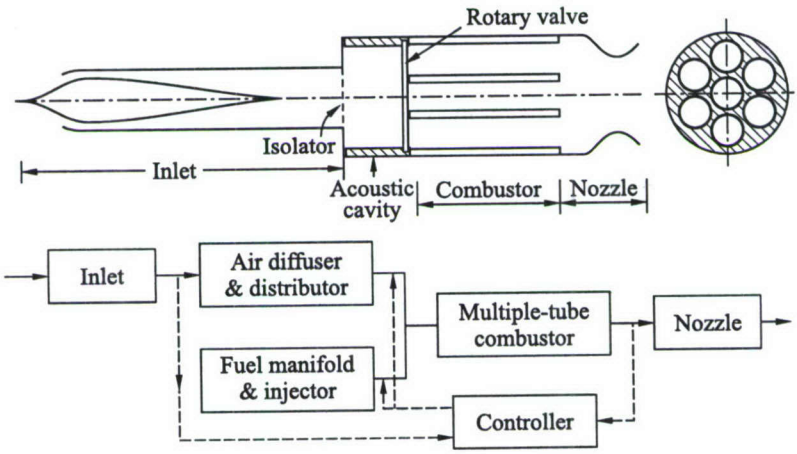

Figure 1 Supersonic air-breathing pulse detonation engine

Mach number of 2.1. A comprehensive study of the inlet aerodynamics is given in [17, 18]. In the following sections, the behaviors of the single-tube PDEs are first studied to serve as a basis for assessing the performance of various multi-tube designs. Analyses are then extended to multitube PDEs, with emphasis placed on the underlying combustion and gasdynamic processes. The effects of operation sequence and cycle frequency on the system performance are examined in detail.

2 THEORETICAL FORMULATION

The analysis is based on the 2D conservation equations of mass, momentum, and energy and takes into account finite-rate chemical kinetics. Diffusive effects are neglected in the current study because of their minor roles in determining the overall flow dynamics and system performance of PDEs. If the chemical reaction rate is expressed by a single progress variable, the resultant governing equations can be written in the following vector form:

$$\frac{\partial Q}{\partial t} + \frac{\partial E}{\partial x} + \frac{\partial F}{\partial y} = H \tag{1}$$

where the dependent variable vector Q, convective flux vectors E, F, and source vector H are defined as:

$$Q = \begin{bmatrix} \rho \\ \rho u \\ \rho v \\ \rho e_t \\ \rho Z \end{bmatrix}, \quad E = \begin{bmatrix} \rho u \\ \rho u^2 + p \\ \rho uv \\ u(\rho e_t + p) \\ \rho uZ \end{bmatrix}, \quad F = \begin{bmatrix} \rho v \\ \rho uv \\ \rho v^2 + p \\ v(\rho e_t + p) \\ \rho vZ \end{bmatrix}, \quad H = \begin{bmatrix} 0 \\ 0 \\ 0 \\ 0 \\ \dot{\omega} \end{bmatrix} \tag{2}$$

In the above equations, ρ, u, v, e_t, and Z represent the density, x-component velocity, y-component velocity, specific total energy, and progress variable (i.e, mass fraction of reactant), respectively. The pressure p is obtained through the equation of state,

$$p = (\gamma - 1)\,\rho \left[e_t - \frac{u^2 + v^2}{2} - Zq \right] \tag{3}$$

where γ is the specific heat ratio and q the heat release per unit mass of reactant. For a one-step irreversible reaction, the mass production rate of reactant $\dot{\omega}$ is

$$\dot{\omega} = -K\rho Z \exp\left(-\frac{E_a}{RT}\right) \tag{4}$$

where K is the preexponential factor, T the temperature, E_a the activation energy per unit mass of reactant, and R the gas constant.

This kind of simplified approach is commonly referred to as the Zel'dovich–von Neumann–Döring (ZND) model in the literature. The five parameters involved for a stoichiometric H_2–air system, $\gamma = 1.29$, $R = 368.9$ J/(kg·K), $q = 2.720 \cdot 10^6$ J/kg, $E_a = 4.794 \cdot 10^6$ J/kg, $K = 7.5 \cdot 10^9$ s^{-1}, are obtained by comparing the model results with the chemical equilibrium calculations in terms of detonation wave properties [19]. The first three are thermodynamic parameters determining the Chapman–Jouguet (CJ) state of detonation. The remaining two are chemical kinetic parameters adopted from [20]. Their primary influence appears in the internal structure of a detonation wave front, with a minor effect on the overall flow evolution.

3 NUMERICAL APPROACH

The governing equations outlined in the previous section are solved numerically using a recently developed CE/SE method. The scheme offers many unique features, such as a unified treatment of space and time, introduction of solution element and conservation element to construct simple stencil, mesh values of dependent variables and their derivatives being considered as independent variables to be solved simultaneously, and no interpolation or extrapolation required to evaluate fluxes at the interface. Furthermore, the CE/SE method has extremely low numerical dissipation and dispersion errors, and thus circumvents

the deficiencies of existing numerical methods for treating detonation waves and shock discontinuities. Detailed descriptions of the CE/SE methods can be found in [21–25].

For a chemically reacting flow, the time scales associated with chemical reactions are much smaller than those with flow evolution, thereby resulting in stiff source terms. The ensuing numerical difficulty can be circumvented using a fractional time-step technique detailed in [24]. The code is also equipped with a 2D unstructured triangular mesh solver to facilitate the calculation of complex configurations. Further efficiency is achieved by parallelizing the code based on the MPI library and a domain-decomposition technique [26]. All of the calculations were executed on an in-house PC cluster consisting of 64 Pentium II processors.

4 SINGLE-TUBE PDE ANALYSIS

The analysis was first performed for a single-tube air-breathing PDE with a CD nozzle. Figure 2 shows the schematic of the computational domain. An external region is included to circumvent the difficulty of specifying boundary conditions at the nozzle exit. The computational domain is discretized into 554,228 unstructured triangular grid cells. The flight condition considered herein has an altitude of 9.3 km and a flight Mach number of 2.1, at which the static pressure, static temperature, total pressure, and total temperature are 0.29 atm, 228 K, 2.65 atm, and 428 K, respectively. The total pressure at the entrance of the detonation tube is 2.12 atm based on a previous study of the inlet aerodynamics [17, 18].

The valve, located at the entrance of the detonation tube, is assumed to be either fully open or fully closed. The engine operation sequence is controlled by three time periods: the period (τ_{close}) during which the valve is closed (including the time for detonation initiation, detonation propagation, and blow-down), the purging period (τ_{purge}) during which a small amount of cold air is injected into the tube to prevent preignition, and the refilling period (τ_{refill}), as shown schematically in Fig. 3. The sum of these three periods equals to the operation cycle time (τ_{cycle}), i.e., $\tau_{\text{cycle}} = \tau_{\text{close}} + \tau_{\text{purge}} + \tau_{\text{refill}}$. In the present study, the purging period is fixed at 0.1 ms for all of the calculations.

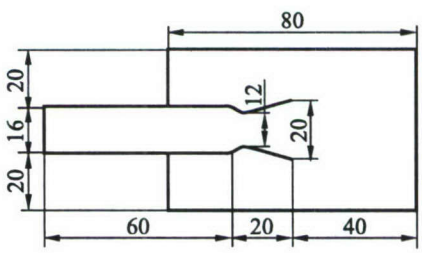

Figure 2 Computational domain for single-tube PDE. Dimensions in cm

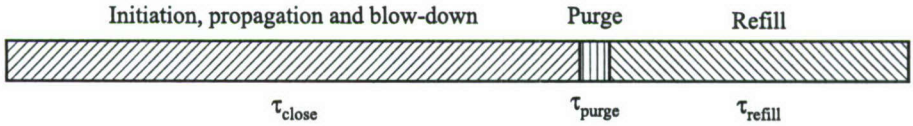

Figure 3 Time periods during one cycle of operation

The boundary conditions at the head-end of the detonation tube are specified according to the engine operation. During the valve close-up stage, the head-end is modeled as a rigid wall. During the purging stage, the total temperature and the total pressure are specified based on the inlet flow condition, and the reactant mass ratio is set to zero. During the refilling stage, the same conditions are used except that the reactant mass ratio is set to unity. The detonation tube is initially filled up with a stoichiometric hydrogen–air mixture at ambient pressure and temperature. A small driver region with a temperature of 2,000 K and a pressure of 30 atm, and a width of 0.2 mm near the head end is implemented for detonation ignition.

Several cases have been studied for a single-tube PDE. The baseline situation has an operation cycle of 3 ms and a valve close-up time of 2.1 ms. The ambient flow is treated as stationary. During the first cycle, the operation begins as the valve closes. Detonation is initiated by the driver gas, propagates downstream, and finally degenerates to a nonreactive shock wave upon its arrival at the reactant–air interface at the end of the tube. The resultant shock wave is then split into two parts, one propagating further downstream, and the other reflecting from the inner walls. Figure 4 shows the snapshots of the pressure and pressure-gradient fields at $t = 0.80$ ms. At this time instant, the primary shock wave resulting from the detonation wave has moved out of the nozzle and transformed to a weakened bow shock. Other common features, including the formation of an oblique shock train due to shock reflection, the presence of vortices due to shock diffraction, and the attachment of secondary shocks onto the vortices, are all clearly resolved. It should be pointed out that the flow structure is more complicated than that for a pure shock diffraction problem because of the nonuniform flowfield resulting from detonation and the existence of the contact surface. Figure 5 shows the density-gradient fields at four different times within the fifth cycle at which a steady operation of the engine is reached. At $t = 12.20$ ms, the detonation wave has already caught up with the leading fresh reactant at about $x = 47.5$ cm instead of 60 cm in the first cycle. The two regions with strong density gradients in the tube represent the resultant shock wave and contact surface, respectively. The second and third snapshots correspond to the blow-down stage. In the fourth snapshot, the refilling process has begun. The two vertical lines within the tube, from left to right, represent the purged-gas/product interface and the shock wave induced by purging, respectively.

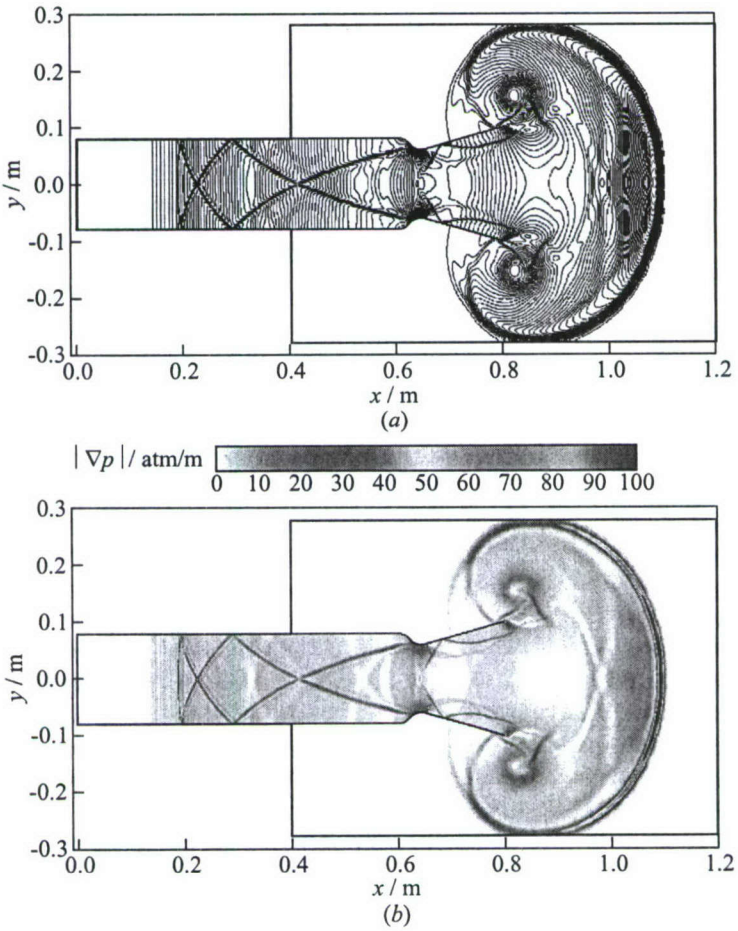

Figure 4 Snapshots of pressure and pressure-gradient fields at $t = 0.80$ ms ($\tau_{\text{cycle}} = 3$ ms, $\tau_{\text{close}} = 2.1$ ms): (a) pressure field: $0 < p < 2.5$ atm; $\Delta p = 0.025$ atm; and (b) pressure-gradient field. (Refer color plate IV.)

Figure 6 presents the time history of the head-end pressure during the first five cycles. Significant differences between the first and later cycles are observed. The pressure plateau during the first 1 ms does not appear in later cycles because of the interaction of waves from the previous cycles. Figure 7 shows the variations of cycle-averaged specific impulse and the filling length, defined as the length at which the detonation wave catches the leading fresh reactant. At steady operation, these values are 3,402 s and 47.5 cm, respectively.

The effect of ambient flow is considered by applying a supersonic inflow at the left boundary of the external region. In spite of the drastic change of the

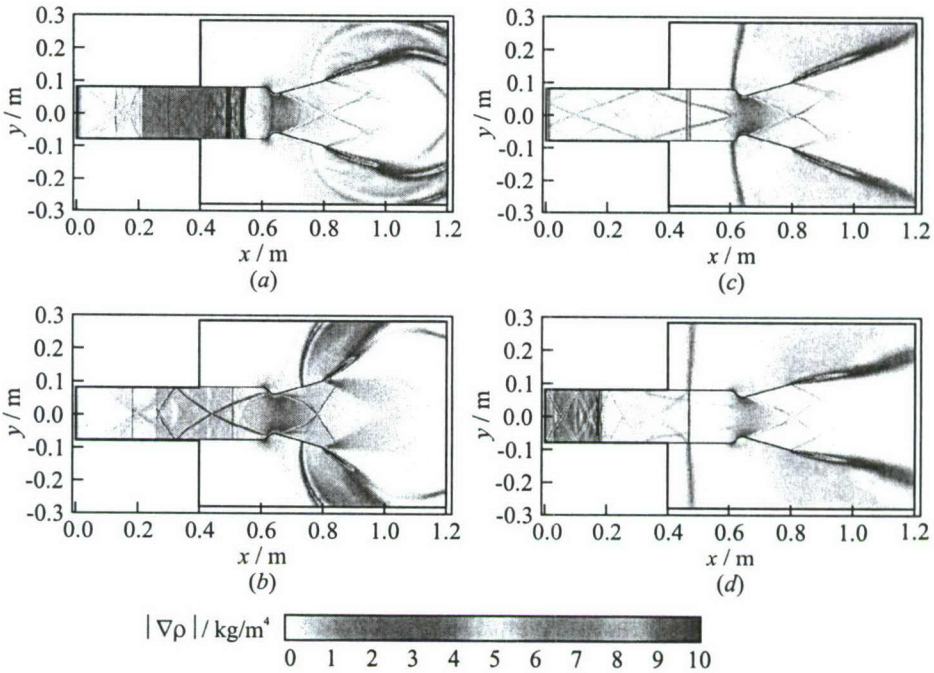

Figure 5 Time evolution of density-gradient field during 5th cycle of operation (τ_{cycle} = 3 ms, τ_{close} = 2.1 ms): (*a*) t = 12.20 ms; (*b*) 12.80; (*c*) 13.50; and (*d*) t = 14.50 ms. (Refer color plate IV.)

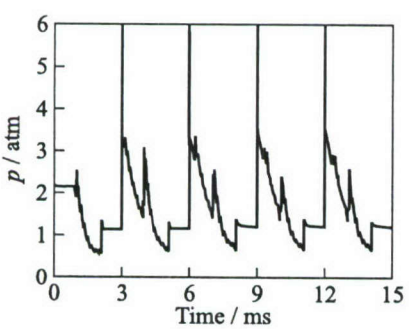

Figure 6 Time history of pressure at head end (τ_{cycle} = 3 ms, τ_{close} = 2.1 ms)

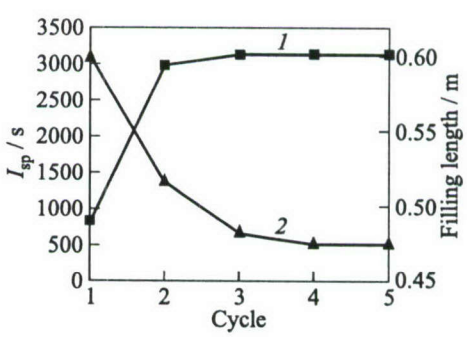

Figure 7 Cycle-average specific impulse (*1*) and filling length (*2*) (τ_{cycle} = 3 ms, τ_{close} = 2.1 ms)

external flowfield, the flowfield within the detonation tube remains nearly the same. Thus, the ambient flow exerts little effect on the system performance in terms of specific impulse and thrust, and will be neglected in later calculations.

5 MULTITUBE PDE ANALYSIS

In this section, the chamber dynamics and system performance of multitube air-breathing PDEs are studied. Figure 8 shows schematically the configuration of concern and the computational domain. The combustor contains three detonation tubes, each with a diameter of 5 cm, and is connected downstream with a CD nozzle. The number of grid cells is 623,254.

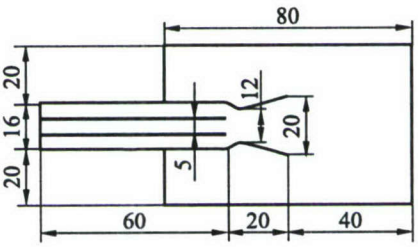

Figure 8 Computational domain for multitube PDE. Dimension in cm

The multiple detonation tubes operate sequentially with a time delay between the tubes, as shown schematically in Fig. 9. The operation sequence of each tube is the same as that for the single-tube case, and is controlled by the cycle period, valve close-up, and purging times. It should be pointed out that the engine operation frequency is the product of tube number and the tube operation frequency. In this paper, the

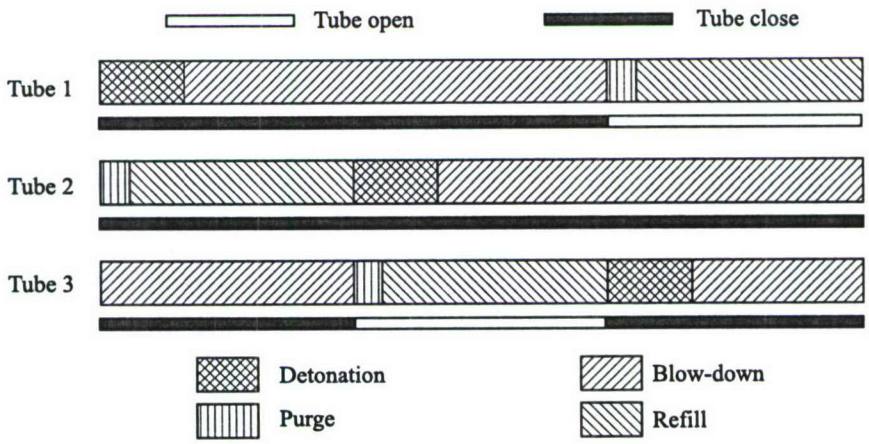

Figure 9 Operation sequence of a triple-tube PDE

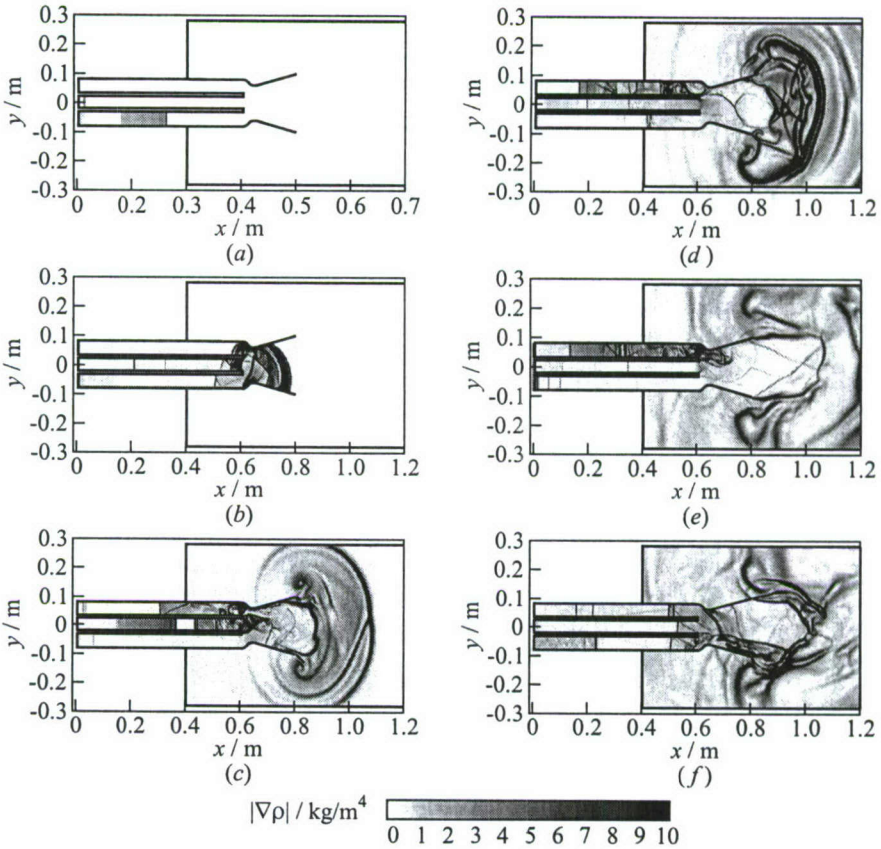

Figure 10 Time evolution of density-gradient field during first cycle of operation ($\tau_{cycle} = 3$ ms, $\tau_{close} = 2.1$ ms): (*a*) $t = 0.15$ ms; (*b*) 0.60; (*c*) 1.15; (*d*) 1.60; (*e*) 2.15; and (*f*) $t = 2.60$ ms

operation period of each cycle is based on that of each individual tube instead of the entire engine.

Figure 10 presents the time evolution of the density-gradient field during the first cycle of operation for a case with a cycle period of 3 ms and a valve close-up period of 2.1 ms. Detonation is initiated in the bottom tube by a driver gas region near the head-end. At $t = 0.15$ ms, the detonation wave has traveled approximately one half of the tube length and the middle tube has begun the refilling process. The detonation wave then propagates downstream, and eventually degenerates to a nonreactive shock wave after passing through the reactant–air interface at the end of the bottom tube. The resultant shock wave proceeds further downstream, diffracts at the exit of the tube, reflects from

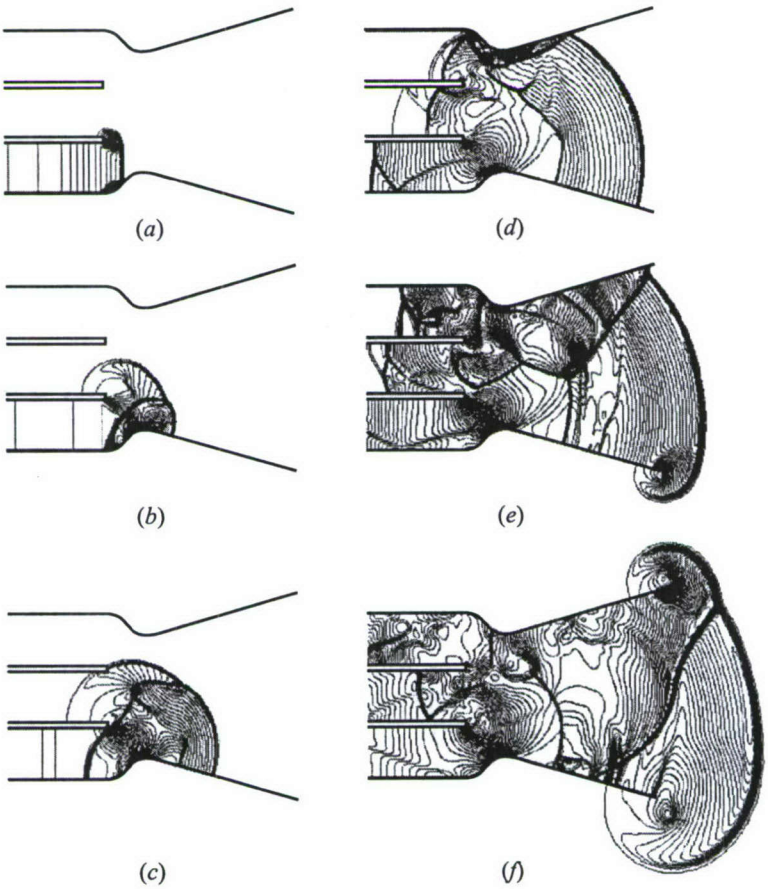

Figure 11 Snapshots of pressure field showing flow development in the nozzle (τ_{cycle} = 3 ms, τ_{close} = 2.1 ms): (*a*) t = 0.40 ms; (*b*) 0.45; (*c*) 0.50; (*d*) 0.60; (*e*) 0.70; and (*f*) t = 0.80 ms

the nozzle walls, and causes complex waves to propagate upstream into all three detonation tubes and downstream into the nozzle, as displayed in Fig. 10*b*. At this instant (t = 0.60 ms), the middle tube is in the refilling stage. The leading shock and the leading purged-gas/product interface, as represented by the two vertical lines in the middle tube, have reached locations of about 30 and 20 cm, respectively. A close-up view of the flow development in the nozzle section is shown in Fig. 11.

The fresh reactant in the middle tube is ignited at 1 ms. Figure 10*c* shows that the detonation wave in the middle tube reaches a distance of 37 cm at $t = 1.15$ ms. The bottom tube undergoes the blow-down process, whereas the top tube is in the purging stage. The shock wave degenerated from the detonation wave in the bottom tube is discharged out of the nozzle and results in a bow shock wave traveling downstream in the external region. Vortices appear near the edge of the nozzle exit, similar to those in the single-tube case. As the detonation wave in the middle tube continues to travel downstream, it interacts with the waves induced previously to cause more complicated wave patterns as evidenced in Fig. 10*d*. On the other hand, in the top tube, the downstream-propagating waves due to the purging and refilling processes meet and interact with the upstream-propagating waves, leading to a highly nonuniform flowfield in the top tube.

After the ignition in the top tube at 2 ms, the detonation wave passes through the leading fresh reactant and transforms to a nonreactive shock wave, as shown in Fig. 10*e*. The flow structure in the top tube is quite complicated, mainly due to the flow nonuniformity in this tube prior to detonation. At $t = 2.6$ ms, the shock wave has propagated out of the nozzle. The middle and the bottom tubes are in the blow-down and refilling stages, respectively.

Steady cyclic operation is reached at the 5th cycle. The cycle-averaged specific impulse and specific thrust are 3,543 s and 896 m/s, respectively, which are about 5% higher than those of the single-tube case discussed in the previous section. The multitube design indeed improves the system performance. Figure 12 shows the time evolution of the density-gradient field during the 5th cycle of operation. The time history of the instantaneous specific thrust is shown in Fig. 13. Also included is the result of the single-tube case for comparison. A very high peak exists for the single-tube case. The deviation of the peak value from the cycle-averaged value represents the degree of unsteadiness of the engine operation. For triple-tube cases, the number of peaks increases to three in each cycle, but the peak magnitudes are significantly reduced, showing a substantial improvement in flow steadiness. It should be noted that there exists considerable lateral thrust in a multitube PDE due to its unsymmetric operations. The maximum lateral thrust of the present triple-tube engine can reach 1,000 N per kg/s of air mass flow rate, thereby causing unnecessary vibration of the vehicle. One way to avoid this problem is the implementation of tube-pairs. Each tube-pair includes two detonation tubes which are located at symmetric positions and operate synchronously in time to ensure symmetric operation and consequently eliminates the lateral thrust.

A parametric study is conducted to study the time effect on system performance by varying τ_{cycle} and τ_{close}. The purge time τ_{purge} is fixed at 0.1 ms. Figure 14 shows the effects of τ_{close} on cycle-averaged specific impulse for two different cycle periods: 3 and 4 ms, corresponding to the operation frequencies of 333 and 250 Hz, respectively. The single-tube result for $\tau_{\text{cycle}} = 3$ ms is also

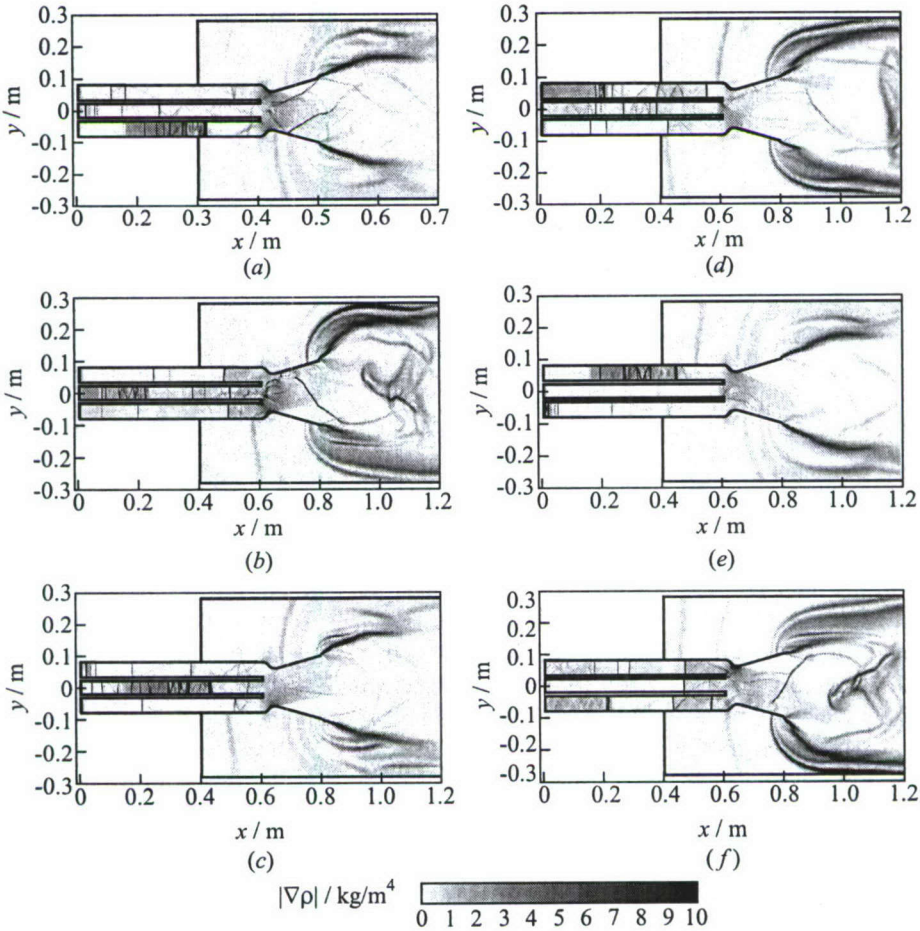

Figure 12 Time evolution of density-gradient field during 5th cycle of operation (τ_{cycle} = 3 ms, τ_{close} = 2.1 ms): (*a*) t = 12.15 ms; (*b*) 12.60; (*c*) 13.15; (*d*) 13.60; (*e*) 14.15; and (*f*) t = 14.60 ms

included for comparison. Clearly, the multitube design helps improve the system performance, and the performance decreases as τ_{close} increases. This can be explained as follows. When the valve close-up time increases, the head-end pressure decreases due to a longer blow-down process. On the other hand, the refilling time decreases, and thus the amount of the reactant refilled decreases. These two factors result in a lower mean chamber pressure and consequently, lower performance. It should be noted, however, that the valve close-up time cannot be too small. Its lower limit is determined by the following two factors.

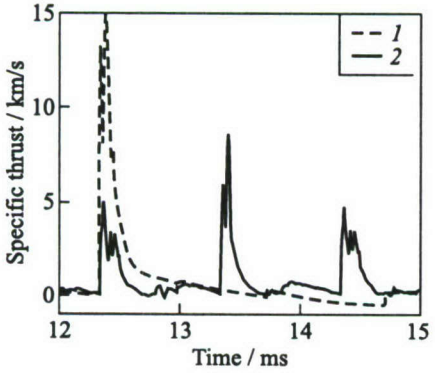

Figure 13 Time history of specific thrust during 5th cycle of operation (τ_{cycle} = 3 ms, τ_{close} = 2.1 ms): *1* — single tube; and *2* — triple tube

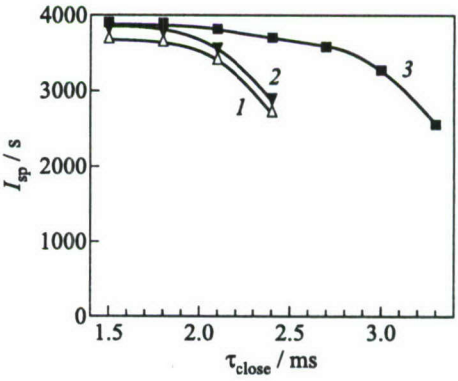

Figure 14 Effects of valve close-up time on specific impulse: *1* — τ_{cycle} = 3 ms, single tube; *2* — τ_{cycle} = 3 ms, triple tube; and *3* — τ_{cycle} = 4 ms, triple tube

One is inlet overpressurization, i.e., the head-end pressure exceeds the inlet air stagnation pressure, thereby prohibiting the detonation tube from purging or refilling when the valve is open. The other is overfilling, i.e., the fresh reactant flows out of the nozzle to the external region before being burned. For the two operation frequencies considered herein, the lower frequency offers a better performance margin for reasons given below. For a lower frequency or a longer cycle period, the refilling time becomes longer and as such more reactant can be delivered into the tube. As a consequence, a higher mean chamber pressure can be achieved and the performance improves. However, an exceedingly large refilling time may result in overfilling and thus degrade the performance. Therefore, an optimum operation frequency exists for a given configuration.

6 CONCLUDING REMARKS

The flow dynamics and system performance of air-breathing PDEs with single and multiple detonation tubes have been studied numerically by means of a 2D model. The effects of various operating parameters (such as cycle frequency and valve close-up period) on engine performance were investigated systematically. Results demonstrate that the multitube design improves the engine performance in terms of specific impulse and the degree of operation steadiness. A smaller valve close-up time increases the system performance in most cases. Furthermore, an optimum frequency exists for a given configuration. The analysis pre-

sented in this paper can be effectively utilized to optimize the engine design and to identify the various loss mechanisms limiting PDE performance.

ACKNOWLEDGMENTS

This work was supported partly by the Pennsylvania State University, and partly by the DoD Multidisciplinary University Research Initiative under ONR Grant No. N00014-99-1-0744 with Dr. Gabriel Roy serving as program manager.

REFERENCES

1. Bussing, T. R. A., and G. Pappas. 1994. An introduction to pulse detonation engines. AIAA Paper No. 1994-0263.
2. Bussing, T. R. A., and G. Pappas. 1996. Pulse detonation engine theory and concepts. In: *Developments in high-speed vehicle propulsion systems*. Progress in astronautics and aeronautics ser. Reston, VA: AIAA Inc. 165:421–72.
3. Hoffman, N. 1940. *Reaction propulsion by intermittent detonative combustion*. Ministry of Supply, Volkenrode Translation.
4. Nicholls, J. A., H. R. Wilkinson, and R. B. Morrison. 1957. Intermittent detonation as a thrust-producing mechanism. *Jet Propulsion* 27:534–41.
5. Dunlap, R., R. L. Brehm, and J. A. Nicholls. 1958. A preliminary study of the application of steady state detonative combustion of a reaction engine. *Jet Propulsion* 27:451–56.
6. Krzycki, L. J. 1962. Performance characteristics of an intermittent-detonation device. U.S. Naval Ordnance Test Station. NAVWEPS Report 7655. China Lake, CA.
7. Helman, D., R. P. Shreeve, and S. Eidelman. 1986. Detonation pulse engine. AIAA Paper No. 1986-1683.
8. Eidelman, S., W. Grossman, and I. Lottati. 1991. Review of propulsion applications and numerical simulations of the pulse detonation engine concept. *J. Propulsion Power* 7(6):857–65.
9. Eidelman, S., and W. I. Grossman. 1992. Pulsed detonation engine: Experimental and theoretical review. AIAA Paper No. 1992-3168.
10. Kailasanath, K. 1999. Applications of detonations to propulsion: A review. AIAA Paper No. 1999-1067.
11. Kailasanath, K. 2000. Review of propulsion applications of detonation waves. *AIAA J.* 38(9):1698–708.
12. Kailasanath, K. 2001. A review of PDE research — performance estimates. AIAA Paper No. 2001-0474.

13. Kailasanath, K. 2001. A review of research on pulse detonation engine nozzles. AIAA Paper No. 2001-3932.

14. Kailasanath, K. 2002. Recent developments in the research on pulse detonation engines. AIAA Paper No. 2002-0470.

15. Mohanraj, R., C. L. Merkle, and H. B. Ebrahimi. 2001. Modeling of pulse detonation engine operation. AIAA Paper No. 2001-0475.

16. Ebrahimi, H. B., R. Mohanraj, and C. L. Merkle. 2001. Modeling of multitube pulse detonation engine operation. AIAA Paper No. 2001-3813.

17. Wu, Y., F. H. Ma, and V. Yang. 2002. System performance and thermodynamics cycle analysis of air-breathing pulse detonation engines. AIAA Paper No. 2002-0317.

18. Oh, J. Y., F. H. Ma, S. Y. Hsieh, and V. Yang. 2002 (submitted). Interactions between shock waves and acoustic waves in a supersonic inlet diffuser. *J. Propulsion Power.*

19. Mcbride, B. J., and S. Gordon. 1996. Computer program for calculation of complex chemical equilibrium compositions and applications. NASA Reference Publication 1311.

20. Mohanraj, R., and C. L. Merkle. 2000. A numerical study of pulse detonation engine performance. AIAA Paper No. 2000-0315.

21. Chang, S. C. 1995. The method of space-time conservation element and solution element — a new approach for solving the Navier–Stokes and Euler equations. *J. Computational Physics* 119:295–324.

22. Wang, X. Y., and S. C. Chang. 1999. A 2D non-splitting unstructured triangular mesh Euler solver based on the space-time conservation element and solution element method. *J. Computational Fluid Dynamic* 8(2):309–25.

23. Chang, S. C., Y. H. Wu, X. Y. Wang, and V. Yang. 2000. Local mesh refinement in space-time conservation element and solution element method. *1st Conference (International) on Computational Fluid Dynamics Proceedings.* Springer-Verlag.

24. Wu, Y. H., V. Yang, and S. C. Chang. 2000. Numerical simulation of chemically reacting flows with detailed kinetics using the space-time method. *1st Conference (International) on Computational Fluid Dynamics Proceedings.* Springer-Verlag.

25. Zhang, Z. C., S. T. Yu, and S. C. Chang. 2002. A space-time conservation element and solution element method for solving the two- and three-dimensional unsteady Euler equations using quadrilateral and hexahedral meshes. *J. Computational Physics* 175:168–99.

26. Karypis, G., and V. Kumar. 1998. Multilevel k-way partitioning scheme for irregular graphs. *J. Parallel Distributed Computing* 48(1):96–129.

EXPERIMENTAL AND NUMERICAL ESTIMATION OF PULSE DETONATION ENGINE PERFORMANCE

N. Tsuboi, K. Fujii, Y. Kenmoku, and A. K. Hayashi

The performance of a pulse detonation engine (PDE) is studied both experimentally and numerically. The experiments were carried out in a single-cycle mode. H_2–air and H_2–O_2 mixtures were filled in a model PDE tube. Measured specific impulse for H_2–O_2 mixture was approximately equal to 180 s in spite of incomplete sustained detonation mode. Measured specific impulse for H_2–air mixture was significantly lower due to the failure of deflagration-to-detonation transition (DDT). The numerical analysis of PDE operation is performed based on the two-dimensional (2D) Euler equations with a detailed reaction model. Extinction of detonations in tubes with sudden expansion was investigated. The numerical results show that the cross-section expansion ratio affects considerably the mode of combustion wave propagation in the combustion chamber.

1 INTRODUCTION

Detonation wave, a dynamic complex comprising a shock wave and flame and propagating at a supersonic speed, has been studied for more than a hundred years and its detailed structure and various properties have been revealed through experiments and numerical simulations as well as theoretical analyses. Motivations to study the detonation phenomenon are (*i*) to better understand the fundamental mechanisms of detonation origin and propagation and (*ii*) to use it for various applications. The former deals, in particular, with the problems of DDT, the existence of irregular cell structure, turbulence and three-dimensional effects, that are left to be explained much more clearly, although many researchers have already addressed these issues. The latter is to study the possibility of applying detonations for propulsion in supersonic aircrafts, e.g., in a scramjet engine or PDE. The basic concept of a PDE is to generate and control pulse propagating detonations. Eidelman & Grossman [1] are one of the pioneers who studied PDEs experimentally, and Kailasanath and his group —

numerically [2–4]. Hanson and his group at Stanford University carried out PDE research experimentally by using advanced laser diagnostics [5]. Some academic groups in Japan also conduct PDE-related basic research as summarized in [6].

This paper presents the experimental setup developed at Aoyama Gakuin University and the results of single-cycle experiments. Furthermore, 2D simulations are conducted and analyzed for detonation transition from the predetonator tube into the combustion chamber, depending on the cross-section expansion ratio.

2 PDE SINGLE-CYCLE EXPERIMENTS

2.1 Experimental Setup

The experimental setup consists of a detonation tube, dump tank, injection system, ignition source, and pressure measurement system as shown in Fig. 1. The facility is capable of operating in a single-cycle or multicycle mode. Both closed-tube and open-tube experiments are possible.

The detonation tube is 1.2 m long with the external diameter of 70 mm and internal 40 × 40 mm rectangular cross-section. A 60-millimeter long Shchelkin spiral made of wire 1 mm in diameter is fixed in the tube to shorten the DDT length. The dump tank is 762 mm long with 762-millimeter internal diameter.

The ignition source consists of a spark plug mounted in a Teflon cap and can be exposed to a maximum voltage of about 5 kV. Four pressure transducers are mounted on the tube to monitor pressure profiles. Detonation velocity and impulse can be derived from the pressure profiles. An optical system with a diode laser for measuring OH distributions is currently under construction.

Prior to experiments, the detonation tube is evacuated to a pressure lower than 4 kPa. Test gas mixtures consist of hydrogen as the fuel and air or oxygen as the oxidizer. Varying parameters in the experiments are mixture type (H_2–air or H_2–O_2 mixture) and the ignition location. Initial pressure and equivalence ratio in all the experiments are 0.1 MPa and 1.0, respectively.

2.2 Experimental Results and Discussion

The experimental pressure histories are presented in Fig. 2. The distances of four pressure transducers from the injector are as follows: 85, 790, 904, and 1044 mm, respectively. The maximum pressure for H_2–O_2 mixture (for example, 2.5 MPa at 904 mm) is significantly larger than that for H_2–air mixture (about 0.2 MPa at 1044 mm) because in the H_2–O_2 mixture, the detonation occurs, but it fails for the H_2–air mixture under similar conditions. As seen from Fig. 2, the

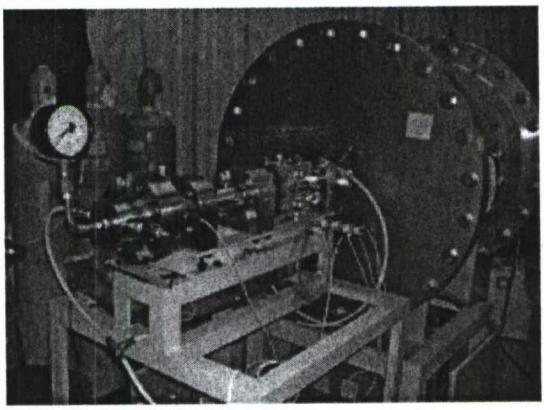

(*a*)

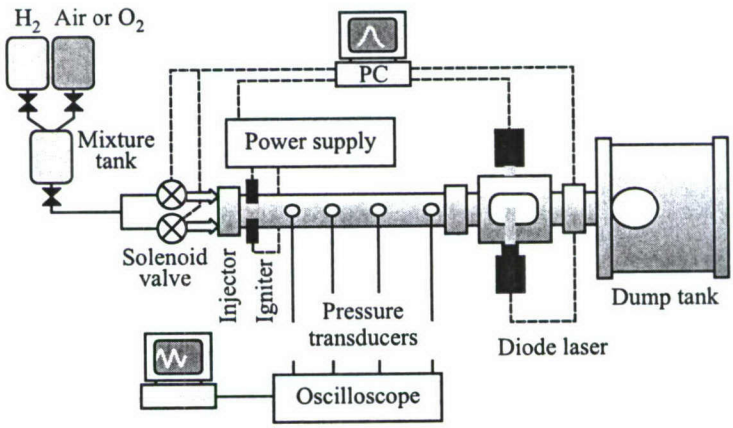

(*b*)

Figure 1 Experimental setup for sdudying DDT: (*a*) photo and (*b*) schematic

detonation in H_2–O_2 mixture propagates much faster than the pressure wave in H_2–air mixture.

In order to understand the effect of the reactive mixture, the detonation velocity is calculated from the pressure history. The Chapman–Jouguet (CJ) detonation velocity, D_{CJ}, for H_2–O_2 mixture is equal to 2806 m/s, while for H_2–air mixture it is 1978 m/s. Figure 3 shows the detonation velocity for both mixtures. The experimental velocities of arising pressure waves have been calculated at measuring bases 85–790 mm, 790–904 mm, and 904–1044 mm for

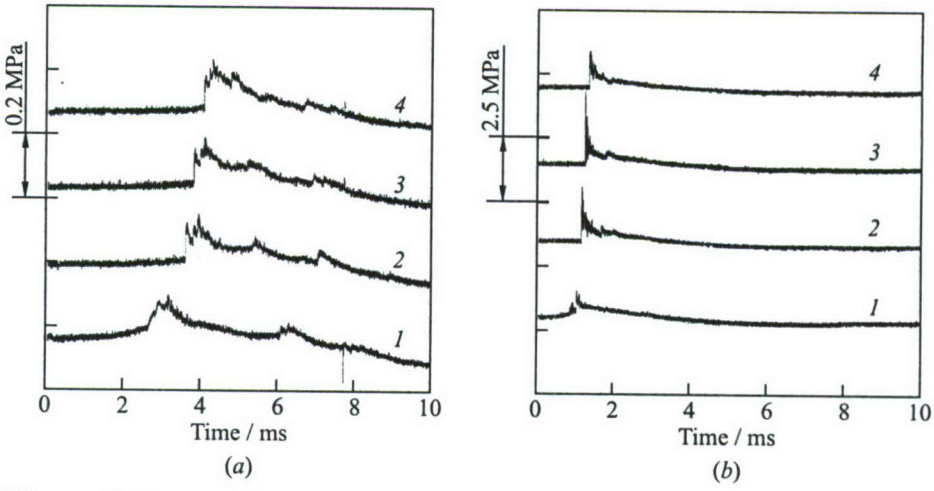

Figure 2 Pressure history at various pressure gauges: *1* — 85 mm; *2* — 790; *3* — 904; and *4* — 1044 mm. (*a*) H_2–air mixture; and (*b*) H_2–O_2 mixture

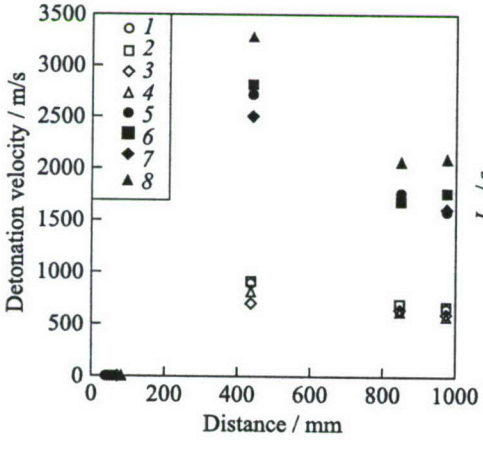

Figure 3 Measured pressure wave velocities for various igniter locations. H_2–air mixture: *1* — 40 mm; *2* — 50; *3* — 70; and *4* — 80 mm; H_2–O_2 mixture: *5* — 40 mm; *6* — 50; *7* — 70; and *8* — 80 mm

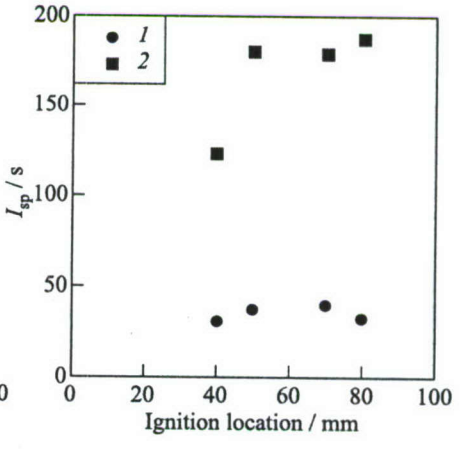

Figure 4 Specific impulse distributions for various iginition locations: *1* — H_2–air mixture; and *2* — H_2–O_2 mixture

various igniter locations. For the H_2–air mixture, the wave velocity does not attain the CJ detonation velocity. The detonation in H_2–O_2 mixture becomes overdriven at the measuring base 85–790 mm for igniter location at 80 mm. Deflagration-to-detonation transition seemed to occur only for the 80-millimeter

ignition location. Note that in all experiments with H_2–O_2 mixture, stable detonation did not occur presumably because the Shchelkin spiral was not long enough to generate DDT. To better understand the reason of detonation failure, the study of the effect of the Shchelkin spiral length should be conducted.

The results of specific impulse measurements are presented in Fig. 4. Specific impulse for H_2–O_2 mixture is approximately equal to 180 s in spite of the incomplete sustained detonation mode. Specific impulse for H_2–air mixture is significantly lower due to the failure of DDT.

3 NUMERICAL SIMULATION OF SUDDEN EXPANSION IN PDE

In the previous section, some preliminary results of experiments were discussed. The numerical simulations of PDE flows in the authors' group have been performed to better understand the experimental results. The numerical simulations have been conducted for single-cycle detonations to study their extinction in tubes with sudden expansion. Though these effects have already been studied by Edwards *et al.* [7] and Pantow *et al.* [8] both experimentally and numerically, the mechanisms of detonation reignition or extinction is still not completely clear. Because of high spatial and temporal resolution in the simulation, the present computational domain is significantly smaller than the size of an actual experimental system.

3.1 Numerical Method

The following assumptions are made to simplify the problem:

(1) the representative reactive species are H_2, O_2, O, H, OH, HO_2, H_2O_2, and H_2O, with N_2 used as a diluent;

(2) the specific heats of the species are the polynomial functions of temperature, and the mixture obeys the ideal gas law;

(3) viscosity, Soret effect, Dufour effect, and diffusion due to the pressure gradient are neglected.

Due to the above assumptions, the governing equations are the 2D, unsteady, compressible Euler equations supplemented with the equations of conservation of mass of each species. A detailed reaction model with 19 elementary forward and backward reactions developed by Hishida & Hayashi [9] is adopted. The forward reaction rates are written in the modified Arrhenius form, and the backward reaction rate constants are calculated by using the forward reaction rates and

the equilibrium constants taken from JANNAF tables [10]. The governing equations are solved explicitly by using the second-order Harten–Yee non-MUSCL modified-flux TVD-upwind scheme [11] for the convective terms and the point implicit scheme for the source terms. The details of the numerical method are reported in [12].

3.2 Simulation Conditions

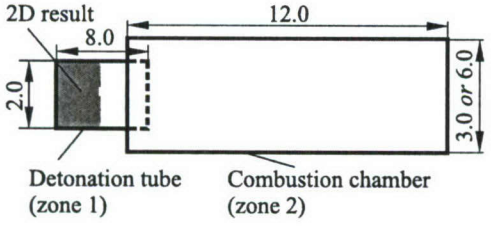

Figure 5 Computational domain. Dimensions in mm

The computational domain includes a detonation tube (zone 1) and a combustion chamber (zone 2). The computational grid is orthogonal with the mesh size of 5 μm. In Case 1, the number of grid points in the detonation tube and combustion chamber is $1601 \times 401 = 642{,}001$ and $2401 \times 601 = 1{,}443{,}001$, respectively. The ratio of cross-section areas of the combustion chamber and detonation tube (expansion ratio) is 1.5. In Case 2, the detonation tube and combustion chamber have $1601 \times 401 = 642{,}001$ and $2401 \times 1201 = 2{,}883{,}601$ grid points, respectively. The corresponding expansion ratio is 3.0. In terms of the width of the computational domain in Cases 1 and 2, zone 1 is 2 mm wide and zone 2 is 3 or 6 mm wide, respectively, as shown in Fig. 5. The initial conditions in zone 1 use the results of 2D detonation simulations as shown in Fig. 6. Initial conditions in zone 2 are: H_2–air mixture, 1 atm, 300 K, and the equivalence ratio of 1.0. The boundary conditions imply adiabatic, slip, and noncatalytic walls. The initial detonation velocity in the detonation tube is approximately 2100 m/s and the detonation is overdriven as compared with the CJ detonation velocity (about 1970 m/s).

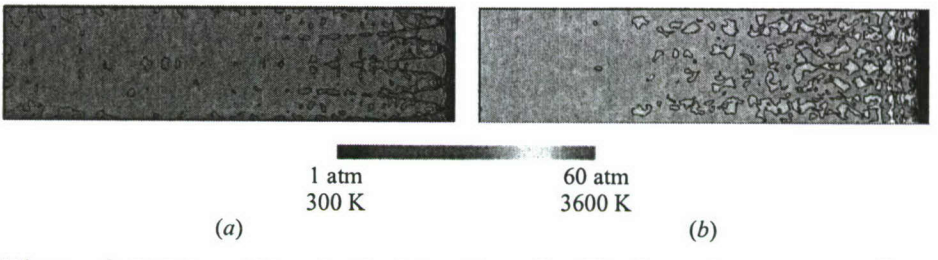

Figure 6 Initial conditions in the detonation tube. The detonation propagates from left to right: (*a*) pressure; and (*b*) temperature. (Refer color plate V.)

3.3 Results of Numerical Simulations and Discussion

Pressure and temperature evolution for Case 1 (expansion ratio of 1.5) are shown in Fig. 7. When the detonation propagates from zone 1 to zone 2, it expands rapidly as shown in Fig. 7*a* (five step number $N = 250$). When the triple points of the detonation collide with the wall in zone 2, the explosion occurs near the wall ($N = 1000$). After the triple points reflect from the wall, they collide again in the center of the tube ($N = 2000$). Then, the detonation is reconstructed with new triple points ($N = 3000, 4000$). Referring to the temperature distributions of Fig. 7*b*, it is seen that the reflected shock wave, after collision with the wall, gives rise to a high-temperature region ($N = 1000$). Next, a high-temperature region appears in the center of the tube ($N = 2000$). A reignition in the Mach stem and transition to detonation are captured at frames $N = 3000$ and 4000.

Evolution of pressure and temperature for Case 2 (expansion ratio of 3.0) are shown in Fig. 8. When the detonation propagates from zone 1 to zone 2, a high-pressure region such as for Case 1 does not appear and triple points are not

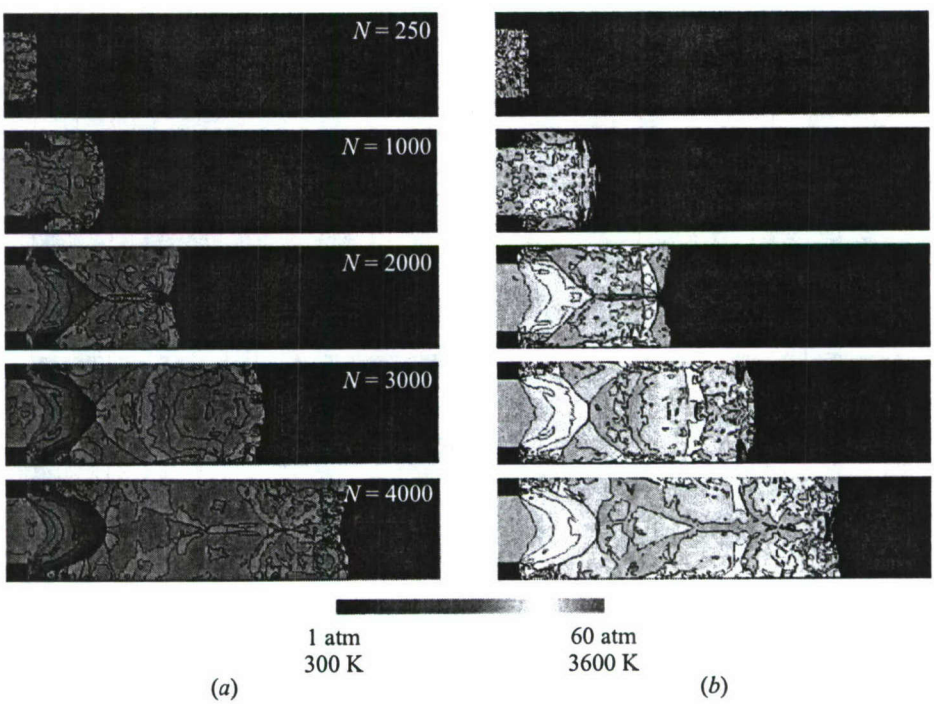

Figure 7 Predicted evolution of pressure (*a*) and temperature (*b*) for Case 1. (Refer color plate V.)

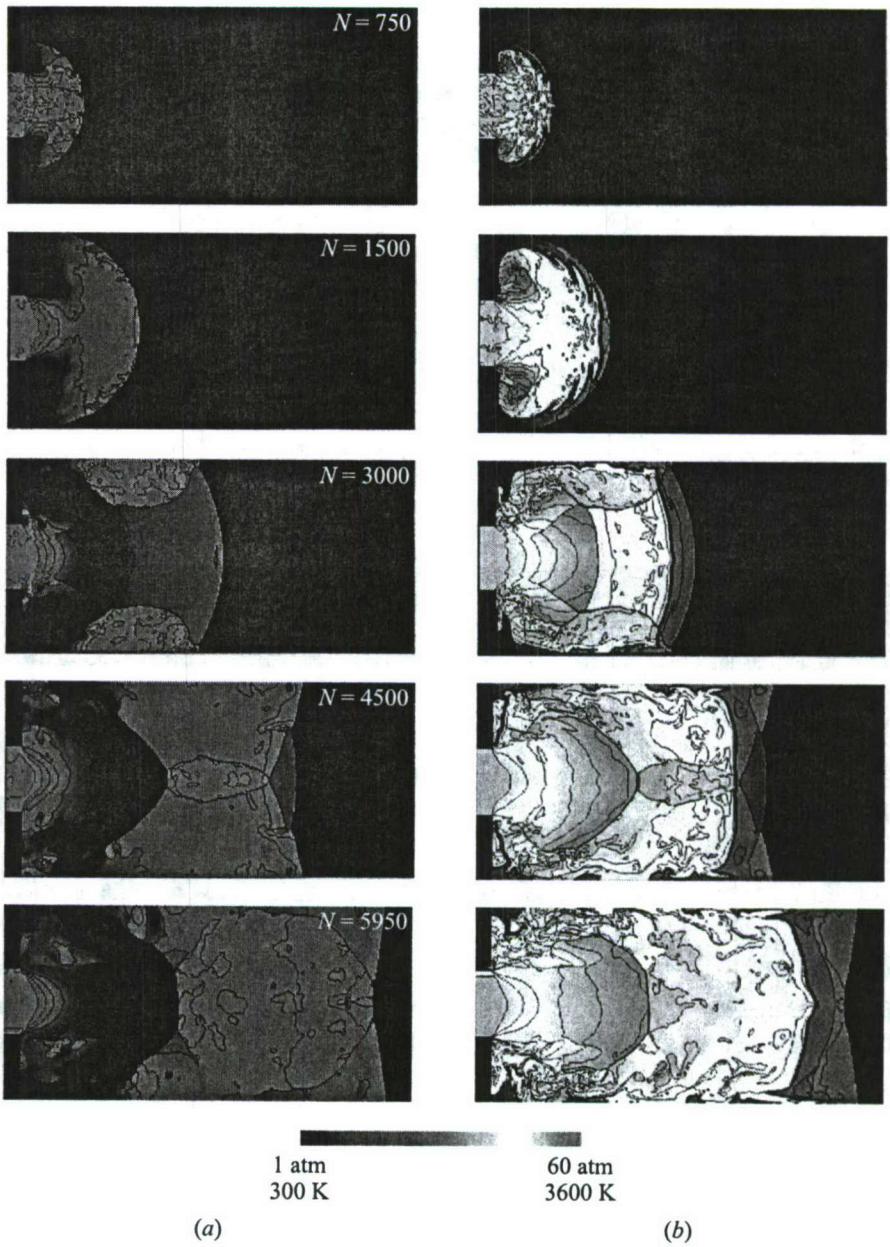

Figure 8 Predicted evolution of pressure (*a*) and temperature (*b*) for Case 2. (Refer color plate VI.)

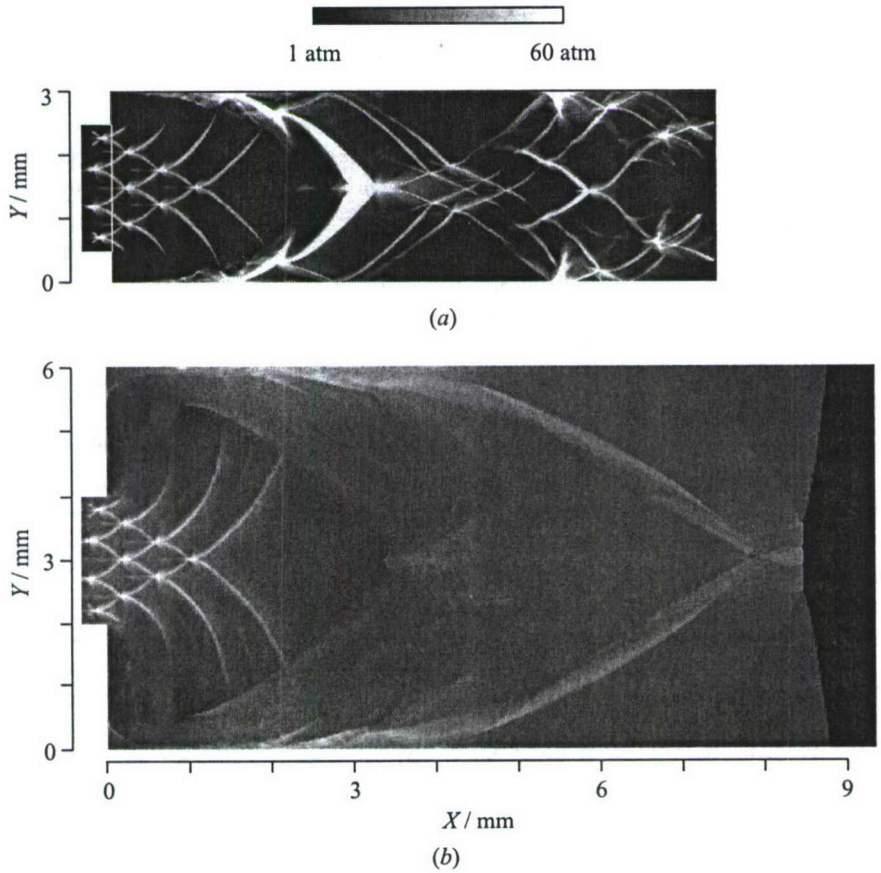

Figure 9 Predicted maximum pressure history: (*a*) Case 1; and (*b*) Case 2

observed (see Fig. 8*a*). Although the temperature near the wall increases due to the collision of triple points with the wall (see Fig. 8*b*, $N = 3000$), secondary explosions are not observed. Finally, the detonation front decouples in zone 2.

The predicted results on the maximum pressure histories for Cases 1 and 2 are shown in Fig. 9. Four triple points are observed in zone 1. When the detonation propagates toward zone 2, the triple points propagate toward the wall without interaction with other triple points. For Case 1, secondary explosions in the vicinity of the wall appear at $x = 1.5$ mm and near the tube center at $x = 3$ mm. Then the detonation is reinitiated, reconstructed and propagates to the right exhibiting irregular cells. For Case 2, all available triple points propagate toward the wall, however, no ignition near the wall is evident. Therefore, the detonation quenches in zone 2.

4 CONCLUDING REMARKS

The performance of a PDE was studied experimentally and numerically. The experimental setup is currently under construction and only the single-cycle performance was evaluated. For a H_2–O_2 mixture, the DDT does occur and detonation was observed in the present experiments. However, the length of the Shchelkin spiral in the experiments was too short so that a stable self-sustained detonation was not obtained for H_2–air mixture. Measured specific impulse for H_2–O_2 mixture is approximately equal to 180 s in spite of incomplete sustained detonation mode. The measured specific impulse of H_2–air mixture was significantly lower due to the failure of DDT.

Two-dimensional H_2–air detonations were simulated for the cases of sudden expansion of the detonation tube. The results showed that the detonation was reinitiated and propagated in a wider channel if the expansion ratio is equal to 1.5. However, the detonation was quenched if the wider channel had the expansion ratio of 3.0 due to failure of ignition near the wall.

REFERENCES

1. Eidelman, S., and W. Grossmann. 1989. A review of propulsion application of the pulsed detonation engine concept. AIAA Paper No. 2000-2446.
2. Kailasanath, K. 2000. Review of propulsion applications of detonation waves. *AIAA J.* 38(9).
3. Chiping, L., K. Kailasanath, and G. Patnaik. 2000. A numerical study of flow field evolution in a pulse detonation engine. AIAA Paper No. 2000-0314.
4. Kailasanath, K. 2002. Recent developments in the research on pulse detonation engines. AIAA Paper No. 2002-0470.
5. Hanson, R. K. 2002. Advanced laser diagnostics for reactive flows. AIAA Paper No. 2002-0196.
6. Hayashi, A. K., and T. Fujiwawa. 2002. The recent progress of Japanese PDE research. AIAA Paper No. 2002-0475.
7. Edwards, D. H., G. O. Thomas, and M. A. Nettleton. 1979. The diffraction of a planar detonation wave at an abrupt area change. *J. Fluid Mechanics* 95(1):79–96.
8. Pantow, E. G., M. Fischer, and T. Kratzel. 1996. Decoupling and recoupling of detonation waves associated with sudden expansion. *Shock Waves* 6:131–37.
9. Hishida, M., and A. K. Hayashi. 1991. Numerical simulation of pulsed jet plume combustion. *13th Colloquium (International) on the Dynamics of Explosions and Reactive Systems.*
10. Stull, D., and H. Prophet. 1971. JANNAF Thermochemical Tables. 2nd ed. NSRDS-NBS37.
11. Yee, H. C. 1987. Upwind and symmetric shock-capturing schemes. NASA Technical Memorandum 89464.
12. Shimizu, H., N. Tsuboi, and A. K. Hayashi. 2001. Study of detailed chemical reaction model on hydrogen–air detonation. AIAA Paper No. 2001-0487.

DDT STUDIES FOR MULTICYCLE PDE APPLICATIONS

R. J. Santoro, S.-Y. Lee, C. Conrad, J. Brumberg, S. Saretto, S. Pal, and R. D. Woodward

A series of studies of the phenomena involved in the transition of a detonation for a geometry in which a significant area change occurs has been investigated. The application of the work is to further the understanding of the appropriate geometry to enhance establishing a detonation in the main thrust tube of a Pulse Detonation Engine (PDE) using a compact predetonator. Results for several geometric configurations have been obtained for a conical transition section in which a transition-enhancing obstacle may be placed. Studies with and without an obstacle in the transition section have been conducted using a conical transition obstacle with a 45-degree half-angle. All experiments were conducted with ethylene as the fuel. Successful detonations in the main thrust tube were achieved for most geometries at nitrogen-to-oxygen ratios less than that for air, that is oxygen-enriched conditions. However, with careful selection of the length of the predetonator, establishment of detonations in the main thrust tube was observed when the region, where a localized explosion has been observed in the predetonator, was located close to the conical transition section. The use of transition-enhancing obstacles was generally observed to be helpful in establishing a detonation in the main thrust tube. However, successful detonation events could be achieved without the presence of obstacles for enriched oxygen conditions. A potential explanation for the observed results is that in the region where localized explosions occur, an overdriven detonation forms which, when combined with shock reflections generated in the conical section or enhanced by the transition-enhancing obstacles, results in establishing a detonation in the main thrust tube.

1 INTRODUCTION

In the past decades, several studies have been devoted to determining the conditions for successful propagation of a Chapman–Jouguet (CJ) detonation wave from a small tube either to an unconfined or a confined environment. It is now

commonly accepted that when the predetonator diameter is large enough to accommodate 9 to 13 detonation cells, depending on the geometry and fuel/oxidizer mixture, successful transition of the detonation occurs [1–3]. Such tube diameter is usually referred to as the critical diameter. Unfortunately, for meeting this requirement one would need predetonator tubes to be of a large diameter, which would, in turn, result in increased difficulty in initiating a detonation. Although this problem could be avoided by using more sensitive mixtures in the predetonator, such as fuel/oxygen mixtures, the added PDE engine complexity discourages pursuing such a solution.

During the same period, another process that leads to the formation of a detonation has been the subject of several studies; namely, the deflagration-to-detonation transition (DDT). The first experiments conducted by Urtiew & Oppenheim [4] on this topic demonstrated that at the time immediately preceding the onset of a detonation wave, an "explosion in the explosion" occurs, which accelerates the flame and leads to the formation of a detonation wave. This explosion can either occur between the leading shock and the flame front, at the flame front, at the shock front, or at the contact discontinuity formed by the coalescence of shock waves that precede the flame [4, 5]. No matter which phenomena cause the onset of a detonation, the detonation wave that emerges from the DDT process presents a high degree of overdrive. Such a highly unsteady state of a detonation wave can be exploited, along with shock-focusing obstacles, to ease the transition of the detonation from the predetonator to the main tube. The same concept can be utilized in multicycle PDE operation. Furthermore, the volume of the predetonator can be significantly reduced by employing obstacles to enhance flame acceleration in the predetonator.

2 EXPERIMENTAL SETUP

A schematic of the tube and injector configuration is shown in Fig. 1. The tube is composed of three sections shown in Fig. 1*a*: a predetonator, 33 mm in diameter and 1118 or 2032 mm long, a conical transition section 215 mm long with a 10° divergence angle (with respect to horizontal), and a main detonator tube, 109 mm in diameter and 1550 mm or 636 mm long. The geometry and angle of divergence of the transition section were designed to minimize diffraction effects at the area change [6]. Fuel and an oxygen/nitrogen mixture, with an equivalence ratio of 1.1, are injected at the head end of the predetonator through an impinging jet injector shown in Fig. 1*b*. The injector design is derived from conventional impinging gas injectors to ensure rapid uniform reactant mixing. The mixture is ignited 28 mm downstream of the injector face by a transversely oriented spark plug. A high-energy ignition system discharges a capacitor, initially containing 4.05 J, into the spark plug. Fuel and oxidizer are delivered to

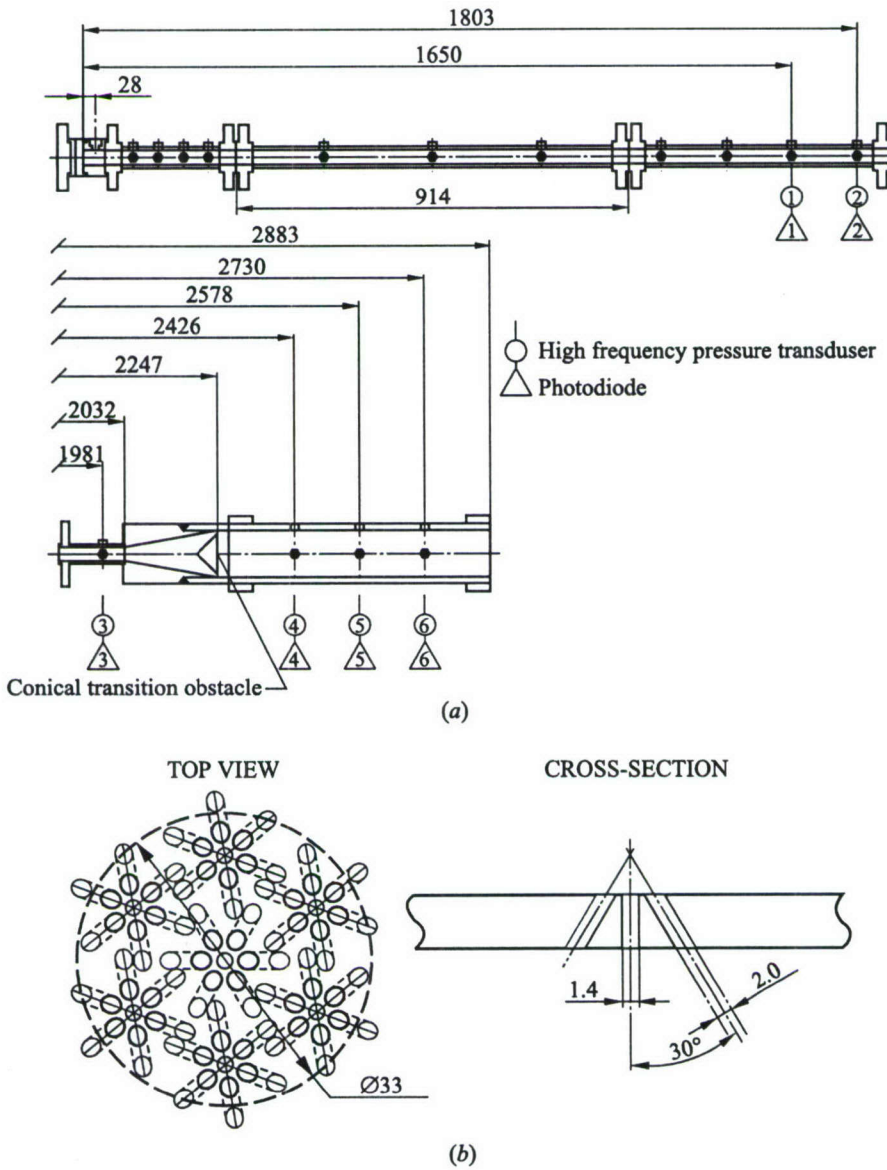

Figure 1 (*a*) Detonator tube including predetonator, transition section, and main detonator. (*b*) Impinging injector face. The fuel is injected along the center holes with surrounding oxidizer holes. Dimensions in mm

the injector through four fast-response solenoid valves. A LabVIEW program remotely controls the valves, spark ignition, and data acquisition system triggering. Calibration of the valves allowed them to be used as metering orifices for all mixture components.

In order to explore the effects of obstacles on the developing detonation wave in and around the transition section, the transition section was modified to position transition-enhancing obstacles of different shapes and blockage ratios (BR) at 50-millimeter increments in the axial direction downstream of the transition exit. A 78% BR, 45-degree half-angle conical transition obstacle was used in the experiments. Here, blockage ratio BR is the ratio of restricted to total tube cross-sectional area.

The evolution of the detonation wave is monitored using high-frequency piezoelectric pressure transducers and photodiodes mounted axially along the tube corresponding to the axial positions shown in Fig. 1*a*. The combination of the pressure and photodiode traces allows the comparison of the compression and reaction front speeds needed to determine the chemical induction time. The traces from the pressure transducers and the photodiodes are sampled at 1 MHz using a data acquisition system.

Throughout the experiments, the mass flow rates of the fuel and oxygen were held constant as the nitrogen flow rate was varied in order to change the nitrogen dilution while maintaining the equivalence ratio. This strategy provided a method by which both the cell size and the location of DDT could be varied. The levels of nitrogen dilution or ratio of moles of nitrogen to oxygen, β, are varied from 0 to 3.76 (air). A side effect of changing the nitrogen content was that the mixture fill velocity increased from 4 m/s, for $\beta = 0$, to 15 m/s, for $\beta = 3.76$.

The fuel concentration was monitored using a hydrocarbon absorption measurement. It has been reported that most hydrocarbon fuels have relatively strong absorption lines at the wavelength of 3.39 μm while the diatomic molecules of oxygen and nitrogen do not. Therefore, the fuel concentration can be determined from the amount of energy that is absorbed by the fuel when the 3.39 μm line of He–Ne infrared laser is passed through the chamber. Using Beer's Law, $I = I_o \exp(-abc)$, the fuel concentration, b [mol/m^3], could be calculated by measuring the ratio of transmitted to input laser energy, I/I_o, and knowing the absorption coefficient, a [m^2/mol], and the optical path length, c [m]. The absorption coefficient for ethylene varies very little with respect to temperature and can be considered constant. The measured value of the absorption coefficient of ethylene fuel was 19.433 m^2/mol. Ethylene combustion can be described by $\phi C_2H_4 + 3(O_2 + \beta N_2) \rightarrow xCO_2 + yH_2O + zN_2$, where ϕ is the equivalence ratio. For all the tests, β is varied at the fixed ϕ of 1.1. Using the ideal gas equation, the concentration of ethylene can be readily obtained as $N_f = P/(1+3(1+\beta)/\phi)RT$. Measured fuel concentrations for mixtures of varying nitrogen dilution are plotted with theoretical values in Fig. 2.

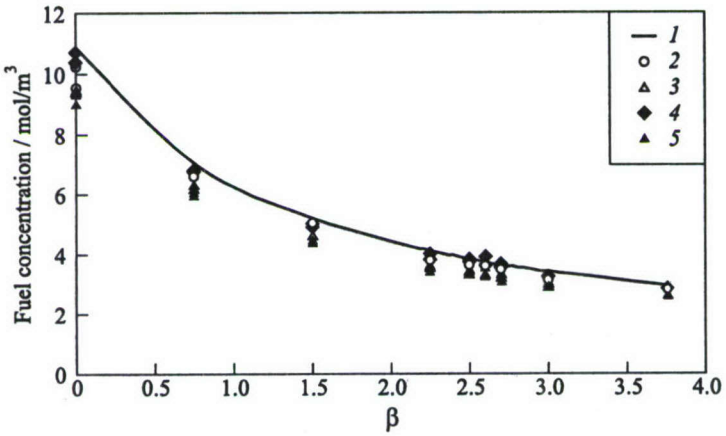

Figure 2 Fuel (ethylene) concentration as a function of molar ratio of nitrogen and oxygen β. Absorption coefficient of ethylene was obtained in the steady state calibration chamber. Theoretical concentration was calculated at the ambient conditions of $T = 300$ K and $P = 1$ atm: *1* — theory, *2* — upstream (with obstacle), *3* — downstream (with obstacle), *4* — upstream (without obstacle), and *5* — downstream (without obstacle)

Absorption measurements have been made at two axial locations with and without the presence of the 45-degree half-angle conical transition obstacle. The first measurement is made in the predetonator, 1498 mm downstream from the injector face, and the second is made in the main chamber, 2578 mm downstream from the injector face. Comparisons between theoretical and measured values of the concentration are in good agreement implying that the injector effectively mixes the reactants and that the valve orifices are calibrated to give the proper flow rates.

3 RESULTS AND DISCUSSION

In order to understand the detailed mechanism that allows a combustion wave to transition into a detonation in the main chamber, a detailed examination of the dynamic pressure and combustion wave traces must be completed. Shown in Fig. 3 is a spatial sketch of the DDT process at several times, a sample set of pressure traces (measurement locations from injector face are identified for each trace), and a space–time diagram of the process. For this case, the mixture dilution is $\beta = 2.25$ and the 45-degree half-angle conical transition obstacle is present at the exit of the transition section.

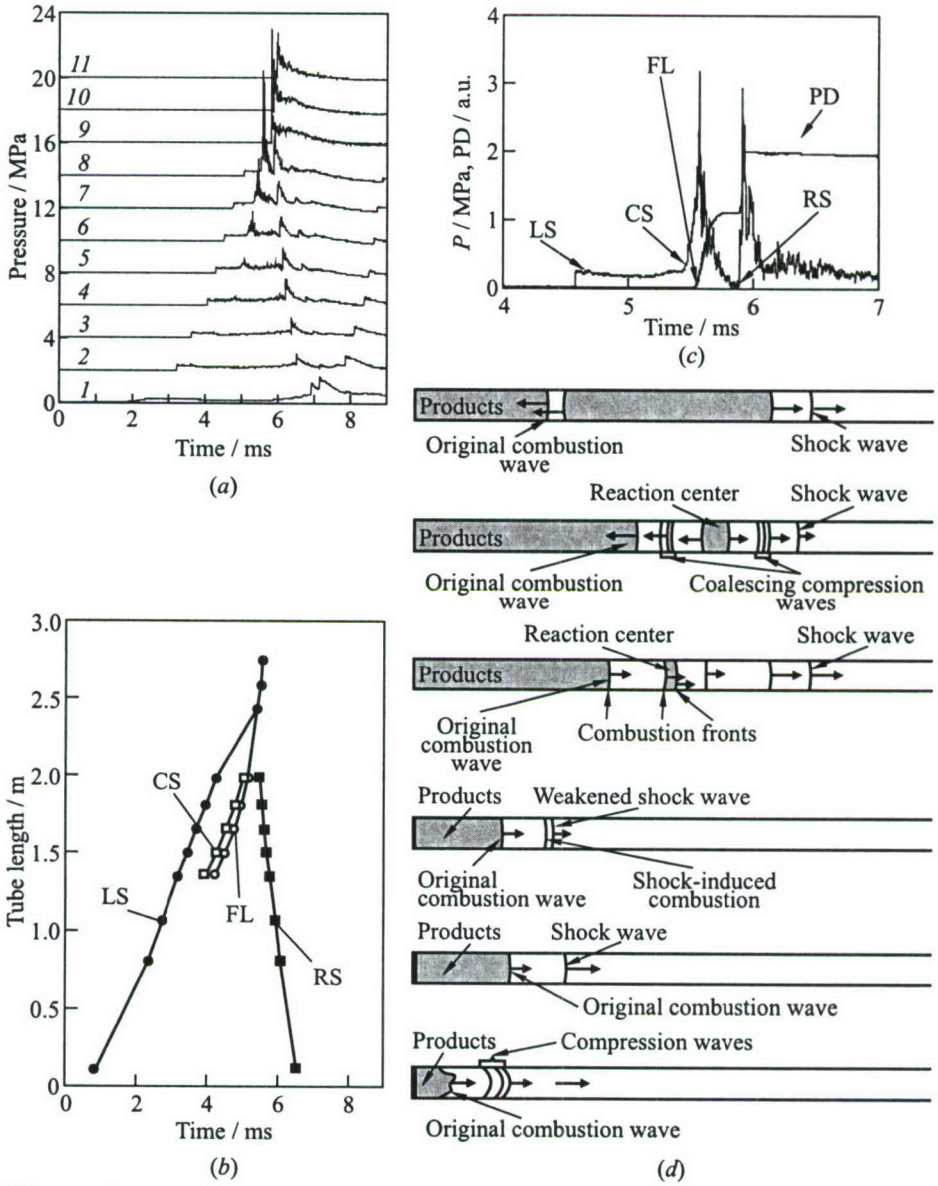

Figure 3 (*a*) Pressure traces up to $x = 1981$ mm in predetonator: *1* — $x = 115$ mm, *2* — 812, *3* — 1066, *4* — 1346, *5* — 1498, *6* — 1650, *7* — 1803, *8* — 1981, *9* — 2426, *10* — 2578, and *11* — $x = 2730$ mm; (*b*) space–time diagram, (*c*) sample of simultaneous pressure and flame traces at $x = 1981$ mm from different run: *LS* — lead shock; *CS* — compression shock, *FL* — flame, *RS* — reflected shock, and *PD* — photodiode; and (*d*) schematic diagram of DDT process

Initially, the tube is filled with a combustible mixture which is ignited at the closed end. The mixture next to the igniter is burned and a combustion wave begins to propagate downstream into the reactant (see bottom pressure trace and spatial sketch in Fig. 3). A lead shock is generated in front of the combustion wave due to the forward motion induced by the initial expansion of hot products behind the combustion front. The flame accelerates due to an increasing level of turbulence and an increase in reactant temperature produced by the lead shock. This additional flame acceleration and product expansion produces a train of compression waves directly in front of the flame, each traveling at a velocity that is sonic with respect to the gas downstream. These compression waves quickly coalesce with one another producing a pressure amplification directly in front of the flame.

This pressure amplification increases the reactant temperature and accelerates the flame. The distance between the amplifying pressure wave and the flame decreases. A localized explosion (secondary ignition) most likely occurs either at a single or at multiple contact surfaces within the train of coalescing compression waves. It is also possible that a portion of the flame accelerates in the boundary layer and ignites the mixture at a contact surface within the train of compression waves. In all of these arguments, a volume of unreacted mixture is bounded by the initial combustion wave and a newly formed reaction center. The temperature and reaction rate of the combustion kernel within the reaction center increases exponentially due to the relatively large compression wave produced by the localized explosion. As a result, the reaction center expands violently and forces the upstream combustion front of the reaction center, the volume of unreacted mixture, and the original combustion front upstream. Compression waves generated by the violent expansion are pushed upstream and are partially supported by the combustion of the volume of unreacted mixture. This can be seen in the upper spatial sketches of Fig. 3 as a compression wave followed by a combustion wave moving upstream.

The compression waves that are sent downstream by the localized explosion coalesce with the lead shock. This newly formed shock wave is stronger and accelerates faster than the previous waves. The combination point represents the beginning of the rapid transition to detonation. The increased shocked gas temperature enhances the combustion wave behind the stronger shock. A closely coupled shock wave and combustion front emerge. The occurrence of this sharp increase in chemical heat release that results in a coupling of the compression and combustion waves represents the end of the transition process. The newly formed self-sustained detonation wave is initially overdriven, but eventually decelerates to the theoretical CJ velocity.

Shown in Fig. 4*a* are a representative set of pressure traces for a class of detonation transitions through the transition section that corresponds to high-energy density, $\beta = 0.0$–1.5. In Fig. 4*a*, there is no transition-enhancing obstacle present at the exit of the transition section. In this set of traces, the detonation has al-

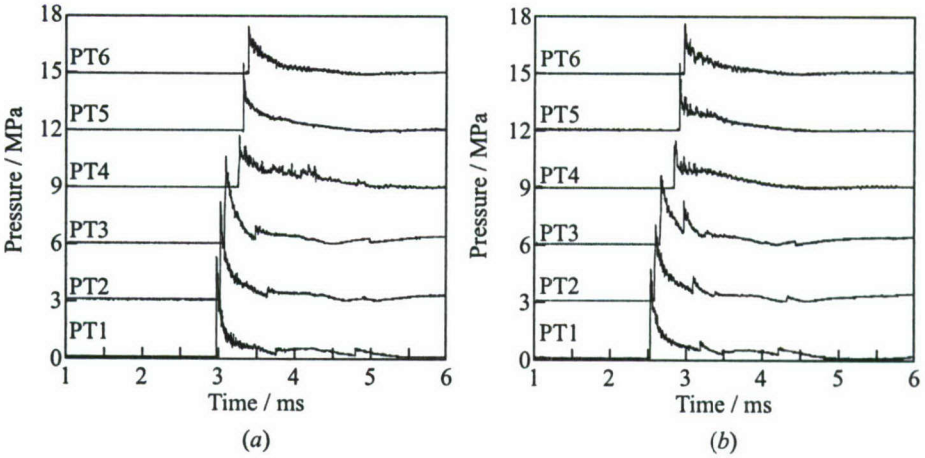

Figure 4 Pressure traces for $\beta = 1.5$: (*a*) without a transition-enhancing obstacle, and (*b*) with the 45-degree half-angle conical transition obstacle positioned at the exit of the transition section

ready developed in the predetonator with the shock and combustion waves being closely coupled. Due to the high-energy density of the mixture, the detonation propagates through the transition section to the main chamber almost unattenuated. After the detonation enters the transition section, a second wave reenters the predetonator and propagates upstream toward the injector face. This could be explained in two ways. First, as the detonation entered the transition section, the combustion wave decelerated away from the shock wave. A localized explosion occurred between the two, which forced compression waves in both directions. The forward compression wave and combustion front accelerated the shock wave and recoupled the two back into a detonation, and the compression wave forced upstream shows up as a retonation wave in Fig. 4*a*. For the second explanation, the initial shock wave of the detonation enters the transition section and reflects off at the compression corner of the transition section exit.

When the 45-degree half-angle conical transition obstacle is placed at the exit of the transition section for the same mixture, as shown in Fig. 4*b*, the only difference occurs in the wave magnitude that travels upstream from the transition section. If a localized explosion occurs in the transition section, shock focusing phenomena resulting from multiple shock reflections between the conical transition obstacle and the transition section wall may result in an acceleration of the reaction within the explosion. This would result in a stronger wave being forced upstream. If the wave that travels upstream is due to a reflection, the increase in magnitude may be due to the increase in compression corner angle from 10° to 0° at the transition exit to 0° to 45° at the apex of the 45-degree half-

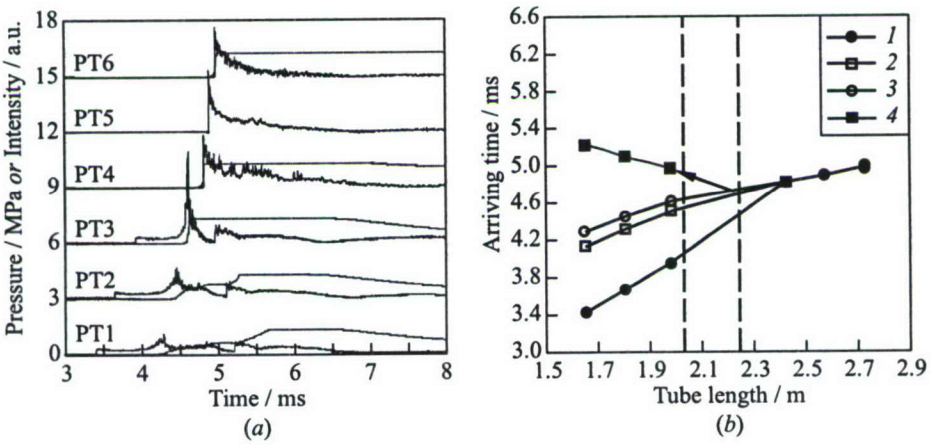

Figure 5 Combustion wave transition through the transition section; $\beta = 2.7$, no transition-enhancing obstacle: (*a*) pressure and flame traces; (*b*) space–time diagram: *1* — lead shock, *2* — compression shock, *3* — flame, and *4* — reflected shock

angle conical transition obstacle. The sharper corner would result in a stronger reflection.

The set of pressure traces shown in Figs. 5 and 6 represents a class of combustion wave transitions through the transition section that corresponds to a moderate energy density, $\beta = 2.25$–3.0. As the dilution increases, the localized explosion moves into and through the transition section in the upstream direction. In Fig. 5*a*, no transition-enhancing obstacle is present, and DDT has not yet been completed. In the first three traces, the developing localized explosion follows the initial compression wave. By looking at the space–time diagram in Fig. 5*b*, the solid line *1* corresponding to the initial shock and the dotted line *3* corresponding to the combustion wave, enter the transition section separated and exit coupled as a detonation wave. Therefore, the localized explosion occurs somewhere between the two transducers surrounding the transition section. Similar to the high-energy-density case, a strong pressure wave propagates upstream from the transition section.

For the pressure traces in Fig. 6, the 45-degree half-angle conical transition obstacle is positioned at the exit of the transition section. When the obstacle is in place, the magnitude of the localized explosion and the compression wave that travels back upstream is increased. This is most likely due to the reaction rate acceleration by the localized explosion resulting from a shock focusing mechanism. Depending on the nature of the shock wave entering the transition section, it may be reflected several times between the transition wall and conical transition obstacle surface. The addition of the conical transition obstacle does

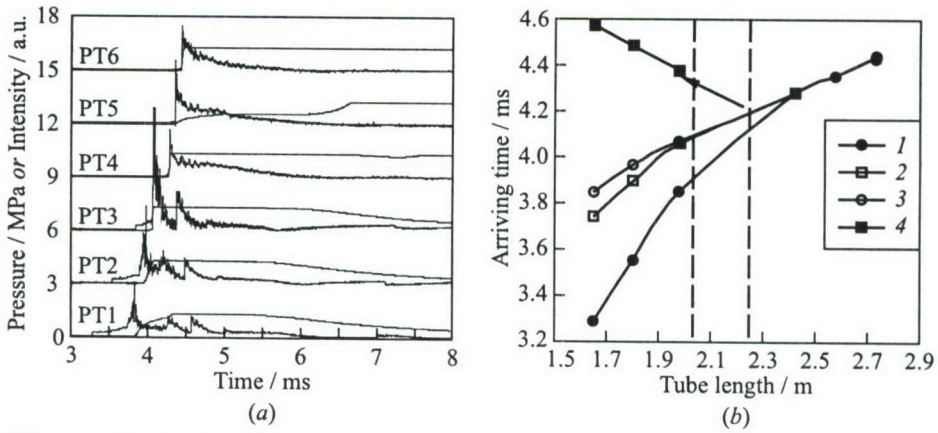

Figure 6 Combustion wave transition through the transition section; $\beta = 2.7$, with 45-degree half-angle conical transition obstacle: (*a*) pressure and flame traces; (*b*) space–time diagram: *1* — lead shock, *2* — compression shock, *3* — flame, and *4* — reflected shock

not change the outcome of combustion wave transition as it propagates into the main chamber as a detonation.

The set of pressure traces shown in Fig. 7 represents a class of combustion wave transitions through the transition section that corresponds to a low energy density, $\beta > 3.0$. For this class of transitions, the localized explosion would have occurred somewhere downstream of the transition section. When no transition-enhancing obstacle is present, the detonation completely uncouples in the transition section and no detonation emerges into the main chamber. When the 45-degree half-angle conical transition obstacle is placed at the exit of the transition section, a coupled detonation emerges into the main chamber. After the combustion wave enters the transition section, a second wave reenters the predetonator and propagates upstream toward the injector face. Two possible explanations could be possible for what occurs in the transition section. First, as the wave entered the transition section, the combustion wave decelerated away from the shock wave. A localized explosion occurred between the two, which forced compression waves in both directions. The forward compression wave and combustion front accelerated the shock wave and recoupled the two back into a detonation, which entered the main chamber. The compression wave forced upstream shows up as a retonation wave in Fig. 7*a*. For the second explanation, the initial shock wave of the detonation enters the transition section and strongly reflects off at the compression corner near the apex of the 45-degree half-angle conical transition obstacle. As the reflected shock passes over the combustion wave, the process leading to the localized explo-

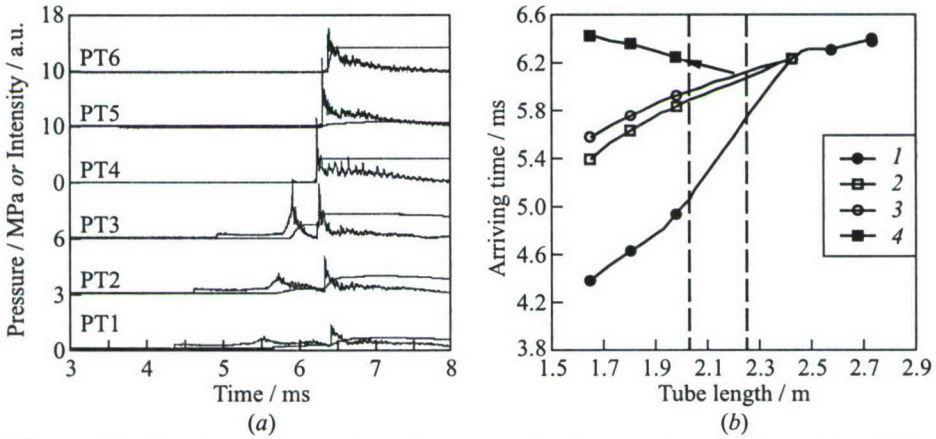

Figure 7 Combustion wave transition through the transition section; $\beta = 3.76$, with 45-degree half-angle conical transition obstacle: (*a*) pressure and flame traces; (*b*) space–time diagram: *1* — lead shock, *2* — compression shock, *3* — flame, and *4* — reflected shock

sion is accelerated leading to the emergence of a detonation in the main chamber.

4 CONCLUDING REMARKS

It has been shown that for ethylene–oxygen mixtures with varying dilutions of nitrogen at an equivalence ratio of 1.1, two types of regimes exist for the current detonator setup consisting of a predetonator, transition section, and main detonator. As the nitrogen dilution is increased, the peak overpressure associated with the final stage of the DDT process moves further downstream and the ignition delay time increases. In the first regime, when β is less than 2.7, the energy content is not only sufficient to initiate a detonation in the predetonator, direct transmission of that detonation to the main detonator occurs. In the second regime, when β is greater than 3.0, a detonation is not developed in the predetonator and the detonation fails in the main detonator.

With the exception of the $\beta = 3.76$ case, employing shock reflection from the transition-enhancing obstacle significantly improves the detonation transmission for mixture dilutions greater than $\beta = 3.0$. Despite the fact that a detonation was not achieved in the predetonator for the cases where the dilution was larger than $\beta = 2.25$, a detonation wave is achieved in the main chamber for all mixtures except for $\beta = 3.76$. For this case, the overpressure was not achieved upstream of

the transition-enhancing obstacle and, therefore, was not available to enhance the reaction in the transition region to a state sufficient to produce a detonation in the main detonator. It is believed by the authors that if the transition-enhancing obstacle was moved further downstream, the overpressure might develop in the additional length producing a stronger reflected wave that is required to intensify the reaction zone. By properly utilizing this concept, the predetonator length can be reduced from a length necessary to produce a detonation to a length necessary to produce an overpressure.

ACKNOWLEDGMENTS

The authors would like to gratefully acknowledge the support of the U.S. Office of Naval Research under Grant N00014-99-1-0744 under the direction of Dr. Gabriel Roy.

REFERENCES

1. Knystautas, R., J. H. Lee, and C. Guirao. 1982. The critical tube diameter for detonation failure in hydrocarbon–air mixtures. *Combustion Flame* 46:63–83.
2. Bartlma, F., and K. Schroder. 1986. The diffraction of a plane detonation wave at a convex corner. *Combustion Flame* 66:237–48.
3. Desbordes, D. 1988. Transmission of overdriven plane detonations: Critical diameter as a function of cell regularity and size. *AIAA J.* 170–85.
4. Urtiew, P., and A. Oppenheim. 1966. Experimental observations of the transition to detonation in an explosive gas. *Proc. Royal Society London A* 295:13–28.
5. Sileem, A., D. Kassoy, and A. Hayashi. 1991. Thermally initiated detonation through deflagration to detonation transition. *Proc. Royal Society London A* 435:459–82.
6. Nettleton, M. 1973. Shock attenuation in a gradual area expansion. *J. Fluid Mechanics* 60:209–23.

DETONATIONS OF HYDROCARBON–AIR MIXTURES IN A PULSE DETONATION CHAMBER

D. I. Baklanov, L. G. Gvozdeva, and N. B. Scherbak

The aim of this study is to determine experimentally detonation velocities, detonation limits, and the predetonation distances for hydrocarbon–air mixtures in a multipulse operation mode of detonation chamber (DC), and to compare the results to those obtained in a single-pulse operation mode. The experiments are conducted in a pulse DC of constant cross-section with valveless injection. Fuel and oxidizer are supplied to the DC separately and mixed inside the chamber. The detonation wave forms and propagates in a flow of combustible mixture after weak ignition by a spark plug with a characteristic energy of about 0.1 J. The frequency of detonations is varied from 0.5 to 6 Hz. Diagnostics include pressure gauges, photodiodes, and ionization probes. Detonations of mixtures of liquid hydrocarbons with oxygen-enriched air and of a methane–oxygen mixture are studied. Detonation velocities, predetonation lengths, and detonability limits are measured as functions of tube diameter and length, mixture composition, cycle frequency, flow velocity in front of the detonation wave, and flow turbulence. For methane–oxygen mixtures, experimental dependencies are compared with experimental data for a single-pulse mode and with the calculated parameters of Chapman–Jouguet (CJ) detonations. It is shown that in a multipulse mode, the characteristics of detonations differ from those for a single-pulse mode. The existence of a turbulent flow of fresh combustible mixture in a multipulse mode affects significantly the predetonation distance and concentration limits of detonation in fuel-lean mixtures. With increasing the flow velocity determining the frequency of detonations, the predetonation lengths decrease and the detonability limits widen.

1 INTRODUCTION

Pulse detonation engines (PDEs) have significant efficiency benefits in comparison to propulsion engines operating in the conventional deflagration mode [1]. To demonstrate this advantage, the calculations of thrust and thermodynamic

efficiency are often made using CJ detonation parameters and assuming that detonation occurs immediately near the ignition source [2]. However, these assumptions can potentially lead to incorrect conclusions, and should be comprehensively checked prior to calculations of realistic engines.

For PDE applications, it is desirable to have liquid hydrocarbons (as fuels) in mixtures with air (as oxidizer) rather than oxygen. Fuel–air mixtures are known to exhibit a large detonation cell size, λ; therefore, the detonation tubes with small diameter, d, to cell size, λ, ratio should be used, as well as with small length, L, to diameter, d, ratios. In addition, a low-energy ignition system and separate delivery of fuel and oxidizer, which leads to poor mixing, should be used for practical reasons. Under these requirements, direct detonation initiation will be difficult to achieve and the predetonation length will be comparable with the PDE tube length as the critical initiation energy for detonation of mixtures of liquid hydrocarbons with air is very large.

As the detonation cell size, λ, for such mixtures is also large, the realistic detonations will most probably differ from a steady-state CJ detonation. It is well known that at $d < \lambda/2$ the detonation cannot propagate in the tube of diameter d, at $d \sim \lambda$ the detonation propagates in a "galloping" mode, at $d \geq \lambda$, the detonation has a complex three-dimensional structure, and only at $d \gg \lambda$, the detonation structure resembles that of the one-dimensional CJ detonation. Thus, for the actual engine with the diameter of several λ, the detonation, even if initiated, is expected to considerably differ from the CJ detonation owing to various losses to the tube walls [3].

Theoretical assessment of PDE performance is thus very dependent on experimentally determined parameters of detonations in conditions representing realistic operation conditions of PDEs.

Besides, a multipulse mode of detonation propagation exhibits some features which are absent in a single-pulse mode. First, when operating in the multipulse mode, the DC is heated nonuniformly with large temperature gradients. Second, in the multipulse mode, the detonation forms and propagates in a flow of fresh mixture rather than in a quiescent gas as in the single-pulse mode. Moreover, the level of turbulence in the flow increases with the operation frequency. It is thus important to find out, whether flow turbulence will effect deflagration-to-detonation transition (DDT) and detonation propagation. These specific features of multipulse detonations are usually not taken into account in theoretical estimates of PDE efficiency, therefore experimental investigations of these effects could be very useful.

For such investigations, it is necessary to have a pulse DC, that is in general rather complex. However, investigations of fuel–air detonations in a multipulse mode in case of liquid fuels are somewhat easier than in a single-pulse mode. In a single-pulse mode, it is difficult to determine the detonation velocity of liquid hydrocarbons because a heated detonation tube should be used (e.g., [4]). In a multipulse mode, the setup is self-heated during operation. In these conditions,

the detonation parameters are measured in the range of temperature and pressure relevant to realistic PDEs.

In this paper, the results of experimental studies of the DDT and propagating self-sustaining detonations in a multipulse mode are presented. Some most perspective and practically important liquid fuels are investigated in mixtures with oxygen-enriched air. Several automobile gasolines with antiknock additives were examined to study the effect of additives on detonability limits. Methane–oxygen mixture was selected to investigate gaseous hydrocarbons, as the experimental results can be readily compared with calculations and experiments in a single-pulse mode.

2 RESULTS OF EXPERIMENTS

2.1 Experimental Setup and Methods

Experiments were performed on the lab-scale PDE model described in [5–9]. The results of experiments on this setup with a DC of variable cross-section operating on gaseous mixtures were reported in [6, 7]. Operation of the setup with a DC of variable cross-section on liquid fuels was reported in [8, 9].

The present experiments are performed on a DC of constant cross-section. The DC diameter varies from 16 to 64 mm; the length varies from 3 to 7 m. The valveless injection system is used, which allows operation in a multipulse mode at frequencies up to 90 Hz. As the injection ports are permanently open, there exists a continuous flow of combustible gases through the DC. Fuel and oxidizer are injected separately, so that mixing occurs in the flow. The flow velocity is determined by the mass flow rates of fuel and oxidizer measured with the help of manometers and rotameters, and is preset by proper opening of the hand-operated central valves installed upstream from the rotameters. The operation frequency is governed by ignition. The ignition is triggered by an electric spark with the energy of about 0.1 J. In the present investigation, the frequency of detonations is 0.5–6 Hz, and the operation time does not exceed 1 hour. The measurements are conducted by using pressure gauges, ionization probes, and photodiodes. Both liquid and gaseous hydrocarbons are used.

The DC (see Fig. 1) consists of different sections, which can be combined. One of the sections, 0.3 m long, is used as the head section. Fuel and oxidizer supply manifolds are connected to the head section. The igniter is also placed inside the head section. Other sections are 1 m long. One of them is used as the measuring section with all measuring devices installed. The pressure gauges, photodiodes, and ionization probes are mounted in four cross-sections 200 mm apart from each other. The ionization probes are nothing else as trivial spark gaps.

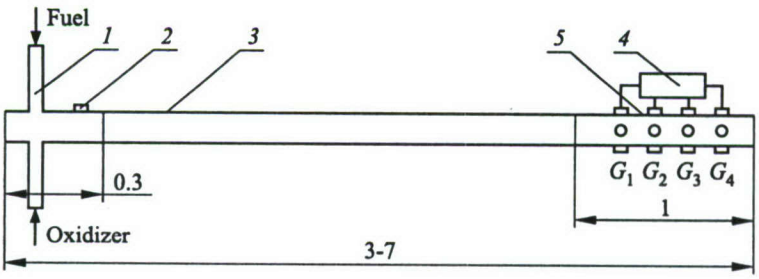

Figure 1 Measuring scheme of detonation parameters in a multipulse mode: *1* — feeding manifolds of fuel and oxidizer; *2* — spark plug; *3* — main section; *4* — measuring unit; *5* — measuring section; G_1, G_2, G_3, G_4 — pressure gauges, ionization probes, and photodiodes. Dimensions in m

The detonation velocity is determined based on the time taken for the wave to pass the distance between ionization probes. The characteristic errors of distance and time measurements are 1 mm and 1 μs, respectively. The photodiodes are adjusted so that they react only to the flame and not to shock waves. Combining pressure gauges and photodiodes at one cross-section, it is possible to measure velocities of both shock waves and flame fronts, i.e., to study the structure of a nonstationary complex "shock wave – flame front" and to register DDT or detonation decay.

To determine the predetonation length, the measuring section is assembled at different distances from the head section. Detonation onset is determined based on simultaneous appearance of signals at a pressure gauge and photodiode in a given cross-section. At this instant, shock wave and flame front merge. After detonation formation, higher velocities are usually observed with the steady-state conditions achieved somewhat later. Therefore, the steady-state detonation velocity is measured at a distance more than 1 m downstream from the site where the detonation occurs.

The detonation tube is water cooled (Fig. 2). It is sunk in a vessel with flowing water. The water level is supported at the stationary value and is registered by the level gauge. As the water level exceeds the nominal height, excess water runs in the drain. The end section of the detonation tube has the U-shaped geometry and is sunk in a silencer so that the detonation products are pushed through water. To prevent water penetration into the detonation tube, a part of the end section is placed slightly higher than the water level. Fuel and oxidizer are injected through tubes 12 mm in diameter, which are partly submerged in water as well. The temperature of water at the vessel exit is measured with a calorimeter. At operating with liquid hydrocarbons, water temperature is supported at the level of 70 °C to prevent hydrocarbon vapor from condensing on the tube interior surface. In case of excessive temperature rise, additional cooling

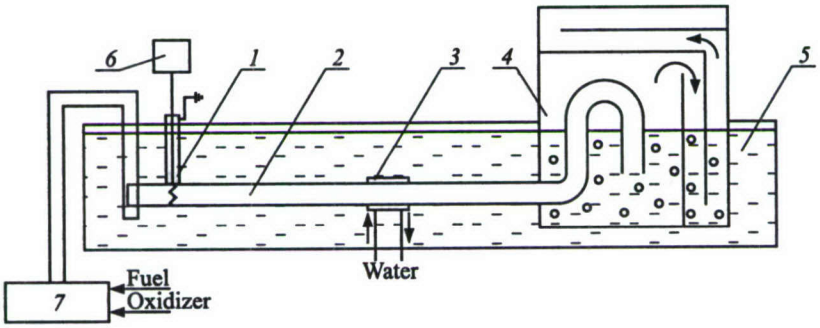

Figure 2 Cooling scheme of detonation chamber operating on liquid hydrocarbons: *1* — spark plug, *2* — detonation tube, *3* — calorimeter, *4* — silencer, *5* — cooling vessel, *6* — ignition block, and *7* — control panel

was used. At operating with the methane–oxygen mixture, water temperature is kept at a level of 10–15 °C.

2.2 Experiments with Liquid Hydrocarbons

Experiments with mixtures of liquid hydrocarbons with oxygen-enriched air are conducted in detonation tubes 7 m long and 36 or 64 mm in diameter. Preliminarily heated liquid fuel is injected through a nozzle. The initial temperature and pressure of the oxidizer are: $t_0 = 20$ °C and $p_0 = 1$ atm, respectively. The pulse repetition rate is 1 Hz.

Different fuels are studied: automobile gasolines (AI-72, AI-80, and AI-93 corresponding to octane number of 72, 80, and 93, respectively); aviation gasoline (B-70); *n*-hexane; acetone; and ethanol. Oxygen-enriched air is used as an oxidizer. Experiments are performed at initial atmospheric pressure.

Measurements of the detonation velocity in mixtures of gasoline and *n*-hexane were performed in tubes of different diameter, at different mixture composition, and different enrichment of air with oxygen. Due to the nonhomogeneity of the fresh mixture in the DC and cycle-to-cycle variation of mixture composition, the characteristic error of detonation velocity measurements is about 3%. The oxidizer-to-fuel ratio is determined as:

$$\alpha = \frac{G_O}{G_F L_0}$$

where G_O is the mass flow rate of oxidizer, G_F is the mass flow rate of fuel, and L_0 is the mass stoichiometric coefficient. The ratio α varies from 0.5 to 1.5.

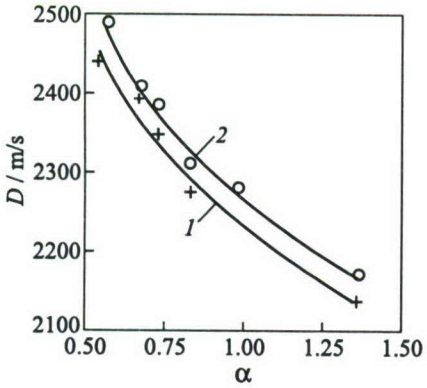

Figure 3 Measured detonation velocity in the mixture of automobile gasoline AI-80 with oxygen-enriched air (A = 95%), in a multipulse mode (f = 1 Hz): *1* (+) — d = 36 mm; and *2* (○) — d = 64 mm

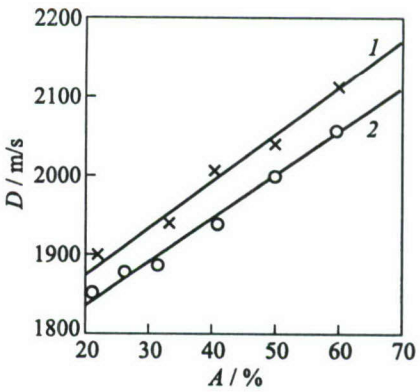

Figure 4 Measured detonation velocity in mixtures of liquid hydrocarbons with oxygen-enriched air (α = 1): *1* (×) — automobile gasoline AI-80, and *2* (○) — n-hexane (C_6H_{14}) in a multipulse mode (f = 1 Hz); d = 36 mm

The measured dependencies of the detonation velocity D vs. oxidizer-to-fuel ratio, α, for gasoline AI-80 are given in Fig. 3 for two detonation tubes. The curves in Fig. 3 are the best fits to experimental points. As expected, the strong dependence of the detonation velocity on α exists.

Also evident is the decrease of the detonation velocity in the tube of smaller diameter as compared with the tube of large diameter. This result testifies the existence of various losses at tube walls according to the Zel'dovich theory and, hence, the arising detonations differ from the CJ detonation [3, 11].

The dependencies of the detonation velocities, D, on the degree of air enrichment with oxygen, A, are also measured. The parameter A is determined as $A = Q_{O_2}/(Q_{O_2} + Q_{N_2}) \cdot 100\%$, where Q_{O_2} is the volume flow rate of oxygen and Q_{N_2} is the volume flow rate of nitrogen, with A = 100% corresponding to pure oxygen. Measured dependencies of the detonation velocities, D, on A in gasoline and n-hexane are presented in Fig. 4. As seen, the detonation velocity depends almost linearly on A.

Note that measured detonation velocities are given in the laboratory frame of reference. It was difficult to find the initial velocity of combustible mixture in front of the detonation wave in the experiments with liquid hydrocarbons. Therefore no recalculation to the moving frame of reference was made in this case. As mentioned above, the measurements were made at the operation frequency of 1 Hz, hence the flow velocities of the combustible mixture were of the order of several meters per second.

Table 1 Measured detonability limits for different fuels mixed with oxygen-enriched air ($A = 95\%$)

Fuel	Lower limit α_1	Upper limit α_2
AI-72	0.74	1.2
AI-80	0.74	1.2
AI-93	0.74	1.1
B-70	0.63	1.25
n-Hexane (C_6H_{14})	0.9	1.2
Ethanol (96%)	0.78	1.0
Acetone	0.75	1.15

The definition of detonability limits is as follows. In the course of experiments, the dependence of the detonation velocity on α is found based on the records provided by ionization probes. In addition, pressure records and electric current records of photodiodes are available at the end of the detonation tube for each experiment. Decreasing α below a certain value α_1 (lower limit), as well as increasing α above a certain value α_2 (upper limit) results in detonation failure which is detected by separation of shock wave from the flame front and by sharp decrease in the detonation velocity. In this manner, the detonability limits in the DC have been found.

The detonability limits for different fuels mixed with oxygen-enriched air ($A = 95\%$) are presented in Table 1.

The table shows that in experiments with automobile gasolines containing antiknock additives, the lower limit of detonation remains identical and corresponds to $\alpha = 0.74$. The upper detonability limit decreases with the octane number in accordance with the increase in the amount of antiknock additive.

It is worth noting that these detonability limits are obtained in a tube with the diameter of 36 mm and length of 7 m ($L/d \approx 200$). It means that, when approaching the concentration limits, the predetonation length becomes longer than the tube length, i.e., the predetonation length exceeds $200d$. It is clear that in longer and wider tubes, the concentration limits will change. It is also essential that current experiments use weak ignition. With strong ignition, detonability limits can be wider. There are eventually no data on detonation velocities and detonability limits in a single-pulse mode for liquid hydrocarbons. For comparison with a single-pulse mode, experiments with gaseous hydrocarbons are made.

2.3 Experiments with Gaseous Hydrocarbons

Experiments with gaseous mixtures are conducted in tubes 3 m long and 16 or 36 mm in diameter. The pulse frequency varies from 0.5 to 6 Hz. Methane–

oxygen mixtures are used, as methane–air mixtures have a cell size too large to be applied in PDEs. Besides, detonations of methane–oxygen mixtures were investigated in detail in a single-pulse mode, and the calculations of parameters of the CJ detonation are also well known [10–13]. Therefore it becomes possible to compare the multipulse experimental data with those obtained in a single-pulse mode and with the calculated data.

The detonation velocities, predetonation lengths, and detonability limits are measured depending on α and operation frequency, f. The influence of vortex generators inserted in the DC on the predetonation length is also studied.

All measurements are made several minutes after firing the experimental setup. The reason is that detonation parameters vary in the course of operation [6]. This fact was explained by the observed appearance of water vapor from the combustion products in the initially dry combustible mixture. As water vapor is a strong inhibitor, the detonability of combustible mixture at the first cycle will be the highest (similar to that in a single-pulse mode) and will lower in subsequent pulses till the establishment of a certain quasi-stationary value.

The detonation velocity in methane–oxygen mixtures as a function of α is measured in a 16-millimeter-diameter tube at a distance of 3 m from the ignition site, i.e., at $190d$. The operation frequency is 1 Hz. In this case, the oxidizer-to-fuel ratio, α, is determined as follows:

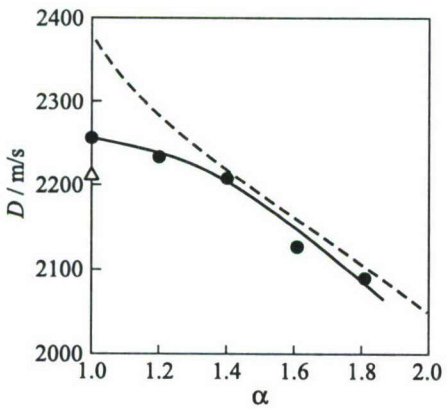

Figure 5 Experimental detonation velocity (relative to the flow in front of the detonation wave) in methane–oxygen mixtures in a multipulse mode (f = 1 Hz) as a function of α, d = 16 mm, distance from ignition is 3 m. Dashed curve — calculated CJ detonation velocity, △ — the detonation velocity in a single-pulse mode (d = 16 mm) obtained from extrapolation of experimental data [13]

$$\alpha = \frac{Q_O}{Q_F L_0}$$

where Q_O is the volume of oxidizer, Q_F is the volume of fuel, and L_0 is the volumetric stoichiometric coefficient.

Experimental data are presented in Fig. 5. The solid curve in Fig. 5 is the best fit of experimental points, while the dashed curve corresponds to the CJ detonation velocity calculated for initial values of pressure p_0 = 1 atm and temperature T_0 = 293 K.

In the experiments, the values of detonation velocities are obtained in a laboratory frame of reference. For gaseous mixtures, the flow velocity in the DC can be readily estimated by measuring the mass flow rates of methane and oxygen. For the ex-

periments of Fig. 5, this velocity is equal to 40 m/s. In Fig. 5, the detonation velocities are given in the frame of reference attached to the flowing gas. Nevertheless, all experimental points are below the calculated curve, in accordance with the Zel'dovich theory [3]. The detonation velocity is found to be insensitive to the operation frequency, f. The experimental value of detonation velocity in a single-pulse mode (triangular point in Fig. 5) is less than the velocity measured in a multipulse mode.

Predetonation lengths are found by assembling the measuring section in different places of the DC. Deflagration-to-detonation transition is detected with the help of ionization probes, pressure gauges, and photodiodes. The measurements are conducted in a tube of diameter 36 mm and 3 m long. The pulse repetition rate is 1 Hz. The dependence of the predetonation length on α is measured.

It is found that the predetonation length, L, is strongly affected by α and the corresponding dependency is the classical U-shaped curve, as shown in Fig. 6 (curve *1*).

A possibility to shorten the predetonation length by means of placing vortex generators in the flow is investigated at low operation frequencies. For this purpose, special experiments are carried out at the same operation frequency of 1 Hz with and without vortex generator. The vortex generator has the shape of the "reverse" Shchelkin spiral. It was created by machining the thread 200 mm long on a part of the inner surface of the DC head section. Curve 2 in Fig. 6 shows the measured predetonation length as a function of α at presence of the vortex generator in the tube. It is seen that fuel-rich mixtures ($\alpha < 1$) are insensitive to the presence of vortex generator. For fuel-lean mixtures ($\alpha > 1$), introduction of the vortex generator into the flow results in decreasing the predetonation length. The shortest predetonation length is obtained for the near-stoichiometric mixture. Without vortex generator, the predetonation length is equal to 0.5 m, i.e., $\approx 14d$. With vortex generator, it decreases to 0.4 m, i.e., $\approx 11d$.

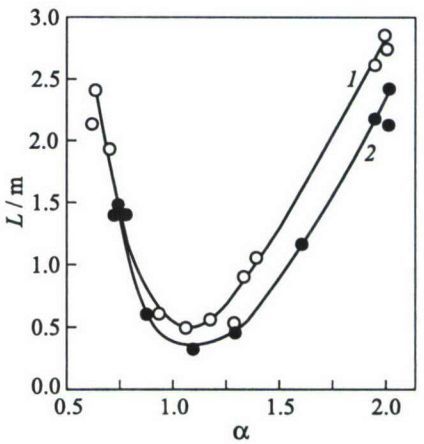

Figure 6 Measured dependence of the predetonation length on α for methane–oxygen mixture in a multipulse mode (f = 1 Hz); d = 36 mm, L = 3 m, without (*1*) and with (*2*) vortex generator

Thus, the experiments show that application of vortex generators in the head section may reduce the predetonation length. It means that vortex generators can also affect the detonability limits. As a matter of fact, for the case under

study, the detonability limits are: $\alpha_1 = 0.3$ and $\alpha_2 = 2.1$ without generator and $\alpha_1 = 0.3$ and $\alpha_2 = 2.3$ with generator, i.e., the presence of vortex generator affects the upper detonability limit.

The effect of Shchelkin spiral on DDT in the initially quiescent gas is known to be due to interactions of shock waves and flame front with roughness elements at the tube wall. It is interesting to investigate the influence of flow turbulence on detonability limits in smooth tubes without turbulizers. In the multipulse device, flow turbulence can be controlled by the operation frequency. In special experiments, it has been found that the increase in gas flow velocity appeared to be much more effective for detonability limits than introduction of vortex generators.

A series of experiments on determining the concentration limits in a multipulse mode was carried out in the tube of 36 mm in diameter and 3 m long ($L/d \approx 90$). For this tube, the predetonation length was preliminarily determined. The measuring section was positioned at the end of the DC. In the course of experiments, parameter α was varied until the predetonation length exceeded 3 m. The measurements were conducted with different operation frequency, i.e., with different Reynolds number of the gaseous flow filling the detonation tube:

$$\mathrm{Re} = \frac{wd}{\nu} = \frac{fLd}{\nu}$$

where ν is the kinematic viscosity of the methane–oxygen mixture, w is the velocity of the mixture, d is the tube diameter, f is the frequency, and L is the tube length.

At $L = 3$ m, $d = 36$ mm, and $\nu = 13.6 \cdot 10^{-6}$ m^2/s, the dependence of the Reynolds number on frequency is: $\mathrm{Re} = 7940f$.

Figure 7 presents the detonability limits of the methane–oxygen mixture in terms of f and Re. Points correspond to experiments where steady-state detonation was observed, i.e., region *1* between solid lines corresponds to the detonation region. Clearly, the detonation limit in a multipulse mode depends strongly on frequency and is wider than in a single-pulse mode, which corresponds to zero frequency. It is also seen from Fig. 7 that the upper boundary of detonation region for fuel-lean mixtures sharply widens with operation frequency and considerable decrease in the predetonation length can be observed. At the same time, no effect of frequency on the lower limit, α_1, for fuel-rich mixtures was detected. With increasing the frequency from 0.5 to 5.6 Hz, the detonability limits are widened twice and the mixtures with $2 < \alpha < 4.5$, which did not detonate at low frequencies, begin to detonate.

Based on Fig. 6, a rough estimate of the predetonation length at $\alpha = 4$ gives the value of 6 m. Due to the effect of turbulence the predetonation length decreases to 3 m as follows from Fig. 7. Thus, the predetonation length is decreased twice as compared to 20% in the case with vortex generator.

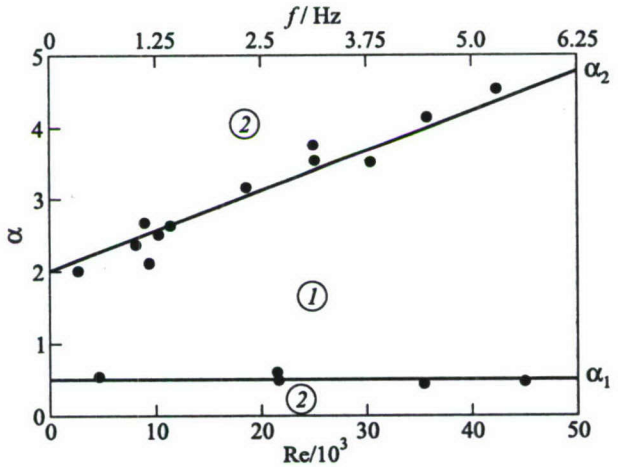

Figure 7 Limiting values of α vs. Re number for CH_4–O_2 mixtures: *1* — detonation; and *2* — no detonation; $d = 36$ mm, $L = 3$ m

3 DISCUSSION

Comparison of the experimental results obtained in a multipulse mode with the data obtained in a single-pulse mode can be conducted using data reported in [10, 12, 13], where detonations of methane–oxygen mixtures were studied experimentally and the calculations of the CJ detonation were made. The results of calculations of the CJ detonations, made in [10, 12, 13], are similar, as they were obtained within the frame of similar assumption that the gas behind the detonation wave is the equilibrium mixture of eight components: CO_2, CO, OH, O, H_2O, O_2, H_2, and H.

Experimental facilities in [10, 12, 13] differ from each other. For example, in [10], the ignition was strong, while in [12, 13] it was weak. In view of these differences, the experimental data seem to be overwhelming and supplement each other. The comparison of current experiments with those in a single-pulse mode is therefore made with [10] in terms of detonability limits, and with [12, 13] in terms of the measured detonation velocity.

3.1 Predetonation Length and Detonability Limits

The most interesting is to compare the data for predetonation lengths and concentration limits of detonation. The comparison indicates that DDT in a turbulent flow is very different from DDT in a quiescent gas.

In [10], the detonation limits of premixed methane–oxygen mixture were determined in the tube 25.4 mm in diameter and 6.1 m long, i.e., with $L/d = 240$. Prior to detonation initiation, the mixture did not move. The detonation was initiated by transition of a detonation wave from the stoichiometric hydrogen–oxygen mixture. The detonation wave existed while the content of methane in the mixture varied from 8.20% (vol.) to 55.64% (vol.)* that corresponds to $\alpha_1 = 0.4$ and $\alpha_2 = 6$. At these concentrations, the predetonation length was nearly 6 m.

Compare these results with the current experiments in a multipulse mode. At low frequency of 0.5 Hz, these experiments are somewhat close to a single-pulse mode. In a tube of 36 mm in diameter and 3 m long ($L/d \approx 90$), the concentration limits are $\alpha_1 = 0.4$ and $\alpha_2 = 2.1$, i.e., for fuel-rich mixtures, the two limits coincides, and for fuel-lean mixtures, concentration limits obtained in [10] are considerably wider than in this study. It is not surprising, because in [10] the length of the tube was twice as long as in the current experiments, the detonation was initiated by strong ignition, and the premixed composition was used. In the current experiments, detonation formation in initially nonpremixed methane–oxygen mixture was induced with weak initiation by a spark plug.

The strong influence of flow turbulence was not expected. It appeared that only proper organization of the gas flow in the detonation tube resulted in a possibility to detonate initially nonpremixed mixture in the tube 3 m long. The same mixture could not detonate at operation frequency less than 1 Hz.

It is still not clear why there is no influence of flow turbulence on the fuel-rich limit, α_1. This question needs further consideration.

In [7], the advantages of the valveless injection of fuel and oxidizer were discussed. The main advantage is a possibility to easily increase the operation frequency, as contrasted to systems with mechanical valves. Now, one more advantage of the valveless system has been revealed — a possibility to widen detonation limits for fuel-lean mixtures.

3.2 Detonation Velocities in Multipulse and Single-Pulse Modes

In a multipulse mode, the stationary detonation propagating in the turbulent flow, has a somewhat higher velocity than in a single-pulse mode. Note that

*According to Pawel, D., H. Vasatko, and H.-Gg. Wagner. 1969. The influence of initial temperature on the limits of detonability. Report AFEOAR67-49, the concentration limits vary from 6.7% (vol.) to 54.3% (vol.) in the tube 26 mm in diameter and 7 m long at normal conditions; extrapolation of the limits to larger tube diameters gives 5.6% (vol.) and 55.3% (vol.), respectively. These data show that fuel-lean limit is considerably wider than in [10]. See also: Guhlmann, K., W. Pusch, and H.-Gg. Wagner. 1966. *Berichte Bunsengesellschaft Physikalische Chemie* 70(2):143–48. (*Editors' remark.*)

the detonation velocity is a parameter almost insensitive to the initial thermodynamic conditions. The other relevant parameters, in particular, the velocity of rarefaction wave behind the detonation front and the pressure in the burned gas, are very sensitive parameters [12, 13]. This means that even small differences in the detonation velocity may result in the strong effect on other sensitive parameters and affect the estimated efficiency of the thermodynamic cycles and PDE thrust.

The detonation velocities in methane–oxygen mixtures measured in a multipulse mode were compared with the values obtained in a single-pulse mode [12, 13]. In those experiments, the two detonation tubes of square cross-section 3×3 cm and 5 m long; 7.2×7.2 cm and 8.3 m long were used. Measuring sections were supplied with optical windows and were assembled at different distances from the ignition site. Detonation was visualized by the Schlieren method using IAB-451 device and high-speed camera SFR. The mixture was ignited with a weak spark plug. The instant of ignition triggering was determined by the SFR, so that the detonation velocities and time intervals between ignition and detonation onset in the measuring section were measured.

The tubes were preliminarily evacuated and then filled with premixed methane–oxygen mixture to a certain pressure. The mixture was so well premixed that the processes of flame propagation and DDT were completely reproducible. The time of detonation formation after mixture ignition was about several milliseconds depending on mixture composition. From experiment to experiment, this time varied no more than by 2–3 μs for the same mixture.

Measurements of the detonation velocity along the tube have shown that after detonation formation at length $\sim$ 30–40 cm from the ignition site the detonation first propagates with a higher speed and then gradually decelerates. After passing the distance of 3 m ($L/d \approx 100$) it propagates with a constant velocity. The following values of the stationary detonation velocity were obtained. In the 3×3 cm detonation tube, the detonation velocity in a stoichiometric methane–oxygen mixture at initial atmospheric pressure and temperature $T = 293$ K was equal 2290 ± 30 m/s. In the 7.2×7.2 cm detonation tube, the detonation velocity was 2350 ± 30 m/s. The calculated value of the CJ detonation velocity was equal to 2392 m/s.

The differences between measured and calculated velocities are due to losses to the walls of the detonation tubes. It is known that the detonation velocity depends linearly on $1/d$ [3]*. Indeed, the extrapolation of the values of the measured detonation velocities $1/d \to 0$, i.e., to an infinitely large diameter, gives the calculated CJ value (Fig. 8). As seen from Fig. 8, the detonation velocity in the tube of 16-millimeter diameter would be equal 2210 m/s in a single-pulse mode. The measured detonation velocity in a multipulse mode (see

*Strictly speaking, the detonation velocity depends almost linearly on $1/d$ only far from the detonability limits. (*Editors' remark.*)

Fig. 5) is equal to 2260 m/s relative to the flow velocity. It is also lower than the calculated CJ velocity (2392 m/s), evidently due to wall losses. As compared with the detonation velocity in a single-pulse mode — 2210 m/s, this velocity appears to be a bit higher. It can be explained by two reasons — the temperature change during the multipulse operation or high turbulence level in the initial gas flow. The first reason seems irrelevant, as in the experiments with methane, the temperature of the cooled water was supported at the level of 10–15 °C, so the temperature of the mixed gas cannot be too high. Besides, the dependence of the CJ detonation velocity on initial temperature is weak and, moreover, the CJ detonation velocity decreases with temperature. It seems probable that the increase of the detonation velocity as compared to the single-pulse mode is explained by a high level of flow turbulence.

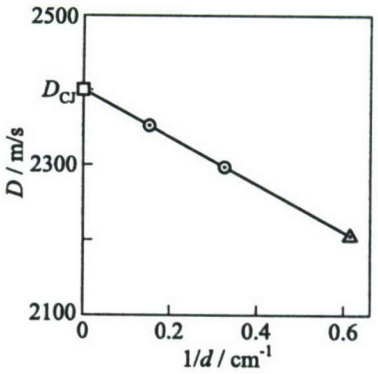

Figure 8 Measured detonation velocities in a single-pulse mode in a stoichiometric methane–oxygen mixture ($p_0 = 1$ atm, $T_0 = 293$ K): △ — the detonation velocity in the tube of diameter $d = 16$ mm, obtained from extrapolation, and □ — calculated CJ detonation velocity

4 CONCLUDING REMARKS

1. Experimental investigations of detonations in the DC operating in a multipulse mode without mechanical valves have been carried out. A detonation tube of a constant diameter (from 16 to 64 mm), 3 to 7 m long was used. The operation frequency was varied from 0.5 to 6 Hz. Prior to detonation initiation in the tube, a flow of fuel and oxidizer with the velocity depending on the pulse repetition rate was established. A weak ignition by a spark plug was used. The tube was cooled with water. The concentration limits of detonation, predetonation lengths, and detonation velocity were measured as functions of tube diameter, mixture composition, presence of vortex generators, and the Reynolds number of gas flow.

2. For mixtures of liquid hydrocarbons with air, the experimental data on detonation velocities have been obtained. For gasoline–air and n-hexane–air mixtures, the dependencies of the detonation velocity on the tube diameter, the oxidizer-to-fuel ratio, α, and the degree of air enrichment with oxygen, A, were investigated. Strong dependencies of the detonation velocities on α and A were obtained, as well as the dependence of the detonation

velocity on tube diameter. Thus, it has been shown that the parameters of detonation do not correspond to the CJ parameters. The experimental data on the detonability limits of automobile gasolines with the antiknock additives were obtained.

3. In experiments with gaseous methane–oxygen mixtures, it has been shown that the detonation parameters in a multipulse mode differ from those obtained in a single-pulse mode. In a multipulse mode, DDT in the turbulent flow of a combustible gas is different from DDT in a quiescent gas. It has been shown that even the detonation velocity in a multipulse mode is higher than in a single-pulse mode.

4. Measurements of the predetonation lengths in methane–oxygen mixtures at low operation frequency (1 Hz) with and without vortex generators have shown that the vortex generators reduce the predetonation length by several dozens percent, and widen detonability limits in fuel-lean mixtures ($\alpha > 1$).

5. The effect of the operation frequency on detonability limits was also investigated. It has been found that with increasing the operation frequency, the detonability limit α_2 (for fuel-lean mixtures) sharply widens. It seems that the flow turbulence diminishes the predetonation length.

ACKNOWLEDGMENTS

This work was implemented partly in the frame of the ONR Propulsion Program, headed by Dr. G. Roy, to whom authors express their gratitude.

REFERENCES

1. Roy, G. D. 1999. Pulsed detonation phenomenon for air breathing propulsion. ISABE Paper No. 99-71.
2. Zitoun, R., and D. Desbordes. 1999. Propulsive characteristics of pulsed detonation. *Combustion Science Technology* 1444:93–114.
3. Zel'dovich, Ya. B., and A. S. Kompaneetz. 1955. *The theory of detonation.* Moscow, Russia: Gostekhteorizdat.
4. Akbar, R. A., P. A. Thibault, *et al.* 2000. Detonation properties of unsensitized and sensitized JP-10 and Jet-A fuels in air for pulse detonation engines. AIAA Paper No. 2000-3592.

5. Baklanov, D. I., L. G. Gvozdeva, and N. B. Scherbak. 1998. The formation of high pressure gas flow in frequency mode during non-stationary propagation of detonation. AIAA Paper No. 98-2562.
6. Baklanov, D. I., L. G. Gvozdeva, and N. B. Scherbak. 1999. Formation of high-speed gas flow at combustion in the regime of multi-step detonation. In: *Gaseous and heterogeneous detonations: Science to applications*. Eds. G. Roy, S. Frolov, K. Kailasanath, and N. Smirnov. Moscow, Russia: Enas Publ. 141–52.
7. Baklanov, D. I., L. G. Gvozdeva, and N. B. Scherbak. 2001. Pulsed detonation combustion chamber for PDE. In: *High-speed deflagration and detonation: Fundamentals and control*. Eds. G. Roy, S. Frolov, D. Netzer, and A. Borisov. Moscow, Russia: Elex-KM Publ. 239–50.
8. Baklanov, D. I., L. G. Gvozdeva, and N. B. Scherbak. 2001. Pulse detonation engine using gasoline–air mixture. *18th ICDERS Proceedings*. Seattle, WA.
9. Baklanov, D. I., L. G. Gvozdeva, and N. B. Scherbak. 2001. Investigation of pulse-detonation engine operating on gasoline–air mixture. *14th ONR Propulsion Meeting*. Eds. G̃. Roy and F. Mashayek. Chicago, IL. 189–94.
10. Michels, H. J., G. Munday, and A. R. Ubbelonde. 1970. Detonation limits in mixtures of oxygen and homologous hydrocarbons. *Proc. Royal Society London A* 319:461–77.
11. Borisov, A. A., and S. A. Loban. 1977. Detonation limits of hydrocarbon–air mixtures in tubes. *Combustion Explosion Shock Waves* 5:729-33.
12. Bazhenova, T. V., L. G. Gvozdeva, Yu. S. Lobastov, I. M. Naboko, R. G. Nemkov, and O. A. Predvoditeleva. 1968. *Shock waves in real gases*. Ch. 6: Reflection and refraction of detonation waves. Ed. A. S. Predvoditelev. NASA TT-F-585.
13. Bazhenova, T. V., L. G. Gvozdeva, Yu. P. Lagutov, V. N. Lyachov, Yu. M. Faresov, and V. P. Fokeev. 1989. *Nonstationary interactions of shock and detonation waves in gases*. Ch. 10: Nonstationary interactions of detonation waves. Ed. P. A. Urtiew. New-York–Washington–Philadelphia–London: Hemisphere Publ. Co.

DETONATION STUDIES AND PERFORMANCE RESULTS FOR A RESEARCH PULSE DETONATION ENGINE

F. Schauer, J. Stutrud, R. Bradley, V. Katta, and J. Hoke

Research results of a combined computational and experimental investigation of an air-breathing pulse detonation engine (PDE) are presented. Models and hardware developed by the Air Force Research Laboratory (AFRL) in-house PDE program examine critical technology issues such as: detonation initiation and propagation; valving; timing and control; instrumentation and diagnostics; variation in tube fill, equivilance ratio, and repetition rate; detonation and deflagration-to-detonation transition (DDT); and performance prediction and analysis. An innovative, premixed four-detonation-tube engine design is currently employed for experimental research and evaluation. Specialized instrumentation and measurement techniques are developed to investigate the unsteady PDE processes. Research objectives include detonation initiation in air without the use of excess oxygen and performance results for various operating conditions. Data are obtained with hydrogen–air as well as hydrocarbon–air mixtures and compared with theoretical results.

1 INTRODUCTION

Renewed interest in pulsed detonation propulsion concepts has prompted recent efforts to develop a low-cost, practical-fueled PDE [1, 2]. Conceptually, the PDE offers few moving parts, high efficiency, high thrust, low weight, low cost, and ease of scaling. These features make the PDE an attractive alternative to jet turbines for small disposable engines. The near constant-volume heat addition process, along with the lack of a compression cycle, lend to the high efficiency and specific impulse, simplicity, and low cost of PDEs. Theoretically, PDEs have the potential for operation at speeds ranging from static to hypersonic with competitive efficiencies, enabling supersonic operation beyond conventional gas-turbine engine technology. Currently, no single-cycle air-breathing engine exists which has such a broad range of operability.

A practical-fueled PDE likely requires detonation of kerosene–air mixture. This requirement creates several technological hurdles that must be overcome in order to develop such a PDE. Complex hydrocarbon fuels, and, particularly, liquid hydrocarbons, are difficult to detonate in air, typically requiring hundreds of kilojoules to directly initiate a detonation [3]. For this reason, development of a practically fueled PDE may become a DDT minimization process since the fuel burned during detonation initiation does not produce thrust efficiently while it is burning at low pressures. Furthermore, since thrust is generated with each detonation cycle, it may be beneficial to raise the operating frequency in order to produce more thrust. Higher operating frequencies also have benefits from an unsteady inlet, nozzle, and noise generation perspective, but create complications in other areas including valving, mixing, shortened residence time requirements, and increased heat loads.

2 TECHNICAL APPROACH

The research approach combines use of analytical and numerical modeling with experimental research. The highly unsteady and severe conditions experienced during PDE operation dictate innovative methodologies to modeling, facilities and instrumentation, and research hardware development and testing, which are explained below.

AFRL's detonation modeling, described in detail elsewhere [4], has been extended to three-dimensional (3D) calculations and studies of detonation initiation schemes such as the Shchelkin spiral calculation in Fig. 1. Both calculations employ weak initiation of hydrogen–air mixtures, but the left frame is a straight channel and the right frame contains a two-dimensional (2D) representation of a Shchelkin spiral. The brighter areas in the Shchelkin spiral calculation indicate that the "hot spots" critical for DDT events are more prevalent with the extra geometry.

The Pulsed Detonation Research Facility (D-Bay) [5] is capable of supporting full-scale engine experiments, with integrated remote control and instrumentation systems. Pulsed thrust measurements from 3 to 1,000 + lbf (13–4500 + N) are made with a damped thrust stand mounted on a conventional static thrust stand. Up to 6 lbm/s (3 kg/s) of 100 psi (680 kPa) air is available and high-capacity inlet and exhaust stacks are useful for self-aspirating designs and atmospheric exhaust. A direct connection to a liquid fuel farm via a high-pressure/high-capacity fuel pump retains the facilities ability to feed large-scale engines.

A hardened remote-control room is adjacent to the 750,000 + ft^3 (25,000 m^3) test cell. A minimum of 2 feet (0.6 m) of reinforced concrete is situated between the test cell and personnel during testing. Such precautions are necessary when

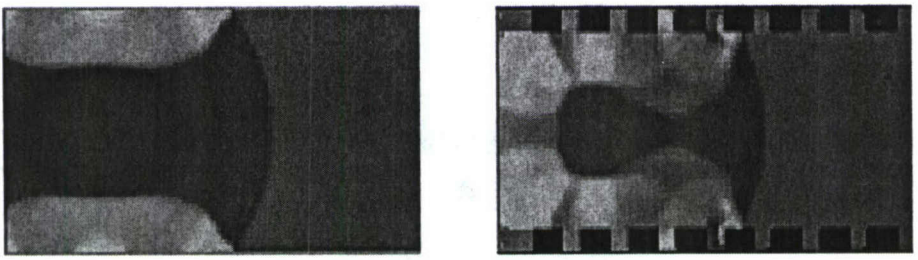

(*a*) (*b*)

Figure 1 Computational fluid dynamics (CFD) model pressure map of DDT event with (*a*) 2D tube and (*b*) Shchelkin spiral

dealing with the high-noise levels associated with PDE operation. Control of all pulsed combustor/detonation engine operations and data acquisition is done via a National Instruments LabVIEW based interface with duplicate manual emergency shutdown and safety system controls.

Choked flow measurements are employed to accurately regulate and measure oxidizer and vapor fuel flow to pulsed engine experiments. These choke points isolate the measurements from the downstream pressure oscillations of pulsed valves. Each flow system contains a pressure controller, a choked orifice plate or critical flow nozzle, and a surge tank to set and hold a required flow rate even with unsteady combustor valve flows.

In addition to conventional (low Hz and kHz frequency) data acquisition and control systems which include intake, fuel, and purge system instrumentation, the facility is equipped with up to 16 channels of high-frequency data acquisition at up to 5 MHz. These may be used for high-frequency pressure transducers, thermocouples, photodiodes, or advanced laser diagnostics. High-speed digital imaging systems, with framing rates varying from kHz to MHz are used for imaging PDE phenomena [6, 7].

Due to the critical timing issues in PDE operations, the high-frequency valving tends to be both expensive and highly constrained. During the design of a research PDE, many options were considered that were either expensive, had severe limitations in operating range, or both. The research engine design is based upon valving found in a General Motors Quad 4, Dual Overhead Cam (DOHC) cylinder head commonly used in the Pontiac Grand Am automobile. This PDE design has an extremely broad operating range and configuration, with up to four detonation tubes operating at up to 40+ Hz each with proven reliability and durability. Valving and tube mount systems have been redesigned to permit higher frequency operation, quick valve system and detonator tube configuration change-outs, and eliminate fatigue problem areas.

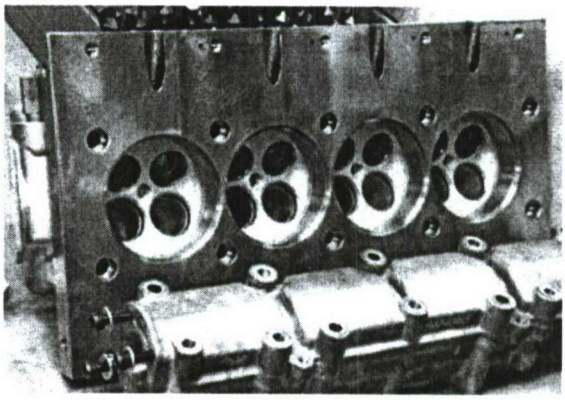

Figure 2 Quad 4 based research PDE valving assembly. Each of the four tube positions contains two intake valves (the upper pairs) and two exhaust valves, which are currently used for purge cycles (the lower pairs of valves). The stock igniter location (smaller central hole between four valves) is typically used for ignition

The operating conditions of PDEs are very similar to internal combustion engines and many of the components can be shared. By driving the overhead cams with an electric motor, the four valves in each of the four cylinders can be made to operate at between 0.5 and 40+ Hz. Many different detonator tube configurations are possible and interfaces are available including single and multiple tube configurations with tubes ranging from 0.75″ (20 mm) to 6″ (150 mm) in diameter and various lengths; 1′ to 6′ (0.3–2 m) being typical. Provisions for lubrication, cooling, ignition, and fuel delivery are integral to the cylinder head/intake manifold assembly.

The two intake valves in each cylinder, visible in Fig. 2, are used to feed premixed air and fuel into detonation tubes, which are attached to an adapter plate secured by the head bolts. In the current configuration, the head and detonation tubes are installed horizontally, and the intake valves are the upper pair. Cold air flows through the exhaust valves in reverse as a purge gas to buffer hot products from igniting the next incoming charge and to convectively cool the inside of the detonation tube walls.

Somewhat uniquely, the research PDE is operated premixed, minimizing mixing and stratification issues. The large pop-off valves and check valves visible in Fig. 3 are some of the precautions used to prevent catastrophic failure in the event of an engine backfire through the premixed intake section. Up to four detonation tubes can be run at 90° out of phase. The main combustion air and purge air lines contain ball valves for each detonation tube feed system so that the engine can be run with one tube, two tubes 180° out of phase, or all four tubes. A rotary position sensor is adapted to the intake camshaft to pro-

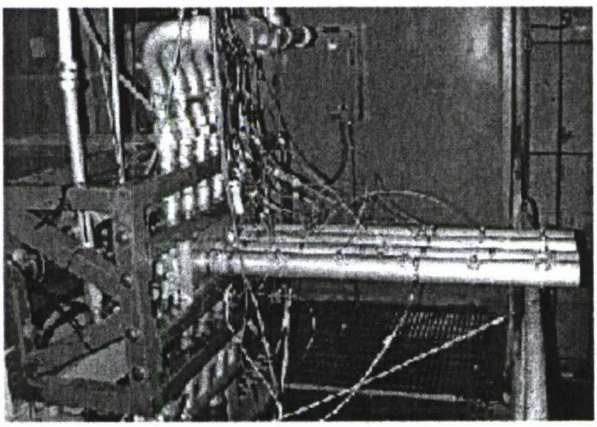

Figure 3 Four-tube research PDE as installed on damped thrust stand. Upper manifold supplies premixed fuel and air; lower manifold provides purge cycle of clean, unfueled air

vide both an index of the valve timing sequence and the relative position of the valves. This signal serves as the master timing signal for the ignition and data acquisition systems.

An eight-channel igniter/fuel injection control box is triggered off the rotary position sensor. Separate control of each detonation tubes' igniter and/or fuel injector can be accomplished with this system. Vapor fuels are premixed with the combustion air via a separate critical flow nozzle and flow control system. Due to the high noise levels associated with PDE testing, all controls and data acquisition are performed remotely from an isolated control room. All of the control systems and data acquisition systems are LabVIEW based and integrated into one 'virtual instrument' with back-up manual shutdown and safety systems. This virtual control panel is extremely flexible and can control all aspects of the PDE's operation including: lubrication, operating valve drive-motor speed, fuel flow, main combustion air flow, purge air flow, fuel systems, timing, ignition delays, and automatic shutdown in the event of a critical system failure.

The research engine is used for performance prediction validations and serves as a test-bed for research of detonation initiation and DDT minimization, heat transfer, noise levels, pulsed ejector concepts, and multitube interactions. A vapor propane system is utilized to conduct research on a complex-hydrocarbon that detonates much like kerosene-based fuels, while avoiding atomization and mixing issues associated with liquid fuels. A variety of liquid fuel injection schemes have also been applied. Further details on the research facility and engine are available elsewhere [5, 8].

3 RESULTS AND DISCUSSION

Although a variety of mechanisms have been studied for detonation initiation [9], only confinement and obstacles will be described briefly here. Confinement has long been a method for prompting detonation initiation via compression of a combustible mixture in an enclosed space. Recently, cavities have been employed to accelerate the transition to detonation downstream of the cavity. Smirnov & Tyurnikov were using cavities to promote DDT in gasoline–air mixtures [10].

Recent CFD models of this cavity effect have provided new insights into the mechanisms responsible for achieving DDT. A typical result in a model of such a cavity geometry is shown in Fig. 4. Subsequent frames, from (*a*) through (*j*), depict pressure levels (white — high / dark — low). A channel corresponding to approximately 1 cell width in height is ignited via a small combusting channel propagating into a cavity approximately 3 cells in both height and width for this 2D simulation. In the first frame, (*a*), weak ignition is achieved via the small channel entering the cavity. Unburned pockets of fuel–air mixture trapped in cavity in frame (*b*), 'explode' in frame (*c*), releasing heat behind the main combustion front. Compression waves from the cavity coalesce near the flame front in frames (*e*) through (*g*) and subsequently create the microexplosion visible in (*g*), which then produces the multiple DDT events visible in frames (*h*) and (*i*). A right-running detonation wave and left-running retonation wave are then evident in frame (*j*). Similar results have been obtained experimentally as well [9].

In addition, to looking at cavities, high-speed digital imaging [6, 7] was used to study the impact of obstacles such as the Shchelkin spiral geometry which produced the hot spots evident in Fig. 1. By utilizing an optically clear polycarbonate detonator tube, flame acceleration and formation of hot spots may be observed in footage such as the frames in Fig. 5. Obtained at 18,000 frames per second, these images depict a classical microexplosion during DDT, the detonation and retonation propagation, as well as the expansion process during tube blow down.

Utilizing detonation initiation methods developed using the techniques illustrated above, DDT is obtained. High-frequency data acquisition systems verify detonative operation. High-frequency pressure transducer measurements in a hydrogen–air detonator tube, as seen in Fig. 6, indicate measured wave speeds of 1959 m/s. Further experimental verification of detonation wave speeds was provided by photodiode measurements shown in Fig. 7 with a derived wave speed of 1959 m/s. These results are in excellent agreement with the stoichiometric hydrogen–air wave speed of 1968 m/s published elsewhere [11].

Similar results are obtained for liquid hydrocarbon fuels (Fig. 8), including the gradual pressure rise near the head wall, the overdriven detonation obtained during DDT, and attainment of the steady Chapman–Jouguet value during detonation propagation down the detonator tube. Evidence of detonation may be

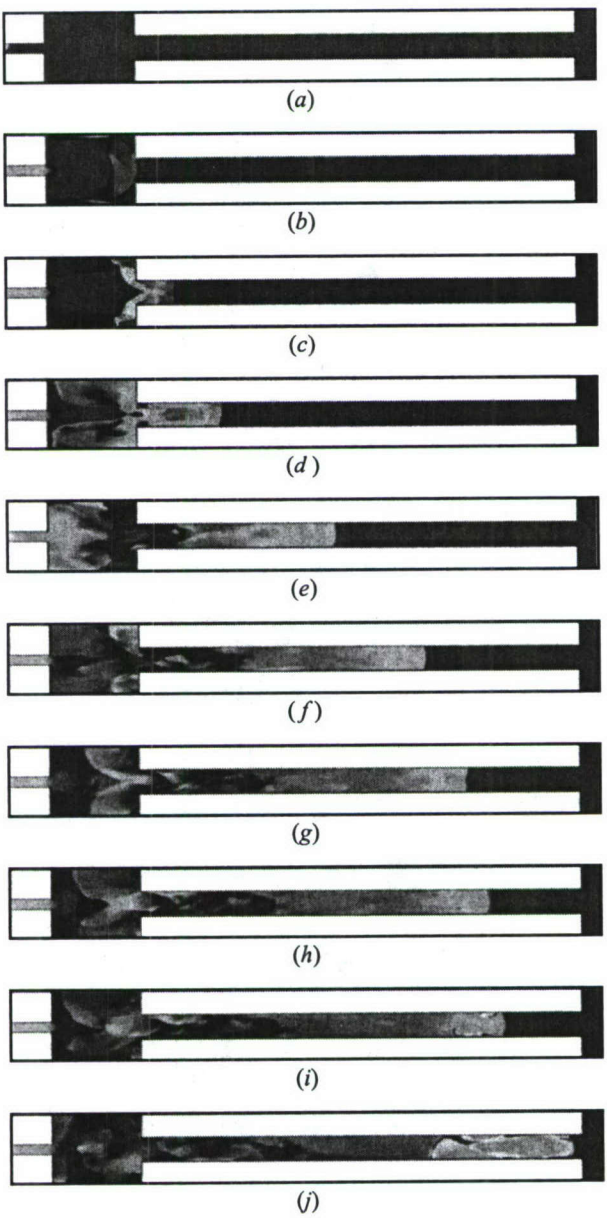

Figure 4 Sequential pressure images of weak ignition and subsequent DDT event in CFD model of cavity geometry

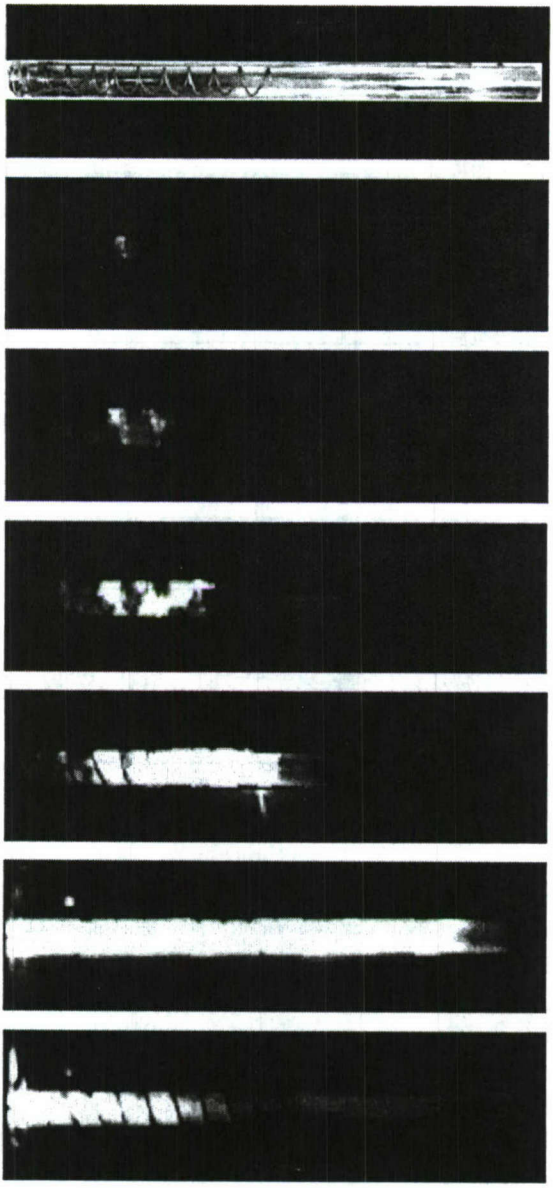

Figure 5 High-speed digital imaging of DDT process with Shchelkin spiral in polycarbonate tube. From top to bottom: still of polycarbonate tube with Shchelkin spiral, formation of hot spot, formation of multiple hot spots, microexplosion, DDT event, subsequent right running detonation and left running retonation, and in the last frame: left running expansion wave during blow-down process

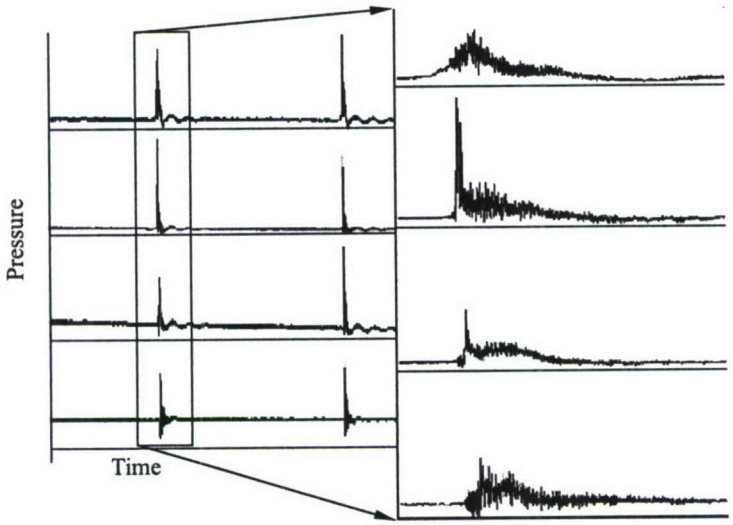

Figure 6 High-frequency pressure traces from in-house PDE at 16 Hz detonation frequency. Measurement locations at 3-, 15-, 21-, and 33-inch (7-, 38-, 53-, and 83-centimeter) axial distances from head; $\sim$ 200-millisecond duration shown

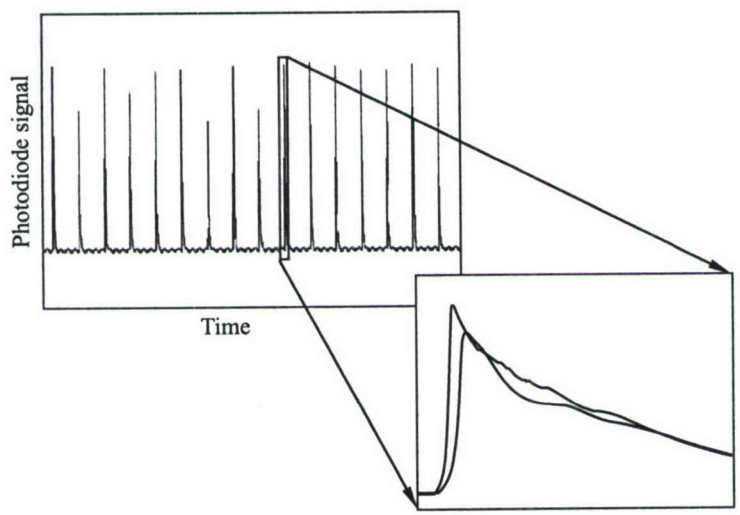

Figure 7 Results of photodiode measurements in a PDE tube at 27- and 33-inch (70- and 83-centimeter) locations

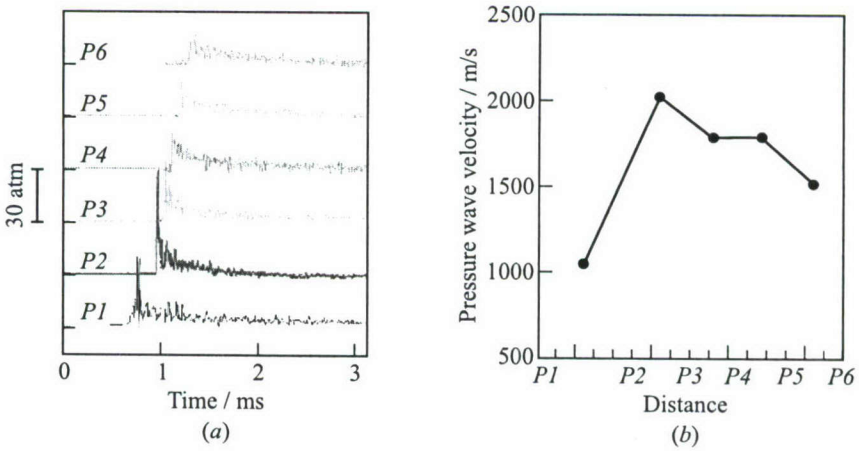

Figure 8 High-frequency pressure traces from research PDE with aviation gasoline. Pressure transducers are distributed from near inlet to near detonator tube exit, *P1* through *P6*, respectively. Pressure wave velocities on right are computed from time of travel between pressure transducers

observed in both the pressure magnitudes on the left side of Fig. 8 and the measured pressure wave velocities on the right.

Typical performance results that follow were obtained with a single aluminum 2.0-inch (50.8-millimeter) inner-diameter tube that was 36″ (915 mm) long, operated at 16 Hz. Conventional weak initiation was employed at the head end (via the spark plugs) with a 5-millisecond ignition delay. The fuel–oxidizer mixture was stoichiometric and premixed hydrogen–air with a 50% clean air purge fill ratio. The above operating parameters apply to all experimental data herein unless stated otherwise.

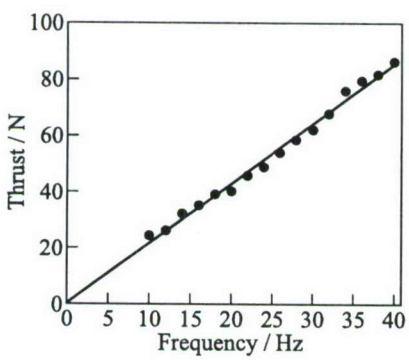

Figure 9 Measured PDE thrust vs. frequency dependence

The research engine has been run in multitube mode, demonstrating both two-tube operation 180° out of phase and four-tube operation 90° out of phase. A wide variety of frequencies have also been demonstrated indicating the simple linear scaling of thrust vs. frequency as shown in Fig. 9. This data also demonstrates the accuracy of the thrust measurements, as the deviation from the straight line is ±0.5 lbf (±2.2 N). Such thrust measurements

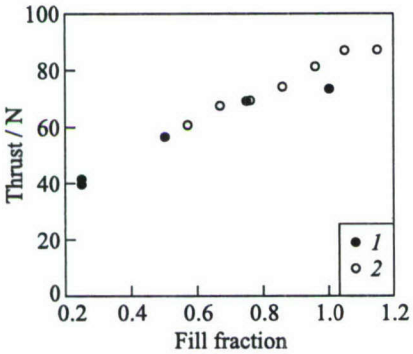

Figure 10 Pulse detonation engine thrust vs. tube fill fraction for hydrogen–air (*1*) and ethanol–air (*2*) mixtures. Fill fraction is defined as filled volume of detonable mixture divided by total tube volume

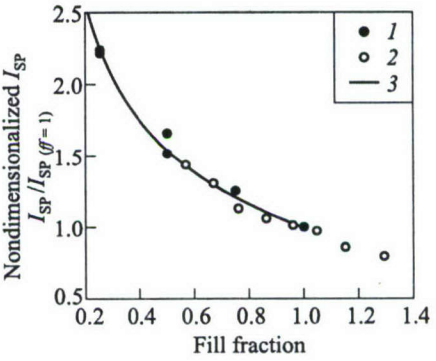

Figure 11 Effect of varying fill fraction on fuel-based specific impulse (nondimensionalized by full tube fill). Experimental data is shown for hydrogen–air (*1*) and ethanol–air (*2*) mixtures along with the analytical results of Mitrofanov (*3*) [13]

have been demonstrated with the current system down to 3 lbf (13 N) but the accuracy and thrust range can be varied with configuration changes.

In addition to frequency alterations, thrust modulation may also be accomplished via variation of the volume of the tube filled with detonable mixture. Via volumetric flow control, the tube fill fraction was varied with the resulting impact upon thrust measured as shown in Fig. 10. Similar results were observed with both hydrogen and liquid fuels. The ratio of the detonable mixture volume to tube volume is referred to as the fill fraction. Fill fractions greater than one typically result in a cloud of combustible mixture around the end of the detonator tube that does not contribute to thrust. Fill fractions less than one result in a detonation driving either purge cycle and/or products from the previous cycle. This results in the same effect as a bypass ratio in a turbo fan engine, in that a bigger mass is moved at a lower change in velocity with resultant gains in efficiency.

This effect has been observed both computationally and experimentally by a number of researchers [8, 12] and has been analytically studied by Mitrofanov [13]. Mitrofanov's calculations, along with authors' experimental results, are plotted in Fig. 11. Specific impulse was normalized via the specific impulse at a fill fraction of 1.0 to collapse the curves for the different fuels. Essentially, this permits data reduction with allowances for differences in the fuel heating value. As seen in the excellent match between the analytical results and the results with two different fuels, the correlation is quite good.

A similar correlation by Shepherd [14] has been compared to a wide variety of experimental data with various tube geometries, wall temperatures, and oper-

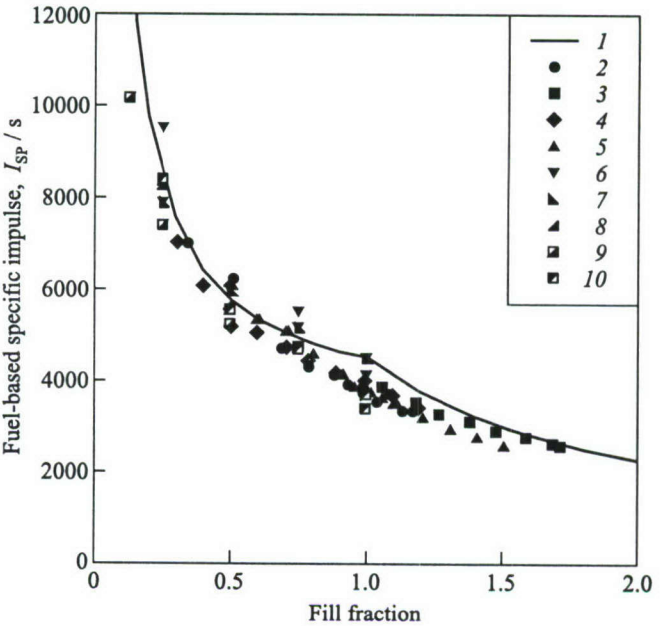

Figure 12 Variation of fuel-based specific impulse vs. tube fill fraction for hydrogen–air mixture. Experimental data from a variety of detonation tube sizes, wall temperatures, and operating frequencies are compared with the analytical model of Shepherd [14]: *1* — I_{sp}, Shepherd model; *2* — med. freq. cooled 99; *3* — low freq. cooled 99; *4* — med. freq. alum. 99; *5* — low freq. alum. 99; *6* — high freq. cooled 00; *7* — high freq. hot steel 01; *8* — 6-foot tube 00; *9* — 6-foot tube 01; and *10* — 3.5-inch diam. 01

ating frequencies (Fig. 12). Again, the results are in good agreement, indicating that performance is easily determined by tube volume and fill conditions.

Along with variations in fill conditions, tube geometry and dynamic effects have been found to dramatically impact the blow down behavior of detonator tubes. The sensitivity of performance to these exit conditions has been identified by Kailasanath *et al.* computationally as the source of much dissension in PDE performance comparisons [15]. Experimentally, high-speed imaging of detonation blow down processes also revealed this sensitivity, as observed in Fig. 13. Slight variations in conditions described above can result in either the spherical shock wrapping at the exit (left image) and resulting in formation of large-scale vortices or the much different behavior depicted by the image on the right, where the detonation blow-down appears to resemble a supersonic jet.

In addition to the effects of frequency and fill fraction, the impact of fuel–air ratio was also examined as shown in Fig. 14. Thrust is plotted vs. a wide range of equivalence ratios. As expected from detonability data [13], a stable region is

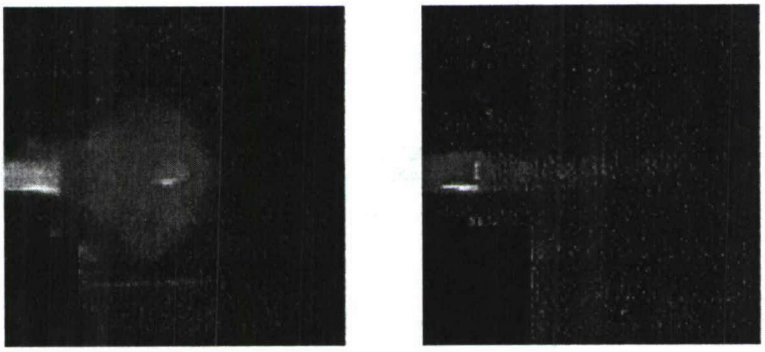

(*a*) (*b*)

Figure 13 High-speed images of detonation blow down. During blow down event on (*a*), a spherical compression wave and vortex roll up is evident. As a result of slight differences in operating conditions, the detonator tube imaged on (*b*) resembles supersonic jet blow down

observed at equivilance ratios near stoichiometric. At fuel-rich conditions, both the detonability and thrust are observed to fall off gradually with increasing fuel-to-air ratio. The detonability and thrust fall off more quickly on the fuel lean side. Similar trends have been observed with other fuel–air mixtures. Despite the loss in thrust due to fuel-lean operation, potential fuel efficiency gains may be made when fuel flow rates are also considered, such as in the following discussion of specific impulse.

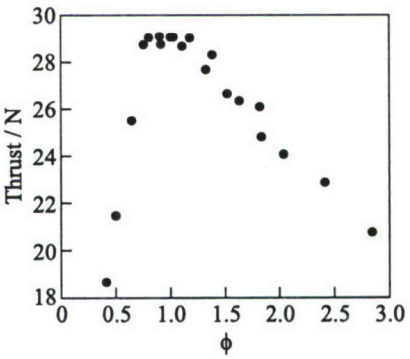

Figure 14 Measured thrust vs. equivalence ratio (ϕ) for hydrogen–air fueled PDE

Specific impulse vs. a wide range of equivilance ratios is shown in Fig. 15 with hydrogen, propane, and various liquid hydrocarbon fuels. Data is compared to analytical predictions by Shepherd [16] along with one experimental point which was initiated with a conventional oxygen predetonator system. Shepherd obtained this experimental data using a single-shot pendulum technique [16]. The heating values for the complex hydrocarbon fuels shown are all similar, except for ethanol, which has a lower heating value and a resultant, lower specific impulse. The analytical predictions assume the mixture detonated from the start, while experimental results required

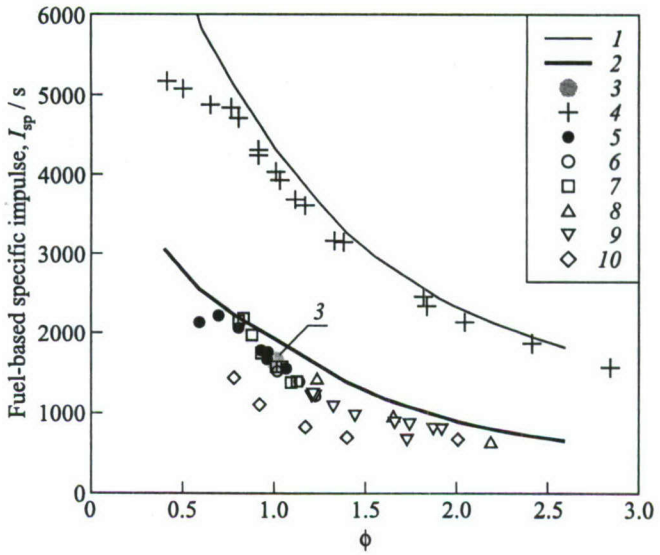

Figure 15 Fuel-based specific impulse I_{sp} vs. equivilance ratio ϕ for a variety of fuel–air mixtures. Calculations *1* (H_2–air) and *2* (C_3H_8–air) and measurement of C_3H_8–air mixture initiated via conventional oxygen predetonator (*3*) are provided by Shepherd [14]. All other experimental measurements were conducted with weak initiation in air. Fuels include: H_2 — *4*, propane (C_3H_8) — *5*, 87-octane motor gasoline (MoGas) — *6*, 100-octane low-lead aviation gasoline (AvGas) — *7*, standard USAF kerosene jet fuels JP-8 — *8* and JP-4 — *9*, and ethanol — *10*

DDT. Despite these differences, good agreement between model and experiments is observed for equivilance ratios above 0.7. Below $\phi = 0.8$, cell size increases rapidly making DDT difficult to obtain [3]; hence the low experimental values.

4 CONCLUDING REMARKS

A brief description of the modeling, research facility, and a research engine used to conduct PDE research has been provided. These tools provided results on detonation initiation, and performance for a wide variety of fuels, detonator tubes, and operating conditions. Results from variations in frequency, equivalence ratio, and tube fill conditions have been presented.

There is much work to be done in developing valving, detonation initiators, noise suppression techniques, thermal protection systems, intake and exhaust nozzles, and control systems before a kerosene–air fueled PDE becomes practical.

The AFRL is exploring PDE technology development (cf. [17–19]) through in-house research and collaboration with other researchers.

ACKNOWLEDGMENTS

This research was funded by the AFOSR and AFRL. Special appreciation must be expressed to the technicians and support personnel, both in-house government employees and on-site contractors who made this work possible, particularly Dwight Fox, Walt Balster, and Jason Parker. Dr. Terry Meyer, Dr. Mike Brown, and Dr. Jim Gord helped provide high-speed imaging. Authors also wish to acknowledge the technical leadership of Dr. Mel Roquemore and Dr. Robert Hancock.

REFERENCES

1. Kailasanath, K. 1999. Recent developments in the research on pulse detonation engine. AIAA Paper No. 2002-0470.
2. Coleman, M. L. 2001. Overview of pulse detonation propulsion technology. CPIA Technical Report CPTR 70.
3. Kaneshige, M., and J. E. Shepherd. 1997. Detonation database. Technical Report FM97-8. GALCIT.
4. Katta, V. R., L. P. Chin, and F. R. Schauer. 1999. Numerical studies on cellular detonation wave subjected to sudden expansion. *17th Colloquium (International) on the Dynamics of Explosions and Reactive Systems Proceedings*. Heidelberg, Germany.
5. Hancock, R. D., J. R. Gord, D. T. Shouse, F. R. Schauer, V. M. Belovich, and W. M. Roquemore. 1999. AFRL combustion branch (PRSC) aero-propulsion research and development activities. *International Test and Evaluation Association (ITEA) Conference Proceedings.*
6. Gord, J. R., C. Tyler, K. D. Grinstead, Jr., G. J. Fiechtner, M. J. Cochran, and J. R. Frus. 1999. Imaging strategies for the study of gas turbine spark ignition. *SPIE's 44th Annual Meeting & Exhibition, Conference 3783 on Optical Diagnostics for Fluids/Heat/Combustion and Photomechanics of Solids.* Denver, CO.
7. Meyer, T. R., J. L. Hoke, M. S. Brown, J. R. Gord, and F. R. Schauer. 2002. Experimental study of deflagration-to-detonation enhancement techniques in a H_2/air pulsed detonation engine. AIAA Paper No. 2002-3720.
8. Schauer, F., J. Stutrud, and R. Bradley. 2001. Detonation initiation studies and performance results for pulsed detonation engine applications. AIAA Paper No. 2001-1129.

9. Schauer, F., J. Stutrud, R. Bradley, V. Katta, and J. Hoke. 2001. Detonation initiation and performance in complex hydrocarbon fueled pulsed detonation engines. *50th JANNAF Propulsion Meeting Proceedings*. Paper I-05. Salt Lake City, UT.
10. Smirnov, N. N., and M. V. Tyurnikov. 1986. Deflagration to detonation transition in gasoline–air mixtures. *Combustion Explosion Shock Waves* 22(2):65–68.
11. Soloukhin, R. I. 1963. *Shock waves and detonations in gases*. Baltimore: Mono Book Corp.
12. Kailasanath, K., G. Patnaik, and C. Li. 1999. Computational studies of pulse detonation engines: A status report. AIAA Paper No. 99-2634.
13. Mitrofanov, V. 2001. Continuous spin detonation of gases and sprayed liquid fuels. *Windows on Science Seminar, EAORD*. Wright-Patterson AFB, OH.
14. Shepherd, J. 2002. *ONR Mid-Term PDE MURI Meeting*. St. Augustine, FL.
15. Kailasanath, K., *et al.* 1999. Pulsed detonation engines — what is its performance? *JANNAF 24th Airbreathing Propulsion Subcommittee* and *36th Combustion Subcommittee Joint Meeting Proceedings*. CPIA Publication 692. Cocoa Beach, FL 1:131–40.
16. Shepherd, J. 2000. Private communications. California Institute of Technology.
17. Rolling, A. J., P. I. King, and F. R. Schauer. 2002. Propagation of detonation waves in tubes split from a PDE thrust tube. AIAA Paper No. 2002-3714.
18. Hoke, J., R. Bradley, J. Stutrud, and F. Schauer. 2002. Integration of a pulsed detonation engine with an ejector pump and with a turbo-charger as methods to self-aspirate. AIAA Paper No. 2002-0615.
19. Frankey, B., F. Schauer, R. Bradley, and J. Hoke. 2002. Evaluation of a hybrid-piston pulsed detonation engine. AIAA Paper No. 2002-0474.

PULSED EJECTOR WAVE PROPAGATION TEST PROGRAM

R. Fernandez, J. W. Slater, and D. E. Paxson

The development of, and initial test data from, a nondetonating Pulse Detonation Engine (PDE) simulator tested in the NASA Glenn 1 × 1 foot Supersonic Wind Tunnel (SWT) is presented in this paper. The concept is a pulsed ejector driven by the simulated exhaust of a PDE. This program is applicable to a PDE entombed in a ramjet flowpath, i.e., a PDE combined-cycle propulsion system. The ejector primary flow is from a pulsed, underexpanded, supersonic nozzle simulating the supersonic waves emanating from a PDE, while the ejector secondary flow is the 1 × 1 foot SWT test section operated at subsonic Mach numbers. The objective is not to study the detonation details, but the wave physics including the starting vortices, the extent of propagation of the wave front, the reflection of the wave from the secondary flowpath walls, and the timing of these events of a pulsed ejector, and correlate these with Computational Fluid Dynamics (CFD) code predictions. Pulsed ejectors have been shown to result in a 3 to 1 improvement in L/D (length-to-diameter) and a near 2 to 1 improvement in thrust augmentation over a steady ejector. This program will also explore the extent of upstream interactions between an inlet and large, periodically applied, backpressures to the inlet as would be present due to combustion tube detonations in a PDE. These interactions could result in inlet unstart or buzz for a supersonic mixed compression inlet. The design of the present experiment entailed the use of an x–t diagram characteristics code to study the nozzle filling and purging timescales as well as a series of CFD analyses conducted using the WIND code. The WIND code is a general purpose CFD code for solution of the Reynolds averaged Navier–Stokes equations and can be applied to both steady state and time-accurate calculations. The first, proof-of-concept, test entry (spring 2001) pressure distributions shown here indicate the simulation concept was successful and therefore the experimental approach is sound. Future testing (planned for mid 2002) will serve to quantify the unsteady ejector performance.

NOMENCLATURE

a^* reference speed of sound used in the nondimensionalized x–t diagrams
A_p primary flow stream cross-section area at mixing region entrance

A_s secondary flow stream equivalent circular cross-section area at mixing region entrance
D ejector diameter
D_p primary flow stream cross-section diameter at mixing region entrance
D_s secondary flow stream equivalent circular cross-section diameter at mixing region entrance
f primary nozzle frequency
L generic length
M_D detonation Mach number
$\mathrm{M}_{\mathrm{noz}}$ Mach number of the nozzle exit
M_0 free-stream Mach number
M_p primary stream Mach number
M_s secondary stream Mach number
p^* reference pressure used to nondimensionaize x–t diagrams
P_a ambient pressure
P_{exit} pressure at nozzle exit
P_T total pressure
$P_{T\mathrm{noz}}$ upstream total pressure of the nozzle
P_{T0} upstream or entrance total pressure
t time (seconds)
T^* reference temperature used to nondimensionalize x–t diagrams
T_{ad} local adiabatic supercooling temperature (Rankine)
T_{dp} local dew point temperature
T_{pn} primary nozzle total temperature
T_s local static temperature
T_T total temperature
$T_{T\mathrm{noz}}$ upstream total temperature of the nozzle
T_{T0} upstream or entrance total temperature
w_p primary stream mass flow
$w_{p\,\mathrm{max}}$ primary nozzle peak instantaneous mass flow
w_s secondary stream mass flow
x axial distance
β ejector entrainment ratio; secondary mass flow to primary mass flow
γ ratio of specific heats (1.4)
ϕ equivalence ratio; $(\text{fuel–air})/(\text{fuel–air})_{\mathrm{stoich}}$
ρ^* reference density used to nondimensionalize x–t diagrams

1 BACKGROUND AND INTRODUCTION

The focus of the test program described in this paper is the design and first exploratory run of an attempt to create a noncombusting simulation of a repeating

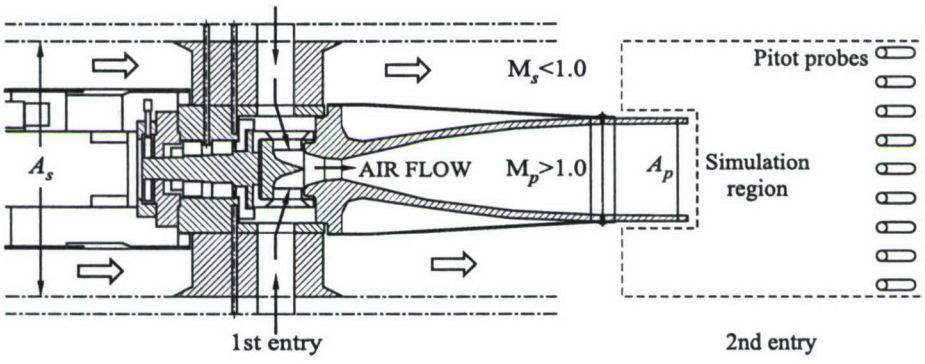

Figure 1 Simulation region: 1st entry: $A_s/A_p = 10$, $D_s/D_p = 3.1$; 2nd entry: $A_s/A_p = 31.2$, $D_s/D_p = 5.6$

series of shock waves exiting a detonation tube into an enclosing chamber that has forced subsonic flow entering the upstream end and the combined streams exiting from the downstream end of the chamber. No attempt is made to actually simulate the chemical reactions, the exhaust products, or the heat release of the detonating wave. The simulation zone starts after the exit of the PDE simulator nozzle and includes the walls of the enclosing chamber, the upstream flow entrance plane, and the downstream mixed flow entrance plane (Fig. 1). Because the detonation chamber is excluded from the simulation, there is no need to reproduce the internal von Neumann pressure spike, nor the thrust generating "plateau" pressure. The parameters that are simulated in the present experiment include: the cycle time or frequency of the disturbances, the detonation tube exit Mach number, a conically shaped (not spherical) shock wave propagating through the confining chamber, the shock reflections off the confining walls, and the associated shock-induced static pressure increases. This simulation should generate any "starting" vortices created, and mixing in the shear layer between the upstream forced flow and the supersonic tube exit.

A pulse detonation engine [1] operates by introducing a fuel–oxidizer mixture into a pressure vessel with an open end and initiating near-constant volume combustion via a detonation. The higher-than-ambient pressure pushing on the closed end of the pressure vessel produces the thrust. An ejector works via the transfer of energy from the primary, or "driving" stream, into the secondary, or "driven" stream. The mixed flow of the two interacting fluid streams exhausts out of the propulsion system at a higher thrust than that of the primary stream alone, i.e., thrust is augmented. The concept discussed in this paper is based on a combination of both concepts to get the greater thermodynamic cycle efficiencies of the PDE when compared to the Brayton cycle with the thrust augmentation of an ejector. This concept involves replacing the traditional steady ejector primary

with a PDE and, thus, employing an unsteady ejector system. Pulsed ejectors have been shown to result in a 3 to 1 improvement in L/D and a near 2 to 1 improvement in thrust augmentation [2].

Many studies have been conducted and papers published on PDE concepts during the last decade. The motivations for all these studies are the promises of lighter weight, high efficiencies, and less complexity (i.e., more robust) [3] than turbine engines. The near-constant volume combustion due to the detonation process [4] produces a higher ideal thermodynamic cycle efficiency for a PDE cycle compared to a Brayton cycle. A PDE system compared to a typical turbomachine has far less moving parts and, thus, far less weight and complexity. Compared to turbojets, PDE systems may offer a reduction in development time, a reduction in engine costs, better thrust-to-weights at higher Mach numbers, decreased parts count, and simplified geometry as well as more flexibility when integrating the propulsion system into the airframe. A PDE propulsion system compared to a ramjet propulsion system has similar levels of lightweight and simplicity but has the added benefit of being able to generate static thrust [5].

Pulse detonation engines may be applicable to a broad range of civil aeropropulsion needs — access-to-space, high-performance aircraft, and Unmanned Air Vehicles (UAVs). Figure 2 shows a possible PDE–ramjet combined-cycle engine configuration for a Single Stage-To-Orbit (SSTO) application using a notional reference vehicle.

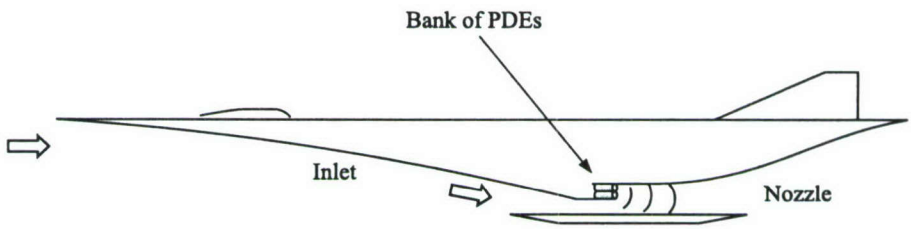

Figure 2 Notional PDE-based combined cycle vehicle

To capitalize on the significant performance benefits of a PDE system, the technical challenges of material limits, combustion-product chemistry, and demonstrated propulsion system component (i.e., vehicle inlet and nozzle, controls, etc.) performance have to be addressed. Material thermal limits [6] and the impact of dissociation and sensible heat release on engine performance [7] have been covered in other papers. Here, the wave propagation information is applicable to how far upstream the interactions between an inlet and large, cyclically applied, backpressures to the inlet, caused by the combustion tube detonations propagating through the mixing section, propagate. For a supersonic mixed-compression inlet, large interactions can result in inlet unstart or buzz.

2 OBJECTIVE

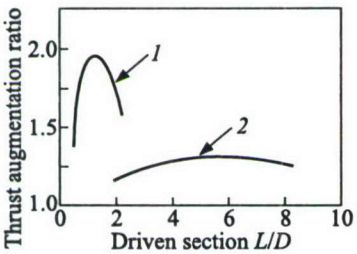

Figure 3 Lockwood's data on comparative thrust augmentation by ejectors [8], area ratio = 10: *1* — pulse jet, and *2* — steady flow

A primary objective of this study is to understand the wave physics of a pulsed ejector including the extent of propagation of the wave front, the reflection of the wave from the secondary flowpath walls, and the timing of these events in order to validate CFD code predictions. The experiment will also quantify the pulsed ejector performance (i.e., thrust augmentation) for this configuration and will be compared to previous studies (Fig. 3) [8]. These past studies show that pulsed ejectors result in a higher thrust augmentation ratio and smaller length-to-diameter ratios than steady state ejectors.

This current test program is one of several studies at the NASA Glenn Research Center (GRC) focused on verifying and understanding unsteady ejector behavior. These various studies encompass the speed regime from subsonic pulsejet-driven ejectors, supersonic pulsed air-jet ejectors (the present paper), to actual PDE-driven pulsed ejectors. The objective being to understand and differentiate the various fluid dynamic phenomena involved in pulsed ejectors. This current test hardware is ideally suited to study pulse or wave shape effects on unsteady ejector performance via the variation of: pulse Mach number, pulse frequency, pulse wave width (via different selections of valve duty cycle), primary-to-secondary area ratios, and primary-to-secondary density ratios.

This test program will also provide data to assess how unsteady downstream conditions affect the performance and operation of inlets. Because inlets are designed to avoid operations near buzz, this dynamic downstream disturbance represents a whole new technology area for inlet designs.

This fundamental experimental program is being conducted in the 1 × 1 SWT and requires operation in subsonic conditions; a regime outside of the facility design. Therefore during this program the flow quality, both spatially and temporally, of the 1 × 1 SWT operating in subsonic mode was quantified and the control of the tunnel in this mode was assessed.

3 MODELING

3.1 Nozzle and Valve Design

The primary stream supersonic nozzle design was challenging due to several constraints:

(1) The need to produce supersonic exit Mach numbers at the exit of the nozzle equivalent to those produced by a detonation tube;

(2) The desire to match the geometric configuration of Lockwood (10-to-1 secondary-to-primary area ratio);

(3) A test facility supply pressure limitation for the primary stream of 465 psia and a supply mass flow limitation of 8 lbm/s;

(4) The wind tunnel itself, the secondary stream, has a low-end static pressure limit at the subsonic Mach numbers governed by the geometry of the installed hardware (and its associated pressure losses induced in the tunnel) and the lower limit the valve control system can hold;

(5) Dew point temperatures on the primary stream low enough to prevent condensation in the nozzle; and

(6) The need for a sharp pressure spike or pulse at the nozzle exit; vs. gradual ramp-ups or ramp-downs which would not properly simulate a PDE.

The first test entry's supersonic nozzle was designed for an exit Mach number of 5.0; a hydrogen–oxygen detonation wave generated with $\phi = 1.0$, $T_T = 536.4$ °R, and a $P_T = 14.7$ psia, produces an actual detonation tube exit Mach number (M_D) of 4.83. Figure 4 presents CFD pressure contours of a detonation wave at the above conditions, with a superimposed sketch of the axisymmetric, or conical, underexpanded nozzle shock plume. The second test entry will also include nozzles designed for lower Mach numbers and different ejector area ratios. The combination of the predefined exit Mach number, and the 10-to-1 secondary-to-primary area ratio (the 1 × 1 SWT's cross-section area equals to 144 sq. in.) defines the supersonic nozzle throat area. With this set, the system mass flow is automatically set for a given pressure. High nozzle Mach number limits are set by the starting pressure ratio needed, with 465 psia being the upstream maximum pressure obtainable, although after flowing through the air valve, the maximum pressure available to the nozzle is about 323 psia. The downstream minimum pressure available is 1.9 psia, although locally lower static pressures are obtainable with the secondary stream flowing. The dew point limit of 445 °R or less is to avoid condensation. The low nozzle Mach number limit is set by the maximum mass flow limit of 8 lbm/s; if the 10-to-1 ejector area ratio is preserved, then the nozzle throat gets larger with decreasing Mach number.

The ejector primary's Mach 5 nozzle was designed with a Method of Characteristics (MOC) FORTRAN code that allows inputs of exit Mach, the ratio of specific heats, γ, and the throat radius. This produces an ideal inviscid nozzle contour that then can be modified to account for boundary layer displacement thickness growth. Because of the small scale of this hardware, there was not a significant change in the nozzle contour due to boundary layer build up. Most

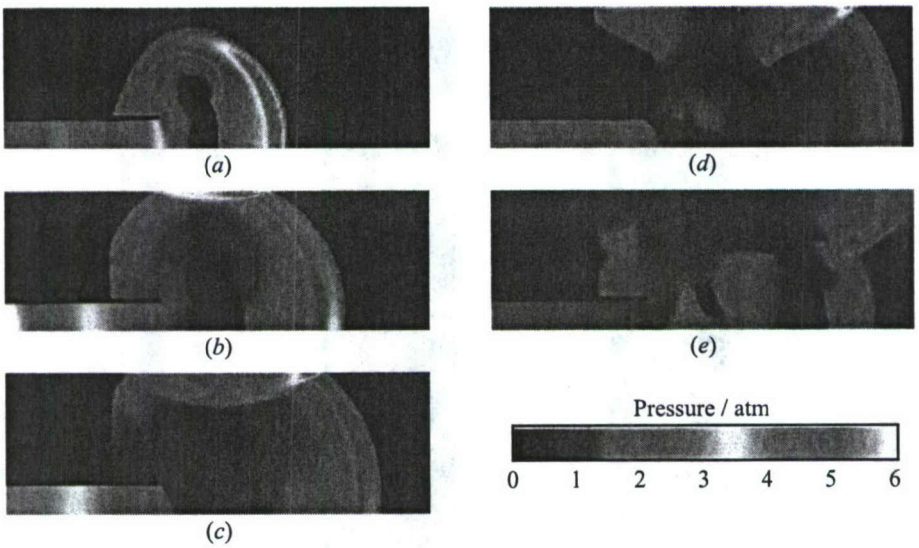

Figure 4 CFD pressure contours of hydrogen–oxygen detonation exiting the PDE tube: (*a*) $t = 0.087$ ms; (*b*) $t = 0.115$ ms, the shock reflects off the tunnel wall; (*c*) $t = 0.142$ ms, the reflected shock has propagated further along the tunnel centerline; (*d*) $t = 0.170$ ms, there is interference between shock waves and expansions; and (*e*) $t = 0.198$ ms. At $t = 0.0188$ ms, the detonation is at the PDE tube exit plane. (Refer color plate VII.)

of the viscous contour offset was smaller than typical machining tolerances until the very end of the nozzle. Therefore, for the following timescale study and CFD analysis, the original inviscid contour was used.

With the primary nozzle starting pressure ratio (spanning the range of 21 to 200), and the peak primary mass flow of 4.8 lbm/s within bounds, there were three remaining items to be studied: valve duty cycle and the associated nozzle filling and emptying time scales; condensation-induced flow breakdown within the nozzle; and the valve performance requirements.

3.2 Timescale Study

In order to arrive at an estimate of the filling and purging process of the supersonic primary nozzle, which determines the pulse wave shape, a quasi-one-dimensional x–t diagram FORTRAN code was run. This computer code will also be used on the other various nozzles to be tested in the facility.

All of the results presented used a 200-point grid and a nondimensional time step of $\Delta\tau = 0.0005$. All of the results to be presented are nondimensional. The

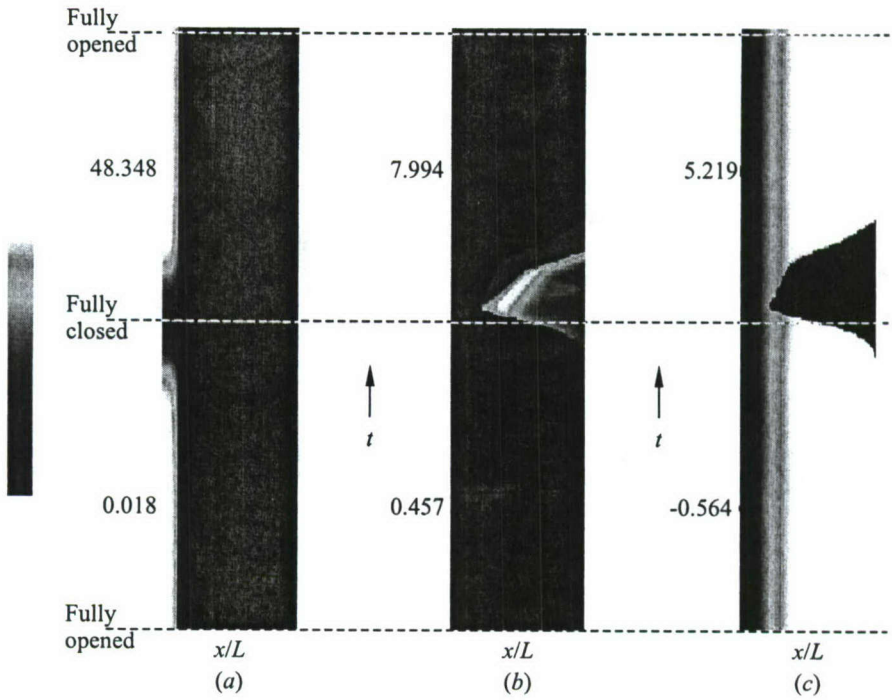

Figure 5 Pressure (a), temperature (b), and Mach contours (c) over one 60-hertz cycle of a Mach 5 nozzle using a linear valve. Numbers beside contours represent high and low values in the x–t space. All values have been nondimensionalized. (Refer color plate VIII.)

Table 1 Reference conditions used to nondimensionalize the Mach 5 nozzle results

p^*, psia	ρ^*, lbm/ft^3	T^*, °R	a^*, ft/s	γ	L, in.
5.75	0.055	281.4	823.0	1.4	16.49

reference conditions used to nondimensionalize the results in Fig. 5 are listed in Table 1.

Because a range of inlet pressure and temperature conditions is tested during the experiment, an average of this range was used as the input. The results are $P_{T0} = 287.5$ psia, $T_{T0} = 985$ °R. These results are for an overexpanded nozzle with an ambient pressure of $P_a = 10.0$ psia.

Because the quasi-one-dimensional x–t code needs a continuous area distribution, a piecewise curve fit was actually used in the code. The fit was made

using a parabola from $0 < x/L < 0.124$ and a sixth order polynomial from $0.124 < x/L < 1.0$.

3.3 Instantaneous Closing

The first simulation is that of an instantaneous closing of the inlet. Practically, this meant imposing a 'wall' boundary condition on the steady flow and running until the exit flow became subsonic. This turned out to be a very short time. Because of the scaling, it appears that almost nothing is going on until the shock abruptly forms at the exhaust end and travels upstream. In reality, the expansion wave arising from stopping the flow at the inlet end travels down the nozzle. The nozzle is quite underexpanded, with a steady state pressure ratio, P_a/P_{exit} of approximately 19. The expansion wave causes the pressure (P_{exit}) to drop and at $t = 0.27$ (0.45 ms) the pressure ratio exceeds 29, the value corresponding to a normal shock with an incoming Mach number of 5.0.

3.4 Instantaneous Opening

After closing the inlet for the simulation described above, the code was run for an extended period of time. Since there is nothing to damp out waves in the code, they continued to rebound in the nozzle. Thus, at some arbitrary time long after the inlet closing, the inlet was instantaneously reopened. An extrapolation was required due to the way that boundary conditions are imposed in the code. With inflow boundaries, one normally imposes a total pressure and temperature. These values are used, along with characteristic information from the interior of the computing domain, to calculate an appropriate state for the image cell just outside the computing domain. In some situations, such as the instantaneous opening of the nozzle inlet, this approach will show that the entering flow is supersonic, and a Mach number must also be imposed. The Mach number for the image cell was simply specified as 1.0. It makes very little difference however, as this supersonic boundary condition persists for only 0.025 time units (0.04 ms). The flow is essentially sonic at the outlet by 0.27 time units (although it drops slightly below for a period after that). At 1.2 time units, the exhaust flow abruptly jumps to Mach 5 flow.

3.5 Linear Valve at 60 Hz

As a final simulation, a linear valve model that is built into the code was placed at the nozzle entrance. The valve opens linearly to the full size of the inlet and then closes the same way. The losses associated with the partially open valve appear

to be fairly realistic based on previous applications of the code. The results of a simulation of the nozzle with this valve after it has reached limit cycle behavior is presented (Fig. 5), which shows contours of pressure, temperature, and Mach number during this process (an x–t diagram). The horizontal dimension in these figures is the distance along the nozzle, and the vertical dimension is time. The contour plot spans a time equivalent to 1 complete cycle; where the cycle shown is one going from full open (at the bottom of the x–t diagram), to full closed (at the middle of the x–t diagram), to full open again at the top. What is evident in this figure is the fact that while the valve is opening and closing in a linear fashion, the exit flow is generally constant at Mach 5. This is quite different from what comes out of the PDE which is low speed most of the time and high speed only for a very short 'spike.' This result has implications when considering the design of the nozzle valve. For example, when using the spinning valve concept, there is a need to design the slots in the spinning valve such that there is considerably more time spent closed than open, i.e., a small valve duty cycle. For other types of valves, it suggests that a simple sinusoid type drive will not be sufficient to simulate PDE like flows.

3.6 Density Changes via Temperature, Condensation, and Molecular Weight

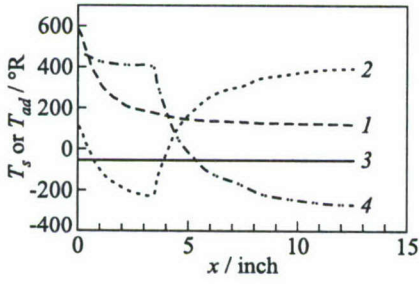

Figure 6 Variation of various temperatures inside the supersonic nozzle: *1* — T_s, *2* — T_{ad}, *3* — −55 limit, and *4* — T_{dp}

An analysis was conducted to determine the local adiabatic supercooling, defined as the cooling of the air below the dew point, along the nozzle's length. An adiabatic supercooling value of less than −55 °F assures that condensation will not occur. Figure 6 shows the variation of local static temperature, T_s, local dew point temperature, T_{dp}, the local adiabatic supercooling, T_{ad}, and the −55-degree Fahrenheit supercooling limit plotted for the test conditions vs. distance traveled along the nozzle. The negative temperature on the ordinate reflects the delta temperature change in supercooling and is not to be interpreted as an absolute temperature value. Notice the strong drop in local dew point as the local static pressure drops. This produces a minimum in the supercooling curve that causes the local supercooling problem to go away the further the air travels down the nozzle.

For the first test entry, the primary nozzle air was heated up to 250 °F (709.6 °R) to generate a density gradient between the primary and secondary air streams, this enhances the flow visualization via shadowgraph and Schlieren

techniques. Side benefits are that the primary stream flow itself will exit relative to the secondary flow ambient temperature at a higher Mach number ($\sim$ 2.4) and that condensation in the nozzle will not be an important factor. For the Mach 5 nozzle, with a total temperature of 250 °F, with dew points in the range of $-$ 15 °F (444.6 °R) to $-$ 40 °F (419.6 °R) (typical run time levels), significant [9] supercooling (i.e., more than $\Delta T = -55$ °F) does not occur until after the flow has traveled 5.6% down the nozzle where it is at approximately Mach 2.1. By then, it takes about 0.5 ms to exit the nozzle; insufficient time to allow significant nucleation [10]. Any water condensation would occur outside of the nozzle, not inside, and so the Mach 5 exit plane condition would be assured. Furthermore, as Fig. 6 indicates, no more nucleation should occur as the air travels down the nozzle and past the minima in the supercooling curve. Since the product of combustion of a "real" H_2–O_2 PDE combined-cycle engine would be water, condensation outside of the primary and into the secondary stream would be acceptable.

In addition to tests of air flowing through the primary nozzle, helium will also be injected through a new primary nozzle and run at the same frequencies. These tests will create a large density gradient between the primary and secondary streams to aid in flow visualization and gather primary-to-secondary density ratio parametric data.

3.7 Valve Performance

The greatest design challenge was the fast-acting rotary air-valve system. Figure 7 shows a typical Mach number and static pressure profile at the exit of a PDE tube for 1 cycle. These profiles represent the features that a valve/nozzle experimental fixture would need to provide and include the von Neumann pressure spike, a plateau pressure level after the spike; and then a decline in the pressure level, that may go subatmospheric until the next detonative pressure spike arrives. Based on this figure, one of the most important features of the valve model and the resultant hardware is a rapid and large build-up of exit pressure followed by its rapid decline. A macro view (i.e., ignoring specific pulse amplitude irregularities of a series of PDE exit pressure traces reveals that a series of narrow triangular waves with a large period between them, or a pulse wave with infinitely small peak duration, would make a good approximation of the trace. As is explained in the following section, for the purposes of this study, the actual PDE detonation tube pressure profiles do not have to be reproduced.

Figure 8 shows the actual valve opening area vs. time of the rotary valve scheme depicted in Fig. 9. The axially flowing valve was designed to deliver a pressure spike satisfying the wave shape (depicted in Fig. 8) by: close coupling between the air supply plenum and the valve (to minimize rise times and hysteresis); fast acting between the start of the opening part of the cycle, the full open

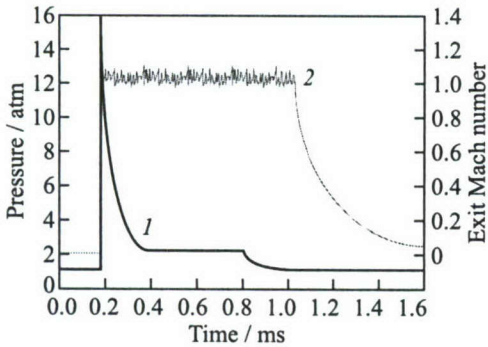

Figure 7 Typical pressure (*1*) and Mach number (*2*) values at the exit of a PDE tube

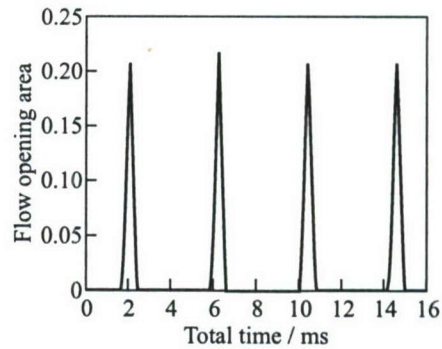

Figure 8 Variation of valve flow area at operating frequency of 240 Hz

peak, and the closing part of the cycle; and close coupling between the valve itself and the supersonic nozzle, again to minimize volume filling and emptying times. The test matrix (Table 2) shows that the pulse frequency was varied at the various test conditions. A significant portion of the data was gathered at 248 Hz. At this operating point, the nozzle will be flowing at Mach 5 for only 0.0009 s (0.9 ms) while for the rest of the 16.13-millisecond cycle, i.e., 0.01523 s (15.23 ms), the nozzle will be either not flowing out or leaking a small amount of flow outwards. Note that Mach 5 is the flow behind the shock wave while the shock wave itself travels through the secondary flow at Mach 1 or less.

4 APPARATUS

4.1 1 × 1-Foot Supersonic Wind Tunnel

The 1 × 1 SWT [11] is a continuous flow facility with test Mach numbers from 1.3 to 6.0. The different Mach numbers are achieved by swapping out the different Mach "blocks" or tunnel nozzles. The upstream high-pressure air is provided by the NASA GRC central air supply service, while the downstream flow is routed to a central exhaust system. The tunnel incorporates an electrical resistance heater to bring the air up to elevated temperature. The air is heated to a high enough temperature to prevent condensation in or liquefaction of the air in the flow. In addition to Mach number and temperature parametrics, Reynolds numbers can be varied via upstream total pressure control. Figure 10 shows the model mounted to the floor and ceiling of the facility test section. The test program used the Mach 1.3 block, with a low enough pressure ratio to assure that the

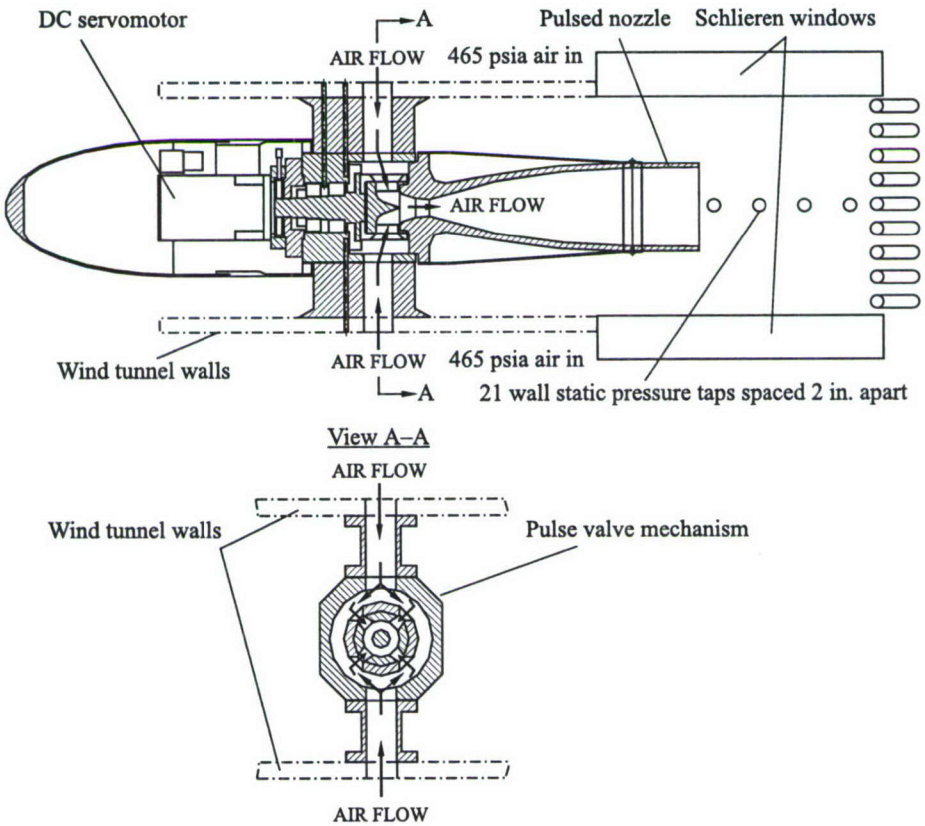

Figure 9 Cross-sectional views of pulse valve mechanism, motor, exhaust nozzle, and wind tunnel walls

Mach block would not start, i.e., was always operating subsonically. For the picture in Fig. 10, the test section wall has been removed to allow access to the model.

The test methodology is relatively straightforward: the tunnel test flow acts as the subsonic secondary flow and a small supersonic nozzle (the primary flow path) is mounted on the tunnel centerline and is pulsed at high frequency. The pulsed shock waves propagating throughout the test section are recorded using high-speed dynamic pressure transducers as well as high-speed Schlieren system and shadowgraph imaging (both film and video were used).

Total pressure measurements were made at the ejector mixing section exit, 14.4 inches aft of the primary nozzle exit. Figure 9 presents a schematic of the hardware items and instrumentation locations. In Fig. 10, one of the 1×1

Table 2 Condensed matrix of tests in stable subsonic tunnel operating mode (without large-amplitude pressure pulses) at primary nozzle air flow Mach number $M_p = 5$

M_0	P_{T0}, psia	T_{T0}, °R	P_{pt}, psia	T_{pn}, °R	$w_{p\max}$, lbm/s	f
0.43	2.2	534	372.0	531	4.987	Hz sweep
	2.0	525	372.0	526,528,531	4.987	Hz sweep
	1.9	532	—	—	—	Turned off
	1.8	533	—	—	—	Turned off
	1.7	533	372.0	535	4.968	Hz sweep
	1.6	526	372.0	532	4.982	Hz sweep
	1.5	532	398.5	553	5.235	Steady
	1.5	532	390.6	553	5.131	Steady
0.42	2.0	525	372.0	525,526,527,532	4.982	Hz sweep
	1.8	531	140.9	540	1.874	Steady
	1.6	526	372.0	532, 537	4.982	Hz sweep
	1.3	532	404.8	572	5.229	Steady
0.41	2.0	525	372.0	532	4.982	Hz sweep
	1.7	531	140.7	539	1.872	Steady
	1.6	526	372.0	538	4.954	Hz sweep
	1.3	531	386.6	600	4.875	Steady
	1.3	532	393.4	613	4.908	Steady
	1.3	539	398.3	650	4.826	Steady
0.40	1.9	525, 526	372.0	527, 528	5.001	Hz sweep
	1.7	533	—	—	—	Turned off
	1.5	526	372.0	531	4.987	Hz sweep
0.39	1.7	538	372.0	579	4.776	Hz sweep
	1.6	532	—	—	—	Turned off
	1.5	526	372.0	531	4.987	Hz sweep
0.38	1.8	525	372.0	527	5.006	Hz sweep
	1.7	533	393.1	617	4.889	Steady
	1.7	537	372.0	565	4.835	Hz sweep
	1.5	533	372.0	535	4.968	Hz sweep
0.36	1.6	533	9.9	532	0.133	Steady
	1.4	533	372.0	536	4.964	Hz sweep
	1.2	532	149.1	539	1.984	Steady
0.35	2.0	535	372.0	531	4.987	Hz sweep
	1.8	532	396.9	554	5.209	Steady
	1.8	526	372.0	528	5.001	Hz sweep
	1.7	533	—	—	—	Turned off
0.34	2.0	531	372.0	534	4.973	Hz sweep
	1.5	530	138.0	540	1.834	Steady
	1.4	532	90.2	533	1.206	Steady

Continued

Table 2 Condensed matrix of tests in stable subsonic tunnel operating mode (without large-amplitude pressure pulses) at primary nozzle air flow Mach number $M_p = 5$ (*Continued*)

M_0	P_{T0}, psia	T_{T0}, °R	P_{pt}, psia	T_{pn}, °R	$w_{p\,max}$, lbm/s	f
0.33	2.0	531	372.0	507 → 535	4.968	Hz sweep
	1.9	534	372.0	528	5.001	Hz sweep
	1.8	528	372.0	527	5.006	Hz sweep
0.32	2.0	531, 534	372.0	508, 532	4.982	Hz sweep
	1.7	525	372.0	527, 531	5.006	Hz sweep
	1.4	532	2.7	532	0.036	Steady
	1.4	532	71.0	533	0.949	Steady
0.31	4.0	532	—	—	—	Turned off
	2.0	533	372.0	529	4.996	Hz sweep
	1.9	534, 535	372.0	531, 527	5.006	Hz sweep
	1.8	530	135.9	540	1.807	Steady
	1.7	525, 527	372.0	526 → 529	4.996	Hz sweep
	1.7	539	—	—	—	Turned off
	1.6	533	5.7	531	0.076	Steady
	1.5	533	—	—	—	Turned off
	1.4	526, 533	372.0	532 → 538	4.982	Hz sweep
	1.1	531	135.4	538	1.803	Steady
	0.9	532	391.4	555	5.132	Steady
0.30	4.1	533	1.6	582	0.021	Steady
	2.0	533	372.0	529	4.996	Hz sweep
	1.8	526	372.0	600	4.691	Hz sweep
	1.4	531	18.6	535	0.249	Steady
	1.4	526	372.0	532	4.982	Hz sweep
	0.9	532	390.1	554	5.120	Steady
	0.7	531	394.0	620	4.888	Steady
0.29	2.0	533	372.0	528	5.001	Hz sweep
0.27	1.7	530	138.9	540	1.846	Steady
0.20	6.0	533	369.4	616	4.598	Steady
	5.7	532	337.1	551	4.436	Steady

Continued

SWT's full span Schlieren windows can be seen below the model. This window is 22.5 inches long and spans the width of the test cabin.

The tunnel was run in a mode (subsonic) outside of its design. Therefore, a calibration of the test section flow was conducted. The tunnel configuration (i.e., nozzle block), total pressure, and flow rate chosen theoretically reflected the combination which provided the most uniform and stable subsonic operation possible; these were verified experimentally. Operational stability was confirmed

Table 2 Condensed matrix of tests in stable subsonic tunnel operating mode (without large-amplitude pressure pulses) at primary nozzle air flow Mach number $M_p = 5$ (*Continued*)

M_0	P_{T0}, psia	T_{T0}, °R	P_{pt}, psia	T_{pn}, °R	$w_{p\,max}$, lbm/s	f
0.00	1.8	524 → 528	372.0	531 → 545	4.922	Hz sweep
	1.8	530	—	—	—	Turned off
	1.8	530 → 538	372.0	520 → 541	4.941	Hz sweep
	1.5	522 → 528	372.0	524 → 529	4.996	Hz sweep
	1.4	523 → 536	372.0	531 → 619	4.987	Steady
	1.3	525	372.0	516	5.059	Hz sweep
	1.3	531, 530	372.0	534 → 589	4.973	Steady
	0.9	538	402.6	658	4.848	Steady
	1.2	525, 532	372.0	532, 524	4.982	Hz sweep
	1.2	522 → 529	372.0	528 → 545	4.922	Steady
	1.1	532	372.0	531	4.987	Steady
	1.1	526	372.0	542	4.936	Hz sweep
	0.9	531	372.0	545	4.922	Steady
	0.6	531, 532	372.0	546 → 628	4.918	Steady
	0.5	532	372.0	630	4.578	Steady
	0.1	528 → 533	372.0	547, 555	4.878	Steady
	1.2	525, 532	372.0	532, 524	4.982	Hz sweep
	1.2	522 → 529	372.0	528 → 545	4.922	Steady
	1.1	532	372.0	531	4.987	Steady
	1.1	526	372.0	542	4.936	Hz sweep
	0.9	531	372.0	545	4.922	Steady
	0.6	531, 532	372.0	546 → 628	4.918	Steady
	0.5	532	372.0	630	4.578	Steady
	0.1	528 → 533	372.0	547, 555	4.878	Steady

by adding dynamic pressure transducers along the tunnel during the subsonic calibration of the 1 × 1 SWT.

4.2 Test Matrix

Table 2 contains the listing of test conditions achieved during the first test entry. Test conditions planned for the second test entry will match these as well as expand the test matrix to higher primary nozzle total pressures when the helium discussed in Section 3.6 is used. Note that the "Hz sweep" primary nozzle frequency shown in the last column implies that several pulse frequencies were recorded at those conditions. The "steady" term means that the rotary valve was not running and therefore steady ejector data was gathered for those conditions.

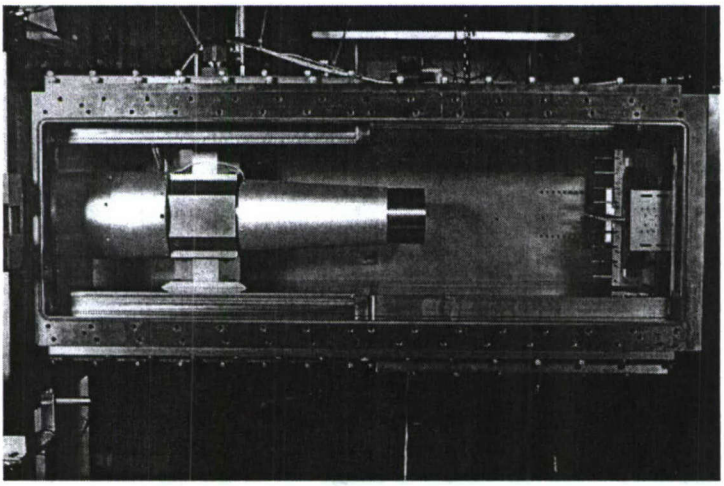

Figure 10 1 × 1 ft. supersonic wind tunnel test section

The $w_{p\,max}$ column refers to the primary nozzle peak instantaneous mass flow, i.e., the mass flow that would occur at the instant the valve reaches its fully opened geometry. The actual mass flow is a time-averaged value dependent on the frequency of operation of the rotary valve.

4.3 Test Hardware and Instrumentation

Although an exact simulation of a pulsed detonation wave train will not be possible with an aerodynamic test, the fact that the simulation region lies outside of the detonation tube means that the von Neumann spike, the plateau pressure, nor the gradual expansion have to be reproduced. The rotary valve and supersonic nozzle combination just have to deliver a periodic pressure spike to the secondary flowpath and the mixing region. Experimental data taken in the NASA GRC's Aero-Acoustic Propulsion Laboratory (AAPL) of a 5-inch PDE acquired by a 15 transducer, 40-foot long instrumentation rake shows that as one travels further downstream of the exit plane, the more the effect of the detonations appears like a pressure spike [12]. The transducer axial locations from the exit of the PDE tube were very similar to those in the 1 × 1 SWT, as well as the positioning of 5.875 inches from the axial centerline of the PDE tube. In the 1 × 1 SWT pulsed ejector test, the transducers mounted along the wall were 6 inches from the axial centerline of the primary nozzle. Future comparisons of the pressure spikes, therefore, should be very comparable between the AAPL test and 1 × 1 SWT test.

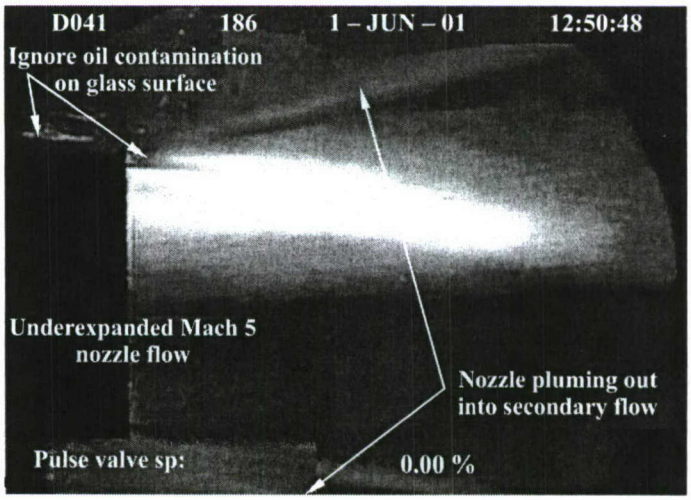

Figure 11 Steady-state ejector Schlieren snapshot

Flow visualization was limited to Schlieren and shadowgraph film and video recorded on a high-speed system (a Kodak Ektapro HS video camera at 4000 frames/s and a Phantom Camera at 8000 frames/s). Because it takes a sonic (Mach 1) pulse on the order 0.44 ms to impact the tunnel wall, some of the highest speed systems out on the market were used. The camera remained running afterwards to capture the interference of the shock waves and expansion waves downstream and any subsequent vortex formations. Figure 11 is a snapshot in time of a color Schlieren image taken of the steady underexpanded Mach 5 exit flow to be discussed in the Results and Discussion section of the paper.

5 CFD ANALYSIS AND COMPARISONS

In order to assess the flow quality of the entrance to the secondary flow region, the test geometry was modeled and studied via CFD. An initial concern was what effect a small step in the hardware fairing would have on the flowfield behind it. A long-term goal of this program is to grid the entire model geometry and perform time-accurate CFD of the entire test setup to support unsteady ejector studies.

The 1 × 1 Pulse Ejector Wave Propagation Model has been analyzed using the WIND 3.0 CFD code [13] assuming a planar, axisymmetric flow domain. The objective was to gain a general insight to the flow field about the external surface of the model and test section of the 1 × 1 SWT with and without flow through the nozzle.

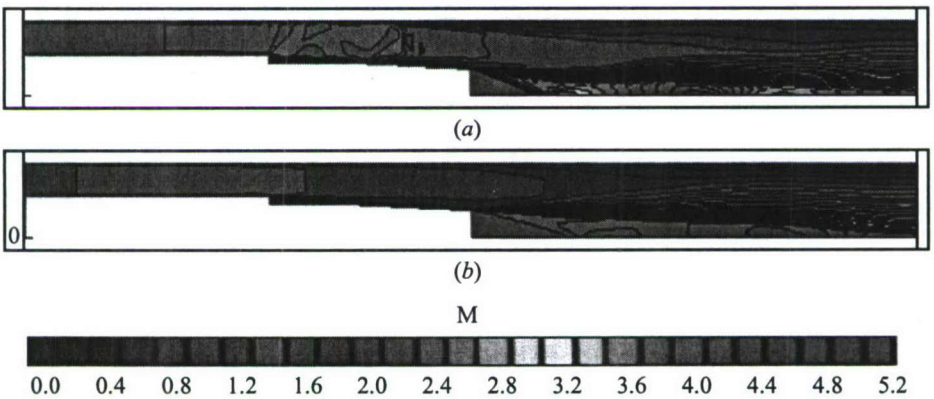

Figure 12 Calculated Mach contours for cases A1 (*a*) and B1 (*b*) with the nozzle flow on. (Refer color plate VII.)

Table 3 CFD cases, tunnel and nozzle conditions

Case	P_{T0}, psi	T_{T0}, °R	P_{exit}, psi	M_{noz}	P_{tnoz}, psi	T_{tnoz}, °R
A1	2.5	520	1.9	5	350	450
A2	2.5	520	1.9	off	off	off
B1	1.25	520	1.75	5	445	860

The analysis used a planar flow domain to model axisymmetric flow about the axis of the nozzle. Figure 12 shows the flow domain. The "top" of the flow domain is the tunnel wall. The tunnel cross-section is a 1 × 1 sq. ft. For the axisymmetric analysis, an assumption is made that the tunnel cross-section is circular with an area of 144 sq. in. The $x = 0$ coordinate is at the nozzle exit. The inflow boundary is located at $x = -40$ in. The downstream/outflow boundary is located at $x = 40$ in. The exterior of the model is at the "bottom" of the flow domain, ahead of the nozzle exit. The "step" in the exterior profile can be seen with a tapering of the radius to the nozzle exit. Ahead of the "step," a straight duct is used rather than trying to model the "bullet" shape of the forward fairing. This approximation is valid as long at the total pressure and total temperature are maintained at the inflow.

The cases examined in this study and the flow conditions of the tunnel and nozzle are summarized in Table 3. P_{T0} and T_{T0} are the total pressure and total temperature of the tunnel, respectively. P_{exit} is the flow domain's downstream exit plane static pressure boundary condition.

Case A1 results in an overexpanded nozzle. Case A2 is for the nozzle off. Case B1 is a slightly underexpanded nozzle.

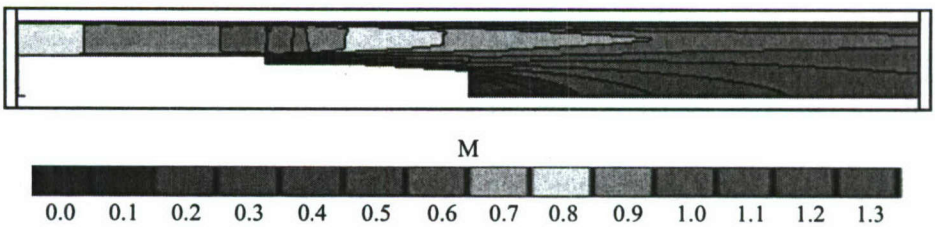

Figure 13 Calculated Mach contours for case A2, the analysis with the nozzle off. (Refer color plate VIII.)

Figure 12 shows the Mach number contours for cases A1 and B1 with the nozzle flow on. Figure 13 shows the Mach number contours for case A2 with the nozzle flow off. The Mach number contours for cases A1 and A2 indicate a slight local acceleration to supersonic Mach number of the flow past the step. The flow field for case A1 indicates the acceleration of up to Mach 1.5. A fairly strong normal shock develops which results in shock/boundary layer interactions and boundary layer separation on the tunnel wall and model exterior. The flow field for case A2 without the nozzle flow indicates the acceleration of up to Mach 1.1, but little flow separation is noticed. Both flow fields indicate a separation region aft of the "step;" however, the flow seems to reattach and become well developed as it flows down the model exterior toward the nozzle exit. Both simulations A1 and A2 draw the same mass flow from ahead of the nozzle exit, 5.618 lbm/s. When the nozzle flow is on, an additional mass flow of 6.785 lbm/s is added to the test section outflow. The flow field with the nozzle on indicates an overexpanded nozzle flow. The shock train is resolved in a fair manner. The simulation with the nozzle off assumes a solid wall at the nozzle exit. The flow field indicates a separation region at the nozzle exit. The flow field for case B1 indicates that the flow past the step remains subsonic; the mass flow drawn from ahead of the nozzle exit is 2.612 lbm/s. The nozzle flow adds another 6.203 lbm/s. The conclusion of this CFD study is that the presence of the step does not seriously affect the flow at the nozzle exit.

6 RESULTS AND DISCUSSION

6.1 Tunnel Calibration

Figure 14*a* presents the measured tunnel total pressure recovery distribution across the width of the test section, at the 46.40-inch axial station, where the pitot pressure rake has been placed midway between the ceiling and floor of

the test section. Presented in Fig. 14*b* is similar data across the height of the test section at the same station, where the pitot pressure rake has been placed midway between the left and right walls of the test section. Varying the upstream supply pressure and the downstream exhaust pressure changed the Mach number. The pressure ratio scale has been expanded to distinguish between the different free-stream Mach numbers, but careful inspection reveals that for all of the Mach numbers, total pressure recovery varies 2.5% or less around the mean value.

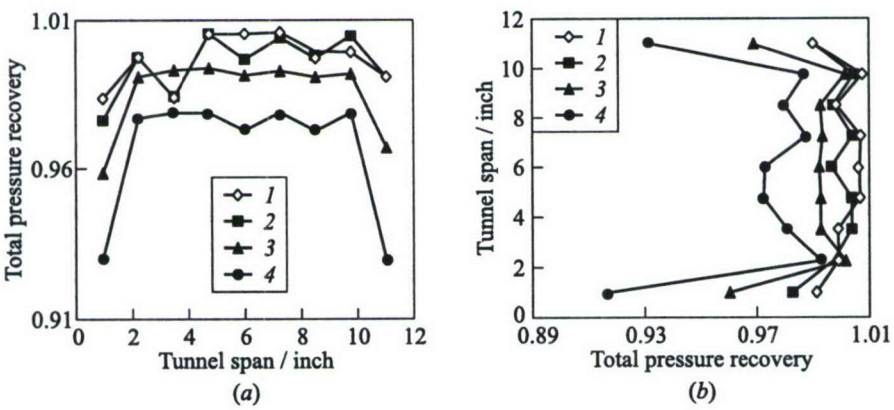

Figure 14 Total pressure distribution at tunnel station 46.4 inch: (*a*) vertical centerline, total pressure divided by upstream total pressure, (*b*) horizontal centerline, total pressure divided by upstream total pressure. *1* — $M_0 = 0.22$; *2* — 0.3; *3* — 0.5; and *4* — $M_0 = 0.7$

6.2 Pulsed Ejector

Because of load problems with the valve's mechanical drive system, the pulsed ejector was only run in the overexpanded mode for these series of "shake out" runs. When the nozzle upstream total pressure reached values of 180 psia or more, the drive system would start slowing down and eventually stop. Several "pulse starts" were performed where the valve was set to a specific frequency with no flow and then the upstream high-pressure air was abruptly turned on. Although these pulse starts did provide 1 to 2 cycles of pressure levels greater than the 180 psia value, they were not enough to get a series of repeatable underexpanded pulsed ejector data. The thrust loads as well as frictional loads greater than the servomotor could overcome were the cause. The rotary valve did provide very repeatable data for all the overexpanded pulsed ejector cases, but with minimal flow entrainment.

6.3 Steady-State Ejector

Figures 15 and 16 present time histories of data down the wind tunnel, the ejector secondary, for 4 discrete points as an initial screening of the ejector concept for use in future tests. These 4 discrete points are: the far upstream supply piping and plenum (portrayed as station 0 in the plot), the station 4 inches upstream of the primary exit plane, the station at the primary nozzle exit plane, and the pitot pressure rake assembly placed at the 46.35-inch station (i.e., approximately 16 inches downstream from the primary exit). Additional stations were measured but these 4 highlight the important results. The 3 cases presented in the figures are for: an overexpanded nozzle, a fully expanded nozzle, and an underexpanded nozzle. All the data in both figures have been area-averaged by the local flow area at that discrete point. For both figures, the secondary air has been turned off, the wind tunnel piping remains closed, and the primary ejector Mach 5 nozzle is pumping the wind tunnel and test section itself.

Figure 15 presents the local mass flow down the duct for the 3 cases mentioned above. For all 3 cases, the far upstream instrumentation, the $x = 0$ inch station, confirms that the forced secondary flow was indeed turned off as no appreciable flow was measured. The second station point shows that while some flow is starting to be pumped down the duct, it is still not significant for all three cases. The third point is where the differences start to show. This is the point at the nozzle exit plane where significant pumping is being produced by the underexpanded and fully expanded cases. The overexpanded case shows very little pumping

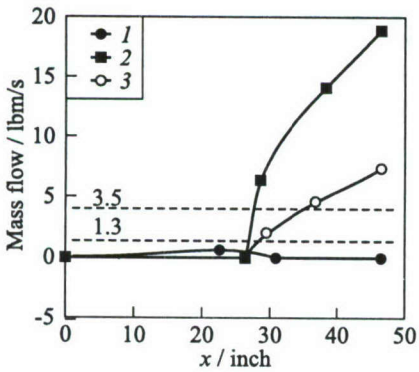

Figure 15 Measured area-averaged local mass flow down the secondary duct: *1* — overexpanded nozzle with p = 1.5 psia; *2* — fully expanded nozzle with p = 1.2 psia; and *3* — underexpanded nozzle with $p = 0.1$ psia

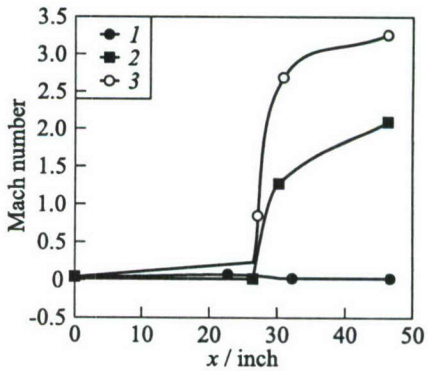

Figure 16 Measured area-averaged local Mach number down the secondary duct: *1* — overexpanded nozzle with p = 1.5 psia; *2* — fully expanded nozzle with p = 1.2 psia; and *3* — underexpanded nozzle with $p = 0.1$ psia

throughout the 4 stations. Also plotted on the figure are the primary stream's mass flow rate; 1.3 lbm/s for the overexpanded case, and 3.5 lbm/s for the fully expanded and underexpanded cases. This is where the area-averaging penalty is noticeable. Because the 1.3 lbm/s was produced by a narrow overexpanded jet that did not expand throughout the secondary region, its area-averaged mass flow was reduced. The last station shows that on an area-averaged basis (and for this quasi-steady case), significant secondary flow was being entrained by the primary stream for the fully expanded and underexpanded jets.

An important point to note is that the fully expanded case with its high entrainment ratio, $\beta = w_s/w_p$, of 4.4 at the pitot rake station was not sustainable. Because the upstream side of the wind tunnel was closed off, the mechanism that occurred is that the ejector evacuated all of the air in the upstream end of the circuit and the static pressure in the test section gradually dropped as the air density dropped. This is consistent with the lack of mass conservation in Fig. 15; there was no conservation of mass in the system since more air was being pumped out than was being put in. Eventually the static pressure dropped enough that the primary nozzle became underexpanded and the stream plumed out throughout the secondary flowpath. The underexpanded entrainment ratio of 1.1 was partially due to the fact that the density of the secondary air was significantly reduced because the test facility had been pumped down by the ejector.

Figure 16 shows the local Mach number down the duct for the corresponding three cases. As is shown, the secondary stream itself became supersonic just ahead of the primary exit due to the significant ejector pumping effect.

7 CONCLUDING REMARKS

Based on the results of the tunnel calibration and preliminary "shake out" wind tunnel tests, the concept of a noncombusting PDE simulator as the driver in the study of pulsed ejectors appears to be valid. The wind tunnel calibration results indicate that the use of the tunnel test section itself as the secondary subsonic flowpath was successful for flow uniformity and stability criteria. The supersonic nozzle design as the ejector primary was validated for the steady-state ejector case with significant pumping potential indicated by the pressure data. The mechanical concept for the rotary valve, in which the flow is shut off and periodically opens to allow a fully flowing nozzle, appears to be valid. That the concept is valid was demonstrated with the overexpanded cases where shock waves were generated and the frequencies were swept from 0 to 400 Hz. The one unknown, currently, is the choice of a large enough motor to overcome the frictional forces in the valve mechanism and the thrust load generated by the fully flowing underexpanded nozzle. With the driving motor problem solved, data will be available to compare this "aerodynamic" simulator of a PDE-driven ejector with actual PDE-ejectors and CFD studies. After the second round of

tests are finished, this facility will be available to perform parametric studies on pulse or wave shape affects on unsteady ejector performance via changes to: pulse Mach number, pulse frequency, pulse wave width, primary-to-secondary area ratios, and primary-to-secondary density ratios. Because this is a cold-flow facility with the associated lower costs in instrumentation, model hardware, and test utilities than a hot-fire facility, it is envisioned that phenomena of interest observed in either CFD or more limited PDE hot firings can be studied in detail.

ACKNOWLEDGMENTS

The authors would like to acknowledge the drafting and mechanical design efforts of Michael W. Henry of QSS Inc., and Raymond P. Homyk of Zinn Technologies. Furthermore, the authors would like to thank the support of the Aeropropulsion Research Program Office at NASA GRC.

REFERENCES

1. Bussing, T. R. A., and G. Pappas. 1994. An introduction to pulse detonation engines. AIAA Paper No.-94-0263.
2. Lockwood, R. M. 1959. Investigation of the physics of energy transfer from an intermittent jet to an ambient fluid: Summary report. ARD-236, Hiller Aircraft Corp.
3. Bratkovich, T. E., and T. R. A. Bussing: 1995. A pulse detonation engine performance model. AIAA Paper No. 95-3155.
4. Bussing, T. R. A., J. B. Hinkey, and L. Kaye. 1994. Pulse detonation engine preliminary design considerations. AIAA Paper No. 94-3220.
5. Kentfield, J. A. C. 2000. The impact and potential of nonsteady flow phenomena in propulsion and elsewhere. Ohio Aerospace Institute presentation.
6. Paxson, D. E. 2001. A performance map for ideal air breathing pulse detonation engines. AIAA Paper No. 2001-3465.
7. Povinelli, L. A. 2001. Impact of dissociation and sensible heat release on pulse detonation and gas turbine engine performance. *15th Symposium (International) on Airbreathing Engines.* ISABE Paper No. 2001-1212.
8. Porter, J. L., and R. A. Squyers. 1979. A summary of ejector augmentor theory and performance, Phase II — Technical Discussion. ONR R-91100/9CR-47A.
9. Pope, A., and K. L. Goin. 1965. *High-speed wind tunnel testing*. New York: John Wiley & Sons, Inc. 56.
10. Wegener, P. P. Gasdynamics of expansion flows with condensation, and homogeneous nucleation of water vapor. Chapter 4.
11. Seablom, K. D., R. H. Soeder, J. F. X. Leone, and M. W. Henry. 1999. NASA Glenn 1-by 1-foot supersonic wind tunnel user manual. NASA/TM-1999-208478.
12. Dittmar, J. H. 2002. Private communications.
13. Bush, R. H., G. D. Power, and C. E. Towne. 1998. WIND: The production flow solver of the NPARC alliance. AIAA Paper No. 98-0935.

PART THREE

AVENUES OF FUTURE RESEARCH

AVENUES OF FUTURE RESEARCH ON PULSE DETONATION ENGINES

G. D. Roy

1 INTRODUCTION

The selected contributions included in this book reflect the state-of-the art in the new, rapidly developing, area of science and technology — Pulse Detonation Propulsion. Currently, it is absolutely clear that there are no fundamental constraints in applying repeatedly propagating confined detonations for producing thrust. Theoretical efficiency of pulse detonation thrusters is considerably higher than that of other thrusters based on deflagrative combustion. In view of this, a breakthrough in efficiency, and, as a consequence, in increased range, payloads, etc. can be expected in both air-breathing and rocket propulsion devices.

Existing idealized schemes of pulse detonation engines (PDEs) imply perfect premixing of fuel and oxidizer, steady-state initial conditions in the combustion chamber, localized instantaneous detonation initiation, thermodynamically equilibrium pressure, temperature, and composition of detonation products in a planar, constant speed, classical Chapman–Jouguet (CJ) detonation, and an adapted nozzle. Idealized schemes of air-breathing PDE, in addition, imply perfect inlets with full pressure recovery and infinitely-fast-response mechanical valves. With this in mind, it is natural to pose a question: "Can the theoretical advantages of PDEs be achieved in realistic conditions or is the PDE another concept that cannot compete successfully with existing technology?" A well-known example is a two-stroke piston engine that, theoretically, is supposed to have twice the power as compared to the four-stroke engine. As a matter of fact, due to various deviations from theoretical operation and presence of unburnt fuel scavenged during the cycle, the actual gain in power is only about 50%, and the fuel consumption grows by 15%–20% as compared to its four-stroke counterpart. Moreover, due to more stringent thermal loading of the piston, the durability issues become critical. Nevertheless, the two-stroke engine has found a number of applications, e.g., in low-speed ship propulsion, high-speed diesels, etc. Hence, it is important that the applications for which a PDE is more suitable must be carefully determined.

2 CURRENT KNOWLEDGE AND CHALLENGES OF FUTURE RESEARCH

To find a definite answer to the question posed, the up-to-date knowledge is still scanty and incomplete. The reader can perceive it from the articles written by world-known experts in detonation physics. First of all, the detonation phenomenon — the kernel of the PDE operation cycle — is not completely understood yet. Most of existing knowledge on fuel detonability is based on empirical and computational findings for academic systems comprising light hydrocarbons (methane, acetylene, ethylene, etc.) as fuel, oxygen as oxidizer, and argon as diluent. Confined fuel–air detonations were studied, with some exceptions, only for light gaseous hydrocarbons. A number of empirical rules and methods exists to estimate the critical initiation energy, as well as the limiting and critical tube diameter of detonation. All these rules and methods are based on the mean size of the detonation cell — a footprint of the propagating detonation (usually measured from tracks on a smoked foil surface). In detonation physics, the cell size has become a rule of thumb of detonation, and is considered as a kind of "phlogiston" released during explosion. It is somewhat disappointing that a growing number of publications dwell on the cell size rather than on the intrinsic characteristics of detonation flows. As the detonation cell structure is quite irregular for practical gaseous explosive systems [1] and depends on many parameters (pressure, temperature, mixture composition, tube diameter, wall roughness, acoustic properties, etc.), it is not surprising that the relevant literature is quite controversial. As for the confined detonation of fuel sprays, i.e., heterogeneous fuel–air mixtures containing fuel drops or particles, there are only a few studies related to this issue.

Evidently, further research is needed to clarify the pros and cons of PDEs. Difficulties inherent in PDE operation can be readily identified. Because of rigorous safety regulations, it is hardly possible that perfectly premixed fuel and air will be utilized in practical devices. Hence, fuel sprays injected into the PDE combustion chamber should be considered as the standard approach and associated mixing techniques can be selectively applied. Obviously, various methods for mixing enhancement used in chemical propulsion could be directly implemented in PDEs. However, as the operation cycle of a PDE is transient and the time available for mixing is very short as compared with steady-state analogs, these techniques may not be as effective, and may even fail. Thus, mixing enhancement may become a crucial issue. In this context, the presence of shock-induced high-speed flow in the PDE combustion chamber, and the consequent influence on the fuel drop breakup should be considered [2].

From all perspectives, the detonation initiation issue is the most challenging. The idealized PDE performance is obtained based on the assumption that detonation is initiated and attains the CJ parameters in the immediate vicinity

of the thrust wall [3–8]. As a matter of fact, it takes about 2 m (in a tube of 33-millimeter diameter) [9], up to 3 m (in a tube of 36-millimeter diameter) [10], or up to 2.5–3 m (in a tube of 100-millimeter diameter) [11] for detonation to be achieved after initiation using a low-energy spark plug in the fuel–oxidizer mixture. It is worth noting that experiments in [9, 10] were performed with separate supplies of gaseous (methane, ethylene, propane) and liquid (ethanol, acetone, *n*-hexane, gasoline) fuel and oxidizer (oxygen-enriched air) to the combustion chamber and the experiments were performed in both single-pulse and multipulse modes. Moreover, in [9–11], various obstacles were used to minimize the length of deflagration-to-detonation transition (DDT). Clearly, as the development of detonation takes a finite time and length, the thrust and specific impulse produced in a single cycle will be different from those obtained in idealized calculations [3–9] and experiments with highly sensitive hydrogen–oxygen mixtures [8].

Deflagration-to-detonation transition is presently considered as one of the most promising approaches to initiate detonation in a PDE. In spite of the fact that qualitatively the DDT phenomenon is sufficiently well understood, there are no prognostic theories so far which would allow predicting the predetonation length and time and pressure evolution at the thrust wall. In view of this, there is a need for comprehensively validated computer codes allowing for modeling noninstantaneous detonation initiation via DDT [12] and unstable modes of predetonation flame propagation in a detonation tube [13].

Based on weight and volume constraints, the reasonable length of the PDE combustion chamber should not exceed 2 m for a tube diameter of the order of 100 mm. This implies that obtaining detonation via DDT is problematic. According to [14], there is an option of using strong reactive shocks rather than detonations for producing thrust. The authors of [14], based on experimental findings, claim that in short PDE tubes, stable fuel–air detonations will not be established anyway. Therefore, instead of looking for efficient ways to initiate fuel–air detonation, they suggest to repeatedly inject high-pressure, partly burned monopropellant (nitromethane or isopropyl nitrate) in a PDE tube filled with air. In this concept, "violent" injection of hot, partly decomposed monopropellant will result in the generation of a strong shock wave in air, while postshock mixing of compressed air with the residual monopropellant will result in secondary explosions and formation of multiple shocks contributing to thrust. Unfortunately, this interesting concept has not yet been substantiated experimentally.

Characteristics inherent in confined detonations are studied in detail in [10, 15–19]. Reported in [15] is an optimization study of initiation of *n*-hexane and *n*-heptane spray detonations in air. The authors have demonstrated the importance of various factors for direct detonation initiation with energy deposited by a powerful electric discharge. It has been shown that various design methodologies can be used to considerably decrease the initiation energy required for

I would like to point out that the inherent energy conversion efficiency for the detonation cycle over a constant-pressure cycle is true for all Mach numbers according to the analysis that I showed at the meeting. However, this advantage refers to a generic propulsion system based on detonations rather than the specific system — the PDE that we are considering. The generic system is steady, utilizes the full heating value of the fuel and assumes isentropic expansion of the detonation products to the ambient conditions. Therefore, it is not surprising that the ideal performance number estimated for this generic detonation propulsion system is significantly larger than the idealized, single-tube PDE system. If the chemical energy losses due to dissociation effects are included, the performance estimate of the generic ideal cycle engine will decrease. If "better" expansion processes are simulated for the single-tube PDE, higher performance numbers for this system is attained. Still there is a difference between the two values, which could be due to the inherent unsteadiness of the PDE. Perhaps, a multitube system with a common inlet and a common nozzle may approach the generic, steady detonation engine cycle and attain the anticipated performance. Such issues, including effects of forward flight, need to be investigated further before one can make more confident assessments of "specific system applications" for the PDE.

Fujiwara (ATES Corporation, Toyota, Japan): Both numerical and experimental efforts have to be directed toward valveless air inlets. The main focuses are: first — feasibility study, and second — evaluation of performance loss that results from continuous opening of air supply valves during supersonic flight. Several Russian studies already exist, which, in my opinion, are done in static environments, but not under supersonic flight conditions. More efforts should be made to PDE design stages, for example, nozzle, ejector, air inlet, wind-tunnel testing, and thrust reinforcement during take-off phase. I do not see too many applications of PDEs for ground-based technologies. One Japanese gas supply company envisions its application in power generation, using their LNG fuel. We can take advantages of PDE thrust characteristics in tunnel digging, rock drilling, etc.

Segal (University of Florida, Gainesville, FL, USA): I would like to outline the issues requiring solution for PDE development. The most critical for efficient operation is, first, rapid detonation wave formation either through rapid DDT or via direct initiation. Several methods discussed at the colloquium require further study. These are: predetonators, electrical discharges, hot gas recirculation, and fuel additives and sensitizers. Increased operational frequency is the second issue of importance for performance improvement. This may suggest valveless and/or multitube PDE configurations. The third issue deals with material science. PDEs are expected to operate with high energy-density release, which, along with the unsteady mechanical stress, require careful studies of ma-

terial strength, reliability, and heat transfer. The last but not the least issue is noise and vibration which needs to be addressed.

Regarding applications, main points are as follows. It is necessary to capitalize on the PDE advantage in terms of few moving parts. In view of this, valveless PDE configurations appear to be particularly attractive. An immediate potential application of PDEs is small diameter, long-range, air-to-air missile. An additional natural application is multitube, long-range unhabitated, terrain following vehicles.

Fernandez (NASA Glenn Research Center, Cleveland, USA): It is important to understand the role of transients in the flow and what effects they may have on the design of inlets and associated frontal area requirements. It may be that demands are larger than with current technologies. There may be potential use for the device in areas such as combined cycle devices and thrust augmentors.

In long-term view, a specific system application of PDE is illustrated in Fig. 1.

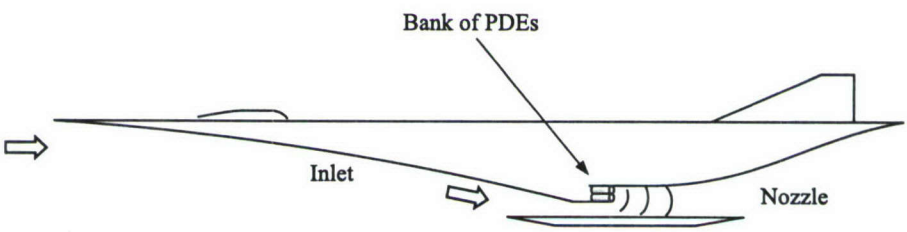

Figure 1 Example of PDE system application

The benefits of the PDE-based design of the vehicle of Fig. 1: contrary to ramjets and/or scramjets, PDE provides static thrust at take-off. No other propulsion system components may be required (i.e., no turbomachinery, no rockets, etc.). With a PDE-based ejector system, it is possible to apply thrust augmentation for vehicle acceleration and cruise flight. Combined cycle system will provide opportunities for acoustic muffling.

Frolov (N. N. Semenov Institute of Chemical Physics, Moscow, Russia): When developing a practical PDE one has to take into account that during transient operation (variation of flight speed and altitude) detonation can fail and deflagrative mode will come into play. Also, deflagration will probably be the operational mode during engine start, when the engine body heats up to the nominal temperature. Elevated nominal temperatures of confinement are needed to partially preevaporate fuel as the detonation of fuel spray is very sensitive to vapor pressure. Hence, the practical PDE should be sort of a modified pulse-jet

engine capable of operating in a pulse-detonation mode at the cruise portion of the flight trajectory. In our recent experiments with multipulse detonations of n-hexane spray in air, we noticed that misfires with detonation failure occurred more often at the beginning of the run. Misfires were also more frequent at lower ambient temperatures.

To demonstrate the importance of the issue, I will give an example. In 1960–1970s, Prof. L. A. Gussak of the Semenov Institute had suggested the idea of using prechamber ignition in automobile piston engines instead of regular spark ignition. In steady-state operation, the engine with prechamber ignition showed excellent performance in terms of fuel consumption and emission of pollutants. However, transient operation of the engine posed so many problems that the nation-wide project was suspended.

Veyssiere (ENSMA CNRS, Poitiers, France): Detonation is the most efficient combustion regime in terms of the rate of energy conversion: indeed, energy conversion occurs within a few microseconds. This property allows considering designs of combustion chambers of very short lengths. PDE designers should keep in mind this determining aspect. To benefit from this advantage, efforts should be made in order to achieve operating conditions for PDE as close to the theoretical ones as possible; that is to let a CJ detonation propagate along the tube as soon as possible after ignition of the mixture. In other respects, the simpler the technical solutions, the more efficient they often are.

As a result, fundamental studies are yet required for getting a better understanding of basic problems such as DDT in a tube, or transmission of a detonation from a small tube to a large volume. This is necessary for reliable monitoring of the whole process. The importance of such studies was illustrated in the presentation of Daniau *et al.* It is possible to achieve direct transmission of a detonation from a tube to semi-infinite volume at tube diameters twice smaller than the classical critical tube diameter. Recently, it was shown at Laboratoire de Combustion et de Détonique that adequate additives to hydrocarbon–air mixtures are able to promote the heat release process in two separate kinetic steps with different characteristic induction times. This results in the existence, at the same time, of two types of cellular detonation structure, with the characteristic dimension of the new structure being ten times or more smaller than the classical one. Since it is recognized that the mixture sensitivity to detonation correlates with the cell size, it is of fundamental importance to investigate the role played by this substructure in the detonation sensitivity. In general, substantial progress in PDE design is strongly dependent on better understanding of the fundamental problems concerning initiation, propagation, and transmission of detonations.

Van Tiggelen (Universite Catholique de Louvain, Louvain, Belgium): The research of last few years has demonstrated the feasibility of a PDE propul-

sion concept. The simulation of PDEs has reached a mature stage and the problem of sufficiently fast transition to detonation using less detonative mixture is to be considered seriously. Although large efforts have been devoted to the modeling of DDT in systems with hydrogen as a fuel, it seems necessary to study experimentally techniques which reduce the transition time to achieve detonation in mixtures with more standard fuels (JP-10, for instance). One way to approach this problem is by using mixtures with nonuniform composition to facilitate the initiation of any kind of fuels. Knowledge about the transition of detonation (or fast deflagration) with composition gradients will then be needed. Data on these are rather scarce in the literature. Perhaps, mixtures with ethylene could provide a possibility; slight enrichment of the air with oxygen has also to be considered. A better understanding of the mechanism of acetylene and ethylene consumption in detonation transition is needed.

Lindstedt (Imperial College, London, United Kingdom): Repeatable detonation initiation appears a critical issue — particularly at high repetition rates. The wish to use standard (e.g., JP-10) fuels leads to the need for innovative geometries that will probably have to utilize significant levels of turbulence enhancement. The possible trend for leaner mixtures, increased I_{sp} and lower NO_x, will only emphasize this trend. The issue of turbulent reacting flows comes to the fore and it would also be good to see more calculations of detonation propagation featuring hydrocarbon fuels and realistic chemistry. The complications caused by liquid fuel injection and the resulting mixing and two-phase flow issues remain to be resolved. The issue of exit losses and geometries are important and the question does arise with respect to how best to utilize the transient outflow in the context of "combined" plants featuring rotating machinery.

Santoro (Pennsylvania State University, University Park, PA, USA): Three main issues remain to be resolved. The first is associated with compact and reliable DDT devices. The second is a reanalysis of transient cycles. The latter represent a paradigm shift in propulsion devices. The third issue that must be considered is associated with cycle fatigue, e.g., the propagation of cracks and failure modes. For example, distributed loads on the side of nozzles can be difficult to deal with and it is expected that repeated transient loads can become problematic. It is also important to find out whether PDE engines can generate a more stable level of thrust through multitube arrangements and relevant technologies need to be developed.

Vasil'ev (M. A. Lavrent'ev Institute of Hydrodynamics, Novosibirsk, Russia): Many important aspects of PDEs were emphasized at this Colloquium. I would like to outline the importance of DDT optimization. The use of atmospheric air as the oxidizer is one of the essential conditions for practical PDEs. If hydrogen is considered as a fuel candidate (based on least energy requirements and ecological constraints), then the energy of about 4 kJ (about

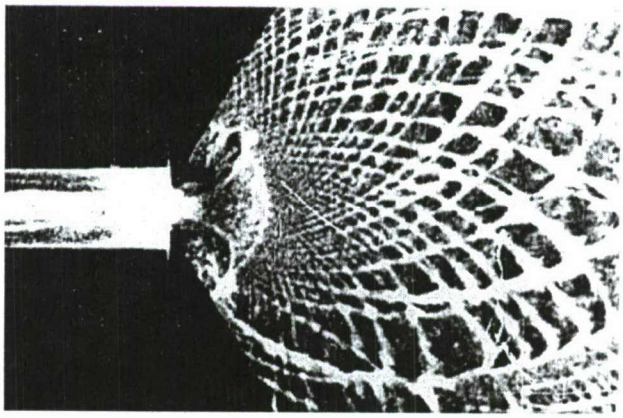

Figure 2 Self-luminosity photograph of spontaneous detonation initiation in the expanding flow at flame diffraction in the nozzle

one gram of TNT) is required for direct detonation initiation in the perfectly mixed near-stoichiometric hydrogen–air mixture (at normal conditions). It is quite problematic to release such energy in each PDE cycle and, moreover, in a high-frequency, multitube PDE operation. In view of this, the enhanced DDT is one of the most promising ways of detonation initiation in PDEs. It must be emphasized, that DDT-accelerators have to ensure the identical DDT processes in each PDE cycle and in each individual detonation tube. In addition, detonation must be initiated in a high-speed (subsonic or supersonic) flow rather than in a quiescent mixture, as is usually the case in relevant studies. It is not evident that the conditions for detonation initiation in a quiescent mixture and in the flow are the same. Therefore new experimental investigations of detonation initiation in a high-speed flow of fuel–air mixture are necessary, e.g., using the wind-tunnel technique in a wide range of flow Mach number. Further studies are also needed to find efficient designs of DDT-accelerators for fuel–air mixtures. Figure 2 demonstrates the efficiency of DDT, obtained by means of the DDT-accelerator with the minimal number of turbulence-generating elements. It is the self-luminosity photograph of spontaneous detonation initiation in the expanding flow at flame diffraction in the nozzle.

Gvozdeva (Institute of High Temperatures, Moscow, Russia): The detonation engines should theoretically give the highest efficiency of transformation of thermal energy into kinetic energy. As shown by Zel'dovich, the combustion products have the minimal entropy on the Hugoniot curve in the case when combustion occurs at the CJ point. It is difficult to expect, that in the PDE, the detonation will propagate in the CJ regime, and it will be established from the very beginning with zero predetonation distance. For the actual sizes of det-

onation tubes and mixtures of liquid hydrocarbons with air, the detonation will never arise at once and even when developed, will not be the CJ detonation, due to considerable heat loss from the reaction zone to tube walls. As a result, the thermodynamic state of combustion products will not be precisely that of the equilibrium Hugoniot curve, but, rather, the Hugoniot curve taking into account the heat loss. Probably the nonideal character of a detonation in a PDE will lead to decreased overall efficiency. However, there exists the other quantity affecting PDE efficiency — a possible maximal frequency. I believe that the nonideal character of detonation will increase the possible operation frequency. It follows from our previous experiments that the velocity of a rarefaction wave in the detonation products relative to the gas flow velocity sharply increases for nonideal detonations. This quantity is directly relevant to the exhaust of burnt gas from the PDE. The increase in the velocity of the rarefaction wave will result in decreasing the time required for the combustion products to leave the engine and will allow increasing the maximum operation frequency, thus improving the PDE performance. The influence of heat loss on the thermal efficiency and maximal operation frequency is, in our opinion, a subject of further examination.

Borisov (N. N. Semenov Institute of Chemical Physics, Moscow, Russia): I would like to address three issues in my comments. The first is the use of detailed kinetics in gasdynamic modeling of nonsteady combustion processes. Most of the modelers believe that the more detailed the kinetic mechanism, the better authenticity of computations. However, one-dimensional simulations and computations with a coarse mesh (which is often inevitable in multidimensional computations) disregard the most important feature of exothermic chemical reactions taking place in a fluid subjected to gasdynamic perturbations, namely, the so-called hot spot nature of ignition. As experiments show, the flow field behind detonation, shock, and compression waves produced by combustion processes is far from being homogeneous because of multiple interactions of weak quasi-acoustic waves, the arising temperature fluctuations result in premature ignition of a combustible mixture in small volumes, which, in turn, extends the effective heat release time in larger volumes. Thus, the modeling procedure should either resolve the hot-spot size or use global kinetics derived from shock-tube experiments (the use of detailed kinetics is justified only in the first case).

The second is mixture preparation, which includes chamber filling with air and fuel and fuel evaporation. These processes can be a decisive factor under real conditions because initiation and propagation of detonation and detonation-like waves are very sensitive to the distribution of concentrations and the amount of vapor phase. Evaporation implies fuel preconditioning, which can also help one to shorten predetonation distances by creating a proper temperature gradient in the mixture. Unfortunately, the problem was properly tackled so far neither experimentally nor by numerical modeling, although it may happen to be even more important than detonating a well-prepared mixture in short chambers.

Finally, steady CJ detonation would never be observed in real combustion chambers because, as experiment and computations show, even in the case of successful direct initiation of detonation in fuel–air mixtures, the CJ detonation sets in within distances exceeding one meter, no doubt that DDT process would take longer distances. Hence, all the thermodynamic estimates of the efficiency of a detonation cycle should be revised to take into account the nonsteady nature of the process. The question arises, do we actually need CJ detonation in the combustion chamber to get better engine performance? As our calculations show, under certain conditions, nonsteady reactive shock waves in the chamber may produce a higher specific impulse than does CJ detonation.

Pakhomov ("Basalt" State Research & Production Enterprise, Moscow, Russia): The concept of specific impulse has been commonly recognized for comparing the efficiencies of various steady-state jet engines. In my opinion, the use of specific impulse as a criterion for estimating PDE performance is not sufficient. This parameter does not allow comparing the performance of PDEs with different characteristic times involved in the operation cycle (e.g., the time of chamber fill with a reactive mixture, time of pressure decay after the detonation leaves the PDE chamber, etc.). In the paper presented at this Colloquium by Koren'kov V. V. and myself [25], an attempt was made to introduce a new criterion of PDE efficiency, taking into account the time of engine operation cycle. However, it seems reasonable to elaborate a number of criteria that completely take into consideration all basic features of PDE performance.

Penyazkov (A. V. Luikov Institue of Heat & Mass Transfer, Minsk, Republic of Belarus): In my opinion, there is a need for three-dimensional consideration of the detonation processes including flow evolution in the propulsion system. Usually, one- and two-dimensional treatments of detonations are used. However, estimations of relevant length and time scales based on the analyses of the predicted flow structure may differ considerably from their realistic values, in particular for insensitive fuels, when the detonation cell size is comparable with the confinement dimensions. This is especially valid for transient processes like DDT, detonation transmission, or unstable detonation. Therefore elaborate numerical and experimental modeling is necessary. In this respect, the PDE design could be, probably, refined if the three-dimensionality of detonations is taken into account. The PDE has to be considered as a self-consistent system, where interactions of transverse flow components with confinement walls regenerate and multiply the local regions of high-energy release in the reacting flow. These feedback effects should sustain the self-amplification of combustion-driven shock waves and facilitate DDT and detonation propagation in the main combustion chamber.

Vasil'ev (M. A. Lavrent'ev Institute of Hydrodynamics, Novosibirsk, Russia): It is the PDE concept that attracts primary attention in the series of

Detonation Colloquia held in Russia during the last five years. My point of view is that PDE is not the only promising concept of detonation-based propulsion. The alternative concept was proposed and realized in the M. A. Lavrent'ev Institute of Hydrodynamics. This is a concept of rotary detonation engine (RDE) in which the reactive mixture burns out in stationary, rotating, multispin detonation waves. Many problems crucial for PDEs (e.g., repeated detonation initiation, DDT, high-frequency operation, cycle-to-cycle repeatability, etc.) appear less important for RDEs. For example, the maximum allowable operation frequency of PDE is limited by the length of an individual detonation tube and may be increased by using a multitube PDE configuration. The operation frequency of RDE is determined only by the tube circumference (or diameter). Moreover, in RDE, the multispin detonation wave, once initiated, rotates stationary in the detonation chamber. One of the main advantages of the spinning wave system is its self-organization at large variation of flow parameters. This allows effec-

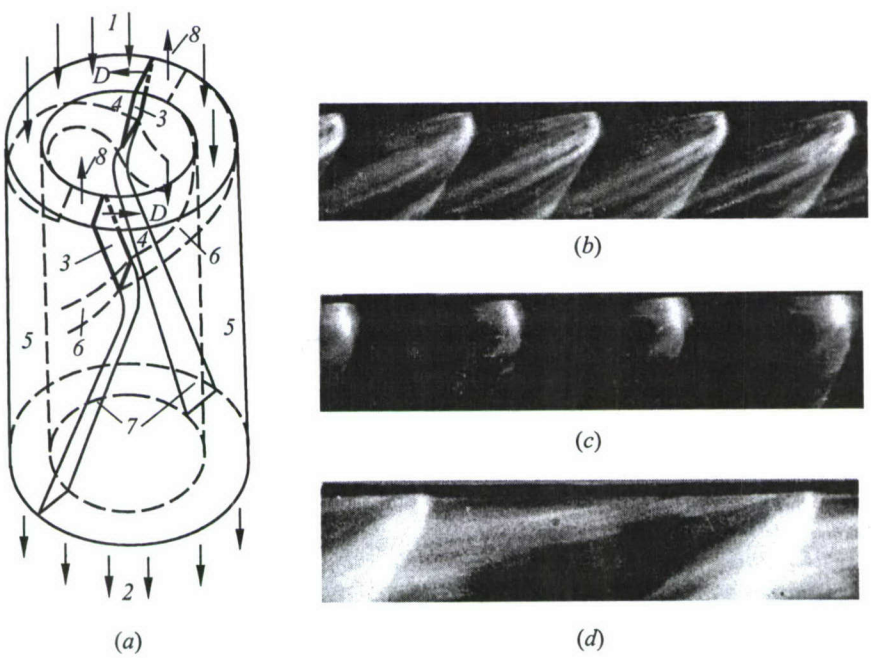

Figure 3 (*a*) Schematic of rotary detonation engine: *1* — initial components; *2* — products; *3* — rotating, transverse, spinning detonation wave; *4* — initial mixture; *5* — annular channel; *6* — contact discontinuity; *7* — tails of detonation waves; *8* — penetration of products into the feed system. Luminosity records shown right are obtained for propane–oxygen (*b*), acetone–oxygen (*c*), and liquid kerosene–oxygen (*d*) mixtures

tive control of the operation of RDE. As for PDE, there are no data on the self-organization of its operation at variable initial conditions. It is likely that adaptive control of PDE operation will become a very important issue. The schematic of Fig. 3*a* shows how the reactive mixture detonates in two rotating, transverse, spinning-like detonation waves. Typical luminosity records of such waves are presented in Fig. 3 for propane–oxygen (*b*), acetone–oxygen (*c*), and liquid kerosene–oxygen (*d*) mixtures. I would like to attract the attention of the audience to the RDE concept as an alternative to PDEs.

Hayashi (Aoyama Gakuin University, Tokyo, Japan): There is a need for worldwide collaboration in the area of PDE research and development and it is good to be focussed to the application. However, fundamental studies remain important for the understanding and optimization of PDEs.

Yu (Wayne State University, Detroit, MA, USA): In computational studies, there is a need to resolve the physics with sufficient accuracy. Benchmark cases are important and it would be good if reliable estimates can be provided with respect to what the resolution requirements are for reliable calculations both in the context of fundamental and cycle analysis studies.

Golub (Institute of High Temperatures, Moscow, Russia): In the literature, there are many PDE related investigations. It would be a good idea to create a targeted database.

Butler (General Electric Aircraft Engines, Cincinnati, USA): General Electric and other aircraft engine manufacturers have spent many years and many millions of dollars improving the Brayton-cycle gas turbine for aircraft. These improvements have been driven by pressure from our customers, the airlines and military operators, for lower operating costs and environmentally friendly propulsion systems. We have been very successful in responding to these pressures — every day millions of passengers travel cheaply and safely to their destinations. The demands for lower cost, reduced noise and lower emissions continue and it is becoming increasingly costly to obtain those improvements to the Brayton-cycle engine. That is why we have a strong interest in alternative cycles such as the pulse detonation cycle.

In this colloquium, there has been much debate about the potential performance benefits of the detonation-based engine. While there is much more work to do before these benefits can be defined with precision, I would like to point out that any improvement in I_{sp} that is in "double digits" is spectacular compared with the yearly improvements in the Brayton engine. Even if the PDE offered no improvement in I_{sp}, the benefits of simplification and reduced manufacturing cost alone may justify its development.

This colloquium was rightly focused on understanding the physics of the detonation phenomenon and the performance improvements that may be derived

from its application. However, we should not forget that in order for any novel propulsion system to be widely adopted, it must not only offer performance improvements, it must also be environmentally acceptable and meet the reliability standards that airlines have come to expect. I would therefore make a plea that in addition to the current lines of research we should begin to look seriously at the noise, emissions (especially NO_x), and the operating life of detonation devices.

Lastly, I would like to thank the organizers and contributors for a very stimulating colloquium.

4 CONCLUDING REMARKS

Substantial progress has been made in detonation research applied to propulsion during the last 5 or 6 years. Recent achievements in confined detonations and PDE efforts are illustrated in this volume. The panel discussion identified some of the possible applications of PDEs, underlying problems that need further research investments, and the potential performance and cost gains of such systems. This discussion, though not complete, has laid the fundamental blocks on which future research and development can be built. The key elements needed for advancement of a new technology: pool of scientists dedicated to the effort, facilities where bench mark experiments can be conducted, computational and predictive capabilities, international colloboration and dissemination of results, and research sponsorship are in place to make this endeavor a reality in the near future.

During the past several years, the U.S. Office of Naval Research (ONR) sponsors fundamental research on detonations with implication of further use of the new knowledge in the development of PDEs. To make the effort more efficacious, ONR collaborates with other research sponsoring agencies, such as the Russian Foundation for Basic Research, in organizing international meetings of specialists and disseminating the scientific results worldwide. As mentioned in the Introduction, a number of subject-oriented books have been published based on this collaboration. This book is intended to make additional contribution in this effort.

REFERENCES

1. Pintgen, F., J. M. Austin, and J. E. Shepherd. 2003. Detonation front structure: Variety and characterization. In: *Confined detonations and pulse detonation engines*. Eds. G. Roy, S. Frolov, R. Santoro, and S. Tsyganov. Moscow, Russia: Torus Press. 105–116.

2. Segal, C., A. Chandy, and D. Mikolaitis. 2003. Break-up of droplets under shock impact. In: *Confined detonations and pulse detonation engines*. Eds. G. Roy, S. Frolov, R. Santoro, and S. Tsyganov. Moscow, Russia: Torus Press. 117–126.
3. Mitrofanov, V. V., and S. A. Zhdan. 2003. Calculation of thrust performance of an ideal pulse detonation engine. In: *Confined detonations and pulse detonation engines*. Eds. G. Roy, S. Frolov, R. Santoro, and S. Tsyganov. Moscow, Russia: Torus Press. 225–232.
4. Miyasaka, T., T. Fujiwara, F. Y. Zhang, Y. Hyodo, Y. Oka, and S. Ito. 2003. Theoretical assessment of PDE performance using two-dimensional numerical analysis. In: *Confined detonations and pulse detonation engines*. Eds. G. Roy, S. Frolov, R. Santoro, and S. Tsyganov. Moscow, Russia: Torus Press. 215–224.
5. Fujiwara, T., T. Endo, T. Miyasaka, F. Y. Zhang, and Y. Oka. 2003. Theoretical assessment of PDE performance at various flight conditions. In: *Confined detonations and pulse detonation engines*. Eds. G. Roy, S. Frolov, R. Santoro, and S. Tsyganov. Moscow, Russia: Torus Press. 203–214.
6. Kailasanath, K. 2003. On the performance of pulse detonation engines. In: *Confined detonations and pulse detonation engines*. Eds. G. Roy, S. Frolov, R. Santoro, and S. Tsyganov. Moscow, Russia: Torus Press. 191–202.
7. Ma, F., J.-Y. Choi, Y. Wu, and V. Yang. 2003. Modeling of multitube pulse detonation engine dynamics. In: *Confined detonations and pulse detonation engines*. Eds. G. Roy, S. Frolov, R. Santoro, and S. Tsyganov. Moscow, Russia: Torus Press. 233–248.
8. Canteins, G., F. Franzetti, R. Zitoun, D. Desbordes, and E. Daniau. 2003. PDE — possible ways for specific impulse improvement. In: *Confined detonations and pulse detonation engines*. Eds. G. Roy, S. Frolov, R. Santoro, and S. Tsyganov. Moscow, Russia: Torus Press. 177–190.
9. Santoro, R. J., S.-Y. Lee, C. Conrad, J. Brumberg, S. Saretto, S. Pal, and R. D. Woodward. 2003. DDT studies for multicycle PDE applications. In: *Confined detonations and pulse detonation engines*. Eds. G. Roy, S. Frolov, R. Santoro, and S. Tsyganov. Moscow, Russia: Torus Press. 259–270.
10. Baklanov, D. I., L. G. Gvozdeva, and N. B. Scherbak. 2003. Detonations of hydrocarbon–air mixtures in a pulse detonation combustion chamber. In: *Confined detonations and pulse detonation engines*. Eds. G. Roy, S. Frolov, R. Santoro, and S. Tsyganov. Moscow, Russia: Torus Press. 271–286.
11. Vasil'ev, A. A. 2003. Some aspects of optimization of accelerators of deflagration-to-detonation transition. In: *Confined detonations and pulse detonation engines*. Eds. G. Roy, S. Frolov, R. Santoro, and S. Tsyganov. Moscow, Russia: Torus Press. 41–48.
12. Kuan, T. S., R. P. Lindstedt, and E. M. Vaos. 2003. Higher moment based modeling of turbulence enhanced explosion kernels in confined fuel–air mixtures. In: *Confined detonations and pulse detonation engines*. Eds. G. Roy, S. Frolov, R. Santoro, and S. Tsyganov. Moscow, Russia: Torus Press. 17–40.
13. Kerampran, S., D. Desbordes, and B. Veyssière. 2003. Influence of the pressure waves generated at the initial stage of flame propagation on the DDT process in smooth tubes. In: *Confined detonations and pulse detonation engines*. Eds. G. Roy, S. Frolov, R. Santoro, and S. Tsyganov. Moscow, Russia: Torus Press. 3–17.

14. Borisov, A. A., A. E. Mailkov, M. A. Silakova, R. N. Elshin, P. V. Komissarov, S. I. Sumskoi, I. O. Samshin, and A. E. Barykin. 2003. Jets of fuel-rich combustion products discharged in air as a source of impulse. In: *Confined detonations and pulse detonation engines*. Eds. G. Roy, S. Frolov, R. Santoro, and S. Tsyganov. Moscow, Russia: Torus Press. 127–140.

15. Frolov, S. M., V. Ya. Basevich, V. S. Aksenov, and S. A. Polikhov. 2003. Initiation of confined spray detonation by electrical discharges. In: *Confined detonations and pulse detonation engines*. Eds. G. Roy, S. Frolov, R. Santoro, and S. Tsyganov. Moscow, Russia: Torus Press. 157–174.

16. Brophy, C. M., J. O. Sinibaldi, D. Netzer, and K. Kailasanath. 2003. Initiator diffraction limits in a pulse detonation engine. In: *Confined detonations and pulse detonation engines*. Eds. G. Roy, S. Frolov, R. Santoro, and S. Tsyganov. Moscow, Russia: Torus Press. 59–73.

17. Tsuboi, N., K. Fujii, Y. Kenmoku, and A. K. Hayashi. 2003. Experimental and numerical estimation of pulse detonation engine performance. In: *Confined detonations and pulse detonation engines*. Eds. G. Roy, S. Frolov, R. Santoro, and S. Tsyganov. Moscow, Russia: Torus Press. 249–258.

18. Trotsyuk, A. V., A. N. Kudryavtsev, and M. S. Ivanov. 2003. Numerical simulation of reflection of detonation and shock waves in supersonic flows. In: *Confined detonations and pulse detonation engines*. Eds. G. Roy, S. Frolov, R. Santoro, and S. Tsyganov. Moscow, Russia: Torus Press. 73–86.

19. Fedorov, A. V., and T. A. Khmel. 2003. Formation of two-dimensional detonation structures in aluminum gas suspension in a channel. In: *Confined detonations and pulse detonation engines*. Eds. G. Roy, S. Frolov, R. Santoro, and S. Tsyganov. Moscow, Russia: Torus Press. 141–156.

20. Penyazkov, O. G. 2003. Near-limit conditions for propagation of detonations in round tubes. In: *Confined detonations and pulse detonation engines*. Eds. G. Roy, S. Frolov, R. Santoro, and S. Tsyganov. Moscow, Russia: Torus Press. 49–58.

21. Shchelkin, K., and A. Sokolik. 1937. The effect of the chemical presensitisation on the initiation of the detonation wave. *Acta Physicochimica URSS* 7:589–96.

22. Fernandez, R., J. W. Slater, and D. E. Paxson. 2003. NASA GLENN'S pulsed ejector wave propagation test program. In: *Confined detonations and pulse detonation engines*. Eds. G. Roy, S. Frolov, R. Santoro, and S. Tsyganov. Moscow, Russia: Torus Press. 303–326.

23. Starik, A. M., and N. S. Titova. 2003. Kinetics of ignition of detonation gaseous mixtures by resonant laser radiation. In: *Confined detonations and pulse detonation engines*. Eds. G. Roy, S. Frolov, R. Santoro, and S. Tsyganov. Moscow, Russia: Torus Press. 87–??.

24. Schauer, F., J. Stutrud, R. Bradley, V. Katta, and J. Hoke. 2003. Detonation studies and performance results for a research pulse detonation engine. In: *Confined detonations and pulse detonation engines*. Eds. G. Roy, S. Frolov, R. Santoro, and S. Tsyganov. Moscow, Russia: Torus Press. 287–302.

25. Koren'kov, V. V., and S. A. Pakhomov. 2002. Estimation of subsonic ramjet pulse detonation engine parameters. In: *Advances in confined detonations*. Eds. G. Roy, S. Frolov, R. Santoro, and S. Tsyganov. Moscow: Torus Press. 235–37.

Научное издание

Confined Detonations and Pulse Detonation Engines
Edited by G. Roy, S. Frolov, R. Santoro, and S. Tsyganov

Титульный редактор: *Т. Торжкова*
Технический редактор: *Л. Кокушкина*
Художественный редактор: *М. Седакова*
Дизайн обложки: *А. Севрюгин*

Н/К

Лицензия ИД № 04600 от 24.04.2001

Сдано в набор 01.08.02. Подписано в печать 15.12.02.
Формат 70 × 100/16. Бумага офсетная. Печать офсетная.
Усл.-печ. л. 30,96. Уч.-изд. л. 28,15. Тираж 500 экз.

Заказ № 7690

Издательство «ТОРУС ПРЕСС»
115201 Москва, а/я 3
torus@torus-press.ru
http://www.torus-press.ru

Отпечатано в соответствии с качеством
предоставленных диапозитивов в ППП «Типография «Наука»
121099 Москва, Шубинский пер., д. 6